Which is the heaviest neutrino? *p. 1555*

Changing goals of nature conservation *p. 1558*

Epigenetic roles in immune cell development *pp. 1578, 1579, & 1580*

Science

$10
26 SEPTEMBER 2014
sciencemag.org

AAAS

The drought you can't see

Geophysical methods detect changes in water storage *pp. 1543 & 1587*

CONTENTS

26 SEPTEMBER 2014 • VOLUME 345 • ISSUE 6204

1569
When pain meets politics, party lines divide

NEWS

IN BRIEF

1544 Roundup of the week's news

IN DEPTH

1547 **EVIDENCE FOR COSMIC INFLATION WANES**
The biggest result in cosmology in a decade fades into dust *By A. Cho*

1548 **RED WOLVES IN THE CROSSHAIRS**
U.S. agency ponders future of innovative reintroduction as animal deaths and controversy mount *By E. Stokstad*

1549 **TESTING NEW EBOLA TESTS**
Identifying infections more quickly and easily could help slow the epidemic *By G. Vogel*

1550 **METABOLIC SHIFT MAY TRAIN IMMUNE CELLS**
BLUEPRINT project studies epigenetics of various blood cells *By E. Pennisi*
▸ RESEARCH ARTICLES PP. 1578, 1579 & 1580

FEATURES

1552 **OVER THE THRESHOLD**
Ecologist Marten Scheffer became a leader in the science of tipping points by studying lakes. Now he's making waves in many other fields *By G. Popkin*

1555 **NOνA'S SHINING MOMENT**
Despite years of delay, Fermilab's massive new experiment has a chance to take the next big step in neutrino physics *By A. Cho*

INSIGHTS

PERSPECTIVES

1558 **WHOSE CONSERVATION?**
Changes in the perception and goals of nature conservation require a solid scientific basis *By G. M. Mace*

1560 **AUTOIMMUNITY BY HAPLOINSUFFICIENCY**
Partial deficiency in the protein CTLA4 underlies severe autoimmune disease with incomplete penetrance
By F. Rieux-Laucat and J.-L. Casanova
▸ REPORT P. 1623

1562 **IMPLEMENTING PASTEUR'S VISION FOR RABIES ELIMINATION**
Human and veterinary health systems must be better integrated if rabies is to be controlled *By F. Lankester* et al.

1564 **WATER'S PLACE IN AU CATALYSIS**
Water plays a key role in gold-catalyzed CO oxidation
By G. M. Mullen and C. B. Mullins
▸ REPORT P. 1599

1565 **MANAGING PATTERNS AND PROPORTIONS OVER TIME**
Tissue patterning is specified relative to growth through differences between cell proliferation and the differentiation rates *By O. Pourquie*
▸ RESEARCH ARTICLE P. 1577

1566 **PEROVSKITES TAKE LEAD IN SOLAR HYDROGEN RACE**
Earth-abundant materials show promise for solar hydrogen production
By T. Hamann
▸ REPORT P. 1593

1568 **A DYNAMIC TOOL FOR NITROGEN REDUCTION**
Carbon monoxide reveals new possibilities for substrate binding in nitrogenase *By M. Högbom*
▸ REPORT P. 1620

BOOKS *ET AL.*

1569 **PAIN**
By K. Wailoo, reviewed by W. Anderson

LETTERS

1571 **BRAZIL'S NEW LAWS BUG COLLECTORS**
By D. B. Ribeiro and A. V. L. Freitas

1571 **PARENTING: SECTION DESERVES A SCOLDING**
By J. Mercer

1571 **PARENTING: ROOTS OF THE SWEET TOOTH**
By A. K. Portella and P. P. Silveira

1572 **ERRATA**

DEPARTMENTS

1543 **EDITORIAL**
The drought you can't see
By Marcia McNutt
▸ REPORT P. 1587

1650 **WORKING LIFE**
The borders I crossed
By Rodica Stan

Science Staff 1542
AAAS News & Notes 1573
Gordon Research Conferences 1628
New Products 1638
Science Careers 1639

Published by AAAS

CONTENTS

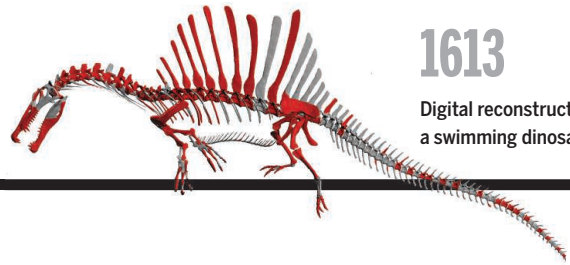

1613
Digital reconstruction of a swimming dinosaur

26 SEPTEMBER 2014 • VOLUME 345 • ISSUE 6204

RESEARCH

IN BRIEF

1574 From *Science* and other journals

RESEARCH ARTICLES

1577 NEURAL DEVELOPMENT
Coordination of progenitor specification and growth in mouse and chick spinal cord *A. Kicheva* et al.
RESEARCH ARTICLE SUMMARY; FOR FULL TEXT: dx.doi.org/10.1126/science.1254927
▸ PERSPECTIVE P. 1565

IMMUNOGENETICS

1578 Epigenetic programming of monocyte-to-macrophage differentiation and trained innate immunity *S. Saeed* et al.
RESEARCH ARTICLE SUMMARY; FOR FULL TEXT: dx.doi.org/10.1126/science.1251086

1579 mTOR- and HIF-1α–mediated aerobic glycolysis as metabolic basis for trained immunity *S.-C. Cheng* et al.
RESEARCH ARTICLE SUMMARY; FOR FULL TEXT: dx.doi.org/10.1126/science.1250684

1580 Transcriptional diversity during lineage commitment of human blood progenitors *L. Chen* et al.
RESEARCH ARTICLE SUMMARY; FOR FULL TEXT: dx.doi.org/10.1126/science.1251033

▸ NEWS STORY P. 1550

REPORTS

1581 JOVIAN ATMOSPHERE
Evidence for global electron transportation into the jovian inner magnetosphere *K. Yoshioka* et al.

1584 INTERSTELLAR CHEMISTRY
Detection of a branched alkyl molecule in the interstellar medium: *iso*-propyl cyanide *A. Belloche* et al.

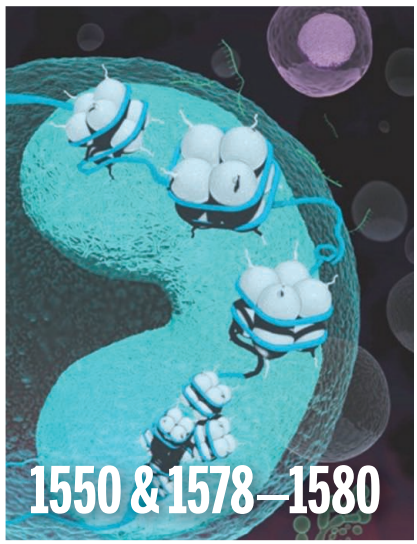

1550 & 1578–1580

1587 REMOTE HYDROLOGY
Ongoing drought-induced uplift in the western United States *A. A. Borsa* et al.
▸ EDITORIAL P. 1543

1590 EARLY SOLAR SYSTEM
The ancient heritage of water ice in the solar system *L. I. Cleeves* et al.

1593 WATER SPLITTING
Water photolysis at 12.3% efficiency via perovskite photovoltaics and Earth-abundant catalysts *J. Luo* et al.
▸ PERSPECTIVE P. 1566

1596 ATMOSPHERIC CHEMISTRY
Infrared-driven unimolecular reaction of CH_3CHOO Criegee intermediates to OH radical products *F. Liu* et al.

1599 CATALYSIS
The critical role of water at the gold-titania interface in catalytic CO oxidation *J. Saavedra* et al.
▸ PERSPECTIVE P. 1564

1602 PLANT ECOLOGY
Environmental filtering explains variation in plant diversity along resource gradients *E. Laliberté* et al.

1605 PLANT DEVELOPMENT
Direct roles of SPEECHLESS in the specification of stomatal self-renewing cells *O. S. Lau* et al.

1609 PALEOLITHIC TOOLS
Early Levallois technology and the Lower to Middle Paleolithic transition in the Southern Caucasus *D. S. Adler* et al.
▸ PODCAST

1613 PALEONTOLOGY
Semiaquatic adaptations in a giant predatory dinosaur *N. Ibrahim* et al.

1616 NEUROSCIENCE
A critical time window for dopamine actions on the structural plasticity of dendritic spines *S. Yagishita* et al.

1620 NITROGEN FIXATION
Ligand binding to the FeMo-cofactor: Structures of CO-bound and reactivated nitrogenase *T. Spatzal* et al.
▸ PERSPECTIVE P. 1568

1623 IMMUNODEFICIENCY
Immune dysregulation in human subjects with heterozygous germline mutations in *CTLA4 H. S. Kuehn* et al.
▸ PERSPECTIVE P. 1560

ON THE COVER

Satellite image from NASA's Gravity Recovery and Climate Experiment (GRACE) mission showing California's devastating loss of fresh water (in red) since 2002. In each of the past 3 years, epic drought has drained the region of more than 15 cubic kilometers of fresh water. Borsa *et al*. report the crustal response to much of this water loss. See page 1587 and the related Editorial on page 1543. *Image: Jay Famiglietti/NASA Jet Propulsion Laboratory, California Institute of Technology; and University of California, Irvine*

ILLUSTRATION: (MIDDLE) SPENCER PHILLIPS, EMBL-EBI

SCIENCE (ISSN 0036-8075) is published weekly on Friday, except the last week in December, by the American Association for the Advancement of Science, 1200 New York Avenue, NW, Washington, DC 20005. Periodicals mail postage (publication No. 484460) paid at Washington, DC, and additional mailing offices. Copyright © 2014 by the American Association for the Advancement of Science. The title SCIENCE is a registered trademark of the AAAS. Domestic individual membership and subscription (51 issues): $153 ($74 allocated to subscription). Domestic institutional subscription (51 issues): $1282; Foreign postage extra: Mexico, Caribbean (surface mail) $55; other countries (air assist delivery) $85. First class, airmail, student, and emeritus rates on request. Canadian rates with GST available upon request, GST #1254 88122. Publications Mail Agreement Number 1069624. **Printed in the U.S.A.**
Change of address: Allow 4 weeks, giving old and new addresses and 8-digit account number. **Postmaster:** Send change of address to AAAS, P.O. Box 96178, Washington, DC 20090–6178. **Single-copy sales:** $10.00 current issue, $15.00 back issue prepaid includes surface postage; bulk rates on request. **Authorization to photocopy** material for internal or personal use under circumstances not falling within the fair use provisions of the Copyright Act is granted by AAAS to libraries and other users registered with the Copyright Clearance Center (CCC) Transactional Reporting Service, provided that $30.00 per article is paid directly to CCC, 222 Rosewood Drive, Danvers, MA 01923. The identification code for *Science* is 0036-8075. *Science* is indexed in the *Reader's Guide to Periodical Literature* and in several specialized indexes.

Published by AAAS

EDITORIAL

The drought you can't see

Marcia McNutt
Editor-in-Chief
Science *journals*

The Western Hemisphere is experiencing a drought of crisis proportions. In Central America, crops are failing, millions are in danger of starvation, and if the drought doesn't break soon, even vessels transiting the Panama Canal will need to lighten their loads, which will increase prices for goods transported globally. In the western United States, the drought-stricken region spans a vast area responsible for much of the nation's fruits, vegetables, and beef. As the drought's grip has tightened, water users have turned to tapping groundwater aquifers to make up the deficit for people, crops, livestock, and industry. But even when the rain does return, regreening the landscape and filling again the streams, lakes, and reservoirs, those aquifers will remain severely depleted. It is this underground drought we can't see that is enduring, worrisome, and in need of attention.

"It is high time we started managing our precious water supplies in harmony with the laws of nature."

The Gravity Recovery And Climate Experiment (GRACE) satellites have provided a global look at groundwater depletion by monitoring small temporal changes in Earth's gravity field. GRACE confirmed massive losses of groundwater from the aquifer underlying California's agriculturally important Central Valley since the 1980s.* In the decade between 2003 and 2012, the drawdown was equivalent to the entire water storage volume of Lake Mead, the nation's largest surface reservoir.† The extraction of groundwater has caused wells to run dry and produced detectable regional uplift or rebound of the land due to water displacement (see Borsa *et al.*, p. 1587).

Underground reservoirs are a natural long-term water storage solution. Taking advantage of aquifers avoids the expense and environmental issues of dam construction. Unlike surface reservoirs, aquifers are not subject to evaporative loss, but under natural conditions they are only recharged slowly as excess precipitation percolates into the aquifer. In some cases, the average age of groundwater can be many thousands of years old, dating back to a time when the climate was wetter. But when water is withdrawn through pumping at prodigious rates, hydrologic processes are not sufficient to fully recharge the reservoirs, especially when land development has created impervious surfaces.

Forty years ago, the state of Arizona reached a critical juncture that called for action, with rapidly falling water tables, dry wells, subsiding land surface, and deteriorating water quality. Now, in the Tucson area for example, water from the Colorado River is used to artificially recharge the aquifers with excess water in wet years that can later be tapped during dry years. The statewide 1980 Groundwater Management Act guarantees that over a 10-year period, the aquifer cannot be overdrawn. The current crisis has prompted the legislature of California—the last state in the west without groundwater regulation—to pass a series of bills that establish state-level oversight of pumping from aquifers.

Surface- and groundwater are all part of one coupled system, responding on different time scales to changes in precipitation. Five years ago when I was director of the U.S. Geological Survey (USGS), an Arizona congressman had some concerns about a USGS report on the impact of overpumping of groundwater on surface stream flows. The congressman declared, "You all should be aware that according to Arizona state law, surface water and groundwater flows are decoupled." Jim Leenhouts, the USGS associate director for the Arizona Water Science Center responded, without hesitation, "Thank you, congressman. Here at the USGS we follow the laws of nature, not the laws of man." It is high time we started managing our precious water supplies in harmony with the laws of nature.

– Marcia McNutt

*http://pubs.er.usgs.gov/publication/fs20093057. †J. S. Famiglietti, M. Rodell, *Science* **340**, 1300 (2013).

10.1126/science.1260795

PHOTOS: (INSET) JUSTIN SULLIVAN/GETTY IMAGES; (RIGHT) STACEY PENTLAND PHOTOGRAPHY

Downloaded from www.sciencemag.org on September 26, 2014

Published by AAAS

NEWS

> “They wanted to impose a scheme of alarm, of psychological terrorism.”
>
> **Venezuela President Nicolás Maduro** in a speech broadcast on 17 September, about his ordered prosecution of doctors who spoke out about nine people who recently died from an unidentified infectious disease, possibly chikungunya.

IN BRIEF

People’s climate march draws 400,000

The climate marchers’ causes ranged from indigenous rights to the Keystone XL Pipeline.

Nearly 400,000 people joined the People’s Climate March on 21 September in New York City, in what organizers called the largest climate demonstration in history. The march was organized by a coalition of more than 1500 organizations and spearheaded by the international environmental organization 350.org. The name refers to the 350 parts per million concentration of CO_2 in the atmosphere proposed as a “safe” upper bound to limit global warming by NASA scientist James Hansen and others in 2008. The march cast a wide net, drawing scientists, politicians, indigenous groups directly affected by changing climate, and numerous famous faces. Among the big names: former Vice President Al Gore, U.N. Secretary General Ban Ki-moon, scientist Jane Goodall, actors Leonardo DiCaprio and Emma Thompson, and musician Sting. People bore posters calling for more clean energy, an end to deforestation, and stopping the Keystone XL Pipeline project. The event came 2 days before a U.N. climate summit and coincided with more than 2800 “solidarity” events in 166 countries, according to the organizers.

AROUND THE WORLD

Deadly vaccine mix-up

IDLIB, SYRIA | Human error appears to be to blame for the deaths of 15 children, all or most under age 2, during a measles immunization campaign in an opposition-held area of northern Syria last week. Up to 50 more children were sickened. Investigations are continuing, but at this point the cause looks like a “terrible, terrible mistake,” in which a strong muscle relaxant was administered along with the measles vaccine, says epidemiologist Chris Maher of the World Health Organization in Amman. He and others worry that the tragic incident and rumors that the vaccine was deliberatly spiked may derail immunization across Syria, which faces the threat of a large measles outbreak next spring. http://scim.ag/Syriameasles

Prize to spot resistant germs

WASHINGTON, D.C. | The U.S. government is offering a new incentive in the fight against antibiotic-resistant bacteria: a $20 million prize for a quick diagnostic test to recognize highly resistant infections. The prize is co-sponsored by the National Institutes of Health and the Biomedical Advanced Research and Development Authority, and its guidelines will be refined after an upcoming public meeting. It is one in a slew of U.S. actions announced last week to signal greater attention to the threat of antibiotic-resistant microbes. The White House also released a national strategy setting goals to be achieved by 2020, and the president signed an executive order creating an advisory council of nongovernmental experts and an interagency task force co-chaired by the secretaries of the Health and Human Services, Defense, and Agriculture departments. http://scim.ag/germprize

NIH cleared of interference

WASHINGTON, D.C. | A federal watchdog office has dismissed allegations that in 2013 National Institutes of Health (NIH) officials improperly interfered with another federal office’s oversight of a

Downloaded from www.sciencemag.org on September 26, 2014

PHOTO: © JASON DECROW/AP/CORBIS

Published by AAAS

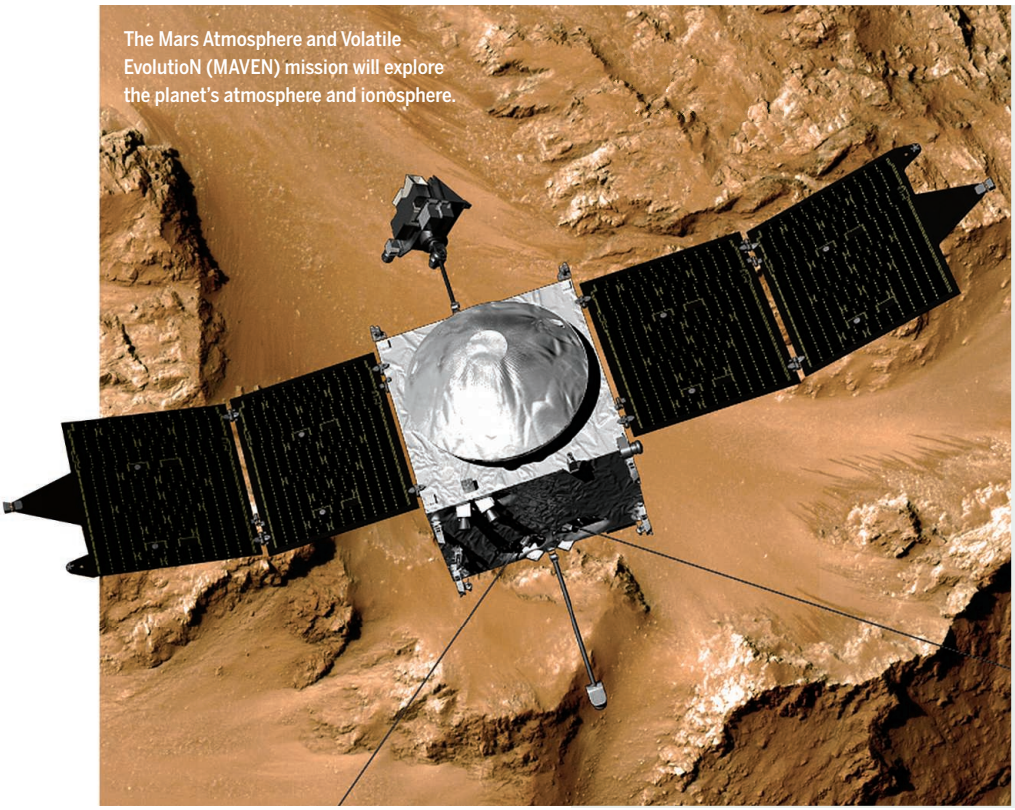

The Mars Atmosphere and Volatile EvolutioN (MAVEN) mission will explore the planet's atmosphere and ionosphere.

MAVEN makes it to Mars orbit

Following a 10-month cruise, NASA's MAVEN spacecraft entered orbit around Mars on 21 September EDT. The spacecraft is the fourth orbiter in operation at Mars, along with NASA's Mars Odyssey and Mars Reconnaissance Orbiter and the European Space Agency's Mars Express. India's Mars Orbiter Mission is supposed to enter orbit on 23 September EDT. MAVEN (Mars Atmosphere and Volatile EvolutioN) will measure the rate at which Mars is losing atmospheric gas molecules to space. Mars had a thicker atmosphere 4 billion years ago—one that could have helped keep temperatures high and the surface wet—and scientists want to understand how the planet's atmosphere became so thin. With its other Mars orbiters starting to show their age, NASA added a communications package to MAVEN, so that it could relay data from rover missions on the surface. MAVEN will just be finishing its system checks when the comet Siding Spring brushes past Mars on 19 October.

controversial NIH-funded study involving premature infants. The Department of Health and Human Services (HHS) inspector general (IG) found that NIH officials encouraged HHS's Office for Human Research Protections to revise a draft letter and reverse a decision sanctioning the University of Alabama, Birmingham, for not fully informing parents about study risks. But NIH's actions were acceptable because no law bars HHS officials from consulting with each other, the IG report found. The matter concerned the $20 million, 23-institution SUPPORT study, which from 2005 to 2009 studied the levels of oxygen that premature infants should receive. **http://scim.ag/NIHpreemie**

STIs on rise in Australia

SYDNEY, AUSTRALIA | Public health experts in Australia are sounding alarms over a record number of new cases of syphilis and a dramatic rise in viral hepatitis deaths. Experts trace the spike in syphilis and other sexually transmitted infections (STIs) to a decrease in condom use, particularly among men who have sex with men, and see the hepatitis death toll as the result of long-term trends in injecting drug use. The alarming numbers and underlying behaviors were examined in two reports on HIV, viral hepatitis, and STIs in Australia released 18 September by the Kirby Institute for Infection and Immunity in Society and the Centre for Social Research in Health, both at the University of New South Wales in Sydney. One bit of good news: Human papillomavirus infections have dropped dramatically since a vaccination program for high school students began in 2007. **http://scim.ag/AustraliaSTI**

Base bad news for dugong

OKINAWA, JAPAN | Land reclamation for a new U.S. Marine Corps air base may sound the death knell for the tiny population of Okinawa dugong, considered by Japan's environment ministry to be critically endangered. The base threatens two of the region's remaining major beds of seagrass, which dugong depend on, says the Nature Conservation Society of Japan (NACS-J), which has petitioned U.S. Ambassador to Japan Caroline Kennedy for permission to conduct a survey. Worldwide, dugong populations have been decimated by hunting, habitat loss due to coastal development, and fishing by-catching. At most 10 of the marine mammals remain in Japan's southernmost prefecture, according to NACS-J. The controversy over the new base is just the latest twist in a protracted dispute over the U.S. military presence on Okinawa. **http://scim.ag/Okinawadugong**

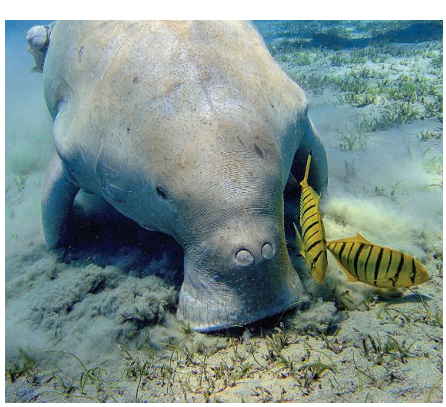

Hurricane drones take flight

MIAMI, FLORIDA | Last week, as Hurricane Edouard churned out in the Atlantic Ocean, the National Oceanic and Atmospheric Administration (NOAA) prepared to get an inside look. But NOAA's hurricane hunters, who have flown into the storms for decades, stayed home; this time, NOAA sent in the drones. During their hourlong flight through the hurricane's winds, four meter-long "Coyote" drones transmitted temperature, pressure, and wind data from below 900 meters—where manned aircraft cannot safely fly—back to NOAA's National Hurricane Center in Miami. One even orbited briefly

PHOTOS: (TOP TO BOTTOM) NASA'S GODDARD SPACE FLIGHT CENTER; JULIEN WILLEM/WIKIMEDIA COMMONS

Published by AAAS

Red colobus monkeys may soon have trouble getting enough protein.

Less nutritious tropical leaves

Even as scientists beef up the nutrient value of human foods, from iron-fortified cereals to vitamin A–enriched rice, the opposite is happening for leaf-eating monkeys. In the 1970s and 1990s, researchers analyzed the nutrient content of leaves in a Ugandan tropical rainforest that was a hotspot for primates. Jessica Rothman, a nutritional ecologist at Hunter College of the City University of New York, has now compared those results with her own analysis, sometimes using the same trees, of 10 species. Increasing temperatures and rainfall variability due to climate change have taken their toll. Over the past 30 years, the leaves' protein content has declined and fiber has increased, she and her colleagues report in an *Ecology* preprint. Monkeys prefer low-fiber, high-protein foliage. Based solely on the leaves in that rainforest, models that predict population growth indicated that leaf-eating primates there may decline by 31% in the coming years.

around the hurricane's eyewall, the intense winds surrounding the eye, before falling into the ocean. A special appropriations bill related to Hurricane Sandy in 2012 funded the $1.25 million project to test the drones this year.

Ig Nobels honor 'Jesus toast'

CAMBRIDGE, MASSACHUSETTS | Seeing Jesus, Elvis, or any other face in the random light and dark spots on a piece of toast means you are "completely normal," according to Kang Lee, a neuroscientist at the University of Toronto in Canada. For their work on the origins within the brain of pareidolia—the perception of nonexistent objects such as faces in a random signal—Lee and colleagues have earned a coveted 2014 Ig Nobel Prize, which celebrates research that "makes you laugh, and then makes you think." The prizes, organized by the *Annals of Improbable Research* and handed out 18 September during a ceremony at Harvard University, include a (worthless) $10 trillion bill in Zimbabwean dollars. This year's winners included: a study of dogs' ability to detect Earth's magnetic field based on how they align with the field while pooping; a measurement of the friction between a shoe and a banana peel; and the modulation of the pain caused by a burning laser while viewing good or bad art.

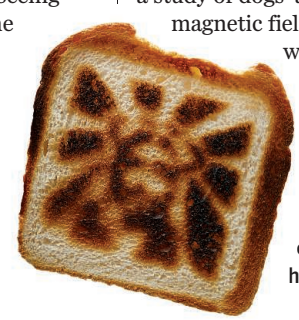

http://scim.ag/IgNobel2014

BY THE NUMBERS

5 million

Minimum extent, in square kilometers, of sea ice in the Arctic Ocean this year, according to the National Snow and Ice Data Center. Measured on 17 September, it's the sixth lowest extent since 1979.

30

Years left, at 2014 CO_2 emissions rates, before we hit a quota of emissions that would warm the planet by more than 2°C compared with preindustrial times, according to *Nature Geoscience* and *Nature Climate Change*.

29%

China's share of global CO_2 emissions in 2013, surpassing the European Union for the first time, according to the Global Carbon Project.

New road map for fusion

WASHINGTON, D.C. | U.S. fusion research should look beyond the ITER reactor project under construction in France and focus instead on a practical energy-generating machine, says a report released this week. The Department of Energy asked the fusion community to draw up a 10-year plan with, at best, modest budget growth. Their report says research should focus on controlling the superhot plasma and on its interface with the reactor material—key issues to generate commercial power. But existing reactors—including Massachusetts's C-Mod—face closure, and under the tightest budget forecast, the United States will likely cede leadership in most areas to overseas researchers.

PHOTOS: (TOP TO BOTTOM) JESSICA M. ROTHMAN; PAUL J. RICHARDS/AFP/GETTY IMAGES

Published by AAAS

IN DEPTH

Evidence for cosmic inflation wanes

The biggest result in cosmology in a decade fades into dust

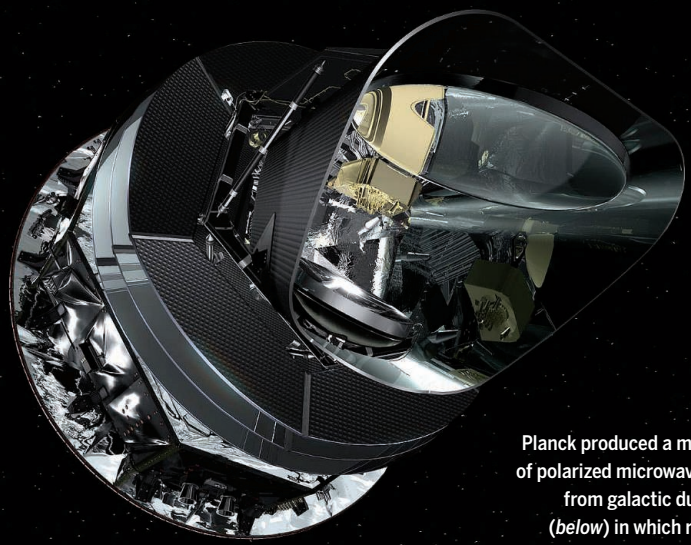

Planck produced a map of polarized microwaves from galactic dust (*below*) in which red means more emissions and blue means less.

By **Adrian Cho**

A beleaguered claim that appeared to reveal the workings of the big bang may instead say more about how science is done in an age of incessant news coverage.

In March, researchers working with a specialized telescope at the South Pole, known as BICEP2, reported extremely faint pinwheel-like swirls in the afterglow of the big bang—the so-called cosmic microwave background (CMB). They claimed they had found traces of gravitational waves rippling through the infant universe—direct evidence that the newborn cosmos had undergone a bizarre exponential growth spurt known as inflation (*Science*, 21 March, p. 1296). But the supposed signal might have been emitted by warm dust within our own galaxy, others argued (*Science*, 23 May, p. 790). Now, data from the European Space Agency's Planck spacecraft show that dust accounts for some, and possibly all, of the BICEP signal.

"We've gone from 'They can't prove that it isn't dust' to 'It's probably dust,' " says David Spergel, a cosmologist at Princeton University who is not a member of the BICEP team. But George Efstathiou, a cosmologist at the University of Cambridge in the United Kingdom and a member of the Planck team, cautions that the new data do not prove that the BICEP signal was entirely spurious.

In fact, to keep people from jumping to that conclusion, the Planck team decided not to issue a press release when it posted its paper to the arXiv preprint server and submitted it to *Astronomy & Astrophysics*, Efstathiou says. "It's very tricky stuff," he says, "so we were anxious that it not go into the press as 'Planck says that BICEP is wrong' because it doesn't."

The new data do show that the BICEP team underestimated the "galactic foreground" radiation. BICEP2—short for Background Imaging of Cosmic Extragalactic Polarization 2—took data from 2010 to 2012, aiming to map the polarization of the primordial microwaves in a small patch of sky. To maximize the instrument's sensitivity, researchers designed it to detect microwaves of only one frequency, 150 gigahertz (GHz).

But the push to improve sensitivity came at a cost. To distinguish radiation from dust and other galactic foregrounds from the CMB, cosmologists generally take data at multiple frequencies. So BICEP researchers had to rely on other groups' estimates of the dust foreground in their field of view—including preliminary numbers presented in a talk by Planck researchers.

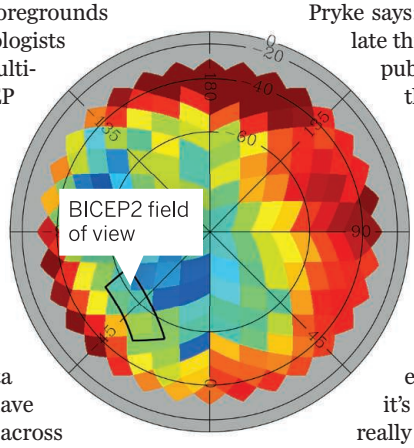

Now researchers with Planck, which took data from 2009 to 2013, have mapped dust emissions across the entire sky and have shown that dust could account for some or all of the BICEP signal. The map shows dust emissions at a frequency of 353 GHz; to estimate emissions at BICEP's frequency of 150 GHz, Planck researchers extrapolated using the average spectrum for dust emissions. But that extrapolation is "solid," Spergel says.

The presence of dust "can only diminish" the BICEP signal, acknowledges Clement Pryke, a cosmologist at the University of Minnesota, Twin Cities, and a co–principal investigator for the BICEP team. "I'm not going to say 'Goddamn it, there's a cosmological signal there,' " Prkye says. "I'm not going to say there isn't, either." The BICEP and Planck teams are working on a joint analysis that should provide a more definitive answer, perhaps by year's end, he says.

Some researchers say the BICEP team made its result seem much stronger than it was by announcing it in a press conference and a press release that proclaimed the "first direct evidence of cosmic inflation." "It's a very bold gamble that's been taken," Princeton cosmologist William Jones said at the time. But BICEP researchers felt pressure from the media to stake a definite claim, Pryke says: "They're trying to translate this into something that the public can understand, and they want a yes or no."

Charles Bennett, a cosmologist at Johns Hopkins University in Baltimore, Maryland, says his impression is that BICEP researchers thought they'd nailed the discovery. "They just got overenthusiastic," he says, "but it's tough to know when you really have something." BICEP researchers might have done better to simply post their preprint as the Planck team has done, Bennett says. "If the result held up, they would have gotten credit anyway," he says.

The new Planck results have sobering implications, Bennett says. They suggest the sky is relatively dusty and that extracting evidence of primordial gravitational waves may take years and multiple experiments, he says. Max Tegmark, a cosmologist at the Massachusetts Institute of Technology in Cambridge, is more optimistic. "There are places in the sky that seem to be twice as clean" as BICEP's field of view, he says. "So people are going to look there." ■

IMAGES (TOP TO BOTTOM): ESA/NASA/JPL-CALTECH; ESA/PLANCK/THE PLANCK COLLABORATION

Downloaded from www.sciencemag.org on September 26, 2014

Published by AAAS

Red wolves reproduce in the wild only in North Carolina. The population is increased with pups born in captivity. A major threat to the population is hybridization with coyotes.

ENDANGERED SPECIES

Red wolves in the crosshairs

U.S. agency ponders future of innovative reintroduction as animal deaths and controversy mount

By **Erik Stokstad**

The fate of the world's only population of red wolves is at stake. In a controversial move, the U.S. Fish and Wildlife Service (FWS) has begun a rapid assessment of its efforts to save the species in the wild. Biologists consider the nearly 3-decade-old program to reintroduce red wolves (*Canis rufus*) to a peninsula in North Carolina a success. It "has served as a model for restoration efforts for large carnivores for years," says Michael Chamberlain, a wildlife biologist at the University of Georgia, Athens.

But the predator now faces two serious threats: growing opposition from hunters and local landowners, and randy coyotes that mate with the wolves, creating problematic hybrids. The worst case, says Ron Sutherland, a conservation biologist with Wildlands Network in Durham, North Carolina, is that federal officials will decide the program isn't viable and pull the remaining 100 or so wolves out of the wild. "All options are on the table," says Tom MacKenzie, an FWS spokesman.

Red wolves, which catch deer and smaller prey, once roamed the eastern United States, but they suffered the same persecution as the larger gray wolf. Hunters and trappers reduced red wolf populations drastically and by the late 1960s biologists had given up on preserving the carnivore in the wild. Fourteen wolves in southeast Texas and southwest Louisiana became the basis of a captive breeding program, which now includes about 190 wolves in more than 40 facilities across the country. (Meanwhile, taxonomists continue to debate whether the red wolf is really a distinct species; many believe it is a gray wolf–coyote hybrid.)

By 1987 the breeding program was successful enough that FWS put red wolves back into the wild, creating what's called a nonessential, experimental population. More than 40 red wolves were released in the Alligator River National Wildlife Refuge on the Albemarle Peninsula of North Carolina. The wolves are reproducing, and biologists have bolstered the population by placing captive-born pups into dens, where they are adopted by wild wolves.

FWS's red wolf recovery plan calls for at least 220 wild wolves in three places. The agency began to establish a second population in 1991, by releasing wolves in the Great Smoky Mountains National Park in Tennessee, but removed the animals 7 years later after too many pups died and adult wolves wandered onto private lands. The population in North Carolina peaked at about 130 in 2001 and has been generally falling since then. Hunting and vehicle collisions account for 58% of wolf deaths.

Coyotes remain a long-term problem. Moving south, they arrived in North Carolina not long after FWS reintroduced the red wolves. Coyotes are such prolific breeders that killing them is not a feasible method of population control. To keep them from diluting the red wolf stock, biologists use so-called sterile placeholders: They trap coyotes living near red wolves and give them vasectomies or tubal ligations. Returned to the wild, these coyotes continue to defend their territories against fertile coyotes, yet can't hybridize with red wolves. "The program has gone well," says Brian Arbogast, a biologist at the University of North Carolina, Wilmington.

Gunshot deaths are a growing concern, however, with an average of seven red wolves killed each year in shootings. Many landowners consider coyotes and wolves a threat to pets, children, and game animals such as deer. The two predators can be easy to confuse, especially when the wolves are young and the same size as adult coyotes. When a red wolf is killed, the loss not only shrinks the population, but it also increases the risk of

Wild predators and private property

Red wolf recovery area includes land held by owners opposed to reintroduction

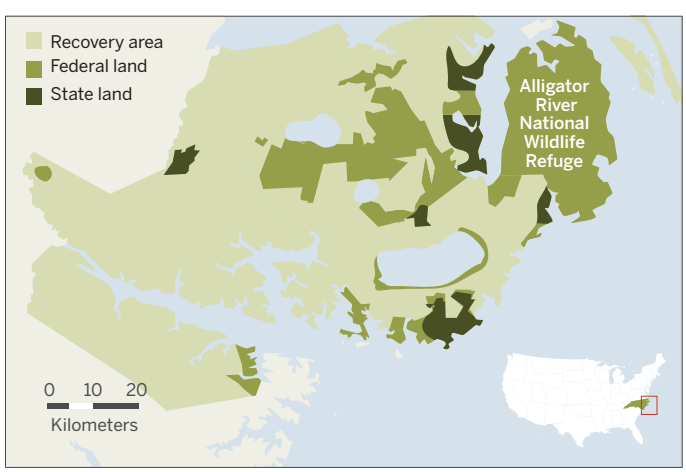

PHOTO: RYAN NORDSVEN/USFWS/FLICKR

Downloaded from www.sciencemag.org on September 26, 2014

Published by AAAS

hybridization. That's because the surviving partner of a wolf pair will seek a new mate—which could be a coyote. (Killing sterilized coyotes compounds the problem, because it opens a coyote territory to fertile newcomers.) The number of red wolf deaths continues to rise. Sometimes, there is evidence of foul play, such as the removal of a radio collar. Concerned, the agency has stopped reporting the location of wolf packs.

The politics of hunting intensified in July 2013, when the North Carolina Wildlife Resources Commission (NCWRC) allowed nighttime coyote hunting, including in the red wolf recovery area (see map, p. 1548). Environmentalists sued, and, this past May, a judge blocked nighttime hunting, pending a trial next year. The judge also prohibited most daytime coyote hunting, citing the danger to red wolves. Less than 3 weeks later, NCWRC Director Gordon Myers asked FWS to launch an "immediate" review of the recovery program. Myers also prohibited the agency from sterilizing and releasing any more coyotes "due to potential for impacts to private landowners and native wildlife." (Others note that this policy may backfire by leading to more coyotes.) The change will be "absolutely catastrophic" to wolf recovery, Chamberlain predicts.

The review is being conducted by the nonprofit Wildlife Management Institute's field office in Kentucky. It will examine the science, management, and "human dimension" of the recovery program. Environmentalists are suspicious of the outcome: The review was announced the Friday afternoon before the Labor Day holiday, a classic gambit to avoid media coverage. And it initially only included a 2-week public comment period (since extended 2 weeks until 26 September). "They're trying to get it done in a hurry before anyone has a chance to react," Sutherland says.

FWS expects the review to be complete by 10 October. That is surprisingly quick, many observers say. "The question for me is how you can do a 60-day assessment of a 27-year program?" says Kim Wheeler, who directs the nonprofit Red Wolf Coalition in Columbia, North Carolina. FWS says it intends to decide the future of the program in early 2015. "We absolutely don't have preconceived conclusions," says Leopoldo Miranda, the FWS assistant regional director in Atlanta. If the agency decides the red wolf recovery plan has been a failure, Sierra Weaver, an attorney with the Southern Environmental Law Center in Chapel Hill, North Carolina, predicts that "there will be a lot of legal groups lining up to take action." ■

INFECTIOUS DISEASES

Testing new Ebola tests

Identifying infections more quickly and easily could help slow the epidemic

By **Gretchen Vogel**

As Ebola continues to rage in three West African countries—and projections for the epidemic's growth look increasingly dire—health officials are hoping they will soon have an additional tool to fight the disease: an easy-to-use, fast, and inexpensive diagnostic test for the responsible virus. Several teams are working on prototype kits—small disposable devices resembling home pregnancy tests—that use just a few drops of blood from a fingertip jab and can be carried easily to remote villages or on door-to-door screening campaigns. At least two of the potential diagnostics will undergo their first field trials in Guinea and Sierra Leone this fall.

Rapid detection of infections would be a huge help in applying the tried-and-true methods that have contained every other Ebola outbreak so far: Identify and isolate infected people quickly enough that they don't pass the virus along to new victims. Ebola isn't easy to spot early in an infection as its symptoms, such as high fever, muscle and abdominal pains, and vomiting, are the same as those of other more common diseases such as malaria and cholera.

Current diagnostic tests take several hours at least, and sometimes days. Clinics—and the teams that trace patients' contacts at risk of infection—rely on a molecular test that detects Ebola virus genes in blood using the polymerase chain reaction (PCR). The test is reliable and accurate, but it requires a blood sample taken by needle and secure transport to a laboratory with a steady supply of electricity, PCR machines, and lab workers equipped to handle highly infectious samples and to run the machines.

That complex process causes some major problems. Suspected patients are often crowded together in makeshift wards, waiting for test results, which means uninfected people may inadvertently become exposed to Ebola. If a suspected case happens very far from the nearest diagnostic facility, it can be days before samples reach the lab and results return.

One of the new tests comes from a company called Senova in Weimar, Germany, which sent 2000 sample kits to Guéckédou, Guinea, earlier this month, where they are being run in parallel to the standard PCR

Members of the European Mobile Laboratory Project use PCR tests in Guéckédou, Guinea.

PHOTO: EUROPEAN MOBILE LABORATORY CONSORTIUM

Published by AAAS

procedure to determine how accurate they are. Meanwhile, researchers from Tulane University in New Orleans, Louisiana, in cooperation with Corgenix in Broomfield, Colorado, and other partners, say they could start testing a prototype rapid diagnostic test as soon as early October in Sierra Leone.

The Corgenix test, based on a test for Lassa fever from the same company, allows a health worker to collect a blood sample directly from a pricked finger onto a pad on one end of a diagnostic test strip. A chemical solution is applied to disinfect the sample and prepare it for the test. The sample then travels through the pad, which separates blood components, and onto the strip itself, which is made of special paper containing dye-tagged antibodies that latch on to a specific Ebola virus protein, if present. As the sample travels farther up the strip, a second antibody binds to the antibody-virus pair, and a dark line appears on the strip, indicating infection.

In Senova's test, a health care worker collects a blood sample from a fingerprick using a minipipette, then mixes the blood with the disinfecting chemical solution before applying it to the test strip; otherwise, the tests are very similar.

Multiple factors influence how well the tests work: the design of the antibodies, the buffer solution, "even what kind of glue you use to stick [the tests] together," says Robert Garry, a virologist at Tulane who is helping coordinate the project with Corgenix. "They look simple, but they're pretty sophisticated devices." Senova says it expects to have early results of its test's performance in 2 to 3 weeks. Researchers hope the tests will be very sensitive as well as very specific—meaning they miss very few Ebola cases, while also producing almost no false positives.

Antibody-based diagnostics are usually not as sensitive as PCR tests, which can copy and detect the tiniest amounts of virus. But even an imperfect test can be helpful, Garry says. It might not be reliable enough to definitively diagnose individuals, he says, but could be used as a screening tool in hard-to-reach villages. "If you test 10 people and none show up positive, you can move on to the next village," he says.

Rapid diagnostic tests could also be helpful in screening patients entering non-Ebola health centers or travelers at airports, says Pierre Formenty of the World Health Organization (WHO) in Geneva, Switzerland. He says WHO is working to develop an "emergency evaluation mechanism" for new diagnostic methods.

If it turns out that the current version of the Senova test doesn't work well enough, finding ways to improve it could take months, says Hans Hermann Söffing, owner of Senova; even getting the prototypes to Guéckédou can take 3 or 4 weeks, he says. Once optimized, however, the tests are relatively easy to produce; Senova could potentially produce thousands per day, he says. Corgenix's tests would probably cost between $1 and $2 each, Garry says.

In the short term, WHO and others are focused on increasing the number of PCR-based labs. While three labs in Guinea are meeting current needs, Formenty says, additional labs are needed in Liberia and Sierra Leone, especially in Monrovia and Freetown, respectively, the hard-hit capital cities.

They will need more staff as well. The European Mobile Laboratory Project, which has established diagnostic facilities in three countries, recently handed its lab in Nigeria over to Nigerians, says Stephan Günther of the Bernhard Nocht Institute for Tropical Medicine in Hamburg, Germany, who helps run the project. European scientists still run the labs in Guinea and Liberia, but they can use reinforcements, Günther says. Special virology expertise isn't required; with 2 weeks of training, "there are thousands of people" who could learn to run the PCR machines safely, he says. ■

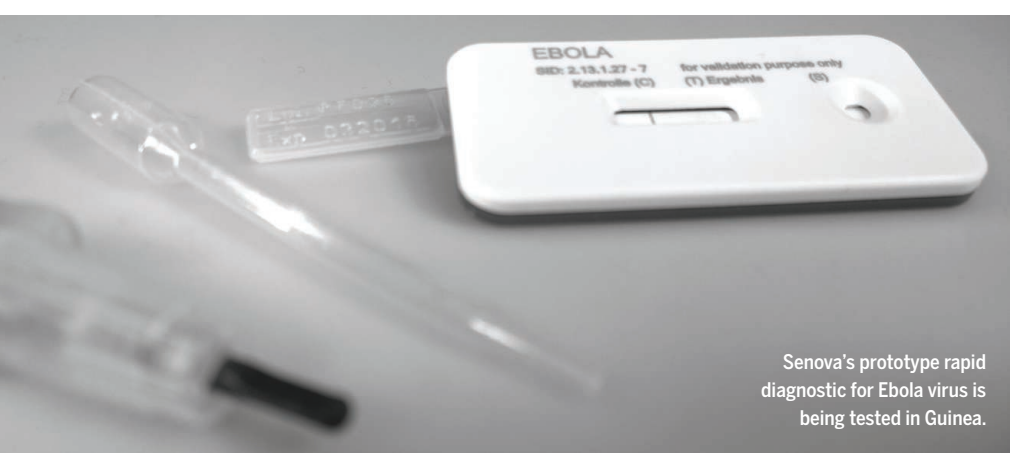

Senova's prototype rapid diagnostic for Ebola virus is being tested in Guinea.

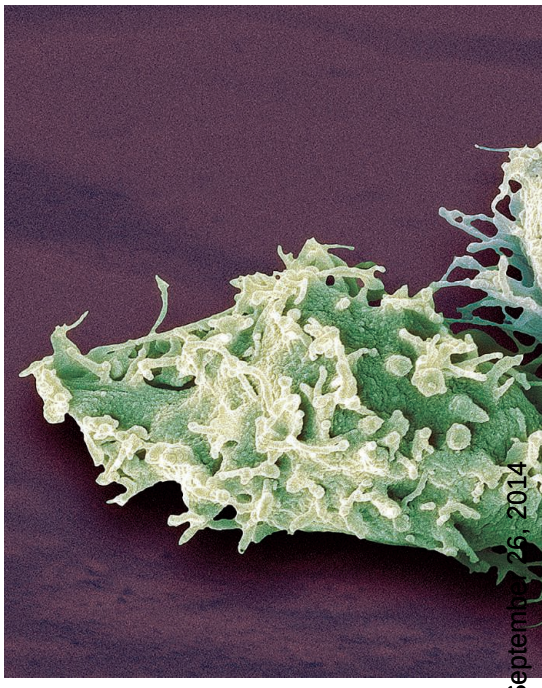

PHOTOS (LEFT TO RIGHT) SENOVA GMBH; STEVE GSCHMEISSNER/SCIENCE SOURCE

IMMUNOLOGY

Metabolic shift may train immune cells

BLUEPRINT project studies epigenetics of various blood cells

By **Elizabeth Pennisi**

The adaptive immune system, which employs the body's T and B cells, is clearly pretty smart—it targets a pathogen with exquisite specificity and can retain a memory of fighting a microbe long ago. But don't call the innate immune system, which recognizes general features of pathogens, stupid. Immunologists are starting to recognize that cellular components of this first line of defense also learn from past battles.

As part of a large-scale program to understand key controllers of gene activity in blood cells, Mihai Netea has now found clues to what may make some innate immune cells, monocytes and macrophages, smarter than once believed. On page 1579, the immunologist from Radboud University Medical Center in Nijmegen, the Netherlands, and his colleagues also suggest a potential way to rev up the body's innate

Downloaded from www.sciencemag.org on September 26, 2014

Published by AAAS

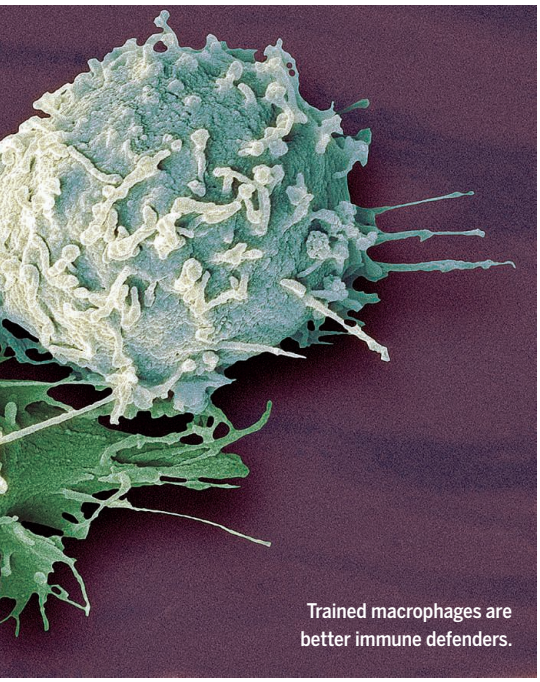

Trained macrophages are better immune defenders.

immunity by "training" those cells. The education would involve turning genes on or off by chemically modifying proteins, called histones, that surround DNA.

Drugs to make such so-called epigenetic modifications are already used to treat cancer and could be adopted for modulating innate immunity, Netea suggests. "We thought innate immunity was just kind of dumb: [Cells] showed up, fired their guns in the air, and died," says James Wynn, a neonatologist at Vanderbilt University School of Medicine in Nashville. "Perhaps the future involves the ability to modify the epigenetics program and change the [innate] response."

The work from Netea emerges out of a pan-European effort called BLUEPRINT that looks at the epigenetics of many types of blood cells, both healthy and diseased, the cells that line blood vessels, and blood's progenitor cells in bone marrow. On page 1578, for example, one BLUEPRINT group surveys the epigenomic landscape of monocytes before and after exposure to several microbial components, tallying up chemical modifications to histones or DNA, such as the addition of methyl or acetyl groups. On page 1580, another BLUEPRINT team assesses how gene activity changes as blood cells develop, a first step toward connecting epigenetic modifications to such activity. "It's a powerful project," says Ross Hardison, a biochemist at Pennsylvania State University, University Park, who is not part of BLUEPRINT. "We are very close to information that has the potential to help the treatment of disease."

Netea wasn't thinking about epigenetics 3 years ago when he first proposed what many considered a heretical idea: that monocytes and macrophages have a memory. These immune cells mount nonspecific responses to various foreign invaders. Typically, adaptive immunity kicks in later, generating customized B and T cells that remember and fight off the specific pathogen for decades. But Netea had noticed that vaccines targeting a specific pathogen subsequently protected mice from other microbial infections, which to him suggested that some form of innate immune memory came into play. In the scientific literature, Netea found examples of similarly improved immune function in plants and insects, which have innate immunity but supposedly no immune memory at all. And others had seen evidence of memory in natural killer cells, another innate immune cell. In 2011, Netea and his colleagues proposed that monocytes are "trained" by early infections to be better prepared for future infections. A year later, they showed training even occurred in mice lacking T and B cells.

A subsequent study suggested that epigenetics influences this training, so Netea turned for help to Radboud molecular biologist Hendrik Stunnenberg, who had put together the €42 million BLUEPRINT effort. Stunnenberg, Netea, and their colleagues first assessed monocytes before and after they converted to the macrophages that settle into specific tissues to do the immune system's dirty work. Specifically, they compared the activity of genes in both cell types, as well as epigenetic marks such as DNA and histone methylation patterns.

For example, they looked at monocytes exposed to a bacterial component called β-glucan and monitored how the epigenome was affected. Previous research has shown that β-glucan trains the monocytes to be more responsive to future microbial infections. "We believe that the innate immune system has a memory [and] that memory could be in the epigenome," Stunnenberg says.

Netea's team wanted to tease out the precise mechanism of this memory. They discerned that several genes involved in an energy-producing process called glycolysis underwent epigenetic changes that turned them on, suggesting that glycolysis had a role in the training phenomenon. They then tested that idea, finding that trained immune cells require more sugar and less oxygen, as would be expected if they were relying on glycolysis for their energy needs. "The data suggest there was a major shift in the metabolic rate of the cell," Stunnenberg says. Furthermore, when they inhibited two master regulator proteins of glycolysis, mTOR and HIF-1α, the cells didn't turn on glycolysis and weren't trained. Immunity training also failed in mice missing the gene for HIF-1α in precursor white blood cells.

Netea envisions one day using medications that modify the epigenome to boost underactive immune systems and improve the immune response to vaccines in infants and the elderly. In people prone to heart attacks, the epigenomic state of some white blood cells may be abnormal and contribute to the inflammation that hurts arteries. "So we need to identify drugs that bring these cells back to reality," says Willem Ouwehand, a hematologist at the University of Cambridge in the United Kingdom.

"We could be seeing the dawning of a new era in immunology, with a greater focus on the innate immune system," notes Kate Jeffrey, an immunologist at Massachusetts General Hospital in Boston. Jeffrey still wants more evidence that epigenetics controls the shift in metabolic pathways seen in trained innate immune cells. Training, she notes, would also need to have a long enough lasting effect to be clinically useful. But if training innate immune cells can work, she adds, "that turns the whole idea of immunity on its head." ■

Training immune cells to have a memory

Exposure to pathogens can boost subsequent responses by altering the activity of genes, including those controlling the energy-generating process glycolysis.

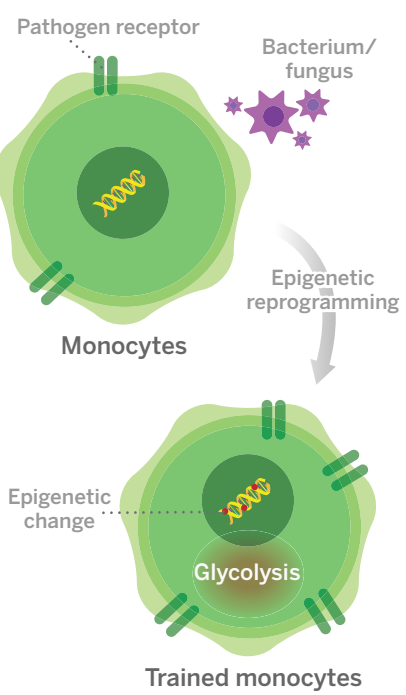

ILLUSTRATION: G. GRULLON/SCIENCE

Published by AAAS

ON THE EDGE

Downloaded from www.sciencemag.org on September 26, 2014

Ecologist Marten Scheffer became a leader in the science of tipping points by studying lakes. Now he's making waves in many other fields

By **Gabriel Popkin**

It was a murky problem. In the late 1980s, scientists in the Netherlands were struggling to reverse an outbreak of cloudy lakes. The source of the scourge was no mystery: Nutrients were running off farm fields and leaking from sewage treatment plants, fueling algae blooms that turned once-clear waters a sickly green.

But researchers had discovered that just cutting off the flow of nutrients often wasn't enough to restore clarity; some lakes and ponds seemed to have tipped into a new, persistently turbid condition. To clear the water, the scientists discovered they needed to give the ecosystems an extra jolt, which they could sometimes do by removing certain kinds of fish. Nobody had a clear theoretical conception of why such "shock therapy" worked.

Marten Scheffer, however, saw something in the gloomy water. The math-savvy ecologist had just arrived at a Dutch environmental agency and had been assigned to study the troubled lakes. He realized they were demonstrating a phenomenon known as bistability—the lakes had two stable states and could abruptly tip from one to the other as a result of a small external nudge. The equations describing such shifts had been around since the 1960s—and even depicted in paintings by Salvador Dalí—but they had found few real-world applications. In the Netherlands, however, Scheffer and his colleagues put them to use, conducting increasingly sophisticated experiments that demonstrated how a better understanding of tipping points could have very practical applications.

That work led in 1993 to a now-classic paper in *Trends in Ecology & Evolution* that has

PHOTO: MANON BRUININGA

Published by AAAS

Before diving into science, Marten Scheffer studied music. He's recorded 15 albums.

helped make Scheffer a leading, and sometimes unorthodox, thinker on the science of tipping points. Now, at 56, the Wageningen University ecologist has crossed a threshold of his own: Flush with funding, he's become the intellectual hub for a global network of scholars who meet for freewheeling discussions, often at a retreat center he built on his family farm in the Netherlands. The collaborations are carrying Scheffer far from the rural lakes where he started, to efforts to identify tipping points in tropical forests, global climate, and communities of gut microbes, and even in the onset of migraine headaches and depression.

Scheffer has become "the social glue … the chief networker in some ways" for a growing community of tipping point researchers, says climate scientist Tim Lenton of the University of Exeter in the United Kingdom. Along the way, he's won hefty science prizes, and his key papers have tallied some 10,000 citations.

Some researchers, however, worry that Scheffer might be moving too far, too fast with his ideas, and that tipping point models, while elegant, are sometimes too rudimentary to be very practical. Still, few question his scientific acumen or skill at shattering disciplinary barriers. Scheffer's "independence is his trademark," says ecologist Wolf Mooij, a colleague at Wageningen University and the Netherlands Institute of Ecology.

THAT AUTONOMY WAS ON DISPLAY in 2009, when Scheffer received the Spinoza Prize, a €2.5 million award that is the Netherlands' most prestigious science honor. Winners typically give a predictable speech. Scheffer, an accomplished musician, instead pulled out a guitar and played an original acoustic composition from *Transitions*, one of 15 albums he has recorded.

Once, Scheffer thought he might play music for a living. Raised in the Dutch countryside by parents who played classical flute and piano, young Scheffer was asked what instrument he wanted to learn. "It was not really a question" of whether he would take lessons, he notes, so "I picked [an instrument] they did not play," the violin, and studied it seriously, well into his college years.

When it came time to choose a career, however, Scheffer tipped toward science. ("I would never be able to be a [classical] violin player," he says, given his eclectic musical tastes.) After earning an undergraduate degree in ecology from Utrecht University, he eventually landed at the Netherlands' Institute for Inland Water Management and Waste Water Treatment.

Soon, Scheffer was wading into the murky lake problem, putting him squarely within a long scientific tradition. Some historians argue that modern ecology itself was launched by the publication of "The Lake as a Microcosm," an 1887 paper by American ecologist Stephen Alfred Forbes. Lakes hit a sweet spot, Scheffer says: ecosystems that are self-contained and experimentally tractable yet intricate enough to yield profound insights. "They're really complex systems but … we understand them relatively well, and can actually manipulate them," he says. And in wet, table-flat Netherlands, Scheffer and his colleagues had plenty of lakes within reach.

Most notably, they showed that clear lakes with plentiful vegetation are resilient to moderate nutrient influxes, whereas murky lakes lacking such vegetation cannot easily return to clarity. The scientists also learned why "shock therapy"—removing bottom-feeding fish—can work. They found that the fish stir up sediment, releasing stored nutrients that keep lakes murky even after external flows are stanched. Once the fish are removed, the water clears enough for aquatic plants to grow; the plants then help hold bottom sediments in place, even if the fish return.

The fish removal method is now used in restoration projects around the world. And the lake experiments helped generate enough high-profile publications for Scheffer that, in 1992, Utrecht University awarded him a Ph.D., despite the fact that he never bothered to formally enroll in graduate classes.

"Marten really formulated very clear, testable theories about shallow lakes," says Stephen Carpenter, a limnologist at the University of Wisconsin, Madison, who studies transitions in North American lakes.

To illustrate the findings, Scheffer introduced a type of graphic that has become a hallmark of his work. It shows a ball rolling across a simple 2D hill-and-valley landscape (see p. 1554). A deep valley represents a resilient, stable state, such as a clear lake with plentiful vegetation and few nutrient inputs. When the ball sits in such a valley, it is difficult to move; if nudged, it quickly rolls back to equilibrium on the valley floor. But if a lake becomes overfertilized, the system resembles a valley with shallow slopes; a slight nudge can push the ball into the next valley—which represents a new stable state like a turbid lake. Restoring clarity means finding ways to lower the hill and reverse the ball's path—such as cutting off nutrients and removing bottom fish.

Such graphics have been invaluable in communicating Scheffer's ideas to policymakers and field workers, who don't typically dabble in complex mathematics. "The ball in a cup pictures really helped get the idea into the minds of managers, and now they're using it all the time," he says. Scheffer "really bridged the gap between the deep theory and the application," Mooij says. "He was very effective in communicating this for both scientific and applied audiences." (In contrast, Dalí's 1983 effort to depict tipping point theory met with less success; the painting, part of his "Catastrophe Series," was his last and is little known.)

SCHEFFER'S CAREER has had its tipping points, each carrying him further from his home in limnology. In the mid-1990s, his lake work helped persuade the more senior Carpenter to invite Scheffer to join the Resilience Alliance, an eclectic confederation of scientists who study what makes some systems stable in the face of change. Scheffer recalls that at his first meeting, in 1997 in the bush in Zimbabwe, the group sat around nightly campfires, trading ideas. "It was very inspiring," he says.

Four years later, he and a group that included several participants in the Zimbabwe retreat published a *Nature* paper that aimed to bring the concept of ecological tipping

Published by AAAS

Scheffer's varied interests include showing off pond life to his children and a colleague.

points into the mainstream. Drawing on studies of lakes, coral reefs, forests, deserts, and oceans, the team argued that ecosystems can often shift abruptly in response to gradual changes, and that managers need to recognize when such "forcings" could cause a catastrophic loss of resilience. The paper has since garnered some 3000 citations.

By the time the *Nature* paper appeared, Scheffer had become head of Wageningen University's Aquatic Ecology and Water Quality Management group. His work over the next decade ranged far beyond aquatic ecosystems, however. He modeled tipping points in climate and other natural and human systems and wandered into fierce ecological debates, including the question of why so many species exist. To advance his brand of freeform transdisciplinary collaboration, Scheffer and a colleague conceived the South American Institute for Resilience and Sustainability Studies, a research center that is now partly funded and under construction in Uruguay.

Scheffer also began wondering whether, with the right kind of data and methods, researchers could detect warning signs that a system was about to tip. Hints of such forecasting methods had appeared in journals as far back as the 1980s, but they received renewed attention after Scheffer and colleagues published a 2009 review paper in *Nature*. One promising statistical signal, they noted, is "critical slowing down," in which an ecosystem or population approaching a tipping point takes longer to recover from a perturbation. To use the ball and valley analogy, when a ball is slower to roll back to the valley floor, that's a sign it is becoming easier to push it into a new stable state.

On the strength of such work, Scheffer won three major awards in 2009 and 2010 that allowed him to do what other scientists dream of: jump off the grants treadmill and pursue his wide-ranging interests. First came the Spinoza Prize, then a €2.5 million European Research Council Advanced Grant (to study early warning signals in a variety of systems), and finally a €2.1 million grant from the Dutch Ministry of Education, Culture and Science (part of a larger project to study climate tipping points).

SCHEFFER WASTED NO TIME in putting his new financial independence to use. Waiting for the Spinoza Prize ceremony to begin, he and his co-awardees, University of Twente physicist Albert van den Berg and Leiden University neurologist Michel Ferrari, began discussing whether tipping point theory could help predict and possibly prevent migraines. The three soon began a joint project, and in 2013 they sketched out a hypothesis in *PLOS ONE*. They are now gathering data to identify neuronal activity patterns that might reliably predict migraine attacks.

Meanwhile, other experimental demonstrations of early warning signals have begun to appear. Scheffer's team, for instance, has used increasing amounts of light to stress laboratory algae and show that populations fluctuate in a recognizable way before crashing. Jeff Gore, a physicist at the Massachusetts Institute of Technology in Cambridge, has achieved a similar result in experiments that stress populations of laboratory yeast. And in a real-world demonstration, Carpenter and colleagues reported in 2011 that they were able to detect early warnings of a food web transition in a lake in northern Wisconsin by tracking signals in fish and plankton populations.

But some researchers urge caution in generalizing from a few results. "My view is that in many cases, the early warning signals [Scheffer] has worked on will be too simplistic to apply to the real world," says Jef Huisman, a microbiologist at the University of Amsterdam and a sometime collaborator with Scheffer. And two psychopathologists from the University of Groningen have challenged a venture Scheffer took into psychiatry, published earlier this year in the *Proceedings of the National Academy of Sciences*. Scheffer and collaborators suggested that signs of "critical slowing down"—and impending depression—may be found in self-reported mood data. The critics were unconvinced, though one of them, Elisabeth Bos, finds the idea exciting. "If you can prove that there's a subset of individuals who really show these critical transitions," she says, "that would be a great tool to use in clinical psychiatry."

Others worry that by trying to apply his ideas too broadly, Scheffer risks creating the kind of hype and blowback that crippled an earlier effort to develop tipping point models, also known as catastrophe theory. "One has to be careful not to kill the baby with the bath water, not to do what happened with elementary catastrophe theory and say it's the solution to everything," says theoretical ecologist Simon Levin of Princeton University.

Scheffer embraces such warnings. He has invited critics to workshops, which often take place at Scheffer's retreat center, built to look like an old Dutch farmhouse. Guests stay in a nearby hotel and bike to the farm. After a morning of heady talk, they might adjourn to pick apples or swim in a nearby lake—in no danger of turning cloudy.

The experience is "very intense yet quite relaxed," says one participant, psychiatrist Kenneth Kendler of Virginia Commonwealth University in Richmond. It's Scheffer's way of nudging his colleagues toward yet another intellectual tipping point. ■

Gabriel Popkin is a science and environmental writer in Mount Rainier, Maryland.

Nudge science

Scheffer uses accessible diagrams to illustrate tipping point concepts.

A resilient system returns to equilibrium quickly after a small push (**black**). It takes a major push (**red**) to tip the system into a new stable state.

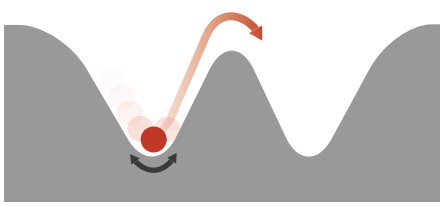

A less resilient system recovers more slowly from small pushes (**black**). This "critical slowing down" can be a warning sign that the system could easily tip into a new state (**red**).

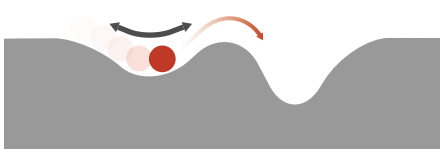

PHOTO: WIM VAN HOF

Published by AAAS

Workers ease one of NOvA's huge modules into place, lined up like slices of bread in a loaf.

Downloaded from www.sciencemag.org on September 26, 2014

NOvA's shining moment

Despite years of delay, Fermilab's massive new experiment has a chance to take the next big step in neutrino physics

By **Adrian Cho**,
in Ash River, Minnesota

It takes a big snare to catch a subatomic ghost. The newly completed NOvA neutrino detector is the size of a warehouse—five stories tall and more than three times that long—and consists of 896 planes of extruded plastic tubes filled with 10 million liters of mineral oil. "This is the world's largest free-standing plastic structure," says Richard Tesarek, a physicist at Fermi National Accelerator Laboratory (Fermilab), 810 kilometers away in Batavia, Illinois, which will fire a beam of the elusive, almost massless particles into the detector. Tesarek says he's applying to Guinness World Records for official recognition of the size claim.

NOvA—short for NuMI (itself an acronym) Off-Axis Electron Neutrino Appearance experiment—has a ghostly feeling. It sits in the middle of nowhere, an hour south of International Falls, population 6357, in a building carved into the pink granite of the Canadian Shield and surrounded by kilometers of birch and red and white pine. Aside from the whir of cooling fans, the place is quiet. There isn't even a barrier or alarm to keep you from wandering into the neutrino beam. (Neutrinos just go through you harmlessly.) Still, for the next several years NOvA will be the new center of action in neutrino physics, perhaps the hottest area of particle physics.

At first blush, NOvA's prospects for making major discoveries might seem dim. The experiment is 2 or 3 years late coming online, having barely survived a budget cut 6 years ago. A neutrino experiment in China beat it to the measurement that had been NOvA's primary goal. And NOvA has been overshadowed by Fermilab's efforts to launch an even bigger neutrino experiment proposed for the next decade.

But fate isn't always cruel. As the 204 members of the NOvA team finish the 14,000-tonne, $278 million detector, they find themselves with an excellent shot at taking the next big step in the global quest to decipher neutrinos, perhaps the most mysterious of the fundamental particles. NOvA could nail down which of the three related kinds of neutrinos is the heaviest and which is lightest. That seemingly esoteric ranking bears on some of the biggest issues in physics, such as why the universe contains so much matter and so little antimatter.

"To me, NOvA has great potential," says Chang Kee Jung, a physicist at Stony Brook University in New York and an international spokesman for T2K, a similar experiment in Japan that is NOvA's direct

PHOTO: REIDAR HAHN

Published by AAAS

competitor. Though some NOvA physicists say they feel like the neglected stepchildren of the U.S. particle physics community, others say the lack of attention has made it easier to get their work done. "We're flying a little under the radar," says Patricia Vahle, a NOvA team member from the College of William & Mary in Williamsburg, Virginia. "I think once we start taking data, things will change pretty quickly."

STUDIED FOR NEARLY 60 YEARS, neutrinos remain shrouded in mystery. "We don't even know their masses," says Mark Messier, a physicist at Indiana University, Bloomington, and co-spokesman for the NOvA team. Physicists do know that neutrinos emerge from particle interactions that involve the weak nuclear force and come in three types—electron, muon, and tau. Neutrinos also undergo a bizarre metamorphosis as they zip along at near light speed. One type morphs into another, as physicists found in 1998 by studying muon neutrinos generated when cosmic rays strike the atmosphere and in 2001 by studying electron neutrinos emanating from the sun.

Since then, physicists around the world have raced to probe such "neutrino oscillations." Scientists once thought that neutrinos were massless, but the morphing means that they can't be. According to relativity, a massless particle must travel at light speed, in which case time stands still for it, and change is impossible. Through various experiments, physicists have shown that neutrino oscillations can be described, at least roughly, by just five parameters. The differences in mass among the three neutrinos provide two of these and determine the rates of the oscillations, faster or slower. Three more numbers known as mixing angles determine the probability that one particular type of neutrino morphs into another.

Neutrino oscillations could help answer a major question about the universe. Neutrinos and their antimatter counterparts, antineutrinos, might oscillate slightly differently. That asymmetry would be an example of a phenomenon called charge-parity (CP) violation, which could help theorists explain how the infant universe produced so much matter and so little antimatter. Quarks, which make up protons and neutrons, also exhibit CP violation, but not enough to explain the matter-antimatter imbalance, so theorists have pinned their hopes on neutrino measurements.

When NOvA was proposed in 2005, a key goal was to measure the one neutrino oscillation parameter that remained unknown—a mixing angle called θ_{13}. To succeed, NOvA would have to improve on an earlier Fermilab experiment called MINOS that in 2005 began firing muon neutrinos to another location in Minnesota, the old Soudan mine. (Fermilab generates the particles in the Neutrinos at the Main Injector, or NuMI, beamline, which blasts protons into a target to make particles called pions. A pion in turn decays into a particle called a muon and a muon neutrino.) MINOS measured a different mixing angle, called θ_{23}, by simply counting muon neutrinos and seeing how many disappeared along the way from Fermilab as they morphed into electron and tau neutrinos. To measure θ_{13}, NOvA would also have to count the much rarer electron neutrinos that appeared in the beam as it traversed the earth.

Straight shooter

Neutrinos change type in flight.

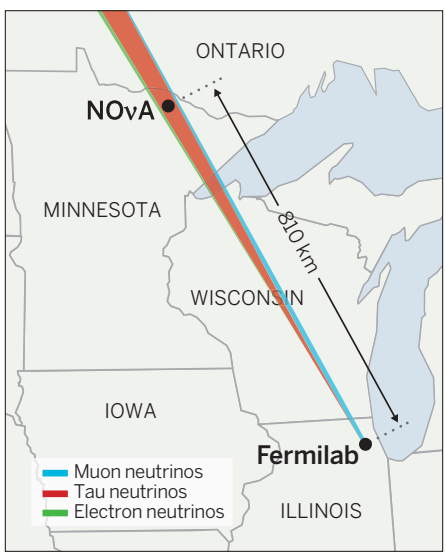

But NOvA had competition. Physicists in Japan were already working on T2K, which shoots muon neutrinos from the Japan Proton Accelerator Research Complex in Tokai to the gargantuan underground Super-Kamiokande neutrino detector in a mine 295 kilometers to the west. Meanwhile, other teams in France, South Korea, and China were all hoping to measure θ_{13} in a different way, by means of the disappearance of electron antineutrinos produced by nuclear reactors.

In the end, NOvA never had a chance to win that race. On 17 December 2007, just as researchers were hoping to get the go-ahead to start construction, Congress zeroed out 2008 funding for the project as part of a last-minute budget bill. "A lot of the [Fermilab] scientists went away and did other things," Vahle says. They "had to be moved into other programs that paid."

One of the reactor teams went on to clinch the θ_{13} measurement. Researchers with the Daya Bay Reactor Neutrino Experiment, 70 kilometers north of Hong Kong, leapfrogged the competition and released the first definitive measurement of the key parameter in March 2012 (*Science*, 16 March 2012, p. 1287). T2K weighed in with a measurement the following year. Tantalizingly, the results proved that CP violation is possible among neutrinos, as it requires that none of the three mixing angles equal zero.

BY THAT TIME, NOvA had risen from the dead, saved in part by the global financial crisis of 2008. Responding to the crisis, the federal government pumped $831 billion into the U.S. economy to stimulate it, partly by investing in public projects. "We were, in the parlance of the time, shovel ready," says John Cooper, a physicist at Fermilab. "We had a design in hand and were ready to go on that building at Ash River." Fermilab received $55 million to start building NOvA.

But haven't Daya Bay and T2K rendered NOvA superfluous? Not quite. Measuring θ_{13} had always been one of a number of targets. NOvA physicists now hope to sort the neutrinos from lightest to heaviest. They know the mass differences: Two types of neutrinos have nearly the same mass and one is different. But they don't know if two neutrinos are light and one heavy or vice versa. Roughly speaking, the first arrangement would make the electron neutrino the lightest, mirroring the mass ranking of the electron and its particle cousins, the muon and the tau. So it's called the normal mass hierarchy. In the second arrangement—the inverted hierarchy—the electron neutrino is one of the two heavier neutrinos.

The hierarchy has broader implications. Theorists suspect that, rather bizarrely, the neutrino may act in a certain sense as its own antiparticle. That would make the neutrino unique among matter particles and would mean it gets its mass in a way that's different from other fundamental particles—which get their masses by interacting with Higgs bosons lurking in the vacuum of empty space. Physicists could prove that was the case if they could observe a hypothesized form of radioactive decay called neutrinoless double beta decay that depends on that oneness of neutrino and antineutrino. But the rate of that decay depends on the electron neutrino's mass, and the decay may be observable only if the hierarchy is inverted.

To determine the hierarchy, NOvA researchers will alternately fire muon neutrinos and muon antineutrinos from Fermilab and compare the numbers of electron neutrinos and electron antineutrinos

ILLUSTRATION: K. ENGMAN/*SCIENCE*

Published by AAAS

appearing at Ash River. En route, electron neutrinos and antineutrinos will interact with electrons in the earth to change their oscillations in opposite ways. That "matter effect" should increase the oscillation rate if the electron neutrino is light and decrease the rate if it is heavy. "The gist of the experiment is if neutrinos oscillate more than antineutrinos, then the mass hierarchy is normal," says Indiana University's Messier, "and if antineutrinos oscillate more than neutrinos, then the hierarchy is inverted."

Compared with Japan's T2K experiment, NOvA has an edge when it comes to probing the hierarchy. Because it fires neutrinos through more earth than T2K does, NOvA is more sensitive to the matter effect and hence the mass hierarchy. NOvA researchers should also get a boost from the measurement they got scooped on. The angle θ_{13} turned out to be several times larger than many theorists anticipated, so more muon neutrinos should turn into electron neutrinos on the way to Ash River than were originally expected. "We'll see all the events we ever hoped to see," Fermilab's Cooper says. After a brief downtime for upgrades of the Fermilab accelerators, physicists will begin taking data in earnest in October.

They will continue collecting data for at least 6 years. To be spotted, an electron neutrino must ping off an atomic nucleus in the detector to produce an electron (or an antielectron in the case of an antineutrino). As the electron zips through the oil-filled tubes, the oil emits light that's detected by optical fibers looping through the tubes, which light up like pixels on a video screen. Of the many billions of neutrinos sent from Fermilab each year, researchers expect to detect about 40 electron neutrinos.

Even that requires a "detector on an industrial scale," Fermilab's Tesarek says. NOvA contains 10,752 extruded groups of tubes—the spares resemble material for prefab buildings or lawn furniture. It took 414 tanker truck loads to ship the oil from a facility in Columbus. The biggest challenges in building NOvA were "logistics, logistics, logistics," Tesarek says.

TO REACH THEIR GOAL, physicists will also need a little luck. The matter-antimatter asymmetry of CP violation—if it exists—could make neutrinos and antineutrinos oscillate differently. And it could counteract the matter effect NOvA researchers are hoping to exploit to determine the mass hierarchy. Or CP violation could enhance the effect.

Reassuringly, by comparing the oscillations of neutrinos and antineutrinos, T2K researchers have seen hints that the effect of CP violation, which is characterized by yet a fourth angle, will improve NOvA's chances of measuring the mass hierarchy, says T2K's Jung. Vahle, the NOvA collaborator from William & Mary, cautiously agrees. "If you take that seriously, it's just right for us," she says. "But it's a very small hint."

NOvA could also have competition. The Daya Bay team has proposed an experiment called the Jiangmen Underground Neutrino Observatory (JUNO) that aims to measure the mass hierarchy by snaring antielectron neutrinos from a pair of nuclear power plants 200 kilometers northwest of Hong Kong. Researchers hope to break ground on the $300 million facility this year and have it running by 2020, says Jun Cao, a physicist at the Chinese Academy of Sciences' Institute of High Energy Physics in Beijing and deputy spokesman for the 250-member JUNO team. "We have some chance to measure [the mass hierarchy] first, but it's hard to predict," he says. "We will do our best."

JUNO would be capable of determining the hierarchy no matter what the effect of CP violation. However, JUNO researchers will have to make very precise measurements of each neutrino's energy, other physicists say. All of that means it may be 10 years before the JUNO team produces a result, Jung says.

By then, Fermilab may have moved on to grander schemes. Even before they started building NOvA, Fermilab began planning a bigger experiment that would shoot a more powerful beam of neutrinos to a detector 1300 kilometers away in an abandoned gold mine in Lead, South Dakota—home to the Sanford Underground Research Facility. The billion-dollar effort, now known as the Long-Baseline Neutrino Facility (LBNF), has long overshadowed NOvA, especially as officials at the U.S. Department of Energy have struggled to find a way to pay for the project, which is key to Fermilab's long-term future.

LBNF would not only measure all the parameters of neutrino oscillations and CP violation, but would also do so precisely enough to test the internal consistency of the entire scenario and look for possible deviations that might point to new physics. The latest plan is to launch the project as a joint venture with Europe and other foreign partners and to share the cost with them (*Science*, 30 May, p. 955).

But until LBNF begins catching neutrinos, NOvA will be the major neutrino facility in the Western Hemisphere, and it may dominate the field until its successor is on the scene in a decade or more. "One could imagine that we just keep running until LBNF is ready to take the beam," Messier says. For now, NOvA researchers are happy to be detecting neutrinos, Cooper says: "It's good to be on the floor running the experiment instead of dreaming for the future." ■

Neutrinos' greatest hits

Progress in neutrino physics has accelerated in the past 16 years and physicists now have a shortlist of key questions they hope to answer.

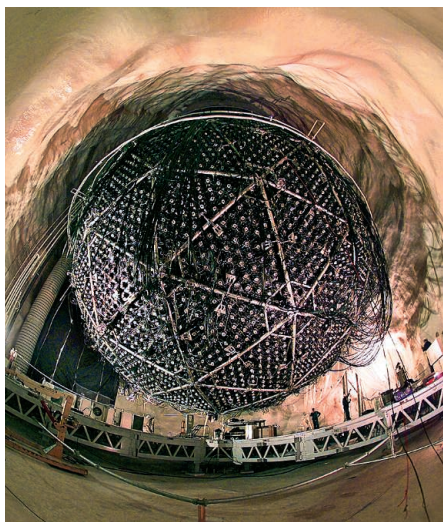

1930
Neutrino hypothesized to explain missing energy in a type of radioactive decay

1956
Neutrinos detected in experiments with nuclear reactors

1962
Electron and muon neutrinos distinguished in accelerator experiments

1968
Shortage of electron neutrinos from sun observed

1969
Neutrino oscillations hypothesized to solve "solar neutrino problem"

1998
Neutrino oscillations observed in study of muon neutrinos generated in atmosphere

2000
Tau neutrino observed

2001
Neutrino oscillations confirmed in study of electron neutrinos from the sun at the Sudbury Neutrino Observatory (above)

2012
Fifth and final parameter describing neutrino oscillations measured

To come
Mass ordering of neutrinos measured

Matter-antimatter asymmetry in neutrinos observed

Absolute masses of neutrinos determined

PHOTO: LAWRENCE BERKELEY NATIONAL LABORATORY

Published by AAAS

A monogenic theory of autoimmunity *p. 1560*

Reactive iron revealed in nitrogenase *p. 1568*

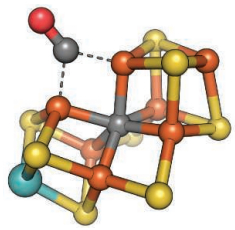

PERSPECTIVES

ECOLOGY

Whose conservation?

Changes in the perception and goals of nature conservation require a solid scientific basis

By **Georgina M. Mace**

Conservation biology is a mission-driven discipline (*1*) and is therefore subject to both drift and the periodic adoption of fads and fashions (*2*). Although many basic conservation principles, conservation organizations, and initiatives of global reach and impact have persisted almost unchanged for decades, the framing and purpose of conservation have shifted (*3*). These shifts mainly relate to how the relationships between people and nature are viewed, with consequences for the science underpinning conservation.

There have been four main phases in the modern framing of conservation in the developed world (see the figure). Conservation thinking before the 1960s was broadly of the "nature for itself" type, which prioritizes wilderness and intact natural habitats, generally without people, and has scientific underpinnings from wildlife ecology, natural history, and theoretical ecology. This thinking continued throughout the 1960s, with a focus on species conservation and protected area management, and remains a dominant ideology for many people today.

In the 1970s and 1980s, rapid increases in the impacts of human activity and awareness of the consequences of habitat destruction, overharvesting, and invasive species led to the emergence of "nature despite people" conservation. Here, the focus is on threats to species and habitats from humans, and on strategies to reverse or reduce them. Ideas concerning minimum viable population sizes and sustainable harvesting levels, as well as intense debates about community-based management and the sustainable use of wild-life, stem from this period (*4*) and persist to the present.

CONSERVATION SERIES

Tropical rain forest, Sinharaja, Sri Lanka. In recent decades, views of the relationship between humans and nature have changed in tandem with increasing impacts of human activities on natural systems.

By the late 1990s, there was ample evidence that pressures on habitats were ubiquitous and persistent, and that the best endeavors of conservation were failing; extinction rates were escalating and pressures on biodiversity increasing relentlessly (*5*). A realization developed that nature provides crucial goods and services that are irreplaceable yet had been consistently ignored (*6*). As the costs of environmental mismanagement started to accumulate, the potential benefits to be gained from taking more seriously these services from nature became clearer (*7*, *8*). Conservation thinking moved away from species and toward ecosystems as a focus for integrated management, with the goal of providing sustainable benefits for people in the form of ecosystem goods and services (*9*)—"nature for people."

The work on the Millennium Ecosystem Assessment (*10*) was a key driver of the widespread adoption of this way of thinking about the natural environment. Many of the ideas were quickly adopted into conservation practice and environmental policy, although not without strong and persistent detractors (*11*). A wider acceptance of the notion that people are part of ecosystems emerged, and the tendency to treat people and nature as separate units in discourse and analysis was much reduced, although not completely eliminated.

The focus on nature's benefits and ecosystem services has been very influential.

PHOTO: THINKSTOCK/GETTY IMAGES

Published by AAAS

However, in recent years the emphasis has moved from a potentially overly utilitarian perspective—managing nature to maximize the overall value of the human condition—to a more nuanced one that recognizes the two-way, dynamic relationships between people and nature (*12*). This "people and nature" thinking emphasizes the importance of cultural structures and institutions for developing sustainable and resilient interactions between human societies and the natural environment. It operates at a range of scales from global to local and has intellectual origins in resource economics, social science, and theoretical ecology (*12*, *13*).

These shifts in focus have occurred over a relatively short period, resulting in a pluralism of views and motives that now underpin conservation. Current conservation science and practice includes all four framings, sometimes in mutually supportive implementations, but increasingly the differences in underlying ideologies can cause frictions and tensions. For example, the North American conservation NGO The Nature Conservancy recently moved away from a focus on preservation, toward exploiting opportunities for conservation outcomes that businesses will invest in for their own benefit. This move has led to lively debates in the literature between some strongly held and divergent viewpoints (*14*).

The multiple framings also have consequences for conservation science, because the scientific tools and techniques have not always kept pace with the concepts and objectives. There are many implications, as shown in the three activities highlighted here: measuring conservation success, designing ecosystem management, and assigning economic value to nature.

Under a "nature for itself" framing, conservation success can be measured with well-established metrics based, for example, on changes in the number of species listed in the IUCN Red List of Threatened Species or on the coverage of protected areas (*15*). In "nature despite people," these measures can be separated by threat type, and efforts made to report on species and areas that are not yet at risk but will soon be if pressures do not abate. But the ecosystem-based framings—"nature for people" and "people and nature"—require metrics that link nature to human well-being, explicitly identifying benefits needed and received by people (*16*). These metrics are very different from those of species and protected areas.

Measuring conservation success is surprisingly difficult when nature and people are considered together. For example, it is widely assumed that conserving the greatest numbers of wild species and intact habitats will be consistent with maximizing the ecosystem services that these areas provide to people. Yet, although most ecosystem functions are enhanced with more ecological and species diversity (*17*), adequate supplies of food or clean water for growing human populations have come from converting intact wilderness into land for agriculture, and canalizing or even draining many rivers and wetlands, thus reducing diversity. The ways in which nature contributes to human well-being are complex (*18*), and the commodification of nature, even with the best intentions, will have unintended and potentially deleterious outcomes for conservation (*11*).

The "people and nature" framing rejects the linear relationship characteristic of "nature for people," instead envisaging a much more multilayered and multidimensional relationship that is difficult to conceptualize, let alone to measure. Attempts to develop large-scale metrics for conservation thus result in a plethora of measures. The strategic plan for the UN Convention on Biological Diversity includes 20 targets and some 100 indicators that include addressing the underlying causes of biodiversity loss, reducing direct pressures on biodiversity, promoting sustainable use, safeguarding ecosystems, promoting species and genetic diversity, and enhancing the benefits to all people (*19*). Given the complex processes and interactions behind these indicators, contradictory messages will inevitably emerge, and unambiguous signals for policy are likely to be hard to find.

The different framings also have implications for ecosystem management. In the "people and nature" view, the science has moved fully away from a focus on species and protected areas and into a shared human-nature environment, where the form, function, adaptability, and resilience provided by nature are valued most highly. However, these terms mean something else in human societies than in ecology. In human societies, a simple behavior change or technological innovation can enhance adaptability and resilience, but for species, ecological communities, and ecosystems, adaptability and resilience result from biophysical processes that require the right components to be in place over scales of space and time that may not be amenable to human management. For example, reversing long-term declines in old-growth forests or recovering the full extent of marine trophic systems may take centuries, far beyond the normal time scale for environmental policies. In these natural systems, once lost, there are complex processes to be recovered that are often not well understood,

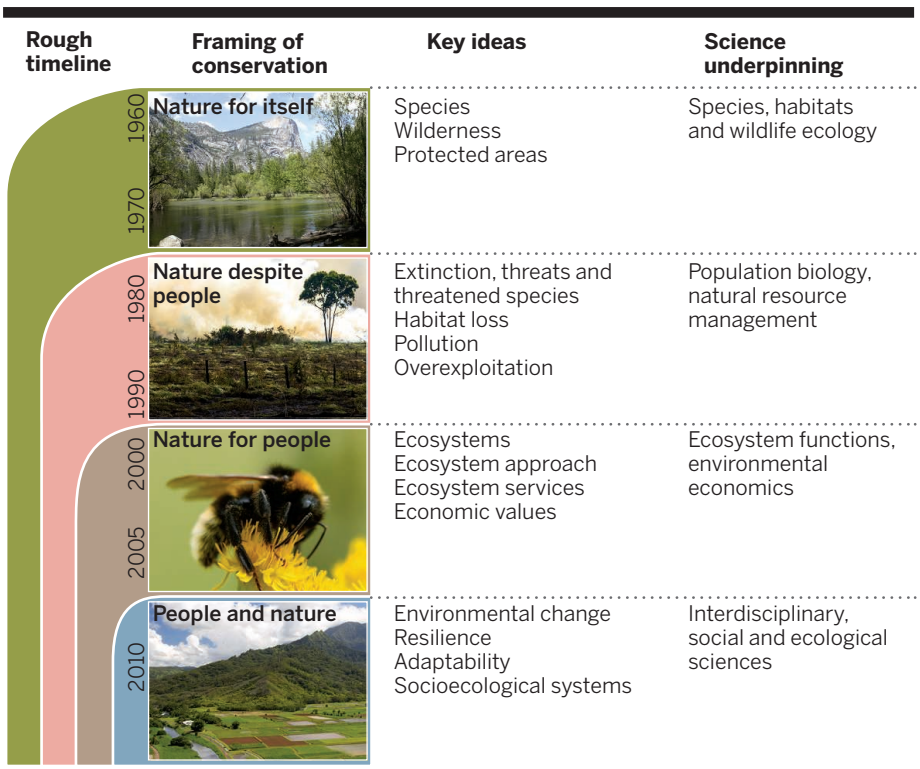

Changing views of nature and conservation. Over the past 50 years, the prevailing view of conservation has changed several times, resulting, for example, in a shift in emphasis from species to ecosystems. None of the framings has been eclipsed as new ones have emerged, resulting in multiple framings in use today.

Centre for Biodiversity and Environment Research, Department of Genetics, Evolution and Environment, University College London, London WC1E 6BT, UK. E-mail: g.mace@ucl.ac.uk

PHOTOS: THINKSTOCK/GETTYIMAGES

Published by AAAS

and a long-term commitment is required to restore or recover them.

A third implication of the multiple framings concerns the role of valuation. Most environmental decisions are made on the basis of economic arguments that consider costs and benefits, usually based on monetary values. By not having good metrics or by rejecting the idea of valuation in principle (*20*) because of its stark formulation in a "nature for people" framing, conservationists may cause nature to be excluded from such decisions. If the benefits provided by nature are assigned no value, they are treated as having no value, and current trends in the decline and deterioration of natural systems will continue.

The differences among the framings are not as stark as they appear. Despite its strong focus on humans, "people and nature" may actually be very similar to "nature for itself." Both framings can include people's hopes and desires about the environment that they wish to live in and leave to their descendants. "People and nature" has traction with other societal needs from the environment and connects better to policy because it has a broader focus. Yet there is a risk that any implementation of "people and nature" will lack the analytical foundations that made the earlier framings both deliverable and measurable.

Hopefully the many important features of "people and nature" will continue to be the focus for conservation over the coming decades. By sustaining a coherent and inclusive focus and by developing the relevant science, tools and decisions should emerge that can ensure a better future for people and nature. ■

REFERENCES

1. M. E. Soulé, *Bioscience* **35**, 727 (1985).
2. K. H. Redford *et al.*, *Conserv. Biol.* **27**, 437 (2013).
3. W. M. Adams, *Against Extinction: The Story of Conservation* (Earthscan, London, 2004).
4. J. Hutton *et al.*, *Forum Dev. Stud.* **32**, 341 (2005).
5. S. L. Pimm, G. J. Russell, J. L. Gittleman, T. M. Brooks, *Science* **269**, 347 (1995).
6. G. C. Daily, *Nature's Services: Societal Dependence on Natural Ecosystems* (Island, Washington, DC, 1997).
7. R. Costanza *et al.*, *Nature* **387**, 253 (1997).
8. A. Balmford *et al.*, *Science* **297**, 950 (2002).
9. R. K. Turner, G. C. Daily, *Environ. Resour. Econ.* **39**, 25 (2008).
10. Millennium Ecosystem Assessment, *Ecosystems and Human Well-Being: Synthesis* (World Resources Institute, Washington, DC, 2005).
11. K. H. Redford, W. M. Adams, *Conserv. Biol.* **23**, 785 (2009).
12. S. R. Carpenter *et al.*, *Proc. Natl. Acad. Sci. U.S.A.* **106**, 1305 (2009).
13. E. Ostrom, *Science* **325**, 419 (2009).
14. M. Soule, *Conserv. Biol.* **28**, 637 (2014).
15. S. H. M. Butchart *et al.*, *Science* **328**, 1164 (2010).
16. B. Fisher *et al.*, *Ecol. Appl.* **18**, 2050 (2008).
17. B. J. Cardinale *et al.*, *Nature* **486**, 59 (2012).
18. G. M. Mace *et al.*, *Trends Ecol. Evol.* **27**, 19 (2012).
19. *UN Convention on Biological Diversity: Strategic Plan for Biodiversity 2011–2020* (Montreal, 2010).
20. D. J. McCauley, *Nature* **443**, 27 (2006).

10.1126/science.1254704

IMMUNOLOGY

Autoimmunity by haploinsufficiency

Partial deficiency in the protein CTLA4 underlies severe autoimmune disease with incomplete penetrance

By **Frédéric Rieux-Laucat**[1,2] *and* **Jean-Laurent Casanova**[2,3,4,5]

Autoimmunity arises from self-reactive T and/or B lymphocytes, and underlies a wide range of conditions, from endocrine disorders to blood cytopenias. Genetic epidemiological studies have long suggested that many autoimmune conditions have an inherited component. Autoimmunity is often described as having polygenic or complex inheritance. However, both descriptions are too general to adequately describe the considerable heterogeneity in patients and conditions. Spectacular progress in the genetic dissection of autoimmunity has come from Mendelian studies of young patients with rare, distinctive conditions. Less has been learned from population-based, genome-wide association studies of more common, clinically less homogeneous conditions. The three best-characterized monogenic autoimmune disorders are autoimmune polyendocrinopathy syndrome type 1, X-linked immunoproliferative enteropathy, and autoimmune lymphoproliferative syndrome (*1*). On page 1623 of this issue, Kuehn *et al.* (*2*) add to this list. Patients with only one functional copy of the gene encoding cytotoxic T lymphocyte antigen 4 (CTLA4) suffer from severe autoimmunity. These heterozygous mutations result in a new phenotype, with infiltration of nonlymphoid organs, such as the intestine, lungs, and brain, by hyperactive T cells and B cells, along with more classic signs of autoimmunity.

CTLA4 is expressed on the surface of T cells. It competes with CD28 to bind B7 molecules expressed on antigen-presenting cells and its activation inhibits the proliferation of effector T cells and stimulates the suppressive functions of regulatory T cells (*3*). These effects help maintain tolerance to self-antigens, as shown by the severe autoimmunity in mice lacking both copies of the *Ctla4* gene (*4*). The physiological importance of human CTLA4 was recently highlighted by the success of treatments based on CTLA4-blocking antibodies in patients with some cancers (*5*). Kuehn *et al.* report that patients heterozygous for a loss-of-function *CTLA4* allele have a phenotype similar to that of mice homozygous for a loss-of-function *Ctla4* allele, whereas heterozygous mice have no detectable phenotype (*2*, *4*). Moreover, autosomal dominant *CTLA4* deficiency displayed incomplete penetrance, as some heterozygous individuals were asymptomatic. This illustrates the similarities and differences between the small number of inbred mouse strains studied in experimental conditions and the large numbers of outbred human kindreds observed in natural conditions (*6*).

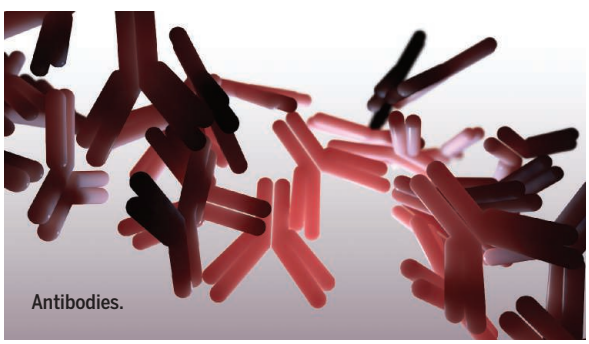

Antibodies.

Since the identification of mutations in the *ADA* gene encoding adenine deaminase as causal for severe combined immunodeficiency in 1985 (*7*), the genetic basis of more than 250 inborn errors of immunity has been determined. Studies initially focused on the conditions underlying severe infections described in the 1950s, but then shifted to the analysis of inherited forms and combinations of infection, allergy, autoinflammation, and autoimmunity (*8*).

The field of primary immunodeficiencies has also diversified considerably in terms of the modes of inheritance. The autosomal dominant pattern of inheritance is common to only about 50 immunological conditions, most of which have been discovered in the past decade. Even more unusual is the underlying mechanism of haploinsufficiency, which was first reported in 1989 for a condition called angioedema (*9*). Haploinsuf-

ILLUSTRATION: V. ALTOUNIAN/*SCIENCE*

Published by AAAS

Autosomal dominant inborn errors of immunity (haploinsufficiency)

GENE	CONDITION	PENETRANCE	DE NOVO
C1INH	Angioedema	High	Yes
CFH	HUS, glomerulonephritis, AMD	High	Yes
TERC	Dyskeratosis congenita, bone marrow failure	High	Yes
CD46	HUS	High	Yes
CFI	HUS, glomerulonephritis, AMD	High	Yes
CHD7	CHARGE syndrome and T cell immunodeficiency	**Complete**	Yes
FAS	Autoimmunity and lymphoproliferative syndrome	Intermediate*	Yes
TERT	Dyskeratosis congenita, bone marrow failure	High	No
NLRP12	Periodic fever syndrome	Complete?†	No†
GATA2	Myeloid disorders, deafness, lymphedema	High	Yes
TBK1	Herpes simplex encephalitis	Intermediate†	No†
IFNGR2	Mendelian susceptibility to mycobacterial disease	Low	No
RPSA	Isolated congenital asplenia	**Complete**	Yes
CTLA4	Autoimmunity	Intermediate	No

Autosomal dominant inborn errors of immunity for which a negative dominance was either experimentally shown or not tested were excluded. Incomplete penetrance is somewhat arbitrarily divided into low, intermediate, and high penetrance. HUS, hemolytic and uremic syndrome; AMD, age-related macular degeneration.

*Penetrant in the presence of a somatic lesion on the other *FAS* locus. †Too few kindreds to draw firm conclusions.

ficiency is defined by the occurrence of a phenotype in heterozygotes despite the lack of negative dominance of the mutant allele over its wild-type counterpart. This is less common than in other fields of human genetics and to our knowledge, only 14 inborn errors of immunity have been confirmed as autosomal dominant by haploinsufficiency. Some of them, such as isolated congenital asplenia (*10*), are actually not typical, hematopoietic-lineage restricted inborn errors of immunity.

Penetrance is incomplete for at least 11 of the 14 autosomal dominant immunological conditions involving haploinsufficiency (see the table). Indeed, haploinsufficiency favors incomplete penetrance more so than dominant negative mutations, given the predicted 50% residual function of the gene product. To date, only the mutations in chromodomain helicase DNA binding protein 7 (CHD7) and ribosomal protein SA (RPSA), which underlie the haploinsufficiency autoimmune disorders called CHARGE syndrome and isolated congental asplenia, respectively, have been convincingly shown to display complete penetrance, but even then, sometimes in association with marked variations in expression (*CHD7*). The observed proportion of de novo mutations (those that arise in a patient's parental germ cell) increases with both the degree of penetrance and the impact of the phenotype on reproduction.

So, what accounts for the incomplete penetrance of CTLA4 haploinsufficiency? Modifier genes as well as environmental factors may be involved. Somatic events may also play an important role, as already shown for haploinsufficiency in FAS, a protein that triggers cell death in activated T and B cells. Surprisingly, somatic *FAS* mutations alone can underlie a condition that is phenotypically similar to autoimmune lymphoproliferative syndrome, which is often caused by germline *FAS* mutations (*11*–*13*). Even more surprisingly, somatic mutations of the second *FAS* allele, or somatic uniparental isodisomy of large regions encompassing the second *FAS* allele (a person harbors two copies of a chromosome segment from one parent only as a result of duplication-deletion events in somatic cells), have been found in symptomatic individuals with autosomal dominant FAS deficiency by haploinsufficiency, but not in those without symptoms (*14*). This suggests that most, if not all, individuals truly heterozygous for a single loss-of-function, nondominant negative mutation of *FAS* require a second, somatic *FAS* lesion for expression of the disease. Somatic variants of *CTLA4*, or of other genes, may also influence the penetrance of autosomal dominant CTLA4 deficiency.

Incomplete penetrance does not imply the absence of a causal relationship between the *CTLA4* genotype and the autoimmune phenotype. On the contrary, it suggests that more common forms of autoimmunity may consist of a myriad of rare monogenic lesions driving disease by haploinsufficiency and with incomplete penetrance. Instead of a polygenic theory of autoimmunity that involves multiple common alleles in an individual patient, we can consider a monogenic theory of autoimmunity, with high locus and allelic heterogeneity at the population level (*15*). Heterozygous, haploinsufficient variants would play an important role in this scenario, given that they account for a higher proportion of variants and have a lower penetrance than dominant negative variants. Of course, monoallelic lesions are more common and less penetrant than biallelic lesions. This would be consistent with the non-Mendelian pattern of inheritance observed for most autoimmune diseases in most families. A condition with strict Mendelian inheritance, as defined by complete penetrance of a monogenic lesion in all genetic backgrounds, is more an exception than a rule, as humans are not single-gene organisms protected against somatic changes and environmental pressure. Although rarely Mendelian, autoimmunity in the general population may therefore often be monogenic—that is, polygenic with a single pilot, one or more co-pilots, and many passengers. Fortunately, a monogenic architecture of autoimmunity would be amenable to in-depth experimental investigation. Causal relationships that are proposed without a clear demonstration of the underlying mechanisms rarely stand the test of time. ■

[1]*Laboratory of Immunogenetics of Pediatric Autoimmunity, INSERM UMR 1163, Necker Hospital for Sick Children, Paris, France.* [2]*Paris Descartes Sorbonne Paris Cité University, Imagine Institute, Paris, France.* [3]*Laboratory of Human Genetics of Infectious Diseases, INSERM UMR 1163, Imagine Institute, Necker Hospital for Sick Children, Paris, France.* [4]*Pediatric Hematology and Immunology Unit, Necker Hospital for Sick Children, AP-HP, Paris, France.* [5]*Howard Hughes Medical Institute and St. Giles Laboratory of Human Genetics of Infectious Diseases, The Rockefeller University, New York, NY 10065, USA. E-mail: jean-laurent.casanova@rockefeller.edu*

REFERENCES

1. M. H. Cheng, M. S. Anderson, *Annu. Rev. Immunol.* **30**, 393 (2012).
2. H. S. Kuehn *et al.*, *Science* **345**, 1623 (2014).
3. M. F. Krummel, J. P. Allison, *J. Exp. Med.* **182**, 495 (1995)
4. P. Waterhouse *et al.*, *Science* **270**, 985 (1995).
5. X. Fan, S. A. Quezada, M. A. Sepulveda, P. Sharma, J. P. Allison, *J. Exp. Med.* **211**, 715 (2014).
6. J. L. Casanova, L. Abel, L. Quintana-Murci, *Cold Spring Harb. Symp. Quant. Biol.* **78**, 157 (2013).
7. D. T. Bonthron, A. F. Markham, D. Ginsburg, S. H. Orkin, *J. Clin. Invest.* **76**, 894 (1985).
8. J. L. Casanova, L. Abel, *Science* **317**, 617 (2007).
9. T. Ariga *et al.*, *J. Clin. Invest.* **83**, 1888 (1989).
10. A. Bolze *et al.*, *Science* **340**, 976 (2013).
11. F. Rieux-Laucat *et al.*, *Science* **268**, 1347 (1995).
12. G. H. Fisher *et al.*, *Cell* **81**, 935 (1995).
13. E. Holzelova *et al.*, *N. Engl. J. Med.* **351**, 1409 (2004).
14. A. Magerus-Chatinet *et al.*, *J. Clin. Invest.* **121**, 106 (2011).
15. J. K. Pritchard, *Am. J. Hum. Genet.* **69**, 124 (2001).

10.1126/science.1260791

Published by AAAS

The human cost of rabies. Having not received post-exposure prophylaxis after a dog bite, a 16-year-old boy suffers the terrifying symptoms of rabies.

CREDIT: MYANMAR-ROHINGYA/REUTERS/DAMIR SAGOLJ

INFECTIOUS DISEASE

Implementing Pasteur's vision for rabies elimination

Human and veterinary health systems must be better integrated if rabies is to be controlled

By **Felix Lankester**,[1,2,3]* **Katie Hampson**,[3] **Tiziana Lembo**,[3] **Guy Palmer**,[1,2] **Louise Taylor**,[4] **Sarah Cleaveland**[2,3]

POLICY

It has been 129 years since Louis Pasteur's experimental protocol saved the life of a child mauled by a rabid dog, despite incomplete understanding of the etiology or mechanisms by which the miracle cure worked (*1*). The disease has since been well understood, and highly effective vaccines are available, yet Pasteur's vision for ridding the world of rabies has not been realized. Rabies remains a threat to half the world's population and kills more than 69,000 people each year, most of them children (*2*). We discuss the basis for this neglect and present evidence supporting the feasibility of eliminating canine-mediated rabies and the required policy actions.

A NEGLECTED PRIORITY. Because of effective control of rabies in domestic dogs, it is no longer a disease of major concern in developed countries. In 2013, the one person diagnosed with rabies in the United States, which was predictably fatal, acquired the infection in Guatemala. In Western Europe no cases were reported in 2013; the one person who died of canine-mediated rabies in 2012 was bitten by a dog in India. With more than 95% of human cases occurring in Africa and Asia (*3*), largely in rural and impoverished communities, rabies threatens the world's most marginalized people (see the first photo). Even in low-income countries, those from more affluent areas rarely die of rabies, as they are likely to promptly access highly effective post-exposure prophylaxis (PEP). It is the poor who die; they are more frequently victims of rabid dog attacks, they suffer fatal delays in trying to access PEP, or simply cannot afford to pay for it (*4*).

Despite recent developments of simple, rapid, and highly accurate diagnostic methods (*5*), underdiagnosis and underreporting contribute to rabies neglect. The true incidence of human rabies in Asia and Africa is estimated to be between 20 and 160 times what is officially reported (*3*). The reasons for this are common among neglected diseases in low-income countries: The afflicted often do not reach medical facilities (*4*, *6*) so are never recorded. For those who attend a medical facility, the similarity of rabies symptoms to other neurologic conditions, including cerebral malaria (*7*), renders clinical diagnosis without laboratory support challenging. Even where laboratory facilities exist, diagnostic samples are rarely collected, and where a clinical diagnosis is made, many cases are not reported to national or international authorities.

Coupled with this structural underdiagnosis and underreporting is the current approach to prioritizing disease interventions. Predominant disease burden metrics, such as disability-adjusted live years (DALYs), are important in focusing research and intervention agendas. However, decisions should also take into account the availability and effectiveness of control interventions and their implementation cost. For rabies, although a DALY score of 1.74 million lost per year is low compared with HIV, malaria, or tuberculosis, highly effective animal vaccines are available to control and eliminate disease in animal reservoirs and to prevent human deaths for a price considered highly cost-effective (*8*, *9*).

Although global concerns relating to avian influenza have helped bridge medical and veterinary disciplines, a responsibility gap remains for zoonotic diseases not considered a global threat. For rabies, prevention through dog vaccination is the province of veterinary medicine, whereas PEP is the responsibility of physicians and nurses. Budgets to address rabies are rarely considered jointly, which results in ever-increasing PEP costs if the disease is not tackled at the animal source. As rabies does not cause a high burden of disease in livestock, compared with many economically important transboundary livestock diseases, dog vaccination has not been prioritized by veterinary services in low-income countries. However, if viewed more broadly as a societal burden, rather than by using a single health or economic metric, the impact of rabies and priority for its control is substantially elevated (*2*, *8*).

A One Health approach, integrating medical and veterinary sectors, is important both to develop appropriate metrics for evaluating the disease burden, and to ensure shared operational responsibility for zoonosis control and prevention. Although international funding can facilitate this coordination (as shown for avian influenza), the most critical requirements are political commitment and building of trust and effective communication between sectors, which need not be prohibitively costly. Establishment of an effective interministerial Zoonotic Disease Unit in Kenya, which has rapidly developed

Downloaded from www.sciencemag.org on September 26, 2014

Published by AAAS

integrated national plans for rabies control and elimination, provides a recent example of One Health coordination involving not only health and veterinary sectors but also wildlife services concerned with the threat that rabies poses to endangered wildlife.

ELIMINATION IS ACHIEVABLE. Although rabies virus is a multihost pathogen, the domestic dog remains the principal reservoir and source of human rabies. The basic reproductive number for rabies (R_0, the average number of new cases generated by a single case) is consistently low ($R_0 < 2$) in dog populations worldwide, despite wide variations in population density (*10*). This suggests that transmission can be relatively easily interrupted through mass dog vaccination (see the chart). In contrast, although reducing dog density has been the first response to many rabies outbreaks (*11*), it has never been successful (*12*).

A growing body of evidence from Central and South America and pilot projects in Southeast Asia and Africa demonstrate the effectiveness of dog vaccination for preventing human rabies in both high- and low-income countries (*13*). Annual vaccination coverage of 70% controls and eventually eliminates the disease (see the second photo) (*10*).

Despite misperceptions of large "stray" dog populations, a high proportion of dogs are accessible for highly efficacious parenteral vaccination campaigns (*14*). Less than 11% of the dog population has been identified as ownerless in Zimbabwe, Chad, Tanzania, and South Africa (*15*). In densely populated Asian settings, where community dogs are common, techniques for vaccinating free-roaming dogs have been successfully applied (*11*).

Studies of rabies epidemiology in the Serengeti National Park in Tanzania and the surrounding communities demonstrate that domestic dogs, not wildlife, drive rabies transmission dynamics (*16*). Where dog rabies has been locally eliminated, the disease disappears in all species (*15*). This generates confidence that control of canine rabies is epidemiologically achievable and that large-scale elimination is a realistic goal. This has been demonstrated by the reduction in canine rabies by around 99% across Latin America, with elimination targets for the region set for 2015 (*17*).

Is elimination of canine rabies economically feasible? Empirical and theoretical studies of mass dog vaccination campaigns in low-income countries reveal that vaccinating dogs against rabies is cost-effective up to the critical 70% vaccination coverage threshold (*9*), is significantly less expensive over the long-term than providing PEP to bite victims, and can result in substantial savings to the public health sector (*8*, *9*, *18*). These savings will be particularly relevant in Asia, where currently 90% of global PEP is administered (*2*, *3*). To realize these savings, initial external financing may be needed to support investments in dog vaccination. However, to ensure sustainability, financing strategies need to involve governments and to have flexibility to encourage community engagement and to exploit new approaches to enhance cost-effectiveness, such as linking dog vaccination with other health-delivery platforms.

ACROSS DISCIPLINES AND BORDERS. The only infectious diseases deliberately eradicated worldwide, smallpox and rinderpest, were within the exclusive domains of human and veterinary medicine, respectively. Eliminating canine rabies as a public health burden will require a One Health approach integrated across sectors. This has proven much easier to advocate in theory than to achieve in practice. Many low-income countries face a considerable challenge in coordinating and integrating activities across decentralized and fragmented veterinary and health care systems. This is exacerbated by a lack of linked regulatory policies.

Although growing scientific evidence is addressing misperceptions about canine rabies epidemiology and control, progress in many countries is still hampered by lack of political commitment and financing mechanisms. Pilot projects in Africa and Asia, which have supported initial investments in dog rabies control, demonstrate the power of catalytic funding to achieve operational progress, and allow veterinary and health

Effect of dog vaccination on rabies and cost

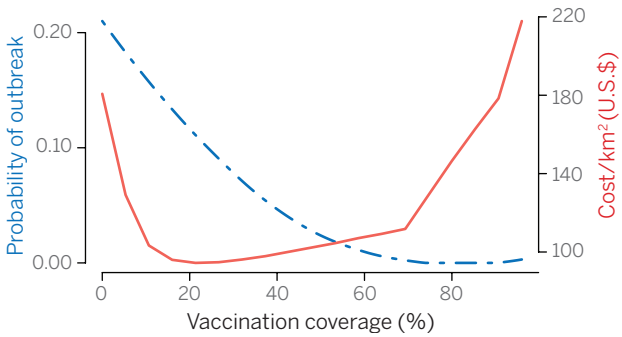

Impact of dog vaccination coverage on rabies outbreak probability and cost. The left axis and the dashed blue line show the probability of an outbreak of 10 or more cases being seeded by an introduced case under different levels of vaccination coverage. The right axis and solid red line indicate the total costs (U.S.$) per km² of rabies control with increasing vaccination coverage. Vaccination coverage of 70% of the canine population reduces outbreak probability close to zero and is cost-effective. Cost data from (*9*), probability data from (*10*).

A mass dog rabies vaccination clinic in Tanzania. This makeshift clinic was set up by the Serengeti Health Initiative.

PHOTO: FELIX LANKESTER

[1]Paul G. Allen School for Global Animal Health, Washington State University, Pullman, WA 99164, USA. [2]School of Life Sciences and Bioengineering, Nelson Mandela African Institution of Science and Technology, Arusha, Tanzania. [3]Boyd Orr Centre for Population and Ecosystem Health, Institute of Biodiversity, Animal Health and Comparative Medicine, University of Glasgow, Glasgow G12 8QQ, UK. [4]Global Alliance for Rabies Control, Manhattan, KS 66502, USA. *E-mail: lankesterf@vetmed.wsu.edu

Published by AAAS

services to move away from short-term or emergency responses toward a more coordinated and proactive program of disease prevention and control. Work is needed to determine how best to scale up from such pilot studies to the national and regional programs that will be needed for eventual elimination. International human and animal health organizations can play an important support role, for example, establishing mechanisms to ensure the affordable supply of human and animal vaccines and their effective cross-sectoral use.

An enduring challenge for global elimination is the ability to work effectively across national boundaries. This has been achieved successfully in the Americas through the REDIPRA network (Directors of National Rabies Control Programs), with specific budgets for cross-border control and the transparent sharing of surveillance and budgetary information resulting in a collective commitment to a public good, as well as constructive peer pressure. Newer regional rabies networks in Asia and Africa could develop along the same lines. Successful rabies control programs in KwaZulu-Natal, South Africa, supported through pilot funding, have resulted in transboundary networks and initiatives in neighboring countries. Initial success provides momentum for further success.

Canine rabies elimination meets all the criteria for a global health priority: It is epidemiologically and logistically feasible, cost-effective, and socially equitable. Pasteur's vision is within our reach—we only need to move the hand forward to grasp it. ■

REFERENCES AND NOTES

1. G. Geison, *The Private Science of Louis Pasteur* (Princeton Univ. Press, Princeton, NJ, 1995).
2. S. Shwiff *et al.*, *Antiviral Res.* **98**, 352 (2013).
3. D. L. Knobel *et al.*, *Bull. World Health Organ.* **83**, 360 (2005).
4. K. Hampson *et al.*, *PLOS Negl. Dis.* **2**, e339 (2008).
5. T. Lembo *et al.*, *Emerg. Infect. Dis.* **12**, 310 (2006).
6. W. Suraweera *et al.*; Million Death Study Collaborators, *PLOS Negl. Trop. Dis.* **6**, e1847 (2012).
7. M. Mallewa *et al.*, *Emerg. Infect. Dis.* **13**, 136 (2007).
8. J. Zinsstag *et al.*, *Proc. Natl. Acad. Sci. U.S.A.* **106**, 14996 (2009).
9. M. C. Fitzpatrick *et al.*, *Ann. Intern. Med.* **160**, 91 (2014).
10. K. Hampson *et al.*, *PLOS Biol.* **7**, e53 (2009).
11. A. A. G. Putra *et al.*, *Emerg. Infect. Dis.* **19**, 648 (2013).
12. M. K. Morters *et al.*, *J. Anim. Ecol.* **82**, 6 (2013).
13. T. Lembo *et al.*, *Dogs, Zoonoses, and Public Health*, C. N. L. Macpherson, F.-X. Meslin, A. I. Wandeler, Eds. (CAB International, Wallingford, UK, ed. 2, 2013), pp. 205–258.
14. S. L. Davlin, H. M. Vonville, *Vaccine* **30**, 3492 (2012).
15. T. Lembo *et al.*, *PLOS Negl. Trop. Dis.* **4**, e626 (2010).
16. T. Lembo *et al.*, *J. Appl. Ecol.* **45**, 1246 (2008).
17. M. A. Vigilato *et al.*, *Philos. Trans. R. Soc. Lond. B Biol. Sci.* **368**, 20120143 (2013).
18. S. E. Townsend *et al.*, *PLOS Negl. Trop. Dis.* **7**, e2372 (2013).

ACKNOWLEDGMENTS

K.H. is supported by the Wellcome Trust (095787/Z/11/Z), and L.T. by the UBS Optimus Foundation. Opinions, findings, conclusions, and recommendations are those of the authors and do not necessarily reflect the views of the supporting institutions.

10.1126/science.1256306

CHEMISTRY

Water's place in Au catalysis

Water plays a key role in gold-catalyzed CO oxidation

By **Gregory M. Mullen**[1] *and* **C. Buddie Mullins**[1,2]

The discovery of highly active gold catalysts for CO oxidation ($CO + \frac{1}{2}O_2 \rightarrow CO_2$) about 25 years ago (*1*) ignited substantial interest in the use of gold as a catalyst. Yet, this seemingly simple reaction has proven to be quite complicated. No consensus exists regarding the mechanism by which gold catalyzes CO oxidation. Confounding the understanding of this process was the discovery that incorporation of minute quantities of water in the reactant feed stream can increase catalytic activity by up to several orders of magnitude (*2*). Many conflicting reports have been proposed for the role of water in the CO oxidation reaction. On page 1599 of this issue, Saavedra *et al.* (*3*) present a compelling mechanism that ties together the conclusions of many of these reports.

There are two key questions regarding water-enhanced CO oxidation on gold catalysts. Does water enhance the reaction by promoting the decomposition of surface intermediates or by assisting in the activation of reactants? And is the active site of the catalyst associated with the gold particle surface or the gold-support interface?

A few reports have suggested that incorporation of water into the feed stream for CO oxidation promotes the decomposition of surface intermediates (*4*, *5*). Such an effect could reduce catalyst deactivation, leading to enhanced activity. For example, hydroxyl groups located on the supporting material near the gold-support interface may abstract hydrogen from a reactive intermediate on the gold surface, resulting in the formation of water and a more stable intermediate that blocks the active site (*4*). Inclusion of water in the feed stream would reverse this process by driving equilibrium toward regeneration of the hydroxyl groups on the support and the less stable intermediate.

Alternatively, water may assist in the activation of reactant species on the catalyst surface. A number of potential active sites and mechanisms exist for this type of process. Studies have proposed that hydroxyl species produced by interactions between water and the gold surface or the gold-support interface can oxidize CO, enhancing catalytic activity relative to the hydroxyl-free surface (*6*–*9*). Different authors have pointed to either cationic gold (*6*, *7*) or metallic gold (*8*, *9*) taking part in this activation process. Others have proposed that the generation of a hydroperoxyl-like surface intermediate via the interaction of water with O_2 on the surface of the gold particle may facilitate CO oxidation (*10*, *11*).

The diversity of proposed active sites and mechanisms has done little to resolve the debate surrounding water-enhanced CO oxidation. Rather than becoming clearer over time, many aspects of this process have become more perplexing.

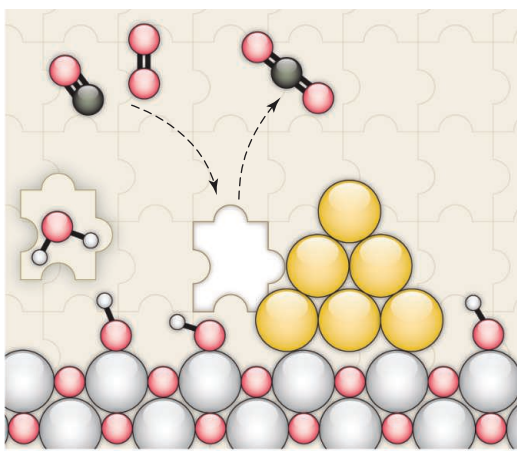

Where water fits in. Many ideas have been proposed for the role of water in gold-catalyzed CO oxidation. The results reported by Saavedra *et al.* indicate that water adsorbed at the gold-support interface plays a key role in this process.

Saavedra *et al.* explored the water-enhanced CO oxidation reaction on a titania-supported gold catalyst. This system has been very well studied, but the authors were nevertheless able to make novel observations with a relatively simple technique. They controlled the amount of water on the catalyst surface by gently drying the material while monitoring adsorbed water and hydroxyl species with infrared (IR) spectroscopy. Removal of weakly adsorbed water from the surface resulted in a substantial decrease in activity for CO oxidation. Furthermore, the authors observed a large kinetic isotope ef-

[1]*McKetta Department of Chemical Engineering, University of Texas at Austin, Austin, TX 78712, USA.* [2]*Department of Chemistry, University of Texas at Austin, Austin, TX 78712, USA. E-mail: mullins@che.utexas.edu*

ILLUSTRATION: P. HUEY/*SCIENCE*

Published by AAAS

fect when H_2O on the catalyst surface was replaced by D_2O, suggesting that cleavage of the O-H or O-D bond is a critical step in the reaction mechanism. These observations indicate that water plays a direct role in the CO oxidation reaction (see the figure).

Saavedra *et al.* supported their experimental results with a comprehensive density functional theory (DFT) investigation. Based on the evidence from the IR spectra, their DFT model incorporates adsorbed water and hydroxyl groups associated with the support. The results show that adsorbed water at the gold-titania interface helps activate O_2 at a very low energetic cost—so low, that the process occurs spontaneously at low temperatures. This is a very surprising revelation given the high energy barriers that gold surfaces display toward O_2 activation. In the authors' model, the most kinetically important step is instead associated with decomposition of a reactive intermediate via proton transfer to water, in agreement with their experimental observations.

In Saavedra *et al.*'s mechanism, hydroperoxyl and hydroxyl species are involved in the water-enhanced CO oxidation reaction. Hydroxyl species associated with both the support and the gold surface play roles in the process. Furthermore, water helps to both activate O_2 and decompose reactive intermediates associated with CO_2 generation. This mechanism not only ties together observations made in several previous studies of the water-enhanced CO oxidation reaction but also lends credence to many seemingly conflicting claims.

Water plays a key role in a number of other reactions carried out on gold catalysts (*12*). By elucidating the role of water in CO oxidation, the study by Saavedra *et al.* may prove key to solving many of the puzzles of gold catalysis. ■

REFERENCES AND NOTES

1. M. Haruta *et al.*, *J. Catal.* **115**, 301 (1989).
2. M. Daté, M. Okumura, S. Tsubota, M. Haruta, *Angew. Chem. Int. Ed.* **43**, 2129 (2004).
3. J. Saavedra *et al.*, *Science* **345**, 1599 (2014).
4. C. K. Costello *et al.*, *Appl. Catal. A Gen.* **243**, 15 (2003).
5. M. M. Schubert, A. Venugopal, M. J. Kahlich, V. Plzak, R. J. Behm, *J. Catal.* **222**, 32 (2004).
6. G. C. Bond, D. T. Thompson, *Gold Bull.* **33**, 41 (2000).
7. H. H. Kung *et al.*, *J. Catal.* **216**, 425 (2003).
8. W. C. Ketchie, Y. Fang, M. Wong, M. Murayama, R. Davis, *J. Catal.* **250**, 94 (2007).
9. R. A. Ojifinni *et al.*, *J. Am. Chem. Soc.* **130**, 6801 (2008).
10. M. Ojeda, B.-Z. Zhan, E. Iglesia, *J. Catal.* **285**, 92 (2012).
11. A. Bongiorno, U. Landman, *Phys. Rev. Lett.* **95**, 106102 (2005).
12. G. M. Mullen, J. Gong, T. Yan, M. Pan, C. B. Mullins, *Top. Catal.* **56**, 1499 (2013).

ACKNOWLEDGEMENTS

We gratefully acknowledge the support of the U.S. Department of Energy (DE-FG02-04ER15587) and the Welch Foundation (F-1436). G.M.M. acknowledges the NSF for a Graduate Research Fellowship.

10.1126/science.1259527

ILLUSTRATION: V. ALTOUNIAN/*SCIENCE*

Neural tube development

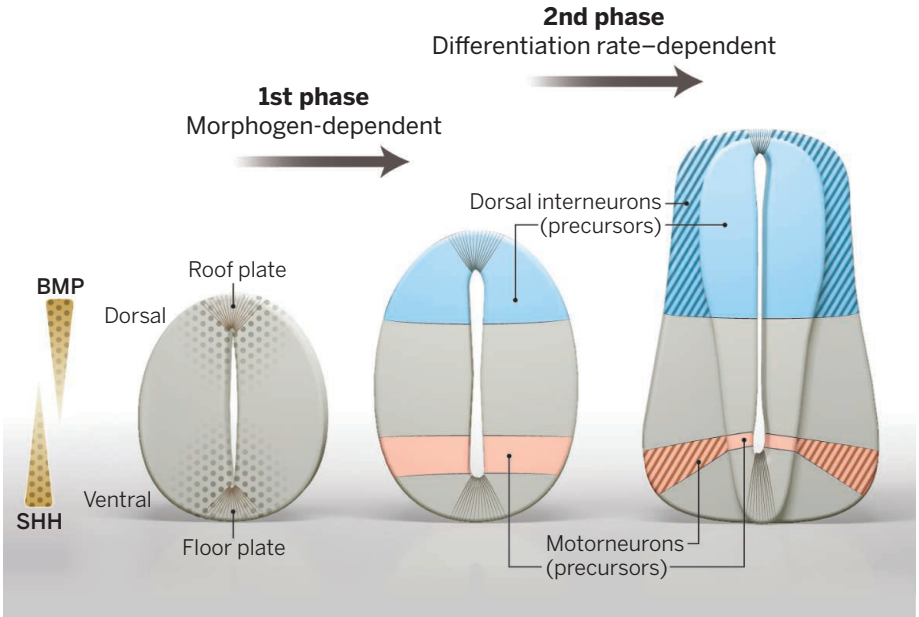

Pattern and size over time. During vertebrate neural tube development, morphogens released dorsally and ventrally specify progenitor cell territories. Growth of the progenitor pools then becomes independent of morphogen concentration and follows a differentiation program defined by transcription factors characteristic of each pool. Growth kinetics is different between each territory and is controlled by a balance between the proliferation and the differentiation rates.

DEVELOPMENTAL BIOLOGY

Managing patterns and proportions over time

Tissue patterning is specified relative to growth through differences between cell proliferation and the differentiation rates

By **Olivier Pourquie**

During vertebrate embryogenesis, new tissues are forged through the development of specific cell types in particular patterns. This patterning happens in the context of tissue growth, but how are these two phenomena coordinated? How does a tissue that changes size over time maintain the proportions of its different domains? Does patterning scale with tissue size? On page 1577 of this issue, Kicheva *et al.* (*1*) answer these long-standing questions. Their analysis of mouse and chick embryos of different sizes reveals that patterning proportions of different progenitor domains in the vertebrate neural tube—the rudiment of the spinal cord—do not scale with growing size. Instead, the authors propose a two-phase process for how tissue regions grow in register to one another, despite different growth rates.

The neural tube is initially composed of a single layer of neural progenitor cells that gives rise to all cell types of the spinal cord. These progenitors produce descendants that stop dividing and migrate to the periphery of the neural tube where they differentiate into the various types of neurons. Neurites from these neurons grow to establish the future functional circuitry, and glial cells develop and occupy specific areas of the spinal cord such as the white matter.

In response to exogenous signals provided by diffusing morphogens such as

Department of Genetics, Harvard Medical School and Department of Pathology, Brigham and Women's Hospital, 77 Avenue Louis Pasteur, Boston, MA 02115, USA. Institut de Génétique et de Biologie Moléculaire et Cellulaire, CNRS (UMR 7104), Inserm U964, Université de Strasbourg, Illkirch, F-64700, France. E-mail: pourquie@genetics.med.harvard.edu

Published by AAAS

sonic hedgehog (SHH) and bone morphogenetic protein (BMP), progenitor cells in the neural tube acquire defined identities characterized by specific transcription factors that condition the type of neurons they can produce (*2*). For example, progenitors located ventrally are exposed to higher concentrations of SHH (produced by the underlying floor plate and notochord tissues) and generate neurons, including motoneurons, that control motor output. Progenitors located dorsally are exposed to high concentrations of BMP (produced by the overlying roof plate tissue) and produce interneurons involved in processing sensory information.

Once morphogens establish the dorsoventral mosaic of precursor territories, the neural tube undergoes massive growth accompanied by an increase in total cell number. In many developmental systems where cell fate is controlled by morphogen gradients (such as the fruit fly imaginal discs), the size of precursor territories increases proportionally when the tissue grows (*3*, *4*). The situation is, however, strikingly different for the neural tube. Kicheva *et al.* show that as the tube grows, the size of its individual precursor territories changes but not in scale with overall neural tube growth. The dimensions of each progenitor pool appear to be independently controlled and follow distinct growth patterns. Remarkably, the different pools keep similar proportions between embryos of different species such as mouse and chicken.

> ***"The model overturns the idea that proportions are determined by scaling morphogen gradients."***

What controls these evolutionarily conserved growth kinetics of neural progenitor pools? The rates of cell proliferation or cell death could vary among the different progenitor territories. Alternatively, newly specified progenitors could be recruited in response to morphogen exposure, thus increasing the pool size. The rate of differentiation that controls cell exit from the progenitor territory could also vary. Kicheva *et al.* performed a thorough quantitative analysis of these three different processes in chicken and mouse embryos. They observed that progenitors in the different territories divide at the same rate and that cell death is negligible in the neural tube during early stages of development. This rules out regulation of the proliferation or cell death rates as mechanisms that control progenitor pool size.

Kicheva *et al.* also analyzed how the progenitor identity re-specification rate varies in time and demonstrate that while it changes early on, this rate rapidly falls to zero, indicating that the identity of the progenitor populations is stabilized early. Remarkably, the commitment of populations to their definitive fate appears to coincide with the peak of BMP and SHH activity in the neural tube. The key parameter that appears to vary across progenitor territories is the differentiation rate.

On the basis of these observations, Kicheva *et al.* propose a two-phase model for neural tube patterning (see the figure). In the first phase, naïve progenitor territories are specified in response to exposure to morphogens such as SHH and BMP. Subsequently, progenitors acquire their definitive identity, which is associated with a characteristic differentiation rate that is specific for each neuronal population. In the second phase, growth of the progenitor pools become largely independent of the morphogen concentration and follows a specific differentiation program imposed by the profile of transcription factors expressed by the progenitors. Growth kinetics of the various progenitor territories is then controlled by the difference between the proliferation and the differentiation rates. The model overturns the idea that proportions are determined by scaling morphogen gradients. Thus, the differentiation rate of motoneurons peaks early, leading to their precocious differentiation in the ventral horn. By contrast, the differentiation rate of interneurons peaks late, allowing the formation of a much larger compartment of progenitors that will form the dorsal interneurons.

A major challenge will be to determine what controls the differentiation rate in different progenitor populations. The signaling pathway controlled by the protein Notch, which regulates cell differentiation in the nervous system (*5*), is an interesting candidate for this role. The findings of Kicheva *et al.* may be relevant to growth dynamics in other tissues as well, and more broadly, may help to explain size variability within and between anatomical domains across species. ■

REFERENCES

1. A. Kicheva *et al.*, *Science* **345**, 1254927 (2014); 10.1126/science.1254927.
2. W. A. Alaynick, T. M. Jessell, S. L. Pfaff, *Cell* **146**, 178 (2011).
3. D. Ben-Zvi, B. Z. Shilo, A. Fainsod, N. Barkai, *Nature* **453**, 1205 (2008).
4. O. Wartlick *et al.*, *Science* **331**, 1154 (2011).
5. A. Louvi, S. Artavanis-Tsakonas, *Nat. Rev. Neurosci.* **7**, 93 (2006).

10.1126/science.1260025

CHEMISTRY

Perovskites take lead in solar hydrogen race

Earth-abundant materials show promise for solar hydrogen production

By **Thomas Hamann**

The world's growing population and industrialization result in an ever-increasing demand for energy. This poses society with a question of critical importance: Are we willing to accept the consequences of climate change linked to the combustion of fossil fuels in order to meet our energy demand? An answer of "no" requires us to quickly solve the challenging problem of developing alternative sources of energy that can replace fossil fuels. On page 1593 of this issue, Luo *et al.* (*1*) report an important step toward achieving that goal.

Sunlight is by far the most abundant energy resource; harvesting just a small fraction of 1% of available solar energy would be enough to indefinitely satisfy the world's entire energy demand (*2*). One major drawback of sunlight, however, is the daily, seasonal, and regional variability of its intensity. Thus, if solar energy is ever to be used at the scale of fossil fuels, a method to store the energy is necessary. Nature provides a great example of solar energy storage by using sunlight to oxidize water to release O_2 and reduce CO_2 to produce hydrocarbon (plant) materials. The overall (sunlight to stored energy) efficiency of photosynthesis is estimated to be only ~1%, which prevents it from being a practical fuel source on a global scale (*3*). Therefore, there has been an ongoing effort to develop artificial photosynthesis systems to convert sunlight and water directly into high-energy-density chemical fuels such as hydrogen gas, a process termed solar water splitting (*4*) (see the figure).

Any viable solar water-splitting system must satisfy four primary criteria: It needs to be efficient, cost effective, and scalable—thus composed of Earth-abundant materials—and stable enough to run for years

Published by AAAS

(*5*). So far, nobody has been able to meet all four requirements. The challenge is to adapt photovoltaic (PV) systems capable of achieving high efficiencies to drive the water-splitting reactions in a scalable fashion. One of the primary difficulties is that splitting water to H_2 and O_2 requires the application of 1.23 V (thermodynamics) plus additional overpotentials associated with driving the hydrogen evolution (HER) and oxygen evolution (OER) half reactions:

$$4H_2O + 4e^- \rightarrow 2H_2 + 4OH^- \text{ (HER)}$$
$$4OH^- \rightarrow O_2 + 4e^- + 2H_2O \text{ (OER)}$$

The HER and OER overpotentials are on the order of 0.1 and 0.3 V, respectively; thus, the overall water-splitting reaction requires a total of ~1.7 V (*6*). This voltage constrains the number of systems that are capable of achieving high solar-to-hydrogen (STH) conversion efficiencies and are not prohibitively expensive.

Mesoscopic and thin-film perovskite-based PV systems have attracted interest because they may break the cost-efficiency paradigm. They are composed entirely of Earth-abundant elements, have low-cost manufacturing processes, and are capable of achieving very high solar-to-electricity power conversion efficiencies (η). The past 2 years have seen the efficiency of methylammonium lead halide perovskite PVs advance considerably, with reported devices producing η > 15% (*7*–*9*). An important aspect of the high-power conversion efficiency is the high photovoltages that are produced.

Luo *et al.* take advantage of these high-photovoltage perovskite PVs by configuring two cells next to each other in electrical series in order to efficiently split water. Integration of solar cells in series produces a sum of the photovoltages, whereas the current from each cell is matched to the others. In this example, the two cells each produce a short-circuit current density (J_{sc}) of more than 20 mA cm^{-2}. Because the cells are situated next to each other, the current from each cell is constant, but the electrode area effectively doubles, producing half the current density (~10 mA cm^{-2}). Importantly, the open-circuit photovoltage (V_{oc}) of each cell was more than 1 V, thus providing a total of up to 2 V to drive the water-splitting reactions. Another advance reported by Luo *et al.* was the introduction of a nickel/iron–layered double hydroxide (NiFe LDH) catalyst deposited on a nickel foam electrode, which can carry out both the HER and OER reactions at 10 mA cm^{-2}, with overpotentials of 0.21 and 0.24 V, respectively.

Department of Chemistry, Michigan State University, 578 South Shaw Lane, Room 411, East Lansing, MI 48824-1322, USA. E-mail: hamann@chemistry.msu.edu

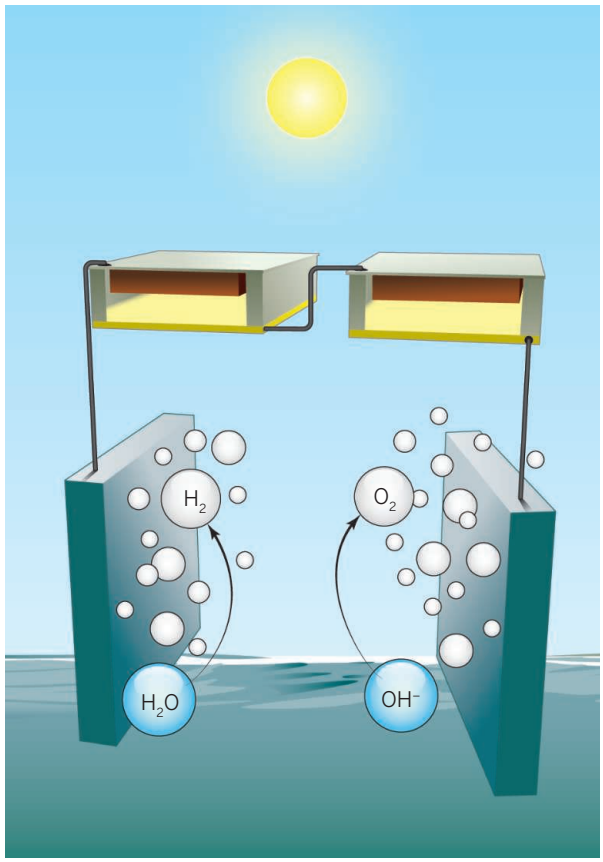

Splitting water. Luo *et al.* (*1*) show that perovskites, materials comprising Earth-abundant elements, are promising for solar hydrogen production.

As the two perovskite cells produce 10 mA cm^{-2} under a load of 1.68 V, a STH efficiency over 12% is achieved. Although the NiFe LDH catalyst is not the best at the HER reaction, the perovskites compensate with their high photovoltage, and using a single catalyst material for both HER and OER reactions offers a potential cost advantage.

While the 12% water-splitting efficiency reported is already exceptional, there are several paths to improvement. Use of a single band-gap material in a tandem configuration is not ideal, and combining a perovskite cell with a smaller band-gap semiconductor such as silicon could produce over 20% STH efficiencies (*6*). Some loss in available photovoltage by substituting a lower-voltage silicon cell for one of the high-voltage perovskite cells in order to increase the photocurrent may be compensated by the use of a better HER catalyst that requires a smaller overpotential. The NiFe LDH catalyst is also opaque and not amenable to an integrated photoelectrochemical system. It is not yet clear if alternative transparent catalysts are absolutely necessary or if the separated PV/electrolyzer configuration used here will ultimately be viable (*5*).

There are very few reports of other systems producing over 10% STH efficiencies. In one notable example, a $GaInP_2$/GaAs tandem cell with platinum catalysts achieved a 12.4% STH water-splitting efficiency (*10*). This high efficiency comes at a high manufacturing cost of the PV, however. In addition, the very rare elements indium and platinum are used, which prevent scalability. There are no previous examples of over 10% STH from systems that have used only Earth-abundant elements and been driven by potentially cheap PV. The combination of high STH efficiency with a cost-effective system composed entirely of Earth-abundant elements reported by Luo *et al.* is thus unrivaled. They have achieved three of the four necessary criteria for a practical water-splitting device. One major drawback of this system is the instability of the perovskite PVs, which results in a degradation of the photocurrent over a period of hours. The cause of the instability is not yet fully understood, and this issue clearly needs to be resolved if these perovskite PVs are ever to be commercially viable (*11*). In addition, use of appropriate protection coatings, as has recently been demonstrated for silicon solar cells, may allow use of these perovskite cells in integrated solar water-splitting systems such as the artificial leaf (*12*–*14*). It will be exciting to see if perovskites will be the first to meet all four criteria to win the solar hydrogen race and beat out fossil fuels for our energy future. ■

REFERENCES

1. J. Luo *et al.*, *Science* **346**, 1593 (2014).
2. N. S. Lewis, D. G. Nocera, *Proc. Natl. Acad. Sci. U.S.A.* **103**, 15729 (2006).
3. J. Barber, *Philos. Trans. R. Soc. A.* **365**, 1007 (2007).
4. A. J. Bard, M. A. Fox, *Acc. Chem. Res.* **28**, 141 (1995).
5. J. R. McKone, N. S. Lewis, H. B. Gray, *Chem. Mater.* **26**, 407 (2014).
6. S. Hu, C. X. Xiang, S. Haussener, A. D. Berger, N. S. Lewis, *Energy Environ. Sci.* **6**, 2984 (, 2013).
7. J. Burschka *et al.*, *Nature* **499**, 316 (2013).
8. M. M. Lee, J. Teuscher, T. Miyasaka, T. N. Murakami, H. J. Snaith, *Science* **338**, 643 (2012).
9. M. Liu, M. B. Johnston, H. J. Snaith, *Nature* **501**, 395 (2013).
10. O. Khaselev, J. A. Turner, *Science* **280**, 425 (1998).
11. T. Leijtens *et al.*, *Nat. Commun.* **4**, 2885 (2013).
12. S. Y. Reece *et al.*, *Science* **334**, 645 (2011).
13. M. J. Kenney *et al.*, *Science* **342**, 836 (2013).
14. S. Hu *et al.*, *Science* **344**, 1005 (2014).

10.1126/science.1260051

ILLUSTRATION: P. HUEY/*SCIENCE*

Published by AAAS

NITROGENASE MECHANISM

A dynamic tool for nitrogen reduction

Carbon monoxide reveals new possibilities for substrate binding in nitrogenase

By **Martin Högbom**

Even though nitrogen makes up almost 80% of the atmosphere, it is a limiting nutrient for biomass production. The low reactivity of nitrogen gas (N_2) is a result of its very strong, unpolarized triple bond. Nitrogenase is the only enzyme known that can break this bond to produce compounds such as ammonia (NH_3) for use in biosynthetic pathways. The atomic structure of this amazing system has been known for more than two decades (*1*, *2*), but the chemical mechanism of this central reaction remains unknown. In a biochemical and structural tour de force, on page 1620 of this issue, Spatzal *et al.* (*3*) report the crystal structure of carbon monoxide (CO) bound to the catalytic metal cluster of the enzyme. This work revealed an unexpected structural rearrangement of the cofactor.

The industrial equivalent of the nitrogenase reaction is the Haber-Bosch process developed during the first decades of the 20th century (*4*). In this process, N_2 is reacted with H_2 to produce NH_3. The overall reaction is energetically favorable but has a very high activation barrier. In the Haber-Bosch process, this barrier is overcome with an iron-based inorganic catalyst at high temperatures and pressures (400°C and 200 atm).

Whereas the Haber-Bosch process uses a big hammer to break the triple bond, nitrogenase uses a much more elegant and complicated catalytic tool to disassemble N_2 at ambient temperature and pressure. Enzymes commonly use transition metal ions to perform the most challenging redox reactions. Nitrogenase houses a dauntingly complicated cofactor consisting of no less than one molybdenum, seven iron, and nine sulfur ions, all beautifully organized around a central carbon. It was only a few years ago that the identity of the central atom was finally determined (*5*, *6*).

Although we know what this complicated tool does and looks like, we have not been able to understand how it functions or to obtain snapshots of it in action. A number of mechanistic proposals have been made that suggest either molybdenum or iron as the central catalytic element. Thus, even the key clue of which part of the cofactor directly interacts with the substrate has been missing (*7*). This issue is commonly studied by determining structures of the protein cofactor with various ligands bound, such as inhibitors or substrate analogs. Carbon monoxide (CO) is a particularly attractive ligand to obtain insight into nitrogenase chemistry. It is a diatomic neutral molecule that is isoelectronic with N_2. It also functions as a reversible inhibitor of N_2 reduction and can even act as a substrate and be chemically modified by the enzyme, albeit very slowly.

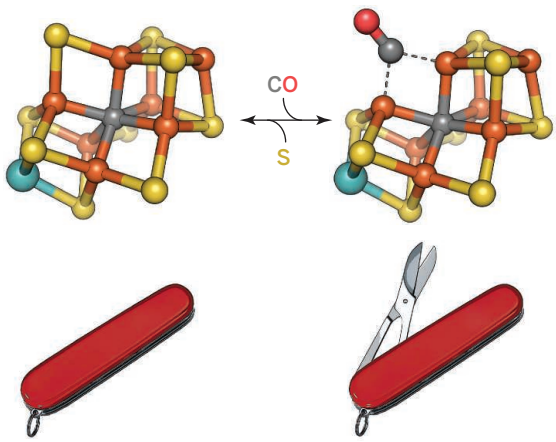

Uncovered potential. The catalytic Mo/Fe/S metal cluster of nitrogenase is shown (molybdenum in turquoise, iron in orange, carbon in gray, and sulfur in yellow). Binding of carbon monoxide rearranges the cluster, revealing new possibilities for substrate binding and reduction.

Such experiments have proven very difficult to perform. To bind any ligand, the cofactor needs to be in its reduced form. Nitrogenase will only accept its natural reductant, an oxygen-sensitive iron-sulfur protein. Also, CO will only bind to the partially reduced protein generated in a reaction mixture during enzymatic turnover, conditions opposite to the very pure protein solutions usually required for crystallization. This resulted in a wall of technical obstacles that had prevented determination of complex structures and a detailed structural understanding of the mechanism.

Spatzal *et al.* overcame these obstacles with a number of elegant procedures—for example, by succeeding to rapidly crystallize the protein directly from enzymatic reaction mixtures. The structure provided a great surprise in that CO binding actually reorganizes the cofactor structure. X-ray anomalous-scattering measurements show that one of the sulfur atoms is removed from the cluster. This vacancy opens a new binding position on the cofactor where a substrate can coordinate two iron ions simultaneously in a bridging manner. Carbon monoxide binds in this position, where it interacts with both iron ions, and it is also in close proximity to the central carbon atom of the cluster.

The direct interaction with iron indicates that there may be mechanistic similarities to the iron-catalyzed Haber-Bosch reaction. Interestingly, the di-iron bridging position also has similarities to substrate-binding modes proposed in other enzymes performing—for example, reduction of O_2 and H_2, as well as other demanding electron-transfer reactions (*8*–*12*). The rearrangement of the nitrogenase metal cluster thus reveals a new reaction surface that appears to provide possibilities for very challenging chemistry.

Together, the results suggest that the previously available picture of the cofactor actually shows a tool protected for storage rather than ready to perform its function. The mode of N_2 binding cannot be conclusively assigned, but the studies of Spatzal *et al.* establish the structurally dynamic nature of the cofactor. The study does not give a complete and final structural description of nitrogenase catalysis, but it does provide the first crack in the wall. ■

Department of Biochemistry and Biophysics, Stockholm University, SE-10691 Stockholm, Sweden. E-mail: hogbom@dbb.su.se

REFERENCES AND NOTES

1. J. Kim, D. C. Rees, *Science* **257**, 1677 (1992).
2. J. Kim, D. C. Rees, *Nature* **360**, 553 (1992).
3. T. Spatzal *et al.*, *Science* **345**, 1620 (2014).
4. V. Smil, *Enriching the Earth: Fritz Haber, Carl Bosch, and the Transformation of World Food Production* (MIT Press, Cambridge, MA, 2004).
5. K. M. Lancaster *et al.*, *Science* **334**, 974 (2011).
6. T. Spatzal *et al.*, *Science* **334**, 940 (2011).
7. B. M. Hoffman, D. Lukoyanov, Z.-Y. Yang, D. R. Dean, L. C. Seefeldt, *Chem. Rev.* **114**, 4041 (2014).
8. M. R. A. Blomberg, T. Borowski, F. Himo, R.-Z. Liao, P. E. M. Siegbahn, *Chem. Rev.* **114**, 3601 (2014).
9. M. H. Sazinsky, S. J. Lippard, *Acc. Chem. Res.* **39**, 558 (2006).
10. C. E. Tinberg, S. J. Lippard, *Acc. Chem. Res.* **44**, 280 (2011).
11. D. Lundin, A. M. A. Poole, B.-M. B. Sjöberg, M. Högbom, *J. Biol. Chem.* **287**, 20565 (2012).
12. R. H. Holm, P. Kennepohl, E. I. Solomon, *Chem. Rev.* **96**, 2239 (1996).

ACKNOWLEDGMENTS

Supported by the Swedish research council and the Knut and Alice Wallenberg Foundation.

10.1126/science.1260021

Published by AAAS

SCIENCE AND POLICY

Feeling your pain

By **Warwick Anderson**

To experience pain, whether acute or chronic, is to know the limits of communication; it is to find ordinary human expression wanting. Yet, as medical historian Keith Wailoo, shows us, that same private experience prompted eloquent professional and public debate in the United States during the late 20th century. We might struggle to articulate our own pain, but some medical and legal experts, along with leading politicians, have been quick to judge the pain of others.

"The claims made about pain and about people in pain," writes Wailoo, "were central to the ongoing battle between liberals and conservatives stretching back to World War II." He tells a compelling story of conflict between liberals sensitive to others' pain and conservatives often suspicious of others' (if not their own) assertions of pain and disability. In his telling, it is a very American story, though he leaves the impression that it might be, in fact, a generic modern tale.

Wailoo artfully uses antithesis in his description of the moral calculus of bodily suffering in American politics. Thus, he positions Bill Clinton's "feeling our pain" against Rush Limbaugh's denunciation of the phoniness of such liberal sympathy. Of course, Wailoo takes care to observe the actual complexity, even messiness, of the postwar politics of pain recognition and evaluation—even so, partisan polarity inevitably organizes his narrative. Democrats and Republicans consistently perceived different boundaries between deserving pain and undeserving fraud. "What it means to be liberal or conservative became ideologically solidified around the problem of pain," Wailoo writes. While readers will learn about the development of pain medicine in the United States during this period, the book's strength and novelty lie in its attention to the political and cultural dimensions of pain. Wailoo reveals how a private experience such as pain can be rendered as a moral calculus and translated into various partisan public programs.

In tracing the connections of personal pathology and national politics, Wailoo covers an extensive terrain. He begins with an account of political ambivalence toward pain and disability during the Eisenhower administration, when respect for disabled veterans conflicted with fears of encouraging welfare and drug dependency. The idiosyncratic character of pain frustrated the efforts of a new cadre of experts to find an objective measure for it. A more-liberal cultural environment in the 1960s emphasized instead subjective criteria in pain evaluation. Pain often became tied to claims for social recognition and demands for medical relief or government support. Ever skeptical, conservatives began to speak more loudly about learned pain, learned helplessness, and dependency. In the Reagan years, Wailoo argues, pain theories came to echo these conservative sensibilities. "Questions of which—and whose—pain mattered most and how to deal with people in pain," he notes, "continued to be socially and politically divisive." Just as 19th-century reformers might distinguish between the deserving and undeserving poor, policy-makers in the late 20th century tried to determine who suffered real pain and therefore warranted treatment or welfare. Nevertheless, efforts have never been disinterested.

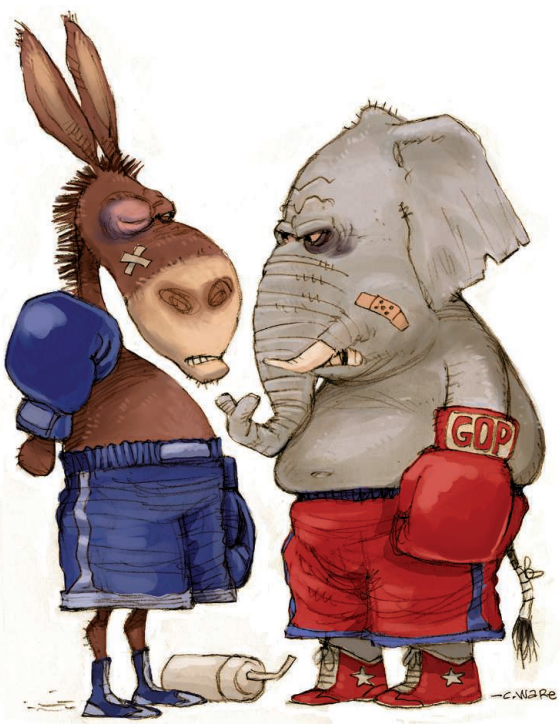

CREDIT: CHRIS WARE

Wailoo provides examples of how the race, gender, and social marginality of sufferers influenced politicians' and bureaucrats' appreciation of pain. He explains the exquisite sensitivity of some conservatives to the presumed pain of fetal innocents and their indifference to the undeniable pain of those tortured by the military. Toward the end of the book, Wailoo describes the effects of deregulating the market for pain medication at the turn of the century, which resulted in some Americans getting overmedicated with opioids and other drugs, while many of those who were more marginalized continued to receive inadequate pain relief. At this point, reenter Limbaugh, stage right. Wailoo makes much of this reactionary celebrity's secret addiction to pain medication, which sat uneasily with his supposed dismissal of the pain of others. For Wailoo, Limbaugh seems to epitomize the hypocrisy of republican virtue.

Pain: A Political History is a deeply felt and provocative history of the political uses to which pain has been put in modern America. Over the course of his distinguished career, Wailoo has moved from meticulous, somewhat inward-looking, historical studies of laboratory research toward more ambitious and politically engaged analysis of what the late Arnold Relman, editor in chief of the *New England Journal of Medicine*, called the medical-industrial complex. In this book, Wailoo mutes discussion of specialty formation, pharmaceutical development, clinical trials, and much else akin to standard medical history; instead he tells, with considerable panache, "the story of how these problems of pain and social welfare came to define American political theater." Recently, Richard Horton, editor in chief of *The Lancet*, complained that medical history has dwindled into a useless form of antiquarianism, when it should be shaping and strengthening the medical struggles of the present (*1*). Contemporary medical history, Horton believes, lacks political clout. Evidently he has not yet read this book.

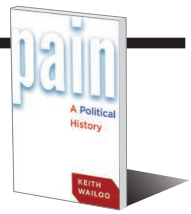

Pain
A Political History
Keith Wailoo
Johns Hopkins University Press, 2014. 292 pp.

The reviewer is at the Department of History and Centre for Values, Ethics, and the Law in Medicine, University of Sydney, SOPHI, Quadrangle A14, Sydney, NSW 2006, Australia. E-mail: warwick.anderson@sydney.edu.au

REFERENCES

1. R. Horton, *Lancet* **384**, 292 (2014).

10.1126/science.1258768

Downloaded from www.sciencemag.org on September 26, 2014

Published by AAAS

LETTERS

Edited by **Jennifer Sills**

Brazil's new laws bug collectors

TROPICAL FORESTS HARBOR diverse and largely unknown insect communities, many of which are threatened species (*1*). Habitat loss has been shown to be the primary threat to insect populations, including all threatened insect species included in the Brazilian Red List (*2*, *3*). Most threatened species reside in the Atlantic Forest, one of the most endangered biomes in Brazil (*4*). Specimen collection has never been proved to be a threat to any insect species in Brazil, and no example of overhunting affecting an insect population has been reported (*5*). Conservation efforts should concentrate on habitat conservation and restoration.

However, recent changes in Brazil's environmental laws include remission of penalties against landowners who illegally remove native vegetation. They also substantially reduce (by 29 million hectares) the areas classified as requiring restoration (*6*). Together, the new laws mean that insect collectors are charged high fines, whereas landowners receive no punishment for previous illegal deforestation. In addition to being ineffective, these actions lead to a general sense of injustice in the population; it appears that those responsible for the main environmental impacts are always forgiven.

Considering the recent debate about the importance of collecting specimens for science (*7*, *8*), Brazilian legislation should focus on the main threats to biodiversity and not on amateur or scientific insect collectors.

***Danilo Bandini Ribeiro*[1]** and *André Victor Lucci Freitas*[2]**

[1]Centro de Ciências Biológicas e da Saúde, Laboratorio de Ecologia, Universidade Federal de Mato Grosso do Sul, Campo Grande, Mato Grosso do Sul, 79070-900, Brazil. [2]Departamento de Biologia Animal, Universidade Estadual de Campinas, Campinas, São Paulo, Brazil.

*Corresponding author. E-mail: biodbr@gmail.com

REFERENCES

1. O. T. Lewis, Y. Basset, in *Insect Conservation Biology*, A. J. A. Stewart, T. R. New, O. T. Lewis, Eds, (CABI, Wallingford, UK, 2007), pp. 34–56.
2. B. M. Machado, G. M. Drummond, A. P. Paglia, *Livro Vermelho da Fauna Brasileira Ameaçada de Extinção* (Fundação Biodiversitas, Belo Horizonte, ed. 1, 2008), vol. 2.
3. K. S. Brown Jr., G. G. Brown, in *Tropical Deforestation and Species Extinction*, T. C. Whitmore, J. A. Sayer, Eds. (Chapman & Hall, London, 1992), pp. 119–142.
4. T. M. Lewinsohn, A. V. L. Freitas, P. I. Prado, *Conserv. Biol.* **19**, 640 (2005).

PHOTO: ANDRÉ VICTOR LUCCI FREITAS

Brazil's endangered butterflies are at greater risk from deforestation than from insect collecting.

5. V. L. Freitas, O. J. Marini-Filho, Eds., *Plano de Ação Nacional para Conservação dos Lepidópteros Ameaçados de Extinção* (ICMBio, Brasília, 2011).
6. B. Soares-Filho *et al.*, *Science* **344**, 363 (2014).
7. L. A. Rocha *et al.*, *Science* **344**, 814 (2014).
8. F. T. Krell, Q. D. Wheeler, *Science* **344**, 815 (2014).

Parenting: Section deserves a scolding

IN HIS NEWS STORY "An experiment in zero parenting" (special section on Parenting, 15 August, p. 752), E. Marshall wrote about the Bucharest Early Intervention Project's (BEIP's) conclusions that foster care is superior to institutional care for unparented children. He noted that the BEIP is famously a randomized design, but did not mention that it did not achieve the goal of isolation of variables. BEIP compared children from socially deprived institutional conditions with those cared for by foster parents trained, funded, and supported at levels far beyond those enjoyed by such caregivers in the United States or Britain (*1*). Having shown that it is better to be rich and healthy than poor and sick, the BEIP researchers concluded that institutions were bad for children (*2*), an inappropriate conclusion that conflicts with a recent nonrandomized study concluding that there were no clear differences between large groups of children from typical institutions and typical foster care arrangements in five low-income countries (*3*).

The Review "The biology of mammalian parenting and its effect on offspring social development" in the same special section (J. K. Rilling and L. J. Young, 15 August, p. 771) also overlooked key points. Rilling and Young described "parenting" behaviors shared by many species, but they omitted the fact that interspecies differences are so great that Harlow's famous monkey study might well have had different results if he had used a different type of monkey (*4*). They also exaggerated the associations between childhood and adult attachment security, and between attachment security and mental health. The related graphic used the ill-defined and outmoded term "parent–child bonding." The graphic also used the term "securely attached" rather than simply "attached," implying that secure attachment is an essential goal, rather than a developmental step whose outcome is not markedly different from some other forms of attachment. The Review also failed to address ongoing disagreements about whether forms of attachment should be measured as separate categories or as points on one or more continua (*5*).

Jean Mercer

Richard Stockton College, Galloway, NJ 08205, USA. E-mail: jean.mercer@stockton.edu

REFERENCES

1. C. H. Zeanah *et al.*, *Devel. Psychopathol.* **15**, 885 (2003).
2. N. A. Fox *et al.*, *Zero Three*, **34**, 4 (2013).
3. K. Whetten *et al.*, *PLOS ONE* **9**, e104872 (2014).
4. B. Seay, N. W. Gottfried, *J. Gen. Psychol.* **75**, 5 (1975).
5. C. Booth-LaForce, G. I. Roisman, Eds., Monographs of the Society for Research in Child Development, Serial No. 314 **79**, 1 (2014).

Parenting: Roots of the sweet tooth

IN HER NEWS STORY "The taste of things to come" (special section on Parenting, 15 August, p. 750), E. Underwood discussed

Downloaded from www.sciencemag.org on September 26, 2014

Published by AAAS

the flavor learning that happens during specific periods in the womb. Fetal life is also a period during which other systems and organs are vulnerable to adaptations in response to a variety of events that may happen during pregnancy (such as maternal infection, hypertension, and tobacco smoking). Most of these events impair fetal growth, affecting its metabolism and risk for diseases over the course of its life (*1*). "Programming" effects, moreover, may influence the neurobiological processes involved in reward sensitivity, impulsivity, and cue interpretation, and therefore persistently shape the individual's response to rewarding stimuli such as palatable foods.

For instance, the hedonic response to sweet taste measured in preterm newborns in their first day of life varies with the degree of their intrauterine growth restriction (IUGR) (*2*). At 3 years of age, IUGR girls are more impulsive in a task that uses a sweet treat as a reward (*3*). In addition, different studies demonstrate that individuals born with low birth weight prefer to eat foods rich in carbohydrates or fat, rather than fruits and vegetables (*4*–*7*). Given that dopamine signals the salience of the rewarding stimuli,

PHOTO: BY EVAN-AMOS (OWN WORK) [CCO], VIA WIKIMEDIA COMMONS

the fetal programming of functional variations in the mesocorticolimbic dopaminergic system facing palatable foods is putatively involved in these behavioral characteristics (*8*).

Considering that the current environment promotes the overconsumption of energy-dense, nutrient-poor food, often leading to obesity, the knowledge that some individuals may be predisposed to spontaneously prefer high-fat, high-sugar foods is relevant. It also justifies investments in prevention research and policy for supporting families and communities to nurture healthy children, considering their vulnerabilities.

André Krumel Portella[1] and Patrícia Pelufo Silveira[2]*

[1]Department of Pediatrics, Universidade Federal de Ciências Médicas de Porto Alegre, 90050-170, Brazil. [2]Department of Pediatrics, Faculty of Medicine, Universidade Federal do Rio Grande do Sul, Ramiro Barcelos, 2350, 90035-903, Porto Alegre, RS, Brazil.

*Corresponding author. E-mail: 00032386@ufrgs.br

REFERENCES

1. C. N. Hales, D. J. Barker, *Diabetologia* **35**, 595 (1992).
2. C. Ayres *et al.*, *Int. J. Pediatr.* **2012**, 657379 (2012).
3. P. P. Silveira *et al.*, *Pediatr. Res.* **71**, 293 (2012).
4. M. A. Barbieri *et al.*, *Pediatr. Res.* **65**, 215 (2009).
5. N. Kaseva *et al.*, *J. Pediatr. Us.* **163**, 43 (2013).
6. M. M. Perala *et al.*, *PLOS ONE* **7**, e46139 (2012).
7. F. Lussana *et al.*, *Am. J. Clin. Nutr.* **88**, 1648 (2008).
8. P. P. Silveira *et al.*, *Appetite* **73**, 15 (2014).

ERRATA

Erratum for the Report: "Observation of the transition state for pressure-induced $BO_3 \rightarrow BO_4$ conversion in glass" by T. Edwards, T. Endo, J. H. Walton, S. Sen, *Science* **345,** 1261201 (2014). Published online 19 September 2014; 10.1126/science. 1261201

AAAS pushes for action on climate change

By **Ginger Pinholster**

Average global temperature has increased by about 1.4°F over the last 100 years, according to a AAAS project.

PHOTO: CHRIS LINDER © WOODS HOLE OCEANOGRAPHIC INSTITUTION

With world leaders convening this week for the United Nations Climate Summit, AAAS called for decisive political action, while also ramping up communication and training activities intended to underscore the reality and urgency of human-caused climate change.

Recognizing that the global financial burden of climate change "could be truly enormous," AAAS CEO Alan I. Leshner commended "President Obama and other world leaders who have signaled their commitment to work toward a legally binding, comprehensive agreement in 2015 by participating in the U.N. Climate Summit." At press time, Leshner was also preparing to co-host a unique dialogue on the financial risks associated with a changing climate.

The 12 November event will bring together economists, policy-makers, and scientists, including Nobel Laureate Mario J. Molina, who chaired the panel that earlier this year produced the AAAS "What We Know" backgrounder on climate change. While scientists have reached consensus that climate change is already causing real physical and ecological losses, quantifying those impacts has been complicated by remaining scientific uncertainties.

Not knowing exactly "how bad the worst-case scenarios might be" has made it difficult to precisely define current and future climate-change costs, said Robert Litterman, a supporter of the "What We Know" report and Chairman of the Risk Committee at Kepos Capital LP, an asset-management firm. "This is basic risk management, but operating in difficult terrain, and clearly any attempt to quantify the appropriate policy response, will require scientists and economists working together, asking tough questions, and breaking the boundaries of their professional silos." The upcoming event, which is co-organized by AAAS and Resources for the Future with support from the Rockefeller Family Fund and Lawrence H. Linden, will be webcast at www.rff.org/mariomolina.

Molina, co-winner of the 1995 Nobel Prize in Chemistry for his role in explaining the ozone hole, has pointed out that the costs of addressing climate change are sure to be lower now than in the future. In 2006, the Stern Review on the Economics of Climate Change estimated the overall costs of climate-change impacts to be at least 5% of global wealth, or gross domestic product (GDP), per year, now and in the future. By comparison, the Stern Review determined that stabilizing those effects would cost about 1% of global GDP annually. Economist Nicholas Stern increased that estimate in 2008, however, and although those findings have been subjected to intense scrutiny, the "What We Know" report also concluded that "the sooner we act, the lower the risk and cost" of climate change.

On other fronts, content for the Association's popular Communicating Science program, which has served some 2100 participants at 46 workshops and 42 lectures so far, has been expanded to help scientists and engineers convey the facts about climate change.

AAAS has also launched a second phase of the "What We Know" project to ensure that climate-change messages reach the U.S. Hispanic community, which represented 17% of the U.S. voting population as of 2011. Molina took part in a television interview with Nuestra Tele Noticias 24 Horas (NTN24), which reaches 8.5 million mostly Spanish-speaking viewers. In concert with Climate Central, a Spanish-language interview with Molina was broadly disseminated to Hispanic meteorologists.

The English-language version of the "What We Know" report, co-chaired by James McCarthy of Harvard University and Diana Wall of Colorado State University and released with help from Climate Nexus, was the subject of at least 442 English-language news stories. The report was provided to U.S. policy-makers, too, and the AAAS Office of Government Relations continues to communicate climate science on Capitol Hill. Most recently, for example, that work has addressed pending amendments such as H.R. 4435 that would prevent the Pentagon from leveraging climate science in support of national security goals. ■

Additional names for AAAS annual election

For more information on the 2014 election, please see AAAS News & Notes in the 29 August issue of *Science*.

GENERAL ELECTION

President-Elect: A. Paul Alivisatos, Lawrence Berkeley National Laboratory/Univ. of California, Berkeley; Barbara A. Schaal, Washington Univ. in St. Louis

Board of Directors: Michael S. Gazzaniga, Univ. of California, Santa Barbara; Steven M. Girvin, Yale Univ.; Mercedes Pascual, Univ. of Michigan; Sean C. Solomon, Lamont-Doherty Earth Observatory/ Columbia Univ.

Committee on Nominations: Peter C. Agre, Johns Hopkins Malaria Research Institute; Frances H. Arnold, California Institute of Technology; Kenneth I. Berns, Univ. of Florida; Robert J. Birgeneau, Univ. of California, Berkeley; W. Carl Lineberger, Univ. of Colorado Boulder; Michael A. Marletta, Scripps Research Institute; Thom Mason, Oak Ridge National Laboratory; Marc Tessier-Lavigne, Rockefeller Univ.

SECTION ELECTIONS

History and Philosophy of Science

Chair Elect: Marsha L. Richmond, Wayne State Univ.

Downloaded from www.sciencemag.org on September 26, 2014

Published by AAAS

RESEARCH

Stone age technology developed independently more than once

Adler et al., *p. 1609*

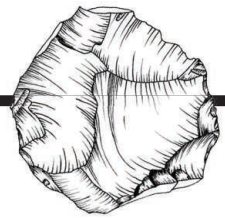

IN *SCIENCE* JOURNALS

Edited by **Stella Hurtley**

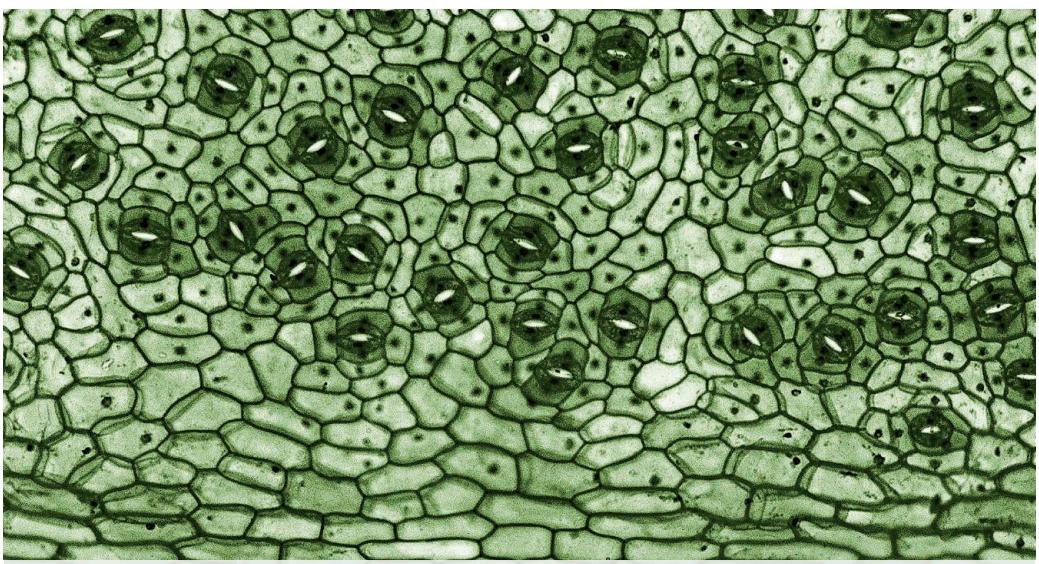

Microscopic view of plant stomata

PLANT DEVELOPMENT

A complex network makes simple pores

Stomata, the pores found on the surface of plant leaves, form at intervals from stem cells. Development of stomata is controlled by the SPEECHLESS transcription factor. Lau *et al*. surveyed the genes that SPEECHLESS itself controls. Targets include genes involved in hormone signaling, control of cell proliferation, and the specification of asymmetric cell fates. Despite the apparent simplicity of a single pore, the genetic network that generates that pore is anything but simple. — PJH

Science, this issue p. 1605

REMOTE HYDROLOGY

Crustal rebound from water drawdown

The ongoing drought across the western United States has taken a toll on underground water storage. Borsa *et al*. use almost imperceptible crustal uplift to estimate the regional water depletion from the drought. Inverting GPS data maps the impact of the drought on local aquifers over the past few years. The deficit so far in the western United States adds up to 240 gigatons of water, the equivalent of a 10-cm layer across the region. Certain areas of California have fared much worse, with local depletions up to five times the regional average. — BG

Science, this issue p. 1587

PALEONTOLOGY

Mysterious dinosaur a swimmer?

Dinosaurs are often appreciated for their size and oddity. In this regard, the North African carnivorous theropod *Spinosaurus,* with its huge dorsal sail and a body larger than *Tyrannosaurus rex,* has long stood out. This species also stands out because of its history. The unfortunate loss of the type specimen during World War II left much of what we know about *Spinosaurus* to be divined through speculation and reconstruction. Ibrahim *et al*. now describe new fossils of this unusual species. They conclude it was, at least partly, aquatic, a first for dinosaurs. — SNV

Science, this issue p. 1613

CATALYSIS

Easier oxidation over gold with added water

Gold adsorbed on metal oxides is an excellent catalyst for the room-temperature oxidation of CO to CO_2. However, there has been continuing disagreement between different studies on the key aspects of this catalyst. Saveeda *et al.* now show through kinetics and infrared spectroscopy that the presence of water can lower the reaction activation barrier by enabling OOH groups to form from adsorbed oxygen (see the Perspective by Mullen and Mullins). The OOH then reacts readily with CO. It thus seems that the main role of oxide support and its interface with the metal is in activating water, but that the steps of the reaction that involve CO occur on gold. — PDS

Science, this issue p. 1599; see also p. 1564

IMMUNOGENETICS

Beware of T cells that don't know how to stop

During an infection, T cells divide extensively and secrete proteins that can severely damage tissues. But T cells know when to stop—they express proteins on their surface such as CTLA4, which put on the brakes. Kuehn *et al*. now report genetic evidence of the importance of CTLA4 in humans (see the Perspective by Rieux-Laucat and Casanova). They identified six patients with mutations in one copy of *CTLA4*. Patients presented with symptoms of an overzealous immune response, with immune cells infiltrating their organs. The findings support the idea that CTLA4

Downloaded from www.sciencemag.org on September 26, 2014

PHOTOS: (TOP TO BOTTOM) ADLER *ET AL.*; DE AGOSTINI PICTURE LIBRARY/SCIENCE SOURCE

Published by AAAS

tells the immune system when enough is enough. — KLM

Science, this issue p. 1623; see also p. 1560

NEUROTECHNOLOGY

Closing the loop on neuroprosthetic control

Patients paralyzed from a spinal cord injury may soon be able to move their legs more naturally. Current neuromodulation devices cause leg movement by electrically stimulating the spinal cord, but they require constant monitoring and adjustment. Wenger *et al.* created a closed-loop system that auto-tunes the device. The authors stimulated the spinal cords of paralyzed rats and then mapped their leg movements while they walked or climbed stairs, creating integrated feedback and feed-forward models for continuous stepping control. — MLF

Sci. Transl. Med. **6**, 255ra133 (2014).

JOVIAN ATMOSPHERE

Hot electron plasma moves in from Io

Scientists have known that solar radiation ionizes the gases from Io's volcanoes to create a torus of plasma around Jupiter, but how that plasma moves is unclear. To investigate this, Yoshioka *et al*. monitored the temperature of the hot electron plasma as a function of distance from the planet with the Hisaki Earth-orbiting satellite. The fraction of hot electrons decreases only gradually with distance from Jupiter, which implies a rapid resupply of these electrons from outside Io's orbit. — MMM

Science, this issue p. 1581

PHYSIOLOGY

Preventing vascular scarring after surgery

The endothelium that lines blood vessels can undergo a change called the endothelial-to-mesenchymal transition (EndMT), which can cause vessel "scarring." Such scarring limits the success of surgical procedures that require blood vessel grafting, including, for example, heart transplantation or coronary bypass surgery. Chen *et al.* found that mice lacking FGFR1 in endothelial cells showed increased EndMT after blood vessel grafting. Moreover, arteries from patients who had rejected heart transplants had lower levels of FGFR1 than those from normal individuals. Thus, enhancing FGFR1 activity could limit vascular scarring in heart disease patients undergoing surgery. — WW

Sci. Signal. **7**, ra90 (2014).

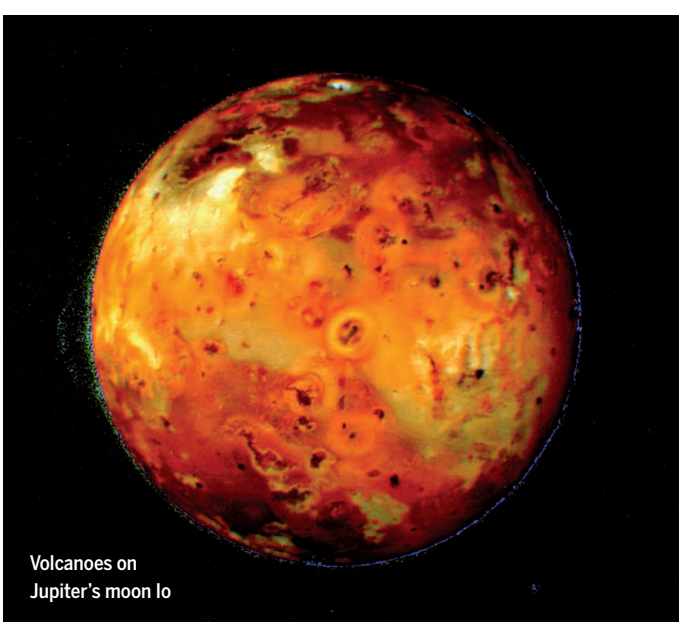

Volcanoes on Jupiter's moon Io

PHOTOS: (LEFT TO RIGHT) NASA/JPL; © 2/LIFE ON WHITE/OCEAN/CORBIS

IN OTHER JOURNALS

Edited by **Kristen Mueller** *and* **Jesse Smith**

NEUROSCIENCE

Timing counts for whisker development

Whiskers help animals to sense the world around them. Each whisker precisely connects to a specific area of the brain. These connections form during early brain development, and protein receptors that bind to the neurotransmitter glutamate (specifically, NMDA-type glutamate receptors) play a key role in their refinement. Fetal and neonatal brains express subunits of the NMDA receptor that regulate its function, called GluN2B and GluN2D. Yamasaki *et al*. discovered that GluN2B and GluN2D play opposing roles as whisker-brain connections develop and mature in mice. Connections formed nearly a day early when mice lacked GluN2D expression. In contrast, reduced expression of the GluN2B subunit delayed the development of the connections by a day. — PRS

J. Neurosci. **34,** 11534 (2014).

NEUROSCIENCE

Animal behavior follows dopamine rewards

In auditory fear conditioning, mice learn to associate auditory cues, such as a tone, with mild footshocks. Forming associations like this, then remembering them long-term (called fear memory consolidation), is an important strategy for navigating one's environment. To understand the molecular basis of fear memory consolidation, Dias *et al*. investigated the contribution microRNAs, small bits of RNA that modulate gene expression. They discovered an important role for the microRNA-34a, which targeted components of a particular signaling pathway (the so-called Notch pathway) that is normally involved in development. MicroRNA-34a caused a transient decrease in Notch-dependent signalling in the amygdala, which was important for fear memory consolidation. — PRS

Neuron **83**, 906 (2014).

PHAGOCYTOSIS

Bring out your dead — hungry receptors await

Every day billions of cells die within the body. Specialized cells called phagocytes patrol the blood and act as cellular

Published by AAAS

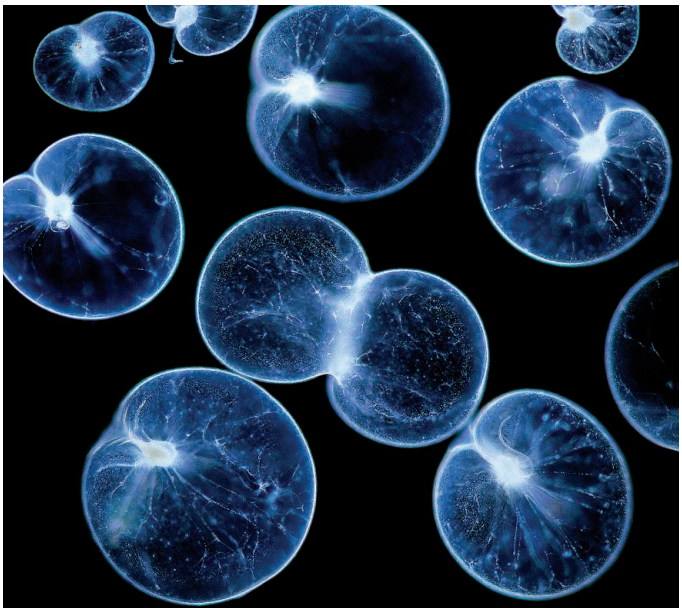

The bioluminescent dinoflagellite *Noctiluca scintillans*

MARINE ECOLOGY

An Arabian wintertime bloom on the rise

Large and widespread wintertime blooms of the dinoflagellate *Noctiluca scintillans* have begun to occur in the Arabian Sea. Until a decade ago, wintertime blooms there were dominated by diatoms, unicellular photosynthetic organisms that thrive in the abundant sunlight and high-nutrient conditions which occur at that time of the year. Now those diatoms are being outcompeted. Gomes *et al.* report that a decrease in the oxygen content of surface waters probably has caused this change, which itself may be caused by high fluxes of organic matter from domestic and industrial wastes. The ascendance of *Noctiluca scintillans* could have a negative impact on the fisheries of the Arabian Sea, which are sustained by the diatom blooms that now are being disrupted by this new order. — HJS

Nat. Commun. 10.1038/ncomms5862 (2014).

garbage collectors, clearing dead cells to prevent tissue damage and inflammation. Phagocytes recognize dead cells because they express molecular "eat me" signals on their surfaces. Zagórska *et al.* examined how mouse phagocytes use different cellular protein receptors, called TAMs, during this process. The TAM receptors Mer and Axl recognize the "eat me" signals on the surface of dead cells. Mer kept the peace by removing the dead cells that accumulate during normal wear and tear. In contrast, during inflammation, Axl protein expression increased and it took over the removal process from Mer. — SMH

Nat. Immunol. 10.1038/ni.2986 (2014).

SOCIAL INTERACTIONS

Hate and violence spread through the air

During the 1994 Rwandan genocide, radio station RTLM aired racist propaganda promoting violence against Tutsis. We now can see quantitatively some of the effects of this propaganda. Yanagizawa-Drott modeled radio signal propagation across this "land of a thousand hills" to determine which villages could receive the RTLM signal. Then they compared their map with court records of the number of people in each village later prosecuted for violent crimes during the genocide. They found that RTLM radio reception was associated with an increase in violence. Militia violence was higher when neighboring villages also had radio coverage, suggesting that social interactions promoted the diffusion of organized violence. The authors estimate that RTLM was responsible for 10% of the total participation in the genocide, by roughly 51,000 people. — BW

Quart. J. Economics 10.1093/qje/qju020 (2014).

ORNITHOLOGY

Social complexity creates brainy parrots

A complex social world of shifting alliances and competitors may be key to the evolution of large brains in humans, dolphins, and spotted hyenas – and, researchers now say, parrots. Hobson et al. observed wild populations of monk parakeets (*Myiopsitta monachus*) in Argentina and captive ones in Florida, finding that the parakeets prefer to spend time with one individual, usually a mate. Captive birds had strong associations with one or two individuals and numerous moderate relationships; their aggressive interactions also suggest a dominance hierarchy of winners and losers. Those layers of relationships require the birds to recognize and remember others—tasks linked to the evolution of cognitive skills. — VM

Auk. 10.1642/AUK-14-14.1 (2014)

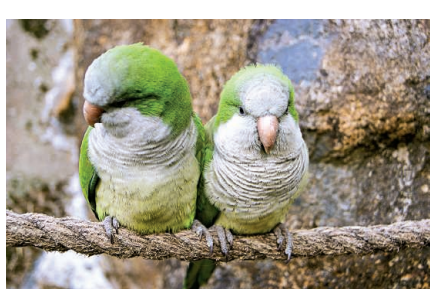

Monk parakeets' relationships are key to their smarts.

MEDICINE

Teaching tolerance stops the bleeding

People with hemophilia A lack a clotting factor [factor VIII (FVIII)] that stops wounds from bleeding. Regular infusions of FVIII can help, but up to 30% of patients make antibodies that attack this treatment. To prevent this, Sherman *et al.* developed a way to teach the immune system to tolerate FVIII, rather than makes antibodies against it. For 2 months, the researchers fed mice leaves from plants engineered to produce fragments of FVIII. The fragments, safely encapsulated in plant cells, entered the area of the gut where immune cells reside and reduced the immune response to FVIII. Treated mice made fewer antibodies against FVIII, suggesting that teaching (immune) tolerance may allow FVIII to stick around and do its job. — LC

Blood **123**, 10 (2014).

CATALYSIS

Constructing a maze full of phosphines

The manufacture of commodity chemicals relies on metals to catalyze, or speed along, the process of making and breaking bonds between lighter elements such as carbon and oxygen. In many cases, the metals are bound to a supporting material to facilitate their separation from the product stream and their subsequent reuse. However, it can be challenging to adopt this approach when the catalyst structure incorporates metal-phosphorus coordination. Sun *et al.* prepared a porous solid by linking phosphine building blocks together. When they introduced rhodium into the structure, the resulting material catalyzed the hydroformylation reaction of octene as well as a free-floating rhodium-phosphine complex. — JSY

Chem. Commun. 10.1039/C4CC03884C (2014).

PHOTOS: (LEFT TO RIGHT) VISUALS UNLIMITED, INC./WIM VAN EGMOND; © LÉLIA VALDUGA/ALAMY; TKTK

Published by AAAS

ALSO IN *SCIENCE* JOURNALS

Edited by **Stella Hurtley**

NEURAL DEVELOPMENT

Differentiation rates regulate pool sizes

Even though a basketball player is bigger than a gymnast, their neural tubes are organized in the same way. Studying chick and mouse embryos, Kicheva *et al.* show that rates of cell differentiation are key (see the Perspective by Pourquie). In a two-phase process, signaling sweeps through the neural tube early on to establish some aspects of cell fate, but later, pools of progenitor cells take on their own regulation. A progenitor that differentiates is no longer a progenitor, and thus the rate of differentiation determines the size of the progenitor pool. The relative sizes of progenitor pools shift as development progresses, to build the spinal cord so that everyone, large or small, has the right proportion of each component. – PJH

Science, this issue p. 1577; see also p. 1565

INTERSTELLAR CHEMISTRY

Carbon chains branch out on space dust

Meteorites found on Earth contain a wide range of complex constituent molecules, including amino acids. Astrochemists proposed the existence of these molecules in interstellar space in the 1980s, but detections have been elusive. Belloche *et al.* used the ALMA telescope array in Chile to observe the massive star-forming region Sgr B2. There, the vast quantities of gas enabled detection of even sparsely distributed species such as *iso*-propyl cyanide. Despite being difficult to detect, such nonlinear organic molecules may be common. The formation of branched molecules is important, given the analogous structure of familiar amino acids — some of the building blocks for life. – MMM

Science, this issue p. 1584

EARLY SOLAR SYSTEM

Nature or nurture for solar system ices?

We know that life's favorite molecule, water, exists throughout the solar system. What we don't know is whether present water levels reflect the chemical conditions of our parent nebula or whether they result from later reprocessing in the young system. The levels of deuterium and hydrogen in solar system water ice offer a tracer for chemical history, and Cleeves *et al.* model the processes at play. The analysis suggests that all nascent planetary systems may have the same water resources that we did. – MMM

Science, this issue p. 1590

IMMUNOGENETICS

A BLUEPRINT of immune cell development

To determine the epigenetic mechanisms that direct blood cells to develop into the many components of our immune system, the BLUEPRINT consortium examined the regulation of DNA and RNA transcription to dissect the molecular traits that govern blood cell differentiation. By inducing immune responses, Saeed *et al.* document the epigenetic changes in the genome that underlie immune cell differentiation. Cheng *et al.* demonstrate that trained monocytes are highly dependent on the breakdown of sugars in the presence of oxygen, which allows cells to produce the energy needed to mount an immune response. Chen *et al.* examine RNA transcripts and find that specific cell lineages use RNA transcripts of different length and composition (isoforms) to form proteins. Together, the studies reveal how epigenetic effects can drive the development of blood cells involved in the immune system. – LMZ

Science, this issue p. 1578, p. 1579, p. 1580

NITROGEN FIXATION

Making nitrogen available for biosynthesis

Nitrogen gas (N_2) is abundant in Earth's atmosphere; however, it must be converted into a bioavailable form before it can be incorporated into biomolecules. The enzyme nitrogenase, which is made up of two metalloproteins, converts N_2 into bioavailable ammonia. One of these, the MoFe-protein, contains a complex metal center, the FeMo cofactor, where the triple N_2 bond is reduced. Understanding how nitrogenase achieves the reduction of N_2 has been a long- term goal. Spatzal *et al.* present the structure of MoFe-protein bound to carbon monoxide (see the Perspective by Hogbom). Although this is an inhibitor rather than the natural substrate,

Published by AAAS

the structure gives insight into how the FeMo metallocluster rearranges to achieve substrate reduction. – VV

Science, this issue p. 1620

WATER SPLITTING

The power of a pair of perovskites

In the past several years, perovskite solar cells have emerged as a low-cost experimental alternative to more traditional silicon devices. Luo *et al.* now show that a pair of perovskite cells connected in series can power the electrochemical breakdown of water into hydrogen and oxygen efficiently (see the Perspective by Hamann). Hydrogen generation from water is being actively studied as a supplement in solar power generation to smooth out the fluctuations due to variations in sunlight. –JSY

Science, this issue p. 1593; see also p. 1566

ATMOSPHERIC CHEMISTRY

Breaking down a Criegee intermediate

Ozone's damaging role in the upper atmosphere is well known, but ozone is also quite active closer down to where we live. In particular, ozone's run-ins with airborne unsaturated hydrocarbons, from natural or anthropogenic sources, produce even more-reactive OH radicals. Liu *et al.* used vibrational spectroscopy to study how OH emerges from a so-called Criegee intermediate formed when ozone attacks 2-butene. The results suggest that OH production is easier than current theory predicts. –JSY

Science, this issue p. 1596

PALEOLITHIC TOOLS

An early assemblage of obsidian artifacts

Levallois technology is the name for the stone knapping technique used to create tools thousands of years ago. The technique appeared in the archeological record across Eurasia 200 to 300 thousand years ago (ka) and appeared earlier in Africa. Adler *et al*. challenge the hypothesis that the technique's appearance in Eurasia was the result of the expansion of hominins from Africa. Levallois obsidian artifacts in the southern Caucasus, dated at 335 to 325 ka, are the oldest in Eurasia. This suggests that Levallois technology may have evolved independently in different hominin populations. Stone technology cannot thus be used as a reliable indicator of Paleolithic human population change and expansion. – AMS

Science, this issue p. 1609

PLANT ECOLOGY

How plant species diversity is shaped

Factors controlling plant species diversity have been teased apart in an ancient dune ecosystem in western Australia. Laliberté *et al.* surveyed plants in the ancient dune, where variation in soil properties is associated with changes in plant diversity. Local plant diversity was mostly determined by environmental filtering from the regional species pool. This process is driven by acidification during long-term soil formation. The findings challenge the prevailing view that resource competition controls local plant diversity. – AMS

Science, this issue p. 1602

NEUROSCIENCE

Animal behavior follows rewards

Animal behavior is learned and reinforced by rewards. On a molecular level, the reward comes in the form of the neurotransmitter, dopamine, which modulates synapses. The exact timing and mechanism of this process remain unknown. Using optical stimulation, Yagishita *et al.* found that dopaminergic modulation involved dendritic spine enlargement only during an extremely narrow time window. Known as reinforcement plasticity, this cellular basis for learning could provide insight into psychiatric disorders involving dopaminergic regulation, such as depression, drug addiction, and schizophrenia. – MM

Science, this issue p. 1616

ECOLOGY

Views of nature, views of conservation

When we think of nature conservation, some of us may imagine wilderness protected in a natural park. Others may think of species closer to home, such as birds and butterflies helped to recovery by the reintroduction of hedges. Mace traces the changes in conversation thinking in the past 50 years. She identifies four different views of nature as emphasis has shifted from individual species to ecosystems, and from viewing nature as separate from humans to considering direct benefits to humans from nature. The different views have important implications for how scientists can measure conservation success and how policy-makers value and manage nature. – JFU

Science, this issue p. 1558

Published by AAAS

RESEARCH ARTICLE SUMMARY

IMMUNOGENETICS

mTOR- and HIF-1α–mediated aerobic glycolysis as metabolic basis for trained immunity

Shih-Chin Cheng, Jessica Quintin, Robert A. Cramer, Kelly M. Shepardson, Sadia Saeed, Vinod Kumar, Evangelos J. Giamarellos-Bourboulis, Joost H. A. Martens, Nagesha Appukudige Rao, Ali Aghajanirefah, Ganesh R. Manjeri, Yang Li, Daniela C. Ifrim, Rob J. W. Arts, Brian M. J. W. van der Meer, Peter M. T. Deen, Colin Logie, Luke A. O'Neill, Peter Willems, Frank L. van de Veerdonk, Jos W. M. van der Meer, Aylwin Ng, Leo A. B. Joosten, Cisca Wijmenga, Hendrik G. Stunnenberg, Ramnik J. Xavier, Mihai G. Netea*

INTRODUCTION: Trained immunity refers to the memory characteristics of the innate immune system. Memory traits of innate immunity have been reported in plants and invertebrates, as well as in mice lacking functional T and B cells that are protected against secondary infections after exposure to certain infections or vaccinations. The underlying mechanism of trained immunity is represented by epigenetic programming through histone modifications, leading to stronger gene transcription upon restimulation. However, the specific cellular processes that mediate trained immunity in monocytes or macrophages are poorly understood.

METHODS: We studied a model of trained immunity, induced by the β-glucan component of *Candida albicans*, that was previously shown to induce nonspecific protection against both infections and malignancies. Genome-wide transcriptome and histone modification profiles were performed and pathway analysis was applied to identify the cellular processes induced during monocyte training. Biological validations were performed in human primary monocytes and in two experimental models in vivo.

RESULTS: In addition to immune signaling pathways, glycolysis genes were strongly upregulated in terms of histone modification profiling, and this was validated by RNA sequencing of cells from β-glucan–treated mice. The biochemical characterizations of the β-glucan–trained monocytes revealed elevated aerobic glycolysis with reduced basal respiration rate, increased glucose consumption and lactate production, and higher intracellular ratio of nicotinamide adenine dinucleotide (NAD^+) to its reduced form (NADH). The dectin-1–Akt–mTOR–HIF-1α pathway (mTOR, mammalian target of rapamycin; HIF-1α, hypoxia-inducible factor–1α) was responsible for the metabolic shift induced by β-glucan. Trained immunity was completely abrogated in monocytes from dectin-1–deficient patients. Blocking of the mTOR–HIF-1α pathway by chemical inhibitors inhibited trained immunity. Mice receiving metformin, an adenosine monophosphate–activated protein kinase (AMPK) activator that subsequently inhibits mTOR, lost the trained immunity–induced protection against lethal *C. albicans* infection. The role of the mTOR–HIF-1α pathway for β-glucan–induced innate immune memory was further validated in myeloid-specific HIF-1α knockout (mHIF-1α KO) mice that, unlike wild-type mice, were not protected against *Staphylococcus aureus* sepsis.

ON OUR WEB SITE

Read the full article at http://dx.doi.org/10.1126/science.1250684

DISCUSSION: The shift of central glucose metabolism from oxidative phosphorylation to aerobic glycolysis (the "Warburg effect") meets the spiked need for energy and biological building blocks for rapid proliferation during carcinogenesis or clonal expansion in activated lymphocytes. We found that an elevated glycolysis is the metabolic basis for trained immunity as well, providing the energy and metabolic substrates for the increased activation of trained immune cells. The identification of glycolysis as a fundamental process in trained immunity further highlights a key regulatory role for metabolism in innate host defense and defines a potential therapeutic target in both infectious and inflammatory diseases. ■

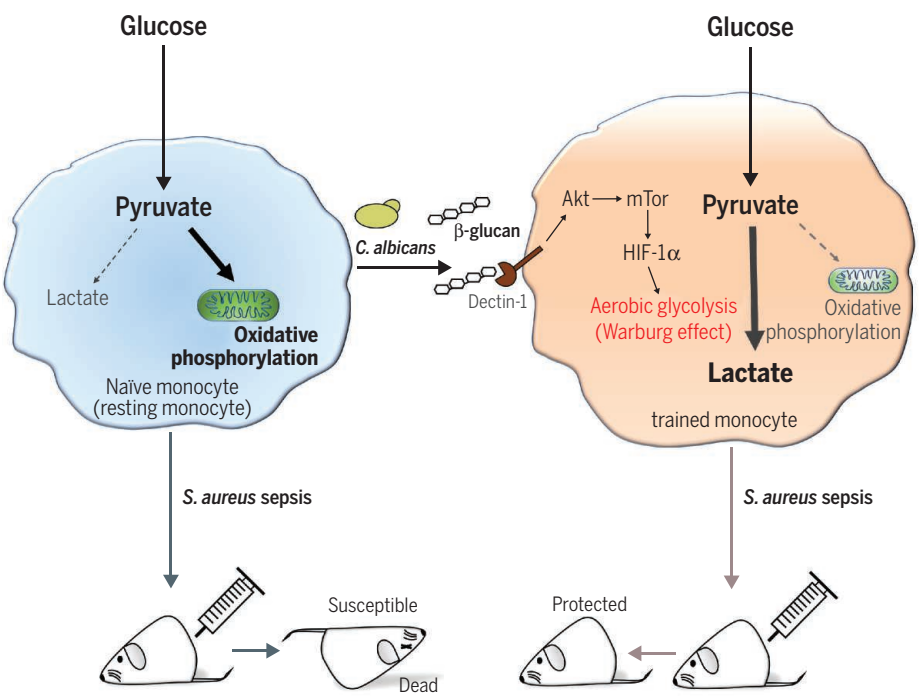

Aerobic glycolysis as metabolic basis for trained immunity. In naïve macrophages during aerobic conditions, glucose metabolism is mainly geared toward oxidative phosphorylation providing adenosine triphosphate (ATP) as the energy source. In contrast, long-term functional reprogramming during trained immunity requires a metabolic shift toward aerobic glycolysis and is induced through a dectin-1–Akt–mTOR–HIF-1α pathway.

The list of author affiliations is available in the full article online.
*Corresponding author. E-mail: mihal.netea@radboudumc.nl
Cite this article as S.-C. Cheng *et al.*, Science 345, 1250684 (2014). DOI: 10.1126/science.1250684

Published by AAAS

RESEARCH ARTICLE

IMMUNOGENETICS

mTOR- and HIF-1α–mediated aerobic glycolysis as metabolic basis for trained immunity

Shih-Chin Cheng,[1] Jessica Quintin,[1] Robert A. Cramer,[2] Kelly M. Shepardson,[2] Sadia Saeed,[3] Vinod Kumar,[4] Evangelos J. Giamarellos-Bourboulis,[5] Joost H. A. Martens,[3] Nagesha Appukudige Rao,[3] Ali Aghajanirefah,[3] Ganesh R. Manjeri,[6] Yang Li,[4] Daniela C. Ifrim,[1] Rob J. W. Arts,[1] Brian M. J. W. van der Meer,[4] Peter M. T. Deen,[7] Colin Logie,[3] Luke A. O'Neill,[8] Peter Willems,[6] Frank L. van de Veerdonk,[1] Jos W. M. van der Meer,[1] Aylwin Ng,[9,10] Leo A. B. Joosten,[1] Cisca Wijmenga,[4] Hendrik G. Stunnenberg,[4] Ramnik J. Xavier,[9,10] Mihai G. Netea[1]*

Epigenetic reprogramming of myeloid cells, also known as trained immunity, confers nonspecific protection from secondary infections. Using histone modification profiles of human monocytes trained with the *Candida albicans* cell wall constituent β-glucan, together with a genome-wide transcriptome, we identified the induced expression of genes involved in glucose metabolism. Trained monocytes display high glucose consumption, high lactate production, and a high ratio of nicotinamide adenine dinucleotide (NAD^+) to its reduced form (NADH), reflecting a shift in metabolism with an increase in glycolysis dependent on the activation of mammalian target of rapamycin (mTOR) through a dectin-1–Akt–HIF-1α (hypoxia-inducible factor–1α) pathway. Inhibition of Akt, mTOR, or HIF-1α blocked monocyte induction of trained immunity, whereas the adenosine monophosphate–activated protein kinase activator metformin inhibited the innate immune response to fungal infection. Mice with a myeloid cell–specific defect in HIF-1α were unable to mount trained immunity against bacterial sepsis. Our results indicate that induction of aerobic glycolysis through an Akt–mTOR–HIF-1α pathway represents the metabolic basis of trained immunity.

In classical descriptions of host defense mechanisms, innate immune responses that are rapid, are nonspecific, and lack memory are distinguished from specific T and B cell–dependent immune responses, which are highly specific and have the capacity to build immunological memory. The hypothesis that the innate immune system is incapable of mounting adaptive responses (*1*) is contradicted by studies showing that organisms lacking a specific immune system, such as plants or insects, are able to respond adaptively to infection (*2*, *3*) and that innate immune cells, such as macrophages, have adaptive characteristics (*4*). In line with the proposal that there are nonspecific adaptive responses in the innate immune system, T and B cell–independent protective effects of monocytes and natural killer (NK) cells have been demonstrated in models of bacterial and viral infections, respectively (*5*, *6*). Furthermore, epigenetic reprogramming at the level of histone H3 methylation has been proposed as the molecular mechanism responsible for long-term memory of innate immunity (*5*, *7*), and this process has been termed trained immunity.

Initiation of innate immune memory through trained immunity is likely to be responsible for the nonspecific protective effects of certain vaccines (*8*). Furthermore, the increased inflammatory responsiveness of monocytes and macrophages due to trained immunity appears to play a central role in inflammatory diseases (*9*). From this perspective, the capacity of innate immunity to mount adaptive responses both redefines the function of innate immunity and identifies a potential therapeutic target in human diseases. It is thus essential to understand the cellular and molecular mechanisms that mediate trained immunity, in hopes of harnessing their therapeutic potential. Although epigenetic modifications are known to underlie information storage during innate immune memory in both plants (*10*) and mammals (*7*), less is known regarding the molecular pathways and downstream mechanisms that lead to trained immunity.

[1]Department of Internal Medicine, Radboud University Medical Center, 6525 GA Nijmegen, Netherlands. [2]Department of Microbiology and Immunology, Geisel School of Medicine at Dartmouth, Hanover, NH 03755, USA. [3]Department of Molecular Biology, Faculties of Science and Medicine, Nijmegen Centre for Molecular Life Sciences, Radboud University, 6500 HB Nijmegen, Netherlands. [4]Department of Genetics, University of Groningen, University Medical Center Groningen, Groningen, Netherlands. [5]4th Department of Internal Medicine, University of Athens Medical School, 12462 Athens, Greece. [6]Department of Biochemistry, Faculties of Science and Medicine, Nijmegen Centre for Molecular Life Sciences, Radboud University, 6500 HB Nijmegen, Netherlands. [7]Department of Physiology, Radboud University Medical Center, 6525 GA Nijmegen, Netherlands. [8]School of Biochemistry and Immunology, Trinity Biomedical Sciences Institute, Trinity College Dublin, Dublin 2, Ireland. [9]Center for Computational and Integrative Biology and Gastrointestinal Unit, Massachusetts General Hospital, Harvard School of Medicine, Boston, MA 02114, USA. [10]Broad Institute of MIT and Harvard, Cambridge, MA 02142, USA.
*Corresponding author. E-mail: mihai.netea@radboudumc.nl

Transcriptome and epigenetics of monocytes

Candida albicans and its main cell wall constituent, β-glucan, induce trained innate immune memory both in vitro and in vivo (*7*). We performed an unbiased assessment of whole-genome mRNA expression, histone methylation, and acetylation patterns after training human primary monocytes with β-glucan, the major *Candida* cell wall structure that mediates trained immunity, which induces nonspecific protection against both infections and malignancies (*11*). An in vitro experimental model of β-glucan–induced trained immunity was established in monocytes (Fig. 1A). β-Glucan training of cells induced a potentiated cytokine production upon restimulation with lipopolysaccharide (LPS) 7 days later (Fig. 1B). An enhanced response was also observed after stimulation with the TLR2 ligand Pam3Cys or with nonrelated Gram-negative and Gram-positive bacteria (fig. S1). Assessment of histone 3 Lys^4 trimethylation (H3K4me3) and histone 3 Lys^{27} acetylation (H3K27Ac) identified promoters that were specifically induced by β-glucan training (Fig. 1C). Pathway analysis of the promoters potentiated by β-glucan identified innate immune and signaling pathways up-regulated in trained cells that are responsible for the induction of trained immunity (*7*, *12*).

In addition to immune signaling pathways, epigenetic profiling of trained monocytes on the basis of both methylation and acetylation patterns identified a signature associated with central metabolism (fig. S2) and an increase in the promoters of genes encoding enzymes involved in glycolysis and its master regulator *mTOR* (mammalian target of rapamycin) (Fig. 1, D and E). Furthermore, after priming of monocytes with β-glucan, genes involved in glycolysis, such as hexokinase and pyruvate kinase, were epigenetically up-regulated 1 week later (Fig. 1F and fig. S3). The gene expressing *mTOR* and the glycolytic genes that are targets of the transcription factor *HIF1α* were also enhanced by β-glucan (fig. S4). In line with this, HIF-1α activation was increased in β-glucan–trained monocytes (fig. S5). In addition, glycolysis genes were also up-regulated in vivo in mice challenged with β-glucan, as revealed by total RNA sequencing analysis in splenocytes of these mice (Fig. 1G and fig. S6).

Glycolysis and monocytes

Monocytes from peritoneal exudates rely on glycolysis as a main energy source (*13*). The role of glucose as an energy substrate for monocytes is demonstrated by the blockade of monocyte stimulation and trained immunity by incubation of cells with 2-deoxy-D-glucose, a glucose analog that cannot be metabolized by the cells and inhibits glycolysis (fig. S7). This is in line with observations that activated macrophages, dendritic cells, and T_H1 and T_H17 lymphocytes undergo a switch from oxidative phosphorylation to aerobic glycolysis (*14*).

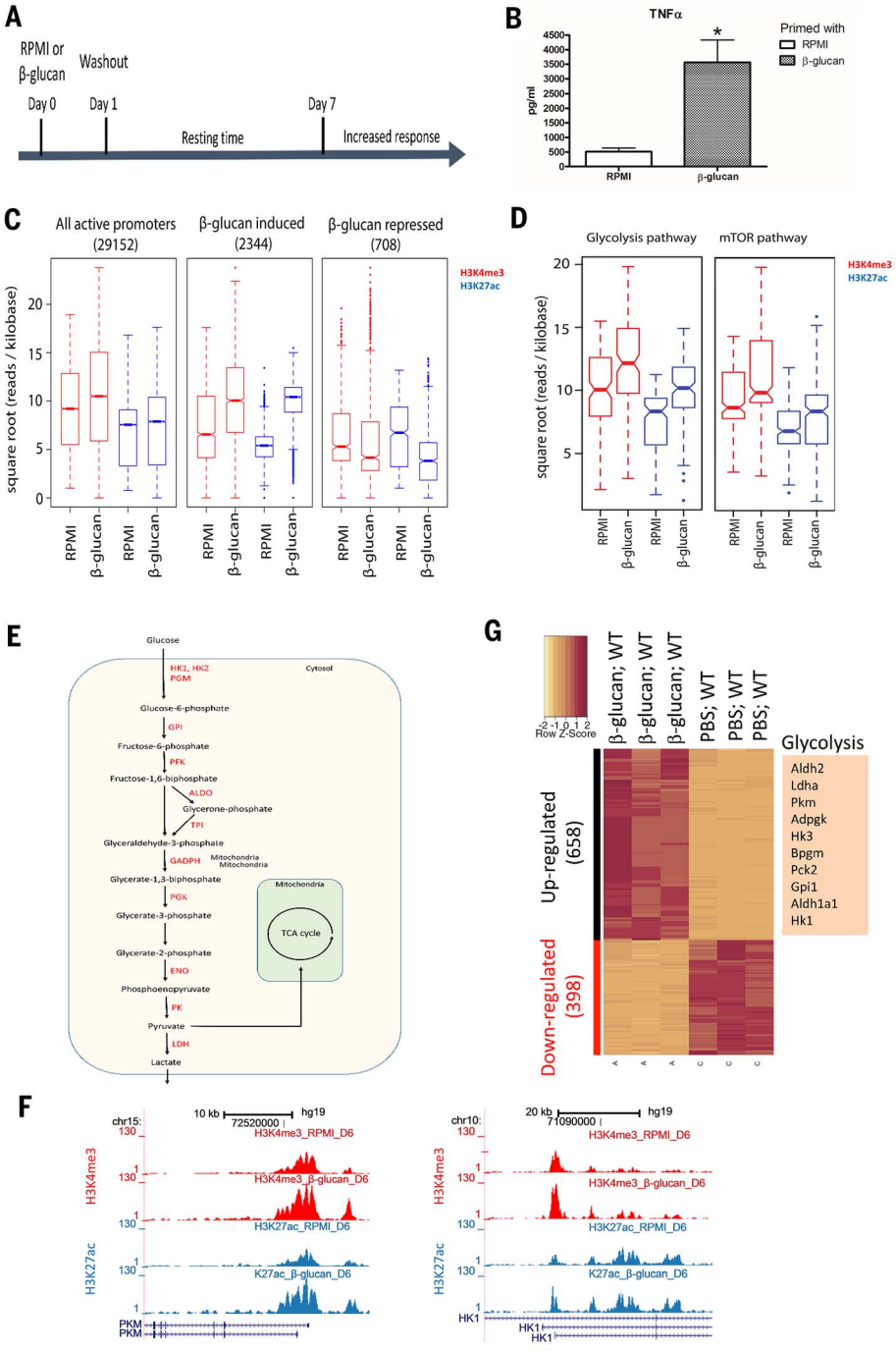

Fig. 1. Trained immunity in monocytes. (**A**) Schematic of in vitro trained immunity experimental setup. (**B**) TNF-α levels after 7 days in β-glucan–treated cells. Data are means ± SEM (n = 8, *P < 0.05, Wilcoxon signed-rank test). (**C**) Genome-wide H3K4me3 (red) and H3K27Ac (blue) epigenetic modifications 7 days after β-glucan treatment. Ratios of β-glucan/RPMI for both H3K4me3 and H3K27Ac modification were calculated for each promoter. The promoters that display significantly higher or lower ratio ($P \leq 0.05$, t test) relative to median values are called β-glucan–induced promoters and β-glucan–repressed promoters, respectively. Box plots show distributions of the sequence read density (reads per kilobase) for all promoters, β-glucan–induced promoters, and β-glucan–repressed promoters in each data set. In each box plot, the band inside each box (midpoint) represents the median value, and upper and lower borders of the box represent the Q3 (third quartile) and Q1 (first quartile) values, respectively. The upper line represents the maximum value within the upper bound [Q3 + 1.5 × (Q3 − Q1)]; the lower line represents the minimum value within the lower bound [Q1 − 1.5 × (Q3 − Q1)]. Dots represent observed points outside the upper and lower bound. (**D**) Epigenetic modifications in the promoter regions of the genes involved in glycolysis and mTOR pathways. The box plots were analyzed as in Fig. 1C. (**E**) Schematic representation of the up-regulated enzymes (red) in the glycolysis pathway. (**F**) Representative screen shots of H3K4me3 (red) and H3K27Ac (blue) modifications in the promoter region of pyruvate kinase (PKM) and hexokinase. (**G**) Differential gene expression analysis between the β-glucan–treated group and the control group. Genes in the glycolysis pathway that are up-regulated by the β-glucan training are highlighted in the box at right. The colors in the heat map represent the normalized RNA levels of identified differential expressed genes (false discovery rate = 0.01, relative change ≥ 1.5) in three mice per group.

Consistent with these findings, monocytes trained with β-glucan showed a reduced baseline oxygen consumption on day 7 relative to naïve cells; this finding is compatible with the hypothesis that these cells underwent a shift from oxidative metabolism toward glycolysis. Moreover, trained cells showed a decreased maximal rate of oxygen consumption after complete uncoupling with carbonyl cyanide *p*-trifluoromethoxyphenylhydrazone (FCCP), a chemical substrate that permeabilizes mitochondrial membranes and uncouples electron transport systems from the oxidative phosphorylation systems (Fig. 2, A and B), whereas the rate of proton leak–dependent oxygen consumption was not altered (table S1). The latter result indicates a reduction of the capacity of the mitochondrial electron transport chain (ETC) as observed after a period of hypoxia (*15*). Hypoxia decreases the activity of the ETC complexes I and IV through HIF-1α (*16*). This hypothesis was reinforced by observations of increased glucose consumption (Fig. 2C), lactate production (Fig. 2D), and ratio of nicotinamide adenine dinucleotide (NAD^+) to its reduced form (NADH) (Fig. 2E) in trained monocytes.

Differences in glucose consumption did not offset the high glucose concentrations in the RPMI medium, which suggests that glucose availability is not the limiting factor for the observed training phenotype (fig. S8). In addition, the training effect induced by β-glucan was likely not due to the presence of pyruvate in the culture medium, an intermediate metabolite in glycolysis, because training occurred even when medium devoid of pyruvate was used during the training process (fig. S9).

Earlier studies have shown that a high cellular NAD^+/NADH ratio acts through sirtuin-1 to decrease the mitochondrial content (*17*). This mechanism may explain the observed β-glucan–induced reduction in ETC capacity. In contrast, LPS stimulation leads to a strong but transient increase in the glycolytic process in monocytes

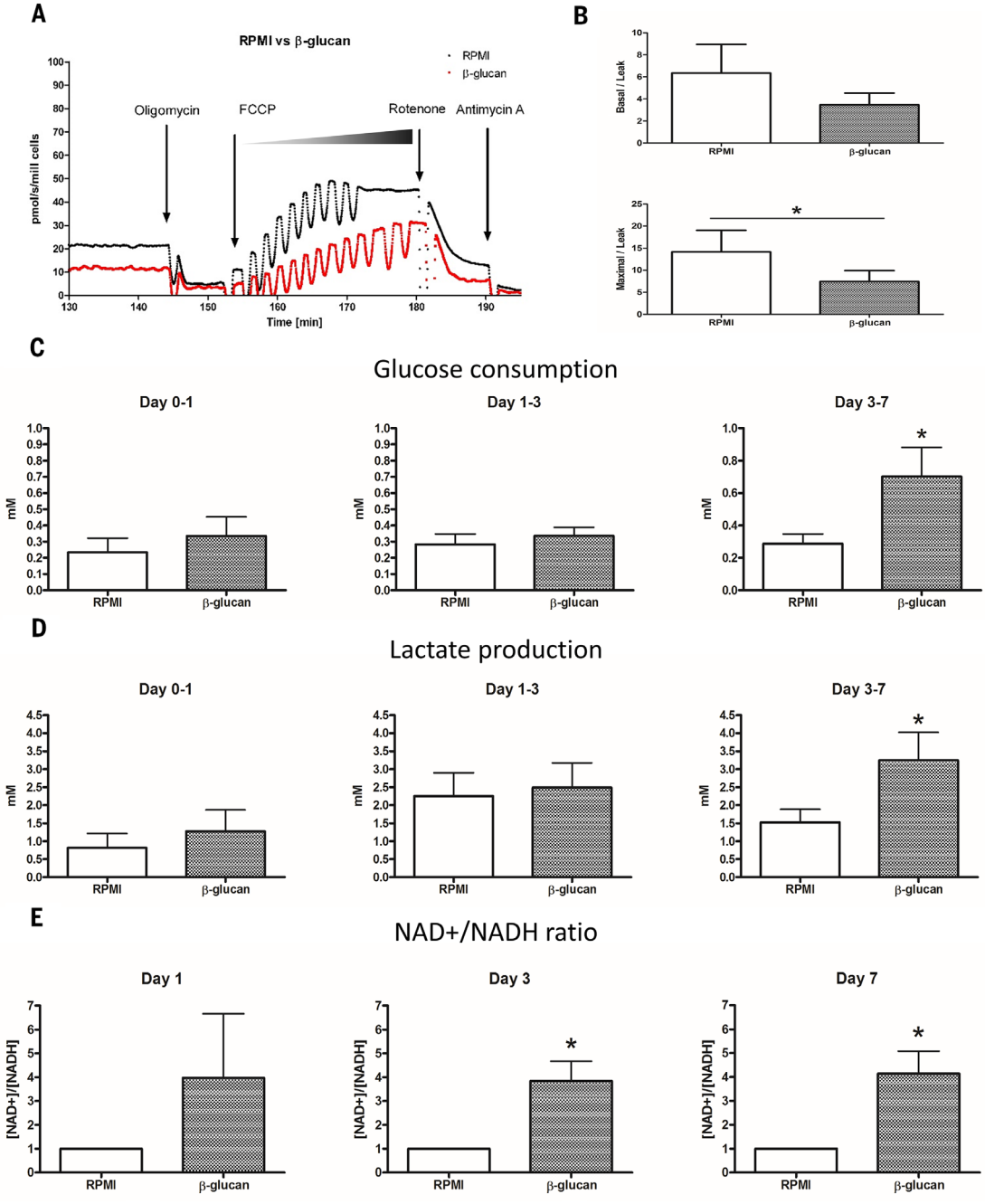

Fig. 2. Physiology after β-glucan treatment. (**A**) Representative oxygen consumption rate of untreated (RPMI, black) and β-glucan–trained (red) monocytes as determined by high-resolution respirometry (Oxygraph; OROBOROS Instruments, Innsbruck). (**B**) Baseline (basal oxygen consumption before oligomycin treatment, upper panel) and maximum oxygen consumption rate (maximum oxygen consumption upon FCCP treatment, lower panel) of untrained (open bar) and β-glucan–trained (solid bar) monocytes determined by respirometry and normalized to the leak oxygen consumption. (**C** and **D**) Kinetic changes of glucose consumption (C) and lactate production (D) from days 1, 3, and 7 of untreated and β-glucan–trained monocytes. (**E**) Kinetics of NAD^+/NADH ratio determined at days 1, 3, and 7. In (B) to (E), data are means ± SEM (n = 5 to 8, *P < 0.05, Wilcoxon signed-rank test).

(fig. S10); this finding supports the suggestion that, although the acute response of monocytes to LPS is characterized by glycolysis (*18*), at later time points this response switches to oxidative phosphorylation—a process that subsequently induces immune tolerance by activation of sirtuin-1 and sirtuin-6 histone deacetylases (*19*). In contrast to LPS-induced tolerance, β-glucan training inhibited the expression of *Sirtuin1* (fig. S11). Moreover, the addition of resveratrol, a sirtuin-1 activator, during the first 24 hours of β-glucan training partially inhibited the enhanced interleukin-6 (IL-6) production (fig. S11). This suggests that sirtuin deacetylases play a role in the modulated monocyte functional phenotype and highlights the complex interaction between the intermediate metabolites and subsequent immune responses through chromatin-modifying enzymes (*20*).

mTOR acts as a sensor of the metabolic environment (*21*) and functions as a master regulator of glucose metabolism in activated lymphocytes (*22*). Epigenetic signals at promoters of genes in the mTOR pathway were significantly higher in β-glucan–trained monocytes (paired t test, P < 0.001) than in cells exposed to culture medium (Fig. 3A). Target genes of mTOR, such as *EIF4EBP1*, displayed a similar pattern (Fig. 3B). In line with this finding, mTOR phosphorylation was up-regulated in trained monocytes as assessed by Western blot (Fig. 3C). Monocytes isolated from patients with a complete deficiency in dectin-1 (*23*) failed to activate mTOR upon stimulation with β-glucan (Fig. 3D) and failed to enhance tumor necrosis factor (TNF) production upon LPS restimulation (fig. S12), supporting the hypothesis that mTOR phosphorylation is dependent on the dectin-1 C-type lectin receptor.

Glycolysis in trained immunity

As the data presented above demonstrate activation of mTOR and glycolysis in trained monocytes, we next investigated the causality between these two processes by blocking glycolysis during β-glucan training. Inhibition of mTOR with rapamycin during the first day of stimulation resulted in a dose-dependent inhibition of the training effect induced by β-glucan (Fig. 3E). Indirect inhibition of mTOR with AICAR, an adenosine

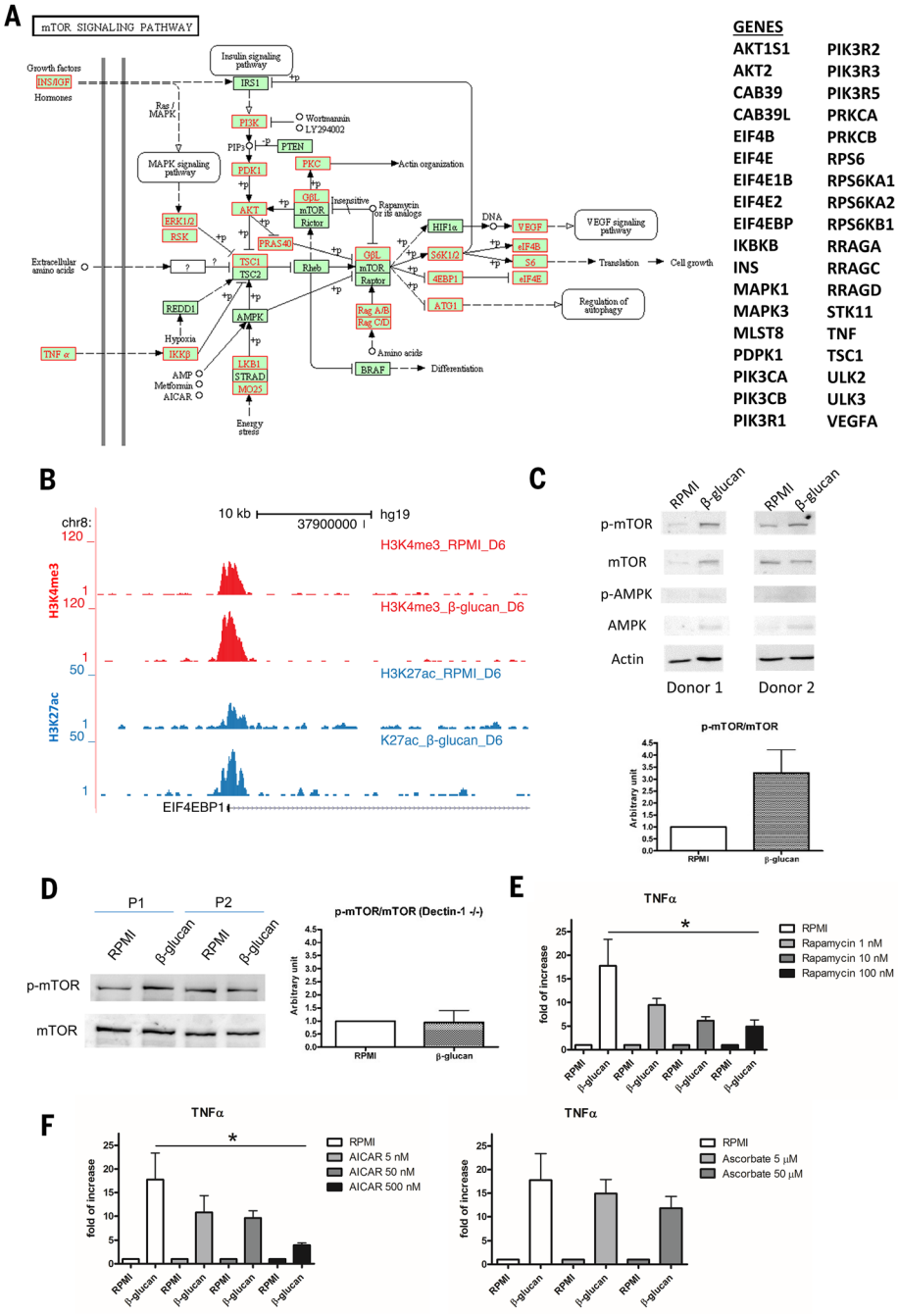

Fig. 3. mTOR signaling in β-glucan–treated monocytes. (**A**) Schematic representation of up-regulated enzymes (red) in mTOR signaling pathway in β-glucan–trained monocytes. (**B**) Screen shot of H3K4me3 (red) and H3K27Ac (blue) modification in the promoter region of *EIF4EBP1* (coding region denoted at bottom), the main target of *mTOR*, in both RPMI- and β-glucan–treated monocytes. (**C**) Western blot from cell lysate harvested at day 7 after RPMI or β-glucan treatment. Antibodies specific for endogenous phospho-mTOR (p-mTOR), total mTOR, phospho-AMPK, AMPK, and actin were used to blot the total and phospho proteins, respectively. Representative blots of five independent experiments are shown. The p-mTOR/mTOR ratio is shown as a bar chart ($n = 5$, $P = 0.0625$, Wilcoxon signed-rank test). (**D** to **F**) The endogenous p-mTOR status of dectin-1–deficient patients was determined by Western blot (D) from cell lysate harvest at day 7 after RPMI of β-glucan treatment and probed with antibodies to p-mTOR and total mTOR, respectively. The p-mTOR/mTOR ratio is shown as a bar chart. Relative cytokine production was determined from cells incubated with rapamycin (mTOR inhibitor) (E) and with AICAR (AMPK inhibitor) and ascorbate (HIF-1α inhibitor) (F) in a dose-dependent manner. In (E) and (F), data are means ± SEM ($n = 6$, $^*P < 0.05$, Wilcoxon signed-rank test).

monophosphate–activated protein kinase (AMPK) activator, had similar effects (Fig. 3F). On the basis of observations that mTOR induction of glycolysis is mediated through activation of HIF-1α and stimulation of glycolytic enzymes (*24*) and that rapamycin inhibits *HIF-1α* expression (*25*), we assessed the effect of a HIF-1α inhibitor on monocyte training. We found that the HIF-1α inhibitor ascorbate also blocked trained immunity in a dose-dependent manner (Fig. 3F).

We further investigated the link between metabolic effects and epigenetic changes by assessing the effects of the epigenetic inhibitors MTA (methylthioadenosine, a methyltransferase inhibitor) and ITF (ITF2357, a histone deacetylase inhibitor) during the training setup on the lactate measurements. As expected, the epigenetic inhibitors had no effect on lactate production in the acute phase (24 hours after β-glucan stimulation; fig. S13). However, lactate production was significantly reduced in the trained monocytes on day 7 when MTA was added to monocytes with β-glucan during the first 24 hours in the incubation period (fig. S13), which suggests that histone methylation also partially modifies the induction of glycolysis in the trained monocytes.

Monocyte mTOR activation

Activation of mTOR by insulin or colony-stimulating factors such as GM-CSF (granulocyte-macrophage colony-stimulating factor) is mediated by intermediary activation of the Akt-PI3K (phosphatidylinositol 3-kinase) pathway (*26*). A similar signal route is induced in monocytes by β-glucan, as stimulation with β-glucan induced a strong phosphorylation of Akt (Fig. 4A). This effect was again dectin-1–dependent, being absent in monocytes isolated from dectin-1–deficient patients (Fig. 4B). Inhibition of Akt phosphorylation also resulted in down-regulation of mTOR activation (Fig. 4C), demonstrating the relationship between Akt and mTOR activation. Finally, the Akt inhibitor wortmannin inhibited monocyte training by β-glucan in a dose-dependent manner (Fig. 4D).

Epigenetic reprogramming of monocytes by trained immunity has been reported as a mechanism of nonspecific protection in different models. Mice were protected from lethal disseminated candidiasis after an initial nonlethal *Candida albicans* infection (*7*). Similarly, β-glucan also induced protection against infection with a lethal *Staphylococcus aureus* inoculum (*27*), while Bacillus Calmette-Guérin (BCG) vaccination protected mice from systemic candidiasis (*5*). We first assessed whether metformin—which acts through AMPK activation and subsequently mTOR inhibition (*28*) and is commonly used for the treatment of type 2 diabetes (*29*)—abrogates the protective effects in these experimental models. In vitro, metformin suppressed trained immunity induced by β-glucan (Fig. 4E), and administration of metformin to mice during and after primary infection with a low-inoculum *C. albicans* inhibited the protective effects induced by it against secondary disseminated candidiasis (Fig. 4F), demonstrating that mTOR-mediated effects mount a protective trained immunity in vivo.

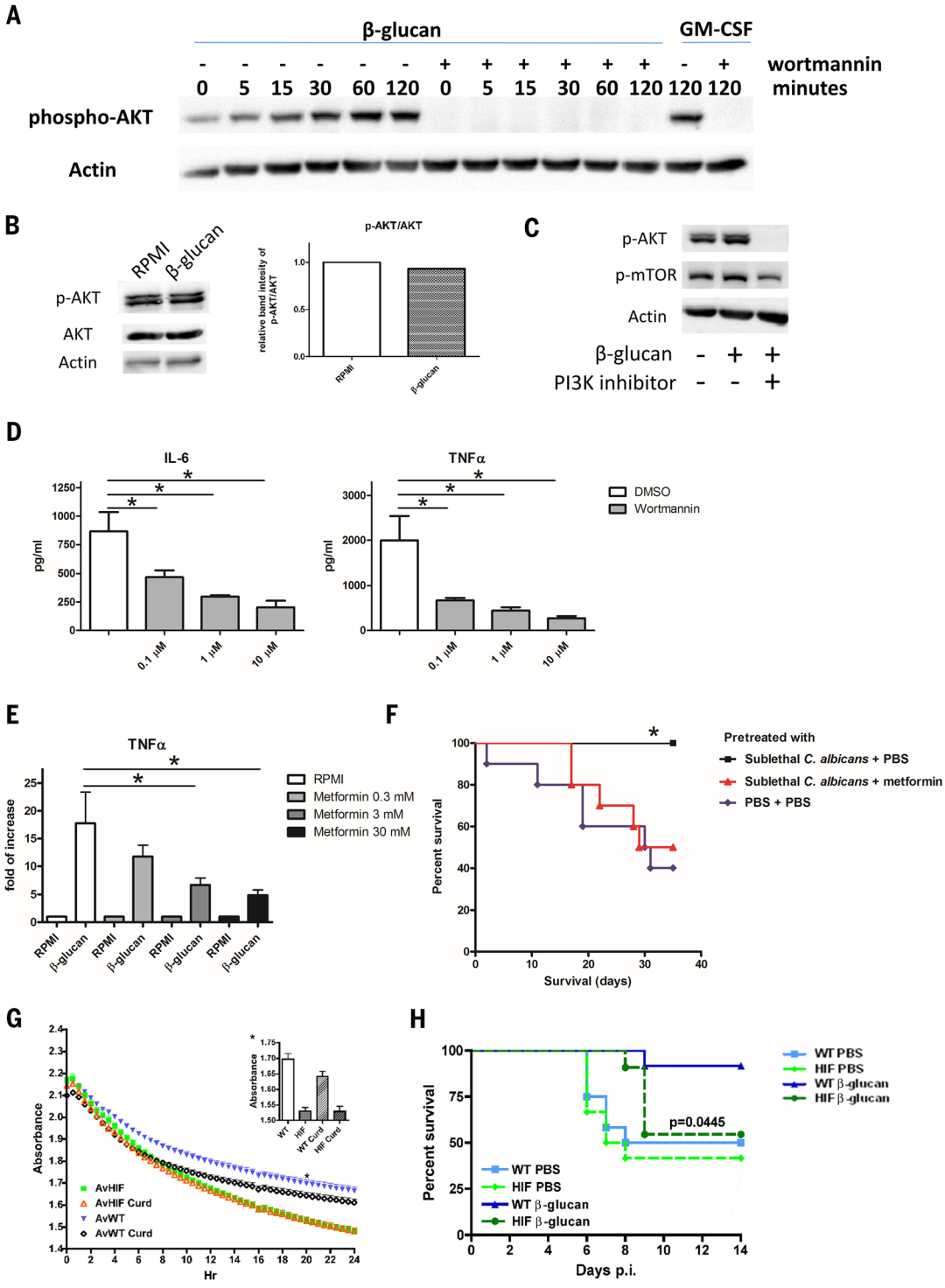

Fig. 4. Akt–mTOR–HIF-1α pathway downstream of β-glucan stimulation. (**A**) Monocytes were treated with either RPMI or β-glucan in the presence or absence of wortmannin, a PI3K inhibitor. GM-CSF stimulation was included as a positive control. Cell lysates were harvested at 5, 15, 30, 60, and 120 min. Akt phosphorylation and actin level were blotted with specific antibodies to p-Akt and actin. Representative blots from three independent experiments are shown. (**B**) Akt phosphorylation and p-Akt/Akt ratio induced by β-glucan from dectin-1 were determined by Western blot by specific antibodies to p-Akt, total Akt, and actin. (**C**) Effects of PI3K inhibitors on Akt and mTOR phosphorylation in β-glucan–treated monocytes were determined by Western blot by probing with specific antibodies to p-AKT and p-mTOR. (**D**) Monocytes were treated with β-glucan in the presence of wortmannin in a dose-dependent manner. Cytokine levels after 7 days were determined by enzyme-linked immunosorbent assay. (**E**) Relative cytokine production was determined from cells incubated with metformin (AMPK inhibitor) in a dose-dependent manner. (**F**) Survival of wild-type C57BL/6J mice infected with live *C. albicans* after training with PBS or β-glucan. Metformin or PBS was given from 1 day before the first nonlethal dose of live *C. albicans* challenge until 3 days after challenge on a daily basis. (**G**) Wild-type (WT) and HIF-KO alveolar macrophages at a concentration of 8×10^4 were incubated with PBS or curdlan (100 μg/ml) for 1 hour. Resazurin was added and absorbance was recorded every 30 min for 24 hours. Inset (*) shows absorbance values at the 20-hour time point. Data are representative of three biological replicates. (**H**) Survival curve of wild-type or mHIF-1α KO mice primed with β-glucan and challenged with a lethal dose of *S. aureus* infection. In (D) and (E), data are means ± SEM ($n = 6$, $^*P < 0.05$, Wilcoxon signed-rank test). In (F) and (H), a log-rank test was used to assess significance of the survival curves ($^*P < 0.05$).

We assessed whether the effects of mTOR were mediated at the level of innate immunity but not at the level of adaptive T and B cell immunity elicited during vaccination. An experimental model of β-glucan–induced protection against *S. aureus* sepsis can be observed in myeloid cell–specific HIF-1α conditional knockout mice (mHIF-1α KO) (*30*). These mice are unable to mount glycolysis specifically in cells of the myeloid lineage. We assessed the metabolic activity of wild-type and mHIF-1α KO macrophages when stimulated with β-glucan. mHIF-1α KO macrophages showed increased chemical reduction of the metabolic indicator resazurin (Fig. 4G), consistent with the hypothesis that HIF-1α induces the switch to aerobic glycolysis in response to β-glucan. In this model, the cells do not undergo the switch in the absence of HIF-1α and are "metabolically" dysregulated. Whereas β-glucan increased the survival of wild-type mice infected with *S. aureus* from 40% to 90%, the

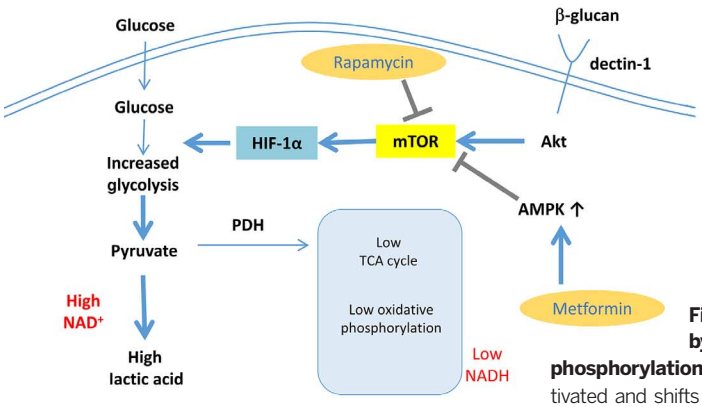

Comparison between naïve monocytes and trained monocytes

	Naïve monocytes	Trained monocyte
Metabolic preference	Oxidative phosphorylation	Aerobic glycolysis
Oxidative phosphorylation	↑	↓
Lactate production	↓	↑
NAD+/NADH ratio	↓	↑

Fig. 5. Model of metabolic activation of trained monocytes, characterized by a shift toward increased aerobic glycolysis and decreased oxidative phosphorylation. Upon β-glucan/dectin-1 recognition, the AKT–mTOR–HIF-1α pathway is activated and shifts the glucose metabolism from oxidative phosphorylation to aerobic glycolysis. The activated glycolysis state prepares β-glucan–trained monocytes to respond to stimulation in a robust manner. The potential role of rapamycin and metformin in inhibition of trained immunity is also depicted. The metabolic differences between a trained monocyte and naïve monocytes are summarized at the right.

induction of trained immunity was completely abrogated in mHIF-1α KO mice (Fig. 4H). To further dissect which pathways are modulated in the mHIF-1α KO mice, we performed RNA sequencing and compared the differential RNA expression profiles of wild-type and mHIF-1α KO mice. Several interesting genes were specifically up-regulated in wild-type but not in mHIF-1α KO mice (fig. S14 and table S2), including those encoding beclin-1 (an autophagy-related protein), STK11 (an AMPK-related serine-threonine kinase), JHDM1D (jumonji C domain containing histone demethylase), and the FOXO4 transcription factor involved in Akt-PI3K stimulation. Thus, these results demonstrate that stimulation of HIF-1α–mediated glycolysis in myeloid cells is crucial for mounting trained immunity in vivo.

Discussion

The role of histone methylation as a mediator of short-term innate immunological memory in macrophages has been described (*7*) and has been referred to as a latent enhancer for the epigenetic elements that mediate this phenomenon (*31*). In this study, whole-genome epigenetic profiling of histone modifications and RNA sequencing analysis have identified both immunologic and metabolic pathways stimulated during trained immunity. A cyclic adenosine monophosphate–dependent pathway mediating trained immunity in monocytes has also been described in an accompanying manuscript (*12*). In the present study, we identified the metabolic pathways induced in trained monocytes, demonstrating a metabolic switch toward aerobic glycolysis, which is in turn crucial for the maintenance of trained immunity (Fig. 5).

A metabolic switch toward aerobic glycolysis was earlier reported to be a feature of cell activation and proliferation [such an effect was first described in neoplastic cells and termed the Warburg effect (*32*)] while also playing a role in effector T helper lymphocytes (*33*) and activated macrophages (*34*). The elevated glycolysis metabolism observed in trained monocytes might be necessary to equip and prepare cells to respond to the intruding pathogens in a robust and rapid manner through proinflammatory cytokine production and possibly also through enhanced phagocytosis capacity (*35*).

Although we observed trained immunity in monocytes, this response should not be restricted to cells in the monocyte lineage. Recently, adaptive features of NK cells have been demonstrated to be involved in resistance to reinfection with viruses (*6*, *36*). The specific NK memory cells, like T cells, rapidly proliferate, degranulate, and produce cytokine upon activation. However, it remains to be determined whether metabolic rewiring also plays a role in NK or in other innate immune cells, such as dendritic cells. In addition, it is of interest to determine whether training is contact-dependent or could also be induced by soluble mediators. This is an important question in the field of autoinflammatory and autoimmune diseases, because these diseases are worsened by the unregulated cytokine production. Our results suggest that proinflammatory cytokines such as IL-1β could also induce trained immunity in monocytes in vitro (fig. S15). This hypothesis is further supported by nonspecific protective effects induced by IL-1β, even when injected several days before an experimental infection is induced (*37*).

One important aspect to note is that the molecular mechanisms investigated in the present study focused on trained immunity in the first 7 days after the initial stimulus. This is the crucial period during which trained immunity offers protection in newborn children against perinatal sepsis (*38*) and thus is relevant from a biological and clinical point of view. Longer-lasting in vivo effects of trained immunity have been demonstrated in humans (*5*), and it is important to assess whether these later effects are mediated through similar mechanisms. However, any such later effects are also likely to be exerted at the level of bone marrow myeloid cell progenitors, as recently demonstrated in the case of Toll-like receptor (TLR)–induced tolerance (*39*).

Our study introduces an interesting preliminary step in understanding the glycolytic process in trained immunity. Hypoxia and glycolysis enhance the proliferative response of macrophages to CSF-1 (*40*) and sustain the survival of activated dendritic cells (*41*). Soluble β-glucan from *Grifola frondosa* induces macrophage proliferation (*42*), although we were not able to observe these effects with trained monocytes by *Candida* β-glucan (*7*). However, epigenetic profiling has identified a cell cycle activation signal in β-glucan–trained cells (*12*), and it is tempting to speculate that trained monocytes are not only capable of increased cytokine production but also primed to respond to proliferative signals, although this remains to be demonstrated. Finally, the identification of glycolysis as a fundamental process in trained immunity further highlights a key regulatory role for metabolism in innate host defense and also defines a novel therapeutic target in both infectious and inflammatory diseases (*9*).

Materials and methods

Isolation of primary human monocytes

Blood was collected from human healthy volunteers and two dectin-1–deficient patients after written informed consent (Ethical Committee Nijmegen-Arnhem, approval no. NL32357.091.10). Peripheral blood mononuclear cells (PBMCs) were isolated by differential centrifugation using Ficoll-Paque (GE Healthcare, Diegem, Belgium) from buffy coats obtained from Sanquin Bloodbank, Nijmegen, Netherlands. Monocytes were purified by MACS depletion of CD3-, CD19-, and CD56-positive cells from the PBMCs; CD3 MicroBeads (130-050-101), CD19 MicroBeads (130-050-301), and CD56 were purchased from Miltenyi Biotec (Leiden, Netherlands) and used according to the manufacturer's protocol. Efficacy of depletion was controlled by flow cytometry (FC500; Beckman-Coulter, Woerden, Netherlands) and was higher than 98%.

Genome-wide sequence analysis

For chromatin immunoprecipitation (ChIP) analysis or RNA sequencing, 10×10^6 $CD3^-CD19^-CD56^-$ pure monocytes were plated on 100-mm dishes. Monocytes were preincubated with cell culture medium (RPMI) or β-glucan (5 μg/ml) for 24 hours in a total volume of 10 ml. After 24 hours, cells were

washed to remove the stimulus and were resuspended in RPMI supplemented with 10% human pool serum. Monocytes were collected before and 6 days after the incubation for ChIP or RNA sequencing. For RNA sequencing, monocytes were collected in TRIzol reagent (Invitrogen, Bleiswijk, Netherlands). The purified materials were then processed to generate genomic DNA for WGBS, RNA (Trizol extraction according to manufacturer instructions; Agilent BioAnalyser RIN >8), and chromatin by fixing the cells in 1% formaldehyde.

Reagents

Candida albicans β-1,3-(D)-glucan (β-glucan) was kindly provided by D. Williams (East Tennessee State University). Reagents used were as follows: LPS (*E. coli* 0B5/B5, Sigma, Diegem, Belgium), rapamycin (Sigma, R0395), metformin (R&D, AF 1730, Abingdon, UK), AICAR (Sigma, A9978), ascorbate (Sigma, A4034), wortmannin (InvivoGen, tlrl-wtm, Toulouse, France). *C. albicans* ATCC MYA-3573 (UC 820) cells were heat-inactivated for 30 min at 95°C.

Stimulation experiments

For training, monocytes were preincubated with β-glucan (10 μg/ml) for 24 hours. After 7 days, cells were restimulated with various microbial ligands: LPS (10 ng/ml), Pam3Cys (10 g/ml), and heat-killed *S. aureus* or heat-killed *E. coli* (both at 10^6 microorganisms/ml). After 24 hours, supernatants were collected and stored at −20°C until cytokine measurement. All the cytokine measurements presented were from at least six donors.

To address the HIF-1α–AMPK–mTOR pathway in trained immunity, we added the specific inhibitors together with β-glucan for the first 24 hours in different doses as follows: rapamycin from 1 to 100 nM, metformin from 0.3 to 30 mM, AICAR from 5 to 500 nM, and ascorbate at 5 and 50 μM.

ChIP-seq data analysis

H3K4me3 and H3K27ac ChIP, sequencing, and processing of the data were performed as described (*7*). The detailed data have been deposited in the GEO database with accession number GSE57206. Sequenced reads of 42-bp length were mapped to human genome (NCBI hg19) using bwa-alignment package mapper (*43*). ChIP-seq data sets were normalized as described (*44*), and the sequenced reads were directionally extended to 300 bp, corresponding to the original length of sequenced DNA fragments. For each base pair in the genome, the number of overlapping sequence reads was determined, averaged over a 10-bp window, and visualized in UCSC browser (http://genome.ucsc.edu). These normalized tracks were used to generate the genome browser screen shots. Putative H3K4me3- and H3K27ac-enriched regions in the genome were identified by using MACS (*45*) with $P < 10^{-8}$. All the transcription start sites (±1 kb) of genes with significant H3K4me3 signal were regarded as active promoters. H3K4me3 and H3K27ac signals at all active promoters were estimated, and $\log_2$ ratios of ChIP-seq signal between treatment and control samples were calculated. Promoters that showed an absolute deviation of 2 times the median (median ± 2 × MAD) of the ratio of ChIP-seq signal (treatment/control) were regarded as regulated promoters (induced or repressed). Sequence reads counted from the normalized ChIP-seq data sets were used to generate the box plots.

Metabolite measurements

Culture medium was collected at days 1, 3, and 7. The glucose and lactate concentrations within the medium were determined by Glucose Colorimetric Assay Kit (K686-100; Biovision, Milpitas, CA) and Lactate Colorimetric Assay Kit (K627-100, Biovision), respectively. NAD^+ and NADH concentration were determined by NAD/NADH Quantification Colorimetric Kit (Biovision, K337-100) from the cell lysate according to manufacturer's protocol. All the metabolite measurement data presented were from at least six donors.

Oxygen consumption measurement

Culture medium was collected from 1 million cells treated with either RPMI or β-glucan. After stimulation, the cells were trypsinized, washed, and resuspended in 60 μl of the collected culture medium. The cell suspensions were then used for cellular O_2 consumption analysis. Oxygen consumption was measured at 37°C using polarographic oxygen sensors in a two-chamber Oxygraph (OROBOROS Instruments, Innsbruck, Austria). First, basal respiration (baseline oxygen consumption) was measured. Next, leak respiration was determined by addition of the specific complex V inhibitor oligomycin A (OLI). Then, maximal electron transport chain complex (ETC) capacity (maximum oxygen consumption) was quantified by applying increasing concentrations of the mitochondrial uncoupler FCCP (1 to 14 μM final maximal concentration). Finally, minimal respiration was assessed by adding a maximal (0.5 μM) concentration of the specific complex I inhibitor rotenone (ROT; 0.5 μM) and the complex III inhibitor antimycin A (AA; 0.5 μM).

After establishment of the baseline oxygen consumption rate, cells were treated with the ATP synthase inhibitor oligomycin to determine the rate of proton leak–dependent oxygen consumption, after which the baseline rate value was normalized to the value of the leak rate. Next, the cells were treated with FCCP to determine the maximum oxygen consumption rate. For normalization, the maximum FCCP value was ratioed to the leak value. The oxygen consumption measurement was repeated in monocytes isolated from five healthy individuals.

Western blot

For Western blotting of AMPK, mTOR, Akt (total and phosphorylated), and actin, training was performed as described in stimulation experiments. Adherent monocytes were trained in 24-well plates. After training and the resting period, cells were lysed in 150 μl of lysis buffer. Equal amounts of protein were subjected to SDS-PAGE electrophoresis using 7.5% polyacrylamide gels. Primary antibodies [1:500 and 1:50 000 (actin)] in 5% (w/v) BSA/TBST (5% bovine serum albumin/TBST) were incubated overnight at 4°C. HRP-conjugated anti-rabbit antibody or HRP-conjugated anti-mouse antibody at a dilution of 1:5000 in 5% (w/v) BSA/TBST was used for 1 hour at room temperature. Quantitative assessment of band intensity was performed by Image Lab statistical software (Bio-Rad, CA, USA). The following antibodies were used: actin antibody (Sigma, A5441), mTOR antibody (Cell Signaling, #2972, Leiden, Netherlands), phospho-mTOR antibody (Ser2448) (Cell Signaling, #2971), AMPKα antibody (Cell Signaling, #2532), phospho-AMPKα (Thr172) (Cell Signaling, #2531), Akt antibody (Cell Signaling, #9272), phosphor-Akt (Ser473) (Cell Signaling, #9271). At least four different individual experiments were repeated for each Western blot experiment.

Analysis of RNA sequencing data

Sequencing reads were mapped to the mouse genome (mm10 assembly) using STAR (version 2.3.0). The aligner was provided with a file containing junctions from Ensembl GRCm38.74. In total, there were 507.5 million reads from 12 samples. Htseq-count of the Python package HTSeq (version 0.5.4p3) was used to quantify the read counts per gene based on annotation version GRCm38.74, using the default union-counting mode (The HTSeq package, www-huber.embl.de/users/anders/HTSeq/doc/overview.html).

Differentially expressed genes were identified by statistics analysis using the edgeR package from bioconductor. The statistically significant threshold [false discovery rate (FDR) = 0.05] was applied. For visualization, relative changes larger than 1.5 and FDR of 0.01 were used to plot the expression level of protein-coding genes.

Animal experimental models

The metformin experiment was done at the University of Athens with the approval of the Ethics Committee on Animal Experiments of the University of Athens (approval no. 2550). C57BL/6J female mice (8 to 12 weeks) were used (Jackson Laboratories, Bar Harbor, ME, USA). Mice were injected with live *C. albicans* blastoconidia (2×10^4 CFU per mouse) or pyrogen-free phosphate-buffered saline (PBS) alone. Seven days later, mice were infected intravenously with a lethal dose of live *C. albicans* (2×10^6 CFU per mouse). Survival was monitored daily. To assess the involvement of the AMPK-mTOR pathway in the training, metformin (250 mg/kg) or PBS was given via intravenous injection from 1 day before the first nonlethal dose of live *C. albicans* challenge until 3 days after challenge on a daily basis.

Wild-type (Cre +/+, HIF flox/flox) and HIF-KO mice 8 to 10 weeks old were trained with 200 μl intraperitoneally (i.p.) of either 1 mg of β-glucan particles or sterile PBS on days −7 and −4 prior to tail vein inoculation with 200 μl of 5×10^6 *S. aureus* strain RN4220 on day 0. Mice were monitored three times daily for survival for 14 days. Data presented are the combined survival data (Kaplan-Meier) from two independent experiments. There were five mice per group in the first survival experiment and seven mice per group in the second survival experiment. A log-rank test was used to assess the statistical significance between

the groups. For the RNA sequence analysis, both wild-type and mHIF1α-KO mice were injected with PBS or β-glucan i.p. and the total RNA was extracted from splenocytes at day 4. The total gene expression profiles were accessed by RNA sequencing. This study was carried out in accordance with the recommendations of the National Research Council (*46*). The protocol was approved by the Dartmouth IACUC (approval no. cram.ra.2).

Metabolic activity assay

Alveolar macrophages were isolated from 6- to 10-week-old HIF-KO and wild-type mice by flushing lungs 10 times with 1 ml of PBS containing 0.5 mM EDTA. Alveolar macrophages were added and allowed to adhere for 1 hour to a 96-well plate at a concentration of 8×10^4 in 200 μl of CO_2-independent media (Leibovitz's L-15, Life Technologies) supplemented with 10% FCS, 5 mM HEPES buffer, 1.1 mM L-glutamine, penicillin (0.5 U/ml), and streptomycin (50 mg/ml). To the media, 10% Resazurin dye (Sigma) was added and the plate was incubated at 37°C for 24 hours, with readings recorded every 30 min at 600 nm. A 690-nm reference wavelength was subtracted from the 600-nm wavelengths and the data were normalized to wells without cells. Curdlan (100 μg/ml, Sigma) was used as a stimulator of metabolic activity.

Statistical analysis

The differences between groups were analyzed using the Wilcoxon signed-rank test (unless otherwise stated). Statistical significance of the survival experiment was calculated using the product limit method of Kaplan and Meier. The level of significance was defined as a P value of <0.05. Cytokine production as well as the band intensity ratio for Western blot were plotted as a bar chart with mean ± SEM. Replicate numbers of the experiments performed are reported in the figure legends.

REFERENCES AND NOTES

1. C. A. Janeway Jr., R. Medzhitov, Innate immune recognition. *Annu. Rev. Immunol.* **20**, 197–216 (2002). doi: 10.1146/annurev.immunol.20.083001.084359; pmid: 11861602
2. Z. Q. Fu, X. Dong, Systemic acquired resistance: Turning local infection into global defense. *Annu. Rev. Plant Biol.* **64**, 839–863 (2013). doi: 10.1146/annurev-arplant-042811-105606; pmid: 23373699
3. J. Kurtz, Specific memory within innate immune systems. *Trends Immunol.* **26**, 186–192 (2005). doi: 10.1016/j.it.2005.02.001; pmid: 15797508
4. D. M. Bowdish, M. S. Loffredo, S. Mukhopadhyay, A. Mantovani, S. Gordon, Macrophage receptors implicated in the "adaptive" form of innate immunity. *Microbes Infect.* **9**, 1680–1687 (2007). doi: 10.1016/j.micinf.2007.09.002; pmid: 18023392
5. J. Kleinnijenhuis *et al*., Bacille Calmette-Guerin induces NOD2-dependent nonspecific protection from reinfection via epigenetic reprogramming of monocytes. *Proc. Natl. Acad. Sci. U.S.A.* **109**, 17537–17542 (2012). doi: 10.1073/pnas.1202870109; pmid: 22988082
6. J. C. Sun, J. N. Beilke, L. L. Lanier, Adaptive immune features of natural killer cells. *Nature* **457**, 557–561 (2009). doi: 10.1038/nature07665; pmid: 19136945
7. J. Quintin *et al*., *Candida albicans* infection affords protection against reinfection via functional reprogramming of monocytes. *Cell Host Microbe* **12**, 223–232 (2012). doi: 10.1016/j.chom.2012.06.006; pmid: 22901542
8. C. S. Benn, M. G. Netea, L. K. Selin, P. Aaby, A small jab—a big effect: Nonspecific immunomodulation by vaccines. *Trends Immunol.* **34**, 431–439 (2013). doi: 10.1016/j.it.2013.04.004; pmid: 23680130
9. S. Bekkering, L. A. Joosten, J. W. van der Meer, M. G. Netea, N. P. Riksen, Trained innate immunity and atherosclerosis. *Curr. Opin. Lipidol.* **24**, 487–492 (2013). doi: 10.1097/MOL.0000000000000023; pmid: 24184939
10. M. Jaskiewicz, U. Conrath, C. Peterhänsel, Chromatin modification acts as a memory for systemic acquired resistance in the plant stress response. *EMBO Rep.* **12**, 50–55 (2011). doi: 10.1038/embor.2010.186; pmid: 21132017
11. G. D. Brown, S. Gordon, Fungal β-glucans and mammalian immunity. *Immunity* **19**, 311–315 (2003). doi: 10.1016/S1074-7613(03)00233-4; pmid: 14499107
12. S. Saeed *et al*., Epigenetic programming of monocyte-to-macrophage differentiation and trained innate immunity. *Science* **345**, 1251086 (2014).
13. R. Oren, A. E. Farnham, K. Saito, E. Milofsky, M. L. Karnovsky, Metabolic patterns in three types of phagocytizing cells. *J. Cell Biol.* **17**, 487–501 (1963). doi: 10.1083/jcb.17.3.487; pmid: 13940299
14. L. A. O'Neill, D. G. Hardie, Metabolism of inflammation limited by AMPK and pseudo-starvation. *Nature* **493**, 346–355 (2013). doi: 10.1038/nature11862; pmid: 23325217
15. D. Tello *et al*., Induction of the mitochondrial NDUFA4L2 protein by HIF-1α decreases oxygen consumption by inhibiting Complex I activity. *Cell Metab.* **14**, 768–779 (2011). doi: 10.1016/j.cmet.2011.10.008; pmid: 22100406
16. T. Klimova, N. S. Chandel, Mitochondrial complex III regulates hypoxic activation of HIF. *Cell Death Differ.* **15**, 660–666 (2008). doi: 10.1038/sj.cdd.4402307; pmid: 18219320
17. S. Y. Jang, H. T. Kang, E. S. Hwang, Nicotinamide-induced mitophagy: Event mediated by high NAD^+/NADH ratio and SIRT1 protein activation. *J. Biol. Chem.* **287**, 19304–19314 (2012). doi: 10.1074/jbc.M112.363747; pmid: 22493485
18. G. M. Tannahill *et al*., Succinate is an inflammatory signal that induces IL-1β through HIF-1α. *Nature* **496**, 238–242 (2013). doi: 10.1038/nature11986; pmid: 23535595
19. T. F. Liu, V. T. Vachharajani, B. K. Yoza, C. E. McCall, NAD^+-dependent sirtuin 1 and 6 proteins coordinate a switch from glucose to fatty acid oxidation during the acute inflammatory response. *J. Biol. Chem.* **287**, 25758–25769 (2012). doi: 10.1074/jbc.M112.362343; pmid: 22700961
20. D. R. Donohoe, S. J. Bultman, Metaboloepigenetics: Interrelationships between energy metabolism and epigenetic control of gene expression. *J. Cell. Physiol.* **227**, 3169–3177 (2012). doi: 10.1002/jcp.24054; pmid: 22261928
21. E. L. Pearce, M. C. Poffenberger, C. H. Chang, R. G. Jones, Fueling immunity: Insights into metabolism and lymphocyte function. *Science* **342**, 1242454 (2013). doi: 10.1126/science.1242454; pmid: 24115444
22. H. Chi, Regulation and function of mTOR signalling in T cell fate decisions. *Nat. Rev. Immunol.* **12**, 325–338 (2012). pmid: 22517423
23. B. Ferwerda *et al*., Human dectin-1 deficiency and mucocutaneous fungal infections. *N. Engl. J. Med.* **361**, 1760–1767 (2009). doi: 10.1056/NEJMoa0901053; pmid: 19864674
24. P. K. Majumder *et al*., mTOR inhibition reverses Akt-dependent prostate intraepithelial neoplasia through regulation of apoptotic and HIF-1-dependent pathways. *Nat. Med.* **10**, 594–601 (2004). doi: 10.1038/nm1052; pmid: 15156201
25. C. C. Hudson *et al*., Regulation of hypoxia-inducible factor 1α expression and function by the mammalian target of rapamycin. *Mol. Cell. Biol.* **22**, 7004–7014 (2002). doi: 10.1128/MCB.22.20.7004-7014.2002; pmid: 12242281
26. T. W. Kelley *et al*., Macrophage colony-stimulating factor promotes cell survival through Akt/protein kinase B. *J. Biol. Chem.* **274**, 26393–26398 (1999). doi: 10.1074/jbc.274.37.26393; pmid: 10473597
27. M. J. Marakalala *et al*., Dectin-1 plays a redundant role in the immunomodulatory activities of β-glucan-rich ligands in vivo. *Microbes Infect.* **15**, 511–515 (2013). doi: 10.1016/j.micinf.2013.03.002; pmid: 23518266
28. D. M. Gwinn *et al*., AMPK phosphorylation of raptor mediates a metabolic checkpoint. *Mol. Cell* **30**, 214–226 (2008). doi: 10.1016/j.molcel.2008.03.003; pmid: 18439900
29. E. Bosi, Metformin—the gold standard in type 2 diabetes: What does the evidence tell us? *Diabetes Obes. Metab.* **11** (suppl. 2), 3–8 (2009). doi: 10.1111/j.1463-1326.2008.01031.x; pmid: 19385978
30. T. Cramer *et al*., HIF-1α is essential for myeloid cell-mediated inflammation. *Cell* **112**, 645–657 (2003). doi: 10.1016/S0092-8674(03)00154-5; pmid: 12628185
31. R. Ostuni *et al*., Latent enhancers activated by stimulation in differentiated cells. *Cell* **152**, 157–171 (2013). doi: 10.1016/j.cell.2012.12.018; pmid: 23332752
32. O. Warburg, Metabolism of tumours. *Biochem. Z.* **142**, 317 (1923).
33. C. H. Chang *et al*., Posttranscriptional control of T cell effector function by aerobic glycolysis. *Cell* **153**, 1239–1251 (2013). doi: 10.1016/j.cell.2013.05.016; pmid: 23746840
34. J. C. Rodríguez-Prados *et al*., Substrate fate in activated macrophages: A comparison between innate, classic, and alternative activation. *J. Immunol.* **185**, 605–614 (2010). doi: 10.4049/jimmunol.0901698; pmid: 20498354
35. A. S. Zinkernagel, C. Peyssonnaux, R. S. Johnson, V. Nizet, Pharmacologic augmentation of hypoxia-inducible factor-1α with mimosine boosts the bactericidal capacity of phagocytes. *J. Infect. Dis.* **197**, 214–217 (2008). doi: 10.1086/524843; pmid: 18173364
36. S. Paust *et al*., Critical role for the chemokine receptor CXCR6 in NK cell-mediated antigen-specific memory of haptens and viruses. *Nat. Immunol.* **11**, 1127–1135 (2010). doi: 10.1038/ni.1953; pmid: 20972432
37. J. W. van der Meer, M. Barza, S. M. Wolff, C. A. Dinarello, A low dose of recombinant interleukin 1 protects granulocytopenic mice from lethal Gram-negative infection. *Proc. Natl. Acad. Sci. U.S.A.* **85**, 1620–1623 (1988). doi: 10.1073/pnas.85.5.1620; pmid: 3125553
38. P. Aaby *et al*., Randomized trial of BCG vaccination at birth to low-birth-weight children: Beneficial nonspecific effects in the neonatal period? *J. Infect. Dis.* **204**, 245–252 (2011). doi: 10.1093/infdis/jir240; pmid: 21673035
39. A. Yáñez *et al*., Detection of a TLR2 agonist by hematopoietic stem and progenitor cells impacts the function of the macrophages they produce. *Eur. J. Immunol.* **43**, 2114–2125 (2013). doi: 10.1002/eji.201343403; pmid: 23661549
40. J. A. Hamilton *et al*., Hypoxia enhances the proliferative response of macrophages to CSF-1 and their pro-survival response to TNF. *PLOS ONE* **7**, e45853 (2012). doi: 10.1371/journal.pone.0045853; pmid: 23029275
41. B. Everts *et al*., Commitment to glycolysis sustains survival of NO-producing inflammatory dendritic cells. *Blood* **120**, 1422–1431 (2012). doi: 10.1182/blood-2012-03-419747; pmid: 22786879
42. Y. Masuda, T. Togo, S. Mizuno, M. Konishi, H. Nanba, Soluble β-glucan from Grifola frondosa induces proliferation and Dectin-1/Syk signaling in resident macrophages via the GM-CSF autocrine pathway. *J. Leukoc. Biol.* **91**, 547–556 (2012). doi: 10.1189/jlb.0711386; pmid: 22028332
43. H. Li, R. Durbin, Fast and accurate short read alignment with Burrows-Wheeler transform. *Bioinformatics* **25**, 1754–1760 (2009). doi: 10.1093/bioinformatics/btp324; pmid: 19451168
44. N. A. Rao *et al*., Coactivation of GR and NFKB alters the repertoire of their binding sites and target genes. *Genome Res.* **21**, 1404–1416 (2011). doi: 10.1101/gr.118042.110; pmid: 21750107
45. Y. Zhang *et al*., Model-based analysis of ChIP-Seq (MACS). *Genome Biol.* **9**, R137 (2008). doi: 10.1186/gb-2008-9-9-r137; pmid: 18798982
46. *Guide for the Care and Use of Laboratory Animals* (National Academies Press, Washington, DC, ed. 8, 2011).

ACKNOWLEDGMENTS

S.-C.C., J.Q., and M.G.N. were supported by a Vici grant of the Netherlands Organization of Scientific Research and ERC Consolidator grant 310372 (both to M.G.N). C.W. is supported by funding from the European Research Council under the European Union's Seventh Framework Programme (FP/2007-2013)/ERC grant agreement 2012-322698). Y.L. is supported by Veni grant 863.13.011 of the Netherlands Organization for Scientific Research. R.A.C. and K.M.S. were supported by National Institute of General Medical Sciences grant 5P30GM103415-03 (William Green, PI) and 1P30GM106394-01 (Bruce Stanton, PI), and National Institute of Allergy and Infectious Diseases grant R01AI81838 (R.A.C., PI). R.A.C./K.M.S. thank B. Berwin for the *S. aureus*. R.J.X funded by DK43351, DK097485, Helmsley Trust, and JDRF. The detailed data have been deposited in the GEO database with accession number GSE57206.

SUPPLEMENTARY MATERIALS

www.sciencemag.org/content/345/6204/1250684/suppl/DC1
Figs. S1 to S15
Tables S1 and S2

10 January 2014; accepted 28 August 2014
10.1126/science.1250684

RESEARCH ARTICLE SUMMARY

IMMUNOGENETICS

Transcriptional diversity during lineage commitment of human blood progenitors

Lu Chen, Myrto Kostadima, Joost H. A. Martens, Giovanni Canu, Sara P. Garcia, Ernest Turro, Kate Downes, Iain C. Macaulay, Ewa Bielczyk-Maczynska, Sophia Coe, Samantha Farrow, Pawan Poudel, Frances Burden, Sjoert B. G. Jansen, William J. Astle, Antony Attwood, Tadbir Bariana, Bernard de Bono, Alessandra Breschi, John C. Chambers, BRIDGE Consortium, Fizzah A. Choudry, Laura Clarke, Paul Coupland, Martijn van der Ent, Wendy N. Erber, Joop H. Jansen, Rémi Favier, Matthew E. Fenech, Nicola Foad, Kathleen Freson, Chris van Geet, Keith Gomez, Roderic Guigo, Daniel Hampshire, Anne M. Kelly, Hindrik H. D. Kerstens, Jaspal S. Kooner, Michael Laffan, Claire Lentaigne, Charlotte Labalette, Tiphaine Martin, Stuart Meacham, Andrew Mumford, Sylvia Nürnberg, Emilio Palumbo, Bert A. van der Reijden, David Richardson, Stephen J. Sammut, Greg Slodkowicz, Asif U. Tamuri, Louella Vasquez, Katrin Voss, Stephen Watt, Sarah Westbury, Paul Flicek, Remco Loos, Nick Goldman, Paul Bertone, Randy J. Read, Sylvia Richardson, Ana Cvejic, Nicole Soranzo, Willem H. Ouwehand, Hendrik G. Stunnenberg, Mattia Frontini,* Augusto Rendon*

INTRODUCTION: Blood production in humans culminates in the daily release of around 10^{11} cells into the circulation, mainly platelets and red blood cells. All blood cells originate from a minute population of hematopoietic stem cells (HSCs) that expands and differentiates into progenitor cells with increasingly restricted lineage choice. Characterizing alternative splicing events involved in hematopoiesis is critical for interpreting the effects of mutations leading to inherited disorders and blood cancers and for the rational design of strategies to advance transplantation and regenerative medicine.

RATIONALE: To address this, we explored the transcriptional diversity of human blood progenitors by sequencing RNA from six progenitor and two precursor populations representing the classical myeloid commitment stages of hematopoiesis and the main lymphoid stage. Data were aligned to the human reference transcriptome and genome to quantify known transcript isoforms and to identify novel splicing events, respectively. We used Bayesian polytomous model selection to classify transcripts into distinct expression patterns across the three cell types that comprise each differentiation step.

RESULTS: We identified extensive transcriptional changes involving 6711 genes and 10,724 transcripts and validated a number of these. Many of the changes at the transcript isoform level did not result in significant changes at the gene expression level. Moreover, we identified transcripts unique to each of the progenitor populations, observing enrichment in non–protein-coding elements at the early stages of differentiation. We discovered 7881 novel splice junctions and 2301 differentially used alternative splicing events, enriched in genes involved in regulatory processes and often resulting in the gain or loss of functional domains. Of the alternative splice sites displaying differential usage, 73% resulted in exon-skipping events involving at least one protein domain (38.5%) or introducing a premature stop codon (26%). Enrichment analysis of RNA-binding motifs provided insights into the regulation of cell type–specific splicing events.

ON OUR WEB SITE

Read the full article at http://dx.doi.org/10.1126/science.1251033

To demonstrate the importance of specific isoforms in driving lineage fating events, we investigated the role of a transcription factor highlighted by our analyses. Our data show that nuclear factor I/B (NFIB) is highly expressed in megakaryocytes and that it is transcribed from an unannotated transcription start site preceding a novel exon. The novel NFIB isoform lacks the DNA binding/dimerization domain and therefore is unable to interact with its binding partner, NFIC. We further show that NFIB and NFIC are important in megakaryocyte differentiation.

CONCLUSION: We produced a quantitative catalog of transcriptional changes and splicing events representing the early progenitors of human blood. Our analyses unveil a previously undetected layer of regulation affecting cell fating, which involves transcriptional isoforms switching without noticeable changes at the gene level and resulting in the gain or loss of protein functions. ■

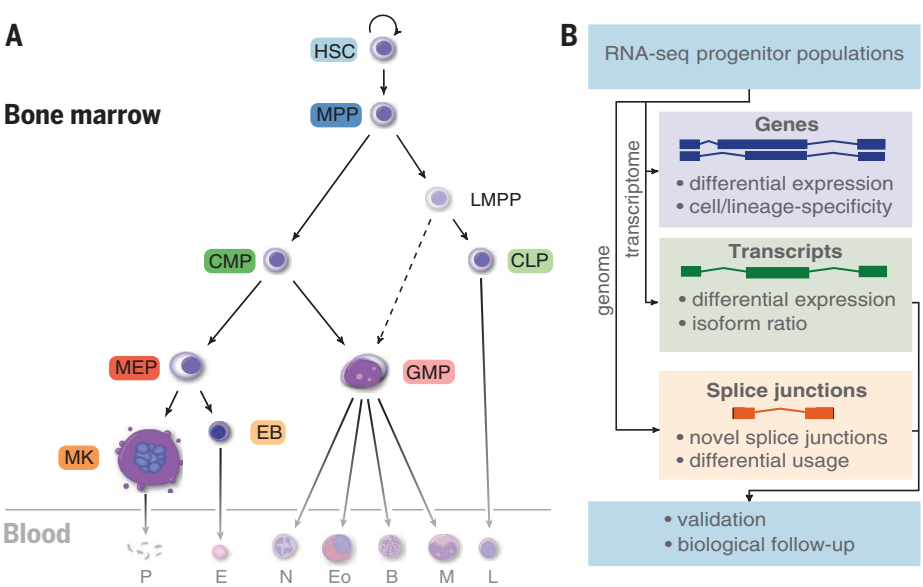

Overview of methodology. RNA-sequencing reads from human blood progenitors [opaque cells in (**A**)] were mapped to the transcriptome to quantify gene and transcript expression. Reads were also mapped to the genome to identify novel splice junctions and characterize alternative splicing events (**B**).

The list of author affiliations is available in the full article online.
*Corresponding author. E-mail: ar506@cam.ac.uk (A.R.); mf471@cam.ac.uk (M.F.)
Cite this article as L. Chen *et al.*, *Science* **345**, 1251033 (2014). DOI: 10.1126/science.1251033

Published by AAAS

RESEARCH ARTICLE

IMMUNOGENETICS

Transcriptional diversity during lineage commitment of human blood progenitors

Lu Chen,[1,2,3]* Myrto Kostadima,[2,4,3]* Joost H. A. Martens,[5]* Giovanni Canu,[2,3] Sara P. Garcia,[2,3] Ernest Turro,[2,3] Kate Downes,[2,3] Iain C. Macaulay,[6] Ewa Bielczyk-Maczynska,[2,3] Sophia Coe,[2,3] Samantha Farrow,[2,3] Pawan Poudel,[2,3] Frances Burden,[2,3] Sjoert B. G. Jansen,[2,3] William J. Astle,[2,3,7] Antony Attwood,[2,3] Tadbir Bariana,[8,9] Bernard de Bono,[10,11] Alessandra Breschi,[12] John C. Chambers,[13,14] BRIDGE Consortium,† Fizzah A. Choudry,[2,3] Laura Clarke,[4] Paul Coupland,[1] Martijn van der Ent,[5] Wendy N. Erber,[15] Joop H. Jansen,[16] Rémi Favier,[17] Matthew E. Fenech,[18] Nicola Foad,[2,3] Kathleen Freson,[19] Chris van Geet,[19] Keith Gomez,[9] Roderic Guigo,[12] Daniel Hampshire,[2,3] Anne M. Kelly,[2,3,20] Hindrik H. D. Kerstens,[5] Jaspal S. Kooner,[13,14] Michael Laffan,[21] Claire Lentaigne,[21] Charlotte Labalette,[2,3] Tiphaine Martin,[2,3,22]‡ Stuart Meacham,[2,3] Andrew Mumford,[23] Sylvia Nürnberg,[2,3]§ Emilio Palumbo,[12] Bert A. van der Reijden,[16] David Richardson,[4] Stephen J. Sammut,[24,25] Greg Slodkowicz,[4] Asif U. Tamuri,[4] Louella Vasquez,[3] Katrin Voss,[2,3]¶ Stephen Watt,[3] Sarah Westbury,[26] Paul Flicek,[4,1] Remco Loos,[4] Nick Goldman,[4] Paul Bertone,[4,27,28] Randy J. Read,[29] Sylvia Richardson,[7] Ana Cvejic,[2,1] Nicole Soranzo,[1,2]* Willem H. Ouwehand,[2,3,1]* Hendrik G. Stunnenberg,[5]* Mattia Frontini,[2,3]*|| Augusto Rendon[2,3,7]*||

Blood cells derive from hematopoietic stem cells through stepwise fating events. To characterize gene expression programs driving lineage choice, we sequenced RNA from eight primary human hematopoietic progenitor populations representing the major myeloid commitment stages and the main lymphoid stage. We identified extensive cell type–specific expression changes: 6711 genes and 10,724 transcripts, enriched in non–protein-coding elements at early stages of differentiation. In addition, we found 7881 novel splice junctions and 2301 differentially used alternative splicing events, enriched in genes involved in regulatory processes. We demonstrated experimentally cell-specific isoform usage, identifying nuclear factor I/B (NFIB) as a regulator of megakaryocyte maturation—the platelet precursor. Our data highlight the complexity of fating events in closely related progenitor populations, the understanding of which is essential for the advancement of transplantation and regenerative medicine.

Hematopoiesis has been extensively studied as a paradigm of stem cell biology and development (*1*). Hematopoietic stem cells (HSCs) and their progeny have been used to pioneer stem cell therapies for malignant and nonmalignant hematological diseases (*2*), and the successful transplantation of genetically repaired HSCs is at the forefront of regenerative medicine in primary immune deficiency and severe combined immunodeficiency (*3*, *4*). HSCs reside in the bone marrow and can undergo asymmetric cell division (*5*), thereby generating an identical copy and a multipotent progenitor cell (MPP). MPPs have the ability to generate all hematopoietic cell types but are incapable of indefinite self-renewal and engraftment (*6*, *7*). This process of expansion, differentiation, and maturation culminates in the daily release of up to 10^{11} newly formed cells into the circulation, mainly red blood cells (RBCs) and platelets (*8*, *9*). The molecular mechanisms driving hematopoiesis have been classically understood as a cascade of gene expression programs propelled by transcription factors (TFs) (*10*) that direct lineage commitment and maturation by the coordinated regulation of gene transcription. Studies of hematological malignancies and model organisms (*1*) have identified many of the critical genes and mechanisms regulating hematopoietic development. Owing to species-specific differences, model organisms only contribute partially toward the detailed characterization of transcriptional cascades regulating human hematopoiesis (*11*–*13*).

Genome-wide transcriptional profiling of human hematopoietic progenitor populations has identified several transcriptional networks coordinating blood formation (*14*). However, gene expression data sets using whole-genome expression arrays only produce an incomplete assessment of the full repertoire of transcript isoforms that underpin the fating and expansion of progenitor cells (*14*–*16*). Alternative splicing is a widespread posttranscriptional process in eukaryotic organisms, wherein multiple distinct transcripts are produced from a single gene (*17*). Analysis of RNA sequencing (RNA-seq) has shown that alternative splicing is used in up to 94% of human multiexonic genes (*18*, *19*), often in a tissue- and developmental stage–specific manner (*18*, *20*, *21*).

Alternative splicing has an important role in disease, with 15% of disease-causing mutations located within splice sites and more than 20% of missense mutations lying within predicted splicing elements (*22*). Studies have also revealed that somatic mutations of splicing factor genes occur frequently in hematological cancers, including

[1]Wellcome Trust Sanger Institute, Wellcome Trust Genome Campus, Hinxton, Cambridge CB10 1SA, UK. [2]Department of Haematology, University of Cambridge, Cambridge Biomedical Campus, Cambridge CB2 0PT, UK. [3]National Health Service (NHS) Blood and Transplant, Cambridge Biomedical Campus, Cambridge CB2 0PT, UK. [4]European Molecular Biology Laboratory, European Bioinformatics Institute, Wellcome Trust Genome Campus, Hinxton, Cambridge CB10 1SD, UK. [5]Department of Molecular Biology, Radboud University, 6525 GA Nijmegen, Netherlands. [6]Sanger Institute–EBI Single-Cell Genomics Centre, Wellcome Trust Sanger Institute, Hinxton, Cambridge CB10 1SA, UK. [7]Medical Research Council Biostatistics Unit, Cambridge Biomedical Campus, Cambridge CB2 0SR, UK. [8]Department of Haematology, University College London Cancer Institute, London WC1E 6DD, UK. [9]The Katharine Dormandy Haemophilia Centre and Thrombosis Unit, Royal Free NHS Trust, London NW3 2QG, UK. [10]CHIME Institute, University College London, Archway Campus, London NW1 2DA, UK. [11]Auckland Bioengineering Institute, University of Auckland, Auckland 1010, New Zealand. [12]Centre for Genomic Regulation and University Pompeu Fabra, 08002 Barcelona, Spain. [13]Imperial College Healthcare NHS Trust, DuCane Road, London W12 0HS, UK. [14]Ealing Hospital NHS Trust, Southall, Middlesex UB1 3HW, UK. [15]Pathology and Laboratory Medicine, University of Western Australia, Crawley, Western Australia 6009, Australia. [16]Department of Laboratory Medicine, Laboratory of Hematology, Radboud University Medical Center, 6525 GA Nijmegen, Netherlands. [17]Assistance Publique–Hopitaux de Paris, INSERM U1009, 94805 Villejuif, France. [18]Biomedical Research Centre, Norwich Medical School, University of East Anglia, Norwich NR4 7TJ, UK. [19]Center for Molecular and Vascular Biology, University of Leuven, 3000 Leuven, Belgium. [20]Cambridge University Hospitals NHS Foundation Trust, Cambridge Biomedical Campus, Cambridge B2 0QQ, UK. [21]Department of Haematology, Hammersmith Campus, Imperial College Academic Health Sciences Centre, Imperial College London, London W12 0HS, UK. [22]Department of Twin Research & Genetic Epidemiology, Genetics and Molecular Medicine Division, St Thomas' Hospital, King's College, London SE1 7EH, UK. [23]School of Cellular and Molecular Medicine, University of Bristol, Bristol BS8 1TD, UK. [24]Department of Oncology, Addenbrooke's Cambridge University Hospital NHS Trust, Cambridge Biomedical Campus, Cambridge CB2 0RE, UK. [25]Cancer Research UK, Cambridge Institute, Cambridge Biomedical Campus, Cambridge CB2 0RE, UK. [26]School of Clinical Sciences, University of Bristol, Bristol BS2 8DZ, UK. [27]Genome Biology and Developmental Biology Units, European Molecular Biology Laboratory, 69117 Heidelberg, Germany. [28]Wellcome Trust—Medical Research Council Stem Cell Institute, University of Cambridge, Cambridge CB2 1QR, UK. [29]Department of Haematology, Cambridge Institute for Medical Research, University of Cambridge, Cambridge Biomedical Campus, Cambridge CB2 0XY, UK.

*These authors contributed equally to this work. †A list of the members of the BRIDGE Bleeding and Platelet Disorders Consortium is available in the supplementary materials. ‡Present address: Department of Twin Research and Genetic Epidemiology, Genetics and Molecular Medicine Division, St Thomas' Hospital, King's College, London SE1 7EH, UK. §Present address: Perelman School of Medicine, University of Pennsylvania, Philadelphia, PA 19104, USA. ¶Present address: Loxxess Neuburg GmbH, Augsburger Straße 133, 86633 Neuburg an der Donau, Germany. ||Corresponding author. E-mail: ar506@cam.ac.uk (A.R.); mf471@cam.ac.uk (M.F.)

myelodysplasia and chronic lymphocytic leukemia (23–25). Thus, knowledge of cell type–specific alternative splicing and transcript isoform usage is required to interpret the consequences of genetic variation and to inform strategies for therapeutic intervention based on gene repair.

Results

Deep transcriptomes of human hematopoietic progenitors

We used fluorescence-activated cell sorting (FACS) of umbilical cord blood (CB) mononuclear cells to obtain highly purified populations of HSCs and five progenitor cells [MPP, CLP (common lymphoid progenitor), CMP (common myeloid progenitor), GMP (granulocyte monocyte progenitor), and MEP (megakaryocyte erythrocyte progenitor)]. In addition, erythroblasts (EBs) and megakaryocytes (MKs), the nucleated precursors of RBCs and platelets, were obtained by in vitro differentiation of CB $CD34^+$ cells (Fig. 1A and fig. S1). For simplicity, we address all eight types of cells as progenitors.

We sequenced 25 polyadenylated [poly(A)$^+$] RNA samples, yielding a total of 2.4×10^9 uniquely aligned reads, ranging from 36×10^6 to 150×10^6 reads per sample (table S1). We used a Bayesian framework implemented in MMSEQ (26) to quantify gene and transcript expression by aligning reads to the transcriptome (Fig. 1B). Transcript usage ratio, the proportion of a gene's expression contributed by each of its transcripts, was also estimated (Fig. 1C). The latter provides an alternative to assessing differential transcript usage, which is less sensitive to depth of coverage and data normalization. To validate MMSEQ transcript expression estimates, we purified 16 additional samples, representing five cell types, and performed quantitative reverse transcription polymerase chain reaction (RT-qPCR) using the Fluidigm BioMark HD system for 36 transcript-specific assays. Linear regression between RNA-seq and RT-qPCR expression estimates indicated high reproducibility in biological replicates (R^2 = 0.70) (fig. S2 and table S2).

We confirmed the identity of each cell population by assessing the expression patterns of a set of well-characterized TF genes that are essential for lineage commitment (Fig. 2A and fig. S3) (1, 27). For instance, *EBF1* expression peaks in CLPs, as expected from its role in B cell development (28). Moreover, the estimated gene expression of *GATA1* and *GATA2* reflects their switch in the differentiation of MEPs to EBs and MKs (29).

Classification of differential expression patterns during lineage commitment

To assess differential expression during hematopoietic lineage commitment at each branching point, such that all possible patterns of expression

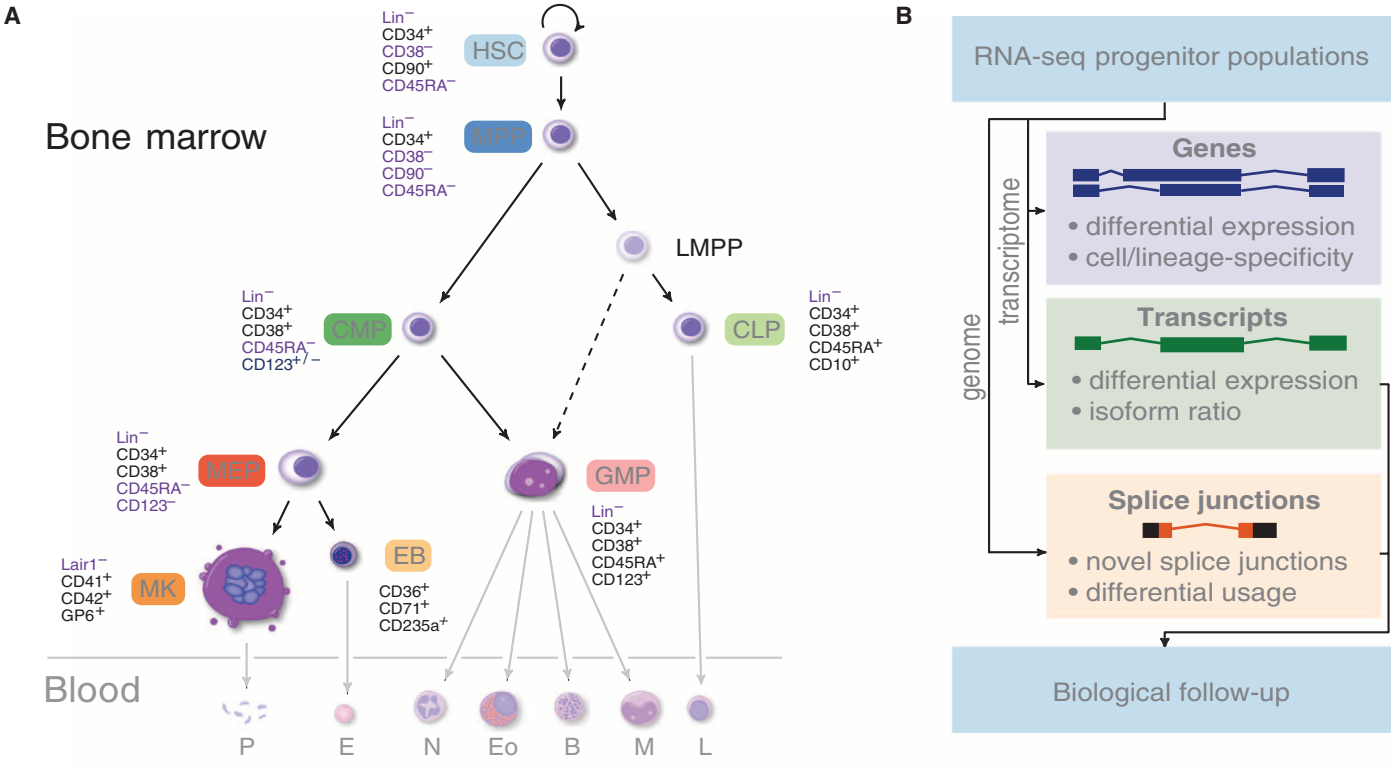

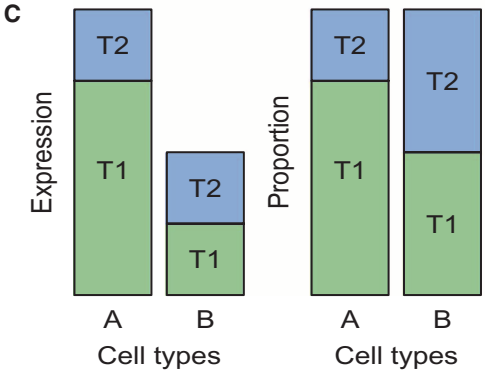

Fig. 1. Transcriptional atlas of hematopoietic progenitors and precursors. (**A**) Schematic representation of the current model of hematopoietic cell ontogeny and samples used in this study. Established ontological relationships are represented as solid lines; emerging ontological relationship are represented as dotted lines. A simplified representation of mature cells is shaded. Antigens used for selecting each population are also indicated. The bone marrow–residing components are the HSC (light blue), MPP (dark blue), lymphoid-primed MPP (LMPP), CLP (light green), CMP (dark green), GMP (light red), MEP (red), EB (light orange), and MK (orange). The blood-residing components are platelets (P), erythrocytes (E), neutrophils (N), eosinophils (Eo), monocytes (M), and lymphocytes (L). (**B**) Data analysis strategy. Reads were mapped to the transcriptome to quantify expression at the gene and transcript levels as well as the transcript proportion (defined as the fraction of gene expression level from a given transcript). Complementary to that, reads were mapped to the genome to identify novel splice junctions and sites where alternative splicing occurs. (**C**) Schematic highlighting the difference between assessing differential expression by looking at transcript expression or transcript proportion.

changes are considered, we used MMDIFF (*30*) to perform Bayesian polytomous model selection between the five possible modes of expression change involving three cell types (see materials and methods for further details and significance thresholds; Fig. 2B). This methodology identifies, for example, transcripts that are down-regulated during the transition from CMP to GMP but retain similar expression between CMP and MEP.

Across all fating events, we detected 6711 genes, 10,724 transcripts, and 7017 transcript usage ratios with significant differences at least at one of the branching points (Fig. 2B). In total, we detected transcriptional changes per cell type in 22

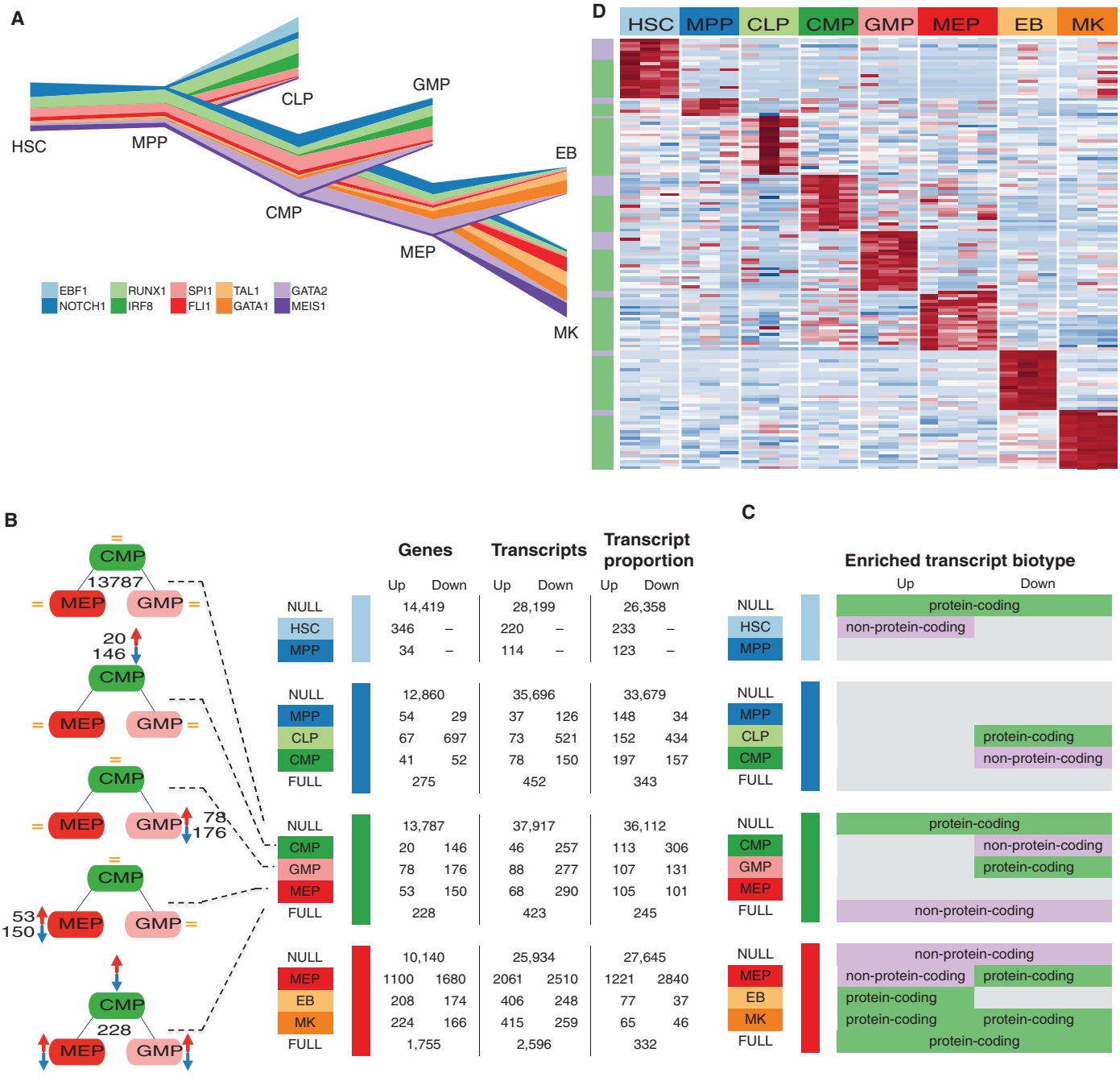

Fig. 2. Transcriptional changes at lineage commitment events. (**A**) River plot representing gene expression levels across cell types for key TFs required for lineage commitment. Line width represents expression level in $\log_2$(FPKM + 1) normalized to the highest expression per gene across cell types. The relative changes in gene expression recapitulate the current understanding of the role of these TFs in hematopoietic differentiation. (**B**) Summary of the number of transcriptional classes—genes, transcripts, and transcript proportions—changing at each lineage commitment point. Bayesian polytomous analysis was used to classify these three quantities into five possible models (top to bottom): NULL model (no change), three single models (only one cell type different), and a FULL model (all three estimates differ). The number of events up- or down-regulated was tallied only when the change occurred in at least two samples at each branching event with an expression FPKM > 1. (**C**) Cell-specific enrichment of protein-coding and non–protein-coding biotypes in up- and down-regulated transcripts for the polytomous models at each branching event. (**D**) Heatmap of expression of lineage-specific transcripts. Polytomous analysis was used to identify genes that were expressed significantly higher in a given cell type relative to all others. Top 20 highest scoring transcripts based on the posterior probability of the model are displayed. The colors along the left axis reflect whether the gene is protein-coding (green) or otherwise (lilac).

to 33% of the 20,459 genes expressed across our data set [defined as expression level ≥ 1 fragment per kilobase of transcript per million fragments mapped (FPKM) in at least two samples]. Changes at the transcript level did not imply measurable differences at the gene level. The overlap between sets of differentially expressed transcripts (at the transcript and usage ratio levels) and of the genes they belong to was low, ranging from 0 to 35% (fig. S4). The extent of overlap did not increase when the threshold applied to ascertain expression (that is, FPKM ≥ 1) was relaxed. Our analysis strategy highlights the advantages of using RNA-seq for assessing the richness of changes in expression at gene and transcript levels compared to probe-based technologies.

Of the 54,386 transcripts expressed at an FPKM ≥ 1 in at least two samples, 28,563 (52.5%) were protein-coding. The second and third most abundant classes were transcripts with retained introns [8661 (15.9%)] and processed transcripts without open reading frames [8140 (15.0%)]. Assessment of the transcript biotypes of differentially expressed transcripts revealed that some modes of expression, at specific branching points, were significantly enriched for non–protein-coding isoforms (Fig. 2C and table S3). For example, during the HSC-to-MPP transition, transcripts up-regulated in HSCs were enriched for non–protein-coding biotypes, such as large intergenic noncoding RNAs (lincRNAs) [false discovery rate (FDR) = 0.043], whereas transcripts with similar expression in both cell types were enriched for protein-coding biotypes (FDR = 0.014). In contrast, differentially expressed transcripts at the terminal differentiation stage (MEP to EB or MK branching point) were enriched for transcripts with protein-coding biotypes (FDR <0.016). These results suggest that a proportion of the regulation of lineage commitment, in the early stages of hematopoiesis, involves non–protein-coding elements and that lincRNAs may counteract differentiation programs, as observed in embryonic stem cells (*31*).

Cell type–specific genes and transcripts

Having evaluated expression patterns for genes differentially expressed between cell types at a branching point, we next focused on those genes and transcripts that were more highly expressed in one given cell population while displaying similar levels of relatively low expression in all other seven cell types (see materials and methods). These cell type–specific genes or transcripts are likely to be important in conferring cellular identity (Fig. 2D and tables S4 and S5). Using conservative thresholds on the posterior probability and the extent of differential expression (see materials and methods), we identified between 6 (for MPP) and 631 (for EB) genes that were cell type–specific. We tested whether our cell type–specific gene sets were able to discriminate between cell populations in two microarray atlases of gene expression in human hematopoiesis (*14*, *16*), achieving high concordance (fig. S5, A to D). The number of cell type–specific transcripts ranged between 19 for MPPs (belonging to 18 genes) and 1807 for EBs (belonging to 1141 genes). The low number of cell type–specific transcripts in MPPs is consistent with the small number of transcripts we identified as up-regulated in this cell type (Fig. 2B). Thus, MPP displayed not only a lower number of up-regulated genes compared to HSCs, CMPs, and CLPs but also an overall lower number of cell-specific transcripts, suggesting a less distinct transcriptional identity of MPPs compared to other progenitor cells.

Consistent with our findings at branching events, cell type–specific gene and transcript sets show different patterns of enrichment of biotypes [Gene Ontology (GO) term enrichment is shown in tables S6 and S7]. Non–protein-coding biotypes were overrepresented in HSC-specific transcripts (FDR = 1.48×10^{-3}), whereas protein-coding transcripts were significantly enriched among transcripts specific in cells at terminally differentiated stages (EBs: FDR < 1.00×10^{-60}; MKs: FDR = 1.96×10^{-55}).

These cell-specific genes may play important roles in determining cell identity and proliferation of the different mature blood cells. We tested the hypothesis that these genes are directly implicated in mature cell differentiation and proliferation by overlapping these sets with genes harboring variants associated with RBC (*32*) and platelet (*33*) quantitative traits through genome-wide association studies. Genes near loci associated with platelet count and volume were enriched in the MK-specific gene set (FDR = 1.7×10^{-8}). In contrast, genes in loci associated with RBC count, RBC volume, and hemoglobin concentration were not enriched in the EB-specific gene set (FDR = 0.42) or in any other cell-specific set. This suggests that the regulation of platelet production is primarily intrinsic to MKs, whereas RBC production is regulated by mechanisms extrinsic to the erythroid lineage.

Our data add to the repertoire of genes and transcripts associated with cell identity in early and late stages of cell development in hematopoiesis, informing downstream examination of the role of transcriptional isoforms expressed in each cell population and their changes at each lineage commitment event.

Identification and characterization of unannotated splice junctions

Owing to their low abundance and anatomical compartmentalization in the bone marrow, blood progenitor cells are systematically underrepresented in existing transcript sequence databases. We analyzed an average of 137 million aligned reads per sample obtained across the 25 samples (table S1 and Fig. 1B) to explore the magnitude of unannotated splice junctions in human hematopoietic progenitors. We intersected splice junction calls from three splice-aware aligners (fig. S6) and required the splice junction to be observed in at least two samples. A total of 159,495 unique splice junctions were detected, of which 29,736 were not annotated in Ensembl v70. We categorized these unannotated splice junctions into four classes, depending on whether their donor and acceptor sites were annotated within Ensembl (Fig. 3A). For 8382 (28.2%) junctions, both donor and acceptor sites were known but not the splicing pattern, whereas 8112 (27.3%) and 8321 (28.0%) splice sites included unannotated splice donors or acceptors. Last, 4921 (16.5%) splice events had both donor and acceptor sites unannotated. The frequency of the four different categories of splicing events did not differ among the eight cell populations (Fig. 3A).

To characterize the 29,736 putative unannotated splice junctions, we investigated their splice site probability scores, degree of conservation, and coding potential. Splice site probability scores (*34*) for unannotated splice sites were similar in known and unannotated donor sites (>0.90, fig. S7). We observed that conservation scores for exonic regions with unannotated splice sites were higher (mean, 0.28) than for intronic regions in the same splice sites (mean, 0.20; $P < 2.2 \times 10^{-16}$, Wilcoxon rank sum test; fig. S8). Last, the protein-coding potential of the unannotated exons was assessed with the frequency of stop codons in all three reading frames for both directions, within a 100–base pair (bp) window around the splice sites. A similar distribution of coding potential was identified in unannotated and annotated exons, with both containing an average of 1.2 fewer stop codons than the equivalent intronic regions (fig. S9).

To identify novel splice junctions, we compared the unannotated splice junctions to splice junctions identified in the University of California Santa Cruz (UCSC) expressed sequence tag (EST)/mRNA data set and in the poly(A)$^+$ RNA-seq data set from 16 human tissues in Illumina BodyMap 2.0 (*35*). In total, 73.5% of our unannotated events were detected in these external data sets, with 23.0% detected in UCSC EST/mRNA data and 72.0% in our reanalysis of the BodyMap 2.0 data set (fig. S10). The remaining 7881 (26.5%) splice junctions were specific to our data set (hereafter called novel). Analysis of novel splice junctions revealed a higher proportion of the noncanonical splicing motif GC-AG (2.2 and 7.3% in unannotated and novel, respectively) compared to annotated sites (0.9%, fig. S11). Whereas both the GT-AG and GC-AG splice sites are processed by the canonical U2-type spliceosome, GC-AG splice sites tend to be alternatively spliced (*36*).

We calculated Shannon's entropy (*37*) for the three classes of splice junctions: annotated, unannotated, and novel (Fig. 3B). A lower entropy distribution in the novel splice junction set indicates that these tend to be population-specific events when compared to the unannotated splice junctions present in BodyMap 2.0 data or all annotated junctions ($P < 2.2 \times 10^{-16}$, Wilcoxon rank sum test; fig. S12). Enrichment analysis of genes containing novel splice junctions highlighted GO terms related to cell cycle, DNA metabolism, and RNA processing (FDR < 5.0×10^{-17}; table S8), suggesting that these novel splice junctions may alter the function of genes involved in critical cellular processes.

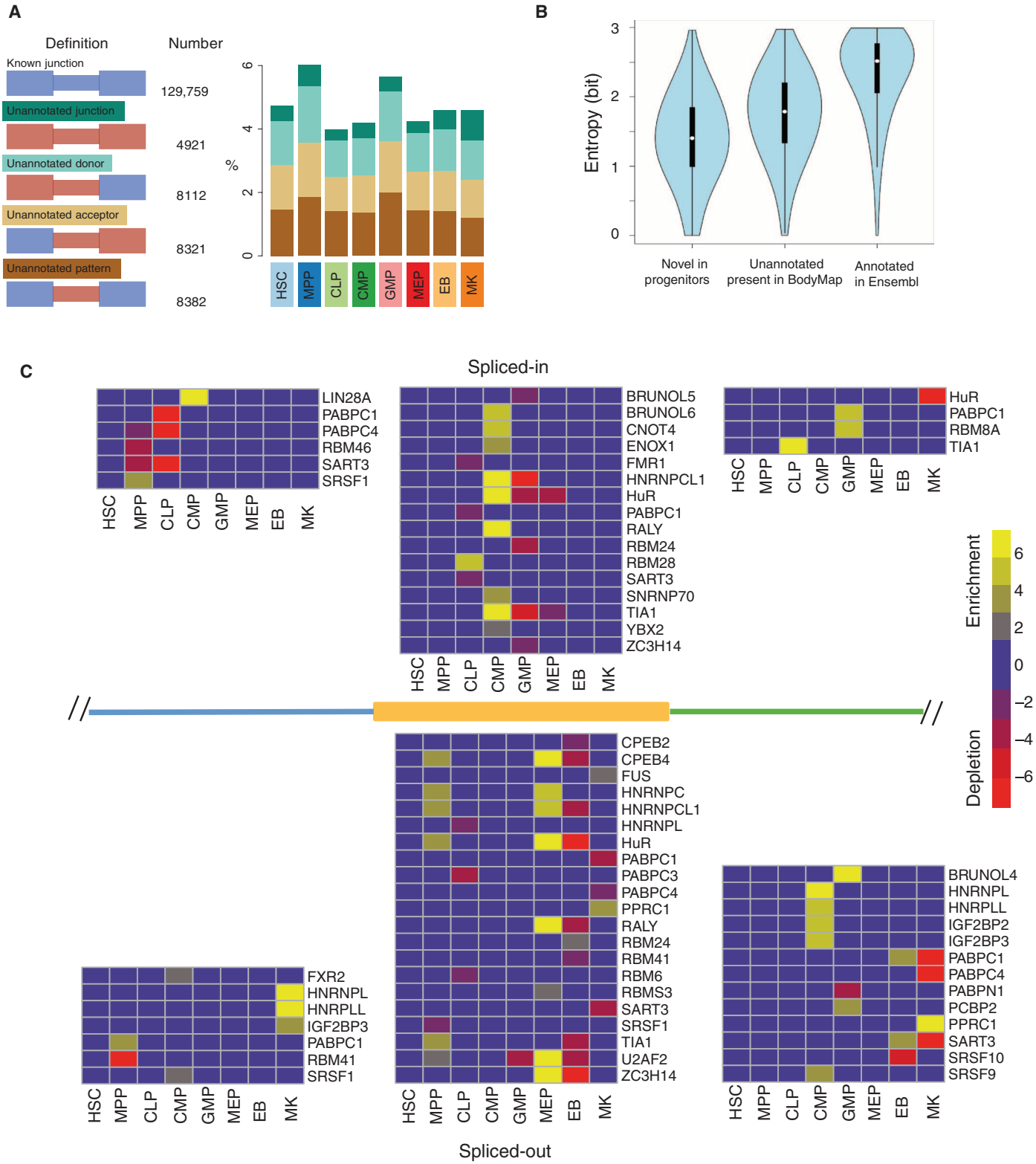

Fig. 3. Cell type–specific splicing and RNA-binding motif enrichment in hematopoiesis. (**A**) Distribution of splice junction definition, absolute count, and cell type–specific fractions within unannotated splice junctions. Blue: annotated exons and junctions; red: unannotated exons and junctions. (**B**) Cell type specificity of known, unannotated, and novel splice junctions measured with Shannon's entropy (*37*). Lower entropy indicates that splice junctions are observed in fewer cell types. (**C**) Region-specific patterns of RNA-binding protein motifs around spliced-in and spliced-out DSU cassette exons. The enrichment or depletion of motifs in three regions: the 300-bp intronic region adjacent to the upstream of the 5′ splice site (blue), the exonic region of the cassette exon (orange), and the 300-bp intronic region adjacent to the downstream of the 3′ splice site (green). The heatmaps present significant enrichment (yellow) or depletion (red) in $-\log_{10}$ *P* value, FDR < 0.05.

Our results suggest that a number of the unannotated and novel splice junctions are indeed functional and used in a cell type–specific manner on the basis of their splice probability, conservation score, coding potential, and entropy.

Validation of novel splice junctions

We used PCR to independently validate 23 of the novel splice junctions. The PCR assays (table S9) performed on five samples showed >90% concordance rate (105 of 115 reactions; figs. S13 to S16 and table S10). We performed additional sequencing of poly(A)$^+$ transcripts from sample MK_3 using the PacBio RS sequencing platform, which enables sequencing of full-length transcripts and overcomes the limitations of transcriptome assembly on the basis of short Illumina reads (*38*). PacBio sequencing yielded 67,110 reads identified as full-length molecules (originating from individual RNA transcripts) ranging between 322 and 13,170 bp in length (median, 2272 bp). These were further combined into 35,663 consensus sequence clusters—transcript structures (see materials and methods). Two novel splice junctions validated by PCR in MKs were also observed within the PacBio data set (fig. S15). Using these data, we investigated the transcriptional context of the novel splice junctions in MKs. Visual inspection of the PacBio alignments indicated that a number of novel splice junctions are part of full-length transcripts, including a previously unobserved intergenic locus on chromosome 12 and an antisense transcript within an annotated protein-encoding region in the *GNG12* locus (fig. S15).

Of the 94,423 splice junctions with 10 or more Illumina reads in MK_3, 54% were supported by PacBio data. In contrast, 7% (66 of 956) of novel and 11% (773 of 7234) of unannotated splice junctions identified in MK_3 were recapitulated in the PacBio data set. We used the annotated splice junctions to estimate the probability of detection by PacBio as a function of read depth and transcript length. The observed validation rates of unannotated and novel junctions, after accounting for read depth, would be consistent with the majority of these junctions originating from transcripts less than 300 bp in length [fig. S17 and (*39*)]. Notwithstanding PacBio's lower depth of sequencing and other unaccounted technical aspects, this analysis provides support to the idea that a large fraction of novel splicing events involve very short transcripts not captured by PacBio.

Differential usage of alternative splice junctions

To investigate the prevalence of cell type–specific alternative splicing, we identified 42,001 splice junction sets where two or more splice junctions shared either the donor or the acceptor sites. Of these, we focused on the 20,924 (49.8%) junctions that contained only two splicing alternatives and were detected in at least two biological replicates. To determine whether an alternative splice site displays differential splicing usage (DSU) [that is, the relative contribution of splicing alternatives (usage proportion) differs between a given cell type and the average proportion across all other cell types], we fitted a beta-binomial model and established statistical significance using a likelihood ratio test. The beta-binomial model accounts for the overdispersion—beyond the expected binomial variance—present in the data. It is an extension to the binomial model (that is, logistic regression) and is akin to using a negative binomial distribution to model overdispersed counts data. This analysis identified 2301 DSU sets (FDR < 0.1). The number of DSU events ranged between 4 for HSC and 1034 for CLP (table S11 and figs. S14, S18, and S19). The DSU set was enriched with novel splice junctions compared to all junctions ($P = 4.39 \times 10^{-7}$, χ^2 test).

To better characterize the biological relevance of cell type–specific DSU, we classified splicing events according to their transcriptional consequences: 73.4% lead to exon skipping events, 8.3% of junctions have an alternative 3′ acceptor, and 6.2% have an alternative 5′ donor; 12.1% of events could not be annotated by using the reference transcriptome (fig. S20). Although unannotated, the length distribution of this fraction suggests that the majority is composed of exon skipping events (fig. S20).

In the alternative spliced regions displaying DSU, 26.1% contained a premature stop codon and 38.5% contained at least one predicted protein structure or domain, therefore resulting in gain or loss of protein functions. No one type of domain was significantly overrepresented in the DSU set. Of the alternative acceptor sites displaying DSU, 39% (84 of 216) resulted from a 3-bp shift in the alternative acceptor sites (fig. S21, left panel), displaying a NAGNAG motif (*40*) (fig. S21, right panel). This motif maintains the translation frame and may introduce a single amino acid insertion or a substitution (fig. S22). The 2301 DSU events could be assigned to 1704 genes. GO enrichment analysis of these genes indicates that these genes may be directly involved in the regulation of transcription and splicing (table S12).

We validated 11 DSU events (4 novel and 7 known events) by using PCR (figs. S14, S15, and S23). Densitometry estimates of the percentage spliced-in (PSI) of these PCRs correlates with the PSI estimated from the RNA-seq data ($n = 26$, $R^2 = 0.78$, fig. S24). In addition, we validated a novel DSU in *nuclear factor I/B* (*NFIB*) (see below and Fig. 4A) and a DSU event in *GFI1B* (*39*). In CMPs, EBs, and MKs, the DSU event in *GFI1B* results in an alternatively spliced-out exon 4 that encodes for two Zn finger domains critical for megakaryopoiesis (*39*). Overall, the DSU analysis confirms alternative splicing as an additional key mechanism through which fundamental processes during hematopoiesis are regulated.

RNA-binding motif enrichment in DSU

Alternative splicing is regulated by trans-acting splicing factors that recognize cis-acting sequences in exons or introns, to promote or suppress the assembly of the spliceosome at the adjacent splice site. We therefore investigated the molecular regulation of cell-specific alternative splicing by examining the sequences around alternatively spliced exons. We used 102 recently described RNA-binding motifs of 80 human RNA-binding proteins (*41*) to identify sets of motifs significantly enriched or depleted in the regions surrounding DSU junctions (table S13). Of the 80 RNA-binding proteins with known binding motifs, 59 were expressed in our data with FPKM > 1 and displayed variable cell type specificity (fig. S25). RNA-binding motif enrichment analysis was performed on cassette exons and proximal intronic regions. The patterns of enrichment and depletion, in addition to the identity of the motifs, varied widely across cell types (Fig. 3C).

The proteins BRUNOL, SRSF, and TIA1 and the HNRNP (heterogeneous ribonucleoprotein) family of proteins are known to regulate tissue-specific splicing (*42*). The patterns of enrichment and depletion in our data set for these proteins suggest that their role in regulating tissue-specific splicing also extends to hematopoietic cells (Fig. 3C). For example, we identified that the motifs of the HNRNP protein family, which typically bind to exonic splicing silencers (*43*), were enriched in exonic regions of MPPs and MEPs that are spliced out.

Novel isoform of NFIB regulates megakaryopoiesis

To investigate the impact of different transcript isoforms in a biological system, we focused our attention on the role of two TFs in megakaryopoiesis, *NFIB*, described below, and *GFI1B* (*39*), as an example of how our analysis informs the interpretation of patient sequencing data. *NFIB* was identified at the MEP/EB/MK branching point (fig. S26), containing a novel MK-specific DSU event (FDR < 0.05). The role of *NFIB* has been extensively studied in lung maturation, the nervous system (*44*), and epithelial stem cell development (*45*). The *NFI* family of TFs, constituted by four members (A, B, C, and X), has previously been implicated in regulating hematopoiesis, with *Nfix* identified as functional in murine HSCs and progenitors (*46*) and *NFIA* implicated in human erythropoiesis (*47*). *NFIC* has been observed as being differentially expressed between MKs of fetal and postnatal origin (*48*). In addition, *NFIB* has been identified as one of the TFs down-regulated in the HSC-to-MPP transition (*49*). However, its role in the later stages of hematopoiesis has remained unexplored.

By examining genomic alignments, we identified a novel *NFIB* transcript (chr9:14,179,779–14,214,332 bp) and annotated the position of the transcription start site (TSS) in the novel first exon. The isoform that results from this novel transcript was primarily expressed in HSCs and MKs and was only present in white blood cells in the BodyMap 2.0 data set, whereas the canonical isoform is widely expressed across other BodyMap 2.0 tissues. The novel TSS lies in a region

of open chromatin in primary MKs (*50*) that is occupied by the TFs MEIS1 (this study), FLI1, GATA1, and SCL/TAL1, but not GATA2 or RUNX1 (*51*). The TSS is also marked by the promoter mark H3K4me3 in MKs (fig. S27). We validated the novel TSS by 5′-RACE RT-PCR and observed multiple PacBio reads supporting it (Fig. 4A). Western blotting confirmed the presence of the protein encoded by the novel short

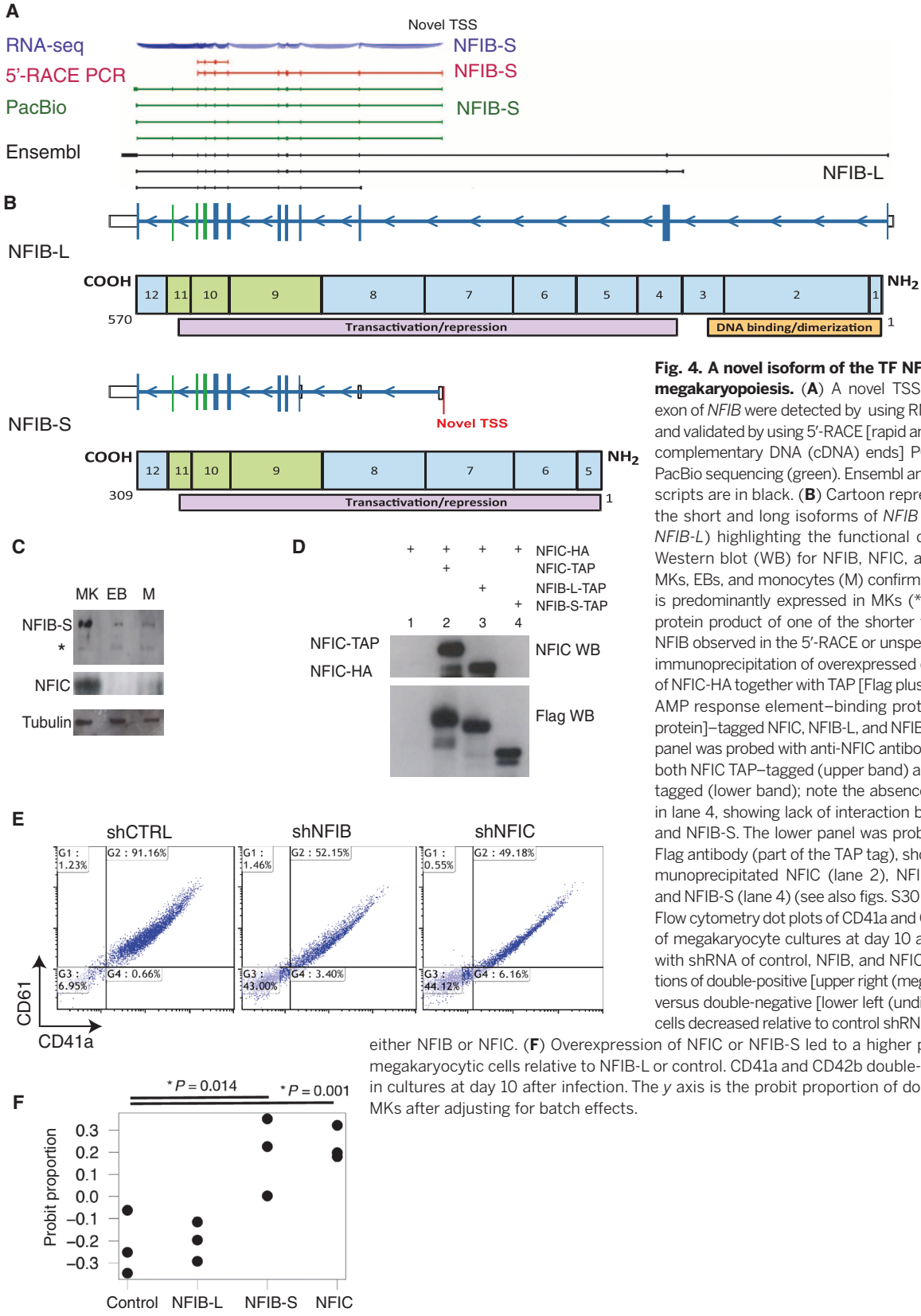

Fig. 4. A novel isoform of the TF NFIB regulates megakaryopoiesis. (**A**) A novel TSS and a novel exon of *NFIB* were detected by using RNA-seq (blue) and validated by using 5′-RACE [rapid amplification of complementary DNA (cDNA) ends] PCR (red) and PacBio sequencing (green). Ensembl annotated transcripts are in black. (**B**) Cartoon representation of the short and long isoforms of *NFIB* (*NFIB-S* and *NFIB-L*) highlighting the functional domains. (**C**) Western blot (WB) for NFIB, NFIC, and tubulin in MKs, EBs, and monocytes (M) confirms that NFIB-S is predominantly expressed in MKs (* is either the protein product of one of the shorter transcripts of NFIB observed in the 5′-RACE or unspecific). (**D**) Co-immunoprecipitation of overexpressed combinations of NFIC-HA together with TAP [Flag plus CREB (cyclic AMP response element–binding protein)–binding protein]–tagged NFIC, NFIB-L, and NFIB-S. The upper panel was probed with anti-NFIC antibodies, showing both NFIC TAP–tagged (upper band) and NFIC-HA–tagged (lower band); note the absence of NFIC-HA in lane 4, showing lack of interaction between NFIC and NFIB-S. The lower panel was probed with anti-Flag antibody (part of the TAP tag), showing the immunoprecipitated NFIC (lane 2), NFIB-L (lane 3), and NFIB-S (lane 4) (see also figs. S30 and S31). (**E**) Flow cytometry dot plots of CD41a and CD61 staining of megakaryocyte cultures at day 10 after infection with shRNA of control, NFIB, and NFIC. The proportions of double-positive [upper right (megakaryocytic)] versus double-negative [lower left (undifferentiated)] cells decreased relative to control shRNA by silencing either NFIB or NFIC. (**F**) Overexpression of NFIC or NFIB-S led to a higher proportion of megakaryocytic cells relative to NFIB-L or control. CD41a and CD42b double-positive MKs in cultures at day 10 after infection. The *y* axis is the probit proportion of double-positive MKs after adjusting for batch effects.

isoform, NFIB-S, as the major isoform in MKs (Fig. 4B and fig. S28), whereas the longer isoform encoded by the canonically spliced transcript could not be detected.

NFIB is known to bind DNA preferentially as a homodimer or a heterodimer in combination with other NFI family members (*52*). Because NFIB-S lacks the DNA binding and protein interaction domains (*53*), we investigated its ability to interact with NFIC in MKs, given its previously hypothesized role in definitive postnatal megakaryopoiesis (*48*). Cotransfection experiments followed by immunoprecipitation showed that the novel isoform, NFIB-S, lacked the ability to interact with NFIC (Fig. 4C). To determine the role of both NFIB and NFIC during megakaryopoiesis, we induced peripheral blood $CD34^+$ cells to differentiate toward MKs and infected them with pools of short hairpin RNA (shRNA) lentiviruses targeting *NFIB*, *NFIC*, or a nonsilencing control. Knockdown of either gene resulted in a marked reduction in differentiation toward MKs as assessed by flow cytometry (Fig. 4D) and confirmed by morphological analysis (fig. S29). This indicated that both NFIB-S and NFIC have an essential role in megakaryopoiesis despite the absence of a DNA binding domain in NFIB-S. Overexpression of both *NFIB*-S and *NFIC* in $CD34^+$ cells increased cell maturation (Fig. 4E, $P = 0.001$ and $P = 0.014$, respectively), measured as double positivity for the MK maturation markers CD41a (ITGA2B) and CD42b (GP1BA) (*54*). In contrast, overexpression of the canonical isoform, *NFIB-L*, had no effect (Fig. 4E). These experiments indicate that both NFIC and the novel isoform NFIB-S, identified in our analysis, play a critical interlinked role in the formation of MKs.

Discussion

Current knowledge of gene expression and function in hematopoiesis is mainly based on observations at gene level. However, it is the transcript, rather than the gene, to which biological function should be ascribed, either as protein-coding or non–protein-coding RNA.

Here, RNA-seq of HSCs and seven progenitor populations have enabled the identification, quantification, and differential expression analysis of cell type–specific transcript isoforms, novel and unannotated splice junctions, and alternative splicing events at a genome-wide level. Analysis of lineage commitment events revealed a wealth of previously undetectable transcript switching and of shifts altering isoform usage ratio, without appreciable changes at gene level, providing evidence of additional layers of regulation in cell fating.

Generating an atlas of splicing events allowed us to explore the diversity and mechanisms behind alternative splicing in human hematopoiesis as well as to contribute further to the human genome functional annotation by reporting 7881 novel splice junctions specific to these rare cell populations.

To demonstrate the importance of specific isoforms in driving lineage-fating events, we investigated the role of a TF highlighted by the polytomous analysis. We envisage that integration of this Blueprint RNA-seq data set with the deep catalogs generated by Blueprint and other epigenome consortia will aid the annotation of the functional genomic landscape of the hematopoietic system. This is essential in the continued effort to interpret the functional consequences of mutations in patients with rare hematological disorders and supports the next enhancements of personalized treatments for patients with hematological malignancies.

Materials and methods

Progenitor cell purification

CB was collected after informed consent (ethical approval REC 12/EE/0040), and mononuclear cells were extracted. $CD34^+$ cells were isolated using the EasySep Human Progenitor Cell Enrichment Kit with Platelet Depletion (STEMCELL Technologies, Vancouver, Canada), stained using a panel of antibodies, and flow-sorted to purify HSC, MPP, CLP, CMP, MEP, and GMP cells that were lysed in TRIzol reagent (Life Technologies, Carlsbad, California).

Cell culture and purification

EBs and MKs were cultured from $CD34^+$ cells isolated from CB mononuclear cells with the human CD34 isolation kit (Miltenyi Biotec, Bergisch Gladbach, Germany). For EBs, $CD34^+$ cells were cultured with erythropoietin, stem cell factor, and interleukin-3 (IL-3) for 14 days. For MKs, $CD34^+$ cells were cultured for 10 days in thrombopoietin and IL-1β. Both populations were immunoselected to >95% purity before lysis.

RNA-seq library preparation and sequencing

RNA was extracted from TRIzol preparations. One hundred picograms of RNA was used to generate poly(A)$^+$ RNA libraries with the SMARTer Ultra Low RNA and Advantage 2 PCR kits (Clontech, Mountain View, California). Samples were indexed with NEXTflex adapters (Bioo Scientific, Austin, Texas), and 100-bp paired-end sequencing was performed on Illumina HiSeq 2000 instruments with TruSeq reagents (Illumina, San Diego, California).

Quality control, trimming, alignment, and expression analysis

RNA-seq libraries were initially subjected to a quality control step, where outliers were identified and discarded from further analysis on the basis of the duplication rates and gene coverage. Paired-end reads of the 25 independent samples were trimmed for both PCR and sequencing adapters with Trim Galore (*55*). Trimmed reads were aligned to the Ensembl v70 human transcriptome using Bowtie (*56*). Quantification of gene and transcript expression was performed with MMSEQ (*26*).

Differential expression analysis through polytomous model classification

Significant differential expression was determined with MMDIFF (*30*) at three different levels: gene, transcript, and isoform usage (generically called features). Polytomous classification was carried out by first performing two-model comparisons to calculate Bayes factors, $B(0,m)$, between a common baseline model and models representing the expression patterns of interest for a given feature. In the baseline model, 0, the feature's mean expression level is the same in all cell types, and in the alternative model, m, the mean expression level is allowed to differ according to the desired pattern (for example, CMP = GMP ≠ MEP). Bayes' theorem was used to compute the posterior probability that the true model γ is equal to m under the assumption that the alternative models are exhaustive: $P(\gamma = m|x) = B(0, m) \times P(\gamma = m)/\Sigma B(0, m') \times P(\gamma = m')$, where x denotes the MMSEQ estimates for that feature.

For the transition from HSCs to MPPs, we used a two-model comparison, where we used a prior probability that the baseline model was true of 0.9. This can be interpreted as a prior belief that 10% of features are differentially expressed. Features with a posterior probability for the alternative model above 0.5 (equivalent to a Bayes factor threshold of 9, representing strong evidence for the alternative model) and an FPKM > 1 in at least two of the samples involved were considered differentially expressed.

At each cell-fating point involving three cell types, we studied all patterns of expression between the progenitor cell and its immediate progeny. We classified feature expression patterns according to five models. The simplest model assumes that the mean expression level is the same across cell types. The most complex model assumes that the mean expression level is different for each cell type. The remaining three models assume that two of the three cell types have the same mean expression level. We specified a prior probability of 80% for the simplest model and distributed the remaining probability evenly across the four alternative models. The model with the highest posterior probability was selected.

Gene set enrichment analysis

Gene and transcript sets derived from the polytomous and the cell type–specific expression analyses of the RNA-seq data were tested for gene set enrichment with the goseq R/Bioconductor package version 1.14.0 (*57*), which accounts for the relationship between power of detection and transcript length. All P values were corrected for multiple testing using the Benjamini-Hochberg method (*58*).

Selection of cell type–specific genes and transcripts

We selected cell type–specific genes and transcripts by performing a nine-model polytomous comparison. The simplest model assumes that the mean expression level is the same across cell types. Each of the remaining eight models assumes that the expression is the same across all cell types except for one of the progenitors. We specified a prior probability of 0.5 for the simplest model and distributed the remaining probability evenly

across the eight alternative models. Genes and transcripts were required to have a posterior probability > 0.5 and a fold change in expression > 1 to be declared cell type–specific. To compare cell type–specific gene expression estimates between our RNA-seq data and publicly available microarray data sets, we retrieved probe annotations for the Illumina (*16*) and Affymetrix (*14*) platforms from Ensembl v70.

Splice junction analysis

Identification of splice junctions for each sample was based on the alignment of the trimmed reads to the human genome (GRCh37) with three different aligners: GSNAP (*59*), STAR (*60*), and GEM (*61*). Splice junctions were considered for further analysis if supported by all three aligners and by at least 10 reads in at least two samples, where reads covered a minimum of 10 bp at both ends of the splice junction. We defined a splice junction as unannotated if not present in Ensembl v70. These were further compared to the EST/mRNA data from UCSC and the Illumina BodyMap 2.0 data set (*35*) to identify novel splice junctions.

Splice site probability scores were extracted from the GSNAP output. PhastCons conservation scores were used to plot evolutionary conservation in the 100 bp surrounding each splice junction. Coding potential was estimated by summing the number of possible stop codons in exonic and intronic regions, in all reading frames and in 100 bp flanking the unannotated splice site. Shannon's entropy (*37*) was calculated on the basis of the read coverage of the splice junctions.

DSU was identified with a beta-binomial model. The characterization of the protein domains in cassette exons with DSU was performed with InterProscan 5 (*62*) to search for domains predicted by Pfam.

Validation of transcript isoform expression and splicing events

To validate the quantification of transcript levels determined by analysis of the RNA-seq data with MMSEQ, we performed RT-PCR assays with 40 transcript-specific assays and 5 positive control assays in multiple cell subsets. Quantitation of each transcript was performed in multiple progenitor cell subsets with the BioMark HD system (Fluidigm, San Francisco, California). After requiring call quality scores >0.9 (Fluidigm Real-Time PCR Analysis software, www.fluidigm.com/software.html), 36 transcripts were analyzed. For each probe, ΔΔCq values were calculated with the B2M transcript as control and the average ΔΔCq for MKs. Linear regression was then performed between ΔΔCq values and the corresponding MMSEQ estimates relative to mean MK.

To validate progenitor-specific novel splice junctions and exon-skipping events, we designed PCR primers to amplify 30 junctions identified by RNA-seq. PCR was performed on pools of the RNA-seq libraries. PCR products were run on agarose gel and imaged, and densitometry was performed.

PacBio libraries were generated (Pacific Biosciences, Menlo Park, California) from cDNA obtained by reverse transcription of 10 ng of MK_3 total RNA and sequenced in five SMRT cells on the PacBio RSII. SMRT Pipe and ICE were used to filter reads to generate consensus sequence clusters that were mapped to the reference human genome (GRCh37) using GMAP.

Enrichment analysis of RNA-binding motifs around cassette exons

Motif enrichment analysis of 102 RNA-binding motifs (*41*) was performed on DSU cassette exons (FDR < 0.05 and usage proportion change > 0.05) over three genomic regions: upstream intronic (300 bp), exonic, and downstream intronic (300 bp). Enrichment and depletion of RNA-binding motifs was determined with cumulative hypergeometric testing, and *P* values were corrected for multiple testing.

Cloning, shRNA, lentivirus production, and transduction

TRC shRNA lentivirus targeting *NFIB* and *NFIC* and a nonsilencing control were purchased from Thermo Scientific Open Biosystems (Little Chalfont, UK). NFIB full length and NFIC cDNA were cloned into pWPI TAP-tagged vector. Packaging was performed in 293T cells, and viral stocks were titrated and quantified using qPCR and, for pWPI, using qPCR and green fluorescent protein FACS. $CD34^+$ cells were purified from NHS Blood and Transplant apheresis filters, as above (Miltenyi), and then infected with lentiviral particles in the presence of polybrene, in medium supplemented with thrombopoietin and IL-1β. On day 2, medium was replaced and cells were cultured toward MKs. At day 10, MKs were counted and assessed by morphology and flow cytometry for maturation.

Transfections, immunoprecipitations, and Western blots

To detect protein-protein interactions, NFI proteins were expressed by cotransfection in 293T cells and immunoprecipitated with an anti-Flag antibody. Western blots were probed with NFIB, NFIC, and β-tubulin.

Data presentation

River plots were generated with the ggplot2 R package (version 0.9.3.1), which was obtained from Bioconductor (www.bioconductor.org/). Heat maps were generated with both the gplots (version 2.13.0) and pheatmap (version 0.7.7) R packages, which were both obtained from CRAN (http://cran.r-project.org/). For sequence logos of the splice site motifs, we used seqLogo R package (version 1.30.0) available from Bioconductor. The IGV genome browser (version 2.3.34) was used for visualization (www.broadinstitute.org/igv/). For further details, please refer to the supplementary materials.

REFERENCES AND NOTES

1. S. H. Orkin, L. I. Zon, Hematopoiesis: An evolving paradigm for stem cell biology. *Cell* **132**, 631–644 (2008). doi: 10.1016/j.cell.2008.01.025; pmid: 18295580
2. J. Hoggatt, J. M. Speth, L. M. Pelus, Concise review: Sowing the seeds of a fruitful harvest: Hematopoietic stem cell mobilization. *Stem Cells* **31**, 2599–2606 (2013). doi: 10.1002/stem.1574; pmid: 24123398
3. I. I. Slukvin, Hematopoietic specification from human pluripotent stem cells: Current advances and challenges toward de novo generation of hematopoietic stem cells. *Blood* **122**, 4035–4046 (2013). doi: 10.1182/blood-2013-07-474825; pmid: 24124087
4. M. P. Lambert, S. K. Sullivan, R. Fuentes, D. L. French, M. Poncz, Challenges and promises for the development of donor-independent platelet transfusions. *Blood* **121**, 3319–3324 (2013). doi: 10.1182/blood-2012-09455428; pmid: 23321255
5. B. Giebel, I. Bruns, Self-renewal versus differentiation in hematopoietic stem and progenitor cells: A focus on asymmetric cell divisions. *Curr. Stem Cell Res. Ther.* **3**, 9–16 (2008). doi: 10.2174/157488808783489444; pmid: 18220918
6. R. Majeti, C. Y. Park, I. L. Weissman, Identification of a hierarchy of multipotent hematopoietic progenitors in human cord blood. *Cell Stem Cell* **1**, 635–645 (2007). doi: 10.1016/j.stem.2007.10.001; pmid: 18371405
7. C. M. Baum, I. L. Weissman, A. S. Tsukamoto, A. M. Buckle, B. Peault, Isolation of a candidate human hematopoietic stem-cell population. *Proc. Natl. Acad. Sci. U.S.A.* **89**, 2804–2808 (1992). doi: 10.1073/pnas.89.7.2804; pmid: 1372992
8. S. H. Orkin, Diversification of haematopoietic stem cells to specific lineages. *Nat. Rev. Genet.* **1**, 57–64 (2000). doi: 10.1038/35049577; pmid: 11262875
9. S. Doulatov, F. Notta, E. Laurenti, J. E. Dick, Hematopoiesis: A human perspective. *Cell Stem Cell* **10**, 120–136 (2012). doi: 10.1016/j.stem.2012.01.006; pmid: 22305562
10. H. Iwasaki *et al*., The order of expression of transcription factors directs hierarchical specification of hematopoietic lineages. *Genes Dev.* **20**, 3010–3021 (2006). doi: 10.1101/gad.1493506; pmid: 17079688
11. J. Mestas, C. C. Hughes, Of mice and not men: Differences between mouse and human immunology. *J. Immunol.* **172**, 2731–2738 (2004). doi: 10.4049/jimmunol.172.5.2731; pmid: 14978070
12. D. G. Tenen, R. Hromas, J. D. Licht, D. E. Zhang, Transcription factors, normal myeloid development, and leukemia. *Blood* **90**, 489–519 (1997). pmid: 9226149
13. R. E. Dickinson *et al*., Exome sequencing identifies GATA-2 mutation as the cause of dendritic cell, monocyte, B and NK lymphoid deficiency. *Blood* **118**, 2656–2658 (2011). doi: 10.1182/blood-2011-06-360313; pmid: 21765025
14. N. Novershtern *et al*., Densely interconnected transcriptional circuits control cell states in human hematopoiesis. *Cell* **144**, 296–309 (2011). doi: 10.1016/j.cell.2011.01.004; pmid: 21241896
15. N. A. Watkins *et al*., A HaemAtlas: Characterizing gene expression in differentiated human blood cells. *Blood* **113**, e1–e9 (2009). doi: 10.1182/blood-2008-06-162958; pmid: 19228925
16. E. Laurenti *et al*., The transcriptional architecture of early human hematopoiesis identifies multilevel control of lymphoid commitment. *Nat. Immunol.* **14**, 756–763 (2013). doi: 10.1038/ni.2615; pmid: 23708252
17. T. W. Nilsen, B. R. Graveley, Expansion of the eukaryotic proteome by alternative splicing. *Nature* **463**, 457–463 (2010). doi: 10.1038/nature08909; pmid: 20110989
18. E. T. Wang *et al*., Alternative isoform regulation in human tissue transcriptomes. *Nature* **456**, 470–476 (2008). doi: 10.1038/nature07509; pmid: 18978772
19. Q. Pan, O. Shai, L. J. Lee, B. J. Frey, B. J. Blencowe, Deep surveying of alternative splicing complexity in the human transcriptome by high-throughput sequencing. *Nat. Genet.* **40**, 1413–1415 (2008). doi: 10.1038/ng.259; pmid: 18978789
20. N. L. Barbosa-Morais *et al*., The evolutionary landscape of alternative splicing in vertebrate species. *Science* **338**, 1587–1593 (2012). doi: 10.1126/science.1230612; pmid: 23258890
21. J. Merkin, C. Russell, P. Chen, C. B. Burge, Evolutionary dynamics of gene and isoform regulation in mammalian tissues. *Science* **338**, 1593–1599 (2012). doi: 10.1126/science.1228186; pmid: 23258891
22. R. K. Singh, T. A. Cooper, Pre-mRNA splicing in disease and therapeutics. *Trends Mol. Med.* **18**, 472–482 (2012). doi: 10.1016/j.molmed.2012.06.006; pmid: 22819011
23. K. Yoshida *et al*., Frequent pathway mutations of splicing machinery in myelodysplasia. *Nature* **478**, 64–69 (2011). doi: 10.1038/nature10496; pmid: 21909114
24. M. Cazzola, M. G. Della Porta, L. Malcovati, The genetic basis of myelodysplasia and its clinical relevance. *Blood* **122**, 4021–4034 (2013). doi: 10.1182/blood-2013-09-381665; pmid: 24136165

25. Y. Wan, C. J. Wu, *SF3B1* mutations in chronic lymphocytic leukemia. *Blood* **121**, 4627–4634 (2013). doi: 10.1182/blood-2013-02-427641; pmid: 23568491
26. E. Turro *et al*., Haplotype and isoform specific expression estimation using multi-mapping RNA-seq reads. *Genome Biol.* **12**, R13 (2011). doi: 10.1186/gb-2011-12-2-r13; pmid: 21310039
27. A. C. Wilkinson, B. Göttgens, Transcriptional regulation of haematopoietic stem cells. *Adv. Exp. Med. Biol.* **786**, 187–212 (2013). doi: 10.1007/978-94-007-6621-1_11; pmid: 23696358
28. D. Bryder, M. Sigvardsson, Shaping up a lineage—Lessons from B lymphopoesis. *Curr. Opin. Immunol.* **22**, 148–153 (2010). doi: 10.1016/j.coi.2010.02.001; pmid: 20207528
29. H. Kaneko, R. Shimizu, M. Yamamoto, GATA factor switching during erythroid differentiation. *Curr. Opin. Hematol.* **17**, 163–168 (2010). doi: 10.1097/MOH.0b013e32833800b8; pmid: 20216212
30. E. Turro, W. J. Astle, S. Tavaré, Flexible analysis of RNA-seq data using mixed effects models. *Bioinformatics* **30**, 180–188 (2014). doi: 10.1093/bioinformatics/btt624; pmid: 24281695
31. M. Guttman *et al*., lincRNAs act in the circuitry controlling pluripotency and differentiation. *Nature* **477**, 295–300 (2011). doi: 10.1038/nature10398; pmid: 21874018
32. P. van der Harst *et al*., Seventy-five genetic loci influencing the human red blood cell. *Nature* **492**, 369–375 (2012). doi: 10.1038/nature11677; pmid: 23222517
33. C. Gieger *et al*., New gene functions in megakaryopoiesis and platelet formation. *Nature* **480**, 201–208 (2011). doi: 10.1038/nature10659; pmid: 22139419
34. G. Yeo, C. B. Burge, Maximum entropy modeling of short sequence motifs with applications to RNA splicing signals. *J. Comput. Biol.* **11**, 377–394 (2004). doi: 10.1089/1066527041410418; pmid: 15285897
35. C. M. Farrell *et al*., Current status and new features of the Consensus Coding Sequence database. *Nucleic Acids Res.* **42**, D865–D872 (2014). doi: 10.1093/nar/gkt1059; pmid: 24217909
36. T. A. Thanaraj, F. Clark, Human GC-AG alternative intron isoforms with weak donor sites show enhanced consensus at acceptor exon positions. *Nucleic Acids Res.* **29**, 2581–2593 (2001). doi: 10.1093/nar/29.12.2581; pmid: 11410667
37. J. Schug *et al*., Promoter features related to tissue specificity as measured by Shannon entropy. *Genome Biol.* **6**, R33 (2005). doi: 10.1186/gb-2005-6-4-r33; pmid: 15833120
38. T. Steijger *et al*., Assessment of transcript reconstruction methods for RNA-seq. *Nat. Methods* **10**, 1177–1184 (2013). doi: 10.1038/nmeth.2714; pmid: 24185837
39. See Supplementary Materials.
40. M. Hiller *et al*., Widespread occurrence of alternative splicing at NAGNAG acceptors contributes to proteome plasticity. *Nat. Genet.* **36**, 1255–1257 (2004). doi: 10.1038/ng1469; pmid: 15516930
41. D. Ray *et al*., A compendium of RNA-binding motifs for decoding gene regulation. *Nature* **499**, 172–177 (2013). doi: 10.1038/nature12311; pmid: 23846655
42. Y. Barash *et al*., Deciphering the splicing code. *Nature* **465**, 53–59 (2010). doi: 10.1038/nature09000; pmid: 20445623
43. D. L. Black, Mechanisms of alternative pre-messenger RNA splicing. *Annu. Rev. Biochem.* **72**, 291–336 (2003). doi: 10.1146/annurev.biochem.72.121801.161720; pmid: 12626338
44. G. Steele-Perkins *et al*., The transcription factor gene *Nfib* is essential for both lung maturation and brain development. *Mol. Cell. Biol.* **25**, 685–698 (2005). doi: 10.1128/mcb.25.2.685-698.2005; pmid: 15632069
45. C. Y. Chang *et al*., NFIB is a governor of epithelial–melanocyte stem cell behaviour in a shared niche. *Nature* **495**, 98–102 (2013). doi: 10.1038/nature11847; pmid: 23389444
46. P. Holmfeldt *et al*., *Nfix* is a novel regulator of murine hematopoietic stem and progenitor cell survival. *Blood* **122**, 2987–2996 (2013). doi: 10.1182/blood-2013-04-493973; pmid: 24041575
47. L. M. Starnes *et al*., A transcriptome-wide approach reveals the key contribution of NFI-A in promoting erythroid differentiation of human $CD34^+$ progenitors and CML cells. *Leukemia* **24**, 1220–1223 (2010). doi: 10.1038/leu.2010.78; pmid: 20428206
48. O. Bluteau *et al*., Developmental changes in human megakaryopoiesis. *J. Thromb. Haemost.* **11**, 1730–1741 (2013). doi: 10.1111/jth.12326; pmid: 23782903
49. F. Notta *et al*., Isolation of single human hematopoietic stem cells capable of long-term multilineage engraftment. *Science* **333**, 218–221 (2011). doi: 10.1126/science.1201219; pmid: 21737740
50. D. S. Paul *et al*., Maps of open chromatin highlight cell type–restricted patterns of regulatory sequence variation at hematological trait loci. *Genome Res.* **23**, 1130–1141 (2013). doi: 10.1101/gr.155127.113; pmid: 23570689
51. M. R. Tijssen *et al*., Genome-wide analysis of simultaneous GATA1/2, RUNX1, FLI1, and SCL binding in megakaryocytes identifies hematopoietic regulators. *Dev. Cell* **20**, 597–609 (2011). doi: 10.1016/j.devcel.2011.04.008; pmid: 21571218
52. D. Apt, T. Chong, Y. Liu, H. U. Bernard, Nuclear factor I and epithelial cell-specific transcription of human papillomavirus type 16. *J. Virol.* **67**, 4455–4463 (1993). pmid: 8392590
53. J. Dekker, J. A. van Oosterhout, P. C. van der Vliet, Two regions within the DNA binding domain of nuclear factor I interact with DNA and stimulate adenovirus DNA replication independently. *Mol. Cell. Biol.* **16**, 4073–4080 (1996). pmid: 8754805
54. S. Poirault-Chassac *et al*., Notch/Delta4 signaling inhibits human megakaryocytic terminal differentiation. *Blood* **116**, 5670–5678 (2010). doi: 10.1182/blood-2010-05-285957; pmid: 20829371
55. www.bioinformatics.babraham.ac.uk/projects/trim_galore/
56. B. Langmead, C. Trapnell, M. Pop, S. L. Salzberg, Ultrafast and memory-efficient alignment of short DNA sequences to the human genome. *Genome Biol.* **10**, R25 (2009). doi: 10.1186/gb-2009-10-3-r25; pmid: 19261174
57. M. D. Young, M. J. Wakefield, G. K. Smyth, A. Oshlack, Gene ontology analysis for RNA-seq: Accounting for selection bias. *Genome Biol.* **11**, R14 (2010). doi: 10.1186/gb-2010-11-2-r14; pmid: 20132535
58. Y. Hochberg, Y. Benjamini, More powerful procedures for multiple significance testing. *Stat. Med.* **9**, 811–818 (1990). doi: 10.1002/sim.4780090710; pmid: 2218183
59. T. D. Wu, S. Nacu, Fast and SNP-tolerant detection of complex variants and splicing in short reads. *Bioinformatics* **26**, 873–881 (2010). doi: 10.1093/bioinformatics/btq057; pmid: 20147302
60. A. Dobin *et al*., STAR: Ultrafast universal RNA-seq aligner. *Bioinformatics* **29**, 15–21 (2013). doi: 10.1093/bioinformatics/bts635; pmid: 23104886
61. S. Marco-Sola, M. Sammeth, R. Guigó, P. Ribeca, The GEM mapper: Fast, accurate and versatile alignment by filtration. *Nat. Methods* **9**, 1185–1188 (2012). doi: 10.1038/nmeth.2221; pmid: 23103880
62. P. Jones *et al*., InterProScan 5: Genome-scale protein function classification. *Bioinformatics* **30**, 1236–1240 (2014). doi: 10.1093/bioinformatics/btu031; pmid: 24451626

ACKNOWLEDGMENTS

The work described in this article was primarily supported by the European Commission Seventh Framework Program through the BLUEPRINT grant with code HEALTH-F5-2011-282510 (D.H., F.B., G.C., J.H.A.M., K.D., L.C., M.F., S.C., S.F., and S.P.G.). Research in the Ouwehand laboratory is further supported by program grants from the National Institute for Health Research (NIHR, www.nihr.ac.uk; to A.A., M.K., P.P., S.B.G.J., S.N., and W.H.O.) and the British Heart Foundation under nos. RP-PG-0310-1002 and RG/09/12/28096 (www.bhf.org.uk; to A.R. and W.J.A.). K.F. and M.K. were supported by Marie Curie funding from the NETSIM FP7 program funded by the European Commission. The laboratory receives funding from the NHS Blood and Transplant for facilities. The Cambridge BioResource (www.cambridgebioresource.org.uk), the Cell Phenotyping Hub, and the Cambridge Translational GenOmics laboratory (www.catgo.org.uk) are supported by an NIHR grant to the Cambridge NIHR Biomedical Research Centre (BRC). The BRIDGE-Bleeding and Platelet Disorders Consortium is supported by the NIHR BioResource—Rare Diseases (http://bioresource.nihr.ac.uk/; to E.T., N.F., and Whole Exome Sequencing effort). Research in the Soranzo laboratory (L.V., N.S., and S. Watt) is further supported by the Wellcome Trust (Grant Codes WT098051 and WT091310) and the EU FP7 EPIGENESYS initiative (Grant Code 257082). Research in the Cvejic laboratory (A. Cvejic and C.L.) is funded by the Cancer Research UK under grant no. C45041/A14953. S.J.S. is funded by NIHR. M.E.F. is supported by a British Heart Foundation Clinical Research Training Fellowship, no. FS/12/27/29405. E.B.-M. is supported by a Wellcome Trust grant, no. 084183/Z/07/Z. Research in the Laffan laboratory is supported by Imperial College BRC. F.A.C., C.L., and S. Westbury are supported by Medical Research Council Clinical Training Fellowships, and T.B. by a British Society of Haematology/NHS Blood and Transplant grant. R.J.R. is a Principal Research Fellow of the Wellcome Trust, grant no. 082961/Z/07/Z. Research in the Flicek laboratory is also supported by the Wellcome Trust (grant no. 095908) and EMBL. Research in the Bertone laboratory is supported by EMBL. K.F. and C.v.G. are supported by FWO-Vlaanderen through grant G.0B17.13N. P.F. is a compensated member of the Omicia Inc. Scientific Advisory Board. This study made use of data generated by the UK10K Consortium, derived from samples from the Cohorts arm of the project. A full list of the investigators who contributed to the generation of the data is available from www.UK10K.org. We wish to acknowledge the following facilities and people: Cambridge BRC Cell Phenotyping Hub, Cambridge BRC Translational Genomics Laboratory, Cambridge BRC Blood and Stem Cell Biobank, NHS Blood and Transplant donation clinic, Sanger Institute–EBI Single-Cell Genomics Centre, J. Garwood, D. Fletcher, L. Guglielmi, team of the Ouwehand laboratory, and M. Bussemakers from the University of Nijmegen. The critical comments from J.-P. Allain and D. Rico are greatly appreciated. The data are available from the Blueprint Consortium Web site www.blueprint-epigenome.eu/ and the European Genome-phenome Archive with accession no. EGAD00001000745. Visualization tools are also accessible from http://blueprint.haem.cam.ac.uk/.

SUPPLEMENTARY MATERIALS

www.sciencemag.org/content/345/6204/1251033/suppl/DC1
Materials and Methods
Figs. S1 to S38
Tables S1 to S15
References (*63*–*88*)

20 January 2014; accepted 28 August 2014
10.1126/science.1251033

RESEARCH ARTICLE SUMMARY

IMMUNOGENETICS

Epigenetic programming of monocyte-to-macrophage differentiation and trained innate immunity

Sadia Saeed,* Jessica Quintin,* Hindrik H. D. Kerstens,* Nagesha A. Rao,* Ali Aghajanirefah,* Filomena Matarese, Shih-Chin Cheng, Jacqueline Ratter, Kim Berentsen, Martijn A. van der Ent, Nilofar Sharifi, Eva M. Janssen-Megens, Menno Ter Huurne, Amit Mandoli, Tom van Schaik, Aylwin Ng, Frances Burden, Kate Downes, Mattia Frontini, Vinod Kumar, Evangelos J. Giamarellos-Bourboulis, Willem H. Ouwehand, Jos W. M. van der Meer, Leo A. B. Joosten, Cisca Wijmenga, Joost H. A. Martens, Ramnik J. Xavier, Colin Logie,† Mihai G. Netea,† Hendrik G. Stunnenberg†

INTRODUCTION: Monocytes circulate in the bloodstream for up to 3 to 5 days. Concomitantly, immunological imprinting of either tolerance (immunosuppression) or trained immunity (innate immune memory) determines the functional fate of monocytes and monocyte-derived macrophages, as observed after infection or vaccination.

METHODS: Purified circulating monocytes from healthy volunteers were differentiated under the homeostatic macrophage colony-stimulating factor concentrations present in human serum. During the first 24 hours, trained immunity was induced by β-glucan (BG) priming, and postsepsis immunoparalysis was mimicked by exposure to lipopolysaccharide (LPS), generating endotoxin-induced tolerance. Epigenomic profiling of the histone marks H3K4me1, H3K4me3, and H3K27ac, DNase I accessibility, and RNA sequencing were performed at both the start of the experiment (ex vivo monocytes) and at the end of the 6 days of in vitro culture (macrophages).

RESULTS: Compared with monocytes (Mo), naïve macrophages (Mf) display a remodeled metabolic enzyme repertoire and attenuated innate inflammatory pathways, most likely necessary to generate functional tissue macrophages. Epigenetic profiling uncovered about 8000 dynamic regions associated with about 11,000 DNase I hypersensitive sites. Changes in histone acetylation identified most dynamic events. Furthermore, these regions of differential histone marks displayed some degree of DNase I accessibility that was already present in monocytes. H3K4me1 mark increased in parallel with de novo H3K27ac deposition at distal regulatory regions; H3K4me1 mark remained even after the loss of H3K27ac, marking decommissioned regulatory elements.

β-glucan priming specifically induced about 3000 distal regulatory elements, whereas LPS tolerization induced H3K27ac at about 500 distal regulatory regions. At the transcriptional level, we identified co-regulated gene modules during monocyte-to-macrophage differentiation, as well as discordant modules between trained and tolerized cells. These indicate that training likely involves an increased expression of modules expressed in naïve macrophages, including genes that code for metabolic enzymes. On the other hand, endotoxin tolerance involves gene modules that are more active in monocytes than in naïve macrophages. About 12% of known human transcription factors display variation in expression during macrophage differentiation, training, and tolerance. We also observed transcription factor motifs in DNase I hypersensitive sites at condition-specific dynamic epigenomic regions, implying that specific transcription factors are required for trained and tolerized macrophage epigenetic and transcriptional programs. Finally, our analyses and functional validation indicate that the inhibition of cyclic adenosine monophosphate generation blocked trained immunity in vitro and during an in vivo model of lethal *Candida albicans* infection, abolishing the protective effects of trained immunity.

ON OUR WEB SITE

Read the full article at http://dx.doi.org/10.1126/science.1251086

DISCUSSION: We documented the importance of epigenetic regulation of the immunological pathways underlying monocyte-to-macrophage differentiation and trained immunity. These dynamic epigenetic elements may inform on potential pharmacological targets that modulate innate immunity. Altogether, we uncovered the epigenetic and transcriptional programs of monocyte differentiation to macrophages that distinguish tolerant and trained macrophage phenotypes, providing a resource to further understand and manipulate immune-mediated responses. ■

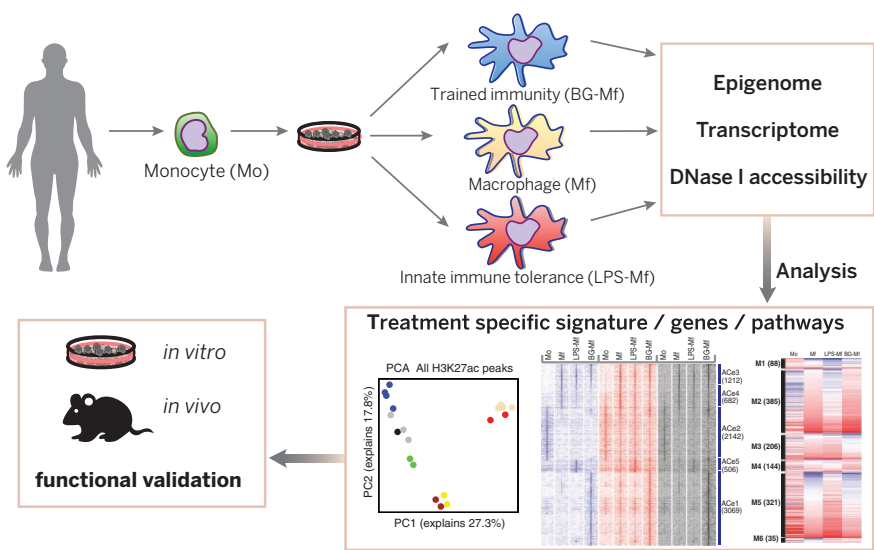

The epigenome, DNase I accessibility, and transcriptome were characterized in purified human circulating monocytes, in vitro differentiated naïve, tolerized (immunosuppression), and trained macrophages (innate immune memory). This allowed the identification of pathways functionally implicated in innate immune memory. This epigenetic signature of human monocyte-to-macrophage differentiation and monocyte training generates hypotheses to understand and manipulate medically relevant immune conditions.

The list of author affiliations is available in the full article online.
*These authors contributed equally to this work.
†Corresponding author. E-mail: h.stunnenberg@ncmls.ru.nl (H.G.S.); mihai.netea@radboudumc.nl (M.G.N.); c.logie@ncmls.ru.nl (C.L.)
Cite this article as S. Saeed *et al.*, *Science* **345**, 1251086 (2014); DOI: 10.1126/science.1251086

Published by AAAS

RESEARCH ARTICLE

IMMUNOGENETICS

Epigenetic programming of monocyte-to-macrophage differentiation and trained innate immunity

Sadia Saeed,[1]* Jessica Quintin,[2]* Hindrik H. D. Kerstens,[1]* Nagesha A. Rao,[1]* Ali Aghajanirefah,[1]* Filomena Matarese,[1] Shih-Chin Cheng,[2] Jacqueline Ratter,[2] Kim Berentsen,[1] Martijn A. van der Ent,[1] Nilofar Sharifi,[1] Eva M. Janssen-Megens,[1] Menno Ter Huurne,[1] Amit Mandoli,[1] Tom van Schaik,[1] Aylwin Ng,[3,4] Frances Burden,[5,6] Kate Downes,[5,6] Mattia Frontini,[5,6] Vinod Kumar,[7] Evangelos J. Giamarellos-Bourboulis,[8] Willem H. Ouwehand,[5,6] Jos W. M. van der Meer,[2] Leo A. B. Joosten,[2] Cisca Wijmenga,[7] Joost H. A. Martens,[1] Ramnik J. Xavier,[3,4] Colin Logie,[1]† Mihai G. Netea,[2]† Hendrik G. Stunnenberg[1]†

Monocyte differentiation into macrophages represents a cornerstone process for host defense. Concomitantly, immunological imprinting of either tolerance or trained immunity determines the functional fate of macrophages and susceptibility to secondary infections. We characterized the transcriptomes and epigenomes in four primary cell types: monocytes and in vitro–differentiated naïve, tolerized, and trained macrophages. Inflammatory and metabolic pathways were modulated in macrophages, including decreased inflammasome activation, and we identified pathways functionally implicated in trained immunity. β-glucan training elicits an exclusive epigenetic signature, revealing a complex network of enhancers and promoters. Analysis of transcription factor motifs in deoxyribonuclease I hypersensitive sites at cell-type–specific epigenetic loci unveiled differentiation and treatment-specific repertoires. Altogether, we provide a resource to understand the epigenetic changes that underlie innate immunity in humans.

Monocytes are generally considered as an intermediate developmental stage between bone marrow precursors and tissue macrophages (*1*). However, circulating monocytes have important effector functions, both during homeostasis through patrol and repair functions (*2*) and during infections by exerting inflammatory effects (*3*). Although several populations of tissue-resident macrophages originate from yolk sac embryonic precursors (*4*), tissues such as dermis and the intestine contain adult monocyte-derived macrophages (*5*–*7*), whereas during infections, adult blood inflammatory monocytes migrate to inflamed tissues and differentiate into monocyte-derived macrophage populations that can eliminate the pathogen and restore tissue integrity (*8*).

In homeostasis or during infections, monocytes can follow different functional programs. During the process of tolerance/immunoparalysis, a common complication of severe sepsis, monocytes enter a refractory functional state, characterized by the incapacity to produce proinflammatory cytokines and decreased human leukocyte antigen DR expression (*9*). Tolerance can be mimicked in vitro and in vivo by challenging the cells with endotoxins such as lipopolysaccharide (LPS): After an initial stimulation phase, cells enter a state of long-term immunotolerance. In contrast, other infections or vaccinations [e.g., *Candida albicans* infection, Bacille Calmette-Guerin (BCG), or measles vaccination] increase the long-term responsiveness of monocytes to microbial stimuli, a state termed "trained immunity" that confers resistance to secondary infections (*10*–*14*). In the case of *Candida* infection, training requires the β-glucan receptor Dectin-1 and the noncanonical Raf-1 pathway and is associated with stable changes in histone trimethylation at H3K4 at a small subset of promoters (*10*). Tolerance and training represent clinically relevant functional states such as the immune paralysis encountered during bacterial sepsis or endotoxin shock (*9*) or the nonspecific protective effects of live microorganism vaccination [e.g., BCG, measles, and yellow fever (*15*)] and strongly influence susceptibility to secondary infections.

Histone and DNA modifications have been hypothesized to play a role in regulating monocyte and macrophage phenotypes (*16*), but data are limited to a few genes and histone modifications (*17*). Moreover, the epigenetic modifications after LPS stimulation were studied for relatively short periods of up to 1 day (*18*). In addition, the two major events that determine the functional fate of monocytes and macrophages—immune tolerance (*19*) and innate immune training (*10*)—have not been thoroughly characterized at the transcriptional and epigenomic level. The BLUEPRINT Consortium aims at defining the epigenomic maps and transcription profiles of a wide variety of blood cells from healthy primary human cells as well as blood-based diseases (*20*, *21*) (www.blueprint-epigenome.eu). Here, we report on the epigenome and transcriptome of monocyte-to-macrophage differentiation and the response to tolerance and training.

Monocyte differentiation in response to external stimuli

Upon migration into the tissues, monocytes differentiate into tissue macrophages. In addition, under differential inflammatory conditions, monocytes can be directed into tolerance or trained immunity functional programs (Fig. 1A). To analyze the different functional programs of monocytes and macrophages, human circulating monocytes (Mo) were purified by triple depletion of T and B lymphocytes and natural killer (NK) cells from the peripheral blood mononuclear cells of healthy human volunteers (fig. S1). Fluorescence-activated cell sorting and transcriptome analyses revealed high-purity monocytes similar to cell surface markers of $CD14^+$ positively selected monocytes (fig. S1).

Using an in vitro approach, we differentiated Mo into macrophages (Mf) by long-term incubation in medium supplemented with human serum (*22*). Alternatively, monocytes were exposed for the first 24 hours to LPS to induce endotoxin tolerance (immune paralysis) (Fig. 1, A and B) (*9*). The LPS exposure of monocytes induced long-term tolerant cells (LPS-Mf) that produce less proinflammatory mediators, such as tumor necrosis factor–α (TNF-α) and interleukin-6 (IL-6), upon an immune challenge with tripalmitoyl glyceryl cysteine (Pam3Cys, a ligand of TLR2) than unprimed naïve Mf. In contrast, a short priming of monocytes with β-glucan induces trained immune cells (BG-Mf) (Fig. 1, A and B) (*10*) that are characterized by an enhanced inflammatory status (*10*) (Fig. 1B). On the basis of the expression of cell surface markers, we concluded that LPS and β-glucan priming followed by continued culture for 5 days yields macrophage-like cells, but with distinct functional programs

[1]Department of Molecular Biology, Faculties of Science and Medicine, Radboud Institute for Molecular Life Sciences, Radboud University, 6500 HB Nijmegen, Netherlands. [2]Department of Internal Medicine, Radboud University Medical Center, 6525 GA Nijmegen, Netherlands. [3]Center for Computational and Integrative Biology and Gastrointestinal Unit, Massachusetts General Hospital, Harvard School of Medicine, Boston, MA 02114, USA. [4]Broad Institute of Massachusetts Institute of Technology and Harvard University, Cambridge, MA 02142, USA. [5]Department of Haematology, University of Cambridge, Cambridge, UK. [6]National Health Service, Blood and Transplant Cambridge Centre, Cambridge Biomedical Campus, Cambridge CB0 2PT, UK. [7]University of Groningen, University Medical Center Groningen, Department of Genetics, Groningen, Netherlands. [8]Fourth Department of Internal Medicine, University of Athens, Medical School, 1 Rimini Street, 12462 Athens, Greece.
*These authors contributed equally to this work. †**Corresponding authors. E-mail: h.stunnenberg@ncmls.ru.nl (H.G.S.); mihai.netea@radboudumc.nl (M.G.N.); c.logie@ncmls.ru.nl (C.L.)**

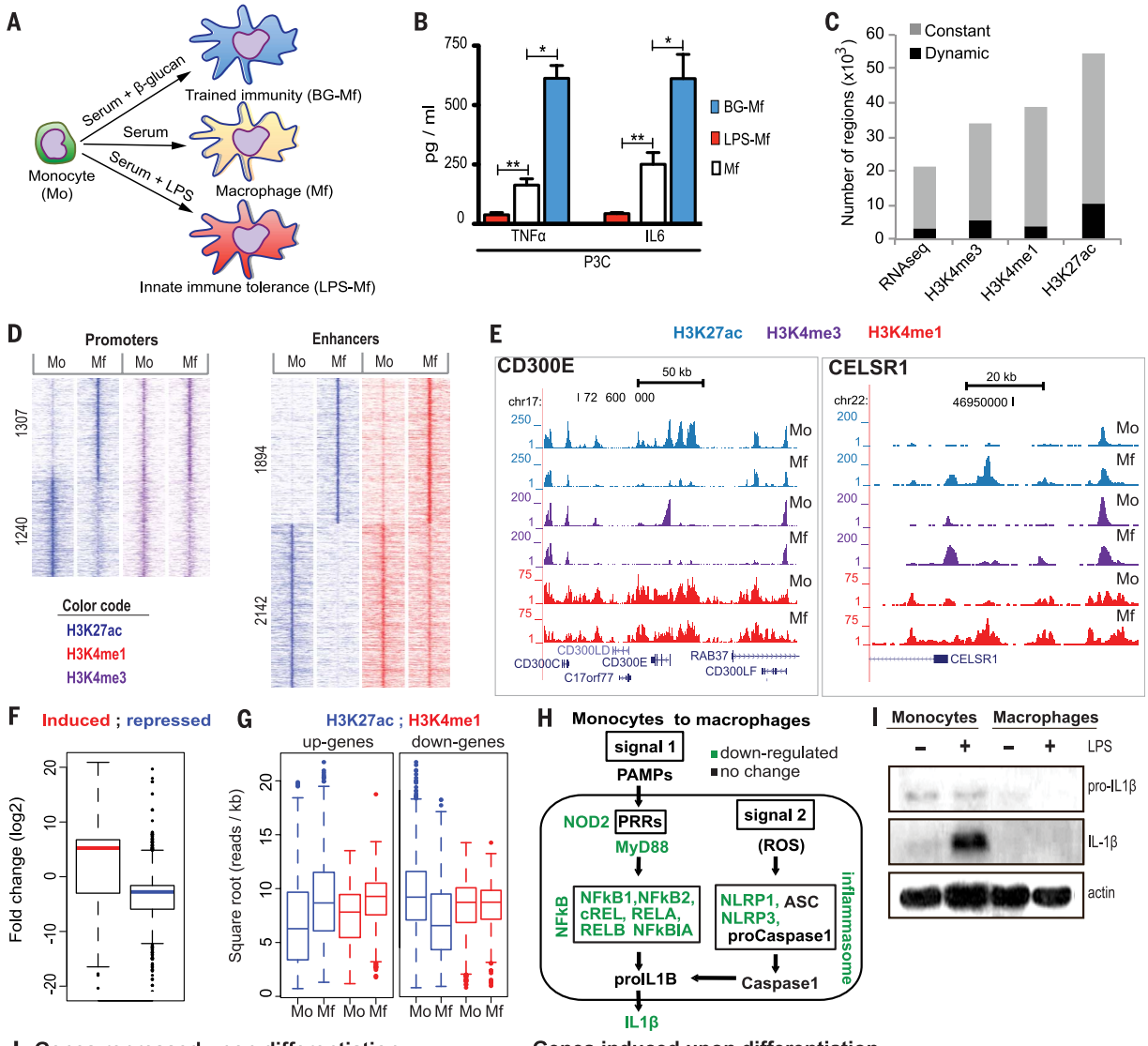

J **Genes repressed upon differentiation**

GO term	Pvalue	Bonferroni
response to wounding	1.30E-16	9.00E-14
inflammatory response	1.10E-15	6.00E-13
cytokine activity	3.80E-09	3.30E-06
extracellular region part	1.50E-06	3.30E-04
chemokine receptor binding	5.60E-05	4.80E-03

Genes induced upon differentiation

GO term	Pvalue	Bonferroni
cytoplasmic part	1.70E-29	8.20E-27
mitochondrion	4.80E-27	1.20E-24
cellular ketone metabolic process	1.10E-20	3.40E-17
carboxylic acid metabolic process	2.70E-20	8.40E-17
organic acid metabolic process	4.60E-20	1.40E-16

Fig. 1. Epigenomic and transcriptional changes during monocyte-to-macrophage differentiation. (**A**) Upon migration into tissues under homeostatic conditions, Mo differentiate into Mf. In addition, monocytes will enter into either a refractory state described as endotoxin "tolerance" that is mimicked in vitro with a short LPS stimulation (LPS-Mf) or a state of increased responsiveness described as trained immunity that is mimicked in vitro with a short ß-glucan incubation (BG-Mf) (see also fig. S4E). (**B**) Cytokine production determined by enzyme-linked immunosorbent assay (ELISA) in supernatants of monocytes primed for 24 hours with cell culture medium (Mf), β-glucan (BG-Mf), or LPS (LPS-Mf) and restimulated on day 6 for an additional 24 hours. *$P < 0.05$ and **$P < 0.005$ (Wilcoxon signed-rank test). Data are presented as mean ± SEM (pooled data from $n \geq 10$ individuals in four independent experiments). (**C**) The proportion of dynamic transcripts and epigenetic regions that differ by at least two median absolute deviations for the H3K27ac, H3K4me3, and H3K4me1 epigenetic marks as a function of monocyte differentiation and/or priming regimens. (**D**) Pile-up heat map of the epigenetic marks from (C) at promoters and enhancers in Mo and Mf. Rows are genomic regions from –12 to +12 kb around the center of the peaks; the signal intensity was determined in windows of 400 bp. (**E**) Screen shots of the epigenetic landscape at the CELSR1 (right) or CD300E (left) loci, two representative examples of loci that display important changes during macrophage differentiation. (**F**) Box-plot presentation of changes in transcript levels during differentiation (Mo to Mf) for the closest differentially expressed genes (within 100 kb) from the dynamic H3K27ac marked regions. (**G**) Box-plot presentation of changes in the H3K27ac and H3K4me1 signal at distal H3K27ac binding sites, in the vicinity (closest within 100 kb) of up-regulated (left) and down-regulated (right) genes during Mo-to-Mf differentiation. (**H**) Modulation of the inflammasome and NF-κB pathways during monocyte-to-macrophage differentiation. (**I**) Mo and Mf were left unstimulated (–) or stimulated with LPS (10 ng/mL) for 24 hours (+). Inflammasome activation was determined by Western blot for IL-1β and pro-interleukin-1β (proIL-1β). The results are representative of at least three independent experiments. (**J**) GO analysis. Enriched GO categories in a set of significantly (4-fold change, RPKM > 2) down- and up-regulated genes when comparing Mo to Mf.

(fig. S1). This was supported by our epigenomic and transcriptomic analyses (fig. S3, see below).

Epigenomic profiles were generated for Mo, naïve Mf, LPS-Mf, and BG-Mf (Fig. 1C) for three histone marks positively associated with gene expression: H3K4me3, which marks promoters; H3K4me1, which marks distal regulatory elements (enhancers); and H3K27ac, which marks active promoters and enhancers (*23*, *24*), following the guidelines of the International Human Epigenome Consortium (www.ihec-epigenomes.org). We also examined the DNA accessibility through deoxyribonuclease I sequencing (DNaseI-seq) and RNA-seq (*25*). In total, 17% of the H3K4me3 peaks, 10% of the H3K4me1 blocks, and 19% of the H3K27ac peaks are dynamic, changing during differentiation (Mo relative to Mf, LPS-Mf, and BG-Mf) by at least two median absolute deviations (Fig. 1C). H3K27ac was by far the most dynamic mark, more often fluctuating distally (7611) [termed acetylated elements (ACe)] compared with the regions within 2.5 kb of an annotated transcription start site (TSS), 3063, [termed acetylated promoters (ACp)]. Importantly, all regions examined displayed some degree of DNase I cleavage sensitivity, indicating that the vast majority of locations, including those with the de novo deposition of H3K27ac, are likely accessible to some extent in monocytes before stimulation. (see also Fig. 2).

Epigenetic and transcriptional changes during monocyte-to-macrophage differentiation

Epigenetic alterations during differentiation of Mo into naïve Mf were considered separately at promoters and distal regulatory elements (Fig. 1D). Promoters were operationally defined as regions within 2.5 kb of a TSS that also bear a detectable H3K4me3 peak. After 6 days of culture, as monocytes develop into macrophages, we observed a decrease in H3K27 acetylation in 1240 promoters and increase in 1307 promoters (z test, $P < 0.05$). Hence, at the epigenetic level, approximately equal numbers of promoters are turned on or off during macrophage differentiation (Fig. 1D). In general, H3K4me3 mark is largely constant at promoters that display dynamic H3K27 acetylation (Fig. 1D), suggesting that H3K27ac appears to function more as a mark of changes in promoter activity than H3K4me3.

In addition, as monocytes develop into macrophages, dynamic distal regulatory elements were operationally defined by H3K27ac at regions that are not known TSSs marked with H3K4me3 signal and that significantly (z test, $P < 0.05$) lose (2142) or gain (1894) acetylation (Fig. 1D). We observed that distal regulatory elements that gain H3K27ac generally gain H3K4me1, starting from a low level of H3K4me1. However, elements that lose H3K27ac generally do not lose their H3K4me1 mark, supporting the notion that H3K4me1 provides an epigenetic memory function in macrophages (Fig. 1, D and E) (*18*). Furthermore, DNase I cleavage frequencies reveal that the majority of distal regulatory DNA elements that lose H3K27ac remain accessible in macrophages (see also Fig. 2A).

To evaluate the relation between H3K27ac-bearing elements and gene expression, we plotted the relative change (fold change) in RNA level of the closest gene against H3K27ac distal elements, revealing a positive correlation between epigenomic marking and transcription from the closest dynamic gene (Fig. 1F). In contrast, the H3K4me1 mark does not correlate well with adjacent gene expression changes (Fig. 1G). This observation is in line with the hypothesis that H3K4me1 marks active (*23*, *24*) as well as latent regulatory elements (*18*). Altogether, our analysis indicates that in the course of monocyte-to-macrophage differentiation, histone H3 marks correlate positively with the activity of promoters (H3K4me3/H3K27ac) and distal regulatory elements that are presumed enhancers (H3K4me1/H3K27ac).

Biological pathways correlated with epigenetic marks

To identify the biological processes affected during differentiation of monocytes into macrophages, we performed a Gene Ontology (GO) analysis on differentially expressed genes (851 down, 1292 up) (table S1). We observed previously described differences in gene expression between monocytes and monocyte-derived macrophages, including the response to wounding (GO:0009611), inflammatory response (GO:0006954), and defense response (GO:0006952) (Fig. 1J and table S2) (*26*–*29*). As expected, pathogen-associated molecular patterns (PAMP)–mediated signal transduction through pattern recognition receptors (PRRs) is remodeled as monocytes differentiate into macrophages through changes in the epigenetic and transcription state of PRR genes. Furthermore, the nuclear factor κB (NF-κB) transcription factor (TF) subunits REL, RELA, RELB, NF-κB1, and NF-κB2, which are key regulators of the cellular response to inflammation (*30*), are all down-regulated (>2-fold lower) (Fig. 1H). Among the modulated inflammatory pathways during monocyte-to-macrophage differentiation, we detected components of the inflammasome (*31*) (Fig. 1H). In line with the expectation that tissue macrophages are more tolerant to challenges of the immune system, in vitro–differentiated macrophages, unlike monocytes, showed no activation of the inflammasome component caspase-1, and they lacked the capacity to secrete the active form of the proinflammatory IL-1β obtained after maturation of pro-IL-1β by caspase-1 (*32*) (Fig. 1I and fig. S4).

The most important GO terms associated with induced RNA expression during monocyte-to-macrophage differentiation (table S2) were monocarboxylic acid and cellular ketone metabolic processes. Up-regulated metabolic enzymes include dehydrogenases HSD17B1, -B4, and -B7—of which HSDB4 has been implicated in the peroxisomal beta-oxidation pathway and peroxisome proliferator–activated receptor (PPAR) signaling—which play essential roles in the regulation of cellular development and metabolism, as well as enzymes involved in glycine, serine, and threonine metabolism (*33*) and the tricarboxylic acid (TCA) cycle. The TCA cycle, which has recently been shown together with glycolysis to enhance endoplasmic reticulum (ER) and Golgi membrane synthesis and induce innate activation of dendritic cells upon Toll-like receptor (TLR)–mediated stimulation (*34*), appears to be remodeled such that the cytoplasmic versions of isocitrate dehydrogenase (IDH1) and malate dehydrogenase (MDH1) are induced >50 and >10-fold respectively, while their mitochondrial counterparts are induced about 2-fold, reaching ~20% of their cytoplasmic equivalents. These data support that re-orchestration of cellular metabolism during macrophage differentiation is an important component of the phenotypic switch between inflammatory and tolerant cells, with resting or tolerant macrophages exhibiting the TCA cycle and oxidative metabolism (*35*). The balance between glycolysis and oxidative metabolism also plays a role in trained immunity and tolerance [see the accompanying manuscript of Cheng *et al.* (*36*)].

The epigenetic profiles of tolerant versus trained cells

After an infectious episode, monocytes can retain an "immunological scar" from a previous encounter, entering either in a refractory state (tolerance) or a state of increased responsiveness (trained). These processes that result in nonspecific innate immune memory have been suggested to be mediated through epigenetic mechanisms (*10*, *19*) and describe very important in vivo phenomena such as postsepsis immunoparalysis (tolerance), or BCG-induced nonspecific (or heterologous) protective effects (training). Tolerance and training can be recapitulated in vitro using Mo exposed for 24 hours with LPS or β-glucan, respectively, followed by culture without additional stimuli for 5 days. These procedures yield differentiated cells that are either tolerant or trained macrophage-like cells (*10*) (Fig. 1A and fig. S4E).

At the epigenomic level, 17% of all dynamic promoters (ACp1) and 40.3% of all dynamic distal elements (ACe1) gain H3K27ac de novo exclusively in BG-Mf. Furthermore, a small subset of the dynamic distal regulatory elements (6%; ACe5) gain de novo H3K27ac marks exclusively in LPS-stimulated cells (LPS-Mf). These changes likely underlie the long-term effects of cell tolerization or training (Fig. 2, A and B, and table S3), mirroring postsepsis immunoparalysis and postvaccination nonspecific (heterologous) protection, respectively.

For the distal regulatory elements, consistent loss of H3K27ac is observed in Mf, LPS-Mf, and BG-Mf at 2142 distal elements (ACe2) (Fig. 2A) relative to the starting Mo. Distal elements that are marked de novo with H3K27ac, following differentiation from Mo to macrophages (Mf, LPS-Mf, and BG-Mf), fall into two clusters: ACe3, which shows a consistent gain of H3K27ac, and ACe4, which are dampened relative to macrophages concordantly in both LPS and β-glucan pretreated

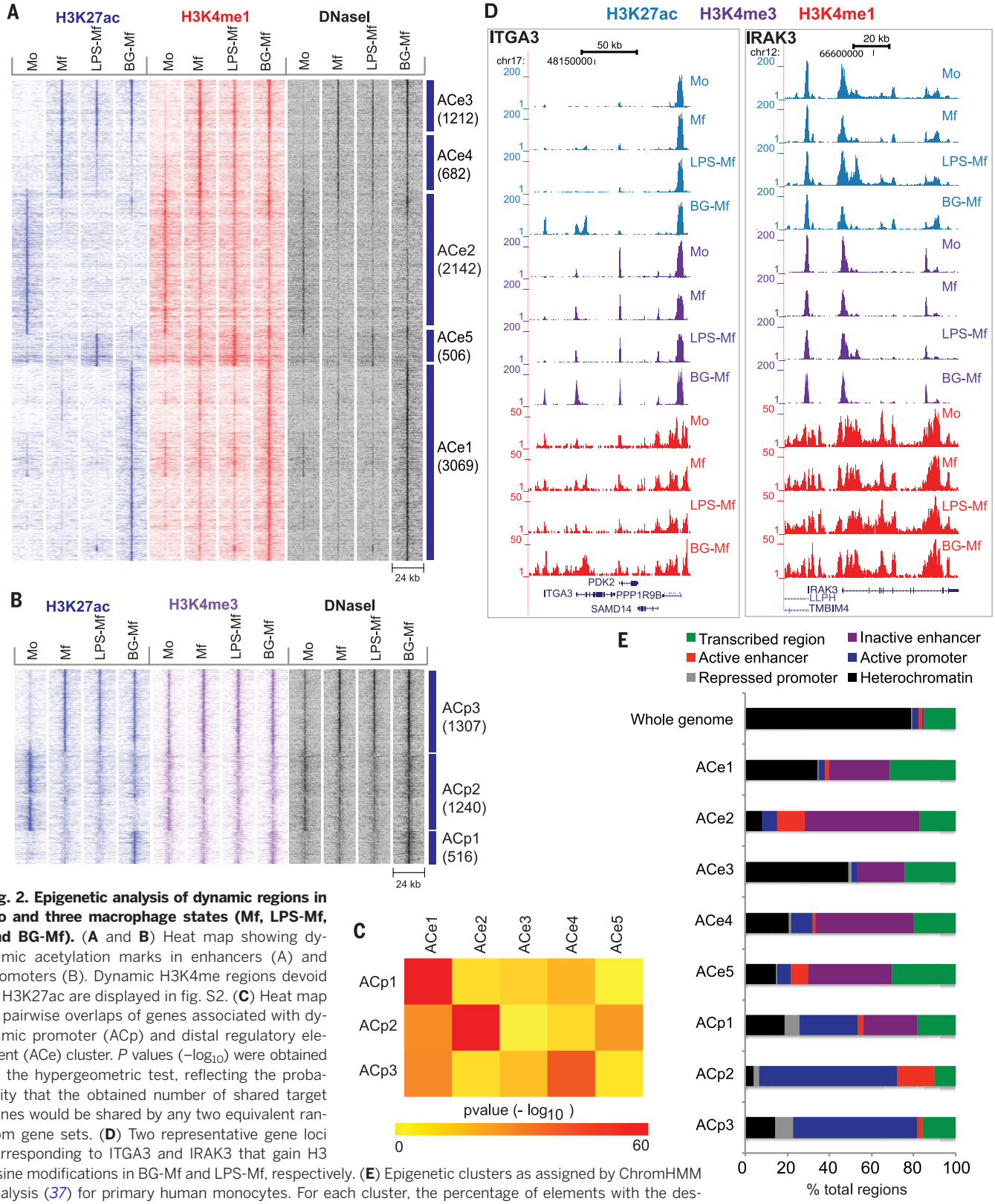

Fig. 2. Epigenetic analysis of dynamic regions in Mo and three macrophage states (Mf, LPS-Mf, and BG-Mf). (**A** and **B**) Heat map showing dynamic acetylation marks in enhancers (A) and promoters (B). Dynamic H3K4me regions devoid of H3K27ac are displayed in fig. S2. (**C**) Heat map of pairwise overlaps of genes associated with dynamic promoter (ACp) and distal regulatory element (ACe) cluster. *P* values ($-\log_{10}$) were obtained by the hypergeometric test, reflecting the probability that the obtained number of shared target genes would be shared by any two equivalent random gene sets. (**D**) Two representative gene loci corresponding to ITGA3 and IRAK3 that gain H3 lysine modifications in BG-Mf and LPS-Mf, respectively. (**E**) Epigenetic clusters as assigned by ChromHMM analysis (*37*) for primary human monocytes. For each cluster, the percentage of elements with the designations heterochromatic (H3K9me3, H3K27me3, or empty), active promoter (H3K4me3), inactive promoter (H3K4me3 and H3K27me3), active regulatory element (H3K4me1 and H3K27ac), inactive regulatory element (H3K4me1), and transcribed segment (H3K36me3) was calculated.

cells (Fig. 2A). The most extensive pretreatment-specific epigenetic response is obtained with β-glucan, whereby 3069 distal elements become marked by H3K27ac (ACe1) (Fig. 2, A and D, left panel). Some diversity in marking of distal elements with H3K27ac in ACe1 can be observed in other states: There are subclusters with low marking in Mf, or in Mo, and there is also a very small subcluster of ACe1 distal elements that is specifically marked upon LPS treatment (Fig. 2A). This indicates a modular, treatment-dependent activation of distinct pathways. Altogether, β-glucan appears to induce an epigenetic program that involves many promoters and distal elements. Some parts of this program are shared with untreated, naïve Mf and others with LPS-Mf, whereas neither LPS-tolerized nor naïve macrophages show such a strong exclusive epigenomic signature (Fig. 2, A and B).

We counted the genes targeted by more than one epigenetically marked cluster and computed the probability of randomly obtaining such overlaps (Fig. 2C). The most significant overlaps (hypergeometric test, $P < 0.01$) are between elements that show similar dynamics (ACp1/ACe1, ACp2/ACe2, and ACp3/ACe4), in keeping with the idea that epigenetically marked promoters and enhancers cooperate to drive gene expression. Notably, β-glucan–induced ACe1 distal elements also appear to be associated with ACp2 and ACp3 promoters more often than expected, suggesting modulation of differentiation-sensitive promoters by β-glucan–induced enhancers. Finally, the ACe5 distal elements, which are marked only upon LPS tolerization, are associated with ACp2 promoters, which are down-regulated upon monocyte differentiation to macrophages. This suggests that LPS-Mf stimulate the activity of a subset of monocyte-specific genes in macrophages via ACe5 elements (Fig. 2C).

To determine the provenance of these epigenetic elements in more detail, we used the ChromHMM data generated by BLUEPRINT for primary human monocytes. ChromHMM indexes chromatin into functional states such as active or repressed promoters, distal regulatory element (enhancer), and heterochromatic (repressed) chromatin (*37*). The majority of dynamic acetylated promoters and distal regulatory elements were already marked with low but appreciable levels of H3K4me3 (promoters) or with H3K4me1 at distal elements in Mo, indicating changes in activity rather than in chromatin state during differentiation to Mf, LPS-Mf, or BG-Mf (Fig. 2E).

Polytomous analysis of the transcriptome of Mf, LPS-Mf, and BG-Mf

To gain insight into the effects of LPS and β-glucan on nonspecific innate immune memory, we grouped genes according to a Bayesian methodology (MMSEQ and MMDIFF) (*38*, *39*) and applied a polytomous model selection approach that allows for classifying genes according to their expression pattern by considering multiple conditions simultaneously instead of generating multiple pairwise comparisons. This approach

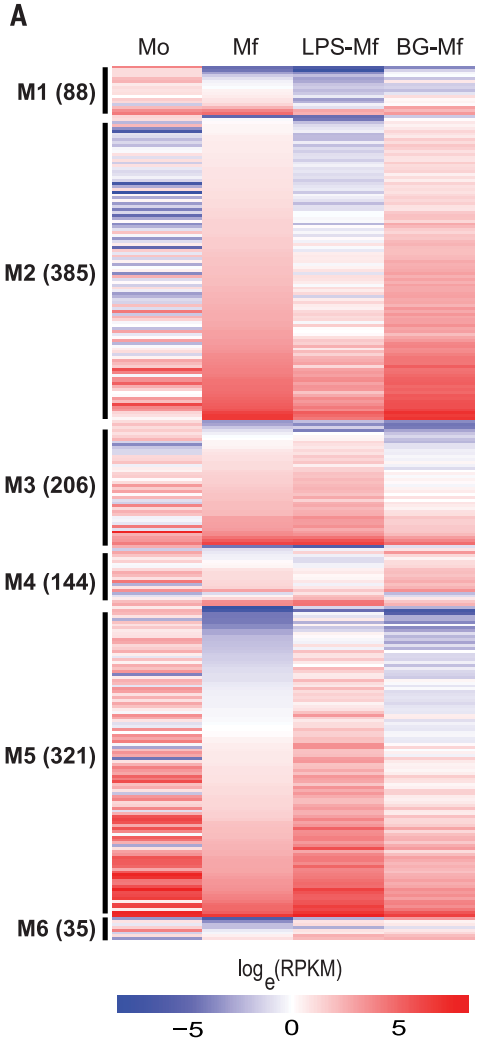

B

Module	GO term	Pvalue	Bonferroni
M1	sugar binding	1.70E-04	3.90E-02
M2	carboxylic acid metabolic process	4.00E-08	7.90E-05
	cellular ketone metabolic process	6.50E-08	1.30E-04
	oxidoreductase activity	2.10E-06	1.40E-03
	lipid metabolic process	5.40E-06	1.10E-02
M3	signal transducer activity	6.20E-06	2.40E-03
	receptor activity	5.60E-05	2.10E-02
M4	cofactor binding	1.00E-05	3.50E-03
M5	immune response	1.40E-22	3.00E-19
	response to wounding	2.30E-20	5.00E-17
	chemotaxis	2.40E-10	5.20E-07
	cytokine activity	1.70E-14	8.00E-12
	chemokine activity	7.80E-12	3.70E-09

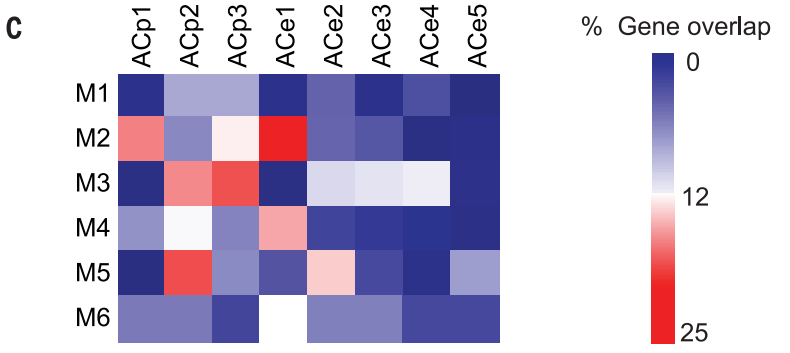

Fig. 3. GO analysis of epigenetic and transcript clusters in Mo and the three macrophage states (Mf, LPS-Mf, and BG-Mf). (**A**) Gene expression patterns were analyzed using a polytomous analysis of gene expression profiles that contrasts LPS-Mf and BG-Mf relative to Mf. Genes plotted are those with a fold change >4 and a polytomous post hoc probability >0.35. (**B**) Enriched GO categories in the major expression modules represented in Fig. 3A. (**C**) Heat map presentation of the percentage of genes in a module that overlap with a dynamic ACp or ACe cluster.

thus allowed us to identify statistically distinct expression patterns with biological relevance at once and define cell state–specific as well as co-regulated gene modules during monocyte-to-macrophage differentiation and in response to training or tolerization. A total of 14 models were compared to the base model of no differential expression and polytomous model selection was applied by computing the posterior probability of each model for each gene. Out of 11,698 genes that expressed >2 RPKM (reads per kilobase per million reads mapped), 7514 showed more than 2-fold changes, and 5847 fit one of the models with a posterior probability > 0.35. The models were condensed into expression modules (M1-6) to bring together genes as a function of their differential expression in LPS-Mf and BG-Mf relative to Mf cells. The genes of the modules that changed 4-fold are plotted in Fig. 3A, and the top associated GO terms are shown (Fig. 3B and tables S2 and S4). Interestingly, GO analysis on these modules (Fig. 3B) resulted in obtaining similar terms from our comparison of Mo and Mf in the absence of LPS or β-glucan (Figs. 1J and 3B). This suggests that both LPS and β-glucan pretreatments modulate the monocyte-to-macrophage differentiation program.

Modules are condition and cell specific

To link the expression modules to the epigenome, we determined the percentage of the genes of each module associated with an epigenetically dynamic promoter or distal element cluster (Fig. 3C and tables S3 and S4). Surprisingly, LPS-Mf do not down-regulate a large set of genes that are expressed in Mo to the same extent as Mf and BG-Mf (Fig. 3A, M5), suggesting that the LPS-Mf retains a monocyte-like expression level for these genes. Indeed, module M5 is enriched in genes from the GO categories "immune response," "response to wounding," and "chemotaxis" (Fig. 3B) and shows up-regulation of monocyte-specific genes (Fig. 1J), as well as a "response to LPS" (table S2). An example of a gene with a monocyte-like expression level in LPS-Mf is interleukin-1 receptor–associated kinase 3 (IRAK3), an essential regulator of innate immune homeostasis that functions as a negative-feedback regulator of Toll-like receptor signaling (*40*) (*41*) (Fig. 2D, right panel). This finding is expected from the perspective of the low inflammatory profile of tolerant macrophages. Module M5 harbors relatively many ACp2, ACe2, and ACe5 elements (Fig. 3C), suggesting that some parts of the monocyte-specific gene expression program are retained in LPS-Mf cells, possibly via induction of a new set of distal elements (ACe5). Furthermore, some of these elements may sustain the expression of target genes that are otherwise down-regulated in Mf and BG-Mf cells. Similarly, module M3 is generally better expressed in LPS-Mf than BG-Mf. M3 includes factors involved in signal transduction, such as IL10RA involved in controlling intestinal inflammation (*42*), the aryl hydrocarbon receptor repressor AHRR that has been shown to be essential for endotoxin tolerance (*43*), and the adenosine receptor ADORA3. Module M3 genes often harbor ACp2, ACp3, ACe2, ACe3, and ACe4 elements, and call the GO terms "signal transducer activity" and "receptor activity" (Fig. 3B), likely reflecting functional linkage between the execution of the naïve macrophage differentiation program and the LPS- and β-glucan–induced epigenetic programs.

Strikingly, module M2 represents a large set of genes that tend to be induced in Mf and are markedly less expressed in LPS-Mf, but equally or even better induced in BG-Mf (Fig. 3A, M2). M2 invokes the GO metabolic terms "cellular ketone metabolic process" and "carboxylic acid metabolic process" that are significant macrophage differentiation markers (Fig. 1J and table S2). Notably, M2 harbors ATF3, a transcription repressor known to target cytokine genes in mouse macrophages (*44*) (see also Fig. 4B). Module M4 is also most up-regulated in β-glucan pretreated cells, and, like M2, it is enriched in ACe1 distal elements (Fig. 3C). This suggests that sustained expression of module M4 in BG-Mf relative to the starting monocytes may depend on the presence of β-glucan–induced distal elements, explaining the apparently paradoxical overlap between the ACe1 elements and ACp2 promoters (Fig. 2C). M4 is enriched in the GO category "cofactor binding," including the pentose phosphate pathway–linked enzymes pyridoxine kinase PDXK and glucose-6-phosphate dehydrogenase G6PD, the glycolysis enzyme pyruvate dehydrogenase subunit DLAT, and the cytoplasmic version of the TCA cycle enzyme malate dehydrogenase MDH1 (table S2); also see (*36*). Intriguingly, a small subset of mitosis-specific genes that were previously reported in the context of monocyte-derived macrophages (*27*, *29*) are also present in module M4 (table S4). However, we assayed DNA replication directly and found no indication that Mf or BG-Mf cells are replicating (fig. S5).

Multiple modules contain G protein–coupled receptors (GPCRs), protein kinases, and epigenetic enzymes (fig. S6 and table S4), indicating extensive remodeling of the trained cell's repertoire of signal transduction molecules. Indeed, the β-adrenergic receptor ADRA2B is specifically induced in β-glucan–trained, rather than in LPS-tolerized, cells. Furthermore, monocytes and the three Mf states could be distinguished by differential expression of human adenosine receptor and Src kinase family members (*27*) (fig. S6). ADORA2B and the Fgr kinase are most strongly expressed in trained BG-Mf cells, whereas Hck kinase transcript levels are highest in LPS-Mf, providing potential pharmacological entry points to modulate immunoparalysis and trained innate immunity-related health conditions.

In summary, the epigenetic effects observed in BG-Mf and LPS-Mf appear to modulate the well-documented M-CSF–induced macrophage differentiation program (*26*), and polytomous transcriptome analysis reveals that LPS-Mf cells sustain expression of certain monocyte pro-inflammatory pathways that are dampened in Mf and BG-Mf cells (M3, M5). On the other hand, β-glucan pretreatment appears to reinforce specific gene expression programs, including metabolic pathway remodeling (M2, M4) through epigenetic modification of both ACp1 promoters and ACe1 distal regulatory elements.

The TF repertoires of differentiation, tolerance, and training

TFs bind to specific DNA sequences and are the effectors of cell phenotype and function, including numerous signal transduction pathways. As they recruit chromatin-modifying enzymes (fig. S6), which modulate gene expression, they are cornerstones of epigenetic signaling. Hence, we focused on the expression patterns of the human TFs to identify those whose expression patterns may determine Mo and the monocyte-derived macrophage fates (Mf, LPS-Mf, and BG-Mf). There are about 1600 bona fide human sequence–specific TFs (table S5). Of these, 74% are expressed at a detectable level (RPKM > 0.1), and 41% are expressed above 2 RPKM (Fig. 4A). Of the highly expressed TFs, 197 TFs change transcript levels more than 4-fold between at least two states (Mo, Mf, LPS-Mf, and BG-Mf) and are henceforth referred to as dynamic TFs. Altogether, 92 TFs are 4-fold down- and 105 TFs are 4-fold up-regulated (Fig. 4, B and C).

From a differentiation program perspective, it is informative to study dynamic changes within TF families (Fig. 4A). The largest TF superfamily is the C2H2 zinc finger Krueppel factors with and without Krueppel-associated box (KRAB) domains, encompassing 559 factors (Fig. 4A). Of these, 15% are dynamic, 14 are down-regulated, and 75 are up-regulated, albeit to low levels (Fig. 4, B and C).

Of the 48 human nuclear receptors, 26 are expressed in at least one of our four cell types, and eight are dynamic. Mo express relatively high levels (RPKM > 100) of the three proinflammatory NR4A1-3 nuclear receptor subfamily members NUR77, NURR1, and NOR1 (*45*), whereas derived macrophages show a dramatic reduction in expression of these nuclear receptors (Fig. 4B). The retinoic acid receptor RARA (NR1B1) also follows this pattern (Fig. 4B). On the other hand, LXRα (NR1H3), a nuclear receptor implicated among others in liver cell and macrophage cholesterol metabolism (*46*, *47*), increases in Mf, LPS-Mf, and BG-Mf cells (85-, 50- and 117-fold), attaining 300 RPKM in BG-Mf (Fig. 4C). Accordingly, the cytochrome (CYP27A1), an enzyme involved in the formation and breakdown of various molecules such as the 25-hydroxy-7-dehydrocholesterol that activates the LXRα (*48*), is itself induced ~25-fold in macrophages. Interestingly, the peroxisome proliferator-activated receptor PPARG (NR1C3) is reduced in Mf and LPS-Mf, but it is maintained in BG-Mf relative to purified Mo, in line with its proposed role in inflammation resolution (*49*) (Fig. 4B). Thus, nuclear receptors appear as major regulators of monocyte and macrophage biology, with LXRα levels qualitatively reflecting the immunological phenotypes of Mf, LPS-Mf, and BG-Mf (Fig. 1A).

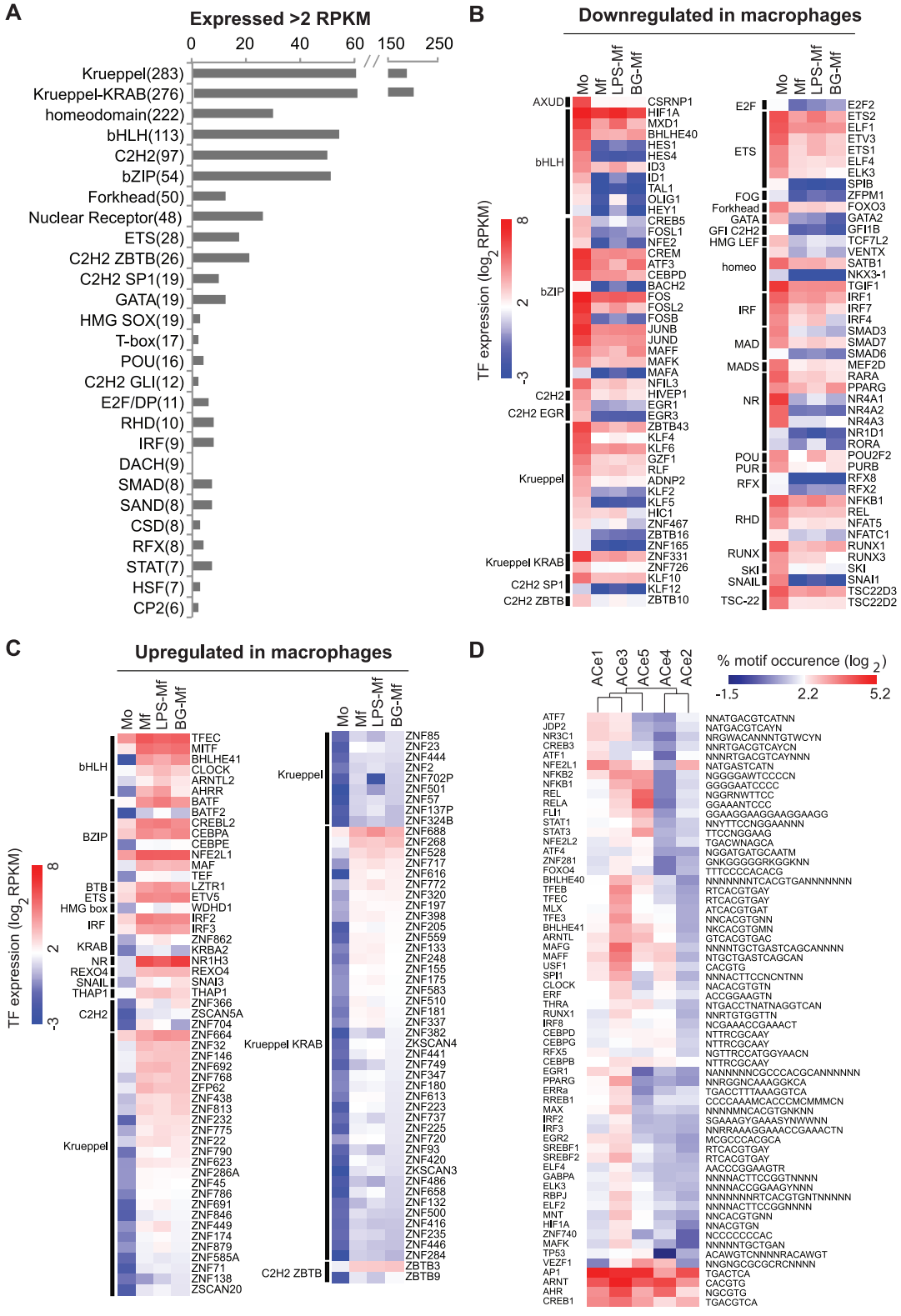

Fig. 4. The TF repertoires of monocytes and derived macrophages. (**A**) Bar representation of the TF family members that are expressed in at least one of the four cell samples (Mo, Mf, LPS-Mf, and BG-Mf). The number of TFs with RPKM values > 2 is plotted, and the total number of TF family members in humans is indicated between brackets. (**B** and **C**) Heat map of the expression levels (log_2 RPKM) of TFs that change expression at least 4-fold in at least one of the four conditions examined. TFs are grouped according to families and whether they are up- or down-regulated upon differentiation. Scale (left) indicates the level of expression (log_2 RPKM). (**D**) Hierarchical clustering of the TF motif occurrence frequency (log_2 percentage, scale at top) in each ACe cluster–associated DHS from all TF motifs that have more than 5% occurrence in at least one instance and that are overrepresented in at least one of the ACe clusters compared with all nondynamic acetylated regions (hypergeometric test, $P < 0.01$).

Aside from nuclear receptors, multiple TF families display coordinated family member switches. For instance, SNAI1, a major mesoderm lineage marker (*50*, *51*), is reduced in expression about 100-fold during macrophage differentiation, but its paralog SNAI3 is 5- to 10-fold higher in macrophages, most likely outcompeting SNAI1 for binding to its cognate DNA binding sites in Mfs (Fig. 4, B and C). Interferons (IFNs) and IFN responses are one essential arm of the host immune responses. Upon infection, PAMPs recognition by PRRs elicits antimicrobial responses by inducing target genes that include those encoding type I IFNs, proinflammatory cytokines, and chemokines. The interferon regulatory factor (IRF) family are transcriptional regulators of type I IFNs and IFN-inducible genes and help regulate facets of innate and adaptive immune responses (*52*). Five of the nine human IRFs are dynamic, as IRF1, IRF4, and IRF7 significantly decrease while IRF2 and IRF3 increase, in a background where IRF8 and IRF9 remain the most abundantly expressed IRF family members. This may reflect the decrease in IRF1 levels, which activates type I interferon IFN-β production, whereas levels of its antagonistic family member IRF2 increase (*53*–*55*). Thus, specific remodeling within TF families occurs in the course of monocyte-to-macrophage differentiation.

The basic leucine zipper domain (bZIP) TFs appear as an influential family in the course of monocyte differentiation, because 94% are expressed above 2 RPKM and 44% are dynamic (Fig. 4, A to C). AP1 complexes composed of heterodimers of the bZIP–FOS (FBJ murine osteosarcoma viral oncogene homolog) and -jun proto-oncogene (JUN) subfamilies are the most abundantly expressed (RPKM > 200) in monocytes and are reduced upon monocyte-to-macrophage differentiation (Fig. 4B), suggesting a down-modulation of AP1 signaling pathways. The CCAAT/enhancer-binding (C/EBP) bZIP subfamily also shows strong dynamics; CEBPA is induced 7-fold, whereas the paralog CEBPD is down-regulated 4-fold, indicating that there may be a coordinated switch in C/EBP heterodimerization which occurs in a complex along with the nondynamic, highly expressed CEBPB (Fig. 4, B and C). The 10-fold down-regulation of cAMP response element modulator (CREM), a bZIP subfamily member, also likely reflects a biological impact (Fig. 4B) because CREM codes for a dominant-negative heterodimerization partner of most cyclic adenosine monophosphate (cAMP) response element (CRE) binding proteins (*56*). CREM down-regulation is therefore likely to capacitate cAMP response element binding factors (see below).

Integration of epigenetic regions with TF binding sites

We used 1406 sequence motifs for 658 human TFs (*57*, *58*) to scan DNase I hypersensitive sites (DHSs) for TF-binding motifs. We determined the overlap between DHSs and dynamic distal elements in our data set. We performed hypergeometric tests using the motif frequency in all distal (nondynamic) H3K27ac regions as the background, to yield TF motifs that are likely candidates to regulate the activity of the distal regulatory regions. As an example, Fig. 4D plots the proportion of dynamically acetylated regions within one cluster that bear a given motif in their associated DHSs. To be included, a motif had to occur in at least 5% of any one epigenetically marked cluster (Fig. 4D and table S6). This reveals enriched TF motifs and permits a comparative analysis of putative TF repertoires in epigenetically marked regions.

The motifs for the bZIP AP1 and CREB1, and basic helix-loop-helix (bHLH) factors ARNT (aryl hydrocarbon receptor nuclear translocator) and AHR (aryl hydrocarbon receptor) are the most abundant occurring in 10 to 36% of ACe1- to ACe5-associated DHSs, in keeping with a broad role for the pathways that control these TFs in monocytes and macrophages, namely MAPKs (mitogen-activated protein kinases), cAMP, and metabolic signaling (*59*). Motifs for bZIP (sub-) family members, most prominently ATF1, ATF7, CREB3, and JDP2, are enriched in the β-glucan–induced ACe1 cluster. Furthermore, motif for the glucocorticoid receptor (NR3C1) is also relatively enriched in ACe1. This suggests that cAMP and cortisol-mediated signaling pathways intersect with the epigenetic response instigated by β-glucan training. By contrast, the immunoparalyzed LPS-Mf cell–specific ACe5 cluster is characterized by NF-κB and REL motifs (Fig. 4D), which are also present in the monocyte-specific ACe2 cluster (Fig. 1H). This is in keeping with the RNA-seq analysis, which points to a large transcriptome module (M5) where LPS-Mf cells resemble Mo more than naïve Mf or BG-Mf (Fig. 3A). In fact, module M5 harbors the NF-κB complex subunit genes that are known to be involved in inflammatory pathways.

Interestingly, the TF motif frequencies in the monocyte-specific ACe2 dynamic distal regions resemble those of ACe4 regions, which are induced in Mf but suppressed when monocytes are challenged with LPS or with β-glucan. However, ACe2 and ACe4 are distinguished by the enrichment of bZIP macrophage (MAFF and MAFG) (*60*, *61*) subfamily motifs in ACe4, which are also relatively more frequent in the differentiation-linked epigenetic clusters ACe1, ACe3, and ACe5, and thus likely drive ACe4 element activity upon differentiation.

The bHLH family, including the cAMP hypoxia inducible factor HIF1A, as well as the circadian factors BHLHE40, BHLHE41, and CLOCK (clock circadian regulator) (fig. S7) (*62*, *63*), show related patterns and are most frequent in the monocyte-to-macrophage differentiation cluster ACe3 and the least frequent in the monocyte-specific cluster ACe2. This suggests that bHLH TFs play important roles in macrophage differentiation. Moreover, IRF motifs are also enriched in the Mf differentiation cluster ACe3, as are smaller TF families such as EGR (early growth response) and ETS (E-twenty-six) factors (Fig. 4D).

In summary, the immune-tolerant phenotype elicited by LPS exposure appears to depend on epigenetically marked putative distal regulatory regions that frequently harbor NF-κB motifs, whereas the motifs that are enriched in the trained BG-Mf–marked epigenetic elements are most frequently also in epigenetic regions turned on in Mf, indicating reinforcement of specific Mf (sub-) programs by monocyte exposure to β-glucan.

Importance of cAMP-dependent intracellular signaling for trained immunity

cAMP signals start with a GPCR and culminate in cAMP-dependent protein kinase (PKA)–mediated CRE binding protein activation. cAMP-dependent signaling has been associated with monocyte function, differentiation, and response to infection (*64*, *65*). In Mf, BG-trained, and LPS-induced tolerant cells, the heterotrimeric G protein repertoire is remodeled: Adenylate cyclase 3 (ADCY3) and the cAMP-degrading phosphodiesterase (PDE3B) are specifically induced in trained cells (Fig. 5A and fig. S8). Strengthening the hypothesis that β-glucan training and LPS tolerization differ with respect to cAMP metabolism, we found that LPS-Mf express significantly more of the monocyte-specific cAMP phosphodiesterase (PDE4B) (Fig. 5A and fig. S8). The PKA regulatory subunit anchoring factor AKAP11 transcript is induced (two-tailed t test, $P < 0.05$) in Mf, BG-Mf, and LPS-Mf cells compared to Mo, and so is the type 1 alpha PKA regulatory subunit PRKAR1A. Furthermore, one of the five human PKA isoforms (PRKACB) is more highly induced (two-tailed t test, $P < 0.05$) in BG-Mf relative to LPS-Mf cells. In addition, the transcripts for CRE binding protein ATF3 and the ER stress response element binding CREB3L2 are higher in BG-Mf than in LPS-Mf (Fig. 5A and fig. S8). Importantly, we identified a known cAMP-inducible bHLH factor (*66*, *67*), BHLHE41, as a likely key TF motif enriched in ACe1, -3, -4, and -5 (Fig. 4D), strongly suggesting that cAMP-mediated molecular signal transduction is important for Mf, LPS-Mf, and BG-Mf cells.

We investigated the role of cAMP-dependent signaling in vitro and in an in vivo experimental model (Fig. 5B). Inhibition of adenylate cyclase and subsequent cAMP synthesis by 2′,5′-dideoxyadenosine significantly (Wilcoxon signed-rank test, $P < 0.05$) impairs training-induced increased cytokine production (Fig. 5C) and, in line with this, the PKA inhibitor H89 also blocks training of monocytes (Fig. 5D). Of note, the PKA inhibitor H89 had no effect on the LPS-triggered immune response (3% increased IL-6 production and 9% decreased TNFα production compared with control stimulation; $P > 0.05$) (fig. S9). Similar effects were observed with propranolol, an inhibitor of β-adrenergic signaling-dependent increase in cAMP (Fig. 5E). Importantly, even though the amplitude of responsiveness to secondary stimulation of each individual varies, the effect of the cAMP-pathway inhibitors on the trained immunity response is consistent and significant among the 18 tested individuals. A nonlethal infection with *C. albicans* protects mice against lethal candidiasis in a T/B cell–independent fashion, due to monocyte-dependent

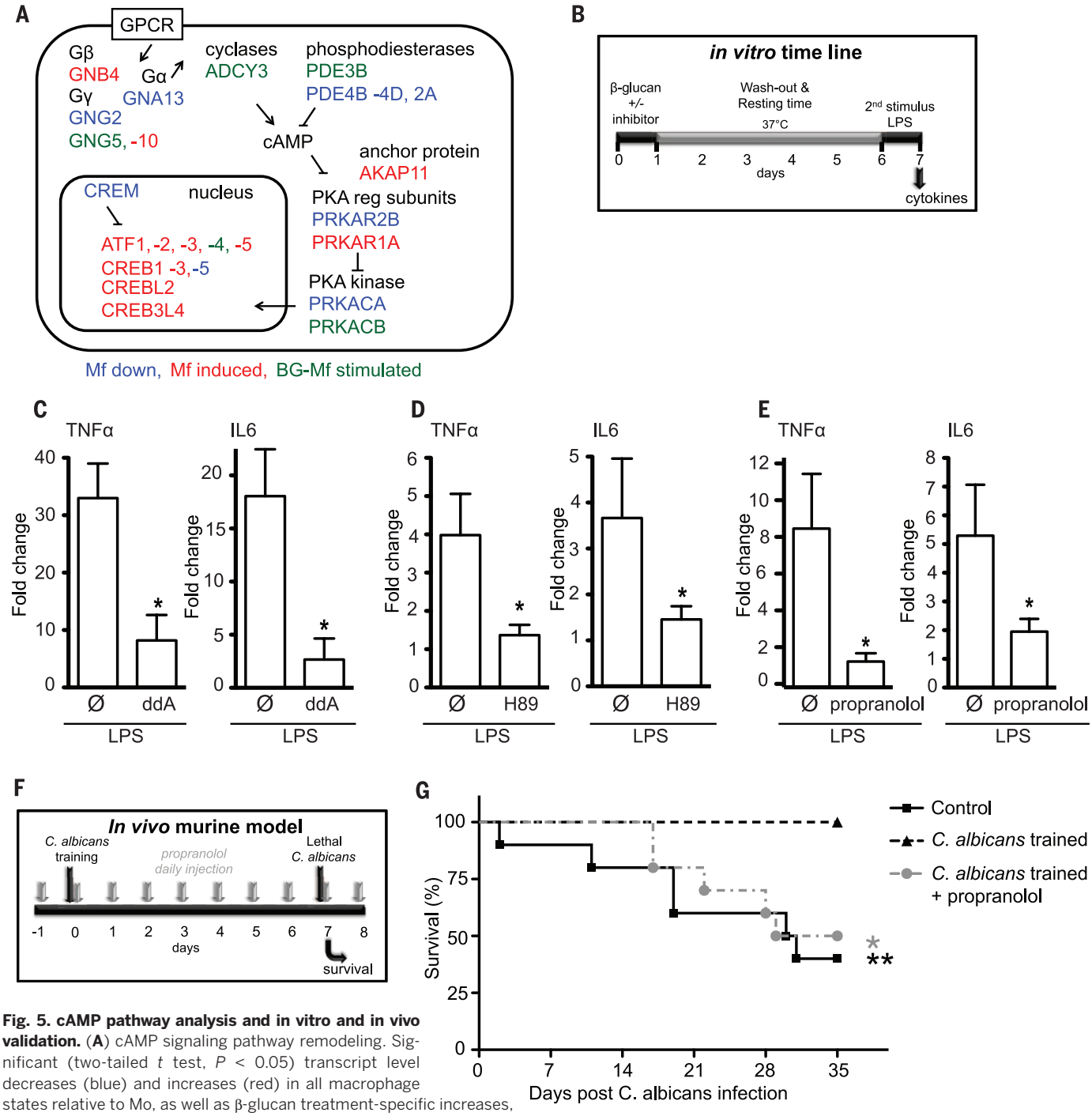

Fig. 5. cAMP pathway analysis and in vitro and in vivo validation. (**A**) cAMP signaling pathway remodeling. Significant (two-tailed *t* test, $P < 0.05$) transcript level decreases (blue) and increases (red) in all macrophage states relative to Mo, as well as β-glucan treatment-specific increases, are indicated; see also fig. S8. (**B**) Diagram of the timeline and experimental setup of the in vitro cAMP inhibition experiment. cAMP inhibitors or vehicle were applied to human primary monocytes during the first 24 hours of "training" [see fig. S4E and (*70*) for details]. After 6 days, secondary stimulation of cells was performed with LPS to induce cytokine production. (**C** to **E**) The inhibitor of adenylate cyclase 2′,5′-dideoxyadenosine (ddA), the PKA inhibitor H89, and the β-adrenergic receptor blocker propranolol inhibited the induction of training by β-glucan, assayed as the response to LPS stimulus on day 6. *$P < 0.05$ (Wilcoxon signed-rank test). Data show the fold increase in cytokine production (ELISA) upon training as compared with untrained Mf cells and are presented as mean ± SEM, $n > 6$ in three independent experiments. (**F**) Timeline of the in vivo training experiment in mice. Mice were either injected intravenously with phosphate-buffered saline (control) or a nonlethal dose of *C. albicans* [2×10^4 colony-forming units (CFU) per mouse] 7 days before intravenous inoculation of a lethal *C. albicans* dose (2×10^6 CFU per mouse). In a third group of mice, propranolol was administered before the inoculation of the nonlethal dose of *C. albicans* (*70*). (**G**) Survival rate of wild-type C57BL/6 mice to a systemic infection with *C. albicans* ($n \geq 8$ per group). Statistical significance between the groups (Kaplan and Meier) was calculated using the log-rank test. *$P < 0.05$, **$P < 0.01$ versus control animals.

trained immunity (*10*). The protection conferred by the nonlethal dose of *C. albicans* was completely abolished by the use of propranolol (Fig. 5, F and G), validating that cAMP-dependent signaling is important for the protective effects of trained immunity.

Discussion

Monocytes and macrophages are prototype mononuclear phagocytes that mediate fundamental innate immune processes such as pathogen clearance, inflammatory cytokine production, and tissue repair. We studied macrophages differentiated from monocytes exclusively in the presence of human serum. This is probably the in vitro model closest to the development of tissue-resident macrophages in vivo, because the differentiation is taking place under the influence of endogenous homeostatic levels of macrophage colony-stimulating factor (M-CSF), rather than stimulated by artificially high concentrations of recombinant CSFs (*68*). In contrast, differentiation with additional recombinant growth factors such as granulocyte macrophage (GM)-CSF, IL-4, or IFN-γ will induce activated M1 or M2 macrophages most often encountered during infectious processes (*68*). Thus, these observations provide clues as to which pathways to tackle in a clinical attempt to reverse immune tolerance to turn on training and activation pathways during immunoparalysis and sepsis.

The present work shows that differentiating monocytes undergo substantial epigenetic changes affecting ~19 mega base pairs (Mbp), equivalent to 0.6%, of the human genome. Using the guidelines of the International Human Epigenome Consortium, we generated genome-wide maps of histone modifications (H3K4me3, H3K4me1, H3K27ac, and DNase I accessibility). We delineated eight epigenetically marked clusters reflecting putative transcription regulatory regions, of which four are differentially modulated when monocytes are exposed to LPS or β-glucan. H3K27 acetylation levels changed at thousands of promoters and distal regions and correlate well with observed changes in gene expression.

Although we cannot ascertain what fraction of the purified monocytes that we cultured participated in any one observed epigenomic or transcriptome change, nor to what extent the laboratory in vitro conditions affect differentiating monocytes relative to the in vivo condition, we can state that monocytes are able to deploy a long-term epigenetic program upon β-glucan–induced training in vitro in the absence of DNA replication. This epigenetic program persists for at least 5 days, is highly reproducible across monocytes from unrelated donors, and represents β-glucan–induced changes in the epigenetic states of promoter and distal elements, indicative of a specific cell differentiation program. Although more modest, a similar epigenomic response of monocytes to LPS is also uncovered, which induces a state akin to post-sepsis immune paralysis. Identification of core signatures of training and tolerance is thus important, as it allows the better characterization of these functional states. Because many epigenetic clusters that differentiate training and tolerance yield significant GO scores, the clusters that we identified appear to report physiologically relevant effects. Indeed, we linked cAMP signaling to the trained phenotype in purified human monocytes, as well as in a mouse model of disseminated candidiasis.

Our TF analysis suggests that monocyte differentiation relies on quantitative remodeling of the TF repertoire, because coordinated changes affect multiple members of many TF families. DNA sequence motifs detected in DHSs adjacent to epigenetically dynamic elements link to cell state–specific epigenetic clusters that fit RNA expression modules. The present data sets, in particular the genomic coordinates of the dynamic epigenomic sites, therefore represent a rich molecular resource to understand and modulate the functionality of monocyte-derived medically important cell types such as macrophages, dendritic cells, foam cells, and osteoclasts (*69*).

Methodology

Monocyte and monocyte-derived cells

To enable analysis of the different functional programs of monocytes, human primary monocytes were purified from three to six healthy human donors (depending on experiment) by first isolating peripheral blood mononuclear cells by differential centrifugation over Ficoll-Paque, followed by depletion of T cells, B cells, and NK cells with beads coated with antibodies directed against CD3, CD19, and CD56, respectively (fig. S1). Mf were obtained by in vitro culture of the purified Mo for 6 days in cell culture medium enriched with human serum (10%). Monocyte tolerance, a state akin to immune paralysis during bacterial sepsis or endotoxin shock, was induced in vitro by exposing the purified monocytes to LPS for 24 hours (*9*). Monocyte training—a functional state in which cells respond more strongly to microbial stimuli that mirror the nonspecific protective effects of live microorganism vaccination [e.g., BCG, measles, and yellow fever (*15*)] (Fig. 1, A and B)—was induced in vitro by exposing the purified monocytes to β-glucan for 24 hours (Fig. 1B) (*10*). The LPS or β-glucan was then washed out from the system, and the cells were incubated in enriched cell-cultured medium for 5 days.

Genome-wide epigenetic profiling

For all the four types of cells described above—Mo, Mf, LPS-Mf, and BG-Mf cells—the epigenomic profiles were generated for three histone H3-borne marks known to be associated with gene expression. They respectively mark promoters (H3K4me3), distal regulatory elements (H3K4me1), and the active forms of both promoters and enhancers (H3K27ac) (*23*, *24*). Additionally, RNA and DNase I accessibility were quantified (*25*). The raw data from the sequencing experiments are available through the European Genome-Phenome Archive (EGA), using the data set identifier EGAD00001001011. Please apply to the Blueprint Data Access Committee (http://www.blueprint-epigenome.eu/index.cfm?p=B5E93EE0-09E2-5736-A708817C27EF2DB7) for permission to access this data set. Processed data can be accessed via Gene Expression Omnibus (GEO) accession no. GSE58310.

REFERENCES AND NOTES

1. J. S. Lewis, J. A. Lee, J. C. Underwood, A. L. Harris, C. E. Lewis, Macrophage responses to hypoxia: Relevance to disease mechanisms. *J. Leukoc. Biol.* **66**, 889–900 (1999). pmid: 10614769
2. F. Geissmann *et al*., Development of monocytes, macrophages, and dendritic cells. *Science* **327**, 656–661 (2010). doi: 10.1126/science.1178331; pmid: 20133564
3. C. Auffray, M. H. Sieweke, F. Geissmann, Blood monocytes: Development, heterogeneity, and relationship with dendritic cells. *Annu. Rev. Immunol.* **27**, 669–692 (2009). doi: 10.1146/annurev.immunol.021908.132557; pmid: 19132917
4. L. C. Davies, S. J. Jenkins, J. E. Allen, P. R. Taylor, Tissue-resident macrophages. *Nat. Immunol.* **14**, 986–995 (2013). doi: 10.1038/ni.2705; pmid: 24048120
5. F. Ginhoux, S. Jung, Monocytes and macrophages: Developmental pathways and tissue homeostasis. *Nat. Rev. Immunol.* **14**, 392–404 (2014). doi: 10.1038/nri3671; pmid: 24854589
6. C. Jakubzick *et al*., Minimal differentiation of classical monocytes as they survey steady-state tissues and transport antigen to lymph nodes. *Immunity* **39**, 599–610 (2013). doi: 10.1016/j.immuni.2013.08.007; pmid: 24012416
7. E. Zigmond *et al*., Ly6C hi monocytes in the inflamed colon give rise to proinflammatory effector cells and migratory antigen-presenting cells. *Immunity* **37**, 1076–1090 (2012). doi: 10.1016/j.immuni.2012.08.026; pmid: 23219392
8. A. Sica, A. Mantovani, Macrophage plasticity and polarization: In vivo veritas. *J. Clin. Invest.* **122**, 787–795 (2012). doi: 10.1172/JCI59643; pmid: 22378047
9. S. K. Biswas, E. Lopez-Collazo, Endotoxin tolerance: New mechanisms, molecules and clinical significance. *Trends Immunol.* **30**, 475–487 (2009). doi: 10.1016/j.it.2009.07.009; pmid: 19781994
10. J. Quintin *et al*., *Candida albicans* infection affords protection against reinfection via functional reprogramming of monocytes. *Cell Host Microbe* **12**, 223–232 (2012). doi: 10.1016/j.chom.2012.06.006; pmid: 22901542
11. M. G. Netea, J. Quintin, J. W. van der Meer, Trained immunity: A memory for innate host defense. *Cell Host Microbe* **9**, 355–361 (2011). doi: 10.1016/j.chom.2011.04.006; pmid: 21575907
12. J. Quintin, S. C. Cheng, J. W. van der Meer, M. G. Netea, Innate immune memory: Towards a better understanding of host defense mechanisms. *Curr. Opin. Immunol.* **29**, 1–7 (2014). doi: 10.1016/j.coi.2014.02.006; pmid: 24637148
13. D. C. Ifrim *et al*., Trained immunity or tolerance: Opposing functional programs induced in human monocytes after engagement of various pattern recognition receptors. *Clin. Vaccine Immunol.* **21**, 534–545 (2014). doi: 10.1128/CVI.00688-13; pmid: 24521784
14. J. Kleinnijenhuis *et al*., Bacille Calmette-Guerin induces NOD2-dependent nonspecific protection from reinfection via epigenetic reprogramming of monocytes. *Proc. Natl. Acad. Sci. U.S.A.* **109**, 17537–17542 (2012). doi: 10.1073/pnas.1202870109; pmid: 22988082
15. C. S. Benn, M. G. Netea, L. K. Selin, P. Aaby, A small jab—a big effect: Nonspecific immunomodulation by vaccines. *Trends Immunol.* **34**, 431–439 (2013). doi: 10.1016/j.it.2013.04.004; pmid: 23680130
16. O. Takeuch, S. Akira, Epigenetic control of macrophage polarization. *Eur. J. Immunol.* **41**, 2490–2493 (2011). doi: 10.1002/eji.201141792; pmid: 21952803
17. M. Ishii *et al*., Epigenetic regulation of the alternatively activated macrophage phenotype. *Blood* **114**, 3244–3254 (2009). doi: 10.1182/blood-2009-04-217620; pmid: 19567879
18. R. Ostuni *et al*., Latent enhancers activated by stimulation in differentiated cells. *Cell* **152**, 157–171 (2013). doi: 10.1016/j.cell.2012.12.018; pmid: 23332752
19. S. L. Foster, D. C. Hargreaves, R. Medzhitov, Gene-specific control of inflammation by TLR-induced chromatin modifications. *Nature* **447**, 972–978 (2007). pmid: 17538624
20. D. Adams *et al*., BLUEPRINT to decode the epigenetic signature written in blood. *Nat. Biotechnol.* **30**, 224–226 (2012). doi: 10.1038/nbt.2153; pmid: 22398613

21. J. H. Martens, H. G. Stunnenberg, BLUEPRINT: Mapping human blood cell epigenomes. *Haematologica* **98**, 1487–1489 (2013). doi: 10.3324/haematol.2013.094243; pmid: 24091925
22. M. G. Netea *et al*., Differential requirement for the activation of the inflammasome for processing and release of IL-1beta in monocytes and macrophages. *Blood* **113**, 2324–2335 (2009). doi: 10.1182/blood-2008-03-146720; pmid: 19104081
23. N. D. Heintzman *et al*., Histone modifications at human enhancers reflect global cell-type-specific gene expression. *Nature* **459**, 108–112 (2009). doi: 10.1038/nature07829; pmid: 19295514
24. A. Rada-Iglesias *et al*., A unique chromatin signature uncovers early developmental enhancers in humans. *Nature* **470**, 279–283 (2011). doi: 10.1038/nature09692; pmid: 21160473
25. R. E. Thurman *et al*., The accessible chromatin landscape of the human genome. *Nature* **489**, 75–82 (2012). doi: 10.1038/nature11232; pmid: 22955617
26. S. Hashimoto, T. Suzuki, H. Y. Dong, N. Yamazaki, K. Matsushima, Serial analysis of gene expression in human monocytes and macrophages. *Blood* **94**, 837–844 (1999). pmid: 10419873
27. F. O. Martinez, S. Gordon, M. Locati, A. Mantovani, Transcriptional profiling of the human monocyte-to-macrophage differentiation and polarization: New molecules and patterns of gene expression. *J. Immunol.* **177**, 7303–7311 (2006). doi: 10.4049/jimmunol.177.10.7303; pmid: 17082649
28. J. Li *et al*., cDNA microarray analysis reveals fundamental differences in the expression profiles of primary human monocytes, monocyte-derived macrophages, and alveolar macrophages. *J. Leukoc. Biol.* **81**, 328–335 (2007). doi: 10.1189/jlb.0206124; pmid: 17046970
29. C. Dong *et al*., RNA sequencing and transcriptomal analysis of human monocyte to macrophage differentiation. *Gene* **519**, 279–287 (2013). doi: 10.1016/j.gene.2013.02.015; pmid: 23458880
30. S. Vallabhapurapu, M. Karin, Regulation and function of NF-kappaB transcription factors in the immune system. *Annu. Rev. Immunol.* **27**, 693–733 (2009). doi: 10.1146/annurev.immunol.021908.132641; pmid: 19302050
31. F. Martinon, J. Tschopp, Inflammatory caspases: Linking an intracellular innate immune system to autoinflammatory diseases. *Cell* **117**, 561–574 (2004). doi: 10.1016/j.cell.2004.05.004; pmid: 15163405
32. J. M. Bruey *et al*., PAN1/NALP2/PYPAF2, an inducible inflammatory mediator that regulates NF-kappaB and caspase-1 activation in macrophages. *J. Biol. Chem.* **279**, 51897–51907 (2004). doi: 10.1074/jbc.M406741200; pmid: 15456791
33. M. Jain *et al*., Metabolite profiling identifies a key role for glycine in rapid cancer cell proliferation. *Science* **336**, 1040–1044 (2012). doi: 10.1126/science.1218595; pmid: 22628656
34. B. Everts *et al*., TLR-driven early glycolytic reprogramming via the kinases TBK1-IKKε supports the anabolic demands of dendritic cell activation. *Nat. Immunol.* **15**, 323–332 (2014). doi: 10.1038/ni.2833; pmid: 24562310
35. S. K. Biswas, A. Mantovani, Orchestration of metabolism by macrophages. *Cell Metab.* **15**, 432–437 (2012). doi: 10.1016/j.cmet.2011.11.013; pmid: 22482726
36. S.-C. Cheng *et al*., mTOR/HIF1α-mediated aerobic glycolysis as metabolic basis for trained immunity. *Science* **345**, 1250684 (2014).
37. J. Ernst, M. Kellis, Discovery and characterization of chromatin states for systematic annotation of the human genome. *Nat. Biotechnol.* **28**, 817–825 (2010). doi: 10.1038/nbt.1662; pmid: 20657582
38. E. Turro *et al*., Haplotype and isoform specific expression estimation using multi-mapping RNA-seq reads. *Genome Biol.* **12**, R13 (2011). doi: 10.1186/gb-2011-12-2-r13; pmid: 21310039
39. E. Turro, W. J. Astle, S. Tavaré, Flexible analysis of RNA-seq data using mixed effects models. *Bioinformatics* **30**, 180–188 (2014). doi: 10.1093/bioinformatics/btt624; pmid: 24281695
40. K. Kobayashi *et al*., IRAK-M is a negative regulator of Toll-like receptor signaling. *Cell* **110**, 191–202 (2002). doi: 10.1016/S0092-8674(02)00827-9; pmid: 12150927
41. L. Balaci *et al*., IRAK-M is involved in the pathogenesis of early-onset persistent asthma. *Am. J. Hum. Genet.* **80**, 1103–1114 (2007). doi: 10.1086/518259; pmid: 17503328
42. D. S. Shouval *et al*., Interleukin 10 receptor signaling: Master regulator of intestinal mucosal homeostasis in mice and humans. *Adv. Immunol.* **122**, 177–210 (2014). doi: 10.1016/B978-0-12-800267-4.00005-5; pmid: 24507158
43. A. Bessede *et al*., Aryl hydrocarbon receptor control of a disease tolerance defence pathway. *Nature* **511**, 184–190 (2014). doi: 10.1038/nature13323; pmid: 24930766
44. C. H. Khuu, R. M. Barrozo, T. Hai, S. L. Weinstein, Activating transcription factor 3 (ATF3) represses the expression of CCL4 in murine macrophages. *Mol. Immunol.* **44**, 1598–1605 (2007). doi: 10.1016/j.molimm.2006.08.006; pmid: 16982098
45. J. P. McMorrow, E. P. Murphy, Inflammation: A role for NR4A orphan nuclear receptors? *Biochem. Soc. Trans.* **39**, 688–693 (2011). doi: 10.1042/BST0390688; pmid: 21428963
46. T. Kohro *et al*., Genomic structure and mapping of human orphan receptor LXR alpha: Upregulation of LXRa mRNA during monocyte to macrophage differentiation. *J. Atheroscler. Thromb.* **7**, 145–151 (2000). doi: 10.5551/jat1994.7.145; pmid: 11480455
47. M. Boergesen *et al*., Genome-wide profiling of liver X receptor, retinoid X receptor, and peroxisome proliferator-activated receptor α in mouse liver reveals extensive sharing of binding sites. *Mol. Cell. Biol.* **32**, 852–867 (2012). doi: 10.1128/MCB.06175-11; pmid: 22158963
48. K. Endo-Umeda *et al*., 7-Dehydrocholesterol metabolites produced by sterol 27-hydroxylase (CYP27A1) modulate liver X receptor activity. *J. Steroid Biochem. Mol. Biol.* **140**, 7–16 (2014). doi: 10.1016/j.jsbmb.2013.11.010; pmid: 24269243
49. E. L. Gautier *et al*., Systemic analysis of PPARγ in mouse macrophage populations reveals marked diversity in expression with critical roles in resolution of inflammation and airway immunity. *J. Immunol.* **189**, 2614–2624 (2012). doi: 10.4049/jimmunol.1200495; pmid: 22855714
50. B. Hotz, A. Visekruna, H. J. Buhr, H. G. Hotz, Beyond epithelial to mesenchymal transition: A novel role for the transcription factor Snail in inflammation and wound healing. *J. Gastrointest. Surg.* **14**, 388–397 (2010). doi: 10.1007/s11605-009-1068-3; pmid: 19856033
51. M. Leptin, twist and snail as positive and negative regulators during Drosophila mesoderm development. *Genes Dev.* **5**, 1568–1576 (1991). doi: 10.1101/gad.5.9.1568; pmid: 1884999
52. K. Ozato, P. Tailor, T. Kubota, The interferon regulatory factor family in host defense: Mechanism of action. *J. Biol. Chem.* **282**, 20065–20069 (2007). doi: 10.1074/jbc.R700003200; pmid: 17502370
53. M. Miyamoto *et al*., Regulated expression of a gene encoding a nuclear factor, IRF-1, that specifically binds to IFN-beta gene regulatory elements. *Cell* **54**, 903–913 (1988). doi: 10.1016/S0092-8674(88)91307-4; pmid: 3409321
54. H. Harada *et al*., Structurally similar but functionally distinct factors, IRF-1 and IRF-2, bind to the same regulatory elements of IFN and IFN-inducible genes. *Cell* **58**, 729–739 (1989). doi: 10.1016/0092-8674(89)90107-4; pmid: 2475256
55. R. Günthner, H. J. Anders, Interferon-regulatory factors determine macrophage phenotype polarization. *Mediators Inflamm.* **2013**, 731023 (2013). doi: 10.1155/2013/731023; pmid: 24379524
56. G. Servillo, M. A. Della Fazia, P. Sassone-Corsi, Coupling cAMP signaling to transcription in the liver: Pivotal role of CREB and CREM. *Exp. Cell Res.* **275**, 143–154 (2002). doi: 10.1006/excr.2002.5491; pmid: 11969286
57. A. Jolma *et al*., DNA-binding specificities of human transcription factors. *Cell* **152**, 327–339 (2013). doi: 10.1016/j.cell.2012.12.009; pmid: 23332764
58. S. J. van Heeringen, G. J. Veenstra, GimmeMotifs: A de novo motif prediction pipeline for ChIP-sequencing experiments. *Bioinformatics* **27**, 270–271 (2011). doi: 10.1093/bioinformatics/btq636; pmid: 21081511
59. K. Newton, V. M. Dixit, Signaling in innate immunity and inflammation. *Cold Spring Harb. Perspect. Biol.* **4**, a006049 (2012). doi: 10.1101/cshperspect.a006049; pmid: 22296764
60. T. Lange, S. Dimitrov, J. Born, Effects of sleep and circadian rhythm on the human immune system. *Ann. N.Y. Acad. Sci.* **1193**, 48–59 (2010). doi: 10.1111/j.1749-6632.2009.05300.x; pmid: 20398008
61. M. H. Sieweke, J. E. Allen, Beyond stem cells: Self-renewal of differentiated macrophages. *Science* **342**, 1242974 (2013). doi: 10.1126/science.1242974; pmid: 24264994
62. A. Aziz, E. Soucie, S. Sarrazin, M. H. Sieweke, MafB/c-Maf deficiency enables self-renewal of differentiated functional macrophages. *Science* **326**, 867–871 (2009). doi: 10.1126/science.1176056; pmid: 19892988
63. K. R. Stenmark *et al*., The adventitia: Essential regulator of vascular wall structure and function. *Annu. Rev. Physiol.* **75**, 23–47 (2013). doi: 10.1146/annurev-physiol-030212-183802; pmid: 23216413
64. G. D. Wenger, M. S. O'Dorisio, Induction of cAMP-dependent protein kinase I during human monocyte differentiation. *J. Immunol.* **134**, 1836–1843 (1985). pmid: 2981923
65. K. C. Bagley, S. F. Abdelwahab, R. G. Tuskan, T. R. Fouts, G. K. Lewis, Cholera toxin and heat-labile enterotoxin activate human monocyte-derived dendritic cells and dominantly inhibit cytokine production through a cyclic AMP-dependent pathway. *Infect. Immun.* **70**, 5533–5539 (2002). doi: 10.1128/IAI.70.10.5533-5539.2002; pmid: 12228279
66. M. Shen *et al*., Induction of basic helix-loop-helix protein DEC1 (BHLHB2)/Stra13/Sharp2 in response to the cyclic adenosine monophosphate pathway. *Eur. J. Cell Biol.* **80**, 329–334 (2001). doi: 10.1078/0171-9335-00167; pmid: 11432722
67. M. Shen *et al*., Molecular characterization of the novel basic helix-loop-helix protein DEC1 expressed in differentiated human embryo chondrocytes. *Biochem. Biophys. Res. Commun.* **236**, 294–298 (1997). doi: 10.1006/bbrc.1997.6960; pmid: 9240428
68. T. A. Wynn, A. Chawla, J. W. Pollard, Macrophage biology in development, homeostasis and disease. *Nature* **496**, 445–455 (2013). doi: 10.1038/nature12034; pmid: 23619691
69. S. Gordon, P. R. Taylor, Monocyte and macrophage heterogeneity. *Nat. Rev. Immunol.* **5**, 953–964 (2005). doi: 10.1038/nri1733; pmid: 16322748
70. Materials and methods are available as supplementary materials on *Science* Online.

ACKNOWLEDGMENTS

The authors are grateful to J. Stamatoyannopoulos for help with DNaseI-seq. We thank S. van Heeringen for access to his databases and expertise. The research leading to the results described in this manuscript has received funding from the European Union's Seventh Framework Programme (FP7/2007-2013) under grant agreement no. 282510-BLUEPRINT. M.G.N. was supported by a Vici grant of the Netherlands Organization for Scientific Research and an ERC Consolidator Grant (no. 310372) and J.H.A.M by a VIDI grant of the Netherlands Organization for Scientific Research. All the genome-wide data generated and analyzed in this study, as well as the sequencing details, can be accessed via GEO accession no. GSE58310.

SUPPLEMENTARY MATERIALS

www.sciencemag.org/content/345/6204/1251086/suppl/DC1
Materials and Methods
Figs. S1 to S9
Tables S1 to S6
References

20 January 2014; accepted 28 August 2014
10.1126/science.1251086

RESEARCH ARTICLE SUMMARY

NEURAL DEVELOPMENT

Coordination of progenitor specification and growth in mouse and chick spinal cord

Anna Kicheva, Tobias Bollenbach, Ana Ribeiro, Helena Pérez Valle, Robin Lovell-Badge, Vasso Episkopou, James Briscoe*

INTRODUCTION: The hallmarks of development are tissue growth and the generation of cell diversity, resulting in reproducibly patterned animals. Yet, how growth and cell fate specification are coordinated to determine the variety of cell types and the proportions of their populations is not well understood. The specification of cell types can be controlled by long-range signals, called morphogens. In some tissues, the shape of morphogen gradients is controlled to match the rate at which the tissue grows, which may keep the pattern proportional to the overall tissue size. To understand whether a similar strategy applies to the patterning of the spinal cord, we measured growth and cell fate specification in chick and mouse embryos of normal size, as well as mutant mice of smaller size.

RATIONALE: Morphogen gradients emanating from the dorsal and ventral sides of the spinal cord establish a striped pattern of gene expression in neural progenitors along the dorsoventral axis. Ventrally, Sonic Hedgehog (Shh) is the key morphogen. As the tissue grows in size, the levels of Shh activity in progenitors decrease and are not constant at progenitor domain boundaries. This prompted us to examine whether growth contributed to pattern formation. To this end, we measured the four parameters that control the number of progenitors in a domain: (i) cell proliferation, (ii) cell death, (iii) terminal differentiation of progenitors into postmitotic neurons, and (iv) switches in cell identity—morphogen-driven changes in gene expression respecifying one progenitor type into another.

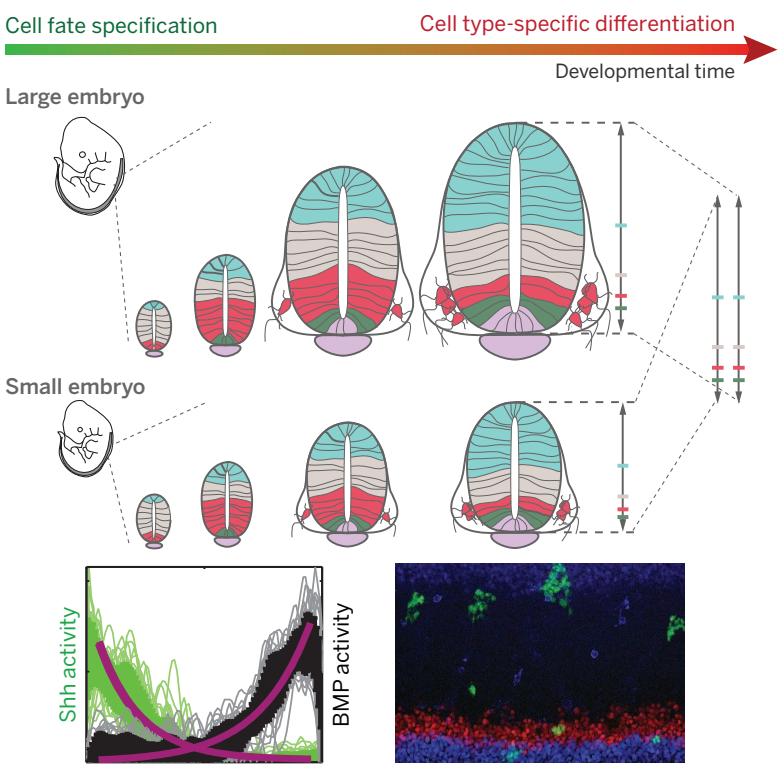

Growth and patterning of the spinal cord. Progenitors are organized in a striped pattern, revealed by their gene expression. In animals of different size, the pattern changes in the same way as the spinal cord grows. This is controlled sequentially, first by progenitor specification by opposing morphogen gradients (bottom left), then by cell-type–specific differentiation resulting in differently shaped clones (green, bottom right).

RESULTS: Unlike systems in which pattern is proportional to size, we found that the relative dorsoventral sizes of neural progenitor domains change continuously during development. These changes in proportions are conserved between mouse, chick, and smaller mouse mutants. Because the proliferation rate of progenitors was spatially uniform and cell death was negligible, neither of these processes could account for the dynamics of pattern formation. Instead, the data revealed two distinct phases of spinal cord development. Initially, the influence of the morphogens dominates, and switches in cell identity establish pattern. During the second phase, domain-specific differentiation rates emerge, causing changes in the relative proportions of progenitor cell populations. Clonal analysis indicated that this effect is anisotropic: Differentiation affects dorsoventral and apicobasal, but not anterioposterior, domain growth. The outcome is that different domains grow in register along the anterioposterior axis. Consistent with the two-phase model, the switches in cell fate and the sensitivity to changes in morphogen signaling decrease as development proceeds. Conversely, experimentally flattening the difference in differentiation rate between domains during the second phase alters pattern.

ON OUR WEB SITE

Read the full article at http://dx.doi.org/10.1126/science.1254927

CONCLUSION: The data reveal two phases of neural tube development and show that sequential control of progenitor cell specification and differentiation elaborates pattern without requiring signaling gradients to expand as tissues grow. Control of the differentiation rate is likely to contribute to pattern formation in other tissues. Furthermore, the domain-specific regulation of the differentiation rates could suggest a means to achieve reproducible development despite differences in individual size. ■

The list of author affiliations is available in the full article online.
*Corresponding author. E-mail: jbrisco@nimr.mrc.ac.uk
Cite this article as A. Kicheva *et al.*, *Science* 345, 1254927 (2014); DOI: 10.1126/science.1254927

Published by AAAS

RESEARCH ARTICLE

NEURAL DEVELOPMENT

Coordination of progenitor specification and growth in mouse and chick spinal cord

Anna Kicheva,[1] Tobias Bollenbach,[2] Ana Ribeiro,[1]* Helena Pérez Valle,[1,3] Robin Lovell-Badge,[1,4,5] Vasso Episkopou,[6] James Briscoe[1]†

Development requires tissue growth as well as cell diversification. To address how these processes are coordinated, we analyzed the development of molecularly distinct domains of neural progenitors in the mouse and chick neural tube. We show that during development, these domains undergo changes in size that do not scale with changes in overall tissue size. Our data show that domain proportions are first established by opposing morphogen gradients and subsequently controlled by domain-specific regulation of differentiation rate but not differences in proliferation rate. Regulation of differentiation rate is key to maintaining domain proportions while accommodating both intra- and interspecies variations in size. Thus, the sequential control of progenitor specification and differentiation elaborates pattern without requiring that signaling gradients grow as tissues expand.

In most developing tissues, the spatiotemporal pattern of gene expression is generated by gene regulatory networks controlled by morphogens (*1*–*3*). This happens at the same time as the tissue grows. Understanding how growth and cell fate specification are coordinated within a tissue to determine the relative proportions of different cell types is of central importance. In some tissues, such as the *Drosophila* wing disc (*4*), early embryo (*5*, *6*), and *Xenopus* gastrula (*7*, *8*) the scaling of the morphogen gradient with tissue size determines the underlying pattern. Whether similar strategies apply to all tissues is unclear.

In the vertebrate neural tube, the dorsoventral pattern of neural progenitors is specified by 13 spatially distinct transcriptional states (*9*). These are encoded by the combinatorial expression of transcription factors in response to opposing morphogen gradients—ventrally secreted sonic hedgehog (Shh) and dorsally secreted bone morphogenetic protein (BMP) and Wnt (Fig. 1A). In mouse, the graded activation of Gli effectors downstream of Shh undergoes temporal adaptation after reaching a peak at embryonic day 9 (E9) (*10*, *11*); hence, it does not correlate with tissue size. Moreover, Gli activity levels are not constant at the boundaries of the target genes Nkx2.2 and Olig2 over time (*11*). Although the transcriptional network is at least in part responsible for this lack of correspondence between Shh signaling and target gene boundary positions (*11*), anisotropic tissue growth might also affect progenitor domain sizes.

During development, neural progenitors proliferate, and this is counterbalanced by their terminal differentiation into neurons, which migrate out of the epithelial progenitor layer (*12*) (Fig. 1, A to C). As a result, the neural tube grows anterioposteriorly, dorsoventrally, and apicobasally, but it is not known how much growth occurs in each dimension. Here, we assess the contribution of morphogen signaling and anisotropic growth to pattern formation and define how pattern adapts to size variability between individuals by measuring the growth characteristics of mouse and chick embryos.

Pattern does not scale with tissue size

To characterize how pattern is specified relative to neural tube growth and Shh signaling, we focused on five progenitor domains that partition the dorsoventral axis (Fig. 1, A and B). We collected transverse sections from the forelimb level of mouse embryos adjacent to somites 7 to 10 between E8 [~10 hours post headfold stage (hph)] and E11.5 [~90 hph, the onset of gliogenesis (*13*)].

During this period, the dorsoventral length of the neural tube increases by a factor of ~4, and the domain boundary positions shift with respect to the ventral midline (Fig. 1D). Before E9, these shifts result, at least in part, from the progressive induction of progenitor domains (*11*, *14*). Moreover, the relative positions of boundaries (as a fraction of the total length) are not constant but also change (Fig. 1E). This could result from changes in cell shape, size, or number. Indeed, the apicobasal thickness of the single-cell layer of Sox2-positive ($Sox2^+$) progenitors changes over time in a domain-specific manner (Fig. 1F), suggesting regulated changes in cell shape. Nevertheless, all progenitors attach to the apical surface; hence, the number of $Sox2^+$ nuclei per section provides a measure of dorsoventral size in units of cells, independent of cell shape (Fig. 1, C and G, and fig. S1). The relative sizes of progenitor domains measured in this way change during development (Fig. 1H), showing that dorsoventral pattern does not change linearly with the overall neural tube size.

In systems where pattern scales with growing tissue size, domain proportions are also preserved between individuals of varying size (*4*–*8*). To study how neural tube pattern accommodates variations in size between individuals, we used a mouse *Minute* strain that is heterozygous for a deletion in Rpl24 (*15*), a large ribosomal subunit component. These smaller *Minute* mice have no apparent locomotion defects, yet they have 19 ± 10% fewer progenitors than wild-type littermates at E11.5 (Fig. 2, A, B, and D), and they produce 60 ± 7% fewer postmitotic neurons (Student's *t* test, $P < 0.05$) (Fig. 2E). Although the neural tube size of Rpl24(Bst)/+ embryos is noticeably smaller than controls after 30 hph, the progenitor domain proportions follow a similar pattern of development [Fig. 2F, 95% confidence intervals (CIs)], and at 90 hph the mice end up with a similarly patterned, albeit smaller, neural tube.

Furthermore, by comparing pattern at equivalent stages and anterioposterior positions, we found that the dynamics of progenitor domain proportions are also conserved between the mouse and chick neural tube (Fig. 2, C and G). Together, this indicates that the dorsoventral domain proportions change during development via a conserved sequence, which is independent of the size of the animal.

Proliferation is uniform but differentiation is cell-type specific

How is the temporal sequence of progenitor domain proportions controlled? Four factors control the number of progenitors in a domain: (i) cell proliferation, (ii) apoptosis, (iii) terminal differentiation leading to cell cycle exit and delamination, and (iv) switches in cell identity—i.e., changes in gene expression that respecify one progenitor type into another. It is possible that spatially nonuniform growth, driven by nonuniform differentiation, proliferation, or apoptosis, together with a memory of the transcriptional state (*11*), could account for the change in proportions independent of signaling. Alternatively, switches in gene expression could increase the size of one progenitor pool at the expense of another. To distinguish between these possibilities, we measured the growth parameters of the mouse spinal cord.

We measured the proliferation rate using sequential pulse labeling with two thymidine

[1]Medical Research Council (MRC), National Institute for Medical Research, The Ridgeway, Mill Hill, London, NW71AA, UK. [2]Institute of Science and Technology (IST) Austria, Am Campus 1, A – 3400 Klosterneuburg, Austria. [3]Imperial College London, UK. [4]Department of Biochemistry, The University of Hong Kong, 3/F Laboratory Block, Faculty of Medicine Building, 21 Sassoon Road, Hong Kong. [5]Division of Biosciences, Faculty of Life Sciences, University College London, UK. [6]Division of Brain Sciences, Faculty of Medicine, Imperial College London, UK.
*Present address: Instituto de Medicina Molecular, Faculdade de Medicina da Universidade de Lisboa, Lisboa, Portugal.
†Corresponding author. E-mail: jbrisco@nimr.mrc.ac.uk

analogs, iododeoxyuridine (IdU) and bromodeoxyuridine (BrdU) (*16*, *17*). The fraction of Sox2$^+$ progenitors labeled only with IdU during the 1.5-hour pulse (IduLI) is directly related to the proliferation rate λ (fig. S2, A and B) (see materials and methods). We also measured the mitotic index (MI), the fraction of phospho-histone H3–labeled Sox2$^+$ progenitors, in combination with progenitor domain markers (Fig. 3A and fig. S2C). The MI/IduLI ratio allows us to determine the duration of mitosis, 27.7 ± 11.3 min, and the domain-specific λ from the MI (see materials and methods). Both approaches indicate that the proliferation rate is uniform in all domains except the Shh-producing floorplate [analysis of variance (ANOVA), $P > 0.05$ for all stages, excluding floorplate].

The proliferation rate is approximately constant before 40 hph (~0.08 hour^{-1}, equivalent to a cell cycle length of ~9 hours) and decreases at later times (Fig. 3A). In parallel, the duration of the G1 phase of the cell cycle increases relative to the cell cycle length (Fig. 3, D and E, and fig. S3, A and B), but this increase is not spatially uniform. Thus, while the overall cell cycle length is similar between the motor neuron progenitor (pMN) and dorsal progenitor (pD) domains at 60 hph, their cell cycle phase distribution is different. This raises the possibility that a homeostatic control mechanism could coordinate G1/S and G2/M progression to maintain uniform proliferation (*18*).

Because the proliferation rate is spatially uniform, it cannot cause the observed changes in domain proportions. Furthermore, the fraction of apoptotic progenitors is less than 0.5% (Fig. 3B), and cleaved Caspase 3, used to detect apoptosis, can persist for more than 2 hours in neural tissues (*19*). Thus, the rate of progenitor apoptosis

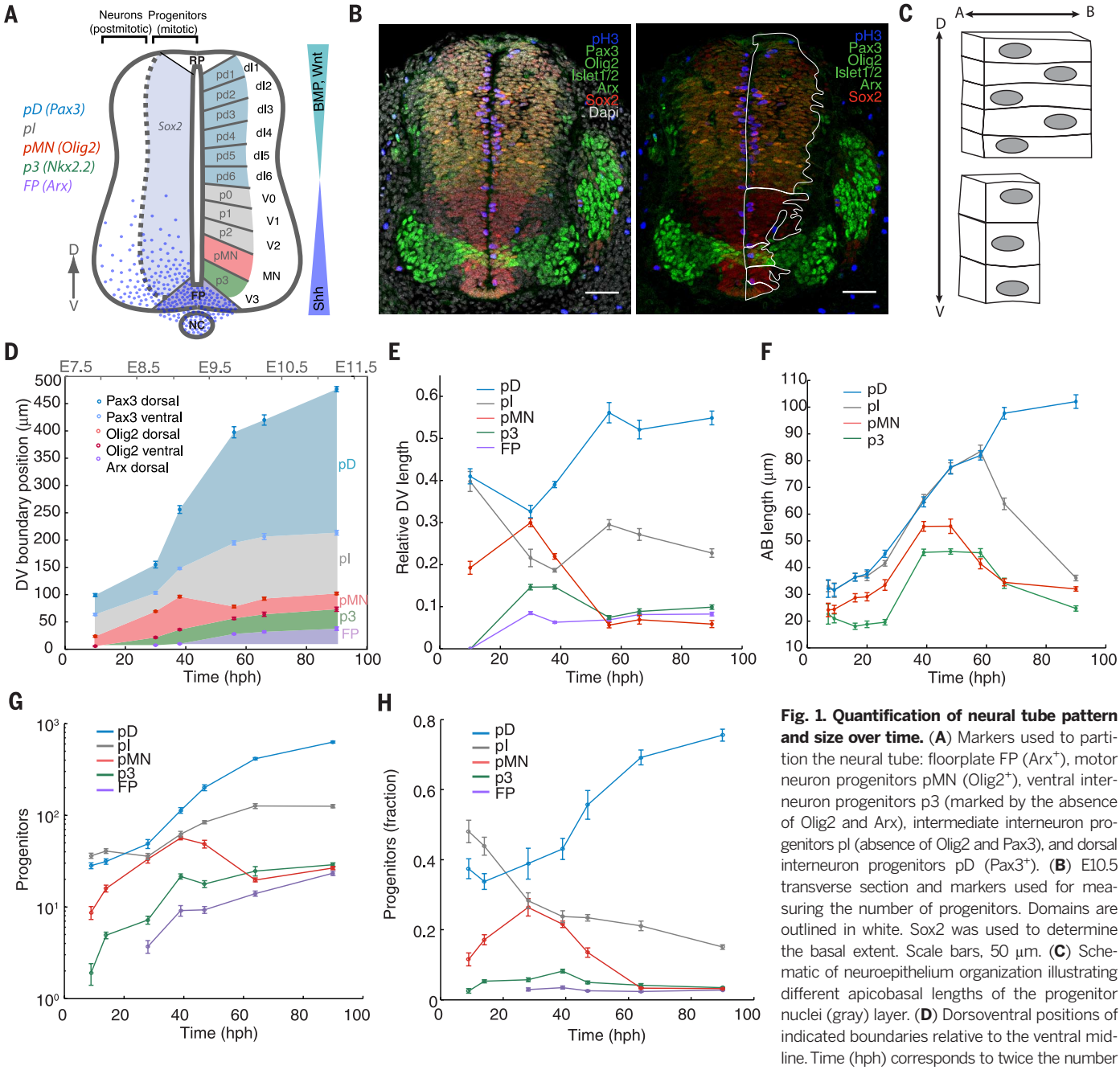

Fig. 1. Quantification of neural tube pattern and size over time. (**A**) Markers used to partition the neural tube: floorplate FP (Arx$^+$), motor neuron progenitors pMN (Olig2$^+$), ventral interneuron progenitors p3 (marked by the absence of Olig2 and Arx), intermediate interneuron progenitors pI (absence of Olig2 and Pax3), and dorsal interneuron progenitors pD (Pax3$^+$). (**B**) E10.5 transverse section and markers used for measuring the number of progenitors. Domains are outlined in white. Sox2 was used to determine the basal extent. Scale bars, 50 μm. (**C**) Schematic of neuroepithelium organization illustrating different apicobasal lengths of the progenitor nuclei (gray) layer. (**D**) Dorsoventral positions of indicated boundaries relative to the ventral midline. Time (hph) corresponds to twice the number of somites. Upper *x* axis, embryonic day (table S1). (**E**) The dorsoventral boundary positions relative to total dorsoventral length change over time. (**F**) Mean apicobasal length of the Sox2$^+$ progenitor layer. (**G**) Mean number of Sox2$^+$ nuclei per hemi-section in each domain based on the markers in (B), representing dorsoventral domain size in units of cells. (**H**) Number of progenitors in G relative to the total. Error bars, mean ± SEM. For sample sizes, see table S2.

(<0.0025 hour^{-1}) is negligible compared with the proliferation rate and does not significantly affect the domain growth rates.

To measure the differentiation rate, we quantified the number of Sox2-negative (Sox2$^-$) postmitotic neurons generated from each progenitor domain before E11 in transverse sections (Fig. 2E). We defined the differentiation rate as the number of neurons produced per unit time relative to the size of the progenitor domain, which reflects the probability of progenitors to exit the cell cycle. The differentiation rate was not constant over time. For MNs, a maximum rate was reached at 60 hph (Fig. 3C). For the intermediate and dorsal interneurons, peak differentiation occurred at ~100 hph (fig. S1, G and H). The differentiation rate differed between domains: Before 90 hph, pMNs differentiated at a higher rate (reaching 0.15 hour^{-1}) than the ventral interneuron progenitors (p3) and more dorsal regions (<0.03 hour^{-1}). The increase in differentiation

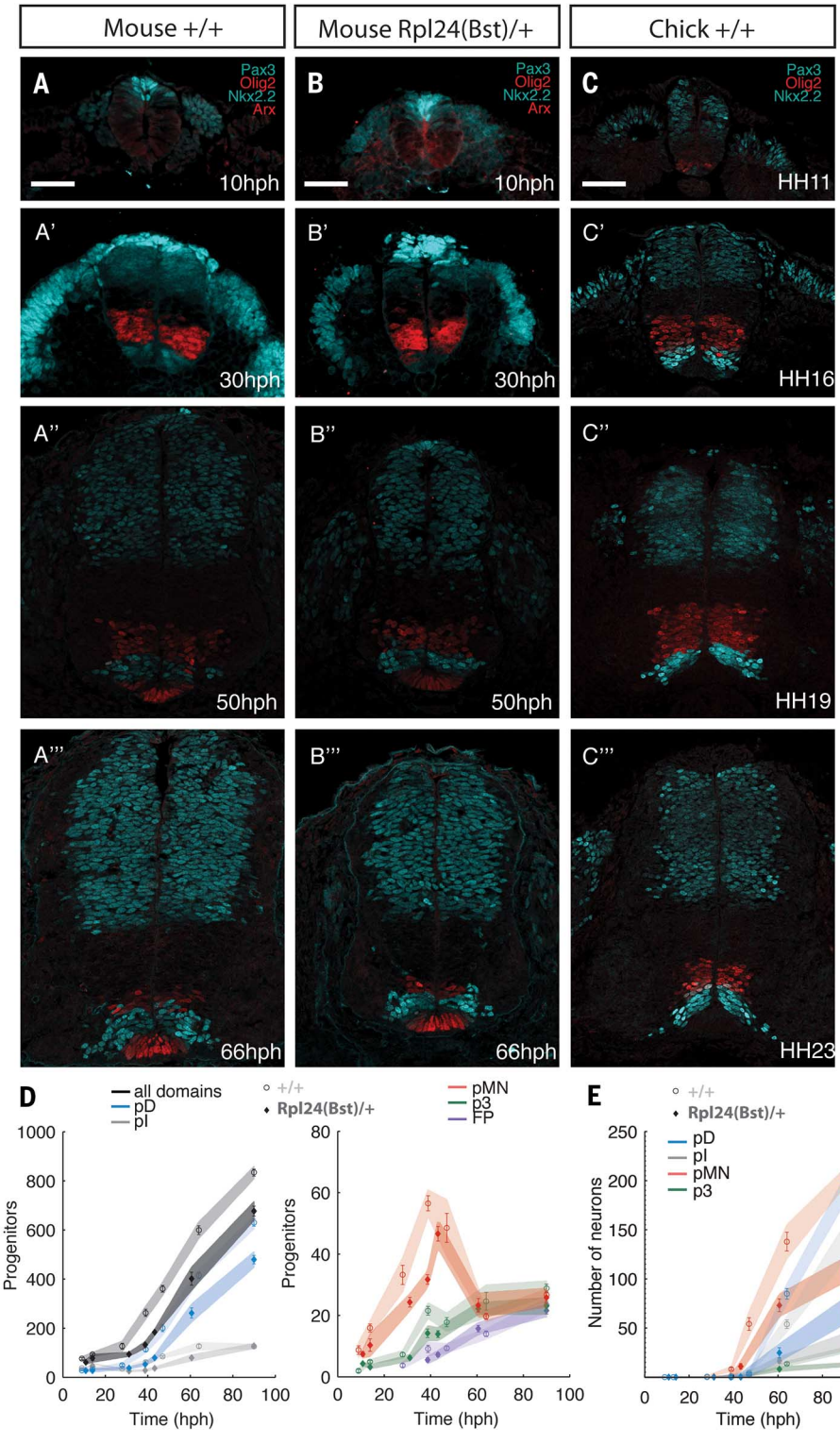

Fig. 2. Comparison of wild-type, Rpl24(Bst)/+ mouse and chick embryos. (**A** to **C'''**) Transverse sections immunostained for Pax3, Olig2, Nkx2.2, and Arx. Identical magnification; scale bars, 50 μm. (**D**) Progenitors per hemisection in wild-type (circles, light shades) versus Rpl24(Bst)/+ (diamonds, dark shades) mouse embryos. The larger, more dorsal domains are plotted on the left panel; the smaller, more ventral domains are on the right. (**E**) Postmitotic neurons in Rpl24(Bst)/+ versus wild-type embryos [legend as in (D)]. (**F**) The progenitors per hemisection in each domain relative to the total number change in a similar way between Rpl24(Bst)/+ and control. (**G**) Wild-type mouse (circles, light shades) versus chick (diamonds, dark shades) comparison as in (F). The chick data set was registered to mouse, so the somite next to which the measurements were made was generated at equivalent corresponding time (table S1). [(D) to (G)] Error bars, mean ± SEM. Shaded areas, 95% CIs. For sample sizes, see table S2.

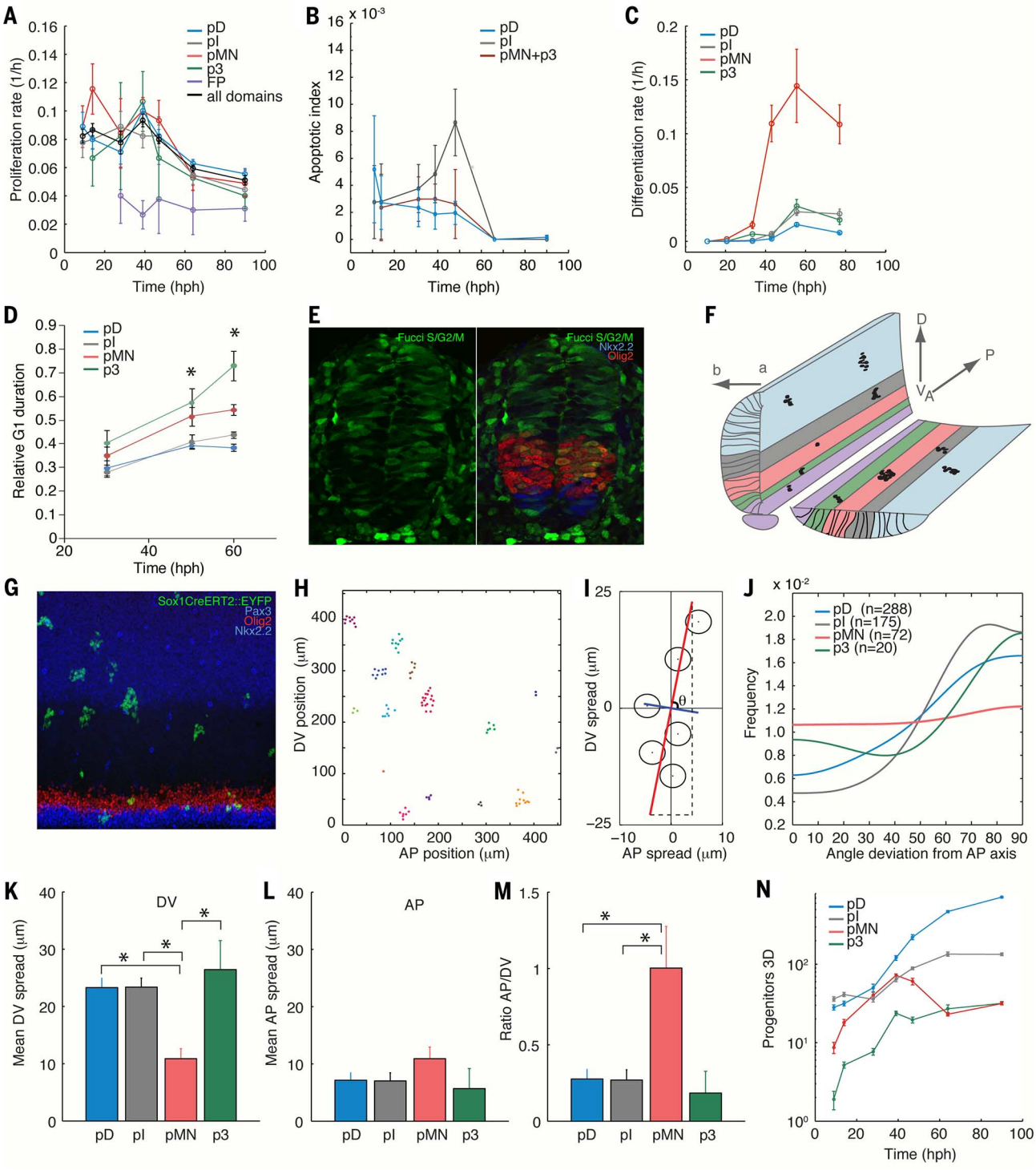

Fig. 3. Mouse growth parameters. (**A**) The proliferation rate determined from MI in sections is similar (ANOVA, $P > 0.05$) for all domains except FP. (**B**) Fraction of Caspase3$^+$ Sox2$^+$ progenitors. (**C**) Differentiation rate determined from transverse sections. (**D** and **E**) G1 length relative to the total cell cycle length (D) estimated from the fraction of S/G2/M-Fucci negative progenitors (E). Asterisks, one-way ANOVA across domains; $P < 0.05$. (**F**) Neural tube geometry and flat-mount preparation. Colors as in Fig. 1A; labeled cells, black. (**G**) Maximum projection though a flat mount, imaged between somites 6 to 13. Dorsal up, anterior left. Clones marked by EYFP expression. (**H**) Coordinates of the EYFP$^+$ cells in (G). Clonal groups are color-coded. (**I**) Example clone. Cell coordinates (dots) and typical cell diameter (circles). First and second eigenvectors of the second moment matrix are shown by red and blue lines, respectively. Clone orientation angle relative to the anterioposterior axis, θ. Anterioposterior and dorsoventral clone spread, dashed lines. (**J**) The density distribution of pD, pI, and p3 clone orientation angles is non uniform (χ^2 test, $P < 0.05$). (**K** to **M**) Mean dorsoventral (K), anterioposterior (L) clone spread and ratio of the mean anterioposterior/dorsoventral spread (M). Asterisks, Student's t test; $P < 0.05$. (**N**) Progenitors in a hemisection with anterioposterior length = 1 cell at $t = 10$ hours and increasing in three dimensions as calculated from the clonal and section data (see the supplementary materials). [(A) to (N)] Error bars, mean ± SEM. For sample sizes, see table S2.

rate of the pMN domain happens at the same time (40 hph) as the size of the domain starts decreasing (Fig. 1G). Thus, differential net growth rates resulting from cell-type–specific differences in the differentiation rate could be the main factor influencing domain size proportions.

Progenitor domain growth is anisotropic

The measurements of the proliferation and differentiation rates can be used to test whether these are sufficient to account for the temporal changes in domain sizes. If this is the case, cell identity does not switch (i.e., the respecification rate is zero) and the change in number of progenitors is given by:

$$\dot{P}(t) = (\lambda(t) - \gamma(t))P(t) \qquad (1)$$

where P is the number of progenitors, $\dot{P}$ is the temporal change in progenitor number, λ is the proliferation rate, and γ is the differentiation rate; all of these change over time. If growth explains the dynamics of patterning, the measured net growth rate $\lambda(t) - \gamma(t)$ should be equal to the relative increase in progenitor number, $\dot{P}/P$.

To measure $\dot{P}/P$, in addition to the dorsoventral and apicobasal sizes, it is necessary to measure the change in progenitor number along the anterioposterior axis (Fig. 3F). To do this, we used a tamoxifen-inducible system, whereby CreERT2 knocked into the Sox1 locus (fig. S4A) excises a loxP-flanked transcription stop sequence resulting in the expression of enhanced yellow fluorescent protein (EYFP). With low tamoxifen doses, EYFP expression was activated in individual progenitors at E9.5 (Fig. 3, F and G). Forty-eight hours later, the sizes of the resulting clones were consistent with the measured proliferation and differentiation rate (fig. S4B). The shape of the clones relates the anterioposterior growth rate to the dorsoventral growth rate calculated from Fig. 1G (see the supplementary materials). This provides a measurement of the growth of a defined volume of the brachial neural tube (Fig. 3N).

Most labeled cells formed coherent groups, suggesting that cell rearrangements after E9.5 are limited (Fig. 3G) (*20*, *21*). The clones often had irregular shape; to quantify these, we used the second moment matrix of cell coordinates (Fig. 3, G to I, and fig. S4). For all but the pMN domain, clones were elongated along the dorsoventral axis, and their orientation was dorsoventrally biased (Fig. 3, J to M, and fig. S4E). By contrast, pMN clones were on average isotropic. Furthermore, although the dorsoventral spread of clones differed between domains, they had a similar anterioposterior spread (Fig. 3, K and L). This implies that mechanical or molecular constraints ensure equivalent anterioposterior growth across the tissue, whereas the dorsoventral growth rates are position and cell-type dependent.

Using these data, we calculated the relative increase in progenitor number in three dimensions $\dot{P}/P$ (see the supplementary materials) and directly compared it to the net growth rate (Eq. 1). To validate the measurements, $\dot{P}/P$ was compared to $\lambda(t) - \gamma(t)$ of the whole tissue, because respecification is irrelevant for the total number of progenitors and Eq. 1 must hold true. This is indeed the case (Fig. 4A), except at 20 hph, which corresponds to the time neural crest delaminates from the neural tube (*22*). Thus $\dot{P}/P$ decreases over time, indicating that the number of progenitors comprising the brachial spinal cord increases at a decelerating rate, by ~0.08 hour^{-1} at 10 hph and by ~0.02 hour^{-1} at later stages.

A two-phase model for neural tube pattern formation

We analyzed individual progenitor domains (Fig. 4, B to F). Before ~40 hph there were discrepancies between $\dot{P}/P$ and $\lambda(t) - \gamma(t)$: The pD and pI domains expanded less than predicted by their growth rate (Fig. 4, B and C), whereas the ventral domains, which are progressively induced in progenitors that initially had pI identity, expanded more (Fig. 4, D to F) (*23*). By contrast, after ~40 hph, there was a good correspondence between the relative increase in progenitor number of each domain and the net growth rate. Thus after ~40 hph, the changes in domain size can be accounted for by proliferation and differentiation, suggesting that the net respecification rate is negligible. Consistent with this, 92.1% of the clones in our data set consisted of a single progenitor type (fig. S4C), indicating that cell identity changes within a lineage are infrequent after E9.5. Because proliferation is spatially uniform (Fig. 3A), the differences in $\dot{P}/P$ between domains, and hence the changes in proportions, must be accounted for by cell-type–specific differences in the differentiation rates (Fig. 3C).

Together, these observations indicate that neural tube patterning can be viewed as a two-phase process: an early phase (before ~40 hph), where there is no differentiation and progenitor identity is actively specified, and a late phase, where progenitor identity does not change significantly and the relative domain sizes are controlled by cell-type–specific differentiation rates (Figs. 3C and 4G).

How are reproducible domain proportions between individuals of different sizes and species achieved during the second phase? In the absence of switches in cell identity and given a spatially uniform proliferation rate, the number of progenitors in any two domains (e.g., the dorsal half P_d, and the ventral half P_v) would each change in accordance to Eq. 1. Hence, the ratio of progenitors in the two domains would change as

$$\frac{d\left(\frac{P_d}{P_v}\right)}{dt} = (\gamma_v(t) - \gamma_d(t))\frac{P_d}{P_v} \qquad (2)$$

where $\gamma_v(t)$ and $\gamma_d(t)$ are the time-dependent differentiation rates in the two domains. Therefore, as long as two individuals have the same differences between the differentiation rates of domains over time, regardless of the absolute tissue size, their progenitor domain proportions would change in the same way. Thus, reproducible pattern proportions are achieved if four criteria are satisfied: (i) absence of net cell identity changes, (ii) conserved cell-type–specific differences in the differentiation rate, (iii) conserved temporal dynamics of the differentiation rate in different individuals, and (iv) reproducible initial proportions established during the early phase.

Because the chick neural tube shows similar changes in proportions as mouse, we hypothesized that the two-phase model also applies to this species and the differentiation rate dynamics are preserved. To test this hypothesis, we determined the change in progenitor number in chick. Photoconverting photoswitchable cyan fluorescent protein (PS-CFP) in a stripe of cells in the neural tube of transfected embryos indicated a homogenous anterioposterior growth rate across domains (fig. S5). The proliferation rate, measured from the mitotic index (Fig. 4H, fig. S2, F and G, and fig. S6) and IdU/BrdU incorporation (fig. S2, D and E), was spatially uniform, except in the floorplate (fig. S2G), and consistent with previous studies (*24*, *25*). At later stages, the proliferation rate in chick was lower than in mouse (Fig. 4H), in agreement with the smaller size of the chick neural tube (fig. S1, D to F). The differentiation rate was cell-type–dependent, highest in the pMN domain, and undergoing similar temporal changes to mouse (Fig. 4I). Finally, comparing $\lambda(t) - \gamma(t)$ to $\dot{P}/P$ (fig. S7) supported the idea that pattern formation in the chick neural tube proceeds in a similar biphasic way as mouse. The similarity in the differentiation dynamics in chick and mouse explains the overall similarity in pattern proportions.

The two-phase model was also consistent with the proportion dynamics observed in *Minute* mouse embryos. In these embryos, the proliferation rate was unaffected (Fig. 4J) (*26*), whereas the fraction of apoptotic cells was higher, particularly at later stages, explaining the smaller progenitor number compared with controls (Fig. 4L). The pMN differentiation rate in Rpl24(Bst)/+ embryos was consistent with the observed changes in proportions (Fig. 4K). Together, these data indicate that pattern formation in the Rpl24(Bst)/+ embryos is consistent with the two-phase model and that the preserved differentiation rate dynamics can account for the reproducible pattern of these mice relative to control.

Experimental validation of the two-phase model

The two-phase model for neural tube patterning makes several predictions. First, the rate of respecification of progenitor identity should decrease significantly at late developmental stages. To test this prediction, we measured the rate of Olig2 identity switching at different stages using a tamoxifen-inducible Olig2^{KICreER} line (*27*) (Fig. 5, A to C). As predicted, the rate of Olig2 identity change decreases from 0.034 per hour^{-1} to 0.004 hour^{-1} the later the Cre activity was induced (Fig. 5C) (ANOVA, $P < 0.05$). Although this decrease occurs in parallel with the increase of G1 phase length (Fig. 3D), analysis of the cell cycle phase distribution in cells undergoing a Olig2-Nkx2.2 switch, marked by the coexpression of

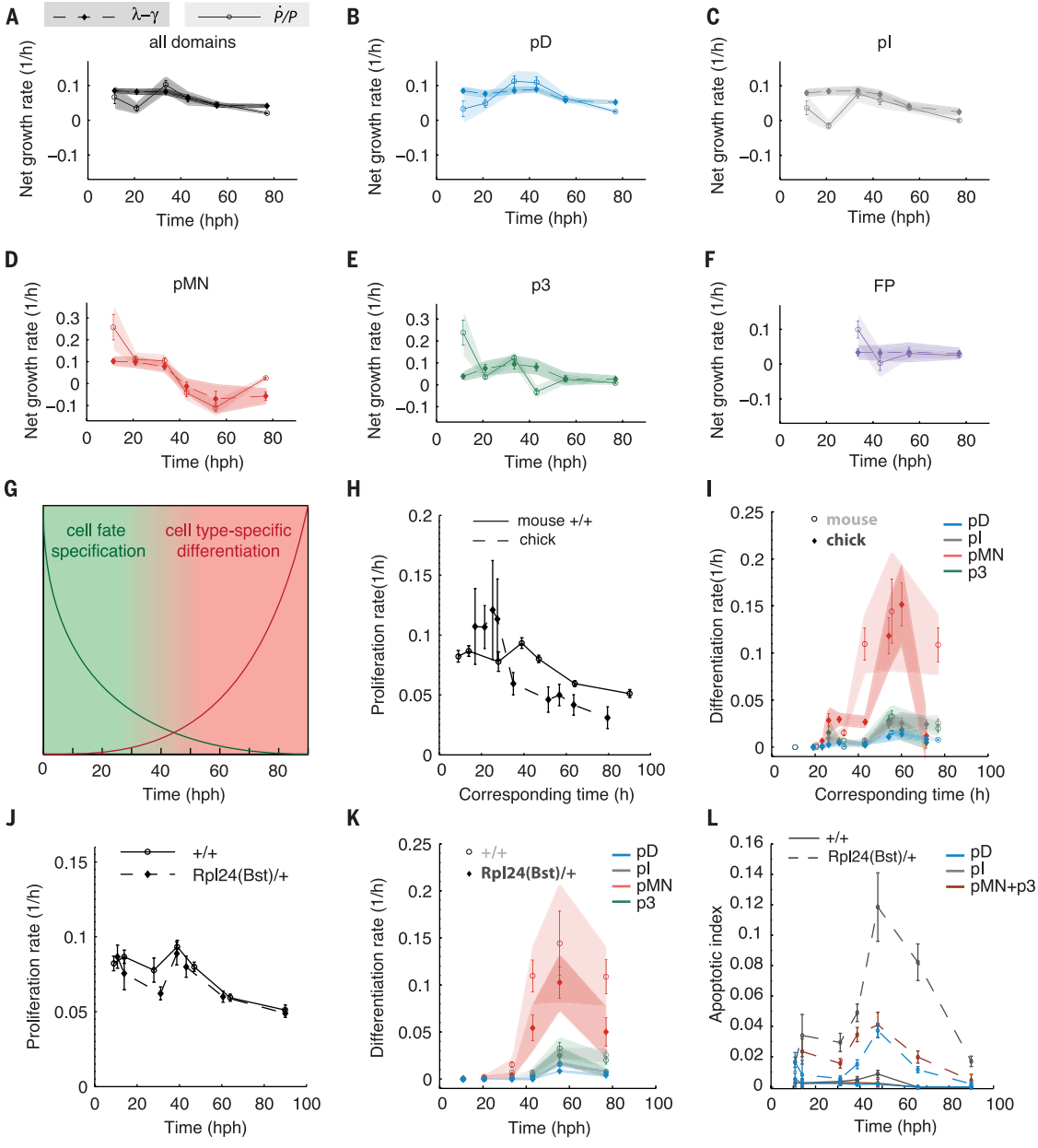

Fig. 4. Growth accounts for changes in pattern at later times. (**A** to **F**) Relative temporal increase in progenitor number in all dimensions ($\dot{P}/P$, solid lines) compared to the net growth rate [$\lambda(t) - \gamma(t)$, dashed lines] for each domain. (**G**) Two-phase model of neural tube development. (**H** and **I**) Comparison of mouse (circles) to chick (diamonds) mean proliferation rate (H) and differentiation rate (I). (**J** to **L**) Comparison of the mean proliferation rate (J), differentiation rate (K), and fraction of Caspase3^{+} progenitors (L) between wild-type mouse (solid lines) and Rpl24^{Bst}/+ embryos (dashed lines). [(A) to (L)] Shaded areas, 95% CIs. Error bars, mean ± SEM. For sample sizes, see table S2.

both genes, suggests that respecification can occur at any time of the cell cycle (Fig. 5D and fig. S3C).

The decrease in Olig2 respecification rate, despite the continuing changes in Gli activity, raises the possibility that progenitors become less sensitive to Shh signaling. To investigate this, we reduced Shh signaling using moderate concentrations of the inhibitor cyclopamine at different stages of development in cultured mouse embryos (Fig. 5, E to K). The domain boundary positions had little sensitivity to 5 μM of cyclopamine at E9.5 of development, but shifted significantly at earlier stages (Fig. 5K). Moreover, the time at which gene expression becomes robust to experimental inhibition of Shh signaling coincided with the time at which Olig2 identity changes decreased (Fig. 5C) and the transition between the two phases of development (Fig. 4G).

Examination of the dynamics of Gli activity indicated that the transition between the two phases of pattern formation occurred when Gli activity levels were close to maximal (Fig. 5L and fig. S8) (*11*). The BMP signaling levels measured by immunostaining for phosphorylated Smad1/5/8 showed similar temporal dynamics (Fig. 5M and fig. S8). These measurements revealed that the maximum ranges and greatest overlap between the two gradients were before 30 hph (Fig. 5N). Thus, progenitors are exposed to the highest levels of BMP and Shh signaling before 30 hph. This suggests that the subsequent decrease in BMP and Shh activity permits the stabilization of lineages, in part through the action of the transcriptional network in progenitors (*11*), and allows for growth-dependent, rather than morphogen-dependent, regulation of progenitor domain proportions.

To investigate direcly whether the differentiation rate affects domain proportions, we reasoned that if the spatial differences in the differentiation rate were removed, the pMN domain, which normally differentiates at a higher rate than other domains, would increase in relative size. We imposed approximately uniform differentiation rates in chick using in ovo electroporation in two ways: (i) increasing differentiation in all domains by overexpressing Ngn2 or p21 (Fig. 6, A and B, and fig. S9, A and B) (*28*, *29*); and (ii) inhibiting differentiation in all domains by overexpressing YAP (Yes-associated protein), an effector of Hippo signaling (Fig. 6, C and D), or the Notch intracellular domain (fig. S9, C and D) (*30*, *31*). These perturbations have an established effect on neuronal differentiation (*28*–*31*) and caused a decrease in progenitor number in the first case and an increase in the second, without a

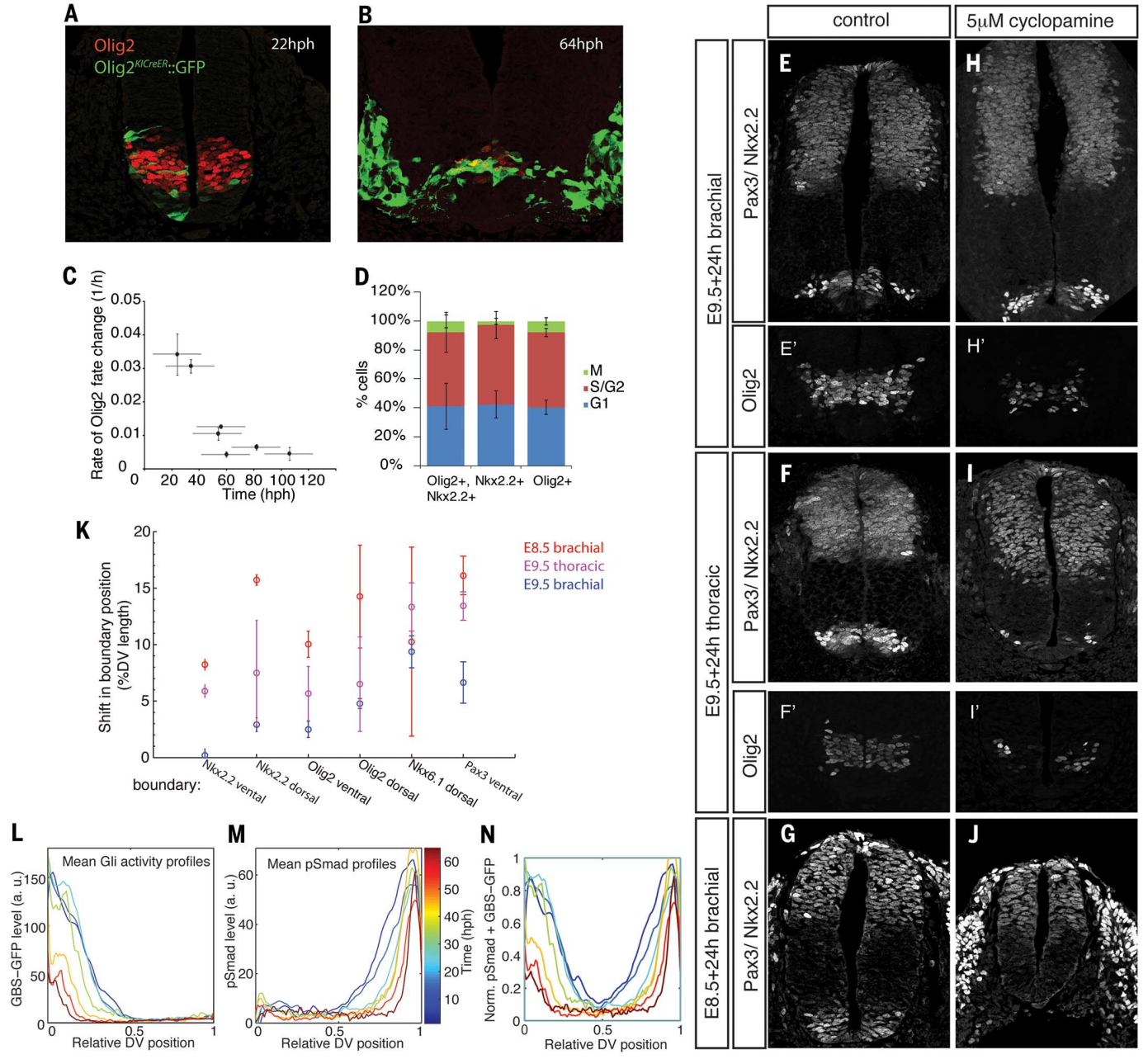

Fig. 5. Validation of the two-phase model. (**A** and **B**) Olig2^{KICreER}-induced EGFP expression (green) from the indicated times. Olig2 immunostaining, red. (**C**) Quantification of rate of loss of Olig2 identity. Period of Olig2^{KICreER} activity, horizontal gray bars. (**D**) Distribution of cell cycle phases (based on S/G2/M-Fucci expression) in progenitors expressing Olig2, Nkx2.2, or both (Fig. 3E). (**E** to **J**) Mouse embryo culture at the indicated stages without [(E) to (G)] or with [(H) to (J)] 5 μM cyclopamine. Sections in (H) and (I) are from the same embryos as (E) and (F), respectively. (**K**) Quantification of the experimental conditions in (E) to (J). The difference in mean boundary position between control and cyclopamine treatment was significant (Student's *t* test, $P < 0.05$) for all boundaries at E8.5 and 3/6 at E9.5-brachial. The different boundaries were measured in independent experiments. Cyclopamine concentration for Nkx6.1 boundary in E8.5 is 3 μM. (**L** and **M**) pSmad and GBS-GFP mean fluorescence intensity versus relative distance from the ventral midline at different stages. (**N**) Profiles in (L) and (M) were normalized to the maximum intensity in each time series and summed to give combined pSmad and GBS-GFP activity. Error bars, mean ± SEM. For sample sizes, see table S2.

significant change in the mitotic index (Fig. 6, A and C, and fig. S9E). In the case of Ngn2 overexpression, the differentiation rate of nonelectroporated cells (fig. S9, F and G) was also affected and became spatially uniform, suggesting that nonautonomous mechanisms—e.g., feedback from postmitotic cells—are involved in differentiation control (*32*). Importantly, in all conditions the relative size of the pMN domain became larger on the electroporated compared to the contralateral side (Fig. 6, B and D) and was similar to the larger pMN relative size at the onset of the experiment (~30 hours) (Fig. 2G). Because these perturbations cause opposite effects on the overall tissue size, this result cannot be explained by changes in the relative range of the signaling gradients and respecification.

Discussion

Here, we show that progenitor domain proportions in the neural tube continuously change through a

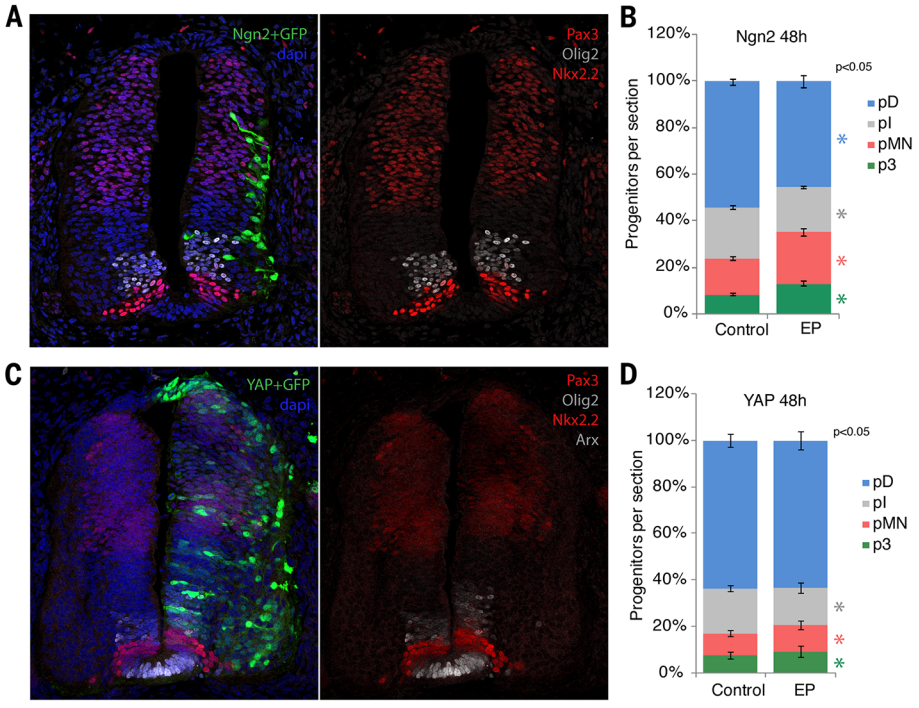

Fig. 6. Perturbing differentiation changes the relative pMN size. (**A**) Chick electroporation at HH14 of Ngn2+GFP assessed after 48 hours. (**B**) Number of $Sox2^{+}$ progenitors per hemisection on the control versus Ngn2 electroporated side for 13 sections (five embryos) as described in (A). (**C**) Electroporation of constitutive YAP+GFP, as in (A). Progenitors expand both dorsoventrally and apicobasally on the electroporated side. (**D**) Quantification of (C) for 12 sections (six embryos). Error bars, mean ± SEM.

conserved sequence that is independent of animal size. Pattern is first established by morphogen-driven cell fate specification and then elaborated by cell-type–specific regulation of differentiation rates.

How the spatiotemporal changes in the differentiation rate are regulated is a key question. The length of G1, Notch signaling, and proneural genes (e.g., Ascl1 and Ngn1/2), which are activated downstream of domain identity regulators such as Olig2, could play a role (*28*, *33*–*38*). The comparison of mouse to chick and *Minute* embryos suggests that the temporal changes in the differentiation rate are conserved and independent of embryo size, thus ensuring that domain proportions are comparable between individuals. This constrains the possible molecular mechanisms controlling the differentiation rate and implies that feedback regulation might ensure its robustness (*32*). The nonautonomous effect after Ngn2 electroporation suggests a possible role for postmitotic neurons in regulating the differentiation rate of progenitors, although other mechanisms cannot be excluded.

The transition from specification to differentiation phase correlates with the dynamics of Shh and BMP signaling. These dynamics depend on transduction cascades but are also likely to be constrained by the effective ligand diffusion, degradation, and the size of the morphogen source (*39*). Despite the decrease in Shh and BMP signaling, progenitor pattern is maintained during the differentiation phase. This could be explained by bistability produced by the transcriptional network (*11*). In the floorplate, a transcriptional network downstream of Fgf signaling contributes to these cells becoming refractory to Shh and BMP before E9.5 (*40*, *41*). Our data suggests that neural progenitors in the other domains tolerate a decrease in Gli and pSmad activity, although some level of Shh signaling is clearly required during the differentiation phase (*23*, *42*).

During the specification phase, chick, mouse, and *Minute* embryos are of similar initial size. This might result from the early period of regulative growth apparent from surgically manipulated embryos (*43*, *44*). Thus, the timing of the transition from specification to differentiation could be connected to an optimal tissue size for the formation and activity of morphogen gradients. Further quantitative analysis will be needed to understand both morphogen-dependent and -independent scaling mechanisms in other tissues and species.

Materials and methods

Mouse strains

To generate $Sox1^{CreER}$, the Sox1 reading frame was replaced with CreERT2 (fig. S4A). The following strains were previously described: Tg(GBS-GFP) (Gli binding sites–green fluorescent protein) (*11*), $Olig2^{KICreER}$ (*27*), CAG-CAT-EGFP (*45*), Fucci-S/G2/M #504 (*46*), and Rpl24(Bst) (*15*, *47*). Strains were maintained on a Parkes background to maximize litter size.

Embryo staging

Embryos were staged according to the number of somites, where one somite is generated every 2 hours in mouse and 1.5 hours in chick (*48*). Hamburger and Hamilton staging criteria were used for late stages of chick development (*49*). The chick data set was registered to mouse, so that the brachial-level somite at which the measurements were made was generated at equivalent corresponding time (table S1).

For GBS-GFP and pSmad measurements, embryos were initially staged by somite number. The dorsoventral lengths of the neural tubes were fitted to DVlength = ae^{bt}, where a and b are fit parameters, t is time (fig. S8F), and then restaged based on the fit.

Immunohistochemistry and imaging

Transverse sections were processed as described (*11*). Idu/BrdU antigens were exposed by 40-min deoxyribonuclease I treatment at 37°C, except mouse E8.5, where 2N HCl was used.

Flat-mount preparation: the neural tube was cut at the roofplate and then fixed in 4% paraformaldehyde and subsequently methanol. Antibody incubations and washes were 24 hours each. The left/right neural-tube halves were split, then mounted with grease spacers between slide and coverslip.

Sections were imaged with 40x/1.25NAOil objective, flat mounts with 20x/0.7NADry on a Leica TCS-SP5-MP. Single optical sections were taken, except for GBS-GFP and pSmad analysis, where a maximum projection of 3 z slices 1 μm apart were used. For flat mounts, the entire apicobasal depth of the progenitor layer was imaged with z slices 1.5 μm apart.

Antibodies used were goat anti-Sox2 (R&D systems, 1:100), rat anti-pH3 (Novus Biologicals, 1:2000), rabbit anti-Olig2 (Millipore, 1:1000), rabbit anti-Arx (*50*) (from J. Chelly, 1:1000), mouse anti-Pax3(c) (Developmental Studies Hybridoma Bank, 1:100), rabbit anti-Islet1 (*51*) (from T. Jessell, 1:3000), sheep anti-GFP (Biogenesis, 1:1000), mouse anti-Nkx2.2 (DSHB, 1:25), rabbit anti-mAzami Green (MBL, 1:100), rabbit anti-cleaved Caspase3 (Cell Signaling, 1:500); rabbit anti-pSmad1/5/8 (from E. Laufer), mouse anti-BrdU/IdU (1:80, BD clone B44), rat anti-BrdU (1:80, Abcam, clone BU1/75).

Chick electroporation

Chick electroporation was performed in ovo at HH14 and analyzed 48 hours later. Plasmids used: pMIW-YAP (from Xinwei Cao), pCAGGS-NICD (from Olivier Pourquie), pCAGGS-p21 (from Cheryll Tickle), pCAGGS-Ngn2-IRES-GFP (from Francois Guillemot), pPS-CFP2-N (Evrogen), and pCI-H2B-EGFP (from Tatjana Sauka-Spengler). The first three were coelectroporated with pCAGGS-NLS-GFP to mark transfected cells. Final concentrations were 0.5 μg/μl for pMIW-YAP and pPS-CFP2-N, and 1 μg/μl for all other plasmids.

Mouse embryo culture

Mouse embryo culture was performed as previously described (*11*).

IdU/BrdU incorporation

Chick: 0.5 mg/ml IdU or 3.3 mg/ml BrdU (Sigma) in PB, 10% sucrose, 0.5% Fast Green, were injected into the neural tube, and 50 μl was added on top of the embryo. Embryos were treated with IdU for 1.5 hours, then BrdU for 50 min.

Mouse: Pregnant mice were intraperitoneally injected with 0.6 mg IdU and after 1.5 hours with 1 mg BrdU. Embryos were harvested after 30 min.

Chick live imaging

Membrane-anchored GFP transgenic chicken eggs were obtained from the Roslin Institute, Edinburgh. Embryos were electroporated with pCI-H2B-EGFP 8-15h before imaging.

For live imaging, we established a sagittal slice culture protocol, based on a "clot" method (*52*, *53*). The brachial and anterior thoracic region was dissected in L15 medium, then transferred to a glass-bottom dish (MatTek) in a small drop of culture medium [DMEM-F12 1:1, supplemented with N2, B27 (Life Technologies)] containing 10 mg/ml fibrinogen (Calbiochem). Thrombin (0.5U/μl, Amersham) was added, and a fibrin gel was allowed to form for a few minutes. The slice was covered with ~0.5 ml culture medium, and the dish was humidified. *Z* stacks were collected for 3 hours on an inverted Leica-SP5 confocal at 37°C.

Photoconversion in chick embryos

Stage HH16 chick embryos electroporated with pPS-CFP2-N were cultured using the EC (early chick) culture method (*54*), dorsal side up, and immediately photoconverted along the entire dorsoventral length using Leica MP-SP5 microscope, 10X/0.7NADry lens, 30% laser (405 nm) power, ~25 s scan time. Either 15 hours or 0 hours after photoconversion, the neural tube was flat-mounted in phosphate-buffered saline and immediately imaged.

DV boundary positions and pSmad and Gli activity profiles

Image analysis was performed in Fiji (http://fiji.sc/Fiji) and data analysis in MATLAB (Mathworks, MA, USA).

The mean fluorescence intensity in immunostained sections was quantified across a 10-μm region adjacent to the apical lumen. The data was background-subtracted and smoothed with a 5-μm moving average. Boundaries were defined as the positions where the intensity increased above 10% of maximum.

pSmad and GBS-GFP intensity profiles were normalized to the mean profile for each time point, similarly to a described procedure (*55*), by *normalized intensity* = $a \times$ (*raw intensity*), where a is a fit parameter. Profiles that correlated poorly with the mean ($R^2 < 0.5$) were discarded. These were usually sections damaged during dissection and represented <5% of the data.

Seven independent time courses of pSmad and GBS-GFP were collected. Sections in each time course were stained and imaged together to minimize technical variability. The seven data sets were pooled by normalizing to the median value of Φ for each data set, where Φ is the 90th percentile of the fluorescence intensity of each profile.

Progenitor and neuron numbers and differentiation rate

The number of progenitors per section was inferred from the Sox2$^+$ domain area (Fig. 1B) and the average density of Sox2$^+$ nuclei for each stage (fig. S1, A and B) determined from a subset of sections. The number of neurons was determined by counting Dapi$^+$,Sox2$^-$ nuclei. Islet1$^+$ and interspersed Islet1$^-$ nuclei [which are HB9/MNR2$^+$ (not shown)] in the ventral horn were considered MNs. The Pax3 boundary was used to separate ventral interneurons V2 - V0 and dorsal interneurons.

Neurons (N) are produced from progenitors (P) with a rate of differentiation γ, i.e., $dN/dt = \gamma P$. We obtained an estimate of γ using $\gamma = \frac{\Delta N}{P_i \Delta t}$, where Δt was the time interval between two time points, ΔN was the difference in neuron number between the end and the beginning of the time interval, and P_i was the progenitor number in the middle of the interval. The error of γ was calculated by propagation of the standard deviations of all participating variables, assuming that the errors are independent and uncorrelated. The 95% CIs, calculated from the mean, SD, sample size, and Student's t value, were linearly interpolated between time points.

Proliferation rate by IdU/BrdU incorporation

Three cell populations were distinguished by anti-IdU/BrdU, anti-BrdU, and anti-Sox2 immunostaining: (i) Sox2$^+$, IdU$^+$, and BrdU$^-$ (denoted IduL) are progenitors labeled by IdU during the 1.5-hour pulse, which have exited S phase before BrdU addition; (ii) Sox2$^+$, IdU$^+$, and BrdU$^+$; (iii) Sox2$^+$, Idu$^-$, and BrdU$^-$.

The IdU labeling index IduLI is defined as the ratio of IduL over the total number of Sox2$^+$ progenitors. It is related to the pulse duration $\theta(IduL) = 1.5$ hours and the total cell cycle length $\theta(tot)$as:

$$IduLI = \frac{IduL}{\text{all Sox2}^+ \text{ cells}} = \frac{\theta(IduL)}{\theta(tot)} \ln 2 \quad (3)$$

In turn, the proliferation rate λ is related to $\theta(tot)$and IduLI as:

$$\lambda = \frac{ln2}{\theta(tot)} = \frac{IduLI}{\theta(IduL)} \quad (4)$$

Two assumptions are made: (i) cells divide asynchronously and (ii) the length of the pulse is shorter than the G2 phase. This is supported by the random appearance of mitotic figures in flat mounts and by the observation that no IduL cells were found in telophase, indicating that they are not completing mitosis within the experiment.

Mitotic index

The relationship between the duration of mitosis, the total cell cycle length, and the fraction of cells in mitosis depends on the exact growth characteristics of the tissue (*56*). The MI for an exponentially growing tissue is defined as

$$MI = \frac{\text{pH3}^+ \text{ progenitors}}{\text{all Sox2}^+ \text{ progenitors}} = \frac{\theta(pH3)}{\theta(tot)} \ln 2 \quad (5)$$

where $\theta(pH3)$ is the duration of the pH3-positive phase of mitosis and $\theta(tot)$ is the cell cycle length. The proliferation rate λ is related to $\theta(tot)$ and MI by:

$$\lambda = \frac{\ln 2}{\theta(tot)} = \frac{MI}{\theta(pH3)} \quad (6)$$

Thus, to calculate λ, it is enough to know MI and the duration of mitosis. MI was directly measured from sections. To determine the duration of mitosis, we used the fact that λ is related to both MI (Eq. 6) and IduLI (Eq. 4). Hence,

$$\theta(pH3) = \theta(IduL)\frac{MI}{IduL} \quad (7)$$

The average values of MI and IduLI from all stages that were identical between the two types of experiments were used for calculating $\theta(pH3)$. The resulting mitosis duration is 24.6 ± 7.0 min for chick and 27.7 ± 11.3 min for mouse. These are similar to published values (*24*, *25*).

MI in flat mounts (fig. S2, C and F) was estimated from the number of pH3$^+$ cells per apical area, normalized to the average apicobasal length for the respective stage and domain measured in sections (Fig. 1F and fig. S1C).

Cell cycle phase distribution

Mitotic cells were identified using Dapi S+G2 cells using the Fucci-S/G2/M-Green fluorescence intensity. The fluorescence intensities of Olig2, Nkx2.2, and Fucci-S/G2/M-Green were measured in individual nuclei. The Olig2 and Nkx2.2 levels were background-subtracted and normalized to the average intensity in the respective domain. Cells with Olig2/Nkx2.2 ratio between 0.1 and 10 were defined as coexpressing.

Coexpressing cells are assumed to undergo a transition from an Olig2 to an Nkx2.2 stable state or, with a smaller probability, vice versa (*11*). If the transition occurs preferentially in G1 or S+G2 phase, the cell cycle phase distribution in cells that are at the onset of the transition could appear different than in noncoexpressing populations. However, the distribution of both G1 and S+G2 phases across the Olig2-Nkx2.2 level difference was normal (fig. S3C), suggesting that the transition may occur at any time of the cell cycle.

Olig2 lineage tracing

Olig2^{KICreER} mice (*27*) were crossed to CAG-CAT-EGFP (*45*). Cre expression was induced in Olig2$^+$ progenitors by injecting 3 mg of tamoxifen. As a result of the recombination, EGFP was induced with a delay of 12 hours (fig. S10), allowing the tracking of cells after they lose Olig2 expression. Embryos were harvested 48 hours after injection; hence, the effective time interval of EGFP labeling was ~36 hours.

The change in the number of labeled progenitors P, regardless of their type, during the time course of the experiment $\Delta t = t_2 - t_1$ (t_1, time at the beginning; t_2, end time) is

$$\frac{P(t_2) - P(t_1)}{\Delta t} = \lambda P(t_1) - \frac{\Delta N}{\Delta t} \quad (8)$$

Here, $P(t_2)$ are all labeled progenitors at t_2 and ΔN are all labeled neurons. Δt = 36 hours, and

the proliferation rate, λ, are known (the values in Fig. 3A were used); hence, the only unknown is $P(t_1)$. Activation at t_1 occurs only in Olig2$^+$ cells; therefore, $P(t_1) = P_{Olig2}(t_1)$. Hence, the change in the Olig2$^+$ progenitors alone is

$$\frac{P_{Olig2}(t_2) - P_{Olig2}(t_1)}{\Delta t} = \lambda P_{Olig2}(t_1) - \frac{\Delta MN}{\Delta t} - \psi P_{Olig2}(t_1) \quad (9)$$

where $P_{Olig2}(t_2)$ are the labeled Olig2 progenitors at t_2, ΔMN the number of labeled motor neurons, and ψ, which remains the only unknown, is the rate of loss of Olig2 identity at the expense of other progenitor types. Because Δt is large, the reported values of ψ (Fig. 5C) are approximate.

Clonal analysis

Sox1^{CreER}/+ mice were crossed to Gt(Rosa)26-FloxSTOP-Flox-EYFP homozygotes. Pregnant mice were intraperitoneally injected with 0.3 mg tamoxifen at E9.5 and sacrificed 48 hours later. The labeled cells formed clusters that were usually >10 cell diameters away from each other, whereas within a cluster, cells were rarely separated by more than 3 unlabeled cells. Therefore, labeled cells were grouped into clones by scanning a 29-μm radius (≈6 cell diameters) around each cell. For most images, changing the radius by ±5 μm preserved clone grouping. Occasional too densely labeled images were discarded.

Clone shape descriptors (table S2) were derived from the second moment matrix of the cell coordinates of each clone, in which the unit eigenvectors represent two orthogonal axes, and the eigenvalues the variance along these axes. The first eigenvector represents the orientation of the clone with respect to the anterioposterior axis. The anterioposterior and dorsoventral spread of a clone were defined as the distance within ±2 SD from its center of mass.

The distribution of clone orientation angles was determined using a kernel density estimation method and was different in the pMN domain compared with pD, pI, and p3 (two-sample Kolmogorov-Smirnov test, $P < 0.05$).

The density of clonal nuclei (estimated by fitting an ellipse around large clones) corresponded to 19 ± 14 μm^2 per cell. The density of nonclonal nuclei, determined in the Pax3 domain in small volumes (~120 cells) was 2.7 ± 0.1 μm^2 per cell, suggesting that clonal nuclei are ~7 times more dispersed than nonclonal nuclei.

REFERENCES AND NOTES

1. A. Kicheva, M. Cohen, J. Briscoe, Developmental pattern formation: Insights from physics and biology. *Science* **338**, 210–212 (2012). doi: 10.1126/science.1225182; pmid: 23066071
2. E. H. Davidson, Emerging properties of animal gene regulatory networks. *Nature* **468**, 911–920 (2010). doi: 10.1038/nature09645; pmid: 21164479
3. J. Jaeger, D. Irons, N. Monk, Regulative feedback in pattern formation: Towards a general relativistic theory of positional information. *Development* **135**, 3175–3183 (2008). doi: 10.1242/dev.018697; pmid: 18776142
4. F. Hamaratoglu, A. M. de Lachapelle, G. Pyrowolakis, S. Bergmann, M. Affolter, Dpp signaling activity requires Pentagone to scale with tissue size in the growing *Drosophila* wing imaginal disc. *PLOS Biol.* **9**, e1001182 (2011). doi: 10.1371/journal.pbio.1001182; pmid: 22039350
5. T. Gregor, W. Bialek, R. R. de Ruyter van Steveninck, D. W. Tank, E. F. Wieschaus, Diffusion and scaling during early embryonic pattern formation. *Proc. Natl. Acad. Sci. U.S.A.* **102**, 18403–18407 (2005). doi: 10.1073/pnas.0509483102; pmid: 16352710
6. D. Cheung, C. Miles, M. Kreitman, J. Ma, Adaptation of the length scale and amplitude of the Bicoid gradient profile to achieve robust patterning in abnormally large *Drosophila melanogaster* embryos. *Development* **141**, 124–135 (2014). doi: 10.1242/dev.098640; pmid: 24284208
7. H. Inomata, T. Shibata, T. Haraguchi, Y. Sasai, Scaling of dorsal-ventral patterning by embryo size-dependent degradation of Spemann's organizer signals. *Cell* **153**, 1296–1311 (2013). doi: 10.1016/j.cell.2013.05.004; pmid: 23746842
8. D. Ben-Zvi, B. Z. Shilo, A. Fainsod, N. Barkai, Scaling of the BMP activation gradient in Xenopus embryos. *Nature* **453**, 1205–1211 (2008). doi: 10.1038/nature07059; pmid: 18580943
9. W. A. Alaynick, T. M. Jessell, S. L. Pfaff, SnapShot: Spinal cord development. *Cell* **146**, 178–178.e1 (2011). doi: 10.1016/j.cell.2011.06.038; pmid: 21729788
10. E. Dessaud *et al*., Interpretation of the sonic hedgehog morphogen gradient by a temporal adaptation mechanism. *Nature* **450**, 717–720 (2007). doi: 10.1038/nature06347; pmid: 18046410
11. N. Balaskas *et al*., Gene regulatory logic for reading the Sonic Hedgehog signaling gradient in the vertebrate neural tube. *Cell* **148**, 273–284 (2012). doi: 10.1016/j.cell.2011.10.047; pmid: 22265416
12. R. M. Das, K. G. Storey, Apical abscission alters cell polarity and dismantles the primary cilium during neurogenesis. *Science* **343**, 200–204 (2014). doi: 10.1126/science.1247521; pmid: 24408437
13. B. Deneen *et al*., The transcription factor NFIA controls the onset of gliogenesis in the developing spinal cord. *Neuron* **52**, 953–968 (2006). doi: 10.1016/j.neuron.2006.11.019; pmid: 17178400
14. J. Jeong, A. P. McMahon, Growth and pattern of the mammalian neural tube are governed by partially overlapping feedback activities of the hedgehog antagonists patched 1 and Hhip1. *Development* **132**, 143–154 (2005). doi: 10.1242/dev.01566; pmid: 15576403
15. E. R. Oliver, T. L. Saunders, S. A. Tarlé, T. Glaser, Ribosomal protein L24 defect in belly spot and tail (*Bst*), a mouse *Minute*. *Development* **131**, 3907–3920 (2004). doi: 10.1242/dev.01268; pmid: 15289434
16. B. Martynoga, H. Morrison, D. J. Price, J. O. Mason, Foxg1 is required for specification of ventral telencephalon and region-specific regulation of dorsal telencephalic precursor proliferation and apoptosis. *Dev. Biol.* **283**, 113–127 (2005). doi: 10.1016/j.ydbio.2005.04.005; pmid: 15893304
17. B. Boehm *et al*., The role of spatially controlled cell proliferation in limb bud morphogenesis. *PLOS Biol.* **8**, e1000420 (2010). doi: 10.1371/journal.pbio.1000420; pmid: 20644711
18. T. Reis, B. A. Edgar, Negative regulation of dE2F1 by cyclin-dependent kinases controls cell cycle timing. *Cell* **117**, 253–264 (2004). doi: 10.1016/S0092-8674(04)00247-8; pmid: 15084262
19. Y. Yamaguchi *et al*., Live imaging of apoptosis in a novel transgenic mouse highlights its role in neural tube closure. *J. Cell Biol.* **195**, 1047–1060 (2011). doi: 10.1083/jcb.201104057; pmid: 22162136
20. S. M. Leber, J. R. Sanes, Migratory paths of neurons and glia in the embryonic chick spinal cord. *J. Neurosci.* **15**, 1236–1248 (1995).pmid: 7869095
21. L. Erskine, K. Patel, J. D. W. Clarke, Progenitor dispersal and the origin of early neuronal phenotypes in the chick embryo spinal cord. *Dev. Biol.* **199**, 26–41 (1998). doi: 10.1006/dbio.1998.8912; pmid: 9676190
22. E. Theveneau, R. Mayor, Neural crest delamination and migration: From epithelium-to-mesenchyme transition to collective cell migration. *Dev. Biol.* **366**, 34–54 (2012). doi: 10.1016/j.ydbio.2011.12.041; pmid: 22261150
23. E. Dessaud *et al*., Dynamic assignment and maintenance of positional identity in the ventral neural tube by the morphogen sonic hedgehog. *PLOS Biol.* **8**, e1000382 (2010). doi: 10.1371/journal.pbio.1000382; pmid: 20532235
24. S. G. Megason, A. P. McMahon, A mitogen gradient of dorsal midline Wnts organizes growth in the CNS. *Development* **129**, 2087–2098 (2002). pmid: 11959819
25. A. C. Wilcock, J. R. Swedlow, K. G. Storey, Mitotic spindle orientation distinguishes stem cell and terminal modes of neuron production in the early spinal cord. *Development* **134**, 1943–1954 (2007). doi: 10.1242/dev.002519; pmid: 17470968
26. M. Barkić *et al*., The p53 tumor suppressor causes congenital malformations in Rpl24-deficient mice and promotes their survival. *Mol. Cell. Biol.* **29**, 2489–2504 (2009). doi: 10.1128/MCB.01588-08; pmid: 19273598
27. H. Takebayashi *et al*., The basic helix-loop-helix factor olig2 is essential for the development of motoneuron and oligodendrocyte lineages. *Curr. Biol.* **12**, 1157–1163 (2002). doi: 10.1016/S0960-9822(02)00926-0; pmid: 12121626
28. B. G. Novitch, A. I. Chen, T. M. Jessell, Coordinate regulation of motor neuron subtype identity and pan-neuronal properties by the bHLH repressor Olig2. *Neuron* **31**, 773–789 (2001). doi: 10.1016/S0896-6273(01)00407-X; pmid: 11567616
29. J. A. Erhardt, R. N. Pittman, Ectopic p21(WAF1) expression induces differentiation-specific cell cycle changes in PC12 cells characteristic of nerve growth factor treatment. *J. Biol. Chem.* **273**, 23517–23523 (1998). doi: 10.1074/jbc.273.36.23517; pmid: 9722590
30. X. Cao, S. L. Pfaff, F. H. Gage, YAP regulates neural progenitor cell number via the TEA domain transcription factor. *Genes Dev.* **22**, 3320–3334 (2008). doi: 10.1101/gad.1726608; pmid: 19015275
31. P. Huang, F. Xiong, S. G. Megason, A. F. Schier, Attenuation of Notch and Hedgehog signaling is required for fate specification in the spinal cord. *PLOS Genet.* **8**, e1002762 (2012). doi: 10.1371/journal.pgen.1002762; pmid: 22685423
32. A. D. Lander, K. K. Gokoffski, F. Y. M. Wan, Q. Nie, A. L. Calof, Cell lineages and the logic of proliferative control. *PLOS Biol.* **7**, e15 (2009). doi: 10.1371/journal.pbio.1000015; pmid: 19166268
33. B. Martynoga, D. Drechsel, F. Guillemot, Molecular control of neurogenesis: A view from the mammalian cerebral cortex. *Cold Spring Harb. Perspect. Biol.* **4**, a008359 (2012). pmid: 23028117
34. F. Calegari, W. B. Huttner, An inhibition of cyclin-dependent kinases that lengthens, but does not arrest, neuroepithelial cell cycle induces premature neurogenesis. *J. Cell Sci.* **116**, 4947–4955 (2003). doi: 10.1242/jcs.00825; pmid: 14625388
35. U. Marklund *et al*., Domain-specific control of neurogenesis achieved through patterned regulation of Notch ligand expression. *Development* **137**, 437–445 (2010). doi: 10.1242/dev.036806; pmid: 20081190
36. S.-K. Lee, B. Lee, E. C. Ruiz, S. L. Pfaff, Olig2 and Ngn2 function in opposition to modulate gene expression in motor neuron progenitor cells. *Genes Dev.* **19**, 282–294 (2005). doi: 10.1101/gad.1257105; pmid: 15655114
37. M. Saade *et al*., Sonic hedgehog signaling switches the mode of division in the developing nervous system. *Cell Reports* **4**, 492–503 (2013). doi: 10.1016/j.celrep.2013.06.038; pmid: 23891002
38. R. Kageyama, S. Nakanishi, Helix-loop-helix factors in growth and differentiation of the vertebrate nervous system. *Curr. Opin. Genet. Dev.* **7**, 659–665 (1997). doi: 10.1016/S0959-437X(97)80014-7; pmid: 9388783
39. O. Wartlick, A. Kicheva, M. González-Gaitán, Morphogen gradient formation. *Cold Spring Harb. Perspect. Biol.* **1**, a001255 (2009). pmid: 20066104
40. V. Ribes *et al*., Distinct Sonic Hedgehog signaling dynamics specify floor plate and ventral neuronal progenitors in the vertebrate neural tube. *Genes Dev.* **24**, 1186–1200 (2010). doi: 10.1101/gad.559910; pmid: 20516201
41. N. Sasai, E. Kutejova, J. Briscoe, Integration of signals along orthogonal axes of the vertebrate neural tube controls progenitor competence and increases cell diversity. *PLOS Biol.* **12**, e1001907 (2014). doi: 10.1371/journal.pbio.1001907; pmid: 25026549
42. J. Ericson, S. Morton, A. Kawakami, H. Roelink, T. M. Jessell, Two critical periods of Sonic Hedgehog signaling required for the specification of motor neuron identity. *Cell* **87**, 661–673 (1996). doi: 10.1016/S0092-8674(00)81386-0; pmid: 8929535
43. N. E. Lewis, J. Rossant, Mechanism of size regulation in mouse embryo aggregates. *J. Embryol. Exp. Morphol.* **72**, 169–181 (1982). pmid: 7183736
44. G. F. Rands, Size regulation in the mouse embryo. II. The development of half embryos. *J. Embryol. Exp. Morphol.* **98**, 209–217 (1986). pmid: 3655648

45. T. Nakamura, M. C. Colbert, J. Robbins, Neural crest cells retain multipotential characteristics in the developing valves and label the cardiac conduction system. *Circ. Res.* **98**, 1547–1554 (2006). doi: 10.1161/01.RES.0000227505.19472.69; pmid: 16709902
46. A. Sakaue-Sawano *et al*., Visualizing spatiotemporal dynamics of multicellular cell-cycle progression. *Cell* **132**, 487–498 (2008). doi: 10.1016/j.cell.2007.12.033; pmid: 18267078
47. J. Southard, E. Eicher, Belly spot and tail (Bst). *Mouse News Lett.* **56**, 40 (1977).
48. C. Gomez *et al*., Control of segment number in vertebrate embryos. *Nature* **454**, 335–339 (2008). doi: 10.1038/nature07020; pmid: 18563087
49. V. Hamburger, H. L. Hamilton, A series of normal stages in the development of the chick embryo. *J. Morphol.* **88**, 49–92 (1951). doi: 10.1002/jmor.1050880104; pmid: 24539719
50. K. Poirier *et al*., Neuroanatomical distribution of ARX in brain and its localisation in GABAergic neurons. *Brain Res. Mol. Brain Res.* **122**, 35–46 (2004). doi: 10.1016/j.molbrainres.2003.11.021; pmid: 14992814
51. T. Tsuchida *et al*., Topographic organization of embryonic motor neurons defined by expression of LIM homeobox genes. *Cell* **79**, 957–970 (1994). doi: 10.1016/0092-8674(94)90027-2; pmid: 7528105
52. A. Forer, J. D. Pickett-Heaps, Cytochalasin D and latrunculin affect chromosome behaviour during meiosis in crane-fly spermatocytes. *Chromosome Res.* **6**, 533–550 (1998). doi: 10.1023/A:1009224322399; pmid: 9886773
53. J. Januschke, C. Gonzalez, The interphase microtubule aster is a determinant of asymmetric division orientation in *Drosophila* neuroblasts. *J. Cell Biol.* **188**, 693–706 (2010). doi: 10.1083/jcb.200905024; pmid: 20194641
54. S. C. Chapman, J. Collignon, G. C. Schoenwolf, A. Lumsden, Improved method for chick whole-embryo culture using a filter paper carrier. *Dev. Dyn.* **220**, 284–289 (2001). doi: 10.1002/1097-0177(20010301)220:3<284::AID-DVDY1102>3.0.CO;2-5; pmid: 11241836
55. T. Gregor, D. W. Tank, E. F. Wieschaus, W. Bialek, Probing the limits to positional information. *Cell* **130**, 153–164 (2007). doi: 10.1016/j.cell.2007.05.025; pmid: 17632062
56. C. L. Smith, P. P. Dendy, Relation between mitotic index, duration of mitosis, generation time and fraction of dividing cells in a cell population. *Nature* **193**, 555–556 (1962). doi: 10.1038/193555a0; pmid: 13914174

ACKNOWLEDGMENTS

We thank B. Simons, C. Tabin, A. Ugur, M. González-Gaitán, N. Bushati, and M. Cohen for comments on the manuscript; B. Simons and G. Zhang for discussions and help with the clonal analysis; R. Pérez and S. Loubéry for discussions; S. Booth, C. Scott, C. Galichet, S. Malas, K. L. Lee, and A. Ekonomou for generating the Sox1^{CreER} strain; X. Cao, T. Sauka-Spengler, E. Laufer, J. Chelly, T. Jessell, C. Tickle, O. Pourquie, and M. Götz for providing reagents; and N. Mousavy for technical assistance. This work was funded by the Medical Research Council (MRC) (U117560541) and the Wellcome Trust (WT098326MA). A.K. was supported by Federation of European Biochemical Societies, Marie-Curie, and MRC fellowships. The supplementary materials contain additional data. Author contributions: A.K. performed the experiments. A.K. and J.B. conceived the work, analyzed the data, and wrote the manuscript. T.B. analyzed the gradient dynamics and helped with the quantitative analysis. A.R. analyzed the patterning dynamics. H.P.V. participated in the photoactivation and live imaging. V.E. and R.L.-B. contributed the Sox1^{CreER} mouse.

SUPPLEMENTARY MATERIALS

www.sciencemag.org/content/345/6204/1254927/suppl/DC1
Supplementary Text
Figs. S1 to S10
Tables S1 to S3
Reference (*57*)

17 April 2014; accepted 28 July 2014
10.1126/science.1254927

REPORTS

JOVIAN ATMOSPHERE

Evidence for global electron transportation into the jovian inner magnetosphere

K. Yoshioka,[1]* G. Murakami,[1] A. Yamazaki,[1] F. Tsuchiya,[2] T. Kimura,[1] M. Kagitani,[2] T. Sakanoi,[2] K. Uemizu,[1,3] Y. Kasaba,[4] I. Yoshikawa,[5] M. Fujimoto[1,6]

Jupiter's magnetosphere is a strong particle accelerator that contains ultrarelativistic electrons in its inner part. They are thought to be accelerated by whistler-mode waves excited by anisotropic hot electrons (>10 kiloelectron volts) injected from the outer magnetosphere. However, electron transportation in the inner magnetosphere is not well understood. By analyzing the extreme ultraviolet line emission from the inner magnetosphere, we show evidence for global inward transport of flux tubes containing hot plasma. High-spectral-resolution scanning observations of the Io plasma torus in the inner magnetosphere enable us to generate radial profiles of the hot electron fraction. It gradually decreases with decreasing radial distance, despite the short collisional time scale that should thermalize them rapidly. This indicates a fast and continuous resupply of hot electrons responsible for exciting the whistler-mode waves.

The jovian inner magnetosphere (<10 jovian radii, R_J, from the planet center) contains ultrarelativistic electrons (~50 MeV), which have the highest energies found anywhere in the solar system (*1*). They are thought to be generated mainly through gyroresonance with whistler-mode waves (*2*). The waves are excited by hot electrons (>10 keV) injected from outside (from the middle magnetosphere, 10 to 30 R_J) that then become anisotropic as they enter a region with a stronger magnetic field. Therefore, the first step toward acceleration to ultrarelativistic energies is hot plasma transport into the inner magnetosphere.

The jovian middle magnetosphere contains abundant moderately energetic particles (>1 keV). Analyses of previous in situ measurements made from the Galileo spacecraft in the late 1990s indicate possible transient and/or partial injections from the middle to the inner magnetosphere (into $6R_J$) accompanied by whistler-mode waves (*3*–*7*). However, observations from a single point probe embedded in the large volume are inherently limited. This has been an obstacle to concluding that the plasma transportation into the inner magnetosphere is of a global and continuous nature.

The inner magnetosphere is filled with ionic sulfur and oxygen. This gas originates from the neutral sulfur dioxide ejected by volcanoes on Io, the innermost galilean satellite located at $5.9R_J$. A large part of the gas is dissociated and ionized by solar ultraviolet radiation, forming a torus-like structure along Io's orbit around the planet, called the Io plasma torus (IPT). Various emission lines from the ions in the extreme ultraviolet (EUV) wavelength range are excited by electron impact and are observable remotely. Therefore, EUV spectroscopy provides a diagnostic window into the jovian inner magnetosphere. Remote monitoring of the inner magnetosphere can be global and continuous when set up properly.

The intensity of each emission line generated by electron-impacted excitation contains information about the ion and electron densities and the temperature of the electrons. Using laboratory-determined atomic parameters, such as the collisional and spontaneous emission probabilities, we can model an IPT plasma that produces an EUV spectrum that best matches the observations. This method (sometimes called spectral diagnosis) has previously been applied to EUV spectra (*8*–*11*).

On 29 November 2013, the Earth-orbiting EUV spectroscope EXCEED (Extreme Ultraviolet Spectroscope for Exospheric Dynamics) onboard the Hisaki spacecraft (*12*, *13*) acquired EUV spectra of the IPT at high spatial and spectral resolution. The total integration time was 550 min, and there were no remarkable transient events noted in any of the bright emission lines throughout the entire observation period. The spectroscope slit was centered on the latitudinal center of the IPT, and both the dawn and dusk sides of torus were observed in each frame (Fig. 1). The spectral resolution as given by the FWHM (full width at half maximum) is ~0.3 nm, and each pixel spanned 4.2 arc sec. The EUV spectra obtained over the whole IPT (Fig. 2) enable us to derive not only the conventional parameters, such as the ion and electron densities and their temperatures, but also the density fraction of the hot electron component as a function of radial distance (from 5.9 to 7.6 R_J at both dawn and dusk).

In our analysis, the model spectrum depends on the following input parameters: electron column density, electron temperatures for both core and hot components, hot electron fraction, and the relative abundances of ions such as S^+, S^{2+}, S^{3+}, and O^+. The atomic parameters used by the model were derived from CHIANTI version 7.1 (*14*, *15*). Following the Voyager-based empirical model (*16*), we assume charge neutrality with the proton fraction being 10% of the electron fraction. We varied the fractions of S^+ and S^{3+} relative to that of S^{2+}. The fraction of O^+ relative to S^{2+} was fixed at 1.5 on the basis of previous studies using Cassini data (*17*). The spectral diagnostic of the oxygen ion line (83.4 nm) was discarded from this study because of possible contamination by geocoronal emissions, so this choice does not greatly affect our conclusions. The relative density of these ions would be constrained by ground-based observations in the visible wavelength range. The temperature of the hot electrons was also fixed at 46 eV, which satisfies the requirement to maintain the total output energy from the IPT (*18*). We chose the best plasma model via a χ^2 minimization (Fig. 2).

We derived plasma parameters as a function of radius with the best-fit model (Fig. 3). We assumed that the density distribution is concentric about the IPT and performed an "onion-peeling analysis" using the column densities of Fig. 3A. This yielded a value for the local electron density of ~1500 cm^{-3} at Io's orbit, which is consistent with the in situ measurement of Voyager 1 (*16*, *19*). Although the core electron temperatures are independent of the radial distance on both sides (Fig. 3B), the hot electron fractions show clear increases with increasing distance on both dawn and dusk sides (Fig. 3C). We construe this as evidence of continuous hot electron transport into the inner magnetosphere from the middle magnetosphere. The hot electron fraction is higher than that seen in previous in situ measurements and model studies (*11*, *18*, *19*). This is due to our usage of a bi-Maxwellian rather than a kappa-distribution function, which gives a more continuous high-energy tail for the electron populations (*11*, *20*).

The collisional relaxation time scale between the hot and core electrons with temperatures of T_h and T_c is given by

$$\tau^{h\to c} = \left\{ 1.8 \times 10^{-19} \times \frac{m_e (1 - f_h) n_e \ln \Lambda}{[m_e (T_h + T_c)]^{3/2}} \right\}^{-1} \quad (1)$$

where m_e is the electron mass, f_h is the hot electron fraction, n_e is the local electron density, and $\ln \Lambda$ is the Coulomb logarithm (*21*, *22*). If the hot and core electron temperatures are 46 eV and 5 eV, respectively, the relaxation time scale is

[1]Institute of Space and Astronautical Science (ISAS), Japan Aerospace Exploration Agency (JAXA), Sagamihara, Japan. [2]Planetary Plasma and Atmospheric Research Center, Tohoku University, Sendai, Japan. [3]National Astronomical Observatory of Japan, Mitaka, Japan. [4]Department of Geophysics, Tohoku University, Sendai, Japan. [5]Department of Earth and Planetary Science, University of Tokyo, Tokyo, Japan. [6]Earth-Life Science Institute, Tokyo Institute of Technology, Tokyo, Japan.
*Corresponding author. E-mail: kazuo@stp.isas.jaxa.jp

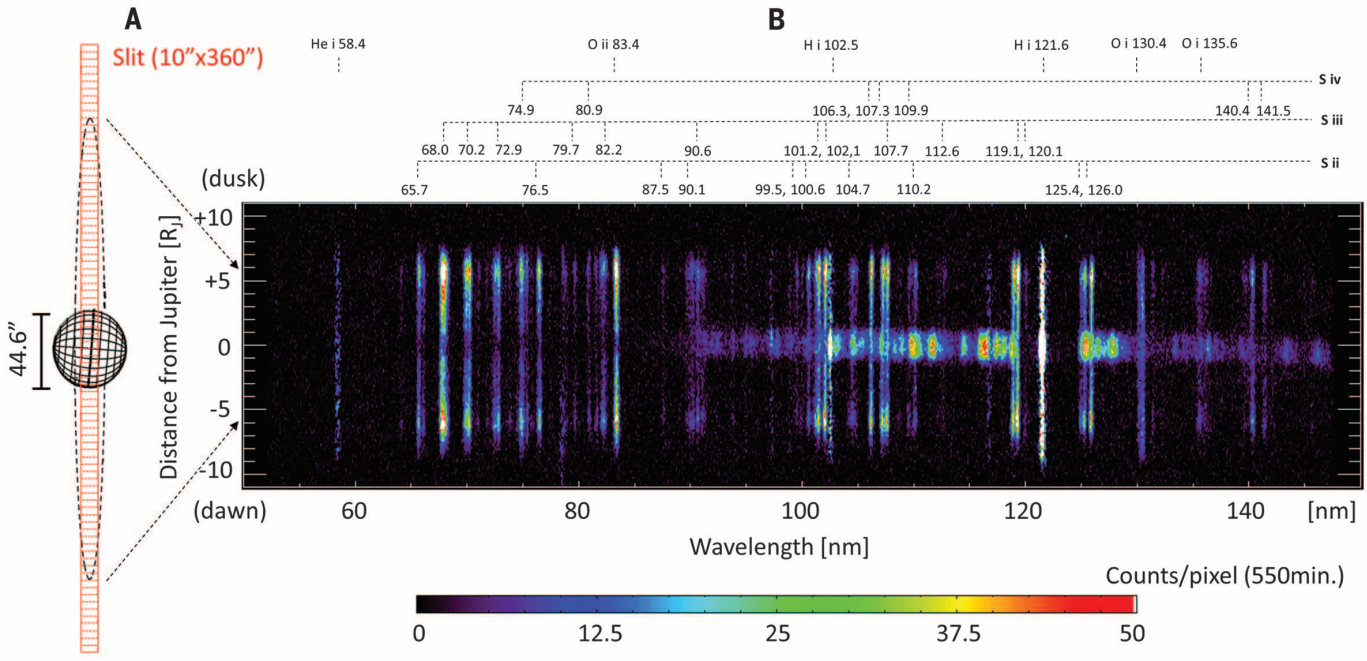

Fig. 1. EUV spectroscopy of the Io plasma torus (IPT) with EXCEED. (**A**) The slit position relative to Jupiter and the IPT. The column of red vertical boxes shows the location of the slit relative to the disk of Jupiter in the center and the black dashed ellipse of the IPT. The slit orientation was aligned parallel to and centered on the IPT latitudinal center during the entire observation period. Spatial information is available only along the longer axis of the slit (360 arc sec in total) and provides a resolution of ~0.2R_J. The shorter axis (10 arc sec in width) corresponds to 0.44R_J. (**B**) The spectrum of Jupiter and the IPT, integrated over 550 min. The vertical axis shows the spatial distribution (bottom corresponds to dawn side); the horizontal axis corresponds to the spectral distribution. Although the geocoronal background has been subtracted, residue at some bright lines (He I 58.4 nm, H I 121.6 nm, etc.) remains. At the top, the major spectral features are labeled by approximate wavelength and responsible ions.

Fig. 2. Absolute brightness–calibrated spectra from radial distances of 5.9 to 7.6 R_J for both dawn and dusk (black lines). Spatial bins are summed over 0.4R_J for the spectra from 5.9 to 7.1 R_J. The outermost bins at 7.6R_J are summed over 0.8R_J to improve the signal-to-noise ratio. For comparison, the best-fit model spectra are also shown as red dashed lines on each spectrum. The shaded areas indicate where geocoronal emissions (He I 58.4 nm, ghost of Lyα 79 nm, O II 83.4 nm, Lyβ 102.5 nm, Lyα 121.6 nm, O I 130.4 nm, and O I 135.6 nm) contaminate the data and were not used in the model parameter fitting.

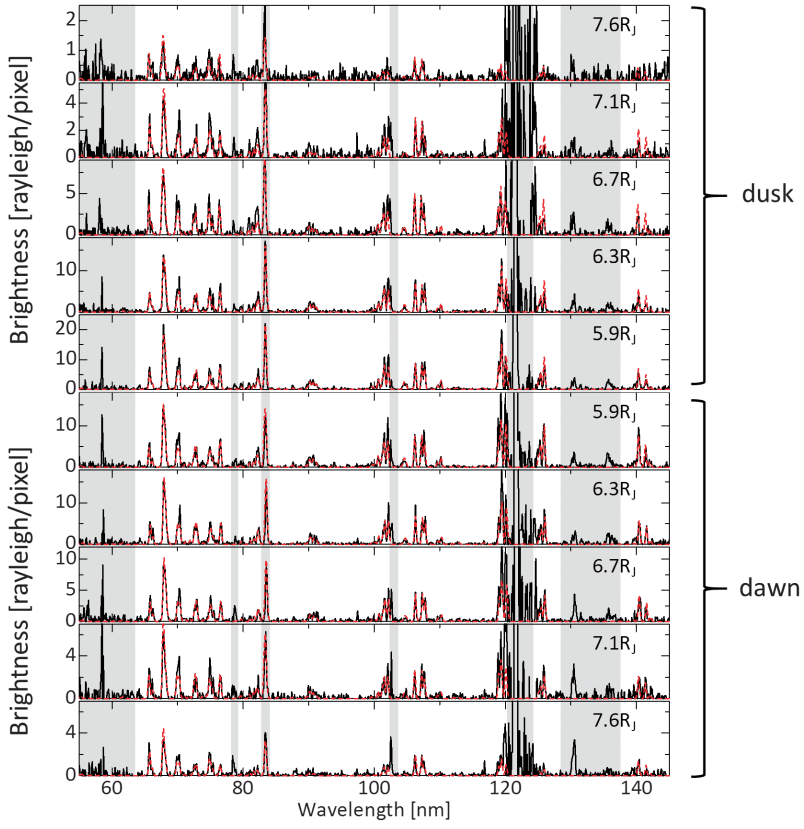

around 45 min (Fig. 4A), which is shorter than the total integration time (550 min) for our data. Therefore, the gradual inward decrease of the hot electron fraction (Fig. 3C) implies a continuous inward hot plasma transportation that balances with its fast collisional loss. The spatial variations seen simultaneously at dawn and dusk, together with a similar profile obtained previously in a post-midnight sector (*11*), imply the presence of an efficient hot plasma transport independent of local time. We note that transport driven by centrifugally driven interchange instability has this property (*23*). Other hypotheses have suggested that the hot electrons could be produced by local heating via interactions with Alfvén or lower-hybrid waves at or near Io's orbit (*19*, *24*–*27*). However, the hot electron fraction increases with radial distance from Io's orbit, which suggests that this mechanism is unlikely. A shorter integration time or careful binning of data by Io's phase angle may reveal the effects of local heating.

Given the decay of the hot electron density according to the time constant of $\tau^{h\to c}$, the inward transport velocity v of hot electrons needed to maintain the density gradient can be estimated by inverting the following formula:

$$R = \exp\left(\frac{D/v}{\tau^{h\to c}}\right) \quad (2)$$

where R is the ratio of hot electron densities between two locations separated radially by a distance D. Using the collisional time scale of 45 min and the derived electron density and hot component fraction, we estimated R and D as follows. We averaged the dawn and dusk data at 5.9, 6.3, and 6.7 R_J to obtain a representative hot electron density at 6.3R_J (inner IPT, 41 ± 14 cm^{-3}). The data at 7.1 and 7.6 R_J were handled likewise to obtain the same metric at 7.35 R_J (outer IPT, 62 ± 32 cm^{-3}). From these, we obtained R ~ 1.5 over the distance D ~ 1.05R_J, which corresponds to a velocity v of ~3.6 R_J/hour. We note that this is comparable to the azimuthal corotation velocity and is consistent with a previous estimate from Galileo in situ measurements (*5*). This inward speed (on the order of 100 km/s), which would reflect the **E** × **B** drift motion of flux tubes, is much faster than the gradient-**B** drift of 10- to 100-keV electrons (at most 1 km/s for <100 keV), indicating that these more energetic electrons are transported inward in mostly the same way as 46-eV electrons.

We can check the validity of setting the hot electron temperature at 46 eV by evaluating the amount of energy that is transported by those hot electrons into the core components. This can be estimated as

$$E_{h\to c} = \frac{f_h \times n_e \times V \times (T_h - T_c)}{\tau^{h\to c}} \quad (3)$$

where V = 1.4 × 10^{31} cm^3 is the torus volume responsible for emissions (*21*). Using the parameters f_h = 2%, n_e = 1500 cm^{-3}, and T_c = 5 eV (derived from Fig. 3), we estimate that the hot electron component contributes 0.5 to 1.2 TW to the IPT (Fig. 4). This value, which is 20 to 60% of the total power emitted from IPT (*11*), is in accord with the widely accepted idea that the ion pickup process and the hot electron injection are the major sources of energy input into IPT (*28*–*30*). Apart from this issue, EUV spectral diagnosis is rather insensitive to the precise temperature; the emission probability for lines excited by impact with hot electrons stays about the same as long as their temperature exceeds 40 eV (460,000 K).

The relative fraction of higher-state ions (S^{3+}) increases toward the outer IPT boundary, which is consistent with the behavior of the hot electrons that contribute to producing such populations (Fig. 3, D and E). A similar radial profile

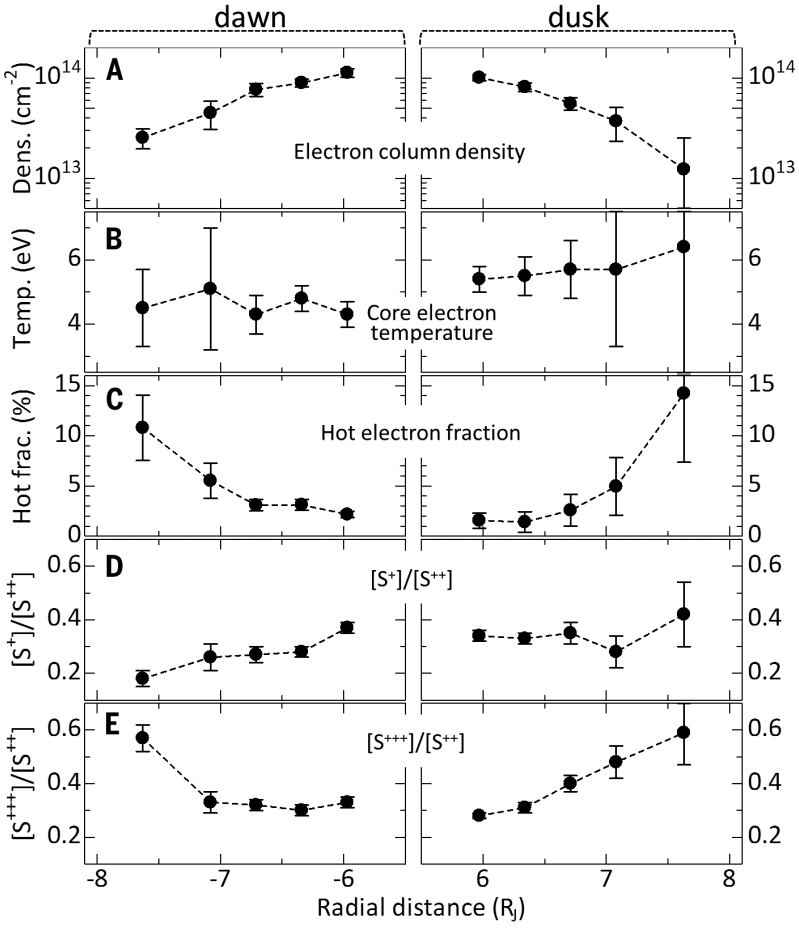

Fig. 3. Plasma parameters derived from the spectral diagnosis as a function of radial distance for dawn (left) and dusk (right). (**A**) electron column density. (**B**) Core electron temperature. (**C**) Hot electron (46 eV) fraction. (**D**) S^+ density relative to S^{2+}. (**E**) S^{3+} density relative to S^{2+}. The error bars show the 1σ errors as reported by the fitting algorithm, which take the statistical and detector sensitivity error into account. The hot electron fraction (C) increasing with radial distance on both dawn and dusk portions is taken as evidence of energy transport into the IPT via centrifugally driven interchange motion.

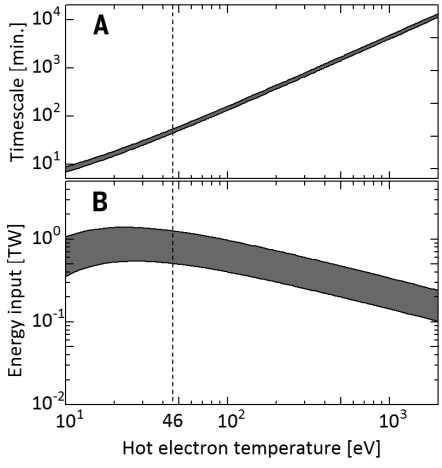

Fig. 4. The time scale and energy dependences on the hot electron temperature. (**A**) The collisional relaxation time scale between the hot and core electrons. (**B**) Total energy input from the hot component to the core component as a function of hot electron temperature. These values are calculated with parameters derived from the innermost regions shown in Fig. 3 (averaged over dawn and dusk). For both panels, the range of the plotted values corresponds to 1σ error. The black dashed line marks the case when the hot electron temperature is 46 eV.

for ion densities was reported by previous in situ measurements in the jovian local night (*16*).

Although there is no clear radial trend in the core electron temperature (Fig. 3B), the temperature is slightly higher on the dusk side. This may reflect the Io-jovian magnetic field interaction leading to electron heating via wave-particle interaction (*24*–*26*). Io was located on the dusk side throughout the whole observation period (phase angle from 200° to 330°). The dawn-dusk temperature asymmetry may also be related to differential magnetic compression heating on the dusk side by the dawn-to-dusk electric field coming from interaction of the Jovian magnetosphere with the flow of solar wind plasma down the magnetotail (*31*, *32*).

REFERENCES AND NOTES

1. S. Bolton *et al.*, in *Jupiter: Planet, Satellites, Magnetosphere* (Cambridge Univ. Press, Cambridge, 2004).
2. R. B. Horne *et al.*, *Nat. Phys.* **4**, 301–304 (2008).
3. L. A. Frank, W. R. Paterson, *J. Geophys. Res.* **107**, 1478 (2002).
4. M. G. Kivelson, K. K. Khurana, C. T. Russell, R. J. Walker, *Geophys. Res. Lett.* **24**, 2127–2130 (1997).
5. R. M. Thorne *et al.*, *Geophys. Res. Lett.* **24**, 2131–2134 (1997).
6. B. H. Mauk, D. J. Williams, R. W. McEntire, *Geophys. Res. Lett.* **24**, 2949–2952 (1997).
7. F. Xiao, R. M. Thorne, D. A. Gurnett, D. J. Williams, *Geophys. Res. Lett.* **30**, 1749 (2003).
8. D. E. Shemansky, G. R. Smith, *J. Geophys. Res.* **86**, 9179–9192 (1981).
9. D. T. Hall *et al.*, *Astrophys. J.* **426**, L51–L54 (1994).
10. P. D. Feldman, D. F. Strobel, H. W. Moos, H. A. Weaver, *Astrophys. J.* **601**, 583–591 (2004).
11. A. J. Steffl *et al.*, *Icarus* **172**, 91–103 (2004).
12. K. Yoshioka *et al.*, *Planet. Space Sci.* **85**, 250–260 (2013).
13. K. Nakaya *et al.*, *Proc. of the 28th ISTS*. 2011-f-19 (2011); http://archive.ists.or.jp.
14. K. P. Dere, E. Landi, H. E. Mason, B. C. Monsignori Fossi, P. R. Young, *Astron. Astrophys. Suppl. Ser.* **125**, 149–173 (1997).
15. E. Landi, P. R. Young, K. P. Dere, G. Del Zanna, H. E. Mason, *Astrophys. J.* **763**, 86–94 (2013).
16. F. Bagenal, *J. Geophys. Res.* **99**, 11043–11062 (1994).
17. K. Yoshioka, I. Yoshikawa, F. Tsuchiya, M. Kagitani, G. Murakami, *J. Geophys. Res.* **116**, A09204 (2011).
18. P. A. Delamere, F. Bagenal, A. Steffl, *J. Geophys. Res.* **110**, A12223 (2005).
19. E. C. Sittler Jr., D. F. Strobel, *J. Geophys. Res.* **92**, 5741–5762 (1987).
20. M. Moncuquet *et al.*, *J. Geophys. Res.* **107**, 1260 (2002).
21. P. A. Delamere, F. Bagenal, *J. Geophys. Res.* **108**, 1276 (2003).
22. J. D. Huba, *Tech. Rep. NRL/PU6790-09-523, 71* (Naval Research Laboratory, Washington, DC, 2009).
23. G. L. Siscoe, D. Summers, *J. Geophys. Res.* **86**, 8471–8479 (1981).
24. F. J. Crary, *J. Geophys. Res.* **102**, 37–49 (1997).
25. L. A. Frank, W. R. Paterson, *J. Geophys. Res.* **105**, 16017–16034 (2000).
26. S. L. G. Hess *et al.*, *J. Geophys. Res.* **115**, A06205 (2010).
27. D. D. Barbosa, F. V. Coroniti, W. S. Kurth, F. L. Scarf, *Astrophys. J.* **289**, 392–408 (1985).
28. D. D. Barbosa, *Astrophys. J.* **430**, 376–386 (1994).
29. R. Schreier, A. Eviatar, V. M. Vasyliūnas, *J. Geophys. Res.* **103**, 19901–19913 (1998).
30. P. A. Delamere *et al.*, *J. Geophys. Res.* **109**, A10216 (2004).
31. D. D. Barbosa, M. G. Kivelson, *Geophys. Res. Lett.* **10**, 210–213 (1983).
32. W. H. Ip, C. K. Goertz, *Nature* **302**, 232–233 (1983).

ACKNOWLEDGMENTS

We thank S. Sawai, S. Fukuda, K. Nakaya, S. Sakai, and all the group members who contributed so much to JAXA's HISAKI project. The HISAKI data sets are archived in the ISAS/JAXA Data Archives and Transmission System (DARTS).

19 May 2014; accepted 21 August 2014
10.1126/science.1256259

INTERSTELLAR CHEMISTRY

Detection of a branched alkyl molecule in the interstellar medium: *iso*-propyl cyanide

Arnaud Belloche,[1]* Robin T. Garrod,[2] Holger S. P. Müller,[3] Karl M. Menten[1]

The largest noncyclic molecules detected in the interstellar medium (ISM) are organic with a straight-chain carbon backbone. We report an interstellar detection of a branched alkyl molecule, *iso*-propyl cyanide (*i*-C_3H_7CN), with an abundance 0.4 times that of its straight-chain structural isomer. This detection suggests that branched carbon-chain molecules may be generally abundant in the ISM. Our astrochemical model indicates that both isomers are produced within or upon dust grain ice mantles through the addition of molecular radicals, albeit via differing reaction pathways. The production of *iso*-propyl cyanide appears to require the addition of a functional group to a nonterminal carbon in the chain. Its detection therefore bodes well for the presence in the ISM of amino acids, for which such side-chain structure is a key characteristic.

Around 180 molecules have been detected so far in the interstellar medium (ISM) (*1*). Apart from the fullerenes that are cyclic, the largest of these interstellar molecules are organic with a straight-chain carbon backbone. However, more complex molecules have been identified in meteorites found on Earth, including more than 80 amino acids (*2*)—the building blocks of proteins. The composition of these meteoritic amino acids suggests that they or their direct precursors have an interstellar origin (*3*). Chemistry at work in the ISM may thus be capable of producing organic molecules more complex than those detected so far and thus of great importance to astrobiology. However, the degree of complexity that may be reached in the ISM is still an open question, as well as how widespread these complex organic molecules are in our Galaxy.

Our previous observations of the star-forming region Sagittarius B2(N), hereafter Sgr B2(N), yielded the first interstellar detection of the straight-chain organic molecule *normal*-propyl cyanide (*n*-C_3H_7CN), the largest molecule yet detected in this source (*4*). This spectral line survey, conducted by using the 30-m single-dish radio telescope of the Institut de Radioastronomie Millimétrique (IRAM), provided continuous spectral coverage throughout the 3-mm transmission window of Earth's atmosphere (*5*). It allowed the identification of other complex organic species, such as ethyl formate (*4*) and aminoacetonitrile (*6*), a possible precursor of the amino acid glycine. On the basis of the success of this single-dish line survey, we performed a survey in the same waveband by using the Atacama

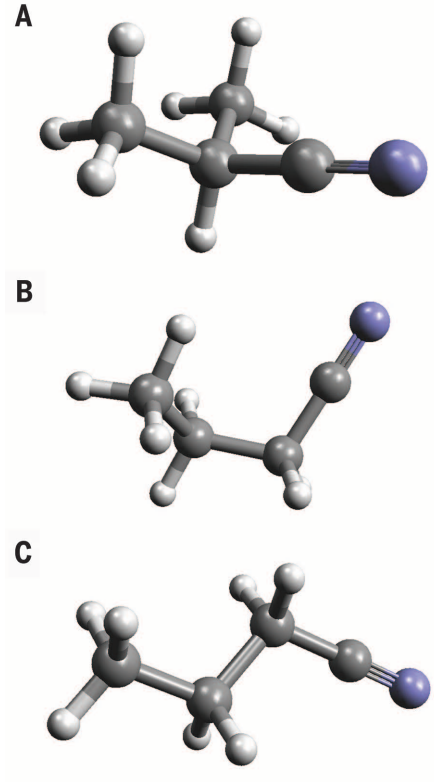

Fig. 1. Models of propyl cyanide isomers and conformers. (**A**) *iso*-propyl cyanide (*i*-C_3H_7CN). (**B**) *gauche-normal*-propyl cyanide (*g-n*-C_3H_7CN). (**C**) *anti-normal*-propyl cyanide (*a-n*-C_3H_7CN). C, H, and N atoms are indicated by gray, small light-gray, and blue spheres, respectively.

[1]Max-Planck-Institut für Radioastronomie (MPIfR), Auf dem Hügel 69, 53121 Bonn, Germany. [2]Center for Radiophysics and Space Research, Cornell University, Ithaca, NY 14853-6801, USA. [3]I. Physikalisches Institut, Universität zu Köln, Zülpicher Straße 77, 50937 Köln, Germany.
*Corresponding author. E-mail: belloche@mpifr-bonn.mpg.de

Large Millimeter/Submillimeter Array (ALMA), resulting in an increase of more than one order of magnitude in both sensitivity and angular resolution. This interferometric project, called EMoCA (Exploring Molecular Complexity with ALMA), aims to decipher the molecular content of Sgr B2(N) in order to test the predictions of astrochemical numerical simulations and to gain insight into the chemical processes at work in the ISM.

Sgr B2 is the most massive star-forming region in our Galaxy. It is located close to the Galactic Center, which is 8.34 ± 0.16 (SEM) kpc from the Sun (*7*). Sgr B2 contains two main sites of star formation, Sgr B2(N) and Sgr B2(M), that, since the early 1970s, have turned out to be the best hunting ground for complex organic molecules in the ISM. Their immense hydrogen column densities that signify large quantities of gas enable the detection of low-abundance species. Sgr B2(N) itself contains two dense, compact, hot cores that are separated by about 5″ [~40,000 astronomical units (AU) in projection] (*6*).

Propyl cyanide (C_3H_7CN, hereafter PrCN) is the smallest alkyl cyanide that exists in several distinct isomers (Fig. 1): the chain isomer *normal*- or *n*-PrCN (also known as butyronitrile or 1-cyanopropane) and the branched isomer *iso*- or *i*-PrCN (also known as *iso*-butyronitrile or 2-cyanopropane). *n*-PrCN is the smallest alkyl cyanide that exists in several distinct conformations. The CN group can be attached to the terminal C of the propyl group in the CCC plane, trans to the CCC chain, leading to the anti conformer, also known as trans (Fig. 1C); it can also be attached to the propyl group rotated by ±120° with respect to the CCC plane, leading to the gauche conformer (Fig. 1B). The rotational spectrum of *i*-PrCN, previously only studied to a limited extent in the microwave region, has recently been recorded extensively in the laboratory from the microwave to the submillimeter wave region along with a redetermination of the dipole moment (*8*).

We used ALMA in 2012 to perform a full spectral line survey toward Sgr B2(N) in the 3-mm atmospheric window between 84 and 111 GHz (*9*). We identified the detected lines by modeling the molecular emission under the assumption of local thermodynamic equilibrium. By using predictions from the Cologne Database for Molecular Spectroscopy (*10*), we assigned emission features to *i*-PrCN or *n*-PrCN (*9*). To interpret the astronomical detections, we performed numerical simulations of the chemistry occurring during the evolution of a hot core (*9*).

Many spectral lines are detected in the ALMA data toward both of the hot cores embedded in Sgr B2(N). These spectra are very close to the confusion limit; that is, signal from a spectral line is detected in nearly every spectral channel. The lines are narrower toward the northern, less-prominent hot core (full width at half maximum, FWHM, ~5 km s^{-1}) than toward the southern, more-prominent one. The detection of faint lines from rare species is therefore easier toward the former, and we focused on this one in the present work. We constructed a preliminary model of the emission of all molecules previously detected,

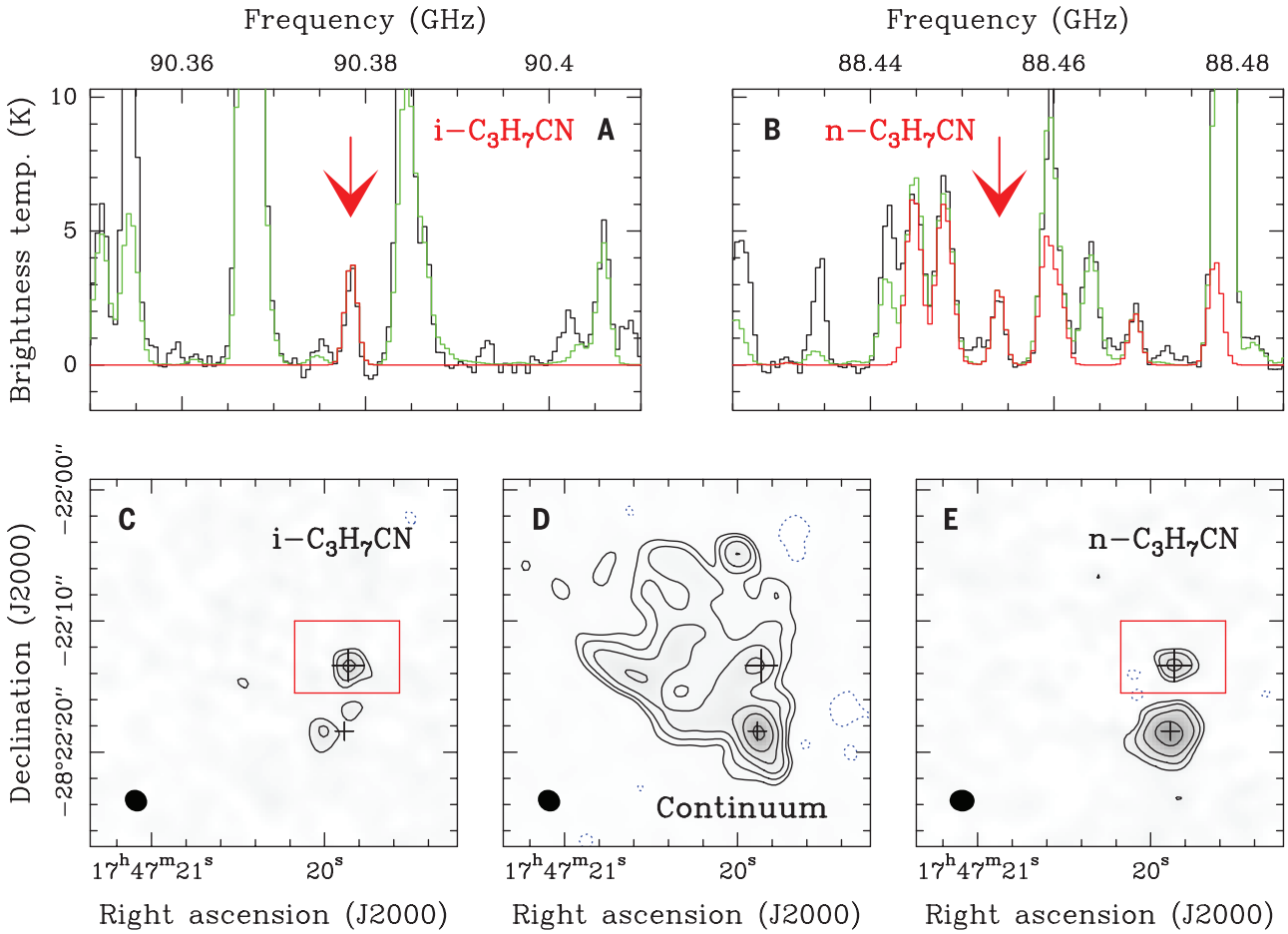

Fig. 2. Examples of transitions of *i*-PrCN and *n*-PrCN toward the northern hot core of Sgr B2(N). (**A** and **B**) Continuum-subtracted spectrum observed with ALMA in black, the preliminary model including all identified molecules in green, and the synthetic spectra of *i*-PrCN and *n*-PrCN, respectively, in red. (**C** and **E**) Integrated intensity maps of the transitions of *i*-PrCN and *n*-PrCN marked with a red arrow in (A) and (B), respectively. The continuum emission at 90.5 GHz is shown in (**D**). The negative contour (dotted blue) is −3σ, and the positive contours (black) are $2^i \times 3\sigma$, with *i* an integer starting at 0 and σ the root-mean-square noise level [23 mJy $beam^{-1}$ km s^{-1}, 8.3 mJy $beam^{-1}$ km s^{-1}, and 20 mJy $beam^{-1}$ km s^{-1} with half-power beam widths of 1.8″ × 1.6″, 1.8″ × 1.6″, and 1.9″ × 1.6″ in (C), (D), and (E), respectively]. The large cross indicates the position of the northern hot core as traced by both molecules. The smaller cross marks the position of the main hot core that has a lower systemic velocity, which implies that the contours outside the red box do not trace the emission of *i*-PrCN and *n*-PrCN in (C) and (E), respectively. The black ellipses show the size of the respective synthetic beams.

on the basis of our analysis of the previous single-dish survey of Sgr B2(N) (*5*). In this way, the risk of misassigning a line to a new species is reduced. About 50 and 120 transitions of *i*-PrCN and *n*-PrCN, respectively, are detected toward the northern hot core (Fig. 2, A and B, and figs. S1 and S2). On the basis of this model, we selected the least-contaminated transitions and produced contour maps of their intensity integrated over their line profile (Fig. 2, C and E, and figs. S3 and S4). From these maps, we derived a deconvolved angular size of 1.0″ ± 0.3″ (FWHM) for the region where both species emit. We used the population diagram method (*11*) to estimate a rotation temperature of 153 ± 12 K (SEM), which characterizes the emission of both molecules (*9*).

With the size and temperature derived above and a linewidth measurement of 5 km s^{-1}, we obtained a good fit to all transitions of *i*-PrCN and *n*-PrCN detected toward the northern hot core of Sgr B2(N). After correction for the contribution of vibrationally excited states (*9*), we derived column densities of $7.2 \times 10^{16} \pm 1.4 \times 10^{16}$ cm^{-2} and $1.8 \times 10^{17} \pm 0.4 \times 10^{17}$ cm^{-2} (SEM), respectively, which yielded an abundance ratio [*i*-PrCN]/[*n*-PrCN] of 0.40 ± 0.06 (SEM). The latter uncertainty assumes the same source size and rotation temperature for both isomers. With the H_2 column density derived from the continuum emission (*9*) (Fig. 2D), we deduced average abundances relative to H_2 of $1.3 \times 10^{-8} \pm 0.2 \times 10^{-8}$ for *i*-PrCN and $3.2 \times 10^{-8} \pm 0.5 \times 10^{-8}$ for *n*-PrCN. The latter uncertainties assume the same rotation and dust temperatures and take neither possible contamination of the continuum emission by free-free emission nor uncertainties on the dust properties into account.

The recently developed chemical kinetics model MAGICKAL [Model for Astrophysical Gas and Ice Chemical Kinetics And Layering (*12*)] was used to simulate the time-dependent chemistry of the source. The model begins with a cold collapse phase, during which abundant ice mantles, composed of simple H-, O-, C-, and N-bearing molecules, are formed on dust-grain surfaces. The cold stage is followed by a warm-up stage, during which the dust and gas temperature rises from ~8 to 400 K. The majority of complex organic molecule formation occurs during this stage, through the addition of simple and complex radicals within and upon the ice mantles.

The model produces time-dependent chemical abundances (with respect to H_2) for various cyanide molecules (Fig. 3). The model temperatures at which each molecule's peak abundance is attained (table S2) may be considered representative of the excitation temperature at which most of the emission from each molecule would occur, assuming local thermodynamic equilibrium. The desorption temperature of each PrCN isomer is ~150 K, with peak gas-phase abundances achieved at 160 K. This agrees well with the rotation temperatures that we determined from observational data for these molecules.

The majority of each of the two PrCN isomers forms in or on the dust-grain ices at around 55 to 75 K in the model. However, the model also indicates that, whereas many similar chemical pathways are open to both *i*-PrCN and *n*-PrCN, the dominant formation route in each case is different. The greatest contribution to *i*-PrCN production comes from the reaction of CN radicals (which are accreted from the gas) with the CH_3CHCH_3 radical. The latter derives from the earlier gas-phase formation of C_3, which is hydrogenated and stored on the grains as C_3H_2, C_3H_4, and C_3H_6. The addition of atomic hydrogen to propylene (C_3H_6) strongly favors the production of CH_3CHCH_3, whose radical site lies at the secondary carbon atom (*13*).

Because the production, either by hydrogen addition or abstraction processes, of radicals such as $CH_2CH_2CH_3$ and CH_2CH_2CN (whose radical site is at the primary carbon atom) is strongly disfavored versus their equivalent iso forms, we find that the dominant formation mechanism for *n*-PrCN is the addition of C_2H_5 and CH_2CN, a process that has no equivalent for the production of *i*-PrCN. The radicals form through the abstraction of hydrogen by OH, from C_2H_6 and CH_3CN, respectively. *i*-PrCN production dominates all reaction mechanisms for which parallel processes are available to both isomers.

Although the overall peak gas-phase values of *i*-PrCN and *n*-PrCN produced by the models are similar, they show a slight bias toward *i*-PrCN production (2.2:1), rather than the observed bias toward *n*-PrCN (0.4:1). This may be caused by the poorly defined rates for barrier-mediated surface reactions, such as $H + C_3H_6 \rightarrow CH_3CHCH_3$ and $OH + CH_3CN \rightarrow CH_2CN + H_2O$, for which only gas-phase rates have been measured and whose behavior may be somewhat different on an ice surface.

Amid the growing understanding that complex organic molecules could form on the surface of dust grains, the formation of branched alkyl molecules in the ISM was suggested theoretically in the 1980s (*14*), but no such molecules were detected until now. The detection of a branched alkyl molecule in Sgr B2, with an abundance similar to that of its straight-chain isomer, indicates a further divergence between the chemistry of star-forming regions like Sgr B2 and quiescent regions. These less-active regions seem to produce only linear molecules—the largest one known to date being $HC_{11}N$ (*15*). The detection of a branched alkyl molecule also suggests a further link between interstellar chemistry and the molecular composition of meteorites for which branched amino acids are even found to dominate over their straight-chain isomers (*16*). The inherent bias toward the production of secondary rather than primary radical sites on precursor radicals suggests that branched molecules may be prevalent, and indeed dominant, in star-forming regions where chemistry of sufficient complexity is reached. The detection of the next member of the alkyl cyanide series, *n*-butyl cyanide (*n*-C_4H_9CN), and its three branched isomers would allow the testing of this conjecture.

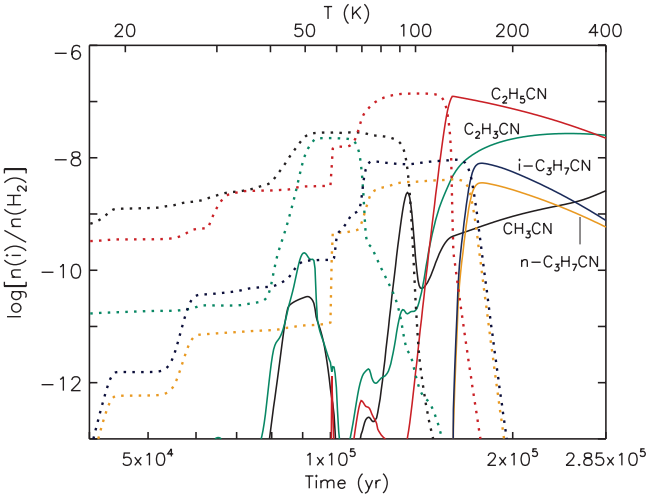

Fig. 3. Simulated fractional chemical abundances of alkyl cyanides with respect to molecular hydrogen, H_2. These abundances represent the warm-up phase of hot-core evolution. Solid lines indicate gas-phase species; dotted lines of the same color indicate the same species in the solid phase. The main phase change from solid to gas for each molecule is caused by thermal desorption from the grain surfaces, according to species-specific binding energies.

REFERENCES AND NOTES

1. See, e.g., www.astro.uni-koeln.de/cdms/molecules.
2. J. E. Elsila, J. P. Dworkin, M. P. Bernstein, M. P. Martin, S. A. Sandford, *Astrophys. J.* **660**, 911–918 (2007).
3. O. Botta, J. L. Bada, *Surv. Geophys.* **23**, 411–467 (2002).
4. A. Belloche *et al.*, *Astron. Astrophys.* **499**, 215–232 (2009).
5. A. Belloche, H. S. P. Müller, K. M. Menten, P. Schilke, C. Comito, *Astron. Astrophys.* **559**, A47 (2013).
6. A. Belloche *et al.*, *Astron. Astrophys.* **482**, 179–196 (2008).
7. M. J. Reid *et al.*, *Astrophys. J.* **783**, 130 (2014).
8. H. S. P. Müller, A. Coutens, A. Walters, J.-U. Grabow, S. Schlemmer, *J. Mol. Spectrosc.* **267**, 100–107 (2011).
9. Additional information is available in the supplementary materials on *Science* Online.
10. H. S. P. Müller, F. Schlöder, J. Stutzki, G. Winnewisser, *J. Mol. Struct.* **742**, 215–227 (2005).
11. P. F. Goldsmith, W. D. Langer, *Astrophys. J.* **517**, 209–225 (1999).
12. R. T. Garrod, *Astrophys. J.* **765**, 60 (2013).
13. H. J. Curran, *Int. J. Chem. Kinet.* **38**, 250–275 (2006).
14. T. J. Millar, P. D. Brown, H. Olofsson, A. Hjalmarson, *Astron. Astrophys.* **205**, L5–L7 (1988).
15. M. B. Bell *et al.*, *Astrophys. J.* **483**, L61–L64 (1997).
16. J. R. Cronin, S. Pizzarello, *Adv. Space Res.* **3**, 5–18 (1983).

ACKNOWLEDGMENTS

We thank D. Petry and E. Humphreys at the European ALMA Regional Center (ARC), F. Gueth at the IRAM ARC node, and D. Muders at the MPIfR for their help with the reduction of the ALMA data; S. Bardeau, S. Maret, J. Pety, M. Lonjaret, and P. Hily-Blant for the new developments implemented in the Weeds software; and M. Koerber for help with preparing Fig. 1. This work made use of the National Institute of Standards and Technology Chemical Kinetics Database. This work has been supported in part by the Deutsche Forschungsgemeinschaft through the collaborative research grant SFB 956 "Conditions and

Impact of Star Formation," project area B3. H.S.P.M. is very grateful to the Bundesministerium für Bildung und Forschung for support through projects FKZ 50OF0901 (ICC HIFI *Herschel*) and 05A11PK3 (ALMA ARC Node). R.T.G. acknowledges support from the NASA Astrophysics Theory Program through grant NNX11AC38G. This paper makes use of the following ALMA data: ADS/JAO.ALMA#2011.0.00017.S. ALMA is a partnership of the European Southern Observatory (ESO) (representing its member states), NSF (USA), and National Institutes of Natural Sciences (Japan), together with National Research Council (Canada) and National Science Council and Academia Sinica Institute of Astronomy and Astrophysics (Taiwan), in cooperation with the Republic of Chile. The Joint ALMA Observatory is operated by ESO, Associated Universities Incorporated/National Radio Astronomy Observatory, and National Astronomical Observatory of Japan. The interferometric data are available in the ALMA archive at https://almascience.eso.org/aq/. The chemical model input files are located at www.astro.cornell.edu/~rgarrod/resources.

SUPPLEMENTARY MATERIALS

www.sciencemag.org/content/345/6204/1584/suppl/DC1
Materials and Methods
Figs. S1 to S6
Tables S1 and S2
References (*17*–*30*)

29 May 2014; accepted 20 August 2014
10.1126/science.1256678

REMOTE HYDROLOGY

Ongoing drought-induced uplift in the western United States

Adrian Antal Borsa,[1]* Duncan Carr Agnew,[1] Daniel R. Cayan[1,2]

The western United States has been experiencing severe drought since 2013. The solid earth response to the accompanying loss of surface and near-surface water mass should be a broad region of uplift. We use seasonally adjusted time series from continuously operating global positioning system stations to measure this uplift, which we invert to estimate mass loss. The median uplift is 5 millimeters (mm), with values up to 15 mm in California's mountains. The associated pattern of mass loss, ranging up to 50 centimeters (cm) of water equivalent, is consistent with observed decreases in precipitation and streamflow. We estimate the total deficit to be ~240 gigatons, equivalent to a 10-cm layer of water over the entire region, or the annual mass loss from the Greenland Ice Sheet.

Over the past few years, the western conterminous United States (WUSA) has experienced large interannual variations in hydrological conditions and is currently undergoing a severe drought. Coincident observations of reduced precipitation and streamflow reflect the impact of the drought but do not directly measure the associated deficit in terrestrial water storage (TWS), which is a comprehensive metric that includes cumulative changes in vegetation and soil moisture, perennial snow and ice, groundwater, and surface water. Satellite gravity measurements from NASA's Gravity Recovery and Climate Experiment (GRACE) have been widely used to observe TWS (*1*, *2*), though these results indicate that for transient signals the intrinsic spatial resolution of these measurements is several hundred kilometers. Additional information about TWS at higher resolution is needed to understand the extent and impact of the current drought at basin to regional scales across the WUSA.

Like other varying loads on Earth's surface, the water mass loss associated with the drought will induce instantaneous vertical and horizontal displacements from elastic deformation (*3*). These can be measured at the millimeter level using the Global Positioning System (GPS), which has been done for seasonal changes in snowpack (*4*) and in hydrologic systems such as lakes (*5*, *6*) and river basins (*7*, *8*). Except very close to the load, these displacements are largely independent of local structure (e.g., sedimentary basins behave the same as bedrock). Displacements from loading provide information about changes at intermediate spatial scales not otherwise observable, and they integrate the effects of all loads—an advantage because displacements provide data from areas otherwise not measured, and a challenge because inversion is required to find the actual spatial distribution.

To study the loading response corresponding to hydrological changes, we have analyzed the past 11 years (2003 to 2014) of daily vertical positions estimated for continuous GPS stations from the National Science Foundation's Plate Boundary Observatory (PBO) and several smaller networks. The stations we used were located on the U.S. mainland west of longitude 109°W and on Vancouver Island. We detrended each time series to remove secular tectonic motion and used the seasonal-trend-loess (STL) method (*9*) to remove seasonal signals due to water loading (*10*–*12*). The STL method is effective on time series like GPS that exhibit modulated behavior (*13*, *14*) that is not well represented by annual and semiannual sinusoids (fig. S1).

GPS records transient displacements from phenomena other than surface loading, including volcanic or tectonic forcing (*15*) and the

[1]Scripps Institution of Oceanography, University of California San Diego, La Jolla, CA 92093, USA. [2]United States Geological Survey, La Jolla, CA 92093, USA.
*Corresponding author. E-mail: aborsa@ucsd.edu

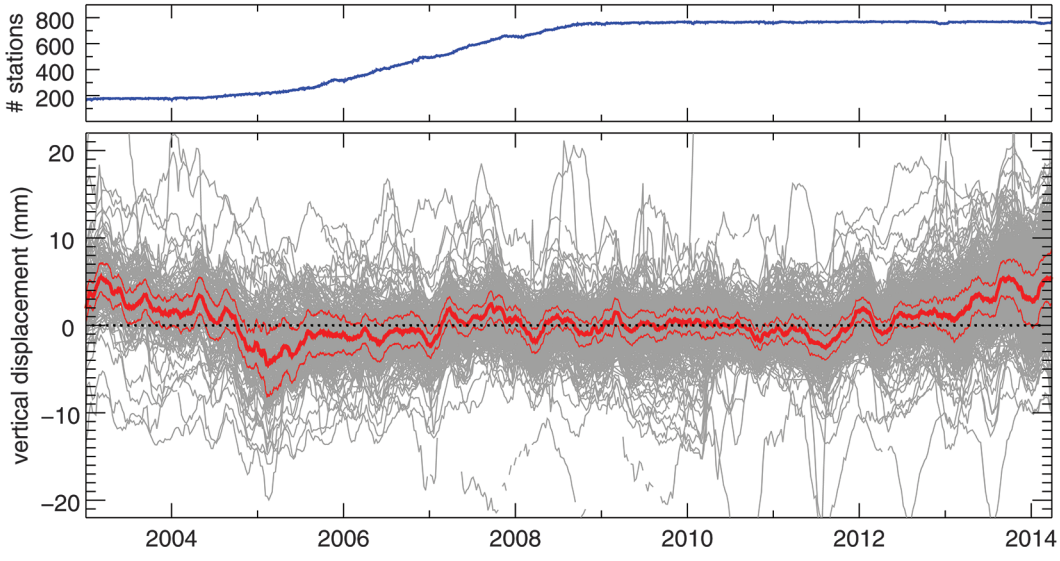

Fig. 1. Vertical GPS displacement time series. Detrended and seasonally adjusted daily vertical displacements from 771 continuous GPS stations in the WUSA, decimated to weekly intervals for plotting (gray lines). The thick red line is the median value of all data for each day, and the light red lines indicate the SD computed from the interquartile range. The uplift that began in 2013 is notable for the period after 2006, when the number and distribution of GPS stations greatly expanded across the region with the building of the PBO (blue line shows the number of stations used in the analysis).

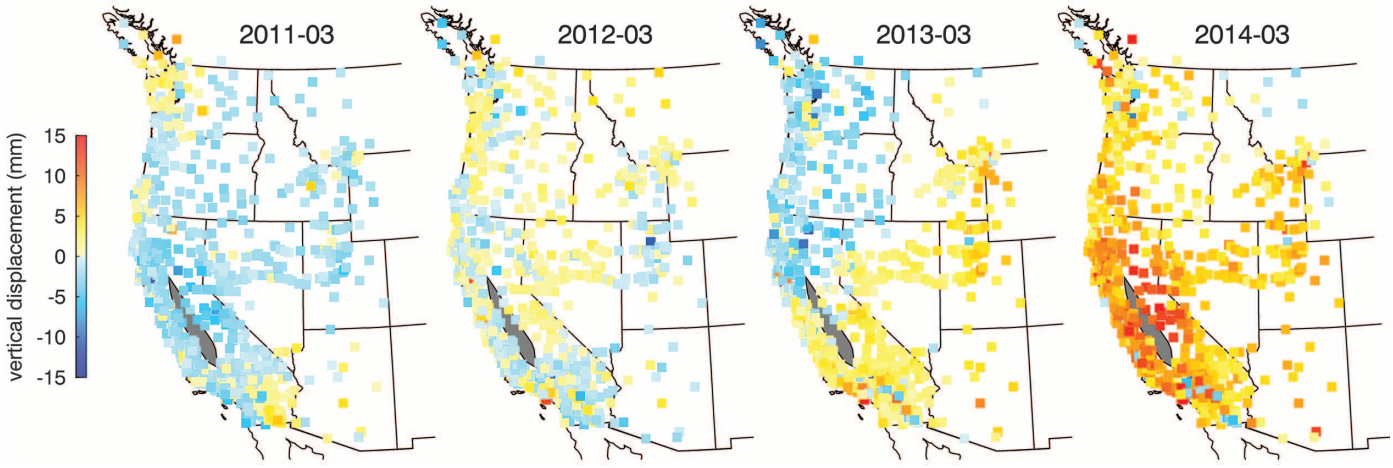

Fig. 2. Maps of vertical GPS displacements. Spatial distribution of displacements from the time series in Fig. 1, from 1 March 2011 through 2014. Uplift is indicated by yellow-red colors and subsidence by shades of blue. The gray region is where stations were excluded in the Central Valley of California.

poroelastic response of aquifers to groundwater extraction and recharge (*16*, *17*). In addition, fictitious vertical displacements can be caused by variations in the signal-scattering environment close to each station (*18*), but these "multipath" effects contribute, on average, only a few millimeters of correlated noise to daily position estimates (*19*) and are not expected to substantially affect our results. We mitigated the impact of nonloading signals by excluding all stations within the actively deforming Long Valley caldera (*20*); all stations in California's Central Valley, where agricultural pumping is widespread (*21*, *22*); stations whose seasonal displacements suggest they are located above an actively pumped aquifer (*11*); and a few gross outliers (*12*).

After removing these stations, we were left with 771 GPS displacement time series (*12*) for our analysis. The median vertical displacement over time reveals a period of uplift beginning in 2013 and continuing through the present (Fig. 1). Before 2013, the median displacement did not deviate more than a few millimeters from zero, at least not since the mid-2005 inception of the PBO network. (We attribute the variability before 2006 to the much smaller number of stations and their concentration in southern California.) Vertical motion in the region is much more dynamic than this overall stability might suggest, as shown by the spatial pattern of displacements (Fig. 2). In March 2011, widespread but modest subsidence prevailed over most of the WUSA, but this had changed to spatially random uplift and subsidence by March 2012. By March 2013, moderate subsidence had returned to the Pacific Northwest and northern California, while moderate uplift had begun elsewhere. A year later, in March 2014, uplift had dramatically increased in California and was widespread across the entire WUSA.

These results demonstrate that interannual vertical displacements vary considerably from year to year, even when the WUSA as a whole is stable. Examining the data at weekly intervals reveals that the spatial displacement patterns

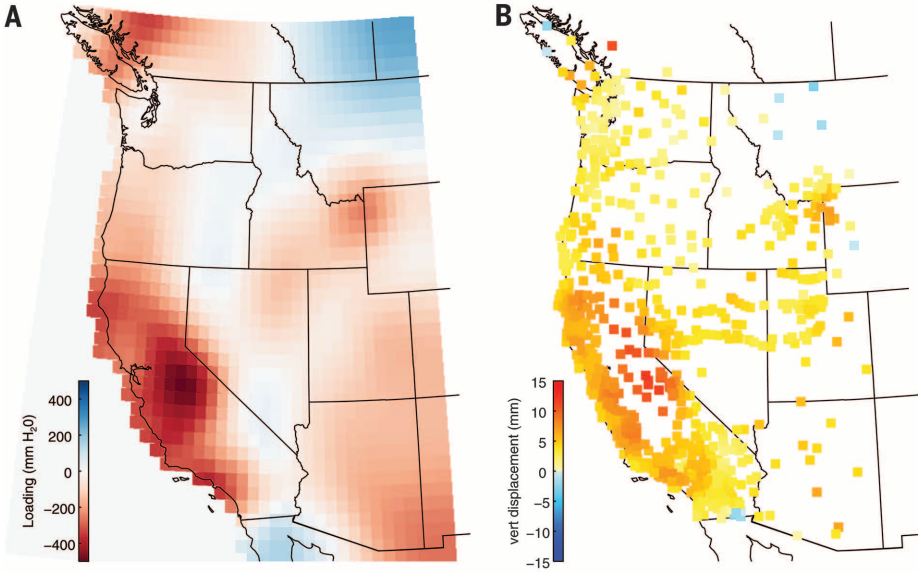

Fig. 3. Maps of estimated loads and predicted displacements. (**A**) Loading estimate for the WUSA in March 2014. Redder areas indicate negative loading (mass deficit), bluer areas indicate positive loading (mass surplus), and white areas are unchanged. (**B**) Vertical displacements, corresponding to the loading model in (A), at the locations of the GPS stations used in this analysis (compare to actual displacements in rightmost panel of Fig. 2).

shown in Fig. 2 evolve coherently over the entire period of analysis on scales of 100 to 1000 km. This behavior is inconsistent with GPS processing error, which would typically cause random noise or motion of the entire network, or with groundwater extraction, which primarily affects agricultural or urban areas (*17*). The GPS stations in our analysis are either attached to solid rock or anchored at several meters depth in soils, so poroelastic effects due to changes in surface soil water content should not affect our results. Finally, interannual horizontal GPS displacements in the region are typically much smaller than their vertical counterparts (Fig. 2 and figs. S2 and S3), which is inconsistent with both volcanic and tectonic processes (*6*, *23*). The only process that can reasonably account for the observed broad-scale deformation is spatiotemporal variation in loading.

We used the observed GPS displacements in March 2014 to estimate the distribution of loads on a 0.5° grid spanning the WUSA. We calculated the vertical displacement at each station for surface loads on an elastic Earth (*3*, *24*, *25*) and used these to invert for loads on the grid (*12*), applying a regularization constraint to balance model misfit and smoothness. Predicted displacements from our preferred load model (Fig. 3) reduce the root mean square of the observed displacements by 53% (fig. S7) and yield spatially random residuals. A checkerboard test (fig. S8) suggests that the spatial resolution of the model is 200 to 300 km, except at the northern and eastern edges of the GPS network, where station spacing is larger.

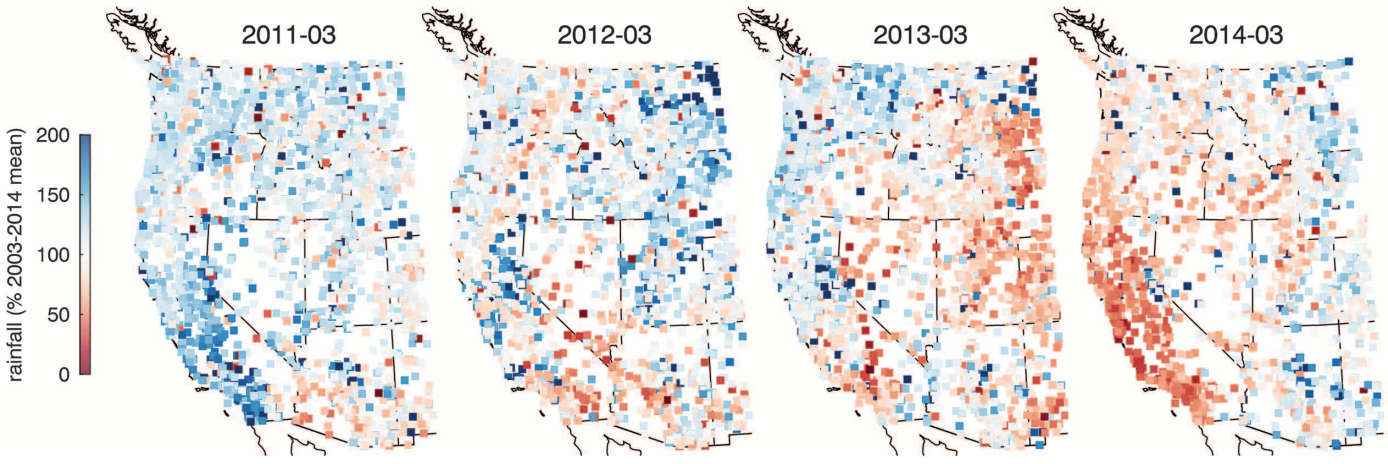

Fig. 4. Maps of annual precipitation anomalies. Deviation of annual precipitation from the 2003-to-2013 mean at meteorological stations in the National Oceanic and Atmospheric Administration's Global Historical Climatology Network, for 2011 to 2014. The pattern of precipitation—in particular, the surplus in California in 2011 and the deficit in 2014—mirrors the pattern of uplift seen in the GPS data.

The inversion produces an estimate of the load that resembles the uplift pattern but is smoother because of the constraints imposed. In March 2014, when most vertical displacements are farthest from their long-term averages, our results show crustal unloading over the entire WUSA, with a maximum in the central Sierra Nevada equivalent to 50 cm of water (Fig. 3). There appears to be a small amount of real nontectonic loading in Montana, whereas the apparent loading just south of the U.S.-Mexico border is probably caused by postseismic effects from the moment magnitude 7.2 El Mayor–Cucapah earthquake in 2010 (*26*). The arid regions of eastern California, Oregon, Washington, and western Nevada show little loading. Estimated loads near the northern and southern boundaries of the grid, as well as in Arizona, Utah, and Montana, are poorly constrained by the GPS data.

We interpret the widespread negative loading, with its central California maximum, to represent changes in terrestrial water storage due to the current WUSA drought. The implied drying relative to the long-term mean appears to be most acute in coastal and mountainous areas and subdued in highly arid regions. This is expected, because the change in precipitation in a drought is proportional to the climatological mean value, so that arid regions lose less water than do wet regions. The area-integrated water deficit over the WUSA in March 2014 is 240 gigatons, a value that is insensitive to the degree of smoothing used in the inversion (fig. S6). For perspective, this deficit is equivalent to a uniform 10-cm layer of water over the entire WUSA and is the magnitude of the current annual mass loss from the Greenland Ice Sheet.

The temporal and spatial water storage variations implied by the observed displacements are consistent with contemporaneous observations of precipitation and streamflow, all of which underscore the extent and severity of the current drought in the WUSA. The departure of annual precipitation from the long-term average (Fig. 4) highlights the changes over the past few years: a wet 2011; a variable 2012; a dry 2013 for the western Rockies, the Great Basin, and parts of California; and severe drought in 2014 along the Pacific coast, with dry conditions extending inland to the Rocky Mountains. Precipitation patterns in 2011 and 2014, in particular, match the pattern of vertical displacements for, respectively, excess (wet) and deficit (dry) loading conditions. Streamflow data from the U.S. Geological Survey (USGS) stream gauge network (fig. S9) exhibit wet/dry patterns similar to the precipitation data, although it is the years 2013 and 2014 that most closely match the vertical displacements. These data sets are consistent with each other and also complementary, each highlighting a different component of the hydrological system.

It has been suggested that long-term and seasonal variations in mass loading due to the hydrological cycle may affect seismicity rates along the San Andreas fault (*27*). We computed the Coulomb stress change on the San Andreas fault from the load shown in Fig. 3 (*12*, *28*) and found that the past 2 years of unloading have increased Coulomb stresses by 100 to 200 Pa, approximately the same amount as a week of tectonic strain accumulation (*29*). Therefore, stress changes from the drought unloading seem unlikely to affect seismicity.

Other methods that can directly monitor changes in total water mass change are sensitive to different spatial scales. Gravimeters allow very sensitive detection of mass changes, but because their sensitivity falls off as r^{-2} (where r is the distance to the mass), they are best at measuring very local changes (*30*). Conversely, perturbations to satellite orbits can be used to detect changing mass distributions over the whole Earth but are insensitive to load variations with wavelengths much less than the orbital height. The nominal resolution for the GRACE satellite is 400 to 500 km (*31*), which is consistent with results from GRACE studies of drought-induced mass changes (*1*, *2*). For vertical displacements from GPS, the loading Green function varies as r^{-1}: Load-induced signals reflect both local and regional changes. Combining these different measurement types offers the greatest promise for monitoring terrestrial water storage.

In the WUSA, interannual changes in crustal loading are driven by changes in cool-season precipitation, which cause variations in surface water, snowpack, soil moisture, and groundwater. We have demonstrated that GPS can be used to recover loading changes due to both wet (e.g., 2011) and dry (e.g., post-2013) climate patterns, which suggests a new role for GPS networks such as that of the PBO. Although precipitation and surface water levels are currently well sampled, other components of terrestrial water storage are monitored only at a limited number of locations, including a growing number of GPS stations for which GPS reflectometry measurements of snow depth and soil moisture are available (*32*–*34*). Our analysis shows that the existing network of continuous GPS stations in the WUSA measures vertical crustal motion at sufficient precision and sampling density to allow the estimation of interannual changes in water loads, providing a new view of the ongoing drought in much of the WUSA. Furthermore, the exceptional stability of the GPS monumentation (*35*) means that this network is also capable of monitoring the long-term effects of regional climate change. Surface displacement observations from GPS, in the WUSA and globally, have the potential to dramatically expand the capabilities of the current hydrological observing network, and continued operation of these instruments will provide considerable value in understanding current and future hydrological changes, with obvious social and economic benefits.

REFERENCES AND NOTES

1. F. Frappart *et al.*, *Environ. Res. Lett.* **7**, 044010 (2012).
2. A. C. Thomas, J. T. Reager, J. S. Famiglietti, M. Rodell, *Geophys. Res. Lett.* **41**, 1537–1545 (2014).
3. W. E. Farrell, *Rev. Geophys.* **10**, 761–797 (1972).
4. K. J. Ouellette, C. de Linage, J. S. Famiglietti, *Water Resour. Res.* **49**, 2508–2518 (2013).
5. P. Elósegui, J. L. Davis, J. X. Mitrovica, R. A. Bennett, B. P. Wernicke, *Geophys. Res. Lett.* **30**, 1111 (2003).

6. J. Wahr *et al.*, *J. Geophys. Res.* **117**, 1795–1806 (2013).
7. M. Bevis *et al.*, *Geophys. Res. Lett.* **32**, L16308 (2005).
8. P. Bettinelli *et al.*, *Earth Planet. Sci. Lett.* **266**, 332–344 (2008).
9. R. B. Cleveland, W. S. Cleveland, J. E. McRae, I. Terpenning, *J. Off. Stat.* **6**, 3–73 (1990).
10. M. S. Steckler *et al.*, *J. Geophys. Res.* **115**, B08407 (2010).
11. D. Argus, Y. Fu, F. Landerer, *Geophys. Res. Lett.* **41**, 1971–1980 (2014).
12. Materials and methods are available as supplementary materials on *Science* Online.
13. R. A. Bennett, *Geophys. J. Int.* **174**, 1052–1064 (2008).
14. J. L. Davis, B. P. Wernicke, M. E. Tamisiea, *J. Geophys. Res.* **117**, B01403 (2012).
15. D. Dzurisin, *Volcano Deformation: Geodetic Monitoring Techniques* (Springer, New York, 2007).
16. N. E. King *et al.*, *J. Geophys. Res.* **112**, B03409 (2007).
17. D. L. Galloway, T. J. Burbey, *Hydrogeol. J.* **19**, 1459–1486 (2011).
18. P. Elósegui *et al.*, *J. Geophys. Res.* **100**, 9921–9934 (1995).
19. M. A. King *et al.*, *Surv. Geophys.* **31**, 465–507 (2010).
20. K.-H. Ji, T. A. Herring, A. L. Llenos, *Geophys. Res. Lett.* **40**, 1054–1058 (2013).
21. M. E. Ikehara, *Hydrol. Sci. J.* **39**, 417–429 (1994).
22. R. T. Hanson *et al.*, in *Land Subsidence, Associated Hazards, and the Role of Natural Resources Development* (International Association of Hydrological Sciences Press, Wallingford, UK, 2010), vol. 339, pp. 467–471.
23. R. Grapenthin, B. G. Ofeigsson, F. Sigmundsson, E. Sturkell, A. Hooper, *Geophys. Res. Lett.* **37**, L20310 (2010).
24. D. C. Agnew, in *Treatise on Geophysics: Geodesy*, T. A. Herring, Ed. (Elsevier, New York, 2007), pp. 163–195.
25. D. C. Agnew, "SPOTL: Some Programs for Ocean-Tide Loading" (SIO Technical Report, Scripps Institution of Oceanography, La Jolla, CA, 2012); http://escholarship.org/uc/item/954322pg.
26. F. Pollitz, R. Bürgmann, W. Thatcher, *Geochem. Geophys. Geosyst.* **13**, Q06002 (2012).
27. C. B. Amos *et al.*, *Nature* **509**, 483–486 (2014).
28. L. Astiz, P. M. Shearer, D. C. Agnew, *J. Geophys. Res.* **105**, 2937–2953 (2000).
29. B. Smith-Konter, D. Sandwell, P. M. Shearer, *J. Geophys. Res.* **116**, B06401 (2011).
30. M. Van Camp, O. de Viron, L. Métivier, B. Meurers, O. Francis, *Geophys. J. Int.* **197**, 192–201 (2014).
31. G. Ramillien, J. S. Famiglietti, J. Wahr, *Surv. Geophys.* **29**, 361–374 (2008).
32. K. M. Larson *et al.*, *IEEE J. Select. Top. Appl. Earth Obs. Remote Sens.* **3**, 91–99 (2010).
33. E. D. Gutmann, K. M. Larson, M. W. Williams, F. G. Nievinski, V. Zavorotny, *Hydrol. Processes* **26**, 2951–2961 (2012).
34. W. Wan, K. M. Larson, E. E. Small, C. C. Chew, J. J. Braun, *GPS Solut.* 10.1007/s10291-014-0383-7 (2014).
35. J. O. Langbein, F. Wyatt, H. Johnson, D. Hamann, P. Zimmer, *Geophys. Res. Lett.* **22**, 3533–3536 (1995).

ACKNOWLEDGMENTS

The GPS data we use come primarily from the PBO and are publicly available from UNAVCO through the Geodesy Advancing Geosciences and EarthScope Facility, which is supported by the NSF and NASA under NSF cooperative agreement no. EAR-1261833. Meteorological data are publicly available from the National Climatic Data Center's Global Historical Climatology Network. The software used for load computation (SPOTL) is publicly available, and the processing software may be obtained from us. We acknowledge the efforts of many at UNAVCO to produce the exceptional PBO GPS data set, especially the station installation efforts of C. Walls, K. Austin, and K. Feaux. We thank M. Dettinger for comments. This work was supported by USGS grant no. G13AP00059.

SUPPLEMENTARY MATERIALS

www.sciencemag.org/content/345/6204/1587/suppl/DC1
Materials and Methods
Figs. S1 to S9
References

20 June 2014; accepted 8 August 2014
Published online 21 August 2014;
10.1126/science.1260279

EARLY SOLAR SYSTEM

The ancient heritage of water ice in the solar system

L. Ilsedore Cleeves,[1]* Edwin A. Bergin,[1] Conel M. O'D. Alexander,[2] Fujun Du,[1] Dawn Graninger,[3] Karin I. Öberg,[3] Tim J. Harries[4]

Identifying the source of Earth's water is central to understanding the origins of life-fostering environments and to assessing the prevalence of such environments in space. Water throughout the solar system exhibits deuterium-to-hydrogen enrichments, a fossil relic of low-temperature, ion-derived chemistry within either (i) the parent molecular cloud or (ii) the solar nebula protoplanetary disk. Using a comprehensive treatment of disk ionization, we find that ion-driven deuterium pathways are inefficient, which curtails the disk's deuterated water formation and its viability as the sole source for the solar system's water. This finding implies that, if the solar system's formation was typical, abundant interstellar ices are available to all nascent planetary systems.

Water is ubiquitous across the solar system, in cometary ices, terrestrial oceans, the icy moons of the giant planets, and the shadowed basins of Mercury (*1*, *2*). Water has left its mark in hydrated minerals in meteorites, in lunar basalts (*3*), and in martian melt inclusions (*4*). The presence of liquid water facilitated the emergence of life on Earth; thus, understanding the origin(s) of water throughout the solar system is a key goal of astrobiology. Comets and asteroids (traced by meteorites) remain the most primitive objects, providing a natural "time capsule" of the conditions present during the epoch of planet formation. Their compositions reflect those of the gas, dust, and—most important—ices encircling the Sun at its birth, i.e., the solar nebula protoplanetary disk. There remain open questions, however, as to when and where these ices formed, whether they (i) originated in the dense interstellar medium (ISM) in the cold molecular cloud core before the Sun's formation or (ii) are products of reprocessing within the solar nebula (*5*–*7*). Scenario (i) would imply that abundant interstellar ices, including water and presolar organic material, are incorporated into all planet-forming disks. By contrast, local formation within the solar nebula in scenario (ii) would potentially result in large water abundance variations from stellar system to system, dependent on the properties of the star and disk.

In this work, we aim to constrain the formation environment of the solar system's water, using deuterium fractionation as our chemical tracer. Water is enriched in deuterium relative to hydrogen (D/H) compared with the initial bulk solar composition across a wide range of solar system bodies, including comets, (*8*, *9*), terrestrial and ancient martian water (*4*), and hydrated minerals in meteorites (*10*). The amount of deuterium relative to hydrogen of a molecule depends on its formation environment; thus, the D/H fraction in water, $[D/H]_{H_2O}$, can be used to differentiate between the proposed source environments. Interstellar ices, as revealed by sublimation in close proximity to forming young stars, also exhibit high degrees of deuterium enrichment, ~2 to 30 times that of terrestrial water (*11*–*14*). It is not known to what extent these extremely deuterated interstellar ices are incorporated into planetesimals or if, instead, the interstellar chemical record is erased by reprocessing during the formation of the disk (*15*, *16*). Owing to water's high binding energy to grain surfaces, theoretical models predict that water is delivered from the dense molecular cloud to the disk primarily as ice, with some fraction sublimated at the accretion shock in the inner tens of astronomical units (AU) (*15*). If a substantial fraction of the interstellar water is thermally reprocessed, the interstellar deuterated record could then be erased. In this instance, the disk is left as primary source for (re-)creating the deuterium-enriched water present throughout our solar system.

The key ingredients necessary to form water with high D/H are cold temperatures, oxygen, and a molecular hydrogen (H_2) ionization source. The two primary chemical pathways for making deuterated water are (i) gas-phase ion-neutral reactions, primarily through H_2D^+ and (ii) grain-surface formation (ices) from ionization-generated hydrogen and deuterium atoms from H_2. Both reaction pathways depend critically on the formation of H_2D^+. In particular, the gas-phase channel (i) involves the reaction of H_2D^+ ions with atomic oxygen or OH through a sequence of steps to form H_2DO^+, which recombines to form a water molecule. The grain-surface channel (ii) is powered by H_2D^+ recombination with electrons or grains, which liberates hydrogen and deuterium atoms that react with oxygen atoms on cold dust grains. H_2D^+ becomes enriched relative to H_3^+ because the deuterated isotopologue is energetically favored at low temperatures. There is

[1]Department of Astronomy, University of Michigan, 311 West Hall, 1085 South University Avenue, Ann Arbor, MI 48109, USA. [2]Department of Terrestrial Magnetism, Carnegie Institution of Washington, Washington, DC 20015, USA. [3]Harvard-Smithsonian Center for Astrophysics, Harvard University, Cambridge, MA 02138, USA. [4]Department of Physics and Astronomy, University of Exeter, Stocker Road, Exeter EX4 4QL, UK.
*Corresponding author. E-mail: cleeves@umich.edu.

an energy barrier ΔE_1 to return to H_3^+, i.e., $H_3^+ + HD \rightleftharpoons H_2D^+ + H_2 + \Delta E_1$, where $\Delta E_1 \approx 124$ K, although the precise value depends on the nuclear spin of the reactants and products (*17*). The relatively modest value of ΔE_1 restricts deuterium enrichments in H_3^+ to the coldest gas, $T \lesssim 50K$. Thus, deuterium-enriched water formation requires the right mix of environmental conditions: cold gas, gas-phase oxygen, and ionization.

The conditions in the dense interstellar medium, i.e., the cloud core, readily satisfy these requirements, where temperatures are typically $T \approx 10$ K and ionization is provided via galactic cosmic rays (GCRs). In this regard, the conditions in the core and in the outermost regions of the solar nebula are often thought of as analogous (*18*). This is because the outskirts of protoplanetary disks typically contain the coldest ($T \lesssim 30K$), lowest-density gas and are often assumed to be fully permeated by GCRs. However, the efficacy of GCRs as ionizing sources in protoplanetary disks has been called into question because of the deflection of GCRs by the stellar winds produced by young stars (*19*). Even in the mild, modern-day solar wind, the GCR ionization rate, ζ_{GCR}, by a factor of ~100, is below that of the unshielded ISM. Limits on protoplanetary disks' molecular ion emission indicate low GCR ionization rates, $\zeta_{GCR} \leq 3 \times 10^{-17}$ s^{-1} (*20*). In the absence of GCRs, disk midplane ionization is instead provided by scattered x-ray photons from the central star and the decay of short-lived radionuclides (SLRs), where the latter's influence decreases with time (*21*). In addition, the core-disk analogy breaks down with regard to gas density. At the outermost radius of the protosolar gaseous disk, $R_{out} \sim 50$ to 80 AU (*17*), the typical disk density is $n \sim 10^{10}$ cm^{-3}. This value is approximately five orders of magnitude higher than typical values within the interstellar molecular core (*22*). The steady-state ion abundance is proportional to $\sqrt{\zeta/n}$, where ζ is the ionization rate and n is the volumetric gas (hydrogen) density. For a constant ionization rate, a density increase of 10^5 coincides with a factor of ~300 drop in the ion abundance. Thus, wind or magnetically driven deflection of ionizing GCRs, coupled with high gas densities, will strongly inhibit the disk from generating deuterium enrichments through the standard cold chemical reactions (i) and (ii), described above.

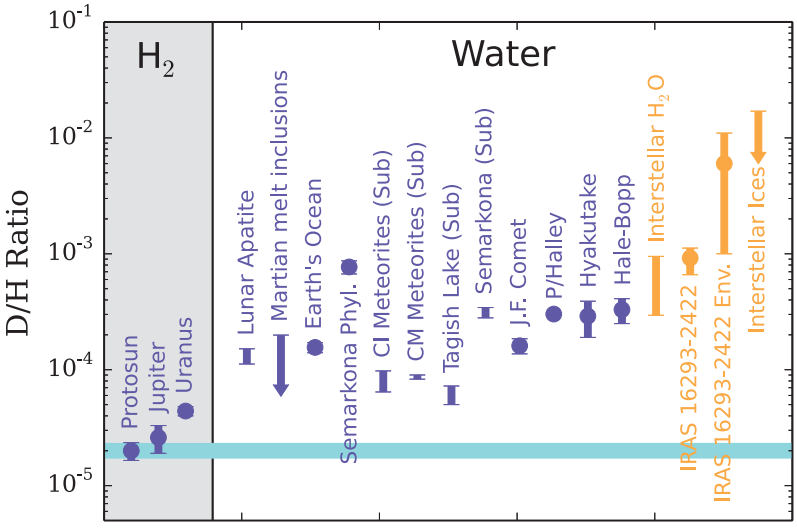

Fig. 1. Atomic D/H ratios in solar system (purple) and interstellar (yellow) sources separated into bulk H_2 and water. Points indicate single measurements, bars without points are ranges over multiple measurements, and arrows correspond to limits. D/H in the bulk gas (i.e., solar) is indicated as a horizontal blue bar. References are provided in table S4 (*17*).

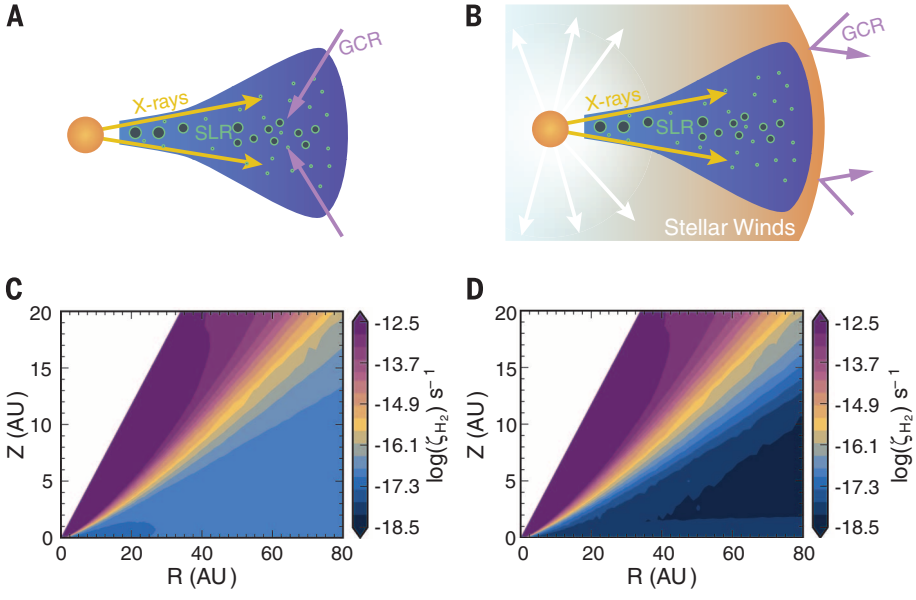

Fig. 2. Schematic of energetic disk ionization sources (top row) and the calculated total H_2 ionization rate (bottom row). (**A**) A "standard" disk ionization model driven by x-rays and GCRs; (**B**) ionization conditions under the influence of a Sun-like wind at solar maximum, now dominated by x-rays in the surface and SLRs in the midplane; (**C**) calculated H_2 ionization rates for the scenario depicted in (A); and (**D**) calculated H_2 ionization rates from the scenario depicted in (B) and that used within this report.

To test the disk hypothesis, we explore whether ionization-driven chemistry within the disk alone is capable of producing the deuterium-enriched water that was present in the early solar system. We have constructed a comprehensive model of disk ionization, including detailed radiative transfer, reduced GCR ionization, and SLR decay. To simulate the "reset" scenario, i.e., all interstellar deuterium enhancement is initially lost, we start with unenriched water with bulk solar D/H composition, $[D/H]_{H_2} = 2.0 \pm 0.35 \times 10^{-5}$ (*23*), and quantify the maximum amount of deuterated water produced by chemical processes in a static protoplanetary disk over 1 million years of evolution. The goal is to determine whether or not the conditions present in the solar nebula were capable of producing at minimum the measured isotopically enriched water in meteorites, ocean water [Vienna Standard Mean Ocean Water (VSMOW)], and comets (see Fig. 1). We do not attempt to address the eventual fate of this water by additional processing, i.e., by radial or vertical mixing, which tends to reduce the bulk D/H ratio in water (*24*, *25*).

Instead, our emphasis is on the physical mechanism necessary for D/H enrichment: ionization. We illustrate the suite of ionization processes considered in the traditional picture of disk ionization (Fig. 2A) alongside a schematic for our new model (Fig. 2B). More specifically, we include "solar-maximum" levels of GCR wind modulation for the incident GCR rate, a factor of ~300 below that of the ISM, Monte Carlo propagation of x-ray photoabsorption and scattering, and ionization by SLR decay products, including losses in the low-density ($\Sigma_{gas} \lesssim 10$ g cm^{-2}) regions of the disk (*17*). The total H_2 ionization rate is shown in Fig. 2, C and D. It can be seen that, whereas the warm surface layers ($\Sigma_{gas} \lesssim 1$ g cm^{-2}) are strongly ionized by stellar x-rays, $\zeta_{XR} \gtrsim 10^{-15}$ s^{-1}, the midplane is comparatively devoid of ionization because of the modulation of incident GCRs (Fig. 2D).

To compute molecular abundances, we compile a simplified deuterium-reaction network designed to robustly predict the D/H in water resulting from gas-phase and grain-surface chemistry (*17*). We include both ion-neutral and the hot-phase neutral-neutral water chemistry (*26*), as well as self-shielding by HD and D_2, in addition to the standard chemical network (*17*). We include an updated treatment of the inherently surface-dependent CO freeze-out process, motivated by new laboratory data on CO ice-binding energies (*17*). CO freeze-out is important for the present study, as CO regulates the amount of oxygen present in gas above $T > 17$ K and available for new water formation. We place the majority of volatile carbon in CO and the rest of the oxygen not in CO in water ice (*15*) [see supplementary materials for additional runs (*17*)]. We examine the final D/H of water ice after 1 million years of chemical evolution, i.e., the approximate lifetime of the gas-rich disk and, correspondingly, the duration over which the disk is able to build up deuterated water (see Fig. 3). The ions are most abundant in the upper, x-ray–dominated surface layers, whose temperatures are too warm for substantial deuterium enrichment in $[D/H]_{H_3^+}$. The bulk ice mass is closest to the cold midplane, where only a meager amount (per unit volume) of H_3^+ and H_2D^+ remain in the gas, a consequence of low ionization rates and high densities.

In addition to spatial abundances, we provide ratios of the vertically integrated column densities of both ions and ices (Fig. 3, bottom). The choice of VSMOW as a benchmark is somewhat arbitrary, considering that comets exceed D/H in VSMOW by factors of one to three times and meteorites have typically lower values, a factor ~2 less (Fig. 1). The column-derived $[D/H]_{H_3^+}$ approaches—but does not reach—VSMOW after 1 million years at the outer edge of the disk. Moreover, most of the molecules that contribute to the column density ratio of $[D/H]_{H_2^+}$ arise in an intermediate layer of cold (T_{gas} ~ 30 to 40 K) gas, where x-ray photons are still present. However, it is readily apparent that this enrichment does not translate into $[D/H]_{H_2O}$. The most deuterium-enriched water, $[D/H]_{H_2O} = 3 \times 10^{-5}$, is colocated with the enriched layer of $[D/H]_{H_3^+}$; however, the water is considerably less enriched than the ions. Over the lifetime of the disk, the gas-phase and grain-surface chemical pathways do not produce deuterated water ices in substantial quantities. Water production is low because of a combination of (i) a lack of sufficient ionization to maintain large amounts of H_2D^+ in the gas and (ii) a lack of atomic oxygen in the gas, locked up in ices. We do find a superdeuterated layer of water at the disk surface ($[D/H]_{H_2O} = 5 \times 10^{-3}$). This layer is a direct consequence of selective self-shielding of HD relative to H_2, which leads to an overabundance of atomic D relative to H. Selective self-shielding is also the cause of the fall of $[D/H]_{H_3^+}$ below the initial bulk gas value inside of $R < 40$ AU. This layer does not, however, contribute substantially to the vertically integrated $[D/H]_{H_2O}$ (Fig. 3, bottom).

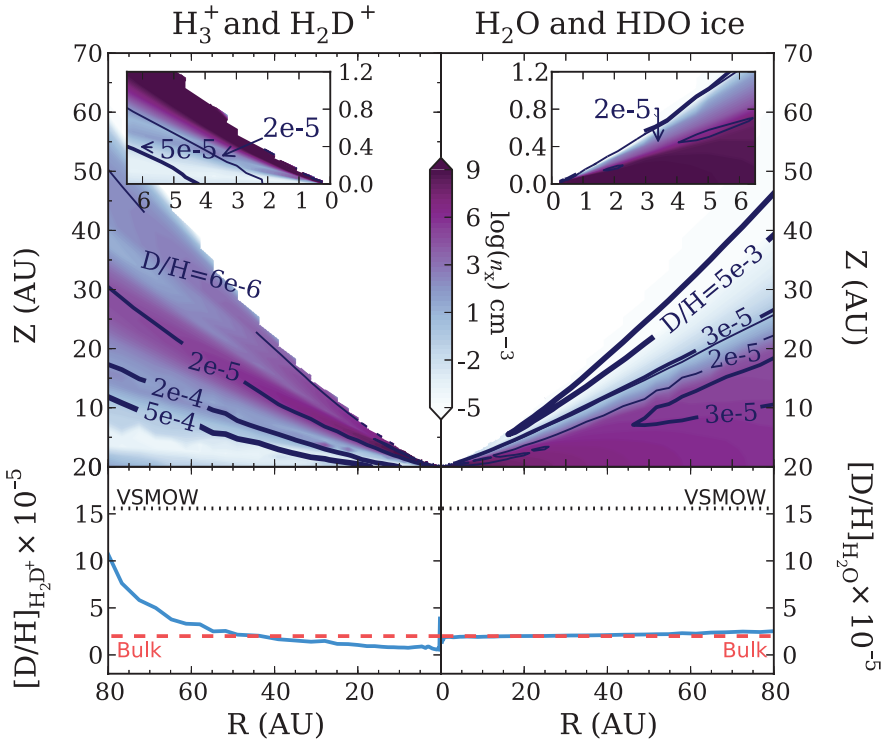

Fig. 3. Chemical abundances and column densities for the drivers of the deuterium enrichment, the ions; and the corresponding products, the ices. (**Top**) Volume densities (cm^{-3}) of all labeled isotopologues for H_3^+ (left) and water (right) in filled purple contours. Solid contour lines indicate local D/H and are as labeled. The color scale applies to both the left and right halves of the plot. (**Insets**) Enlarged inner disk with the same axis units. (**Bottom**) Plots of the vertically integrated D/H ratio of column densities versus radius. The bulk gas (protosolar) value is labeled by the red dashed line, and Earth's ocean value (VSMOW) is labeled with the black dotted line.

In summary, using a detailed physical ionization model, updated treatment of oxygen-bearing (CO) ice chemistry, and a simplified deuterium chemical network, we find that chemical processes in disks are not efficient at producing noteworthy levels of highly deuterated water. Our model predicts that disk chemistry can only produce a volume-integrated $[D/H]_{H_2O} \lesssim 2.1 \times 10^{-5}$, which is only slightly enriched from the bulk solar value (2×10^{-5}). In terms of column density, we find that, even in the most radially distant (coldest) regions, water only attains $[D/H]_{H_2O} \lesssim 2.5 \times 10^{-5}$. This finding implies that ion chemistry within the disk cannot create the deuterium-enriched water present during the epoch of planet formation. When we begin our models with interstellar $[D/H]_{H_2O} \sim 10^{-3}$, however, it is hard to "erase" D/H ratios with low-temperature disk chemistry alone. A number of studies have invoked turbulent mixing of gas in the radial and/or vertical directions, which can reduce inner-disk deuterium enrichments in water (*24*, *25*, *27*). Moreover, a common feature of such models is that they begin with high levels of deuterated water, as high as $[D/H]_{H_2O} \sim 10^{-2}$. In general, mixing in the vertical direction transports highly deuterium–enriched ices from the shielded midplane into the x-ray– and ultraviolet-irradiated warm surface layers (*28*, *29*), where they can be reprocessed to lower D/H. Ices transported radially inward, either entrained by gas accretion or subjected to radial migration, evaporate in the warm and dense inner disk and isotopically reequilibrate with H_2 or ion-neutral chemistry in hot ($T > 100$ K) gas. With our updated disk ionization model, we can now exclude chemical processes within the disk as an enrichment source term and conclude that the solar nebula accreted and retained some amount of pristine interstellar ices. One potential explanation is that during the formation of the disk, there was an early high-temperature episode followed by continued infall from deuterium-enriched interstellar ices (*16*). If we ignore the negligible contribution to deuterated water formation from the disk, we can estimate the fraction of water in a particular solar system body, X, that is presolar, $f_{ISM} = (D/H_X - D/H_\odot)/(D/H_{ISM} - D/H_\odot)$, where D/H_X refers to $[D/H]_{H_2O}$ in X and $D/H_\odot = 2 \times 10^{-5}$. Water in the ISM ranges from a limit of $[D/H]_{H_2O} < 2 \times 10^{-3}$ in interstellar ice (*11*) to $[D/H]_{H_2O} = (3 \text{ to } 5) \times 10^{-4}$ for low-mass protostars, i.e., analogs to the Sun's formation environment (*14*). If the former, higher value reflects the ices accreted by the solar nebular disk, then, at the very least, terrestrial oceans and comets should contain ≳7% and ≳14% interstellar water, respectively. If the low-mass protostellar values are representative, the numbers become 30 to 50% for terrestrial oceans and 60 to 100% for comets. Thus, a considerable fraction of the solar system's water predates the Sun. These findings imply that some amount of interstellar ice survived

the formation of the solar system and was incorporated into planetesimal bodies. Consequently, if the formation of the solar nebula was typical, our work implies that interstellar ices from the parent molecular cloud core—including the most fundamental life-fostering ingredient, water—are widely available to all young planetary systems.

REFERENCES AND NOTES

1. T. Encrenaz, *Annu. Rev. Astron. Astrophys.* **46**, 57–87 (2008).
2. D. J. Lawrence *et al.*, *Science* **339**, 292–296 (2013).
3. J. J. Barnes *et al.*, *Earth Planet. Sci. Lett.* **390**, 244–252 (2014).
4. T. Usui, C. M. O'D. Alexander, J. Wang, J. I. Simon, J. H. Jones, *Earth Planet. Sci. Lett.* **357-358**, 119–129 (2012).
5. F. Robert, D. Gautier, B. Dubrulle, *Space Sci. Rev.* **92**, 201–224 (2000).
6. C. Ceccarelli *et al.*, in *Protostars and Planets VI*, H. Beuther *et al.*, Eds. (Univ. of Arizona, Tucson, 2014), pp. 859–882.
7. E. F. van Dishoeck, E. A. Bergin, D. C. Lis, J. I. Lunine, in *Protostars and Planets VI*, H. Beuther *et al.*, Eds. (Univ. of Arizona, Tucson, 2014), pp. 835–858.
8. D. Bockelée-Morvan *et al.*, *Icarus* **133**, 147–162 (1998).
9. P. Eberhardt, M. Reber, D. Krankowsky, R. R. Hodges, *Astron. Astrophys.* **302**, 301 (1995).
10. C. M. O'D. Alexander *et al.*, *Science* **337**, 721–723 (2012).
11. E. Dartois *et al.*, *Astron. Astrophys.* **399**, 1009–1020 (2003).
12. A. Coutens *et al.*, *Astron. Astrophys.* **539**, A132 (2012).
13. M. V. Persson, J. K. Jørgensen, E. F. van Dishoeck, *Astron. Astrophys.* **541**, A39 (2012).
14. M. V. Persson, J. K. Jørgensen, E. F. van Dishoeck, D. Harsono, *Astron. Astrophys.* **563**, A74 (2014).
15. R. Visser, E. F. van Dishoeck, S. D. Doty, C. P. Dullemond, *Astron. Astrophys.* **495**, 881–897 (2009).
16. L. Yang, F. J. Ciesla, C. M. O'D. Alexander, *Icarus* **226**, 256–267 (2013).
17. Materials and methods are available as supplementary material on *Science* Online.
18. Y. Aikawa, E. Herbst, *Astrophys. J.* **526**, 314–326 (1999).
19. L. I. Cleeves, F. C. Adams, E. A. Bergin, *Astrophys. J.* **772**, 5 (2013).
20. E. Chapillon, B. Parise, S. Guilloteau, F. Du, *Astron. Astrophys.* **533**, A143 (2011).
21. T. Umebayashi, N. Katsuma, H. Nomura, *Astrophys. J.* **764**, 104 (2013).
22. T. Minamidani *et al.*, *Astron. J.* **141**, 73 (2011).
23. J. Geiss, G. Gloeckler, *Space Sci. Rev.* **106**, 3–18 (2003).
24. K. Willacy, P. M. Woods, *Astrophys. J.* **703**, 479–499 (2009).
25. T. Albertsson, D. Semenov, T. Henning, *Astrophys. J.* **784**, 39 (2014).
26. E. A. Bergin, W. D. Langer, P. F. Goldsmith, *Astrophys. J.* **441**, 222 (1995).
27. K. Furuya, Y. Aikawa, H. Nomura, F. Hersant, V. Wakelam, *Astrophys. J.* **779**, 11 (2013).
28. F. J. Ciesla, S. A. Sandford, *Science* **336**, 452–454 (2012).
29. F. J. Ciesla, *Astrophys. J.* **784**, L1 (2014).

ACKNOWLEDGMENTS

L.I.C. and E.A.B. acknowledge support by NSF grant AST-1008800. C.M.O'D.A. was partially supported by NASA Astrobiology grant NNA09DA81A and by NASA Cosmochemistry grant NNX11AG67G. F.D. was supported by NASA grant NNX12A193G. T.J.H. was supported by U.K. Science and Technology Facilities Council grant ST/J001627/1.

SUPPLEMENTARY MATERIALS

www.sciencemag.org/content/345/6204/1590/suppl/DC1
Materials and Methods
Figs. S1 to S4
Tables S1 to S4
References (*30*–*71*)

30 June 2014; accepted 21 August 2014
10.1126/science.1258066

WATER SPLITTING

Water photolysis at 12.3% efficiency via perovskite photovoltaics and Earth-abundant catalysts

Jingshan Luo,[1,2] Jeong-Hyeok Im,[1,3] Matthew T. Mayer,[1] Marcel Schreier,[1] Mohammad Khaja Nazeeruddin,[1] Nam-Gyu Park,[3] S. David Tilley,[1] Hong Jin Fan,[2] Michael Grätzel[1]*

Although sunlight-driven water splitting is a promising route to sustainable hydrogen fuel production, widespread implementation is hampered by the expense of the necessary photovoltaic and photoelectrochemical apparatus. Here, we describe a highly efficient and low-cost water-splitting cell combining a state-of-the-art solution-processed perovskite tandem solar cell and a bifunctional Earth-abundant catalyst. The catalyst electrode, a NiFe layered double hydroxide, exhibits high activity toward both the oxygen and hydrogen evolution reactions in alkaline electrolyte. The combination of the two yields a water-splitting photocurrent density of around 10 milliamperes per square centimeter, corresponding to a solar-to-hydrogen efficiency of 12.3%. Currently, the perovskite instability limits the cell lifetime.

Compared with other energy resources, solar energy is sustainable and far more abundant than our projected energy needs as a species; thus, it is considered as the most promising energy source for the future. Because of the diffuse nature of solar energy, large arrays of solar cells will have to be implemented. Currently, electricity produced by silicon (Si) solar cells is too costly to achieve grid parity. In contrast, the dye-sensitized solar cell (DSSC) (*1*, *2*) uses cheap materials and facile solution processes. A related type of low-cost solution-processed solar cell based on a perovskite formulation has recently emerged (*3*–*10*). The rapid rise of the solar-to-electric power conversion efficiency (currently 17.9% certified) in less than 5 years makes it highly promising for large-scale commercialization (*11*). Long-term stability, however, is currently a challenge with these solar cells.

The conversion of solar energy directly into fuels is a promising solution to the challenge of intermittency in renewable energy sources, addressing the issues of effective storage and transport. In nature, plants harvest solar energy and convert it into chemical fuel via photosynthesis. Inspired by nature, artificial photosynthesis has been proposed as a viable way to store the solar energy as fuel (*12*, *13*). Hydrogen, which is the simplest form of energy carrier, can be generated renewably with solar energy through photoelectrochemical water splitting or by photovoltaic (PV)–driven electrolysis. Intensive research has been conducted in the past several decades to develop efficient photoelectrodes, catalysts, and device architectures for solar hydrogen generation (*14*–*20*). However, it still remains a great challenge to develop solar water-splitting systems that are both low-cost and efficient enough to generate fuel at a price that is competitive with fossil fuels (*21*).

Splitting water requires an applied voltage of at least 1.23 V to provide the thermodynamic driving

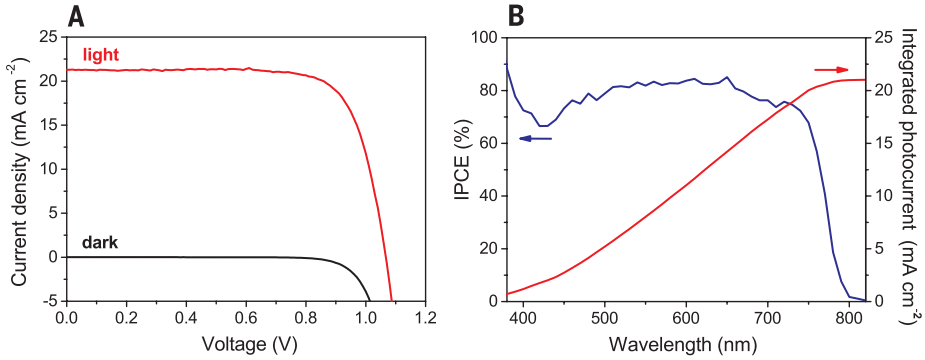

Fig. 1. Performance of perovskite solar cell. (**A**) Current density–potential curve (*J*–*V*) of the perovskite solar cell under dark and simulated AM 1.5G 100 mW cm^{-2} illumination. (**B**) IPCE spectrum of the perovskite solar cell and the integrated photocurrent with the AM 1.5G solar spectrum.

[1]Laboratory of Photonics and Interfaces, Institute of Chemical Sciences and Engineering, School of Basic Sciences, Ecole Polytechnique Fédérale de Lausanne (EPFL), CH-1015 Lausanne, Switzerland. [2]Division of Physics and Applied Physics, School of Physical and Mathematical Sciences, Nanyang Technological University (NTU), 637371 Singapore. [3]School of Chemical Engineering and Department of Energy Science, Sungkyunkwan University (SKKU), Suwon 440-746, Korea.
***Corresponding author. E-mail: michael.graetzel@epfl.ch**

force. Because of the practical overpotentials associated with the reaction kinetics, a substantially larger voltage is generally required, and commercial electrolysers typically operate at a voltage of 1.8 to 2.0 V (*22*). This complicates PV-driven electrolysis using conventional solar cells—such as Si, thin-film copper indium gallium selenide (CIGS), and cadmium telluride (CdTe)—because of their incompatibly low open-circuit voltages. To drive electrolysis with these conventional devices, three to four cells must be connected in series or a DC–DC power converter must be used in order to achieve reasonable efficiency. Multijunction solar cells—such as triple-junction silicon (*18*, *23*), III-V–based solar cells (*16*), and most recently CIGS solar cells in tandem—have also been applied to water splitting (*24*). In contrast, perovskite solar cells have achieved open-circuit voltages of at least 0.9 V and up to 1.5 V according to recent reports (*25*–*27*), which is sufficient for efficient water splitting by connecting just two in series.

Here, we present our results on water splitting using state-of-the-art perovskite solar cells. Our cell was based on $CH_3NH_3PbI_3$, which is processed by means of a two-step spin coating method at 100°C (*28*). The current density–voltage (*J*–*V*) characteristic of a representative perovskite solar cell is shown in Fig. 1A under simulated AM 1.5G solar irradiation (100 mW cm^{-2}) and in the dark. The cell has a short-circuit photocurrent density, open-circuit voltage, and fill factor of 21.3 mA cm^{-2}, 1.06 V, and 0.76, respectively, yielding a solar-to-electric power conversion efficiency (PCE) of 17.3%. The incident photon-to-current conversion efficiency (IPCE) (Fig. 1B) shows that the perovskite solar cell is active from the ultraviolet to 800 nm, which is in good agreement with the band gap (1.5 eV). An integration of the IPCE spectrum with the AM 1.5G solar photon flux yields a current density of 21.1 mA cm^{-2}, corroborating the value that we obtained from the *J*–*V* measurements.

With the highly efficient perovskite solar cell in hand, the next step was to overcome the large water-splitting overpotentials that are typically required to generate H_2 and O_2 at a practical rate. For this purpose, efficient electrocatalysts must be implemented. Our intention was to avoid using the conventional expensive noble metals of low abundance, such as Pt, RuO_2, and IrO_2. In the past decades, tremendous efforts have been devoted to developing low-cost and high-efficiency electrocatalysts for water splitting—for example, MoS_2 and NiMo for the H_2 evolution reaction (HER) (*29*–*31*), and cobalt-phosphate, metal oxides, and hydroxides for the O_2 evolution reaction (OER) (*17*, *32*–*34*). For sustained overall water splitting, the catalysts for the HER and OER must be operated in the same electrolyte. Furthermore, in order to minimize overpotentials in the electrolyte, water splitting should be carried out in either strongly acidic or alkaline electrolyte (*35*). This requirement is a challenge for most of the Earth-abundant catalysts because a highly active catalyst in acidic electrolyte may not be active or even stable in basic electrolyte. For example, MoS_2 is highly active for the HER in acidic electrolyte (*36*), but it is unstable in base. Similarly, most of the metal oxides and hydroxides for the OER are not stable in acidic electrolyte. Thus, it is crucial to develop a bifunctional catalyst that has high activity toward both the HER and OER in the same electrolyte (either strongly acidic or strongly basic). Moreover, the use of a bifunctional catalyst simplifies the system, lowering the manufacturing cost and thus the cost of the resulting hydrogen.

Nickel (Ni) foam is used as the electrode for commercial alkaline electrolysers because of its Earth abundance and porous three-dimensional structure (*22*). Recently, $Ni(OH)_2$ has received great attention for the OER (*33*, *37*, *38*), and it has been shown that the activity could be improved by the incorporation of iron (*39*–*41*). Furthermore, the $Ni(OH)_2$ modified nickel surface has shown an HER rate around four times higher than bare nickel in alkaline electrolyte (*42*, *43*). The high performance of $Ni(OH)_2$ toward both the OER and HER in strongly basic solutions makes it an exceptional bifunctional catalyst. Here, we incorporated iron (Fe) into $Ni(OH)_2$ to form NiFe layered double hydroxides (LDHs), which were directly grown on the surface of the Ni foam by means of a simple one-step hydrothermal growth method (*28*, *40*). For comparison, pristine Ni foam, $Ni(OH)_2$ on Ni foam, and Ni foam with ~3.5-nm Pt nanoparticles (deposited by sputtering on both sides of the foam) electrodes were also studied. The OER characteristics of these different electrodes in 1 M NaOH are shown in Fig. 2A at a scan rate of 1 mV s^{-1}, with the scan direction from positive to negative on the reversible hydrogen electrode (RHE) scale (currents

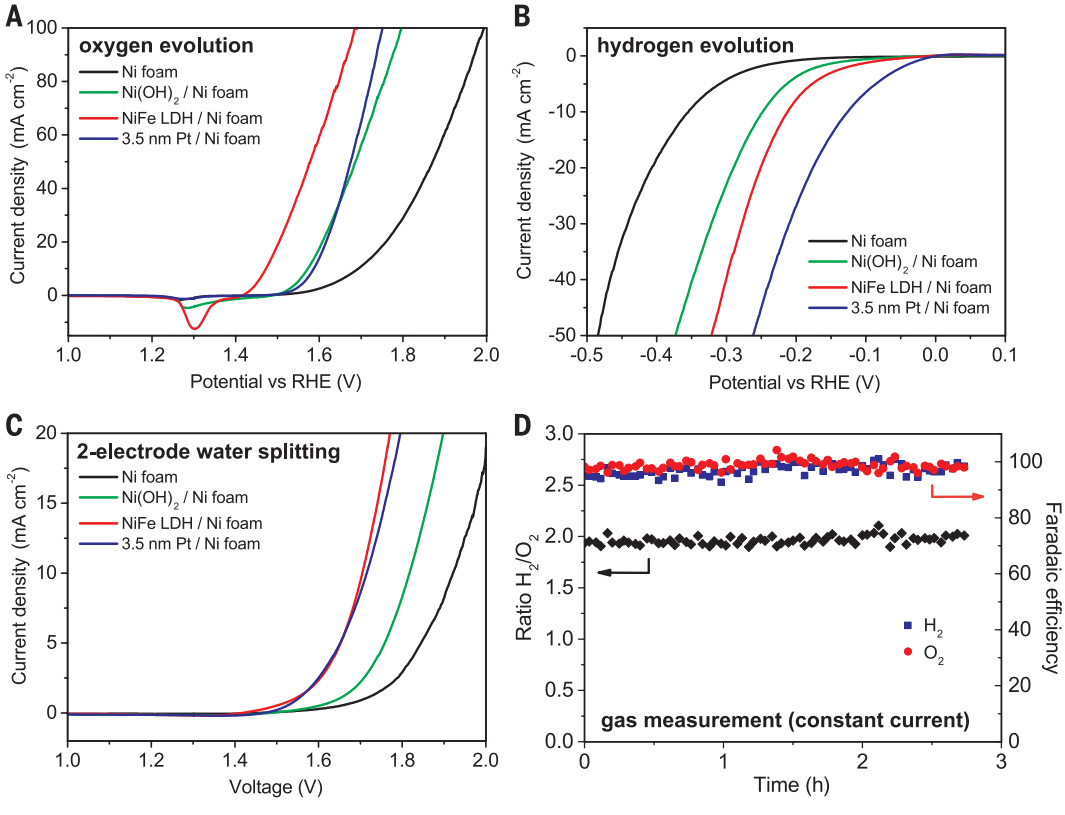

Fig. 2. Electrochemical performance of different catalyst electrodes by linear sweep voltammetry in 1 M NaOH aqueous electrolyte, and gas chromatography measurement of gases evolved from NiFe LDH electrodes. (**A**) OER characteristics of different catalyst electrodes in a three-electrode configuration, scanned in the direction from positive to negative potential on the RHE scale. (**B**) HER characteristics of different catalyst electrodes in a three-electrode configuration, scanned in the direction from negative to positive potential. (**C**) Overall water-splitting characteristics of different catalyst electrodes in a two-electrode configuration, scanned from 2.0 V to 1.0 V. All scan rates were 1 mV s^{-1}. (**D**) Gas ratio and Faradaic efficiency from gas chromatography measurement of evolved H_2 and O_2 from NiFe LDH/Ni foam electrodes in two-electrode configuration, driven by a galvanostat at a current density of 6 mA cm^{-2} (geometric).

are uncorrected and thus include resistive losses in the electrolyte). In the three-electrode configuration, the NiFe LDH/Ni foam electrode requires an overpotential (η_{OER}) of only 240 mV to reach a (projected geometric area) current density of 10 mA cm^{-2}. This potential is 100 mV less than the Pt/Ni foam electrode, whereas $Ni(OH)_2$/Ni foam electrode has nearly the same performance as the Pt/Ni foam for the OER. All of the modified electrodes show improved performance compared with pristine Ni foam. The small cathodic peak at 1.3 V versus RHE is due to the reduction of the oxidized NiFe LDH.

For the measurement of the catalytic activity toward the HER, the electrodes were swept at 1 mV s^{-1} from negative to positive potential on the RHE scale. The performance of the NiFe LDH/Ni foam electrode is much better than the bare Ni foam and slightly better than $Ni(OH)_2$/Ni foam, but worse than the Pt/Ni foam electrode (Fig. 2B). The NiFe LDH/Ni foam electrode requires an overpotential (η_{HER}) of 210 mV to achieve a current density of 10 mA cm^{-2}, which is 100 mV greater than the Pt/Ni foam electrode. The gains that we achieve on the practical level through the use of Earth-abundant catalysts offset the small loss in voltage that we observe. Considering that the HER activity in strong base is usually two to three orders lower than in acidic solution (*43*), the performance of this electrode is remarkable.

To go a step closer to the real application, overall water splitting in a two-electrode configuration was investigated (Fig. 2C). Overall, the NiFe LDH/Ni foam electrode shows nearly the same performance as the Pt/Ni foam electrode, with 10 mA cm^{-2} water-splitting current reached by applying just 1.7 V across the electrodes. To confirm the bifunctional activity of the NiFe LDH/Ni foam electrodes, the evolved gaseous products were quantified by means of gas chromatography. We confirmed quantitative Faradaic gas evolution at the predicted 2:1 ratio for hydrogen and oxygen, within experimental error (Fig. 2D). The exceptional bifunctionality, high activity, and low cost of the NiFe LDH/Ni foam electrode make it highly competitive for potential large-scale industrial applications.

The stability of the catalyst is very important because a practical water-splitting device should ideally last for several years (the longer the lifetime of the device, the lower the cost of the resulting hydrogen). To assess the stability of the NiFe LDH/Ni foam catalyst electrode, 1.8 V was applied to the electrodes, and there is a small degradation over a 10-hour test (fig. S1). However, the performance of the catalyst electrodes fully recovered in the second and third repeat experiments on the same electrode. Thus, although the mechanism of this decrease is yet unclear, the system benefits from the diurnal cycle, in which any slight reduction in photocurrent during daytime illumination is recovered at night. Further characterization of the catalyst electrodes can be found in figs. S2 to S4 and movie S1.

Using the above-demonstrated high-efficiency, low-cost perovskite solar cell and bifunctional water-splitting catalyst, an overall water-splitting cell was assembled (*28*). The schematic diagram of the device is shown in Fig. 3A. The perovskite solar cells were placed side by side and connected with wires to the immersed catalyst electrodes, and simulated solar irradiation provided the energy to split water. A generalized energy diagram is shown in Fig. 3B of the two perovskite solar cells connected in series as a tandem cell for water splitting. The tandem cell used in the integrated device exhibited the *J*–*V* response depicted in Fig. 3C, yielding a V_{OC} of 2.00 V while retaining a high PCE of 15.7%. The predicted operating current density of the combined system (normalized to the total illuminated area of the solar cells) is defined by the intersection of the *J*–*V* curves of both the perovskite tandem solar cell and the catalyst electrodes in the two-electrode configuration (Fig. 3C), giving a value of 10.0 mA cm^{-2}. This operating current, which corresponds to a solar-to-hydrogen efficiency of 12.3%, was confirmed with measurement in the standalone, unbiased light-driven configuration (Fig. 3D). To show the current more clearly, we present only the results of the initial 8 min in Fig. 3D. The performance of the device is further characterized under AM 1.5G chopped light illumination without applying any external bias for 2 hours (fig. S5). The fluctuation of the current under illumination is caused by bubble formation on the surface, which affects the effective surface area. The overall decrease in current on longer time scales is mainly due to the instability of the perovskite solar cell, a challenge that could be addressed by proper passivation and encapsulation techniques. A second representative device, featuring cells with greater stability but lower overall efficiency, is shown in fig. S6.

The operating point of the water-splitting cell occurs very close to the maximum power point of the perovskite tandem cell (9.61 mA cm^{-2} at 1.63 V) (Fig. 3C), indicating that minimal energy is lost in converting electrical to chemical energy in this system. In fact, we have achieved close to the maximum solar-to-hydrogen efficiency possible with the current state-of-the-art perovskite solar cell (in a side-by-side configuration). However, a solar-to-hydrogen efficiency up to 15% is reasonably possible with the fast development of perovskite solar cells (the theoretical upper limit for hydrogen generation in this configuration, as defined by a 1.5 eV band gap and the solar flux, is 17.8%). Improved stability of the device performance can be achieved through passivation of the perovskite solar cells. Furthermore, in the current study, the solar cells are wired with the Ni foam electrodes; however, alternative architectures are possible, for example, by directly attaching the water-splitting catalysts onto the back sides of the solar cells to form an integrated system.

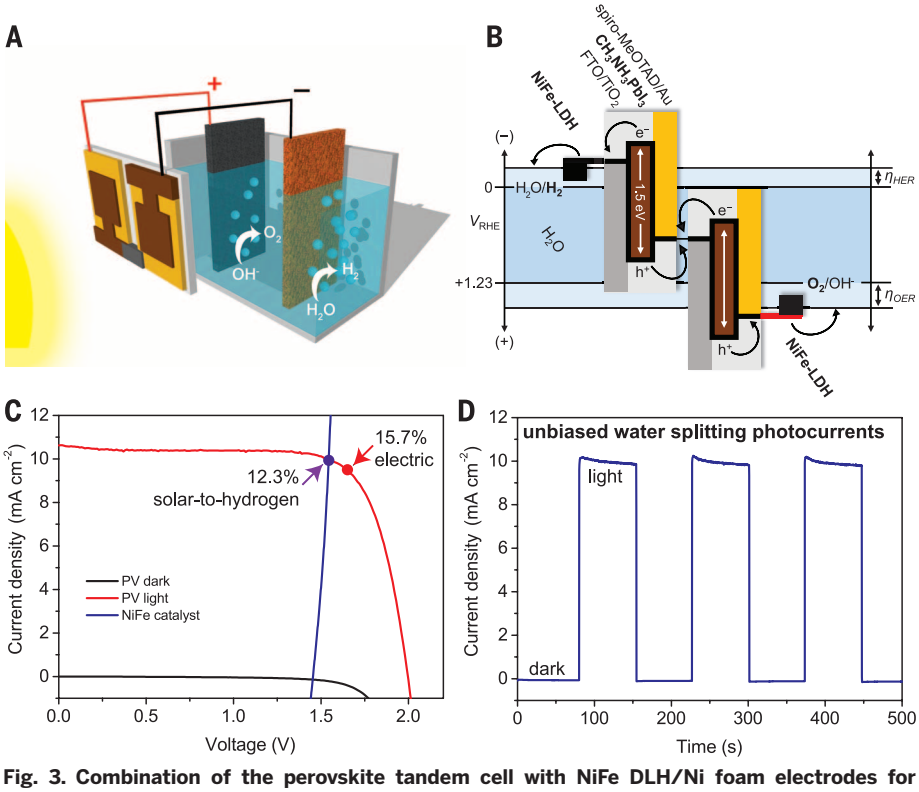

Fig. 3. Combination of the perovskite tandem cell with NiFe DLH/Ni foam electrodes for water splitting. (**A**) Schematic diagram of the water-splitting device. (**B**) A generalized energy schematic of the perovskite tandem cell for water splitting. (**C**) *J*–*V* curves of the perovskite tandem cell under dark and simulated AM 1.5G 100 mW cm^{-2} illumination, and the NiFe/Ni foam electrodes in a two-electrode configuration. The illuminated surface area of the perovskite cell was 0.318 cm^2, and the catalyst electrode areas (geometric) were ~5 cm^2 each. (**D**) Current density–time curve of the integrated water-splitting device without external bias under chopped simulated AM 1.5G 100 mW cm^{-2} illumination.

REFERENCES AND NOTES

1. B. O'Regan, M. Gratzel, *Nature* **353**, 737–740 (1991).
2. M. Grätzel, *Nature* **414**, 338–344 (2001).
3. A. Kojima, K. Teshima, Y. Shirai, T. Miyasaka, *J. Am. Chem. Soc.* **131**, 6050–6051 (2009).
4. J.-H. Im, C.-R. Lee, J.-W. Lee, S.-W. Park, N.-G. Park, *Nanoscale* **3**, 4088–4093 (2011).
5. H.-S. Kim *et al.*, *Sci. Rep.* **2**, 591 (2012).
6. M. M. Lee, J. Teuscher, T. Miyasaka, T. N. Murakami, H. J. Snaith, *Science* **338**, 643–647 (2012).
7. L. Etgar *et al.*, *J. Am. Chem. Soc.* **134**, 17396–17399 (2012).
8. J. Burschka *et al.*, *Nature* **499**, 316–319 (2013).
9. M. Liu, M. B. Johnston, H. J. Snaith, *Nature* **501**, 395–398 (2013).
10. J. H. Heo *et al.*, *Nat. Photonics* **7**, 486–491 (2013).
11. www.nrel.gov/ncpv/images/efficiency_chart.jpg.
12. A. J. Bard, M. A. Fox, *Acc. Chem. Res.* **28**, 141–145 (1995).
13. Y. Tachibana, L. Vayssieres, J. R. Durrant, *Nat. Photonics* **6**, 511–518 (2012).
14. M. G. Walter *et al.*, *Chem. Rev.* **110**, 6446–6473 (2010).
15. A. Fujishima, K. Honda, *Nature* **238**, 37–38 (1972).
16. O. Khaselev, J. A. Turner, *Science* **280**, 425–427 (1998).
17. M. W. Kanan, D. G. Nocera, *Science* **321**, 1072–1075 (2008).
18. S. Y. Reece *et al.*, *Science* **334**, 645–648 (2011).
19. J. Brillet *et al.*, *Nat. Photonics* **6**, 824–828 (2012).
20. J. Luo *et al.*, *Sci. Rep.* **2**, 451 (2012).
21. B. A. Pinaud *et al.*, *Energy Environ. Sci.* **6**, 1983–2002 (2013).
22. K. Zeng, D. Zhang, *Pror. Energy Combust. Sci.* **36**, 307–326 (2010).
23. R. E. Rocheleau, E. L. Miller, A. Misra, *Energy Fuels* **12**, 3–10 (1998).
24. T. J. Jacobsson, V. Fjallstrom, M. Sahlberg, M. Edoff, T. Edvinsson, *Energy Environ. Sci.* **6**, 3676–3683 (2013).
25. E. Edri, S. Kirmayer, M. Kulbak, G. Hodes, D. Cahen, *J. Phys. Chem. Lett.* **5**, 429–433 (2014).
26. E. Edri, S. Kirmayer, D. Cahen, G. Hodes, *J. Phys. Chem. Lett.* **4**, 897–902 (2013).
27. S. Ryu *et al.*, *Energy Environ. Sci.* **7**, 2614–2618 (2014).
28. Materials and methods are available as supplementary materials on *Science* Online.
29. J. Greeley, T. F. Jaramillo, J. Bonde, I. B. Chorkendorff, J. K. Nørskov, *Nat. Mater.* **5**, 909–913 (2006).
30. T. F. Jaramillo *et al.*, *Science* **317**, 100–102 (2007).
31. J. R. McKone, B. F. Sadtler, C. A. Werlang, N. S. Lewis, H. B. Gray, *ACS Catalysis* **3**, 166–169 (2012).
32. R. D. L. Smith *et al.*, *Science* **340**, 60–63 (2013).
33. F. Lin, S. W. Boettcher, *Nat. Mater.* **13**, 81–86 (2014).
34. T. W. Kim, K.-S. Choi, *Science* **343**, 990–994 (2014).
35. E. A. Hernández-Pagán *et al.*, *Energy Environ. Sci.* **5**, 7582–7589 (2012).
36. D. Merki, S. Fierro, H. Vrubel, X. Hu, *Chem. Sci.* **2**, 1262–1267 (2011).
37. M. Gao *et al.*, *J. Am. Chem. Soc.* **136**, 7077–7084 (2014).
38. X. Xia *et al.*, *Sci. Rep.* **2**, 981 (2012).
39. M. Gong *et al.*, *J. Am. Chem. Soc.* **135**, 8452–8455 (2013).
40. Z. Lu *et al.*, *Chem. Commun. (Camb.)* **50**, 6479–6482 (2014).
41. L. Trotochaud, S. L. Young, J. K. Ranney, S. W. Boettcher, *J. Am. Chem. Soc.* **136**, 6744–6753 (2014).
42. R. Subbaraman *et al.*, *Nat. Mater.* **11**, 550–557 (2012).
43. N. Danilovic *et al.*, *Angew. Chem. Int. Ed. Engl.* **51**, 12495–12498 (2012).

ACKNOWLEDGMENTS

The authors thank the Swiss Federal Office for Energy (PECHouse Competence Center, contract SI/500090–02), Nano-Tera NTF project TANDEM, the PECDEMO project, cofunded by Europe's Fuel Cell and Hydrogen Joint Undertaking under Grant Agreement 621252, the European Union for supporting the following projects: NANOMATCELL, under grant agreement 308997, MESO, and GLOBASOL, under the grant agreement 577490. In addition, we are grateful to the Swiss National Science Foundation and Swiss National Center of Competence in Research Molecular Ultrafast Science and Technology for financial support. M.G. thanks the European Research Council for financial support under the Advanced Research Grant (ARG 247404) "Mesolight" and acknowledges his affiliation as a visiting faculty member with Nanyang Technological University Singapore; the King Abdulaziz University Jeddah, Saudi Arabia; and the Advanced Institute for Nanotechnology at SKKU, Suwon, Korea. M.K.N. acknowledges his affiliation as a visiting faculty member to the King Abdulaziz University Jeddah, Saudi Arabia. H.J.F is thankful for the support from Singapore-Berkeley Research Initiative for Sustainable Energy (SinBeRISE) program. J.-H.I and N.-G.P are grateful to the National Research Foundation of Korea grants funded by the Ministry of Science, ICT & Future Planning (MSIP) of Korea under contracts NRF-2012M1A2A2671721 and NRF-2012M3A6A7054861 (Global Frontier R&D Program on Center for Multiscale Energy System).

SUPPLEMENTARY MATERIALS

www.sciencemag.org/content/345/6204/1593/suppl/DC1
Materials and Methods
Figs. S1 to S6
Reference (*44*)
Movies S1 and S2

3 July 2014; accepted 20 August 2014
10.1126/science.1258307

ATMOSPHERIC CHEMISTRY

Infrared-driven unimolecular reaction of CH_3CHOO Criegee intermediates to OH radical products

Fang Liu,[1] Joseph M. Beames,[1] Andrew S. Petit,[1] Anne B. McCoy,[2] Marsha I. Lester[1]*

Ozonolysis of alkenes, an important nonphotolytic source of hydroxyl (OH) radicals in the troposphere, proceeds through energized Criegee intermediates that undergo unimolecular decay to produce OH radicals. Here, we used infrared (IR) activation of cold CH_3CHOO Criegee intermediates to drive hydrogen transfer from the methyl group to the terminal oxygen, followed by dissociation to OH radicals. State-selective excitation of CH_3CHOO in the CH stretch overtone region combined with sensitive OH detection revealed the IR spectrum of CH_3CHOO, effective barrier height for the critical hydrogen transfer step, and rapid decay dynamics to OH products. Complementary theory provides insights on the IR overtone spectrum, as well as vibrational excitations, structural changes, and energy required to move from the minimum-energy configuration of CH_3CHOO to the transition state for the hydrogen transfer reaction.

Hydroxyl (OH) radicals, often termed the atmosphere's detergent, initiate the oxidative breakdown of most trace species in the lower atmosphere (*1*). Photolytic sources dominate the production of OH radicals in the daytime through solar photolysis of ozone, which generates $O(^1D)$ atoms that react with H_2O to form OH radicals, and nitrous acid, with sizable amounts of the latter being produced under high-NO_x conditions. The principal nonphotolytic source of atmospheric OH radicals is alkene ozonolysis, which is an important OH radical initiator in low-light conditions, urban environments, and heavily forested areas (*2*, *3*). Recent field campaigns indicate that alkene ozonolysis accounts for ~30% of tropospheric OH radicals in the daytime and essentially all of the smaller, yet appreciable, OH radical concentration at night (*4*, *5*).

Alkene ozonolysis occurs by cycloaddition of ozone across the C=C double bond and subsequent decomposition of the resultant primary ozonide, releasing ~50 kcal mol^{-1} of excess energy, to produce an energized carbonyl oxide species, known as the Criegee intermediate, and an aldehyde or ketone product (*6*). Further unimolecular decay of the Criegee intermediate leads to formation of OH radicals (*7*, *8*). The OH yield from ozonolysis changes substantially with alkene structure, increasing from ~10% for ethene via the simplest Criegee intermediate CH_2OO to more than 60% for ozonolysis of *trans*-2-butene (*9*, *10*), which proceeds through the methyl-substituted Criegee intermediate CH_3CHOO, the focus of the present study. (See table S1 for chemical structures of relevant species.) Concurrent detection of Criegee intermediates and OH products by photoionization mass spectrometry also shows a large increase in OH yield for alkyl-substituted Criegee intermediates compared to CH_2OO (*11*, *12*).

The efficient production of OH radicals upon ozonolysis of alkenes has been proposed to follow a 1,4-hydrogen atom shift mechanism for alkyl-substituted Criegee intermediates. The computed reaction coordinate, depicted in Fig. 1 for the more stable syn-conformer of CH_3CHOO, involves passage over a transition state with a five-membered, ringlike structure and migration of a hydrogen on the methyl group (an α-hydrogen) to the terminal oxygen to generate vinyl hydroperoxide (VHP, H_2C=CHOOH). This leads directly to O-O bond breakage, yielding OH radical and vinoxy products. A different mechanism is predicted for CH_2OO (and anticonformers of Criegee intermediates), with a substantially higher barrier to reaction that leads to dioxirane (*13*, *14*) and, based on kinetic studies, a much smaller yield of OH products under laboratory and atmospheric conditions (*9*).

This study focuses on infrared (IR) activation of cold Criegee intermediates to drive unimolecular decay to OH products. Specifically, we used IR excitation of *syn*-CH_3CHOO in the CH stretch overtone ($2\nu_{CH}$) region near 6000 cm^{-1} to surmount the barrier associated with 1,4-hydrogen transfer

[1]Department of Chemistry, University of Pennsylvania, Philadelphia, PA 19104-6323, USA. [2]Department of Chemistry and Biochemistry, The Ohio State University, Columbus, OH 43210-1173, USA.
*Corresponding author. E-mail: milester@sas.upenn.edu

from the methyl group to the terminal oxygen, yielding OH radical products under collision-free conditions. This state-selective excitation of cold Criegee intermediates coupled with detection of the OH reaction products enabled direct examination of the IR spectrum of CH_3CHOO, barrier height for hydrogen transfer, and ensuing unimolecular dynamics. This critical hydrogen transfer step in alkene ozonolysis reactions, demonstrated here as a direct unimolecular pathway from a prototypical alkyl-substituted Criegee intermediate to OH products, is responsible for the nonphotolytic generation of OH radicals in the troposphere.

A highly selective IR action spectrum of jet-cooled CH_3CHOO was obtained by scanning the IR laser in the CH overtone region while sensitively probing OH products by laser-induced fluorescence (LIF) on the OH A-X (1,0) $Q_1(3)$ transition. The selectivity of the experiment is twofold: First, the IR action spectrum reveals only those CH_3CHOO vibrational states that couple to the hydrogen transfer reaction coordinate, thereby producing OH. Second, the vibrational states prepared must contain sufficient energy to surmount or tunnel through the barrier to OH products, revealing the effective barrier height. Approximately 11 features are observed in the IR action spectrum from 5600 to 6100 cm^{-1}, as shown in Fig. 2. The central wave numbers and relative intensities of the observed features are listed in table S2. The numerous vibrational features observed indicate that the CH-stretching vibrations in this region are coupled to the reaction coordinate either directly or indirectly through intramolecular vibrational energy redistribution (IVR), as discussed later. The intensities of the IR features reflect a combination of the oscillator strength for the CH overtone or combination bands and the yield of OH products.

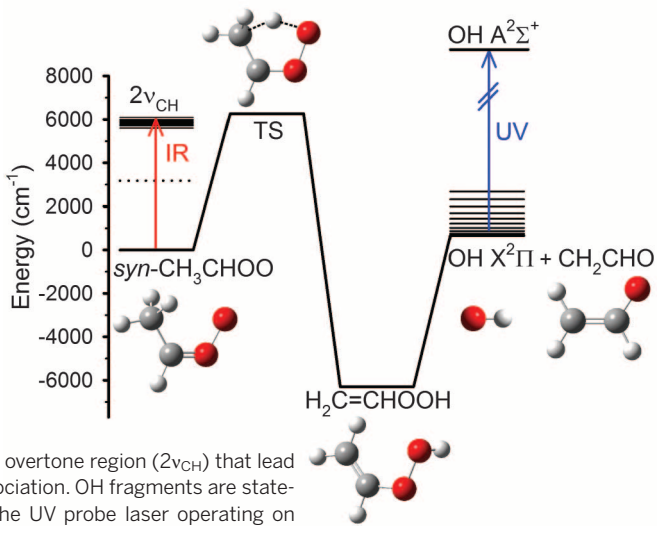

Fig. 1. Reaction coordinate for OH production from the Criegee intermediate. Theoretically computed stationary points including harmonic zero-point energy corrections are shown for *syn*-CH_3CHOO passing over a transition state (TS) to VHP (H_2C=CHOOH) and OH + vinoxy products. In the experiment, the IR pump laser prepares vibrational states in the CH overtone region ($2\nu_{CH}$) that lead to rearrangement and dissociation. OH fragments are state-selectively detected with the UV probe laser operating on the OH A-X (1,0) transition.

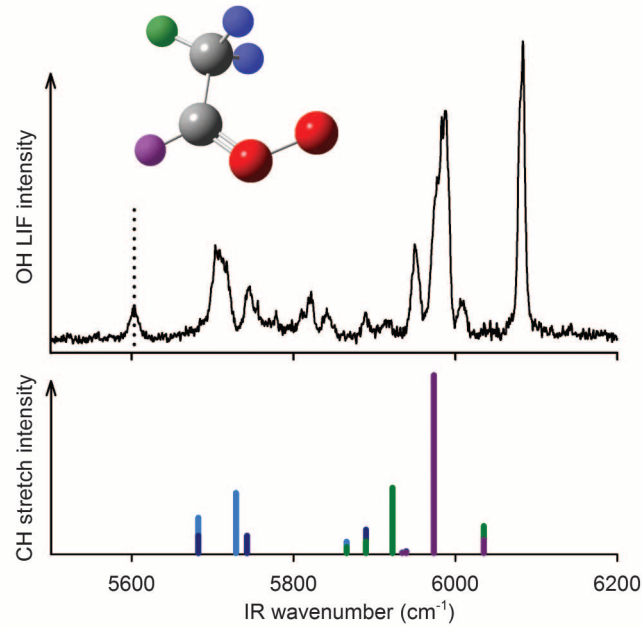

Fig. 2. Experimental and theoretical vibrational spectra. Upper panel: IR action spectrum observed for *syn*-CH_3CHOO in the CH stretch overtone region via LIF detection of OH products. The lowest experimentally observed feature, denoted with a dashed line, sets an upper limit for the effective barrier to reaction. Lower panel: Anharmonic IR spectrum calculated for CH stretches of *syn*-CH_3CHOO using DFT//B3LYP/6-311+G(2d,p). Only vibrational positions, not intensities, are directly comparable between experiment and theory. The colors represent different vibrational modes involved in pure overtones and combination bands (two-color bars), ν_1 (purple), ν_2 (green), ν_3 (light blue), and ν_{13} (dark blue), corresponding to the motions of color-coded hydrogen atoms in the molecular model.

The UV probe transition was selected to obtain the largest IR-induced OH A-X (1,0) LIF signal for the most intense features in the IR action spectrum. A representative OH product-state distribution is shown in fig. S1. The OH products appear within the 5-ns temporal pulse widths of the lasers.

The features observed in the IR action spectrum are attributed to the more stable syn-conformer of CH_3CHOO (depicted in Fig. 2), which was the predominant conformer observed in prior photoionization, ultraviolet (UV) absorption, and microwave spectroscopy studies (*11*, *15*, *16*). *syn*-CH_3CHOO with C_s symmetry has four high-frequency normal mode vibrations ascribed to CH-stretching motions, two of which result from the motion of hydrogen atoms that lie in the COO plane (ν_1, ν_2) and two of which involve motions of the out-of-plane hydrogens, one symmetric and one asymmetric (ν_3, ν_{13}), as listed in table S3; the hydrogen atoms involved in these vibrational motions are color coded in Fig. 2. Thus, 10 IR transitions for *syn*-CH_3CHOO in the CH overtone region should arise from four CH stretch overtone bands (e.g., $2\nu_1$) and six CH stretch combination bands comprising one quantum in each of two CH stretches (e.g., $\nu_2 + \nu_3$). The anharmonic IR frequencies and intensities of these 10 transitions for *syn*-CH_3CHOO were predicted by using density functional theory (DFT) and compared with experiment in Fig. 2; additional comparisons with MP2 and CCSD(T) calculations are presented in fig. S2. The calculated vibrational spectra, specifically the positions and span of the vibrational features, compare favorably with those observed experimentally, suggesting that overtones and combination bands involving all four CH-stretching modes are observed. As discussed below, both the frequencies and intensities of the CH overtone transitions are influenced by higher-order anharmonic couplings to modes that access the transition state to reaction directly.

A few of the IR features exhibit distinctive rotational band contours, although most appear to involve transitions to strongly mixed or overlapping vibrational states. Expanded views of the vibrational features at 5951 and 6081 cm^{-1} are shown in Fig. 3, along with simulations of the band contours based on rotational constants for *syn*-CH_3CHOO (*16*). The fits reveal an initial cold rotational temperature of ~10 K and spectral line broadening arising from rapid (~3 ps) IVR and/or reaction dynamics upon CH stretch overtone excitation. The highest-energy feature in the IR action spectrum at 6081 cm^{-1} appears to be an in-plane CH stretch (hybrid *a*,*b*-type with equal contributions), corresponding to a zeroth-order bright state with $2\nu_1$ character. The feature at 5951 cm^{-1} (purely *c*-type) is attributed to an out-of-plane asymmetric CH stretch (ν_{13}), likely in combination with an in-plane CH stretch (ν_1 or ν_2). The lowest-energy

feature observed at 5603 cm^{-1} is also indicative of an out-of-plane asymmetric CH stretch (ν_{13}); a simulation of the band contour is shown in fig. S3.

Most notably, the lowest-energy feature at 5603 cm^{-1} sets an upper limit of 16.0 kcal mol^{-1} for the effective barrier to unimolecular decay to OH products. This experimental determination of the barrier height is nearly 2 kcal mol^{-1} lower than recent theoretical predictions for the transition state separating the *syn*-CH_3CHOO Criegee intermediate from VHP and OH products of 17.9 kcal mol^{-1} (including zero-point corrections) (*12*, *14*); similar barrier heights are predicted for several alkyl-substituted Criegee intermediates with α-hydrogens (*12*, *17*). This lower estimate for surmounting and/or tunneling through the barrier reveals that unimolecular decay to OH products is more facile than predicted by current theoretical models.

An intrinsic reaction coordinate (IRC) has been computed to obtain insight on the potential energy and structural changes required to move from the minimum-energy configuration of *syn*-CH_3CHOO to the transition state leading to OH products. The IRC is displayed in Fig. 4 as a function of decreasing separation between the transferring α-hydrogen and terminal oxygen (R_{OH}). Other important structural changes along the IRC are a heavy-atom backbone motion to close the HCCOO ring, denoted by the distance between the methyl carbon and terminal oxygen (R_{CO}); the α-hydrogen to methyl carbon bond length (R_{CH}); and a HCCO torsion (τ) associated with internal rotation of the methyl group that moves the α-hydrogen toward the heavy-atom plane. The IRC also reveals that as the α-hydrogen is brought closer to the terminal oxygen, first the CH_3 group rotates and then the CH bond elongates.

Further theoretical analysis (see supplementary materials) identifies the vibrational excitations required to distort *syn*-CH_3CHOO from the minimum-energy configuration toward the transition state for the hydrogen transfer reaction (table S3). Four modes are most relevant: the out-of-plane CH stretch vibrations (ν_3 and ν_{13}), the mode associated with closing of the HCCOO ring (ν_{12}), and the HCCO torsion (ν_{18}). Of these, many quanta of mode ν_{12} are required to reach the transition state, indicating that this mode plays an important role in the unimolecular decomposition mechanism. Excitation of the in-plane CH stretches (ν_1 and ν_2), however, does not lead directly toward the transition state. Nevertheless, analysis of quartic coupling terms in the expansion of the potential (see table S4) shows appreciable coupling among the four CH stretch vibrations (modes ν_1, ν_2, ν_3, and ν_{13}), consistent with the mixed nature of many of the observed bands. These CH stretches are further coupled to states with excitation in the ring-closing (ν_{12}) or HCCO torsion (ν_{18}) mode (see tables S5 to S7). These higher-order couplings enable overtones and combination bands involving all four CH stretch vibrations to access the transition-state region required for reaction.

The theoretical analysis supports the experimental finding that energized Criegee intermediates, prepared here through vibrational activation of CH-stretching vibrations, undergo direct 1,4-hydrogen transfer to produce OH radicals. Both in-plane and out-of-plane CH-stretching vibrations of *syn*-CH_3CHOO, identified as overtone and combination bands by using IR action spectroscopy with OH radical detection, are shown to be coupled to the reaction coordinate. The effective barrier to reaction established by the lowest-energy feature observed at 5603 cm^{-1} indicates that unimolecular decay of methyl-substituted Criegee intermediates, and likely other alkyl-substituted carbonyl oxides with an α-hydrogen, should be more facile in producing OH radicals than anticipated from current models of alkene ozonolysis in the troposphere.

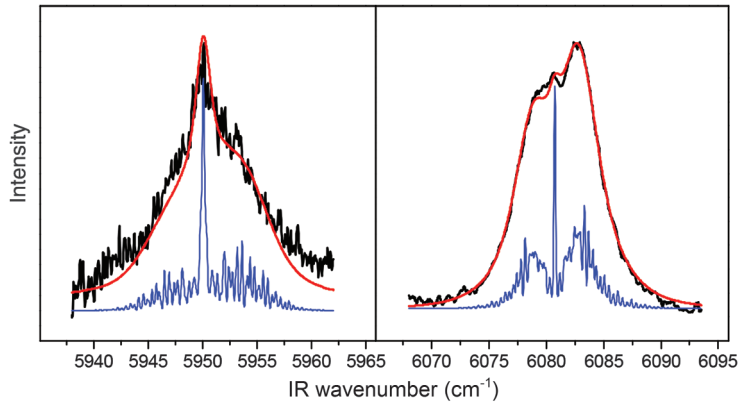

Fig. 3. Expanded views of 5951 and 6081 cm^{-1} features in the IR action spectrum of jet-cooled *syn*-CH_3CHOO. Simulations of rotational band contours for *syn*-CH_3CHOO are superimposed with homogeneous line broadening (red), indicative of rapid (~3 ps) IVR and/or reaction dynamics upon CH stretch overtone excitation, and at the laser bandwidth (blue).

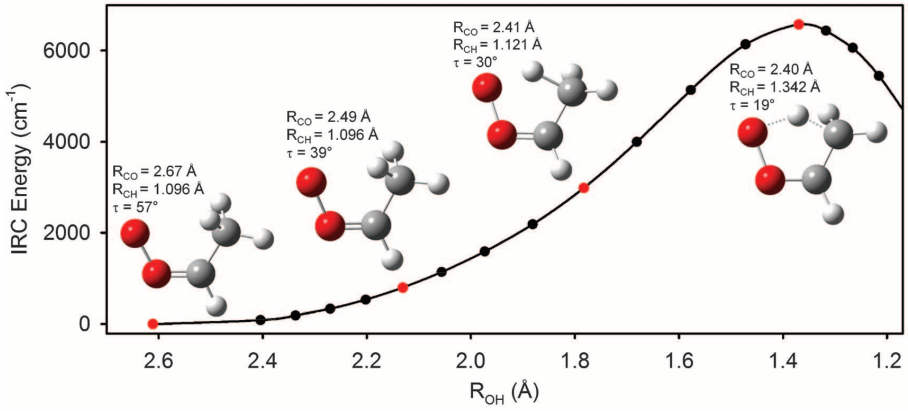

Fig. 4. IRC from the minimum-energy configuration of the Criegee intermediate to the transition state leading to OH products. The IRC is displayed as a function of the terminal oxygen to α-hydrogen distance (R_{OH}). Representative geometric structures along the path (red points) are shown with the methyl carbon to terminal oxygen distance (R_{CO}), the α-hydrogen to methyl carbon bond length (R_{CH}), and HCCO torsional angle (τ, with τ = 0 corresponding to the α-hydrogen lying in the heavy-atom plane) indicated.

REFERENCES AND NOTES

1. B. J. Finlayson-Pitts, J. N. Pitts, *Chemistry of the Upper and Lower Atmosphere* (Academic Press, San Diego, 2000).
2. D. Stone, L. K. Whalley, D. E. Heard, *Chem. Soc. Rev.* **41**, 6348–6404 (2012).
3. R. M. Harrison *et al.*, *Sci. Total Environ.* **360**, 5–25 (2006).
4. K. M. Emmerson *et al.*, *Atmos. Chem. Phys.* **7**, 167–181 (2007).
5. K. M. Emmerson, N. Carslaw, *Atmos. Environ.* **43**, 3220–3226 (2009).
6. D. Johnson, G. Marston, *Chem. Soc. Rev.* **37**, 699–716 (2008).
7. N. M. Donahue, G. T. Drozd, S. A. Epstein, A. A. Presto, J. H. Kroll, *Phys. Chem. Chem. Phys.* **13**, 10848–10857 (2011).
8. A. Novelli, L. Vereecken, J. Lelieveld, H. Harder, *Phys. Chem. Chem. Phys.* **16**, 19941–19951 (2014).
9. J. D. Fenske *et al.*, *J. Phys. Chem. A* **104**, 7821–7833 (2000).
10. A. S. Hasson *et al.*, *J. Phys. Chem. A* **107**, 6176–6182 (2003).
11. J. M. Beames, F. Liu, L. Lu, M. I. Lester, *J. Chem. Phys.* **138**, 244307 (2013).
12. F. Liu, J. M. Beames, A. M. Green, M. I. Lester, *J. Phys. Chem. A* **118**, 2298–2306 (2014).
13. J. M. Anglada, J. M. Bofill, S. Olivella, A. Solé, *J. Am. Chem. Soc.* **118**, 4636–4647 (1996).
14. K. T. Kuwata, M. R. Hermes, M. J. Carlson, C. K. Zogg, *J. Phys. Chem. A* **114**, 9192–9204 (2010).
15. C. A. Taatjes *et al.*, *Science* **340**, 177–180 (2013).
16. M. Nakajima, Y. Endo, *J. Chem. Phys.* **140**, 011101 (2014).
17. L. Vereecken, J. S. Francisco, *Chem. Soc. Rev.* **41**, 6259–6293 (2012).

ACKNOWLEDGMENTS

Additional details of the experiments and calculations are presented in the supplementary materials. This research was supported, in part, through NSF grants CHE-1112016 (M.I.L.), CHE-1362835 (M.I.L.), and CHE-1213347 (A.B.M.). J.M.B. acknowledges support through the Dreyfus Postdoctoral Program in Environmental Chemistry (EP-12-025). Acknowledgment is made to the Donors of the American Chemical Society Petroleum Research Fund for partial support of this research (ACS PRF 53320-ND6). A.S.P. acknowledges support from the U.S. Air Force Office of Scientific Research (USAFOSR) PECASE award under AFOSR grant FA9950-13-1-0157.

SUPPLEMENTARY MATERIALS

www.sciencemag.org/content/345/6204/1596/suppl/DC1
Materials and Methods
Supplementary Text
Figs. S1 to S3
Tables S1 to S7
References (*18*–*33*)

9 June 2014; accepted 20 August 2014
10.1126/science.1257158

CATALYSIS

The critical role of water at the gold-titania interface in catalytic CO oxidation

Johnny Saavedra,[1] Hieu A. Doan,[2] Christopher J. Pursell,[1] Lars C. Grabow,[2]* Bert D. Chandler[1]*

We provide direct evidence of a water-mediated reaction mechanism for room-temperature CO oxidation over Au/TiO_2 catalysts. A hydrogen/deuterium kinetic isotope effect of nearly 2 implicates O-H(D) bond breaking in the rate-determining step. Kinetics and in situ infrared spectroscopy experiments showed that the coverage of weakly adsorbed water on TiO_2 largely determines catalyst activity by changing the number of active sites. Density functional theory calculations indicated that proton transfer at the metal-support interface facilitates O_2 binding and activation; the resulting Au-OOH species readily reacts with adsorbed Au-CO, yielding Au-COOH. Au-COOH decomposition involves proton transfer to water and was suggested to be rate determining. These results provide a unified explanation to disparate literature results, clearly defining the mechanistic roles of water, support OH groups, and the metal-support interface.

The interactions between transition-metal nanoparticles and their metal-oxide supports are often critical for heterogeneous metal nanoparticle catalysts (*1*). However, the roles of the species involved are often not well understood, especially for supported Au catalysts, which are active for selective hydrogenations (*2*, *3*), oxidations (*3*–*5*), and the water-gas shift (WGS) reaction (*3*, *6*). Several factors have been suggested for the exceptionally high activity of Au catalysts, including quantum size effects (*7*), particle geometry (*8*, *9*), and undercoordinated Au atoms (*10*–*12*).

Oxygen activation at the metal-support interface is widely regarded as the key step in room-temperature CO oxidation (*13*–*17*), but substantial debate remains regarding the nature of the active site (*9*, *12*, *17*–*23*). Experimental studies indicate that materials lacking OH groups are inactive (*24*, *25*), yet, the dominant mechanistic models vary in the suggested role of support OH groups and generally highlight the possible role of oxygen vacancies (*16*, *17*, *22*–*24*, *26*). Computational models also have not indicated a clear mechanistic role for the support OH groups, and isotope-labeling studies indicate that CO and O_2 react without incorporating oxygen from the support (*21*, *27*). Perhaps most importantly, as Fig. 1A shows, water markedly increases catalytic activity (*20*, *21*, *26*, *27*), yet only one proposed mechanism suggests a direct potential role for water (*21*).

We performed an experimental and computational study to better understand how water, surface hydroxyls, and the metal-support interface interact during CO oxidation over Au/TiO_2 catalysts. The surface water and hydroxyl groups of a commercial Au/TiO_2 catalyst were deuterated in situ with flowing D_2O/N_2 [supplementary materials (SM) 3.1 and 3.2]. The exchanged catalyst was then flushed with N_2 to remove excess D_2O. Under these conditions, we measured a large kinetic isotope effect (KIE, k_H/k_D = 1.8 ± 0.1, Fig. 1B), consistent with a primary KIE, indicating O-H(D) bond cleavage in the rate-determining step (RDS). Previous studies on Au/Al_2O_3 catalysts (*21*, *28*) found almost no rate difference ($k_H/k_D \approx 1$ to 1.2) upon switching H_2O for D_2O in the feed and concluded that an equilibrium isotope effect might be involved (*21*). Our studies (Fig. 1C) showed that adding 700-Pa H_2O/D_2O to the feed reduced the observed KIE to 1.4. This change was reversible: 60 min after removing H_2O/D_2O from the feed, the KIE approached the original value (Fig. 1C). The large KIE under relatively dry conditions indicates that water or support OH must be involved in the reaction mechanism and that O-H(D) bond cleavage occurs in a kinetically important step. Further, the reaction is subject to saturation kinetics, with added water affecting the kinetics of the RDS.

We explored potential mechanistic roles of O-H bonds with density functional theory (DFT) studies using a 10-atom gold nanocluster residing on four layers of TiO_2(110) support. Unlike previous studies, our computational model (SM 2.5 and 2.6) includes both support OH groups and adsorbed water (*13*, *14*, *18*, *29*). This model substantially simplifies the real system, using a small Au cluster and a single water molecule to represent 3-nm particles and multiple water molecules. Thus, the DFT calculations provide substantial insight into likely elementary reaction steps, but need to be interpreted in the context of the more complex real system.

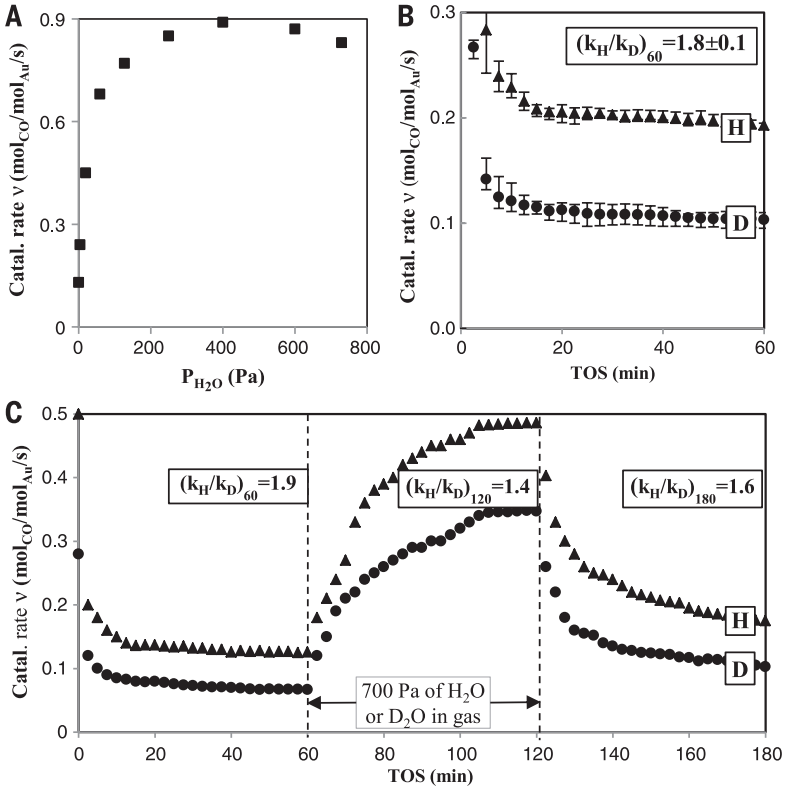

Fig. 1. Water and kinetic isotopic effects on CO oxidation over Au/TiO_2. (**A**) Effects of water on the overall reaction rate. (**B**) Reaction rate for protonated (▲**H**) and deuterated (•**D**) catalysts in the absence of added water (six trials averaged). (**C**) Changes in reaction rate induced by adding 700 Pa of H_2O/D_2O. Reaction conditions: 20°C, 1% CO, 20% O_2, space velocity (SV) = 36 liters g catalyst^{-1} min^{-1}.

[1]Department of Chemistry, Trinity University, San Antonio, TX 78212-7200, USA. [2]Department of Chemical and Biomolecular Engineering, University of Houston, Houston, TX 77204-4004, USA.
*Corresponding author. E-mail: bert.chandler@trinity.edu (B.D.C.); grabow@uh.edu (L.C.G.)

The H_2O molecule adsorbed on a bridging OH group at the metal-support interface through hydrogen bonding interactions; this adsorption motif was ~1.0 eV more stable than adsorption on the Au cluster and ~1.4 eV more stable than adsorption on a bridging OH group away from the interface (SM 6.1). Although we studied several O_2 adsorption and activation pathways (Fig. 2, SM 6.2 and 6.3), we did not find an intermediate species with O_2 bound only to Au atoms near the metal-support interface. In all cases, an essentially barrier-free proton transfer lowered the overall energy of the system, generating H_2O_2* or *OOH (Fig. 2; "*" references species adsorbed to Au). Once *OOH formed, it migrated along the Au particle, allowing atoms near, but not strictly at, the metal-support interface to participate in the reaction.

The KIE and DFT studies indicate proton transfer in a key reaction step, but they do not provide sufficient information to determine if the reaction is initiated by adsorbed water or support OH groups. In situ infrared spectroscopy was therefore used to quantify these species (SM 4.1) and compare catalyst activity to their relative surface concentrations. The non–hydrogen-bonded ν_{OH} stretching vibration centered near 3650 cm^{-1} is exclusively associated with support OH groups, whereas the δ_{HOH} bending vibration centered at 1623 cm^{-1} is exclusively due to adsorbed water. There is also a broad band centered around 3400 cm^{-1} assigned to ν_{OH} for OH groups involved in hydrogen bonding that may have contributions from both water and Ti-OH [complete infrared (IR) analysis in SM 4.1].

Our catalysis studies do not indicate a direct role for support OH groups in the reaction mechanism. Gentle drying with flowing N_2 (Table 1 and Fig. 3A) only removed water and had little effect on the support OH bands. Catalytic activity, however, dropped by an order of magnitude, indicating that adsorbed water, not support OH, is the key proton donor. Further, a constrained ab initio thermodynamic analysis (SM 2.6) indicates that the support OH groups at the metal-support interface are thermodynamically unstable relative to gas-phase water under dry conditions and therefore would be unavailable as proton donors. As water is added to the system, the interfacial support OH groups and weakly adsorbed water are equilibrated and ultimately become indistinguishable.

Several mechanisms reported in the literature invoke OH transfer from the support to Au (*17*, *23*) as an elementary step. Our experimental and DFT studies do not support such a step. The calculated barrier for transferring a Ti^{cus}-OH group to Au [activation energy (E_a) = 1.63 eV, SM 6.5] is too large to be a viable room-temperature pathway. Further, generating *COOH from *CO and *OOH (ΔE = –2.23 eV, E_a = 0.10 eV) is thermodynamically and kinetically far more favorable than the reaction between *CO and Ti^{cus}-OH (ΔE = 0.60 eV, E_a = 0.72 eV, SM 6.5).

To quantify the effects of adsorbed water, we performed a series of adsorption, thermogravimetric analysis (TGA), and kinetics experiments. IR spectroscopy showed water adsorption on titania (not on Au, SM 4.1), consistent with DFT calculations (SM 6.1). The adsorption isotherm quasi-saturated around 700 Pa (1.7 weight %, 13 molecules/nm^2), corresponding to roughly 1.5 monolayers of water on titania, suggesting a bilayer adsorption structure typical for water (*30*). The reaction rate correlates extremely well with the amount of weakly adsorbed water, and the reaction order (1.33, Fig. 3B) is substantially larger than the reaction orders for CO or O_2 (0.01 and 0.1 to 0.3, respectively; SM 5.1 to 5.3).

We further evaluated the reaction kinetics using a Michaelis-Menten (M-M) kinetic model (SM 5.2), which provides quantitative metrics that characterize heterogeneous catalysts (*31*). This model helps distinguish between changes in the inherent activity of the active site (measured with K_R—analogous to the conventional K_M) and the relative number of active sites (associated with ν_{max}). Double-reciprocal plots of the O_2 dependence data (Fig. 3C) yield K_R values that are independent of the water coverage (Fig. 3D), indicating that H_2O did not affect the inherent reactivity of the active sites. The ν_{max} values, however, increased linearly with adsorbed water. Because K_R was essentially constant, this indicates that weakly adsorbed water increased the effective number of active sites rather than changing their inherent reactivity.

Two explanations for increasing the number of active sites are consistent with the DFT studies and recognize the importance of the metal-support interface (*9*, *12*, *18*–*23*). First, if oxygen binding requires protons from weakly adsorbed water, then increasing the water coverage should increase the number of available protons and facilitate O_2 binding. Second, the DFT studies suggest that *OOH can interact with Au atoms that are near, but not strictly at, the metal-support interface. As additional Au sites gain access to protons from water, a greater number of O_2/peroxo-binding sites become available. This increase in active-site density also argues strongly against O atom vacancies on the support being the active sites for O_2 activation, as surface water would be expected to rapidly fill those vacancies.

The conclusion that support OH groups do not directly participate in the reaction mechanism requires a new model to explain why the support and surface OHs strongly influence CO oxidation activity (*13*–*15*, *24*, *25*). Our results indicate that the support OH groups' primary role is to anchor active water near the Au particle and possibly help activate it through hydrogen bonding. The relative number of support OHs near Au particles and their ability to anchor enough water to facilitate the reaction may partially explain the strong support effects reported in the literature (*3*, *17*, *22*, *23*).

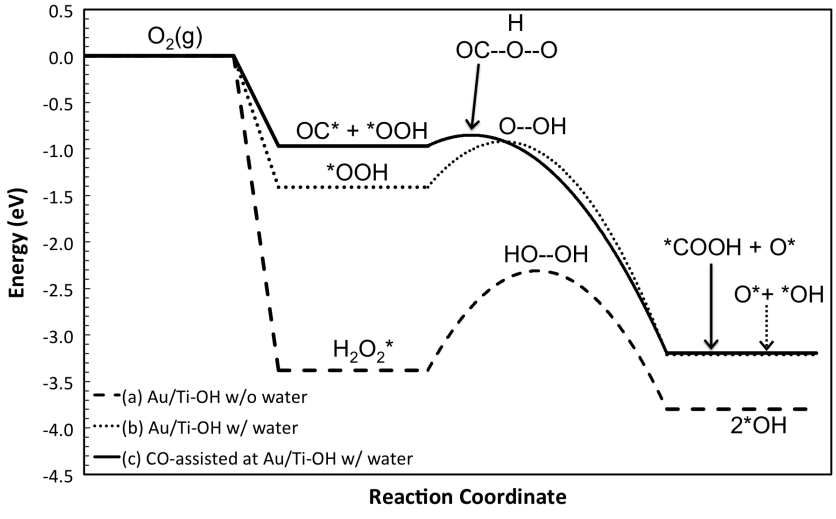

Fig. 2. Potential energy diagrams for O_2 binding and O-O bond activation near the Au/TiO_2 interface. (a): In the absence of H_2O (dashed pathway), O_2 adsorption at the Au/TiO_2 interface initiates a spontaneous transfer of two protons, forming H_2O_2*; (b): with an adsorbed H_2O (dotted pathway), O-O bond activation leads preferentially to O* and *OH; (c): with adsorbed H_2O and CO (solid pathway), O-O scission is facilitated by nucleophilic attack of *CO, resulting in *COOH (carboxyl).

Table 1. Effects of drying treatments on IR spectra and catalytic activity.

Drying treatment*	Ti-OH area†	H_2O area‡	υ (s^{-1})
None	14.3	842	0.32
20°C, 0.5 hour	14.1	503	0.22
70°C, 0.5 hour	14.0	228	0.18
20°C, 16 hours	13.9	131	0.09
70°C, 16 hours	13.8	102	0.03

*N_2 flowing at 50 ml/min. †3741–3645 cm^{-1}. ‡3800–1800 cm^{-1}.

Although the DFT results for O_2 adsorption are congruent with proton transfer as part of the mechanism, they do not explain the observed KIE. The *OOH species have moderate direct decomposition barriers (E_a ~0.5 eV, Fig. 2 and SM 6.3). However, CO-assisted *OOH activation yielding *O and *COOH was found to be extremely facile (E_a = 0.10 eV, Fig. 2). This O-OH dissociation barrier is lower than the previously reported barriers for the related CO-assisted O_2* dissociation on supported and unsupported Au clusters (*10*, *13*, *14*, *18*, *32*). In contrast to the predominant opinion reported in the literature (*16*), the extremely low barriers associated with this pathway suggest that O_2 activation is quite facile in the presence of water and CO.

To explain the observed KIE and close the catalytic cycle, we explored possible *COOH decomposition pathways (SM 6.6); Fig. 4 shows the two most relevant pathways. In the first pathway, the proton is spontaneously transferred from *COOH to the coadsorbed O* (green, ΔE = –0.27 eV, E_a = 0.0 eV), leaving *OH on the surface after CO_2 desorption. Closing the catalytic cycle requires the direct reaction between *OH and *CO (ΔE = 0.10 eV, E_a = 0.40 eV, SM 6.4) to yield *COOH, followed by *COOH decomposition, which returns the proton and restores the active site. The second pathway is initiated by an endothermic proton transfer from *COOH to an adsorbed water molecule (simultaneously transferring a proton to the support) (purple, ΔE = 0.61 eV; E_a = 0.76 eV), followed by CO_2 desorption. The remaining O* reacts with *CO in a well-studied reaction (ΔE = –1.03 eV; E_a = 0.65 eV, SM 6.4).

These pathways are chemically similar, differing primarily in the order of the steps. The reactions between *CO and *O or *OH have fairly similar barriers, and both pathways also go through the same endothermic *COOH decomposition step. This step is the likely RDS because it involves a proton transfer (*COOH to water) and has the highest computed activation-energy barrier (movie S1). DFT calculations based on this transition state (involving a single water molecule) yielded a calculated KIE of 2.55 (SM 6.7), which represents an upper limit to the experimentally determined KIE at low water coverage. The predicted lower limit of the equilibrium isotope effect associated with this step is 1.08. This is somewhat lower than the value we measured at 700-Pa water, but is similar to low values previously reported using higher water pressures (*21*, *28*).

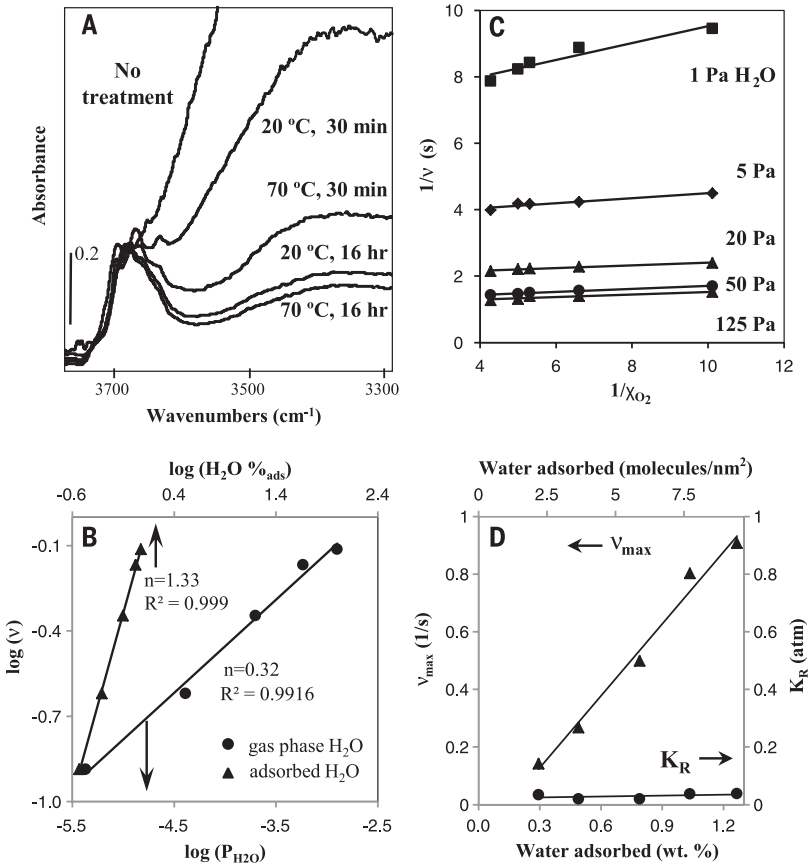

Fig. 3. Infrared spectroscopy and kinetics data showing the changes associated with weakly adsorbed water. (**A**) IR spectra and treatment conditions for gently dried catalysts. (**B**) Reaction order based on gas phase (•) and weakly adsorbed (▲) water (20°C, 1% CO, 20% O_2, SV = 35 liters g catalyst^{-1} min^{-1}). (**C**) Double-reciprocal plots used in Michaelis-Menten kinetic treatment. (**D**) Michaelis-Menten kinetic parameters versus catalyst water content.

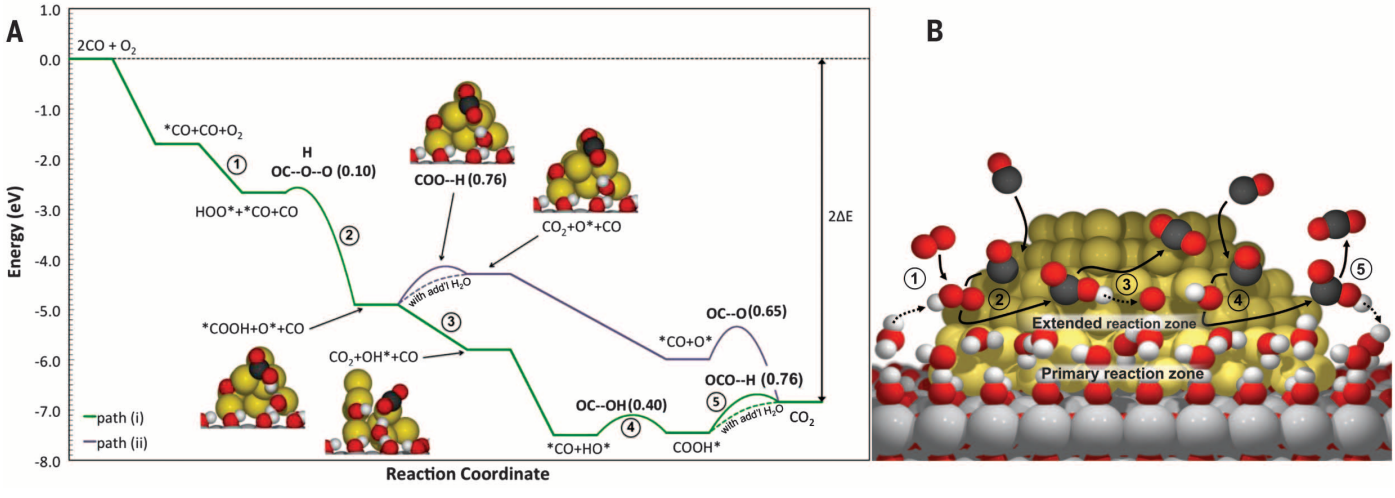

Fig. 4. Proposed reaction mechanism. (**A**) Potential energy diagram; both pathways are limited by a combination of *COOH decomposition and the reaction between *CO and *O(H). (**B**) Schematic representation of the lower (green) pathway.

The involvement of weakly adsorbed water in multiple mechanistic steps is also consistent with the large reaction order (1.3). DFT calculations also indicate that a second adsorbed water molecule in the vicinity of the *COOH species facilitates the proton transfer, which only needs to overcome the thermodynamic barrier (ΔE = 0.70 eV, E_a = 0.70 eV, SM 6.6). Further, at higher water coverage, rapid proton mobility (*33*) can explain the shift to an equilibrium isotope effect. *COOH decomposition has also been identified as the RDS in the related WGS reaction on Cu and Pt (*34*, *35*), and this elementary step is consistent with reports of NaOH promoting CO oxidation over Au catalysts (*17*, *36*).

The CO oxidation mechanism shown in Fig. 4, along with the structural model of support OH groups anchoring and activating water near Au particles, provides a fresh framework for interpreting previous results. This model provides a single active-site description that unifies some very disparate mechanistic information, accounts for the promotional effects of water, and is consistent with previously reported isotope exchange studies (*21*, *27*) that indicate that CO and O_2 must react directly on the Au particles without exchanging O atoms with the support or adsorbed water. At the same time, it maintains the importance of the support OH groups and the metal-support interface without directly involving them in the reaction mechanism. The likely active sites bear a strong resemblance to the WGS mechanism over Au catalysts, where the support anchors water near Au-CO sites (*6*).

This proposed mechanism explains why the O_2 adsorption and activation steps, which are widely regarded as the critical mechanistic steps, have been so difficult to characterize. The fast room-temperature catalysis mechanism requires both water and CO for O_2 binding and activation. Experiments performed without water, particularly ultrahigh-vacuum and DFT studies, ultimately probe different reaction mechanisms than what appears to be the dominant room-temperature pathway on supported catalysts. Similarly, most traditional catalyst studies rarely control or report feedwater contents, which has likely contributed to the wide range of reported CO oxidation activities for Au/TiO_2 catalysts and to the difficulties in understanding the key features of the best catalysts. Finally, this new mechanism brings the interpretation of traditional supported catalyst experiments more in line with computational and surface-science studies, which have largely indicated that the key reaction steps occur on Au (*7*, *9*–*14*, *17*, *29*), without direct participation of the support.

REFERENCES AND NOTES

1. M. Cargnello *et al.*, *Science* **341**, 771–773 (2013).
2. A. Corma, P. Serna, *Science* **313**, 332–334 (2006).
3. T. Takei *et al.*, *Adv. Catal.* **55**, 1–126 (2012).
4. B. N. Zope, D. D. Hibbitts, M. Neurock, R. J. Davis, *Science* **330**, 74–78 (2010).
5. C. Della Pina, E. Falletta, M. Rossi, *Chem. Soc. Rev.* **41**, 350–369 (2012).
6. M. Shekhar *et al.*, *J. Am. Chem. Soc.* **134**, 4700–4708 (2012).
7. M. Valden, X. Lai, D. W. Goodman, *Science* **281**, 1647–1650 (1998).
8. A. A. Herzing, C. J. Kiely, A. F. Carley, P. Landon, G. J. Hutchings, *Science* **321**, 1331–1335 (2008).
9. M. S. Chen, D. W. Goodman, *Science* **306**, 252–255 (2004).
10. H. Falsig *et al.*, *Angew. Chem. Int. Ed.* **47**, 4835–4839 (2008).
11. C. Lemire, R. Meyer, S. Shaikhutdinov, H.-J. Freund, *Angew. Chem. Int. Ed.* **43**, 118–121 (2004).
12. G. Mills, M. S. Gordon, H. Metiu, *J. Chem. Phys.* **118**, 4198 (2003).
13. I. N. Remediakis, N. Lopez, J. K. Nørskov, *Angew. Chem. Int. Ed.* **44**, 1824–1826 (2005).
14. L. M. Molina, M. D. Rasmussen, B. Hammer, *J. Chem. Phys.* **120**, 7673–7680 (2004).
15. R. A. Ojifinni *et al.*, *J. Am. Chem. Soc.* **130**, 6801–6812 (2008).
16. D. Widmann, R. J. Behm, *Acc. Chem. Res.* **47**, 740–749 (2014).
17. M. S. Ide, R. J. Davis, *Acc. Chem. Res.* **47**, 825–833 (2014).
18. I. X. Green, W. Tang, M. Neurock, J. T. Yates Jr., *Science* **333**, 736–739 (2011).
19. T. Fujitani, I. Nakamura, *Angew. Chem. Int. Ed.* **50**, 10144–10147 (2011).
20. M. Daté, M. Okumura, S. Tsubota, M. Haruta, *Angew. Chem. Int. Ed.* **43**, 2129–2132 (2004).
21. M. Ojeda, B.-Z. Zhan, E. Iglesia, *J. Catal.* **285**, 92–102 (2012).
22. M. C. Kung, R. J. Davis, H. H. Kung, *J. Phys. Chem. C* **111**, 11767–11775 (2007).
23. M. Haruta, *Faraday Discuss.* **152**, 11–32, discussion 99–120 (2011).
24. J. A. Singh, S. H. Overbury, N. J. Dudney, M. Li, G. M. Veith, *ACS Catal.* **2**, 1138–1146 (2012).
25. W. C. Ketchie, M. Murayama, R. J. Davis, *Top. Catal.* **44**, 307–317 (2007).
26. H. H. Kung, M. C. Kung, C. K. Costello, *J. Catal.* **216**, 425–432 (2003).
27. J. T. Calla, R. J. Davis, *J. Catal.* **241**, 407–416 (2006).
28. C. K. Costello *et al.*, *Appl. Catal. A* **243**, 15–24 (2003).
29. S. Laursen, S. Linic, *Phys. Chem. Chem. Phys.* **11**, 11006–11012 (2009).
30. J. Carrasco, A. Hodgson, A. Michaelides, *Nat. Mater.* **11**, 667–674 (2012).
31. C. G. Long *et al.*, *J. Am. Chem. Soc.* **130**, 10103–10115 (2008).
32. Z.-P. Liu, P. Hu, A. Alavi, *J. Am. Chem. Soc.* **124**, 14770–14779 (2002).
33. L. R. Merte *et al.*, *Science* **336**, 889–893 (2012).
34. A. A. Gokhale, J. A. Dumesic, M. Mavrikakis, *J. Am. Chem. Soc.* **130**, 1402–1414 (2008).
35. L. C. Grabow, A. A. Gokhale, S. T. Evans, J. A. Dumesic, M. Mavrikakis, *J. Phys. Chem. C* **112**, 4608–4617 (2008).
36. G. M. Veith, A. R. Lupini, N. J. Dudney, *J. Phys. Chem. C* **113**, 269–280 (2009).

ACKNOWLEDGMENTS

We gratefully acknowledge the U.S. National Science Foundation (grants CBET-1160217, CHE-1012395, and CHE-1300619) and the U.S. Department of Energy (NSF/DOE CBET-1258688) for financial support of this work. We also thank R. Rioux (Pennsylvania State University) and Z. Tonzetich (University of Texas at San Antonio) for assistance with transmission electron microscopy and thermogravimetric analysis measurements, respectively. Additional financial support was provided to L.C.G. and H.A.D. through a University of Houston New Faculty Grant. Use of the computational resources at the Center for Nanoscale Materials was supported by the U.S. DOE, Office of Science, Office of Basic Energy Sciences, under contract no. DE-AC02-06CH11357. This work also used the Extreme Science and Engineering Discovery Environment (XSEDE, supported by NSF grant OCI-1053575) and the Kraken computing resource at the National Institute for Computational Sciences (supported by NSF grants 0711134, 0933959, 1041709, and 1041710 and the University of Tennessee). We acknowledge the Texas Advanced Computing Center (TACC) at The University of Texas at Austin for providing high-performance computing resources that have contributed to the research results reported in this paper. Additional computational resources were provided by the Center for Advanced Computing and Data Systems (CACDS, formerly Texas Learning and Computation Center, TLC^2) and the Research Computing Center (RCC) at the University of Houston.

SUPPLEMENTARY MATERIALS

www.sciencemag.org/content/345/6204/1599/suppl/DC1
Materials and Methods
Supplementary Text
Figs. S1 to S12
Scheme S1
Tables S1 to S8
Movie S1

13 May 2014; accepted 8 August 2014
Published online 4 September 2014;
10.1126/science.1256018

PLANT ECOLOGY

Environmental filtering explains variation in plant diversity along resource gradients

Etienne Laliberté,[1]* Graham Zemunik,[1] Benjamin L. Turner[2]

The mechanisms that shape plant diversity along resource gradients remain unresolved because competing theories have been evaluated in isolation. By testing multiple theories simultaneously across a >2-million-year dune chronosequence in an Australian biodiversity hotspot, we show that variation in plant diversity is not explained by local resource heterogeneity, resource partitioning, nutrient stoichiometry, or soil fertility along this strong resource gradient. Rather, our results suggest that diversity is determined by environmental filtering from the regional flora, driven by soil acidification during long-term pedogenesis. This finding challenges the prevailing view that resource competition controls local plant diversity along resource gradients, and instead reflects processes shaping species pools over evolutionary time scales.

For decades, ecologists have sought to understand patterns in terrestrial plant diversity along environmental gradients (*1*). Prominent theories emphasize resource competition as a key driver of diversity (*2*–*4*). Alternatively, it has been proposed that variation in local plant diversity along gradients reflects the filtering of species that are poorly adapted to local environmental conditions (*5*–*7*), highlighting the importance of long-term evolutionary processes in shaping species pools and present-day patterns of plant diversity. These competing hypotheses have been considered in isolation, and further progress can be made only by considering the

multivariate links between resource supply, species pools, and local plant diversity (*8*).

To disentangle how resource supply and species pools interact to control local plant diversity, we studied a >2-million-year coastal dune chronosequence near Jurien Bay in southwestern Australia (30°01′ to 30°24′S; 114°57′ to 115°11′E) (*9*) (also see supplementary materials and methods). The chronosequence provides a distinctive opportunity to explore controls over local plant diversity for several reasons (*10*). First, the broad range in soil age leads to an exceptionally strong natural gradient in nutrient availability and stoichiometry while minimizing variation in other important ecosystem factors such as climate, topography, and parent material (*9*, *11*). Additionally, the fact that all chronosequence stages are found within a short (~10-km) distance ensures that differences in species pool sizes among stages can be due to environmental filters only, thus ruling out dispersal limitation as a causal factor. Further, previous studies showed that nutrient availability strongly constrains plant growth along the chronosequence (*9*, *11*), whereas the open canopy of the shrubland vegetation (average leaf area index <0.5) rules out light as a limiting resource. Finally, the chronosequence is located in one of the most floristically diverse regions on Earth (*12*), enabling us to further our understanding of the controls over plant diversity in species-rich ecosystems.

We evaluated prominent hypotheses about how local soil resources might drive local plant diversity along this resource gradient (*10*) (Fig. 1). First, spatial heterogeneity in soil properties might allow more niches for species with different resource requirements to coexist locally (*13*, *14*). Second, plant diversity might show a unimodal ("hump-shaped") response to soil fertility, declining under higher fertility due to competitive exclusion (*2*, *4*). Third, plant diversity might be greatest where no single soil nutrient strongly limits plant growth (i.e., colimitation) if species show trade-offs in their ability to acquire different nutrients (*15*). Here, we focus on nitrogen (N) and phosphorus (P) because these are the two nutrients that most strongly limit or colimit plant growth along this chronosequence (*9*, *11*). Fourth, a greater diversity in the forms of N or P present in soils might promote plant diversity through resource partitioning, if species differ in their preference for different forms of these nutrients (*16*, *17*). Finally, variation in plant diversity along resource gradients might simply reflect environmental filtering from the regional flora due to key abiotic properties (e.g., soil pH or total [P]), thus leading to species pools of varying sizes, with no need to invoke factors that might influence resource competition (*5*–*7*, *18*) (Fig. 1).

To test these hypotheses, we studied vegetation and soils from 60 permanent 10-by-10–m plots encompassing six chronosequence stages (i.e., 10 replicate plots per stage) for which soils ranged in age from the present day (stage 1) to >2 million years old (stage 6) (*9*). In each plot, we measured species composition, density, and canopy cover of all vascular plants. We use rarefied plant species richness as our measure of local plant diversity, thus controlling for differences in plant density (fig. S1) or sampling effort (*19*). We collected seven surface (0 to 20 cm) soil samples per plot and determined pH and a range of soil nutrients. We also collected leaf samples and analyzed them for nutrients (*11*). Finally, we grew canola (*Brassica napus*) in soils collected from each plot to derive a plant-based index of soil fertility.

To determine the relative importance of soil resource factors and species pool effects on local plant species richness, we translated our conceptual causal model (Fig. 1) into one that could be evaluated quantitatively (*10*). The resulting structural equation model (Fig. 2A) was well supported by the data (χ^2 = 40.1, df = 42, P = 0.555), and none of the independence claims implied by the model were statistically significant (P > 0.05), suggesting that all of the important relationships were specified in the model. As expected from previous results (*9*, *11*), long-term pedogenesis led to strong shifts in the local soil resource factors that have been hypothesized to influence plant species richness, either directly or indirectly via declines in soil total P and pH (Figs. 2 and 3A). However, despite the marked changes in soil resources along the chronosequence, variation in local plant species richness was explained almost entirely by soil pH (Figs. 2A and 3C). By contrast, there were no significant effects on local plant species richness of soil spatial heterogeneity, N:P stoichiometry, or diversity of N and P forms (Fig. 2A), although species richness showed a weak but statistically significant hump-shaped relationship with soil fertility after accounting for all other factors (fig. S2). Still, adding local soil resource factors as predictors to a model that considered only soil pH provided a worse fit to the data [model with only soil pH as predictor: Akaike's information criterion (AIC) = 353; model with soil pH and all local resource factors presented in Fig. 2A as predictors: AIC = 360; likelihood-ratio test: L = 10.1, df = 9, P = 0.344], reinforcing the importance of soil pH as a causal factor.

To determine whether the effect of soil pH on local species richness was the result of environmental filtering from the regional flora, we estimated the species pool size for each chronosequence stage (fig. S3) using the second-order jackknife estimator (*20*) and included this variable in a second model (Fig. 2B). This model was well supported by our data (χ^2 = 48.6, df = 58, P = 0.804) and showed that the negative effect of soil pH on local plant diversity could be explained by environmental filtering from the regional flora (Figs. 2A and 3, C to E).

Our results thus reveal that environmental filtering from the regional flora is the dominant factor explaining variation in local plant diversity along this strong resource gradient, overriding factors associated with local resource competition that have been the focus of several prominent theories. A negative effect of high soil pH on local plant diversity is expected in regions where acidic soils have been common throughout evolutionary history (*18*). Accordingly, the species-rich flora of southwestern Australia has evolved predominantly on ancient, strongly weathered and, therefore, acidic soils (*12*). One explanation underlying the negative effect of high pH on plant diversity is a poor capacity of many plant species to acquire micronutrients or P from calcareous soils (*21*). However, although pH best explained variation in the size of species pools along this

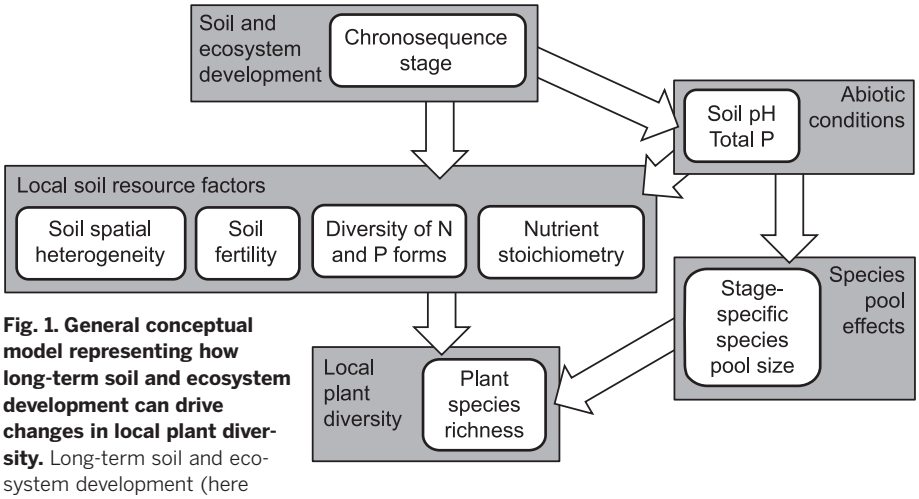

Fig. 1. General conceptual model representing how long-term soil and ecosystem development can drive changes in local plant diversity. Long-term soil and ecosystem development (here represented by "chronosequence stage") can lead to changes in the local soil resource factors that prominent theories emphasize as key drivers of local plant diversity along resource gradients (*10*). In addition, pedogenesis leads to changes in abiotic conditions such as soil P concentrations and pH, which can also affect those local soil resource factors (*10*). Finally, abiotic conditions such as pH can lead to environmental filtering from the regional flora to give rise to stage-specific species pools of varying sizes, which can influence local plant diversity through proportional sampling (*6*).

[1]School of Plant Biology, The University of Western Australia, Crawley, WA 6009, Australia. [2]Smithsonian Tropical Research Institute, Apartado 0843-03092, Balboa, Ancon, Republic of Panama.
*Corresponding author. E-mail: etienne.laliberte@uwa.edu.au

gradient (Fig. 2B), we note that pH and soil total [P] are strongly correlated (correlation coefficient $r = 0.97, P < 0.0001$) (fig. S4). As such, it is possible that environmental filtering from the regional flora along this gradient reflects P toxicity on P-rich soils in species adapted to infertile conditions (*21*) and, conversely, inefficient use of P on P-impoverished soils in species adapted to fertile conditions (*11*).

For completeness, we also tested the effect of individual soil resource factors on local plant diversity separately to explore whether some of these effects could have been deemed significant had the influence of pH and species pools not been appropriately considered (i.e., not included in the models). When tested independently, both the diversity of P forms and leaf N:P ratio showed positive and significant ($P < 0.05$) effects on local plant diversity (table S1), which could have been interpreted as a role for P partitioning (*17*) or greater plant diversity under P limitation (*22*). However, both of these effects disappeared once variation in soil pH and species pool sizes among chronosequence stages were taken into account (Fig. 2).

The importance of evolutionary or biogeographical history in shaping floras to explain global patterns of plant diversity (e.g., the latitudinal gradient of plant diversity) has long been recognized (*23*). However, species pools have received less attention (*6*) than resource competition (*2*, *3*) as explanations for patterns of plant diversity along local resource gradients. Although previous studies have highlighted the importance of environmental filtering and species pools in explaining local plant diversity patterns (*7*, *24*–*27*), our study provides the strongest support to date for this hypothesis by simultaneously evaluating prominent theoretical predictions about the role of soil resources in driving local plant diversity (*10*)—namely those associated with spatial resource heterogeneity (*13*, *14*), resource partitioning (*16*, *17*), nutrient stoichiometry (*3*, *15*), and soil fertility (*2*, *4*). Our finding that environmental filtering from the regional flora is the dominant driver of local plant diversity along this resource gradient is important because our design allows us to rule out dispersal filters while minimizing variation in ecosystem properties (e.g., climate, soil texture, topography, parent material) that can amplify species pool effects. That said, the relatively low productivity and frequent disturbance by fire, coupled with a species-rich flora, might partly explain the strong species pool effects over local plant diversity in this system (*28*). Further research should explore whether local resource factors become more important in more productive and less frequently disturbed systems, as well as in less species-rich systems.

An improved mechanistic understanding of the controls over terrestrial plant diversity is critical for predicting how diversity may respond to environmental change (*29*, *30*). Overall, our study supports the view that local plant diversity patterns along resource gradients cannot be understood without considering the interaction between evolutionary history and local abiotic

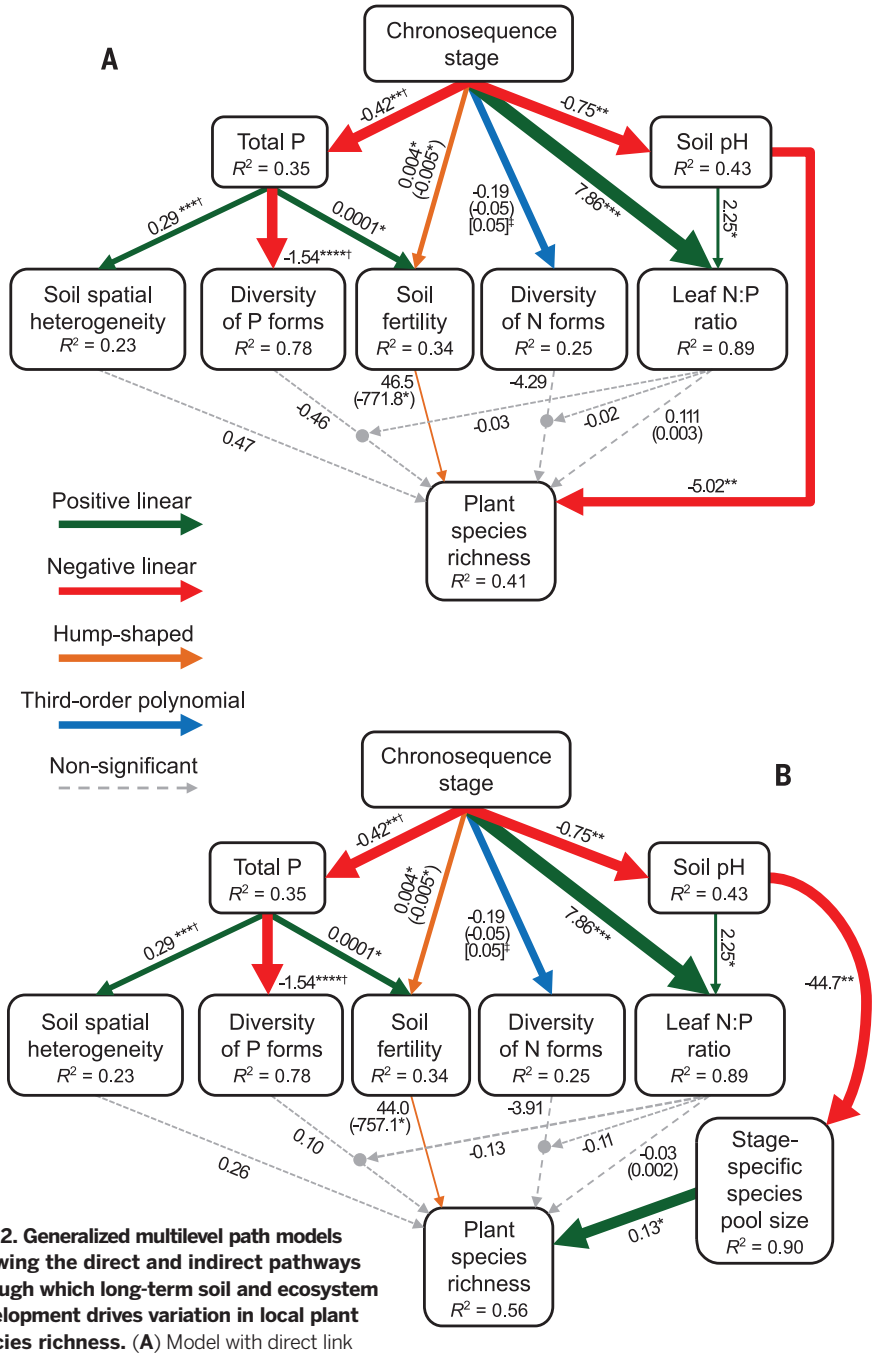

Fig. 2. Generalized multilevel path models showing the direct and indirect pathways through which long-term soil and ecosystem development drives variation in local plant species richness. (**A**) Model with direct link from soil pH to local plant species richness. (**B**) Model with effect of soil pH on local plant species richness mediated via changes in the size of each stage-specific species pool. Rarefaction was used to remove effects of plant density on species richness. Arrows represent the flow of causality. Arrows pointing to other arrows represent interactive effects, whereby one variable is expected to influence the strength and direction of the relationship between two other variables. Both models were well supported by our data [(A): $\chi^2 = 40.1$, df = 42, $P = 0.555$; (B): $\chi^2 = 48.6$, df = 58, $P = 0.804$], and none of the independence claims implied by the model were statistically significant at $\alpha = 0.05$. Path coefficients (i.e., numbers associated with each arrow) are unstandardized regression coefficients. Arrow width is proportional to the standardized path coefficient and can be interpreted as the relative importance of each factor. For nonlinear relationships involving polynomial terms, path coefficients for second-order polynomials are shown in parentheses, whereas those for third-order polynomials are in shown in square brackets. Standardized path coefficients for nonlinear relationships involving polynomial terms were computed using composite variables. Statistical significance for nonlinear relationships was tested using likelihood-ratio tests. Gray dashed arrows represent nonsignificant ($P > 0.05$) relationships. †Total phosphorus (P) was log-transformed in these analyses. ‡$0.05 < P \leq 0.1$; *$P \leq 0.05$; **$P \leq 0.01$; ***$P \leq 0.001$; ****$P \leq 0.0001$. N, nitrogen. R^2, coefficient of determination.

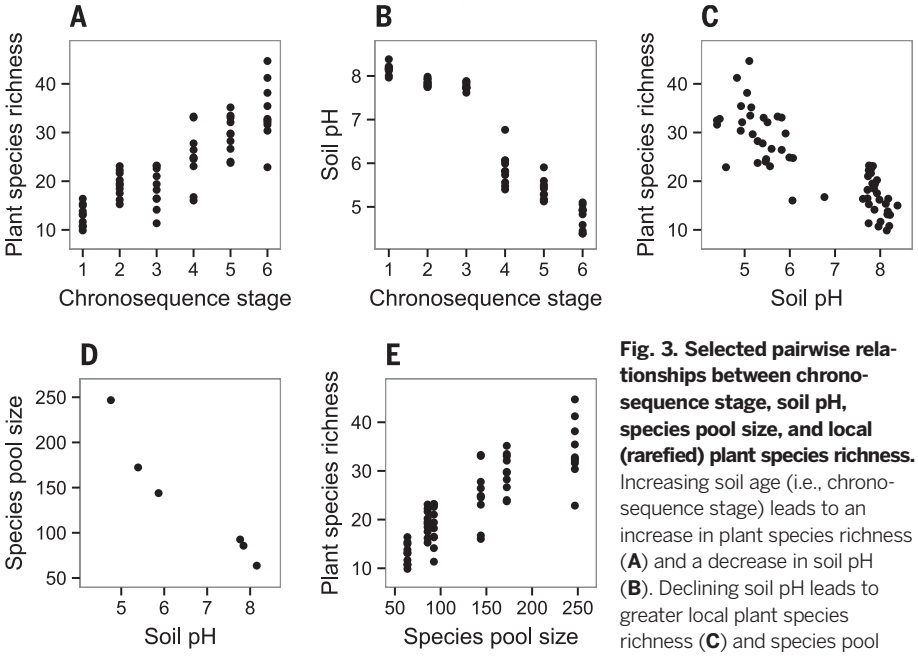

Fig. 3. Selected pairwise relationships between chronosequence stage, soil pH, species pool size, and local (rarefied) plant species richness. Increasing soil age (i.e., chronosequence stage) leads to an increase in plant species richness (**A**) and a decrease in soil pH (**B**). Declining soil pH leads to greater local plant species richness (**C**) and species pool sizes (**D**). Local plant species richness is greater with larger species pools (**E**). In (D), there are only six data points (i.e., one per chronosequence stage) because species pool size was estimated for each stage.

conditions (*5*, *6*). Moreover, it suggests that the prevailing view by which mechanisms associated with local resource competition best explain patterns in local plant diversity along resource gradients should be revisited (*6*). Our results do not imply that local resource factors and niches are unimportant in promoting local plant species coexistence within individual communities (*31*); rather, they suggest that such factors may not explain variation in plant diversity among communities. Our finding about the importance of environmental filtering and species pools in shaping local plant diversity patterns along resource gradients might also help to explain why studies find inconsistent responses of plant diversity to productivity (*8*).

REFERENCES AND NOTES

1. R. H. Whittaker, *Science* **147**, 250–260 (1965).
2. J. P. Grime, *Nature* **242**, 344–347 (1973).
3. D. Tilman, *Plant Strategies and the Dynamics and Structure of Plant Communities* (Princeton Univ. Press, Princeton, NJ, 1988).
4. M. A. Huston, *Am. Nat.* **113**, 81–101 (1979).
5. D. R. Taylor, L. W. Aarssen, C. Loehle, *Oikos* **58**, 239–250 (1990).
6. M. Zobel, *Trends Ecol. Evol.* **12**, 266–269 (1997).
7. J. B. Grace, *Perspect. Plant Ecol. Evol. Syst.* **2**, 1–28 (1999).
8. P. B. Adler *et al.*, *Science* **333**, 1750–1753 (2011).
9. E. Laliberté *et al.*, *J. Ecol.* **100**, 631–642 (2012).
10. E. Laliberté *et al.*, *Trends Ecol. Evol.* **28**, 331–340 (2013).
11. P. Hayes, B. L. Turner, H. Lambers, E. Laliberté, *J. Ecol.* **102**, 396–410 (2014).
12. S. D. Hopper, P. Gioia, *Annu. Rev. Ecol. Evol. Syst.* **35**, 623–650 (2004).
13. G. E. Hutchinson, *Am. Nat.* **93**, 145–159 (1959).
14. D. Tilman, S. Pacala, in *Species Diversity in Ecological Communities* (Univ. of Chicago Press, Chicago, 1993), pp. 13–25.
15. W. S. Harpole, D. Tilman, *Nature* **446**, 791–793 (2007).
16. R. B. McKane *et al.*, *Nature* **415**, 68–71 (2002).
17. B. L. Turner, *J. Ecol.* **96**, 698–702 (2008).
18. M. Pärtel, *Ecology* **83**, 2361–2366 (2002).
19. N. J. Gotelli, R. K. Colwell, *Ecol. Lett.* **4**, 379–391 (2001).
20. A. Chiarucci, N. J. Enright, G. L. W. Perry, B. P. Miller, B. B. Lamont, *Divers. Distrib.* **9**, 283–295 (2003).
21. H. Lambers, F. S. Chapin, T. L. Pons, *Plant Physiological Ecology* (Springer, New York, 2008).
22. H. Olde Venterink, *Plant Soil* **345**, 1–9 (2011).
23. J. Terborgh, *Am. Nat.* **107**, 481–501 (1973).
24. J. B. Grace, S. Harrison, E. I. Damschen, *Ecology* **92**, 108–120 (2011).
25. S. Harrison, H. D. Safford, J. B. Grace, J. H. Viers, K. F. Davies, *Ecol. Monogr.* **76**, 41–56 (2006).
26. L. Gough, J. B. Grace, K. L. Taylor, *Oikos* **70**, 271–279 (1994).
27. M. Pärtel, M. Zobel, *Ecography* **22**, 153–159 (1999).
28. M. A. Huston, *Oikos* **86**, 393–401 (1999).
29. C. J. Stevens, N. B. Dise, J. O. Mountford, D. J. Gowing, *Science* **303**, 1876–1879 (2004).
30. M. J. Wassen, H. O. Venterink, E. D. Lapshina, F. Tanneberger, *Nature* **437**, 547–550 (2005).
31. J. M. Levine, J. HilleRisLambers, *Nature* **461**, 254–257 (2009).

ACKNOWLEDGMENTS

We thank the Western Australia Department of Parks and Wildlife for access to field sites and facilities. This research was supported by a Discovery Early Career Research Award (DE120100352) from the Australian Research Council and research grants from the University of Western Australia to E.L. and a Ph.D. scholarship to G.Z. from the Paul Hasluck Bequest, administered by the Kwongan Foundation. We thank P. Hayes for collection of leaf nutrient data and J. Grace and H. Lambers for providing comments on the manuscript. The vegetation and soil data are available on Dryad (www.datadryad.org).

SUPPLEMENTARY MATERIALS

www.sciencemag.org/content/345/6204/1602/suppl/DC1
Materials and Methods
Figs. S1 to S5
Table S1
References (*32*–*64*)

21 May 2014; accepted 2 September 2014
10.1126/science.1256330

PLANT DEVELOPMENT

Direct roles of SPEECHLESS in the specification of stomatal self-renewing cells

On Sun Lau,[1] Kelli A. Davies,[1] Jessica Chang,[1]* Jessika Adrian,[1] Matthew H. Rowe,[1]† Catherine E. Ballenger,[2] Dominique C. Bergmann[1,2,3]‡

Lineage-specific stem cells are critical for the production and maintenance of specific cell types and tissues in multicellular organisms. In *Arabidopsis*, the initiation and proliferation of stomatal lineage cells is controlled by the basic helix-loop-helix transcription factor SPEECHLESS (SPCH). SPCH-driven asymmetric and self-renewing divisions allow flexibility in stomatal production and overall organ growth. How SPCH directs stomatal lineage cell behaviors, however, is unclear. Here, we improved the chromatin immunoprecipitation (ChIP) assay and profiled the genome-wide targets of *Arabidopsis* SPCH in vivo. We found that SPCH controls key regulators of cell fate and asymmetric cell divisions and modulates responsiveness to peptide and phytohormone-mediated intercellular communication. Our results delineate the molecular pathways that regulate an essential adult stem cell lineage in plants.

In multicellular organisms, the need to generate and maintain diverse cell types and tissues is fulfilled by lineage-specific stem cells (*1*). These stem cell lineages, active postembryonically, produce a defined set of cell types. Although the origins of these lineage-specific stem cells during development are largely obscure, master transcription factors are implicated in their specification in both animals and plants (*1*–*3*). However, low expression levels and/or presence in a limited number of cells makes genome-wide study of these transcriptional regulators by standard chromatin immunoprecipitation (ChIP) assays, the most common technique for studying protein-DNA interactions, technically challenging.

Stomata are epidermal valves that mediate gas exchange between the plant and atmosphere. In *Arabidopsis*, stomatal guard cells are derived

from an epidermal cell lineage (Fig. 1A) (*4*, *5*). Two populations of stomatal precursor stem cells, meristemoid mother cells and meristemoids, have limited self-renewing properties and proliferate without the benefit of a stem cell niche (*4*–*6*). These stem cells are created through the postembryonic activity of SPEECHLESS (SPCH) in a subset of protodermal cells (*7*, *8*). SPCH is a control point through which developmental, environmental, and phytohormone signals are integrated (*4*, *5*). However, no targets of SPCH have been reported, and thus the sphere of its regulatory influence is unknown. Here, we develop a ChIP method optimized for rare developmental regulators and profile the genome-wide binding of SPCH in vivo. In combination with multiple transcriptional response data sets, our ChIP-sequencing (ChIP-seq) data indicate that SPCH programs an entire lineage by promoting fate transitions and asymmetric cell divisions (ACDs). SPCH also modulates the sensitivity of stomatal lineage cells to hormone and peptide/receptor–mediated signaling. Our results suggest how this lineage exhibits considerable autonomy while still coordinating with the overall organ development program.

Like many developmental regulators, SPCH expression is transient and limited to few cells (Fig. 1A). Standard ChIP assays on SPCH yielded only modest target enrichment (~4-fold, Fig. 1C, blue box), and thus we needed improved ChIP sensitivity for the detection of endogenously weak signals. We hypothesized that if background signals in a ChIP assay could be kept low, increasing the experimental scale would lead to a disproportional increase in signals from targets (true signal) over background (Fig. 1B). Therefore, performing ChIP at a large scale may achieve high target enrichment even for low-abundance proteins. We tested this hypothesis with ChIPs at three different scales on a *spch* mutant line bearing a complementing, Myc-tagged SPCH variant driven by its native promoter (SPCHpro:SPCH2-4A-MYC) (fig. S1). The scales represented 4, 8, and 16 times (or 6, 12, and 24 g) the input materials used in a typical *Arabidopsis* ChIP experiment. ChIP-qPCR (quantitative polymerase chain reaction) assays of SPCH on the promoter of *TOO MANY MOUTHS* (*TMM*) showed that scale increase improves target enrichment up to 600-fold at 16x (or a >30-fold increase in enrichment with a 4-fold scale increase) (Fig. 1C, three rightmost columns). Thus, weak signals can be enhanced by maximizing input. We termed this method Maximized Objects for Better Enrichment (MOBE)–ChIP.

To profile genome-wide binding events of SPCH, we performed and pooled six MOBE-ChIPs on SPCHpro:SPCH2-4A-MYC and on a wild-type (WT) control for high-throughput sequencing (scale, 16x; total, 144 grams per genotype) (Fig. 1C, red box, and fig. S2B). For comparison, standard ChIP-seq was also included [pooled from nine independent ChIPs on SPCHpro:SPCH2-4A-YFP (yellow fluorescent protein) and nucGFP (green fluorescent protein) at 4x] (Fig. 1C, blue box, and fig. S2A). MOBE-ChIP-seq confirmed the ChIP-qPCR results at the *TMM* promoter, revealing a single peak with an enrichment score of 178 [$-\log_{10}(q\text{ value})$, 1.2×10^{6}]; the corresponding peak from our 4x run had a score of 1.2 [$-\log_{10}(q\text{-value})$, 5.7] (Fig. 1D). Low background signal is also a genome-wide trend. Using the peak-calling algorithm ChIP-seq Analysis in R (CSAR) (*9*), we detected peaks with an enrichment score as low as 1.62 at a false discovery rate (FDR) of 1×10^{-6}, in contrast to other studies whose peaks above threshold scores of 1.85 and 79.6 were detected at FDRs of 0.01 and 0.001, respectively (table S1) (*10*, *11*). The ability to identify these low-coverage peaks is indicative of the power of signal enrichment. Thus, through MOBE-ChIP-seq, we generated a comprehensive in vivo genome-wide binding map of SPCH.

Using two complementary peak-calling pipelines, we identified 8327 SPCH-bound regions (tables S2 and S3). Seventy percent of the SPCH binding peaks are associated with gene promoters, mostly within 500 base pairs upstream of the transcriptional start site (Fig. 2A and fig. S3). De novo discovery of enriched motifs in the binding peaks identified CDCGTG as the top-scoring motif; this variant of the E-box (CACGTG), to which basic helix-loop-helix (bHLH) proteins typically bind, is enriched at the summit of the SPCH peaks (Fig. 2B and fig. S4).

To focus on loci most likely to respond transcriptionally to SPCH binding, we generated a "high-confidence" subset of peaks that were nonintergenic with enrichment scores ≥10 (table S2). Among the high-confidence targets, Gene Ontology (GO) terms for genes involved in regulation of transcription, signaling, response to stimulus, and regulation of hormone levels were significantly enriched (Fig. 2E, fig. S5, and table S4). This suggests that in the initiation of the stomatal lineage, SPCH could act as a mediator of environmental and hormone inputs that are translated into further downstream transcriptional and signaling networks. The enrichment of the GO term "protein targeting to membrane" is interesting given the membrane-associated polarization of stomatal lineage proteins BASL and POLAR during asymmetric divisions (*12*, *13*).

To correlate SPCH binding with transcriptional responses on a genome-wide scale, we compared the high-confidence SPCH targets to data sets representing genes expressed in response to SPCH induction (fig. S6 and table S5) and those enriched for genes preferentially expressed in the stomatal lineage (*13*) (fig. S7). Significant enrichment of the SPCH targets was found among genes both up- and down-regulated in response to SPCH induction (27 and 20%, respectively) (Fig. 2C) and in plants with excess or no meristemoids (31 and 12%) (Fig. 2D). By chance, SPCH would be predicted to bind to ~4.5% of genes in the data sets (1517 targets out of 33,602 *Arabidopsis* genes). Overall, these comparisons indicate that nearly a

[1]Department of Biology, Stanford University, Stanford, CA 94305, USA. [2]Howard Hughes Medical Institute, Stanford University, Stanford, CA 94305, USA. [3]Carnegie Institution for Science, Stanford, CA 94305, USA.
*Present address: Department of Genetics, Stanford Medical School, Stanford, CA 94305, USA. †Present address: Agricultural Research Service, 800 Buchanan Street, Albany, CA 94710, USA.
‡Corresponding author. E-mail: dbergmann@stanford.edu

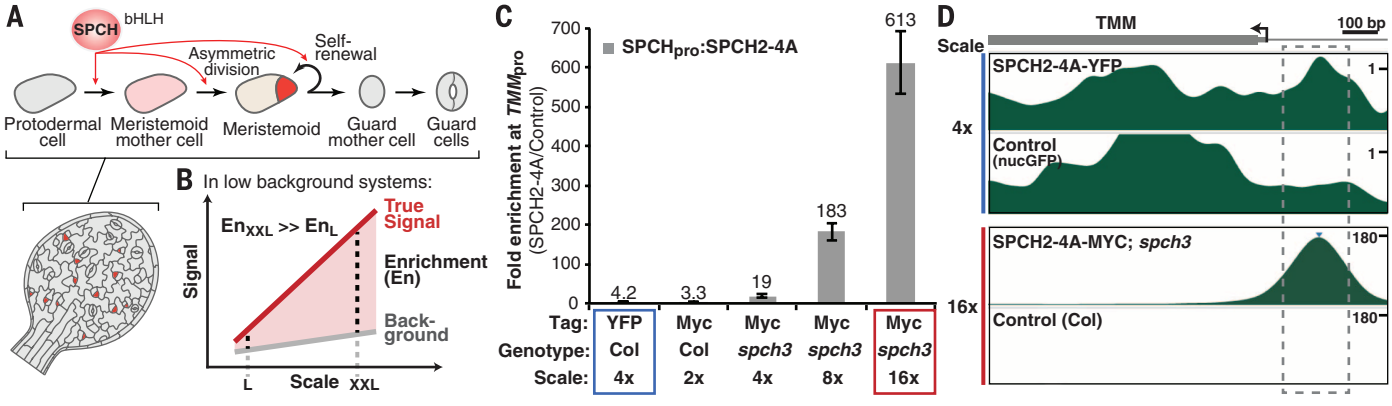

Fig. 1. Chromatin immunoprecipitation (ChIP) optimized for cell-type–specific studies in vivo. (**A**) *Arabidopsis* stomatal development scheme. SPCH controls the initiation and proliferation of the stem cell–like stomatal lineage precursors (pink and red cells). (**B**) Model for improving target enrichment in ChIPs through increasing experimental scale. (**C** and **D**) ChIPs at larger scales improve target enrichments. ChIP-qPCR assays of a SPCH variant on the *TMM* promoter performed at the indicated conditions (C). SPCH ChIP-seq profiles at *TMM* (D) generated from ChIPs at 4x and 16x [blue and red box in (C), respectively]. The *y* axis represents the enrichment values; note scales. Dashed box marks the SPCH-binding region.

quarter (23%) of the SPCH targets are differentially expressed (table S6) and SPCH may activate or repress a large number of its targets directly.

Meristemoid-active stomatal regulators are among the direct SPCH targets (Fig. 2F, fig. S8A, fig. S9, and table S7). SPCH binds to its own promoter and to the promoter of genes that encode its heterodimeric bHLH partners, ICE1/SCRM and SCRM2 (*14*), and induces their expression (Fig. 2, F and G, and fig. S8A). Although initial activation of *SPCH* may not require SPCH protein (fig. S10), this positive feedback loop may be an essential part of a bistable switch that converts the initially low and stochastic expression of SPCH into an active SPCH-SCRM heterodimer to drive stomatal lineage fates. SPCH also binds and activates expression of genes encoding the secreted ligand EPF2, the receptor TMM, and the ERECTA family of receptor-like kinases (Fig. 2, F and G, and fig. S8A), all of which enforce proper patterning by restricting proliferation in the early stomatal lineage and act upstream of kinases that target SPCH for posttranslational down-regulation (*4*, *15*–*17*). Further, SPCH binds to the promoters and activates expression of *BASL* and *POLAR*, which encode polarly localized proteins, suggesting a direct role in regulating the ACD process (Fig. 2, F and G). SPCH binding is not associated with genes that encode a later expressed stomatal lineage EPF (*EPF1*), an EPF not expressed in the stomatal lineage (*CHALLAH*) or the broadly expressed mitogen-activated protein kinase kinase kinase (MAPKKK) YODA (fig. S8B). Taken together, our ChIP-seq and RNA-seq data reveal the broad and direct roles of SPCH in sustaining a SPCH transcriptional cascade, establishing meristemoid identity and mediating ACDs.

The CDCGTG motif appears in the SPCH-bound regions of stomatal targets like *ICE1*, *TMM*, and *ERL2*. In *ICE1*, SPCH binds in two peaks centered on the locations of two CDCGTG motifs (fig. S11). To test the role of SPCH-binding motifs in *ICE1* expression, we generated a reporter bearing point mutations in the two peak-associated motifs (Fig. 2H) to compare to the WT reporter. Consistent with previous reports (*14*), expression of the WT promoter reporter (ICE1pro) was observed in the stomatal lineage; however, the mutant reporter (mICE1pro) was nearly undetectable (Fig. 2H and fig. S12). Similar dependence was seen with the SPCH–up-regulated gene At2g34510, which contains CDCGTG within a strong intronic SPCH binding peak. Deletion of the SPCH binding region abrogated early stomatal lineage-specific expression (fig. S13).

An intriguing meristemoid behavior is the ability to self-renew through ACDs. Beyond requirements for SPCH activity and the polarly localized BASL (Fig. 2F), however, little is known about the ACD process. Among SPCH targets, *ARK3/AtKINUa* (Fig. 3A) caught our attention as it encodes a plant-specific kinesin in the preprophase band (*18*). In plants, the preprophase band marks the future division plane (*19*). Confocal analysis of ARK3pro:ARK3-YFP showed localization to preprophase bands of asymmetrically

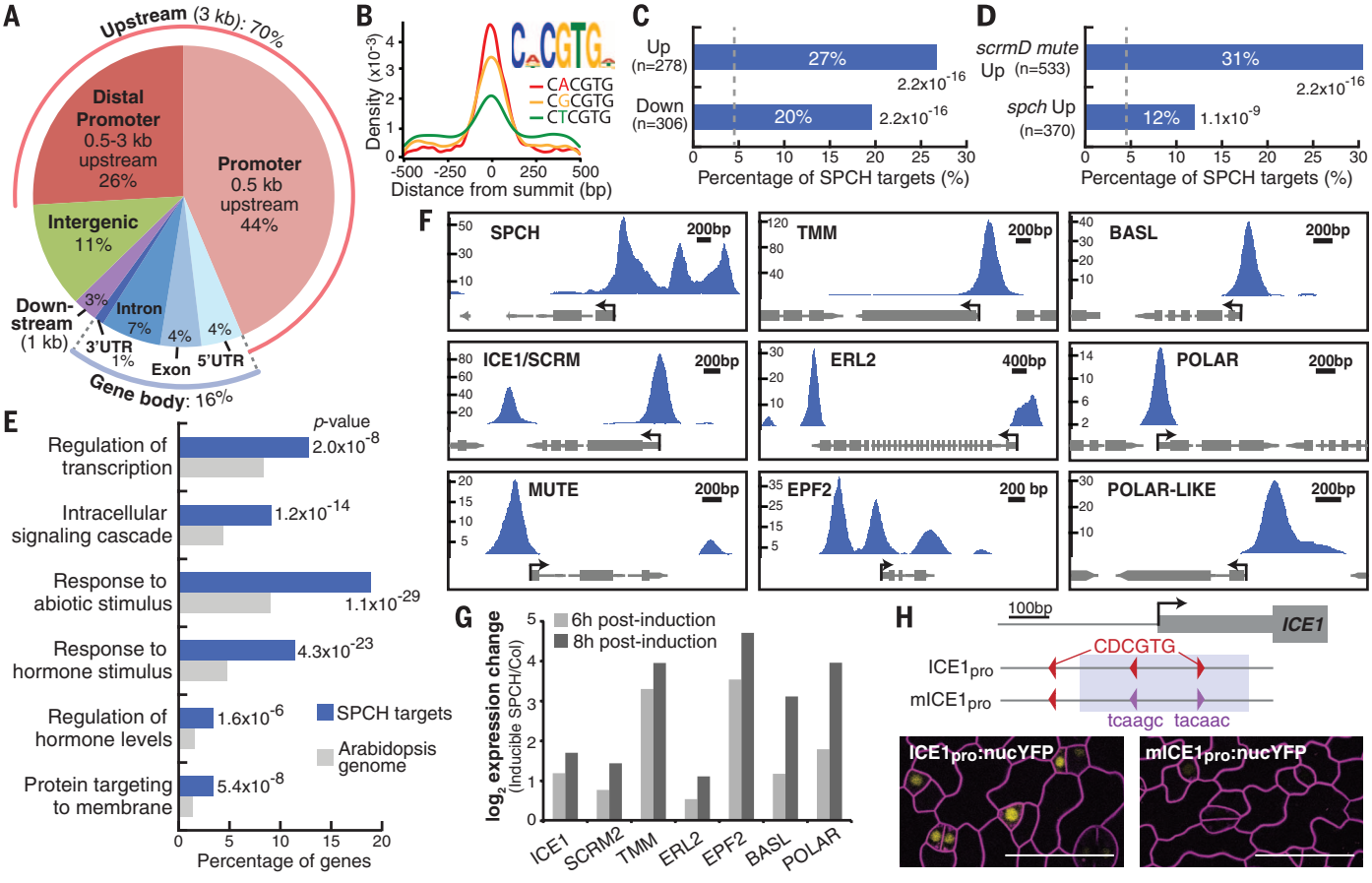

Fig. 2. Genome-wide analysis of SPCH-binding targets reveals direct roles in lineage specification and asymmetric cell divisions. (**A**) Distribution of SPCH-binding peaks relative to gene structure. (**B**) Top-scoring motif (E value, 7.5 × 10^{-365}) and the position of its three variants in SPCH-binding peaks. (**C** and **D**) Percentage of SPCH targets among differentially expressed genes in RNA-seq analysis of inducible SPCH1-4A (C), and microarray analysis of meristemoid-enriched (*scrmD mute*) or -depleted (*spch*) mutants (*13*) (D). *P* values are calculated by Fisher's exact test. Dashed line indicates percentage by chance. (**E**) Select enriched GO terms of SPCH target genes. (**F** and **G**) SPCH binds and activates key stomatal regulators. ChIP-seq profiles of select stomatal genes (F). The *y* axis represents peak score (CSAR), and arrows indicate gene orientation and transcriptional start sites. Gene expression changes upon induction of SPCH in RNA-seq analysis (G). (**H**) Importance of SPCH-binding motif (red) on *ICE1* expression. Mutation of two motifs (purple, mICE1pro) within the SPCH-binding peak (blue shading) abrogates *ICE1* expression (yellow). Confocal images of 4-dpg abaxial cotyledons have ML1pro:mCherry-RCI2A–marked cell outlines (purple). Scale bar, 40 μm.

dividing meristemoids (Fig. 3B). Coexpression with SPCHpro:SPCH-CFP indicated that SPCH precedes ARK3, consistent with SPCH activating *ARK3* expression (Fig. 3, C to E). To ascertain its function in the stomatal lineage, we reduced ARK3 expression by driving an artificial microRNA against it with the SPCH promoter (*SPCHpro:amiR-ark3*). In the cotyledon epidermis of *amiR-ark3*–expressing plants, we observed clusters of meristemoid-like small cells at 4 days postgermination (dpg) that developed into clusters of stomata at 11 days (Fig. 3, G and I, brackets). These small cell clusters, which displayed diminished physical asymmetry, appear to arise from misplaced but complete division planes. Notably, cell wall stubs or other evidence of incomplete divisions were not observed. The *amiR-ark3* phenotypes resembled those associated with *basl* mutants (*12*) and are hallmarks of loss of ACD capacity. Thus, ARK3 appears to be a new player essential for ACD, possibly through regulating preprophase band placement, and establishes a direct link between SPCH and the ACD machinery.

SPCH initiates a lineage with autonomous control over cell division and fate determination. Nonetheless, the stomatal lineage is also coordinated with developmental programs operating across tissues and organs. Phytohormones play critical roles in coordinating development, and recent reports indicate that auxin, brassinosteroid (BR), and abscisic acid regulate stomatal development (*20*–*23*). BR controls stomatal development through phosphorylation of YODA and SPCH by its central glycogen synthase kinase 3–like kinase, BIN2 (Fig. 4F) (*21*, *22*). Among SPCH target categories, BR biosynthetic and response genes show significant enrichment (fig. S14). Notably, SPCH binds to the promoters of *BIN2* and *CPD*, which encodes an essential enzyme for BR biosynthesis (Fig. 4, A and F), and the absence of *CPD* results in stomatal overproduction (*24*). We tested the effect of SPCH on the expression of BR genes by reverse transcription qPCR (RT-qPCR) in the meristemoid-enriched line SPCHpro:SPCH2-4A-YFP (Fig. 4B). Consistent with inhibition of BR signaling, we found that *BIN2* expression is elevated, whereas *CPD* is repressed (Fig. 4B). Supporting BIN2's role in promoting SPCH function, stomatal lineage-specific expression of BIN2-1 led to small cell clusters in cotyledons, similar to those observed upon SPCH overexpression (Fig. 4C). Thus, our results suggest the presence of feedback by SPCH counteracting BR signaling (Fig. 4F). SPCH also binds to genes encoding the BR signaling effectors, the BZR1 family of transcription factors (BZR1, BES1/BZR2, and BEH1 to BEH4), and BIM2, the putative dimeric partner of BES1 (*25*–*27*). *BEH1* to *BEH4* and *BIM2* were up-regulated in the meristemoid-enriched mutant, and *BIM2* exhibited stomatal lineage-specific expression (Fig. 4, B and D). Epidermal expression of *bes1-D* (*26*) correlates with an increase in stomatal density, whereas a *bes1* RNA interference (RNAi) knockdown line (*27*) exhibited a trend toward lower stomatal density (Fig. 4E). This role in promoting stomatal development may be explained through the known repression of the BR biosynthetic genes by the BZR1 family (*28*). Thus, SPCH-mediated induction of *BIN2* and repression of *CPD* (either

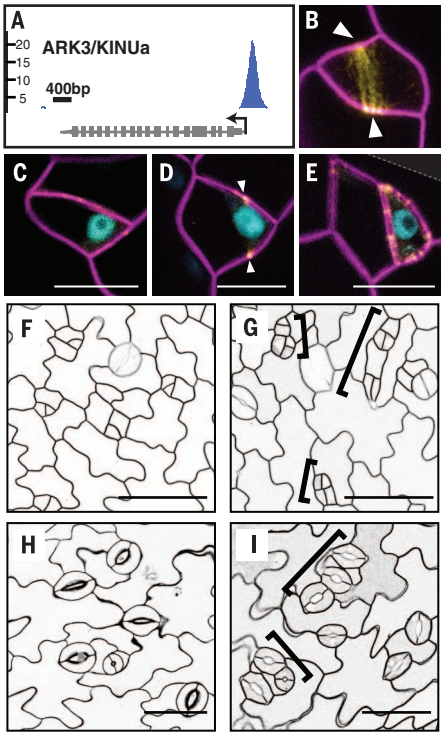

Fig. 3. SPCH regulates ACD through a preprophase band-localized kinesin. (**A**) SPCH ChIP-seq profile of *ARK3/KINUa*. (**B** to **E**) Expression of ARK3pro:ARK3-YFP (yellow) (B) and its coexpression with SPCHpro:SPCH-CFP (blue) [(C) to (E)] before (C), during (B) and (D), and after (E) a stomatal ACD. Arrowheads indicate the preprophase band. (**F** to **I**) ACD defects in SPCHpro:amiR-ark3 [(G) and (I)], compared with Col [(F) and (H)]. Brackets mark clusters of small cells (G) or guard cells (I). Confocal images are of 3- [(B) to (E)], 4- [(F) and (G)] and 11-day [(H) and (I)] abaxial cotyledons with ML1pro:mCherry-RCI2A–marked cell outlines. To display the cells in (E) in the same orientation as panels (C) and (D), we rotated the image in (E) and filled in the nonimaged space in the upper right corner with a black triangle (dashed line). Scale bars, 10 μm [(C) to (E)], 50 μm [(F) to (I)].

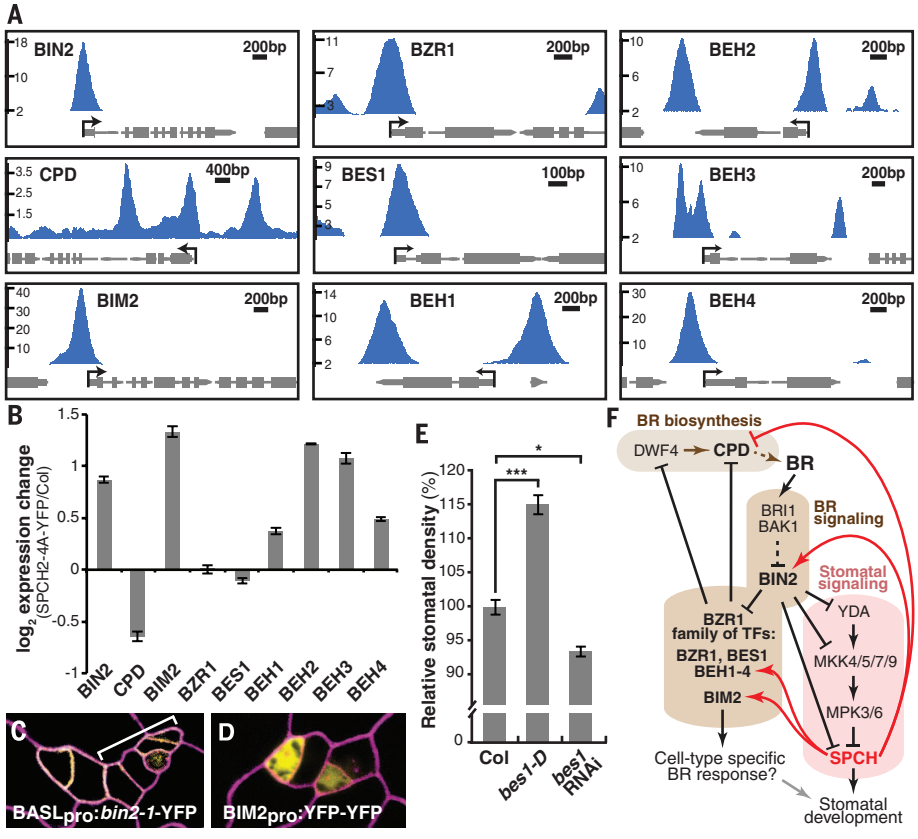

Fig. 4. Feedback regulation of brassinosteroid biosynthesis and signaling by SPCH. (**A**) ChIP-seq profiles of select brassinosteroid (BR) pathway genes (labeled as in Fig. 2F). (**B**) RT-qPCR analysis of BR genes in 4-dpg SPCHpro:SPCH2-4A-YFP and Col seedlings. Values are means ± SEM. (**C** and **D**) Confocal images of 3-dpg adaxial cotyledons with propidium iodide-stained cell outlines (purple). Stomatal lineage-specific expression of hyperactive BIN2 (yellow) induces lineage proliferation (bracket) (C). Stomatal lineage expression pattern of BIM2pro:YFP-YFP (yellow) (D). (**E**) Alteration of stomatal density in gain-of-function BES1pro:*bes1-D* and *bes1*-RNAi knockdown. *P < 0.05, ***P < 0.001 (Wilcoxon rank sum test). (**F**) Model of SPCH-BR pathway interactions. SPCH, a target of BR signaling, feeds back (positively, red arrows, or negatively, red T-bar) upon transcription of multiple pathway members.

directly or indirectly through the BZR1 family) leads to higher BIN2 activity and derepression of SPCH, promoting accumulation of SPCH in active meristemoids (Fig. 4F). Overall, this feedback mechanism by SPCH would serve to reinforce differences between SPCH-expressing meristemoids and nonexpressing neighbors, which may be important for local patterning and coordinating the lineage with overall BR-mediated growth controls.

Here, we revealed the broad influence of SPCH in stomatal lineage specification through MOBE-ChIP. This technique, which is based on a simple scale increase, could be widely applicable in other tissues or organisms to obtain high-quality binding information about cell-type–specific regulators. The large number of SPCH-binding regions reported here is reminiscent of the behavior of the bHLH transcription factor MyoD, a master regulator of mammalian myogenesis, which associates with more than 30,000 regions in the human genome and is responsible for resetting global transcriptional and epigenetic states during development (*29*). Additional experiments are needed to establish definitively how often and by what mechanisms SPCH binding alters gene expression. However, our data that hundreds of genes, including those mediating abiotic and hormone responses, are directly regulated by SPCH supports previous functional studies (*20*, *22*) that place SPCH in a critical position to integrate physiological and environmental information into a developmental program that optimizes leaf properties (stomatal density and size) for prevailing environments.

REFERENCES AND NOTES

1. R. Heidstra, S. Sabatini, *Nat. Rev. Mol. Cell Biol.* **15**, 301–312 (2014).
2. A. P. Fong, S. J. Tapscott, *Curr. Opin. Genet. Dev.* **23**, 568–573 (2013).
3. A. García-Bellido, J. F. de Celis, *Genetics* **182**, 631–639 (2009).
4. O. S. Lau, D. C. Bergmann, *Development* **139**, 3683–3692 (2012).
5. L. J. Pillitteri, J. Dong, *Arabidopsis Book* **11**, e0162 (2013).
6. S. Robinson *et al.*, *Science* **333**, 1436–1440 (2011).
7. C. A. MacAlister, K. Ohashi-Ito, D. C. Bergmann, *Nature* **445**, 537–540 (2007).
8. L. J. Pillitteri, D. B. Sloan, N. L. Bogenschutz, K. U. Torii, *Nature* **445**, 501–505 (2007).
9. J. M. Muiño, K. Kaufmann, R. C. van Ham, G. C. Angenent, P. Krajewski, *Plant Methods* **7**, 11 (2011).
10. K. Schiessl, J. M. Muiño, R. Sablowski, *Proc. Natl. Acad. Sci. U.S.A.* **111**, 2830–2835 (2014).
11. K. Kaufmann *et al.*, *Science* **328**, 85–89 (2010).
12. J. Dong, C. A. MacAlister, D. C. Bergmann, *Cell* **137**, 1320–1330 (2009).
13. L. J. Pillitteri, K. M. Peterson, R. J. Horst, K. U. Torii, *Plant Cell* **23**, 3260–3275 (2011).
14. M. M. Kanaoka *et al.*, *Plant Cell* **20**, 1775–1785 (2008).
15. J. A. Nadeau, F. D. Sack, *Science* **296**, 1697–1700 (2002).
16. E. D. Shpak, J. M. McAbee, L. J. Pillitteri, K. U. Torii, *Science* **309**, 290–293 (2005).
17. L. Hunt, J. E. Gray, *Curr. Biol.* **19**, 864–869 (2009).
18. J. L. Malcos, R. J. Cyr, *Cytoskeleton (Hoboken)* **68**, 247–258 (2011).
19. C. G. Rasmussen, J. A. Humphries, L. G. Smith, *Annu. Rev. Plant Biol.* **62**, 387–409 (2011).
20. J. Le *et al.*, *Nat. Commun.* **5**, 3090 (2014).
21. T.-W. Kim, M. Michniewicz, D. C. Bergmann, Z.-Y. Wang, *Nature* **482**, 419–422 (2012).
22. G. E. Gudesblat *et al.*, *Nat. Cell Biol.* **14**, 548–554 (2012).
23. Y. Tanaka, T. Nose, Y. Jikumaru, Y. Kamiya, *Plant J.* **74**, 448–457 (2013).
24. M. Szekeres *et al.*, *Cell* **85**, 171–182 (1996).
25. Z. Y. Wang *et al.*, *Dev. Cell* **2**, 505–513 (2002).
26. Y. Yin *et al.*, *Cell* **109**, 181–191 (2002).
27. Y. Yin *et al.*, *Cell* **120**, 249–259 (2005).
28. J.-X. He *et al.*, *Science* **307**, 1634–1638 (2005).
29. Y. Cao *et al.*, *Dev. Cell* **18**, 662–674 (2010).

ACKNOWLEDGMENTS

We thank Z.-Y. Wang (Carnegie) for the antibody to YFP and the *bin2-1* allele; Y. Yin (Iowa State University) for the BES1pro:*bes1*-D-GFP construct; J. Chory (SALK) for the *bes1* RNAi line; and members of our laboratory for critical comments. Funding for this work was provided by National Institutes of Health (NIH) 1R01GM086632. O.S.L. was a Croucher Fellow, K.A.D. was supported by Cellular and Molecular Biology Training Program NIH5T32GM007276 and by a National Science Foundation graduate research fellowship, and J.A. was supported by the DAAD. D.C.B. is a Gordon and Betty Moore Foundation Investigator of the Howard Hughes Medical Institute. The ChIP-seq and RNA-seq data in this study can be found in National Center for Biotechnology Information's Gene Expression Omnibus repository (www.ncbi.nlm.nih.gov/geo) as GSE57954. The supplementary materials contain additional data.

SUPPLEMENTARY MATERIALS

www.sciencemag.org/content/345/6204/1605/suppl/DC1
Materials and Methods
Figs. S1 to S15
Tables S1 to S8
References (*30*–*62*)

3 June 2014; accepted 25 August 2014
Published online 4 September 2014;
10.1126/science.1256888

PALEOLITHIC TOOLS

Early Levallois technology and the Lower to Middle Paleolithic transition in the Southern Caucasus

D. S. Adler,[1*] K. N. Wilkinson,[2] S. Blockley,[3] D. F. Mark,[4] R. Pinhasi,[5] B. A. Schmidt-Magee,[1] S. Nahapetyan,[6] C. Mallol,[7] F. Berna,[8] P. J. Glauberman,[1] Y. Raczynski-Henk,[9] N. Wales,[1,10] E. Frahm,[11] O. Jöris,[12] A. MacLeod,[3] V. C. Smith,[13] V. L. Cullen,[13] B. Gasparian[14]

The Lower to Middle Paleolithic transition (~400,000 to 200,000 years ago) is marked by technical, behavioral, and anatomical changes among hominin populations throughout Africa and Eurasia. The replacement of bifacial stone tools, such as handaxes, by tools made on flakes detached from Levallois cores documents the most important conceptual shift in stone tool production strategies since the advent of bifacial technology more than one million years earlier and has been argued to result from the expansion of archaic *Homo sapiens* out of Africa. Our data from Nor Geghi 1, Armenia, record the earliest synchronic use of bifacial and Levallois technology outside Africa and are consistent with the hypothesis that this transition occurred independently within geographically dispersed, technologically precocious hominin populations with a shared technological ancestry.

The Late Middle Pleistocene [LMP, oxygen isotope stage (OIS) 12/11e to OIS 6/5e, ~425 to 130 thousand years ago (ka)] witnessed the evolution of *Homo sapiens* in Africa and Neandertals in western Eurasia (*1*, *2*). In Africa, the Early Stone Age (ESA)–Middle Stone Age (MSA) transition is characterized by the slow replacement of bifaces by flakes, points, and blades produced through various hierarchical core reduction strategies, among which Levallois concepts are the most notable (*3*–*6*). In Western Europe, lithic assemblages from Late Acheulian contexts highlight the asynchronous, geographically discontiguous evolution from bifacial to Levallois technology and the gradual transition from the Lower Paleolithic (LP) to the Middle Paleolithic (MP) ~300 to 200 ka (*7*–*9*). Levantine sites assigned to the Acheulo-Yabrudian (AY, ~400 to 200 ka) document non-Levallois methods for the manufacture of blades, broad flakes, and thick scrapers with scalar retouch (Quina) and the gradual disappearance of bifaces (*10*, *11*). The technological variability apparent in these regions reflects the complex hominin behavioral mosaic in place before the MSA and the MP (*12*) (Fig. 1). Within the Southern Caucasus, a region situated between Africa and Europe, this critical period of technological and behavioral evolution remains uncharted and undated (*13*).

In bifacial technology (Mode 2), a mass of stone is shaped through the serial removal of interrelated flakes (façonnage) until the remaining volume takes on a desired form, such as a handaxe. This method of stone tool production originated in Africa ~1.75 million years ago and spread to Eurasia with the initial Acheulian dispersal <900 ka. In contrast, Levallois technology (Mode 3), a specific hierarchical core reduction strategy, entails the multistage shaping (façonnage) of a mass of stone (core) in preparation to detach a flake of predetermined size and shape from a single preferred surface (débitage) (*14*, *15*). Flakes resulting from biface production were generally treated as waste, whereas particular flakes detached from a

Levallois core are the desired products. The novel combination of the shaping and flaking systems in Levallois technology during the Late Acheulian and the eventual replacement of bifacial technology by Levallois methods denote the beginning of the MSA/MP.

In Levallois technology, the volume of the core is conceived as two hierarchically related surfaces separated by a plane of intersection, with the upper, or flake release surface representing the exploitable volume and the lower, or striking platform surface representing the unexploited volume (*14*, *15*). The flake release surface is shaped through the management of lateral and distal convexities so as to control the morphology of the resulting products (flakes), and the flake release surface is parallel to the plane of intersection. The intersection between the flake release surface and the striking platform is perpendicular to the axis of percussion, and all stages of reduction are achieved through hard-hammer percussion.

Levallois technology is subdivided into the preferential method, in which a single Levallois flake is produced before the repreparation of core convexities, and the recurrent method, in which multiple Levallois flakes are detached before repreparation (*14*, *15*). Core convexities are created through the detachment of preparatory flakes (e.g., débordants), which in turn influence the pattern of detachments from the flake release surface. Three main patterns are typically observed among Levallois cores and flakes: removals from one direction (unidirectional, parallel, or convergent), from two directions (opposed or orthogonal), or along the circumference of the core (radial or centripetal).

Recent studies highlight a specific set of multiple functional/adaptive advantages, or "coinciding optima" (*16*–*18*), that might help explain the broad temporal and geographic distribution of Levallois reduction methods after OIS 8. For example, Levallois technology is shown to be optimal in terms of raw material economy and flake utility (*17*), and Levallois flakes detached from preferential Levallois cores form a statistically robust group with morphologically desirable characteristics that are distinguishable from those of other flakes (*19*).

The diffusion of ideas or movement of populations is routinely implicated in the distribution of Levallois technology, with some scholars arguing that its geographic proliferation in Eurasia was predicated on the expansion of archaic *Homo sapiens* from Africa (*20*). This and allied hypotheses imply that the appearance of Levallois technology outside Africa was sudden, reflecting a behavioral, if not an actual biological replacement event. Therefore, technological discontinuity with the preceding Acheulian (Mode 2) is to be expected. Such hypotheses also assume direct correlations between specific hominin species and certain stone tool technologies, with movements of the former taken to explain complex geographic and temporal patterns in material culture evolution and distribution (*20*–*22*). These expectations and assumptions are ill suited to the LMP, during which the poorly sampled archaeological record exhibits substantial technological variability across great spans of time and space, the sparse chronometric record is of limited accuracy and precision, and significant variability in the ancient DNA and hominin fossil records

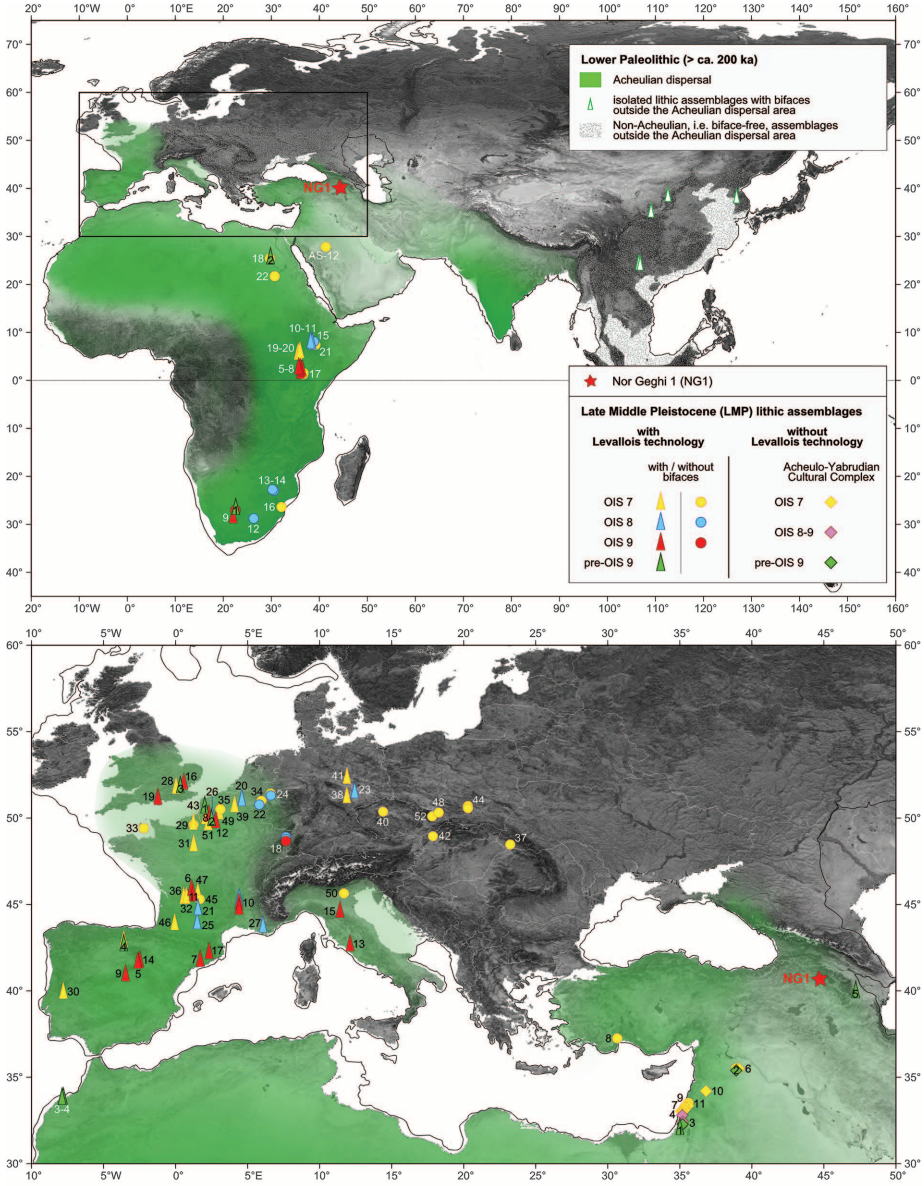

Fig. 1. Spatiotemporal distribution of early Levallois and biface technology during the LMP (>200 ka, >OIS 9 to OIS 7) in the Old World. Data are correlated with table S6, which provides detailed information on each site. The inset illustrates the spatiotemporal distribution of the Eurasian data correlated with technology. Landmasses conform to modern coastlines, and ancient coastlines are drawn to ~ –75 m (average glacial levels). Ice cover is not depicted. The background map is modified after (*37*).

[1]Department of Anthropology, University of Connecticut, 354 Mansfield Road, Unit 1176, Storrs, CT 06269, USA. [2]Department of Archaeology, University of Winchester, Winchester, SO22 4NR, UK. [3]Department of Geography, Royal Holloway, University of London, Egham, Surrey, TW20 0EX, UK. [4]Natural Environmental Research Council Argon Isotope Facility, Scottish Universities Environmental Research Centre, Scottish Enterprise and Technology Park, Rankine Avenue, East Kilbride, G75 0QF, UK. [5]School of Archaeology, University College Dublin, Newman Building, Belfield, Dublin 4, Ireland. [6]Department of Cartography and Geomorphology, Yerevan State University, Alek Manukyan 1, 0025 Yerevan, Armenia. [7]Departamento de Geografía e Historia, Universidad de La Laguna, Tenerife, Spain. [8]Department of Archaeology, Simon Fraser University, 8888 University Drive, Burnaby, British Columbia, V5A 1S6, Canada. [9]Ex-Situ Silex, Leiden, Netherlands. [10]Centre for GeoGenetics, University of Copenhagen, Øster Voldgade 5-7, 1350 Copenhagen K, Denmark. [11]Department of Archaeology, University of Sheffield, Northgate House, West Street, Sheffield, S1 4ET, UK. [12]MONREPOS Archaeological Research Centre and Museum for Human Behavioural Evolution, Römisch-Germanisches Zentralmuseum Mainz, Schloss Monrepos, D-56567 Neuwied, Germany. [13]Research Laboratory for Archaeology and the History of Art, University of Oxford, Dyson Perrins Building, South Parks Road, Oxford, OX1 3QY, UK. [14]Institute of Archaeology and Ethnology, National Academy of Sciences of the Republic of Armenia, Charents 15, 0025 Yerevan, Armenia.
***Corresponding author. E-mail: daniel.adler@uconn.edu**

defy simple taxonomic attributions (*23*, *24*). Our research at Nor Geghi 1 (NG1), a stratified Late Acheulian open-air site at the edge of the Armenian Volcanic Highlands (Fig. 1 and fig. S1), challenges the single-origin and dispersal hypothesis by providing the earliest evidence outside Africa for a transitional site at which hominins engaged in the simultaneous practice of bifacial and Levallois technology (*25*).

NG1 was discovered in 2008 when obsidian artifacts were found eroding from a 135-m-long section exposed on the western wall of the Hrazdan Gorge (40°20.8'N, 44°35.823'E, 1375 m above sea level). The Hrazdan River connects Lake Sevan (36 km north) with the Arax River (38 km southwest), and in its central 40-km stretch the Hrazdan cuts through basaltic lava flows emanating from volcanoes in the western part of the Gegham range (fig. S1). A broad chronology for these flows is provided by $^{40}K/^{40}Ar$ and $^{40}Ar/^{39}Ar$ dating of lavas from the Hatis, Gutanasar, and Mensakar volcanoes, suggesting that the vents formed ~700 ka and had eruptive histories spanning ~550,000 to 200,000 years (*26*–*28*).

The archaeology of NG1 is contained within alluvial sediments sandwiched between an upper (Basalt 1) and a lower (Basalt 7) lava flow (figs. S2 to S5). The $^{40}Ar/^{39}Ar$ technique was used to date Basalt 7 (441 ± 6 ka) and Basalt 1 (197 ± 7 ka) (fig. S8 and database S2), thereby bracketing the stratified alluvial sediments between late OIS 12 and the end of OIS 7 (Fig. 2). The five stratigraphic units recorded between the basalts (from bottom to top, Units 5 to 1) form a normally bedded sequence of fine-grained sedimentary beds, with a minor proportion of sands and gravels toward the base. The grain sizes and structural properties of the sediments indicate that they were deposited first within channels (Unit 5), later at the channel/floodplain interface (Unit 4), and finally on the floodplain of the paleo-Hrazdan River (Units 3 to 1). Micromorphological analysis shows that the alluvial layers are primarily composed of pyroclastic silt and sand. Unit 2 is the humic A horizon and Unit 3 the Bt horizon of a floodplain soil, whereas Unit 1 represents renewed alluvial deposition. Two unconformities exist within the alluvial sequence. The first, of unknown age and duration, is located at the contact between Units 2 and 1 and represents the missing O horizon of the floodplain soil profile. The second, located between Unit 1 and Basalt 1, is associated with the truncation of the former before the passage of the latter and represents roughly 100,000 years, based on $^{40}Ar/^{39}Ar$ dating of sanidine grains from cryptotephra obtained from the uppermost 5 cm of Unit 1 (308 ± 3 ka) (Fig. 2, fig. S9, and databases S1 and S2). A third unconformity is documented at the contact between Unit 5 and Basalt 7.

Strong links between paleoclimate variations and environmental changes have been identified at Early Pleistocene localities within the region and show that the environmental responses to past climate changes in western Asia were broadly comparable to those from Europe and the Mediterranean, with cooler and drier glacial periods, and warmer and more humid interglacials (*29*, *30*). Pedogenic processes in the Southern Caucasus probably coincided with warm, humid interglacials that led to soil development over most of Europe and vast parts of Asia. Consequently, based on the $^{40}Ar/^{39}Ar$ ages of the Unit 1 tephra and Basalt 7 and the unconformity identified between Units 1 and 2, we correlate the deposition of Units 5 to 4 with late OIS 10/early OIS 9e, deposition of and pedogenesis within Units 3 to 2 with OIS 9e (335 to 325 ka), and accretion of the overlying truncated basal remnant of Unit 1 with OIS 9c/b (Fig. 3).

The NG1 lithic assemblage (Fig. 4, table S5, and figs. S10 to S14) is produced entirely on obsidian, and all stages of reduction and manufacture are represented. All cores exhibit a volumetric core concept, with hierarchically organized surfaces separated by a plane of intersection. Seventeen of these cores conform to criteria that define Levallois technology (*14*, *15*), and both the preferential and recurrent Levallois methods are present. Core dorsal scar patterns are predominantly unidirectional, bidirectional, and centripetal, and débordants document the management of core flake release surfaces. Levallois flakes and blades typically exhibit plain or faceted platforms, and dorsal scar patterns are principally unidirectional with evidence at their distal extremities for the lateral and distal preparation of the cores from which they were detached. The bifaces are of variable sizes and morphologies; however, the larger specimens are morphologically similar to Late Acheulian bifaces found throughout Eurasia. Scrapers of various types (e.g., déjeté

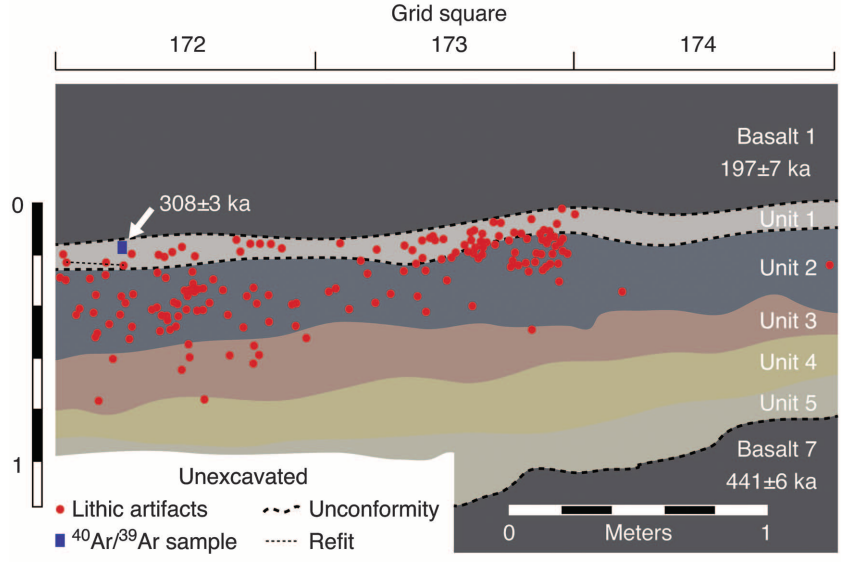

Fig. 2. Representative stratigraphic section of NG1. See figs. S4 and S5 for section location.

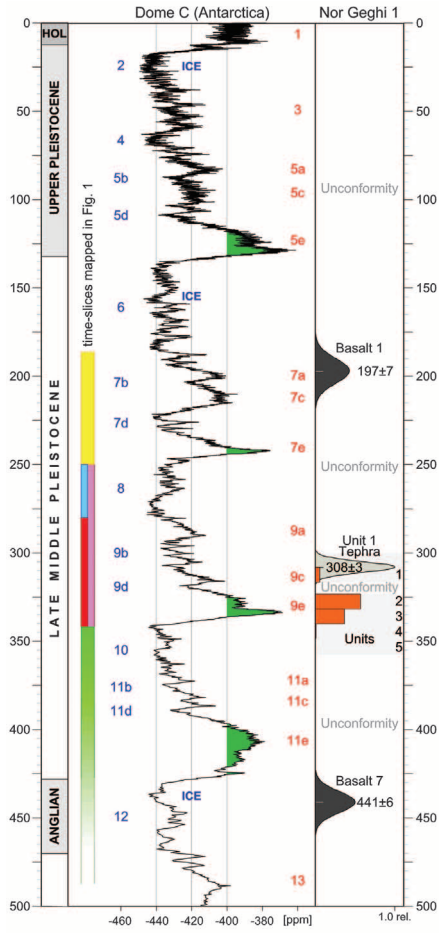

Fig. 3. Age model of the NG1 geostratigraphic sequence. The sequence is based on the $^{40}Ar/^{39}Ar$ age chronology, stratigraphic, and micromorphological results, correlated with the last 500 ka of the European Project for Ice Coring in Antarctica Dome C deuterium isotope record of Pleistocene climate change {delta deuterium [parts per million] (ppm) (*38*)}. Left/even blue numbers indicate cold dry stages; right/odd red numbers indicate warm, humid stages; and green shading (delta deuterium levels > −400 ppm) indicates peak interglacial periods, during which most of Europe was densely forested.

and transverse, with Quina retouch) dominate the retouched tool assemblage, and resharpening flakes indicate the onsite production and maintenance of these implements.

The elemental composition of 316 artifacts was measured nondestructively using portable x-ray florescence (pXRF) (*31*). The results indicate that 93.7% of the artifacts derive from the Gutanasar volcano obsidian flows (2 to 8 km northeast), 2.8% from Hatis (12 km east-southeast), 3.2% from Pokr Arteni (70 km west), and 0.3% from Pokr Sevkar (120 km southeast) (figs. S15 and S16). The latter two sources are located within distant drainages not linked to the Hrazdan, and therefore hominin transport is the only mechanism to explain their presence at NG1. The procurement of obsidian from a variety of local and nonlocal sources suggests that hominins at NG1 were exploiting large, environmentally diverse territories.

Early evidence for Levallois technology is found in assemblages from Western Europe dated to late OIS 9 and perhaps earlier (Fig. 1 and table S6), but these are often from secondary contexts or assigned to the "Final Acheulian" because of the presence of bifaces and the low frequency or absence of the preferential Levallois method. In addition, these assemblages lack the Quina scrapers that in part define the AY, where the Levallois method is rare or absent (*32*). The lithic assemblage from NG1 is unique in its combination of bifacial and Levallois technology, with Quina retouch and blade production, all recovered from a secure stratigraphic context.

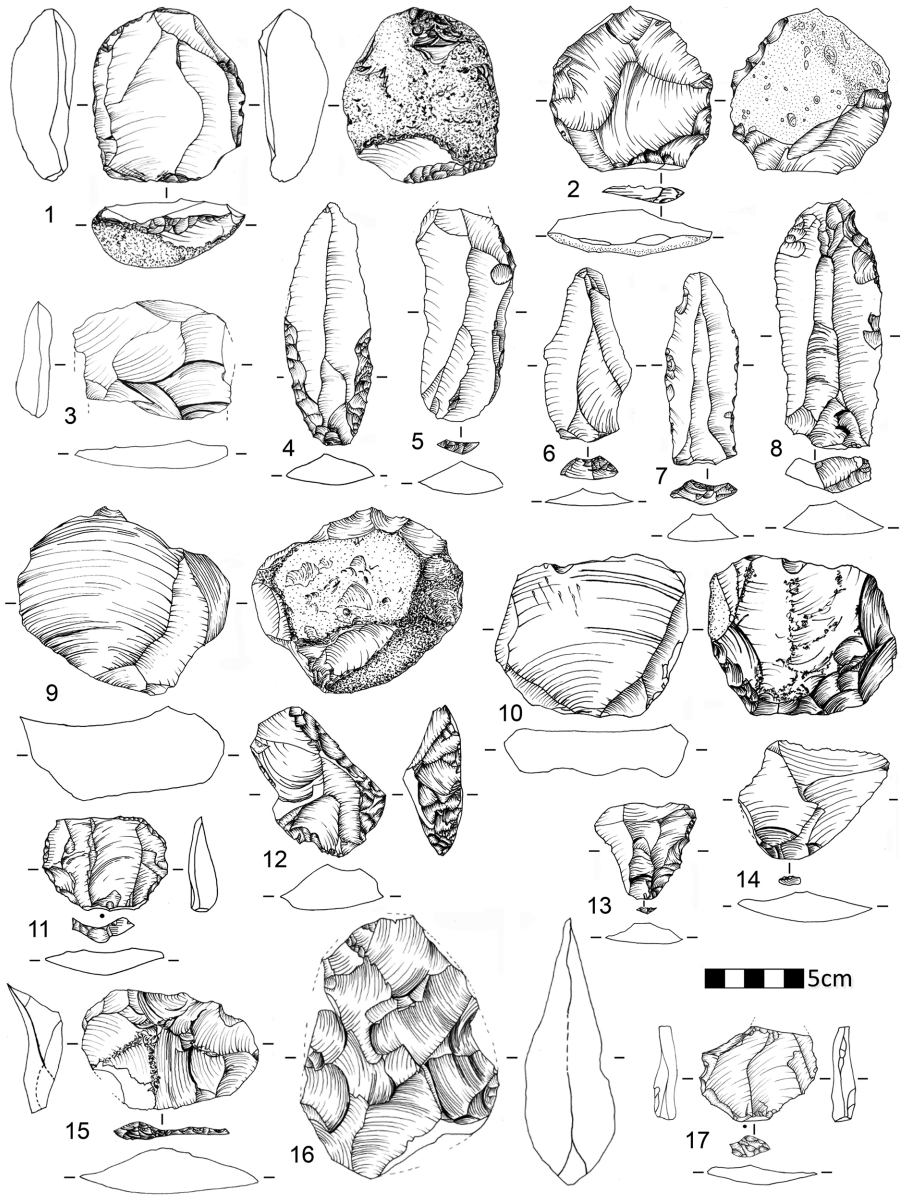

Fig. 4. Obsidian artifacts from NG1. Levallois: 1 and 2, recurrent cores; 3, 11, 13 to 15, and 17, flakes; 4, point with retouched base; 5 to 8, blades; 9 and 10, preferential cores. Non-Levallois: 12, scraper with Quina retouch; 16, biface.

Given the absence of taphonomic mixing, the intimate archaeological association of these technologies and artifact types could result from multiple hominin groups with distinct lithic traditions occupying NG1 alternately over thousands of years, thus producing a "mixed" lithic signature. However, this hypothesis would require us to accept that LMP hominins were less technologically flexible than indicated by the African and Eurasian archaeological evidence (*6*, *33*, *34*). Our data are consistent with the hypothesis that the synchronic technological variance documented at NG1 reflects the behavioral variability and technological evolution of a local Late Acheulian population and are thus inconsistent with the expectations and assumptions of the single-origin and dispersal model for Levallois technology.

Empirical evidence supports the contention that Levallois technology is an inherent property of the Acheulian that evolves out of the existing, but previously separate technological systems of façonnage and débitage (*7*, *35*), and shows that Acheulian bifacial technology and Levallois technology are homologous, reflecting an ancestor-descendant relationship (*36*). Rather than a "technical breakthrough" that spread from a single point of origin, Levallois technology resulted from the gradual synthesis of stone knapping behaviors shared among hominins in Africa and those indigenous to the Acheulian dispersal area in Eurasia (Fig. 1). Consequently, the development of Levallois technology within Late Acheulian contexts represents instances of technological convergence.

The geographically and temporally discontiguous pattern of early Levallois technology and the presence of Acheulian-like assemblages in the LMP (≤late OIS 6) suggest that hominins shifted between different technological options and/or that technological change was not always maintained, perhaps due to small effective population sizes, geographically restricted social networks, or high extinction rates (*35*). The eventual proliferation of Levallois technology during OIS 8 to OIS 7 and its continued ubiquity into late OIS 3 (Fig. 1 and table S6) establish it as an evolutionarily significant adaptation practiced by diverse hominin populations irrespective of taxonomic affiliation or environment. As such, variations in lithic technology cannot be considered proxies for hominin demographic changes during the LMP. At NG1, the early synchronic use of bifacial and Levallois technology is consistent with the hypothesis that developments in the technological realm of LMP hominins resulted from deep-rooted evolutionary processes based on a common technological ancestry.

REFERENCES AND NOTES

1. I. McDougall, F. H. Brown, J. G. Fleagle, *Nature* **433**, 733–736 (2005).
2. J. J. Hublin, *Proc. Natl. Acad. Sci. U.S.A.* **106**, 16022–16027 (2009).
3. G. Clark, *World Prehistory: A New Outline* (Cambridge Univ. Press, London, 1969).
4. N. Porat *et al.*, *J. Archaeol. Sci.* **37**, 269–283 (2010).
5. A. I. R. Herries, *Int. J. Evol. Biol.* **2011**, 1–25 (2011).
6. C. A. Tryon, J. T. Faith, *Curr. Anthropol.* **54** (S8), S234–S254 (2013).

7. M. White, N. Ashton, *Curr. Anthropol.* **44**, 598–609 (2003).
8. F. Fontana *et al.*, *J. Anthropol. Archaeol.* **32**, 478–498 (2013).
9. A. Picin, M. Peresani, C. Falguères, G. Gruppioni, J.-J. Bahain, *PLOS ONE* **8**, e76182 (2013).
10. R. Barkai, A. Gopher, S. E. Lauritzen, A. Frumkin, *Nature* **423**, 977–979 (2003).
11. R. Shimelmitz, R. Barkai, A. Gopher, *J. Hum. Evol.* **61**, 458–479 (2011).
12. S. L. Kuhn, *Curr. Anthropol.* **54**, S255–S268 (2013).
13. V. B. Doronichev, *PaleoAnthropol.* **2008**, 107 (2008).
14. E. Boëda, in *The Definition and Interpretation of Levallois Technology*, H. L. Dibble, O. Bar-Yosef, Eds. (Prehistory Press, Madison, WI, 1995), pp. 41–69.
15. E. Boëda, *Le Concept Levallois: Variabilité des Méthodes* (CNRS Éditions, Paris, 1994).
16. P. J. Brantingham, S. L. Kuhn, *J. Archaeol. Sci.* **28**, 747–761 (2001).
17. S. J. Lycett, M. I. Eren, *J. Archaeol. Sci.* **40**, 2384–2392 (2013).
18. S. J. Lycett, M. I. Eren, *World Archaeol.* **45**, 519–538 (2013).
19. M. I. Eren, S. J. Lycett, *PLOS ONE* **7**, e29273 (2012).
20. R. Foley, M. M. Lahr, *Camb. Archaeol. J.* **7**, 3 (1997).
21. S. J. Armitage *et al.*, *Science* **331**, 453–456 (2011).
22. H. Valladas *et al.*, *J. Hum. Evol.* **65**, 585–593 (2013).
23. M. Meyer *et al.*, *Nature* **505**, 403–406 (2014).
24. K. Prüfer *et al.*, *Nature* **505**, 43–49 (2014).
25. Materials and methods are available as supporting material on *Science* Online.
26. R. Badalian *et al.*, *Radiat. Meas.* **34**, 373–378 (2001).
27. E. V. Arutyunyan, V. A. Lebedev, I. V. Chernyshev, A. K. Sagatelyan, *Dokl. Earth Sci.* **416**, 1042–1046 (2007).
28. V. A. Lebedev, I. V. Chernyshev, K. N. Shatagin, S. N. Bubnov, A. I. Yakushev, *J. Volcanol. Seismol.* **7**, 204–229 (2013).
29. S. Joannin *et al.*, *Earth Planet. Sci. Lett.* **291**, 149–158 (2010).
30. V. Ollivier *et al.*, *Quat. Int.* **223-224**, 312–326 (2010).
31. E. Frahm *et al.*, *J. Archaeol. Sci.* **41**, 333–348 (2014).
32. A. J. Jelinek, *Science* **216**, 1369–1375 (1982).
33. S. McBrearty, *J. Archaeol. Res.* **69**, 7 (2013).
34. J. J. Shea, *Curr. Anthropol.* **52**, 1–35 (2011).
35. T. Hopkinson, A. Nowell, M. White, *PaleoAnthropology* **2013**, 61 (2013).
36. S. Lycett, *J. Anthropol. Archaeol.* **26**, 541–575 (2007).
37. R. Stöckli, E. Vermote, N. Saleous, R. Simmon, D. Herring, The Blue Marble Next Generation - A true color earth dataset including seasonal dynamics from MODIS (NASA Earth Observatory, 2005); http://earthobservatory.nasa.gov/Features/BlueMarble/bmng.pdf.
38. L. Augustin *et al.*, *Nature* **429**, 623–628 (2004).

ACKNOWLEDGMENTS

Data discussed in this paper can be found in the supplementary materials. All artifacts are stored at the Institute of Archeology and Ethnography, Yerevan, Armenia. We thank the following organizations for their financial support: the University of Connecticut [2008–2014: Norian Armenian Programs Committee, College of Liberal Arts and Sciences (CLAS), Office of Global Affairs, Study Abroad; and CLAS Book Committee]; the UK Natural Environment Research Council (grant IP-1186-0510), the L. S. B. Leakey Foundation (2010 and 2011), the Irish Research Council (2008 and 2009), and the University of Winchester. We also thank P. Avetisyan and B. Yeritsyan, Institute of Archeology and Ethnography, Republic of Armenia, for their collaboration.

SUPPLEMENTARY MATERIALS

www.sciencemag.org/content/345/6204/1609/suppl/DC1
Materials and Methods
Supplementary Text
Figs. S1 to S16
Tables S1 to S7
References (*39*–*192*)
Databases S1 and S2

27 May 2014; accepted 19 August 2014
10.1126/science.1256484

PALEONTOLOGY

Semiaquatic adaptations in a giant predatory dinosaur

Nizar Ibrahim,[1]* Paul C. Sereno,[1] Cristiano Dal Sasso,[2] Simone Maganuco,[2] Matteo Fabbri,[3] David M. Martill,[4] Samir Zouhri,[5] Nathan Myhrvold,[6] Dawid A. Iurino[7]

We describe adaptations for a semiaquatic lifestyle in the dinosaur *Spinosaurus aegyptiacus*. These adaptations include retraction of the fleshy nostrils to a position near the mid-region of the skull and an elongate neck and trunk that shift the center of body mass anterior to the knee joint. Unlike terrestrial theropods, the pelvic girdle is downsized, the hindlimbs are short, and all of the limb bones are solid without an open medullary cavity, for buoyancy control in water. The short, robust femur with hypertrophied flexor attachment and the low, flat-bottomed pedal claws are consistent with aquatic foot-propelled locomotion. Surface striations and bone microstructure suggest that the dorsal "sail" may have been enveloped in skin that functioned primarily for display on land and in water.

Bones of the predatory dinosaur *Spinosaurus aegyptiacus* first came to light over a century ago from Upper Cretaceous rocks in Egypt (*1*–*3*) but were destroyed in World War II (*4*). More recently, isolated teeth and bones (*5*) and the anterior half of an adult skull (*6*) have been discovered in the Kem Kem beds of eastern Morocco (Fig. 1A) and equivalent horizons in Algeria, but are insufficiently complete to estimate the size, proportions, and functional adaptations of this species. Here we report the discovery of a partial skeleton of *S. aegyptiacus* from the middle of the Kem Kem sequence (Fig. 1B), which is probably Cenomanian in age (~97 million years ago) (*7*).

The subadult skeleton, here designated the neotype of *S. aegyptiacus* (*8*), preserves portions of the skull, axial column, pelvic girdle, and limbs. It was discovered in fluvial sandstone that has yielded remains of the sauropod *Rebbachisaurus* (*9*) and three other medium-to-large theropods (an abelisaurid, *Deltadromeus*, and *Carcharodontosaurus*) (*7*, *10*). We regard two additional Kem Kem theropods, *Sigilmassasaurus brevicollis* and *S. maroccanus* (*11*, *12*), to be referable to *S. aegyptiacus* (*8*).

The neotype skeleton and isolated bones referable to *S. aegyptiacus* were scanned with computed tomography, size-adjusted, and combined with a digital recreation of the original Egyptian fossils (Fig. 2A, red). Missing bones were extrapolated between known bones or estimated from those of other spinosaurids (*6*, *13*, *14*). The digital model of the adult skeleton of *Spinosaurus* (Fig. 2A), when printed and mounted, measures over 15 m in length, longer than *Tyrannosaurus* specimens (~12.5 m) (*15*).

A concentrated array of neurovascular foramina open on the anterior end of the snout and appear similar to foramina in crocodilians that house pressure receptors that detect water movement (*8*, *16*) (Fig. 2B and fig. S6). The enlarged, procumbent, interlocking anterior teeth are well adapted for snaring fish (*5*, *6*) (Fig. 2B and fig. S4). The fossa for the fleshy nostril is small and, unlike any other nonavian dinosaur, is retracted to a posterior position to inhibit the intake of water (Fig. 2C and figs. S4 and S6) (*8*).

Most cervical and dorsal centra are elongate compared to the sacral centra, resulting in a proportionately long neck and trunk (Figs. 2A and 3 and tables S1 and S2). The anteriormost dorsal centra, however, are proportionately short, exceptionally broad, and concavoconvex (Fig. 2D). These characteristic vertebrae, the affinity of which has been controversial (*7*, *11*, *12*), are referred here to *S. aegyptiacus*, based on their association with spinosaurid skeletons in Niger (*8*) and Egypt (*2*). The horizontal cervicodorsal hinge created by these broad centra would facilitate dorsoventral excursion of the neck and skull in the pursuit of prey underwater.

The distal two-thirds of the tail comprises vertebrae with relatively short centra, diminutive zygapophyses, and anteroposteriorly compressed neural spines (Fig. 2G). The affinity of these caudal elements has been uncertain (*17*), but comparisons with associated remains from Egypt (*2*) and more proximal caudals in the neotype (Fig. 2A) allow referral to *Spinosaurus*. Short centra and reduced neural arch articulations enhance lateral bending during tail propulsion in bony fish (*18*).

The forelimb has hypertrophied deltopectoral and olecranon processes for powerful flexion and extension (Fig. 2A). Elongate manual phalanges (Fig. 2H) and less recurved, manual unguals that

[1]Department of Organismal Biology and Anatomy, University of Chicago, Chicago, IL 60637, USA. [2]Museo di Storia Naturale di Milano, Corso Venezia 55, 20121 Milan, Italy. [3]School of Earth Sciences, University of Bristol, Queen's Road, Bristol, BS8 1RJ, UK. [4]School of Earth and Environmental Sciences, University of Portsmouth, Burnaby Road, Portsmouth, PO1 3QL, UK. [5]Laboratoire de Géosciences, Faculté des Sciences Aïn Chock, Université Hassan II, Casablanca, Morocco. [6]Intellectual Ventures, 3150 139th Avenue Southeast, Bellevue, WA 98005, USA. [7]Dipartimento di Scienze della Terra, Sapienza Università di Roma, Piazzale Aldo Moro 5, 00185 Rome, Italy.
*Corresponding author. E-mail: nibrahim@uchicago.edu

are probably referable to *Spinosaurus* (*11*) and were possibly used in gaffing and slicing aquatic prey suggest that the manus is proportionately longer than in earlier spinosaurids (*13*, *14*).

The pelvic girdle and hindlimb are considerably reduced in *Spinosaurus* (Fig. 2A). The surface area of the iliac blade is approximately one-half that in most other theropods (table S1), and the supraacetabular crest that supports the hindlimb is low (Fig. 2F). Hindlimb length is just over 25% of body length (table S1). In a plot of forelimb, hindlimb, and body length (Fig. 3), *Spinosaurus* and other large theropods maintain fairly similar forelimb lengths. Relative hindlimb length, however, is noticeably less in the spinosaurid *Suchomimus* (25%) and especially in *Spinosaurus* (19%) than in other large tetanuran theropods.

Unlike other mid- or large-sized dinosaurs, the femur in *Spinosaurus* is substantially shorter than the tibia (Fig. 2, I and J, and table S1). In smaller-bodied bipedal dinosaurs, short femoral proportions indicate increased stride length and enhanced speed. In *Spinosaurus* this is clearly not the case, given the short hindlimb. The femur in *Spinosaurus* has an unusually robust attachment for the caudofemoral musculature, which is anchored along nearly one-third of the femoral shaft (Fig. 2I), suggesting powerful posterior flexion of the hindlimb. The articulation at the knee joint for vertical limb support, in contrast, is reduced. The distal condyles of the femur are narrow, and the cnemial crest of the tibia is only moderately expanded (Fig. 2, I and J). Together these features recall the shortened condition of the femur in early cetaceans (*19*, *20*) and in extant semiaquatic mammals that use their hindlimbs in foot-propelled paddling (*21*).

Pedal digit I is unusually robust and long in *Spinosaurus*: Unlike *Allosaurus* or *Tyrannosaurus*,

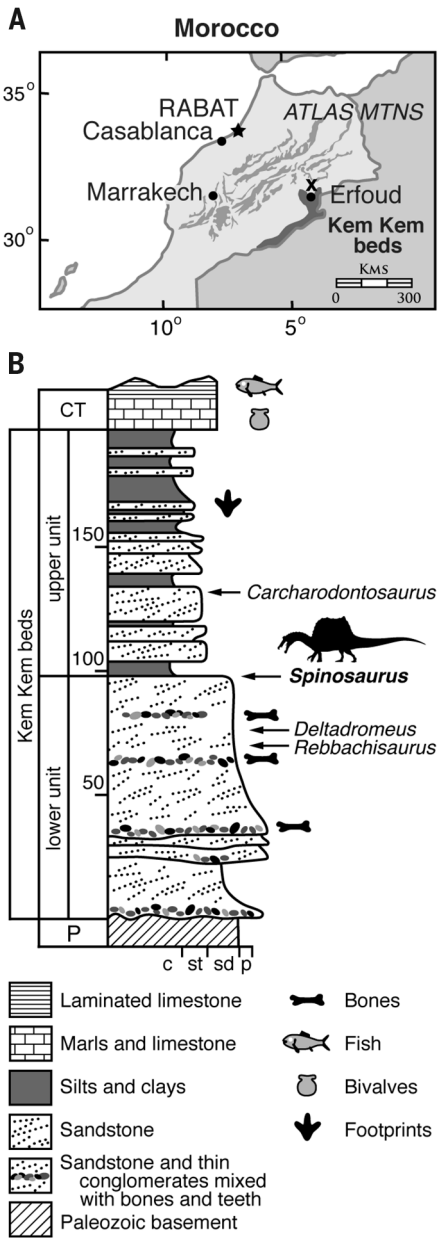

Fig. 1. Geographic location and stratigraphic position of the neotype skeleton of *S. aegyptiacus*. (**A**) Locality (X), situated 18 km northeast of Erfoud in southeastern Morocco. (**B**) Stratigraphic position at the base of the upper unit of the Kem Kem beds, with correlative positions of associated remains of contemporary dinosaurs. Abbreviations: c, clay; CT, Cenomanian-Turonian limestone; p, pebbles; P, Paleozoic; sd, sandstone; st, siltstone.

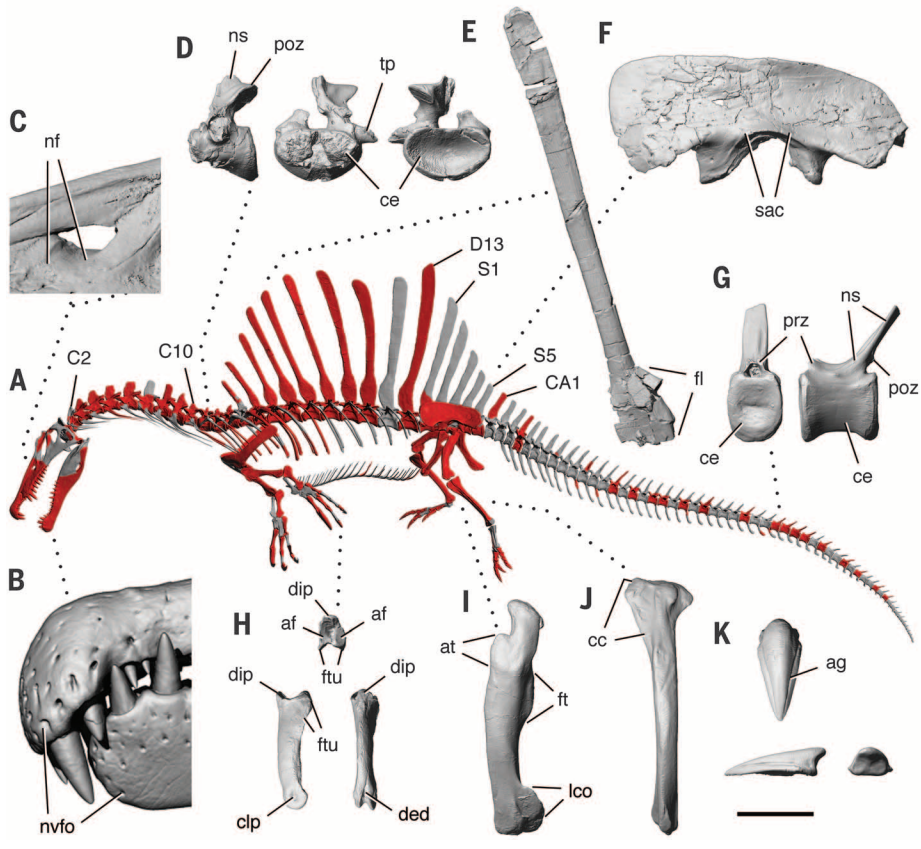

Fig. 2. Semiaquatic skeletal adaptations in *S. aegyptiacus*. (**A**) Skeletal reconstruction in swimming pose showing known bones (red) based on size-adjusted, computed tomographic scans of the neotype (FSAC-KK 11888), referred specimens, and drawings of original bones (*1*). (**B**) Rostral neurovascular foramina in lateral view (MSNM V4047 and a digital restoration of the holotypic lower jaw). (**C**) Narial fossa in lateral view (MSNM V4047). (**D**) Anterior dorsal vertebra (~D1) in lateral, anterior, and posterior views (UCRC PV601). (**E**) Dorsal neural spine (D8) in left lateral view (FSAC-KK 11888). (**F**) Left ilium in lateral view (FSAC-KK 11888). (**G**) Mid-caudal vertebra (~CA30, reversed) in anterior and left lateral views (UCRC PV5). (**H**) Right manual II-1 phalanx in proximal, lateral, and dorsal views (FSAC-KK 11888). (**I**) Left femur in lateral view (FSAC-KK 11888). (**J**) Right tibia (reversed) in lateral view (FSAC-KK 11888). (**K**) Right pedal digit III ungual in dorsal, lateral, and proximal views (FSAC-KK 11888). Abbreviations: af, articular facet; ag, attachment groove; at, anterior trochanter; C2, 10, cervical vertebra 2, 10; CA1, caudal vertebra 1; cc, cnemial crest; ce, centrum; clp, collateral ligament pit; D13, dorsal vertebra 13; ded, dorsal extensor depression; dip, dorsal intercondylar process; fl, flange; ft, fourth trochanter; ftu, flexor tubercle; lco, lateral condyle; nf, narial fossa; ns, neural spine; nvfo, neurovascular foramina; poz, postzygapophysis; prz, prezygapophysis; S1, 5, sacral vertebra 1, 5; sac, supraacetabular crest; tp, transverse process. Institutional abbreviations: FSAC, Faculté des Sciences Aïn Chock, Casablanca; MSNM, Museo di Storia Naturale di Milano; UCRC, University of Chicago Research Collection, Chicago. Scale bars, 10 cm in (B) to (D), (G), (H), and (K); and 20 cm in (E), (F), (I), and (J).

the first phalanx of digit I in *Spinosaurus* is the longest nonungual phalanx in the pes (fig. S1) and would have been in contact with the substrate in a stationary pose. The pedal unguals are proportionally large, long, low, and flat-bottomed (Fig. 2K and figs. S1 and S2), features that differ markedly from the deeper recurved unguals in other large theropods. The unguals in *Spinosaurus* are reminiscent of the flattened pedal unguals of shorebirds that do not perch (*22*). In addition, the toes of some shorebirds have fleshy lobes and interdigital webbing that enhance foot-propelled propulsion. The lengthened digit I and flattened pedal unguals in *Spinosaurus* suggest that the foot may have been adapted to traversing soft substrates or webbed for paddling.

Increases in bone mass and density are common skeletal modifications in terrestrial vertebrates transitioning to a semiaquatic existence (*23*). In *Spinosaurus*, this was achieved by enlarging midline display structures, eliminating open medullary cavities in the long bones, and increasing bone density. In subadult *Spinosaurus*, the dorsal neural spines are composed primarily of dense bone with only a narrow central zone of cancellous bone (Fig. 4D), and long bones have solid shafts (Fig. 4, A and C) with no development of the open medullary cavity that is present in other theropods, including early spinosaurids (Fig. 4B). Bone density within the long bones, in addition, is 30 to 40% greater in *Spinosaurus* than in other theropods (*8*).

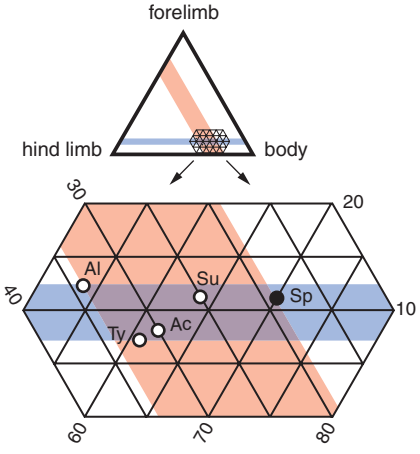

Fig. 3. Ternary morphospace plot comparing forelimb, hindlimb, and body length. Forelimb (humerus + radius + metacarpal II), hindlimb (femur + tibia + metatarsal III), and body length (from snout tip to posterior extremity of pelvic girdle) are plotted as percentages of the sum of forelimb, hindlimb, and body lengths in *S. aegyptiacus* and other large tetanuran theropods (data from Table 1). Blue zone shows the range of forelimb length, from 7% (*Tyrannosaurus*) to 12% (*Allosaurus*). Hindlimb length (red zone) ranges from 34% (*Allosaurus*) to 19% (*Spinosaurus*). Abbreviations: Ac, *Acrocanthosaurus*; Al, *Allosaurus*; Sp, *Spinosaurus*; Su, *Suchomimus*; Ty, *Tyrannosaurus*.

We estimated a center-of-body mass for a flesh rendering of *Spinosaurus* created over the digital skeleton (*8*). Center-of-mass estimates for several theropods have been expressed as a percentage of femoral length measured anteriorly from the hip joint (*24*). The center of mass in a biped must be located over the middle one-third of the pes to generate a plausible mid-stance pose (*25*). In our flesh rendering of *Spinosaurus*, the center of body mass is positioned in front of both the hip and knee joints at a distance greater than femur length (fig. S3), suggesting that forelimb support was required during terrestrial locomotion. *Spinosaurus* appears to have been poorly adapted to bipedal terrestrial locomotion. The forward position of the center of mass within the ribcage may have enhanced balance during foot-propelled locomotion in water.

These adaptations suggest that *Spinosaurus* was primarily a piscivore, subsisting on sharks, sawfish, coelacanths, lungfish, and actinopterygians that were common in the Kem Kem river system (*5*, *7*, *11*). A long narrow skull and powerful forelimbs are also present in earlier spinosaurids, which like *Spinosaurus* (*26*) have been interpreted as predominantly piscivorous (*13*, *14*, *27*, *28*).

The locomotor adaptations outlined above, however, mark a profound departure in form and function from early spinosaurids. Prominent among these are the reduced pelvic girdle; short hindlimb; short femur; and long, low, flat-bottomed pedal unguals, all of which can be verified in the second partial skeleton described by Stromer as "*Spinosaurus* B" (*2*, *8*). We note here that *Spinosaurus* must have been an obligate quadruped on land, the first discovered among theropod dinosaurs, given the usual horizontal sacroiliac joint and the anterior location of the estimated center of body mass (*8*). *Baryonyx* was interpreted as a facultative quadruped, based on its long skull and neck and robust humerus (*27*), but this was not confirmed by the discovery of more complete hindlimb remains of the related *Suchomimus* (*13*).

In *Spinosaurus* we infer foot-powered paddling from the relatively short femur with hypertrophied flexor attachment and strong pedal digit I, as occurs in semiaquatic mammals such as early cetaceans (*19*–*21*). Low, flat-bottomed pedal unguals are coincident with digital lobes or webbing in

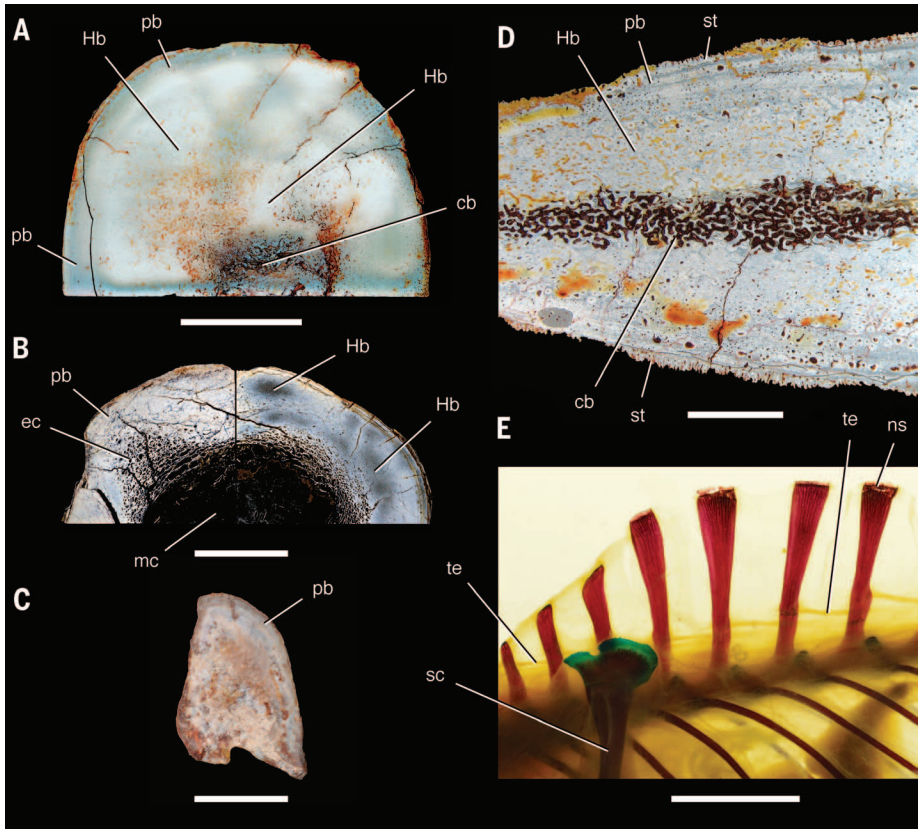

Fig. 4. Bone microstructure and dorsal spine form. (**A**) Mid-shaft thin section of the right femur of *S. aegyptiacus* (FSAC-KK 11888). (**B**) Mid-shaft thin section of the right femur of *Suchomimus tenerensis* (MNN GAD608). (**C**) Cross-sectional view of right manual II-1 phalanx of *S. aegyptiacus* (FSAC-KK 11888). (**D**) Thin section of a dorsal neural spine (distal section) in *S. aegyptiacus* (FSAC-KK 11888). (**E**) Dorsal vertebrae with tall neural spines and spinal tendons in a cleared and stained specimen of *Trioceros* (*Chamaeleo*) *cristatus* (FMNH 19886). Abbreviations: cb, cancellous bone; ec, erosional cavities; Hb, Haversian bone; mc, medullary cavity; ns, neural spine; pb, primary bone; sc, scapula; st, striae; te, tendon of multisegment spinal muscle. Institutional abbreviations: FMNH, Field Museum of Natural History. Scale bars, 2 cm in (A) and (C), 3 cm in (B), 5 mm in (D), and 1 cm in (E).

shore birds (*22*), and interdigital webbing has been reported in theropod dinosaurs (*29*).

Reduction of the pelvic girdle and hindlimb and the concomitant enhancement of axial-powered locomotion are common among semiaquatic vertebrates. The flexibility of the tail and the form of the neural spines in *Spinosaurus* suggest tail-assisted swimming. Like extinct and extant semiaquatic reptiles, *Spinosaurus* used lateral undulation of the tail, in contrast to the vertical axial undulation adopted repeatedly by semiaquatic mammals (*20*, *21*).

The dorsal "sail" in *Spinosaurus*, the tallest axial structure documented among dinosaurs, has been argued to be a thermoregulatory surface, a muscle- or fat-lined hump (*30*), or a display structure. Stromer (*1*) drew an analogy to the skin-covered neural spines of the crested chameleon, *Trioceros cristatus* (Fig. 4E). As in *T. cristatus*, the sail of *Spinosaurus* is centered over the trunk (Fig. 2A). The shape and positioning of the spine are also similar, and the base of the neural spine is expanded anteroposteriorly, with edges marked by ligament scars (Fig. 2E). In *Trioceros*, a tendon of multisegmental axial musculature attaches to the expanded base of the neural spine (Fig. 4E). The upper portion of the spine has sharp anterior and posterior edges, is marked by fine vertical striae (Figs. 2E and 4D), and is spaced away from adjacent spines, unlike the broader, contiguous, paddle-shaped dorsal spines of other spinosaurids (*13*). The striated surface, sharp edges, and dense, poorly vascularized internal bone of the spines suggest that they were wrapped snugly in skin and functioned as a display structure that would have remained visible while swimming.

REFERENCES AND NOTES

1. E. Stromer, *Ahb. Königl. Bayer. Akad. Wissen. Math-Phys. Kl.* **28**, 1–32 (1915).
2. E. Stromer, *Abh. Königl. Bayer. Akad. Wissen. Math-Naturwissen. Abt.* **22**, 1–79 (1934).
3. J. B. Smith, M. C. Lamanna, H. Mayr, K. J. Lacovara, *J. Paleontol.* **80**, 400–406 (2006).
4. W. Nothdurft, J. Smith, *The Lost Dinosaurs of Egypt* (Random House, New York, 2002).
5. P. Taquet, D. Russell, *C. R. Acad. Sci. Paris* **299**, 347–353 (1998).
6. C. Dal Sasso, S. Maganuco, E. Buffetaut, M. A. Mendez, *J. Vert. Paleontol.* **25**, 888–896 (2005).
7. P. C. Sereno *et al.*, *Science* **272**, 986–991 (1996).
8. See the supplementary materials on *Science* Online.
9. R. Lavocat, in *Comptes Rendus de la 19ème Congrès Géologique International*, Alger, 1952, session XII-3, 15 (1954), pp. 65–68.
10. L. Mahler, *J. Vert. Paleont.* **25**, 236–239 (2005).
11. D. A. Russell, *Bull. Mus. Hist. Nat. Paris* **18**, 349–402 (1996).
12. B. McFeeters, M. J. Ryan, S. Hinic-Frlog, C. Schröder-Adams, H. Sues, *Can. J. Earth Sci.* **50**, 636–649 (2013).
13. P. C. Sereno *et al.*, *Science* **282**, 1298–1302 (1998).
14. A. J. Charig, A. C. Milner, *Bull. Nat. Hist. Mus* **53**, 11–70 (1997).
15. C. Brochu, *J. Vert. Paleontol. Mem. 7*, **22** (suppl. 4), 1–138 (2002).
16. D. B. Leitch, K. C. Catania, *J. Exp. Biol.* **215**, 4217–4230 (2012).
17. F. E. Novas, F. Dalla Vecchia, D. F. Pais, *Rev. Mus. Argent. Cien. Nat.* **7**, 167–175 (2005).
18. F. E. Fish, G. V. Lauder, *Annu. Rev. Fluid Mech.* **38**, 193–224 (2006).
19. S. I. Madar, *Adv. Vert. Paleobiol.* **1**, 353–378 (1998).
20. P. D. Gingerich, *Paleobiology* **29**, 429–454 (2003).
21. F. E. Fish, *IEEE J. Oceanic Eng.* **29**, 605–621 (2004).
22. A. Manegold, *Acta Ornithol.* **41**, 79–82 (2006).
23. E. Amson, C. de Muizon, M. Laurin, C. Argot, V. de Buffrénil, *Proc. Biol. Sci.* **281**, 20140192 (2014).
24. K. T. Bates, R. B. J. Benson, P. L. Falkingham, *Paleobiology* **38**, 486–507 (2012).
25. S. M. Gatesy, M. Bäker, J. R. Hutchinson, *Paleobiology* **29**, 535–544 (2009).
26. E. Stromer, *Abh. Königl. Bayer. Akad. Wissen. Math.-Naturwissen. Abt.* **33**, 1–102 (1936).
27. A. J. Charig, A. C. Milner, *Nature* **324**, 359–361 (1986).
28. E. J. Rayfield, A. C. Milner, V. B. Xuan, P. G. Young, *J. Vert. Paleontol.* **27**, 892–901 (2007).
29. M. L. Casanovas Cladellas *et al.*, *España Zub. Monogr.* **5**, 135–163 (1993).
30. J. B. Bailey, *J. Paleontol.* **71**, 1124–1146 (1997).

ACKNOWLEDGMENTS

We thank C. Abraczinskas for final drafts of all text figures; M. Auditore for discussions and drawings; T. Keillor, L. Conroy, and E. Fitzgerald for image processing and modeling; R. Masek, T. Keillor, E. Fitzgerald, and F. Bacchia for fossil preparation; C. Straus, N. Gruszauskas, D. Klein, and the University of Chicago Medical Center for computed tomographic scanning; M. Zilioli, F. Marchesini, M. Pacini, E. Lamm, and P. Vignola for preparation of histological samples; A. Di Marzio (Siemens Milano) and P. Biondetti (Fondazione Ospedale Maggiore Istituto di Ricovero e Cura a Carattere Scientifico, Milan) for computed tomography scanning and rendering of MSNM V4047; and the Island Fund of the New York Community Trust and National Geographic Society (grant SP-13-12) for support of this research. N.I. was also supported by NSF grant DBI-1062542. We also thank the embassy of the Kingdom of Morocco in Washington, DC, for their continued interest in this project. Skeletal measurements and geologic data are included in the supplementary materials. The neotype is going to be deposited at the Faculté des Sciences Aïn Chock (University of Casablanca), Casablanca, Morocco.

SUPPLEMENTARY MATERIALS

www.sciencemag.org/content/345/6204/1613/suppl/DC1
Supplementary Text
Figs. S1 to S8
Tables S1 to S5
References (*31*–*48*)

15 July 2014; accepted 3 September 2014
10.1126/science.1258750

NEUROSCIENCE

A critical time window for dopamine actions on the structural plasticity of dendritic spines

Sho Yagishita,[1,2] Akiko Hayashi-Takagi,[1,2,3] Graham C.R. Ellis-Davies,[4] Hidetoshi Urakubo,[5] Shin Ishii,[5] Haruo Kasai[1,2]*

Animal behaviors are reinforced by subsequent rewards following within a narrow time window. Such reward signals are primarily coded by dopamine, which modulates the synaptic connections of medium spiny neurons in the striatum. The mechanisms of the narrow timing detection, however, remain unknown. Here, we optically stimulated dopaminergic and glutamatergic inputs separately and found that dopamine promoted spine enlargement only during a narrow time window (0.3 to 2 seconds) after the glutamatergic inputs. The temporal contingency was detected by rapid regulation of adenosine 3′,5′-cyclic monophosphate in thin distal dendrites, in which protein-kinase A was activated only within the time window because of a high phosphodiesterase activity. Thus, we describe a molecular basis of reinforcement plasticity at the level of single dendritic spines.

Animal behaviors are reinforced only when rewarded shortly after a motor or sensory event (*1*, *2*). The neocortex, hippocampus, and amygdala process the sensorimotor signals and send glutamatergic synaptic output to the striatum (*3*), where connections can be modified by Hebbian learning mechanisms, such as spike-timing-dependent plasticity (STDP) (*4*). Animals learn to associate the sensorimotor signals with subsequent rewards through reinforcement of the neuronal circuits involving dopamine (*5*–*7*). Despite its importance, this narrow timing detection has never been demonstrated at the cellular level and might be ascribed to neural network properties (*6*, *8*).

Dendritic spine morphology is correlated with spine function (*9*), and dendritic spines enlarge during long-term potentiation in the cortices (*10*–*12*). We examined the effects of dopamine on the structural plasticity in striatal medium spiny neurons (MSNs). Results show that dopamine affected spine structural plasticity in a narrow time window consistent with behavioral conditioning (*5*). Functional imaging revealed the molecular interrelationships between the reinforcement and Hebbian plasticity.

We investigated dopamine actions on glutamatergic synapses on MSNs using optogenetics and

[1]Laboratory of Structural Physiology, Center for Disease Biology and Integrative Medicine, Faculty of Medicine, The University of Tokyo, Bunkyo-ku, Tokyo 113-0033, Japan. [2]Core Research for Evolutional Science and Technology, Japan Science and Technology Agency, Japan Science and Technology Agency, 4-1-8 Honcho, Kawaguchi, Saitama 332-0012, Japan. [3]Precursory Research for Embryonic Science and Technology, Japan Science and Technology Agency, Japan Science and Technology Agency, 4-1-8 Honcho, Kawaguchi, Saitama 332-0012, Japan. [4]Department of Neuroscience, Mount Sinai School of Medicine, New York, NY 10029, USA. [5]Integrated Systems Biology Laboratory, Department of Systems Science, Graduate School of Informatics, Kyoto University, Sakyo-ku, Kyoto 606-8501, Japan.
***Corresponding author. E-mail: hkasai@m.u-tokyo.ac.jp**

two-photon uncaging. For optogenetic stimulation of dopaminergic fibers, a Cre-dependent adeno-associated virus (AAV) vector expressing channelrhodopsin-2 (ChR2) was injected into the ventral tegmental area (VTA) of DAT-Cre mice expressing Cre specific to dopaminergic neurons (Fig. 1A and fig. S1). The direct pathway–constituting MSNs, which mainly express dopamine 1 receptors (D1Rs) (*13*), were labeled by an AAV vector with a specific promoter for D1R-MSNs (Fig. 1A and fig. S1). In acute coronal slices, including the nucleus accumbens (NAc) core, whole-cell recordings were obtained from the identified D1R-MSNs. Dendritic spines were visualized by means of two-photon microscopy (980 nm) detecting

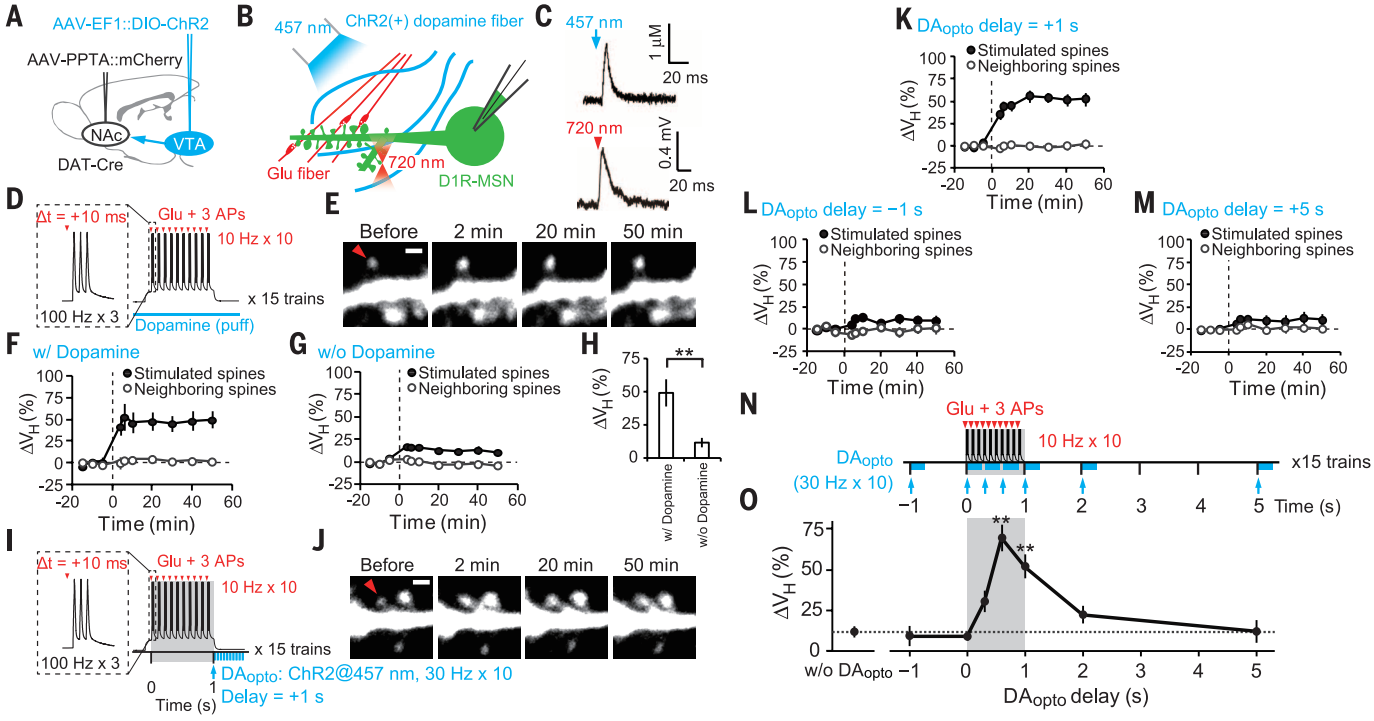

Fig. 1. A temporal profile of dopamine actions on spine enlargement. (**A**) Injection of AAV vectors for ChR2 and the D1R-MSN marker (PPTA-mCherry) in 3-week-old DAT-Cre mice. (**B**) Selective stimulation of dopaminergic and glutamatergic inputs by means of blue laser field irradiation to ChR2 and two-photon uncaging of caged-glutamate at a single spine, respectively, in acute slices of NAc obtained from 5- to 7-week-old mice. (**C**) An amperometric measurement of dopamine (top) by carbon-fiber electrode and whole-cell recording of glutamate-induced current (bottom, 2pEPSP) in identified D1R-MSNs. (**D**) An STDP protocol with dopamine puff application. (**E**) Images of the dendritic spine (red arrowhead) that received STDP stimulation in the presence of dopamine (100 μM). (**F** and **G**) Time courses of spine enlargement in the presence [(F), 13 spines, 4 dendrites] and absence of dopamine [(G), 58 spines, 14 dendrites]. (**H**) Amplitudes of spine enlargements with or without dopamine. $^{**}P = 0.0041$ by Mann-Whitney U test. (**I**) STDP with repetitive activation of dopaminergic fibers containing ChR2 (blue lines) at 30 Hz, 10 times (DA_{opto}). (**J**) Images of the dendritic spine (arrowhead) that received STDP + DA_{opto} with a delay of 1 s. (**K** to **M**) Time courses of spine enlargement induced by STDP + DA_{opto} at 1 s [(K), 48 spines, 14 dendrites], –1 s [(L), 20 spines, 5 dendrites] and 5 s [(M), 28 spines, 7 dendrites] after STDP onset. (**N**) Timings of DA_{opto} application. (**O**) Increases in spine volumes by STDP + DA_{opto} plotted versus DA_{opto} delay (fig. S2, A to C). Data are presented as mean ± SEM. $P = 4.2 \times 10^{-6}$ with Kruskal-Wallis and $^{**}P = 0.0018$ (0.6 s) and 0.0027 (1 s) by Steel test in comparison with STDP in the absence of DA_{opto}. Scale bars, 1 μm.

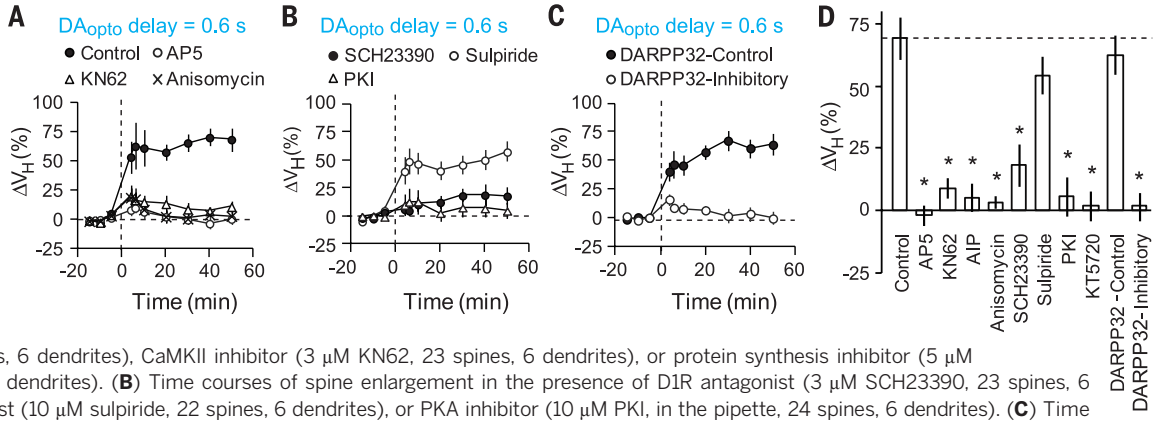

Fig. 2. Pharmacology of spine enlargement induced by STDP plus DA_{opto} with a 0.6-s delay. (**A**) Time courses of spine enlargement induced by STDP + DA_{opto} with a 0.6-s delay in the absence (control, 24 spines, 7 dendrites) and presence of NMDAR antagonist (50 μM D-AP5, 22 spines, 6 dendrites), CaMKII inhibitor (3 μM KN62, 23 spines, 6 dendrites), or protein synthesis inhibitor (5 μM anisomycin, 25 spines, 6 dendrites). (**B**) Time courses of spine enlargement in the presence of D1R antagonist (3 μM SCH23390, 23 spines, 6 dendrites), D2R antagonist (10 μM sulpiride, 22 spines, 6 dendrites), or PKA inhibitor (10 μM PKI, in the pipette, 24 spines, 6 dendrites). (**C**) Time courses of spine enlargement in the presence of inhibitory (100 μM, in the pipette, 24 spines, 6 dendrites) or control peptide for DARPP-32 (100 μM, in the pipette, 24 spines, 6 dendrites). (**D**) Averaged volume changes in the absence and presence of the compounds. Data are presented as mean ± SEM. $P = 3.4 \times 10^{-6}$ with Kruskal-Wallis and $^{*}P = 0.023$ (AP5), 0.023 (KN62), 0.037 (AIP) (fig. S5A), 0.023 (anisomycin), 0.035 (SCH23390), 0.023 (PKI), 0.037 (KT5720) (fig. S5A), and 0.023 (DARPP-32.inhibitory peptide) with Steel test.

fluorescence of Alexa488 loaded through a recording pipette (Fig. 1B and fig. S1C). Stimulation of a single spine by means of two-photon uncaging (720 nm) of CDNI-Glu (Fig. 1B) induced two-photon excitatory postsynaptic potentials (2pEPSPs) with amplitudes similar to miniature EPSPs (mEPSPs) (Fig. 1C and fig. S1D). The amplitudes of 2pEPSCs positively correlated with spine volumes, as they did with pyramidal neurons (fig. S1E) (*9*). The STDP protocol of repetitive uncaging of glutamate paired with action potentials (APs) (Glu + AP) (Fig. 1D) (*14*) induced robust spine enlargement that was selective for the stimulated spine (Fig. 1, E and F) when dopamine (100 μM) was puff applied, whereas only a weak enlargement occurred in the absence of dopamine (Fig. 1G), which is consistent with previous findings (*14*, *15*).

A single pulse of blue laser stimulation of ChR2-expressing dopaminergic fibers induced a transient increase in the tissue dopamine concentration (Fig. 1C). We tested the actions of a physiologically relevant phasic release of dopamine (30 Hz, 10 times) induced by the optogenetic stimulation of dopaminergic fibers (DA_{opto}) and found that DA_{opto} just after STDP stimulation (DA_{opto} delay = 1 s) (Fig. 1I) induced

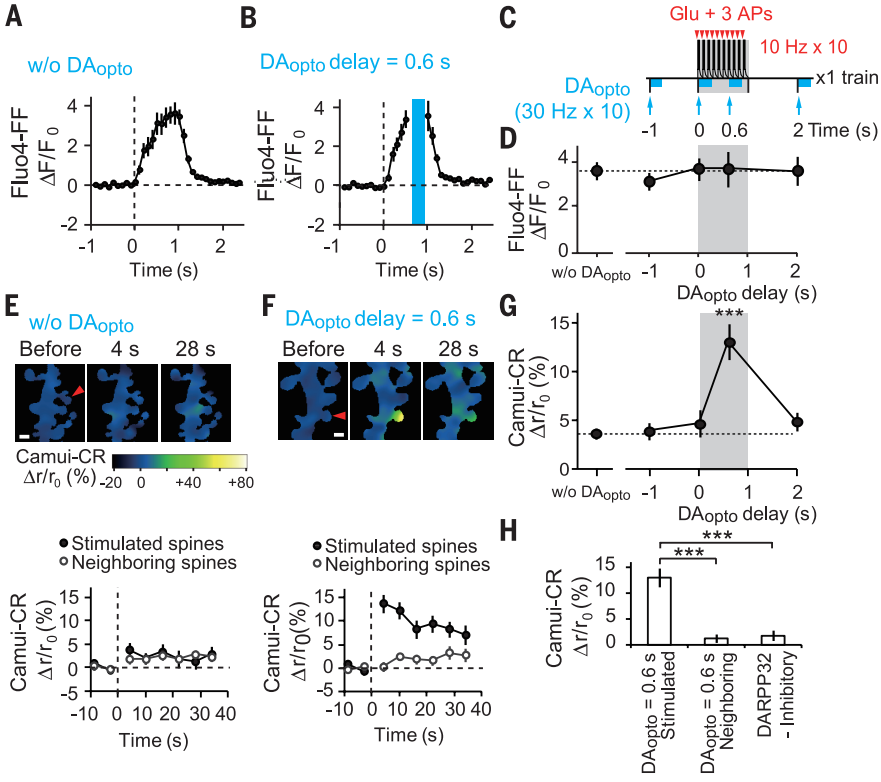

Fig. 3. DA_{opto} effects on STDP stimulation-induced increases in $[Ca^{2+}]_i$ and CaMKII activities. (**A** and **B**) Increases in Fluo4-FF fluorescence, representing $[Ca^{2+}]_i$ increases, within single spines in response to a train of STDP stimulation in the absence [(A), 20 spines, 15 dendrites] and presence of DA_{opto} with a 0.6-s delay [(B), 15 spines, 8 dendrites]. Blue laser irradiation during DA_{opto} is blanked by the blue bar. (**C**) STDP and DA_{opto} protocols for Ca^{2+} and CaMKII imaging. Unlike plasticity induction (Fig. 1N), only one train was applied. (**D**) No effect of DA_{opto} on the peak values of $[Ca^{2+}]_i$ (fig. S6, A to C). P = 0.91 with Kruskal-Wallis test. (**E** and **F**) Ratiometric imaging with Camuiα-CR during STDP stimulation in the absence [(E), 33 spines, 14 dendrites] or presence of DA_{opto} with a 0.6-s delay [(F), 42 spines, 14 dendrites]. Relative increases in the ratio are shown as pseudocolor coding in (E). (Bottom) Time courses of FRET ratios in the spines stimulated with glutamate uncaging or the neighboring spines. Scale bars, 1 μm. (**G**) Dependence of the peak Camuiα-CR FRET ratios on the DA_{opto} delay (fig. S6, D to F). $P = 1.3 \times 10^{-5}$ with Kruskal-Wallis test and $^{***}P = 8.4 \times 10^{-5}$ with Steel test versus those without DA_{opto}. (**H**) Normalized increases in Camuiα-CR ratios by STDP + DA_{opto} with a 0.6-s delay in the stimulated (42 spines, 14 dendrites) and neighboring spines (42 spines, 14 dendrites), and in the presence of DARPP-32 inhibitory peptide in the stimulated spines (43 spines, 10 dendrites) (fig. S6G). Data are presented as mean ± SEM. $P = 8.8 \times 10^{-9}$ with Kruskal-Wallis test and *** $P = 2.6 \times 10^{-9}$ and 1.1×10^{-6} with Steel test.

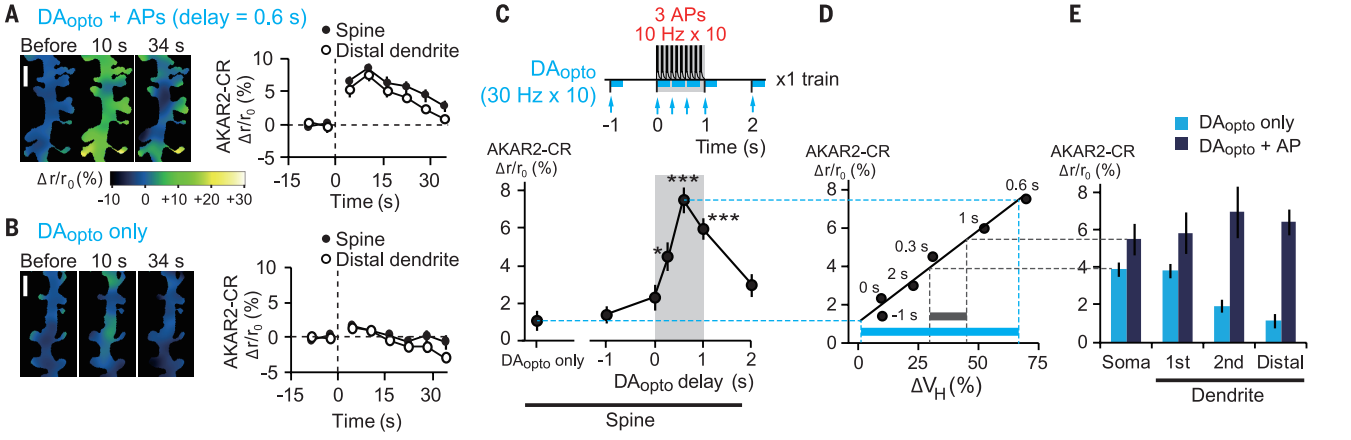

Fig. 4. AP effects on DA_{opto}-induced PKA activation in proximal and distal dendrites. (**A** and **B**) Images and time courses of FRET ratios of AKAR2-CR in the spine and distal dendrites stimulated by APs + DA_{opto} with a 0.6-s delay [(A), 153 spines, 25 dendrites] or DA_{opto} only [(B), 158 spines, 26 dendrites]. The relative increases in the ratio were pseudocolor coded as shown in (A). Scale bar, 2 μm. (**C**) AKAR2-CR responses to APs + DA_{opto} with various delays (fig. S7, E to I). $P = 5.3 \times 10^{-10}$ with Kruskal-Wallis test and $^{*}P$ = 0.012, $^{***}P = 1.3 \times 10^{-6}$ (0.6 s), and 4.0×10^{-4} (1 s) with Steel test versus DA_{opto} only. (**D**) AKAR2-CR response (C) plotted against spine volume changes (Fig. 1O) for various DA_{opto} timings. The Spearman's correlation coefficient was 0.94, and P = 0.0048. The blue and gray bars indicate the dynamic ranges of volume changes predicted by the dynamic ranges of AKAR2 responses at dendritic spine (blue) and soma (gray). (**E**) AKAR2-CR responses at the soma and first, second, and distal dendrites in response to DA_{opto} only and DA_{opto} + APs with a 0.6-s delay (fig. S8, A and B).

robust spine enlargement (Fig. 1, J and K). Stimulation of dopaminergic fibers 1 s before (DA_{opto} delay = −1 s) or 5 s after (DA_{opto} delay = 5 s) STDP (Fig. 1, L and M) resulted in only a slight enhancement. The actions of DA_{opto} were examined with various timings (Fig. 1N), revealing that DA_{opto} timing was critical to enhance plasticity, with maximal effects for a delay of 0.6 s (Fig. 1O and fig. S2, A to C), and decayed in a few seconds, which is consistent with behavioral study results (*5*, *16*). The spine enlargement was accompanied by an increase in the 2pEPSC (fig. S3). A similar DA_{opto} timing was observed when we induced STDP through electrical stimulation of presynaptic fibers (fig. S4).

Pharmacological studies revealed that D1R-MSN structural plasticity was dependent on *N*-methyl-D-aspartate receptors (NMDARs), Ca^{2+}/calmodulin–dependent protein kinase II (CaMKII), and protein synthesis (Fig. 2A and fig. S5A), suggesting that the molecular mechanisms for D1R-MSN plasticity are similar to those underlying structural plasticity in hippocampal pyramidal neurons (*10*–*12*). Plasticity also depended on D1R and protein kinase A (PKA), but not on D2R (Fig. 2B and fig. S5A). Spine enlargement was prevented by an inhibitory peptide blocking the interaction of dopamine- and adenosine 3′,5′-cyclic monophosphate (cAMP)–regulated phosphoprotein 32 kD (DARPP-32) with protein phosphatase 1 (PP-1) (*17*), but not its control peptide (Fig. 2, C and D). Moreover, spine enlargement was induced even in the absence of DA_{opto} when PP-1 was inhibited by calyculin A (fig. S5, B and C). These results suggest that similar to hippocampal preparations (*18*), the phosphorylation of DARPP-32 by PKA would inhibit PP-1 and disinhibit CaMKII.

To test whether changes in Ca^{2+} signaling account for DA_{opto} timing (*19*), we imaged increases in cytosolic Ca^{2+} concentrations ($[Ca^{2+}]_i$) in spines using a low-affinity calcium indicator Fluo-4FF (K_{Ca} = 10 μM) to avoid saturation. The $[Ca^{2+}]_i$ increases gradually built up and quickly waned after cessation of the STDP protocol (Fig. 3A). We found that DA_{opto} did not affect Ca^{2+} transients (Fig. 3, B to D, and fig. S6, A to C), indicating that Ca^{2+} signaling modulation did not play a major role.

We examined whether CaMKII activation was related to DA_{opto} timing by using the Förster resonance energy transfer (FRET) indicator of CaMKII, Camuiα-CR (*20*–*22*), which was virally transfected into D1R-MSNs. CaMKII activation was weak in the absence of DA_{opto} (Fig. 3E) but was greatly potentiated by DA_{opto} (Fig. 3F), with timing similar to DA_{opto} timing for spine enlargement (Fig. 3G and fig. S6, D to F). This enhancement was specific to the stimulated spine (Fig. 3H), abolished by the inhibitory peptide for DARPP-32 (Fig. 3H and fig. S6G), and mimicked by PP-1 inhibitors, calyculin A and tautomycetin (fig. S6, H and I). These results support the hypothesis that PKA/DARPP-32 disinhibits CaMKII via PP-1 (fig. S11).

We addressed whether the DA_{opto} timing was formed at the level of PKA activation by using a FRET probe of PKA, AKAR2-CR (*22*), which was virally delivered to the D1R-MSNs. Unlike structural plasticity or Camuiα-CR activation, PKA activation in response to stimulation of a dendritic spine by STDP and DA_{opto} was not restricted to the stimulated spine; neighboring spines also exhibited significant PKA activation (fig. S7, A to D). Even without glutamate uncaging, PKA activation was observed in the spine and dendritic shaft (Fig. 4A) in an AP-dependent manner (Fig. 4B), suggesting that PKA activation is a cell-wide phenomenon. When DA_{opto} was applied at various times relative to APs, we obtained a timing (Fig. 4C and fig. S7, E to I) similar to DA_{opto} timing on spine enlargement and CaMKII activation (Fig. 1O). The extent of spine enlargement positively correlated with that of PKA activation (Fig. 4D). APs themselves were not sufficient to activate PKA (fig. S8, C to E). The contingency between APs and DA_{opto} might be detected by Ca^{2+}/calmodulin–dependent adenylyl cyclase 1 (AC1), which is synergistically activated by Ca^{2+}/calmodulin and Gs (*23*). Consistent with this, AC1 blocker (NB001) eliminated AKAR2 activation, as well as structural plasticity (fig. S9, A to D).

In the soma and proximal (first branch) dendrites, however, DA_{opto} alone was sufficient to activate PKA (Fig. 4E and fig S8, A and B) (*24*), and APs could only slightly enhance PKA. We predict that APs might have modulated spine enlargement to a small degree in these regions, if there had been spines (Fig. 4D). Thus, DA_{opto}-induced PKA activation must be suppressed in distal dendrites in order to attain the large dynamic range for the timing detection. In fact, when phosphodiesterase 10A (PDE10A), the major phosphodiesterase in MSNs, was blocked by its inhibitor papaverine (*25*), PKA activations were similarly induced in distal dendrites as in the soma (fig. S9, E to G). Papaverine also disrupted the time window for structural plasticity (fig. S9, H and I). Why were PDE10A actions particularly potent in the distal dendrites? Subcellular differences in PDE10A expression might not account for this, considering that PDE10A is expressed at the plasma membrane and is uniformly distributed along the dendrites (*26*). Instead, we found a negative correlation between dendrite diameter and DA_{opto}-induced PKA activity (fig. S10A, blue), which was lost when the phosphodiesterase was inhibited (fig. S10A, orange). Therefore, PDE10A might counteract the increases in cAMP more potently in the thin distal dendrites because of its high surface-to-volume ratios (fig. S10, B and C). Spines are only found in the distal thin dendrites of MSNs (fig. S10, D to E) (*27*), suggesting that spines are distributed to be efficiently modulated by dopamine timing in MSNs.

It has been enigmatic why dopamine reinforces preceding, but not subsequent, sensorimotor events. If dopamine always activates PKA, its effects should last long enough to reinforce the subsequent events over tens of seconds (Fig. 4A). However, dopamine did not activate PKA unless $[Ca^{2+}]_i$ primed AC1 to outcompete the high phosphodiesterase activity in thin dendrites (fig. S11). Our data show that $[Ca^{2+}]_i$ priming should occur strictly before dopamine delivery (0 s) (Figs. 1O, 3G, and 4C), which is reminiscent of serotonin's action in the classical conditioning of the siphon withdrawal reflex in *Aplysia* (*28*), in which serotonin, carrying an aversive signal, was only effective when it was preceded by increases in $[Ca^{2+}]_i$ for activation of calcium-dependent adenylyl cyclase (AC) and PKA in presynaptic terminals (*29*). The delay in $[Ca^{2+}]_i$ priming of AC may compensate the time lag of monoaminergic signals after reward or punishment. Our data suggest that reinforcement plasticity occurs at the single spine level, even though PKA activation is a cell-wide phenomenon, in such a way that dopamine regulates the gain of NMDAR-dependent Hebbian plasticity via CaMKII activity (fig. S11). This interdependence between Hebbian and reinforcement plasticity has been implicitly assumed in the reinforcement learning theory, in which the Hebbian term is used for the credit assignment (*6*, *30*), and the dopamine timing in our study corresponds to the eligibility trace that determines the time window for reward action (*30*). Thus, we have clarified a molecular and cellular basis of reinforcement plasticity at the level of single dendritic spines.

REFERENCES AND NOTES

1. E. L. Thorndike, *Animal Intelligence* (Macmillan, New York, 1911).
2. I. P. Pavlov, *Conditioned Reflexes; An Investigation of the Physiological Activity of the Cerebral Cortex* (Oxford Univ. Press, Humphrey Milford, London, 1927).
3. M. F. Roitman, R. A. Wheeler, R. M. Carelli, *Neuron* **45**, 587–597 (2005).
4. Y. Dan, M. M. Poo, *Physiol. Rev.* **86**, 1033–1048 (2006).
5. J. Black, J. D. Belluzzi, L. Stein, *Brain Res.* **359**, 113–119 (1985).
6. W. Schultz, *J. Neurophysiol.* **80**, 1–27 (1998).
7. S. L. Smith-Roe, A. E. Kelley, *J. Neurosci.* **20**, 7737–7742 (2000).
8. T. Nakano, J. Yoshimoto, K. Doya, *Front. Comput. Neurosci.* **7**, 119 (2013).
9. M. Matsuzaki *et al.*, *Nat. Neurosci.* **4**, 1086–1092 (2001).
10. M. Matsuzaki, N. Honkura, G. C. R. Ellis-Davies, H. Kasai, *Nature* **429**, 761–766 (2004).
11. J. Tanaka *et al.*, *Science* **319**, 1683–1687 (2008).
12. C. D. Harvey, R. Yasuda, H. Zhong, K. Svoboda, *Science* **321**, 136–140 (2008).
13. C. R. Gerfen *et al.*, *Science* **250**, 1429–1432 (1990).
14. W. Shen, M. Flajolet, P. Greengard, D. J. Surmeier, *Science* **321**, 848–851 (2008).
15. J. N. J. Reynolds, B. I. Hyland, J. R. Wickens, *Nature* **413**, 67–70 (2001).
16. R. A. Rescorla, *Annu. Rev. Neurosci.* **11**, 329–352 (1988).
17. Y. G. Kwon *et al.*, *Proc. Natl. Acad. Sci. U.S.A.* **94**, 3536–3541 (1997).
18. R. D. Blitzer *et al.*, *Science* **280**, 1940–1943 (1998).
19. C. Cepeda, M. S. Levine, *Sci. STKE* **2006**, pe20 (2006).
20. K. Takao *et al.*, *J. Neurosci.* **25**, 3107–3112 (2005).
21. S. J. R. Lee, Y. Escobedo-Lozoya, E. M. Szatmari, R. Yasuda, *Nature* **458**, 299–304 (2009).
22. A. J. Lam *et al.*, *Nat. Methods* **9**, 1005–1012 (2012).
23. G. D. Ferguson, D. R. Storm, *Physiology (Bethesda)* **19**, 271–276 (2004).
24. L. R. V. Castro *et al.*, *J. Physiol.* **591**, 3197–3214 (2013).
25. A. Nishi *et al.*, *J. Neurosci.* **28**, 10460–10471 (2008).
26. E. I. Charych, L. X. Jiang, F. Lo, K. Sullivan, N. J. Brandon, *J. Neurosci.* **30**, 9027–9037 (2010).
27. C. J. Wilson, P. M. Groves, *J. Comp. Neurol.* **194**, 599–615 (1980).
28. R. D. Hawkins, T. W. Abrams, T. J. Carew, E. R. Kandel, *Science* **219**, 400–405 (1983).
29. Y. Yovell, T. W. Abrams, *Proc. Natl. Acad. Sci. U.S.A.* **89**, 6526–6530 (1992).
30. R. S. Sutton, A. G. Barto, *Reinforcemnet Learning* (MIT Press, Cambridge, MA, 1998).

ACKNOWLEDGMENTS

We thank K. Kaibuchi, M. Mishina, T. Tanabe, K. Doya, J. Wickens, T. Toyoizumi, and K. Kasai for helpful discussion; K. Deisseroth for the channelrhodopsin-2 plasmids; M. Z. Lin for the Camuiα-CR and AKAR2-CR plasmids; K. Iwamoto and S. Jinde for confocal microscopy; M. Ikeda for technical assistance; and M. Ogasawara and M. Tamura for laboratory facility. This work was supported by the Strategic Research Program for Brain Sciences ("Bioinformatics for Brain Sciences" to H.K. and S.I.) and Grants-in-Aid (2000009 and 26221011 to H.K.) from the Ministry of Education, Culture, Sports, Science, and Technology and by the National Institutes of Health GM53395, DA035612, and NS069720 (G.C.R.E.-D.). This work was also supported by the Human Frontier Science Program (H.K.). G.C.R.E.-D. has a patent in the United States for the synthesis of dinitroindolinyl-caged neurotransmitters.

SUPPLEMENTARY MATERIALS

www.sciencemag.org/content/345/6204/1616/suppl/DC1
Materials and Methods
Figs. S1 to S11
References (*31*–*39*)

1 May 2014; accepted 29 August 2014
10.1126/science.1255514

NITROGEN FIXATION

Ligand binding to the FeMo-cofactor: Structures of CO-bound and reactivated nitrogenase

Thomas Spatzal,[1]* Kathryn A. Perez,[1] Oliver Einsle,[2,3] James B. Howard,[1,4] Douglas C. Rees[1]*

The mechanism of nitrogenase remains enigmatic, with a major unresolved issue concerning how inhibitors and substrates bind to the active site. We report a crystal structure of carbon monoxide (CO)–inhibited nitrogenase molybdenum-iron (MoFe)–protein at 1.50 angstrom resolution, which reveals a CO molecule bridging Fe2 and Fe6 of the FeMo-cofactor. The μ_2 binding geometry is achieved by replacing a belt-sulfur atom (S2B) and highlights the generation of a reactive iron species uncovered by the displacement of sulfur. The CO inhibition is fully reversible as established by regain of enzyme activity and reappearance of S2B in the 1.43 angstrom resolution structure of the reactivated enzyme. The substantial and reversible reorganization of the FeMo-cofactor accompanying CO binding was unanticipated and provides insights into a catalytically competent state of nitrogenase.

Biological nitrogen fixation is nature's pathway to convert atmospheric dinitrogen (N_2) into a bioavailable form, ammonia (NH_3). Nitrogenase, the only known enzyme capable of performing this multielectron reduction, consists of two component metalloproteins, the iron (Fe)–protein (Av2) and the molybdenum-iron (MoFe)–protein (Av1) (*1*–*3*). The Fe-protein, containing a [4Fe:4S]-cluster, mediates the adenosine triphosphate (ATP)–dependent electron transfer to the MoFe-protein to support dinitrogen reduction (*4*). The MoFe-protein is an $\alpha_2\beta_2$ heterotetramer with one catalytic unit per αβ heterodimer (*5*). To achieve the elaborate redox properties required for reducing the N–N triple bond, two metal centers are present in the MoFe-protein: the P-cluster and the FeMo-cofactor. The P-cluster, an [8Fe:7S] entity, is the initial acceptor for electrons, donated from the Fe-protein during complex formation between the two proteins (*6*–*8*). Electrons are subsequently transferred to the FeMo-cofactor, a [7Fe:9S:C:Mo]-*R*-homocitrate cluster that constitutes the active site for substrate reduction and is the most complex metal center known in biological systems (*5*, *9*–*12*).

Substrates and inhibitors bind only to forms of the MoFe-protein reduced by two to four electrons relative to the resting, "as-isolated" state, which can only be generated in the presence of reduced Fe-protein and ATP (*1*). Mechanistic studies must take into account the dynamic nature of the nitrogenase system, which requires multiple association and dissociation events between the two component proteins, as well as the ubiquitous presence of protons that are reduced to dihydrogen even in competition with other substrates (*1*, *13*–*15*). The resulting distribution of intermediates under turnover conditions complicates the structural and spectroscopic investigation of substrate interactions. Hence, even the fundamental question of whether molybdenum or iron represents the site for substrate binding at the FeMo-cofactor is still under debate, and as a consequence, a variety of mechanistic pathways have been proposed based on either molybdenum or iron as the catalytic center, mainly following Chatt-type chemistry (*16*).

Inhibitors are potentially powerful tools for the preparation of stably trapped transient states that could provide insight into the multielectron reduction mechanism. In this regard, carbon monoxide (CO), a noncompetitive inhibitor for all substrates except protons (*17*, *18*), has a number of attractive properties; CO is isoelectronic to the physiological substrate, is a reversible inhibitor, and only binds to partially reduced MoFe-protein generated under turnover conditions. Although noncompetitive inhibitors are traditionally considered to bind at distinct sites from the substrate, for complex enzymes—such as nitrogenase—with multiple oxidation states and potential substrate-binding modes, this distinction is not required (*19*). More recently, it has also been shown that CO is a substrate, albeit a very poor one, whose reduction includes concomitant C–C bond formation to generate C2 and longer-chain hydrocarbons, in a reaction reminiscent of the Fischer-Tropsch synthesis (*20*, *21*). Therefore, CO binding as inhibitor or substrate must involve important active-site properties common to the reduction of the natural substrate dinitrogen. For this reason, CO binding has been investigated by a variety of spectroscopic methods, most notably electron paramagnetic resonance and infrared spectroscopy, and depending on the partial pressure, multiple CO-bound species have been observed; yet, a structurally explicit description of any CO-binding site has been elusive (*18*, *22*–*27*).

Building on these observations, we have determined a high-resolution crystal structure of a CO-bound state of the MoFe-protein from *Azotobacter vinelandii*. This necessitated overcoming several obstacles. First, the experimental setup for all protein-handling steps, including crystallization, was deemed to require the continuous presence of CO. Second, because inhibition requires enzyme turnover, a prerequisite was the ability to obtain crystals of the MoFe-protein from activity assay mixtures, rather than from isolated protein (see supplementary material for assay details), conditions that are typically contradictory to crystallization requirements. Finally, rapid MoFe-protein crystallization (≤5 hours) was crucial and was achieved on the basis of previously developed protocols in combination with seeding strategies and in the presence of CO (*10*).

Crystals of the inhibited MoFe-protein (Av1-CO) yielded structural data at 1.50 Å resolution, which allowed clear identification of a CO ligand (Fig. 1, A and C, and fig. S1, A to D). The Av1-CO structure directly demonstrates the binding of one molecule of CO per active site in a μ_2-bridging mode between Fe2 and Fe6 that forms one edge of the trigonal six-iron prism (Fe2-3-4-5-6-7) of the FeMo-cofactor (Fig. 1, A, C, and D). CO binding is accompanied by a displacement of one of the belt sulfur atoms (S2B), although it retains the essentially tetrahedral coordination spheres for Fe2 and Fe6. As a result, the two Fe are coordinated by two sulfur and two carbon atoms—a geometry, to our knowledge, not previously observed in metalloclusters [although higher–coordination number geometries have

[1]Howard Hughes Medical Institute and Division of Chemistry and Chemical Engineering, MailCode 114-96, California Institute of Technology, Pasadena, CA 91125, USA. [2]Institut für Biochemie, Albert-Ludwigs-Universität Freiburg, 79104 Freiburg, Germany. [3]BIOSS Centre for Biological Signalling Studies, Albert-Ludwigs-Universität Freiburg, 79104 Freiburg, Germany. [4]Department of Biochemistry, Molecular Biology and Biophysics, University of Minnesota, Minneapolis, MN 55455, USA.
*Corresponding author. E-mail: spatzal@caltech.edu (T.S.); dcrees@caltech.edu (D.C.R.)

been observed in FeFe-hydrogenases (*28*)]. Confirmation of the S2B displacement was provided by anomalous difference Fourier maps calculated with diffraction data measured at 7100 eV (Fig. 1B); this energy is just below the Fe K-edge so that the anomalous scattering from S is substantially enhanced relative to Fe. The carbon atom of CO is located at a distance of 1.86 Å from each of the irons (Fe2 and Fe6), compared with a previous distance of 2.2 Å for S2B (Fig. 1C). The altered ligand environment results in a small adjustment of the FeMo-cofactor geometry, with the Fe2-Fe6 distance (2.5 Å) slightly shortened relative to the unchanged Fe4-Fe5 and Fe3-Fe7 distances (2.6 Å) (Fig. 1C).

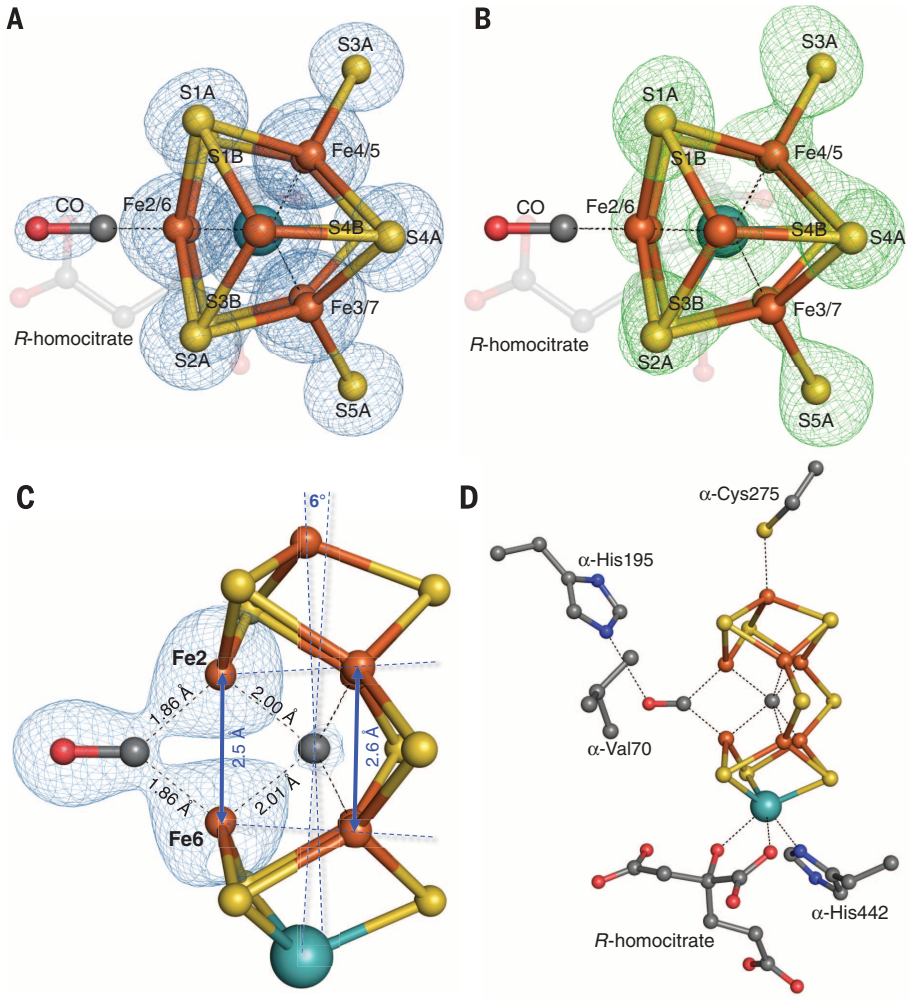

Fig. 1. CO-inhibited MoFe-protein (Av1-CO). Refined structure of the CO-bound FeMo-cofactor at a resolution of 1.50 Å. (**A**) View along the Fe1-C-Mo direction. The electron density ($2F_{obs} - F_{calc}$) map is contoured at 4.0 σ and represented as blue mesh. The density at the former S2B site is substantially decreased and in excellent agreement with bound CO [see also (C)]. (**B**) Same orientation as (A) superimposed with the anomalous density map calculated at 7100 eV (green) at a resolution of 2.1 Å contoured at 4.0 σ, showing the absence of anomalous electron density at the CO site. (**C**) Side view of FeMo-cofactor highlighting the μ_2 binding geometry of CO. The electron density ($2F_{obs} - F_{calc}$) map (blue mesh) surrounding CO-Fe2-Fe6-C is contoured at 1.5 σ. (**D**) Same orientation as (C) highlighting the ligand environment of the metal center. The catalytically important side-chain residues α-Val70 and α-His195 are in close proximity to the CO-binding site. Iron atoms are shown in orange, sulfur in yellow, molybdenum in turquoise, carbon in gray, nitrogen in blue, and oxygen in red.

Table 1. Nitrogenase activity. The acetylene reduction activity of "as-isolated" Av1, Av1-CO, and Av1 reactivated was measured by the quantification of ethylene production. Nitrogenase activity is quantitatively recovered upon reactivation. Errors represent standard deviations of three measurements.

Sample	Specific reduction activity	
	Amount [nmol(acetylene) min^{-1} $mg(Av1)^{-1}$]	Percent (%)
Av1 as isolated	1930 ± 90	100 ± 5
Av1-CO	< 2 ± 2	< 0.1 ± 0.1
Av1 reactivated	1820 ± 80	94 ± 4

Given the complete displacement of S2B, we assessed whether the CO-inhibited protein could be reactivated or if it was irreversibly modified. Crystals of CO-inhibited MoFe-protein were active when dissolved in an assay mixture in the absence of CO. Furthermore, when we newly assayed CO-inhibited MoFe-protein from the original inhibition preparations after removal of CO (see supplementary material for assay details), a quantitative recovery (94 ± 4%) of the initial activity was obtained (Table 1). The reactivated MoFe-protein was subsequently reisolated from activity assay mixtures and crystallized, which yielded a structure at 1.43 Å resolution. The structural data of the protein (Av1 reactivated) revealed that S2B is regained by replacing the previously bound CO ligand, which results in the recovery of the resting state FeMo-cofactor. The full occupancy of the sulfur at the S2B site in the reactivated enzyme is evident by inspecting the $2F_{obs} - F_{calc}$ electron density map, as well as the anomalous electron density map verifying the anomalous scattering contribution expected for S2B (Fig. 2, A and B).

The finding that S2B can be reversibly replaced by CO raises the question of where this atom is located in the CO-inhibited state. If the S2B binding site is ordered, candidate locations should be evident by an inspection of the 7100 eV anomalous difference Fourier map. In this manner, one site per catalytic unit was identified with anomalous density compatible with sulfur. This potential sulfur binding site (SBS) is positioned ~22 Å away from the S2B position in the FeMo-cofactor and consists of a small protein pocket at the interface of the α and β subunits, formed by the side chains of residues α-Arg*93*, α-Thr104, α-Thr111, α-Met112, β-Asn*65*, β-Trp428, β-Phe450, and β-Arg*453* (Fig. 3, A and B). The positive surface charge of the cavity is suited to accommodate an anionic species such as HS^- or S^{2-} (Fig. 3B). In previous structures of the resting state enzyme [Protein Data Bank (PDB) IDs: 1M1N and 3U7Q], this site has been assigned as water; note that the density at this site is also decreased in the structure of reactivated Av1 (fig. S2). The potential SBS is connected to the FeMo-cofactor–binding pocket by a noncontinuous water channel, and conformational rearrangements would be needed to accommodate the reversible migration of S2B from and to the active site. Although we have observed a correlation between density at the potential SBS and the CO-inhibited state of the MoFe-protein, the identity of this site as the displaced S2B cannot be achieved solely based on crystallographic data. In assessing the relevance of this site, it should be noted that the residues forming the pocket are poorly conserved, the site seems rather remote from the FeMo-cofactor, and because sulfur and chloride

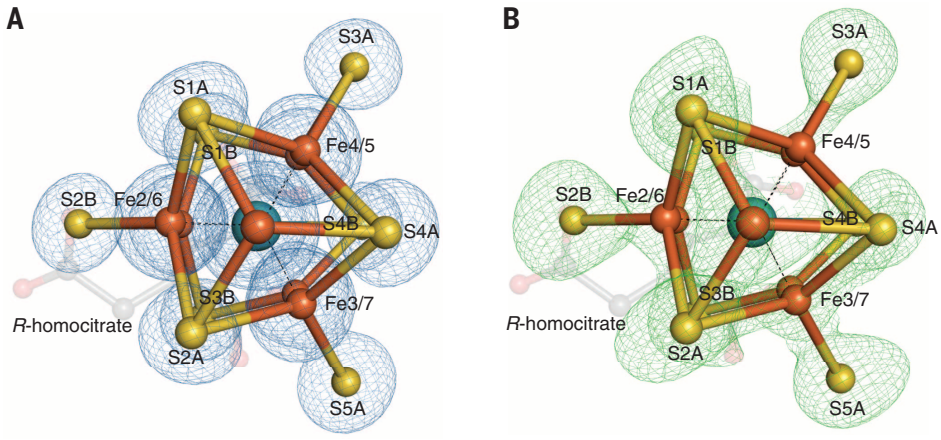

Fig. 2. Reactivated MoFe-protein (Av1 reactivated). Refined structure of the FeMo-cofactor at a resolution of 1.43 Å. (**A**) View along the Fe1-C-Mo direction. The electron density ($2F_{obs} - F_{calc}$) map is contoured at 4.0 σ and represented as blue mesh. Electron density at the S2B site is in excellent agreement with a regained sulfur. (**B**) Same orientation as (A) superimposed with the anomalous density map (green) at a resolution of 2.15 Å contoured at 4.0 σ, showing the presence of anomalous density at the S2B site. Color scheme is according to Fig. 1.

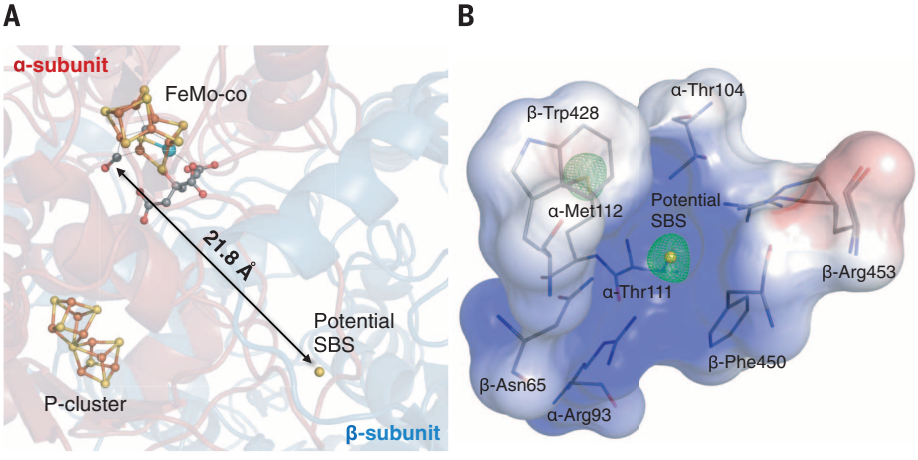

Fig. 3. Overview of the potential sulfur binding site (SBS) in the CO-inhibited MoFe-protein (Av1-CO). (**A**) Location of the potentially bound sulfur in a protein cavity on the interface between the α and β subunits of the $\alpha_2\beta_2$ MoFe-protein. The potential SBS is located 22 Å away from its former position in the FeMo-cofactor (S2B-site). (**B**) Close-up view of the binding cavity. Positive surface charge is represented in blue, negative surface charge in red. The anomalous density map at a resolution of 2.1 Å is represented as green mesh and contoured at 4.0 σ, showing the presence of anomalous density at the potential SBS. The side-chain sulfur of α-Met112 provides an internal standard for full occupancy. Alternate conformations for β-Arg453 are indicated. The color scheme is according to Fig. 1.

have similar anomalous scattering properties at 7100 eV, it is possible that this is a general anion-binding site in Av1.

The crystallographic characterization of CO-bound FeMo-cofactor of the MoFe-protein has important implications for the mechanism of substrate reduction by nitrogenase: The CO-binding site is close to the side chains of residues α-His195 (2.8 Å, NE2–OC distance) and α-Val70 (3.4 Å, closest methyl–OC distance). Modifications to both side chains were reported to substantially alter the catalytic properties of the enzyme. An α-His195 to α-Gln195 mutation resulted in the loss of N_2 reduction activity, while an α-Val70 to α-Ala/Gly70 alteration was reported to enable the reduction of longer carbon-chain substrates and highlighted the potential involvement of Fe6 in substrate reduction (*29*–*33*). In the structure presented here, α-His195 is in hydrogen bonding distance to the oxygen of CO, and α-Val70 directly flanks the binding site (Fig. 1D).

The displacement of S2B could be facilitated by a proton donation from α-His195 to yield either HS^- or H_2S, which would generate a better leaving group than S^{2-}. Although the dissociation of a sulfur may seem surprising, it opens up the ligand binding site, because the large radius of S^{2-} effectively shields the cofactor Fe atoms in the resting state from substrate and/or inhibitor attack (*2*). The more general implication that binding of exogenous ligands can be accompanied by the reversible dissociation of at least one belt sulfur from the metal sites of the FeMo-cofactor changes the present view of the structural inertness of the [7Fe:9S:C:Mo]-*R*-homocitrate cluster toward ligand exchange. The relative lack of reactivity of the resting state is a striking property of the FeMo-cofactor, and the requirement for more highly reduced forms to bind substrate and inhibitors may reflect the need to dissociate sulfur ligands from Fe sites.

The displacement of the belt sulfur S2B by carbon monoxide causes the FeMo-cofactor scaffold to lose its intrinsic three-fold symmetry. Additionally, Fe1, the interstitial carbon, and molybdenum are no longer aligned, creating an asymmetry in the resulting [7Fe:8S:C:Mo] cluster (Fig. 1C). The modest adjustments of the remaining scaffold upon CO binding are suggestive of an important role for the interstitial carbon in stabilizing the cofactor during rearrangements and substitutions to the coordination environment of the irons (*34*, *35*).

The experimental manipulations used to generate the CO-inhibited structure are distinct from those reported in previous spectroscopic studies; hence, it is not possible to unambiguously assign the structure to one of the many annotated spectroscopic states. Note that many of the previously identified states undergo dynamic interchanges, including photoinduced transitions between states (*25*). Like the structure presented here, the spectroscopically identified "lo-CO" state has been proposed to involve one molecule of CO bound to the active site in a bridging mode (*22*, *26*). A state with two CO bound to Fe2 and Fe6 could correspond to the "high-CO" form (*22*, *23*) and might represent an intermediate relevant to the C–C coupling reaction.

The generation and successful stabilization of CO-bound MoFe protein under turnover conditions has culminated in a crystal structure that provides a detailed view of a ligand bound to the nitrogenase active site. The observations that CO is isoelectric to N_2, is a potent yet reversible inhibitor of substrate reduction without impeding proton reduction to dihydrogen, and is bound in close proximity to previously determined catalytically important residues emphasize the relevance of the CO-bound structure toward understanding dinitrogen binding and reduction. This sheds light on N_2 activation based on a di-iron edge of the FeMo-cofactor and in this respect resembles the Haber-Bosch catalyst that also uses an iron surface to break the N–N triple bond. The demonstrated structural accessibility of CO-bound MoFe-protein opens the door for comparable studies on a variety of inhibitors and substrates, with the goal of understanding the detailed molecular mechanism of dinitrogen reduction by nitrogenase.

REFERENCES AND NOTES

1. B. K. Burgess, D. J. Lowe, *Chem. Rev.* **96**, 2983–3012 (1996).
2. J. B. Howard, D. C. Rees, *Proc. Natl. Acad. Sci. U.S.A.* **103**, 17088–17093 (2006).
3. L. C. Seefeldt, B. M. Hoffman, D. R. Dean, *Annu. Rev. Biochem.* **78**, 701–722 (2009).
4. M. M. Georgiadis *et al*., *Science* **257**, 1653–1659 (1992).
5. J. Kim, D. C. Rees, *Nature* **360**, 553–560 (1992).
6. H. Schindelin, C. Kisker, J. L. Schlessman, J. B. Howard, D. C. Rees, *Nature* **387**, 370–376 (1997).
7. J. W. Peters, K. Fisher, W. E. Newton, D. R. Dean, *J. Biol. Chem.* **270**, 27007–27013 (1995).
8. D. J. Lowe, K. Fisher, R. N. F. Thorneley, *Biochem. J.* **292**, 93–98 (1993).
9. O. Einsle *et al*., *Science* **297**, 1696–1700 (2002).
10. T. Spatzal *et al*., *Science* **334**, 940 (2011).
11. K. M. Lancaster *et al*., *Science* **334**, 974–977 (2011).
12. Y. Hu, M. W. Ribbe, *Coord. Chem. Rev.* **255**, 1218–1224 (2011).
13. D. C. Rees *et al*., *Philos. Trans. A Math. Phys. Eng. Sci.* **363**, 971–984 (2005).
14. D. J. Lowe, R. N. F. Thorneley, *Biochem. J.* **224**, 895–901 (1984).
15. R. N. F. Thorneley, D. J. Lowe, *Biochem. J.* **215**, 393–403 (1983).
16. J. Chatt, J. R. Dilworth, R. L. Richards, *Chem. Rev.* **78**, 589–625 (1978).
17. J. C. Hwang, C. H. Chen, R. H. Burris, *Biochim. Biophys. Acta* **292**, 256–270 (1973).
18. L. M. Cameron, B. J. Hales, *Biochemistry* **37**, 9449–9456 (1998).
19. L. C. Davis, M. T. Henzl, R. H. Burris, W. H. Orme-Johnson, *Biochemistry* **18**, 4860–4869 (1979).
20. C. C. Lee, Y. Hu, M. W. Ribbe, *Science* **329**, 642–642 (2010).
21. Y. Hu, C. C. Lee, M. W. Ribbe, *Science* **333**, 753–755 (2011).
22. H.-I. Lee, L. M. Cameron, B. J. Hales, B. J. Hoffman, *J. Am. Chem. Soc.* **119**, 10121–10126 (1997).
23. L. Yan *et al*., *Eur. J. Inorg. Chem.* **2011**, 2064–2074 (2011).
24. S. J. George, G. A. Ashby, C. W. Wharton, R. N. F. Thorneley, *J. Am. Chem. Soc.* **119**, 6450–6451 (1997).
25. Z. Maskos, B. J. Hales, *J. Inorg. Biochem.* **93**, 11–17 (2003).
26. R. C. Pollock *et al*., *J. Am. Chem. Soc.* **117**, 8686–8687 (1995).
27. L. C. Davis, M. T. Henzl, R. H. Burris, W. H. Orme-Johnson, *Biochemistry* **18**, 4860–4869 (1979).
28. D. W. Mulder *et al*., *Structure* **19**, 1038–1052 (2011).
29. P. M. C. Benton *et al*., *Biochemistry* **42**, 9102–9109 (2003).
30. C. H. Kim, W. E. Newton, D. R. Dean, *Biochemistry* **34**, 2798–2808 (1995).
31. P. C. Dos Santos, S. M. Mayer, B. M. Barney, L. C. Seefeldt, D. R. Dean, *J. Inorg. Biochem.* **101**, 1642–1648 (2007).
32. D. J. Scott, H. D. May, W. E. Newton, K. E. Brigle, D. R. Dean, *Nature* **343**, 188–190 (1990).
33. J. Christiansen, V. L. Cash, L. C. Seefeldt, D. R. Dean, *J. Biol. Chem.* **275**, 11459–11464 (2000).
34. J. Rittle, J. C. Peters, *Proc. Natl. Acad. Sci. U.S.A.* **110**, 15898–15903 (2013).
35. I. Dance, *Chem. Asian J.* **2**, 936–946 (2007).

ACKNOWLEDGMENTS

We thank J. Peters, L. Zhang, J. Rittle, C. Morrison, B. Wenke, and K. Dörner for informative discussions. This work was supported by NIH grant GM45162 (D.C.R.), Deutsche Forschungsgemeinschaft grants EI-520/7 and RTG 1976, and the European Research Council N-ABLE project (O.E.). We gratefully acknowledge the Gordon and Betty Moore Foundation, the Beckman Institute, and the Sanofi-Aventis Bioengineering Research Program at Caltech for their generous support of the Molecular Observatory at Caltech and the staff at Beamline 12–2, Stanford Synchrotron Radiation Lightsource (SSRL), for their assistance with data collection. SSRL is operated for the U.S. Department of Energy and supported by its Office of Biological and Environmental Research and by the NIH: National Institute of General Medical Sciences (P41GM103393) and the National Center for Research Resources (P41RR001209). We thank the Center for Environmental Microbial Interactions for its support of microbiology research at Caltech. Coordinates and structure factors have been deposited in the Protein Data Bank of the Research Collaboratory for Structural Bioinformatics, with IDs 4TKV (Av1-CO) and 4TKU (Av1 reactivated).

SUPPLEMENTARY MATERIALS

www.sciencemag.org/content/345/6204/1620/suppl/DC1
Materials and Methods
Figs. S1 and S2
Tables S1 and S2
References (*36*–*43*)

29 May 2014; accepted 31 July 2014
10.1126/science.1256679

IMMUNODEFICIENCY

Immune dysregulation in human subjects with heterozygous germline mutations in *CTLA4*

Hye Sun Kuehn,[1]* Weiming Ouyang,[2]* Bernice Lo,[3,4]* Elissa K. Deenick,[5,6] Julie E. Niemela,[1] Danielle T. Avery,[5] Jean-Nicolas Schickel,[7] Dat Q. Tran,[8] Jennifer Stoddard,[1] Yu Zhang,[4,9] David M. Frucht,[2] Bogdan Dumitriu,[10] Phillip Scheinberg,[10] Les R. Folio,[11] Cathleen A. Frein,[12] Susan Price,[3,4] Christopher Koh,[13] Theo Heller,[13] Christine M. Seroogy,[14] Anna Huttenlocher,[14,15] V. Koneti Rao,[3,4] Helen C. Su,[4,9] David Kleiner,[16] Luigi D. Notarangelo,[17] Yajesh Rampertaap,[18] Kenneth N. Olivier,[18] Joshua McElwee,[19] Jason Hughes,[19] Stefania Pittaluga,[16] Joao B. Oliveira,[20] Eric Meffre,[7] Thomas A. Fleisher,[1]† Steven M. Holland,[4,18] Michael J. Lenardo,[3,4]† Stuart G. Tangye,[5,6] Gulbu Uzel[18]†

Cytotoxic T lymphocyte antigen–4 (CTLA-4) is an inhibitory receptor found on immune cells. The consequences of mutations in *CTLA4* in humans are unknown. We identified germline heterozygous mutations in *CTLA4* in subjects with severe immune dysregulation from four unrelated families. Whereas *Ctla4* heterozygous mice have no obvious phenotype, human *CTLA4* haploinsufficiency caused dysregulation of FoxP3$^+$ regulatory T (T_{reg}) cells, hyperactivation of effector T cells, and lymphocytic infiltration of target organs. Patients also exhibited progressive loss of circulating B cells, associated with an increase of predominantly autoreactive CD21^{lo} B cells and accumulation of B cells in nonlymphoid organs. Inherited human *CTLA4* haploinsufficiency demonstrates a critical quantitative role for CTLA-4 in governing T and B lymphocyte homeostasis.

Immune tolerance is controlled by multiple mechanisms (*1*, *2*), including regulatory T (T_{reg}) cells (*3*–*5*) and inhibitory receptors (*6*, *7*). T_{reg} cells constitutively express the inhibitory receptor CTLA-4, which confers suppressive functions (*8*, *9*). CTLA-4, also known as CD152, is also expressed by activated T cells and, upon ligation, inhibits their proliferation (*10*). Homozygous deficiency of *Ctla4* in mice causes fatal multiorgan lymphocytic infiltration and destruction (*11*–*13*); hence, CTLA-4 functions at a key "checkpoint" in immune tolerance. CTLA-4–immunoglobulin (Ig) fusion protein and neutralizing CTLA-4 antibody are used to modulate immunity in autoimmune and cancer patients (*14*, *15*), respectively. Studies have given conflicting results regarding the association of *CTLA4* single-nucleotide variants (SNVs) with organ-specific autoimmunity (*16*). The consequences of genetic CTLA-4 deficiency in humans are unknown.

Our index patient—a 22-year-old female (A.II.1)—developed brain, gastrointestinal (GI), and lung lymphocytic infiltrates, autoimmune thrombocytopenia, and hypogammaglobulinemia in early childhood (Fig. 1A and table S1). Her 43-year-old father (A.I.1) manifested lung and GI infiltrates, hypogammaglobulinemia, and clonally expanded γδ-CD8$^+$ T cells infiltrating and suppressing the bone marrow (fig. S1A). Four additional cases from three unrelated families (families B, C, and D) (fig. S1 and table S1) were identified among a cohort of 23 patients with autoimmune cytopenias, hypogammaglobulinemia, CD4 T cell lymphopenia, and lymphocytic infiltration of nonlymphoid organs. Patient B.I.1, previously diagnosed with common variable immunodeficiency

[1]Department of Laboratory Medicine, Clinical Center, National Institutes of Health, Bethesda, MD 20892, USA. [2]Laboratory of Cell Biology, Division of Monoclonal Antibodies, Office of Biotechnology Products, Center for Drug Evaluation and Research, U.S. Food and Drug Administration, Bethesda, MD 20892, USA. [3]Molecular Development of the Immune System Section, Laboratory of Immunology, National Institute of Allergy and Infectious Diseases, Bethesda, MD 20892, USA. [4]NIAID Clinical Genomics Program, National Institute of Allergy and Infectious Diseases, Bethesda, MD 20892, USA. [5]Immunology and Immunodeficiency Group, Immunology Division, Garvan Institute of Medical Research, Sydney, NSW 2010, Australia. [6]St. Vincent's Clinical School Faculty of Medicine, University of New South Wales, Sydney, NSW 2010, Australia. [7]Department of Immunobiology, Yale University School of Medicine, New Haven, CT 06511, USA. [8]Department of Pediatrics, University of Texas Medical School, Houston, TX 77030, USA. [9]Immunological Diseases Unit, Laboratory of Host Defenses, National Institute of Allergy and Infectious Diseases, Bethesda, MD 20892, USA. [10]Hematology Branch, National Heart, Lung and Blood Institute, Bethesda, MD 20892, USA. [11]Radiology and Imaging and Sciences, Clinical Center, National Institutes of Health, Bethesda, MD 20892, USA. [12]Clinical Research Directorate, Clinical Monitoring Research Program, Leidos Biomedical Research Inc., Frederick National Laboratory for Cancer Research, Frederick, MD 21702, USA. [13]Liver Diseases Branch, National Institute of Diabetes and Digestive and Kidney Diseases, Bethesda, MD 20892, USA. [14]Department of Pediatrics, University of Wisconsin, Madison, WI 53706, USA. [15]Department of Medical Microbiology and Immunology, University of Wisconsin, Madison, WI 53706, USA. [16]Laboratory of Pathology, National Cancer Institute, Bethesda, MD 20892, USA. [17]Division of Immunology and Manton Center for Orphan Disease Research, Children's Hospital, Harvard Medical School, Boston, MA 10217, USA. [18]Laboratory of Clinical Infectious Diseases, National Institute of Allergy and Infectious Diseases, Bethesda, MD 20892, USA. [19]Merck Research Laboratories, Merck & Co., Boston, MA 02130, USA. [20]Instituto de Medicina Integral Prof. Fernando Figueira–IMIP, 50070 Recife-PE, Brazil.
*These authors contributed equally to this work.
†Corresponding author. E-mail: tfleishe@cc.nih.gov (T.A.F.); lenardo@nih.gov (M.J.L.); guzel@niaid.nih.gov (G.U.)

Fig. 1. Clinical phenotype and pedigree of the patients. (**A**) Top: Computed tomography images of lung and brain from patient A.II.1. Bottom: Histological section (magnification 20×) from a duodenal biopsy from a healthy donor (HD) and patient A.II.1 stained for CD3 (brown cells), showing an increased number of transepithelial T cells within the villi. (**B**) Flow cytometric analyses of CD4$^+$ cells or total lymphocytes stained for the indicated surface markers from a healthy donor and patient A.I.1. Data showing decreased CD45RA$^+$CD62L$^+$ naïve CD4$^+$ T cells are representative of three patients (A.I.1, A.II.1, and B.I.1). Programmed cell death–1 (PD1) expression data shown are representative of five patients (A.I.1, A.II.1, B.I.1, C.II.1, and D.II.1) and three healthy donors. Data showing decreased circulating B cells are representative of two patients (A.I.1 and A.II.1). (**C**) Mutations in patient alleles displayed on a schematic of the four exons of *CTLA4*, pedigrees, and phenotype summary highlighting organs (gray) with inflammatory infiltrates and autoimmune cytopenias for affected family members. TM, transmembrane domain. (**D**) Protein and mRNA expression of CTLA-4 in T_{reg} cells. Left: Levels of CTLA-4 expression in T_{reg} cells (CD4$^+$CD25$^+$FoxP3$^+$) were assessed by intracellular staining. The numbers in the upper right corner depict mean fluorescence intensity (MFI) of anti-CD152 (CTLA-4) staining. Dotted line indicates the peak of CTLA-4 expression in a healthy donor. Data shown are representative of three experiments. Right: Levels of *CTLA4* mRNA in T_{reg} cells (CD4$^+$CD25$^+$CD127^{lo}) sorted from seven different healthy donors and four patients were measured by real-time PCR using the probe for *CTLA4* transcript variant 1 (full length) and normalized to GAPDH. Data are means of replicates from six experiments. For relative gene expression, all data were normalized to the same HD. The horizontal lines indicate mean values from healthy donors or patients.

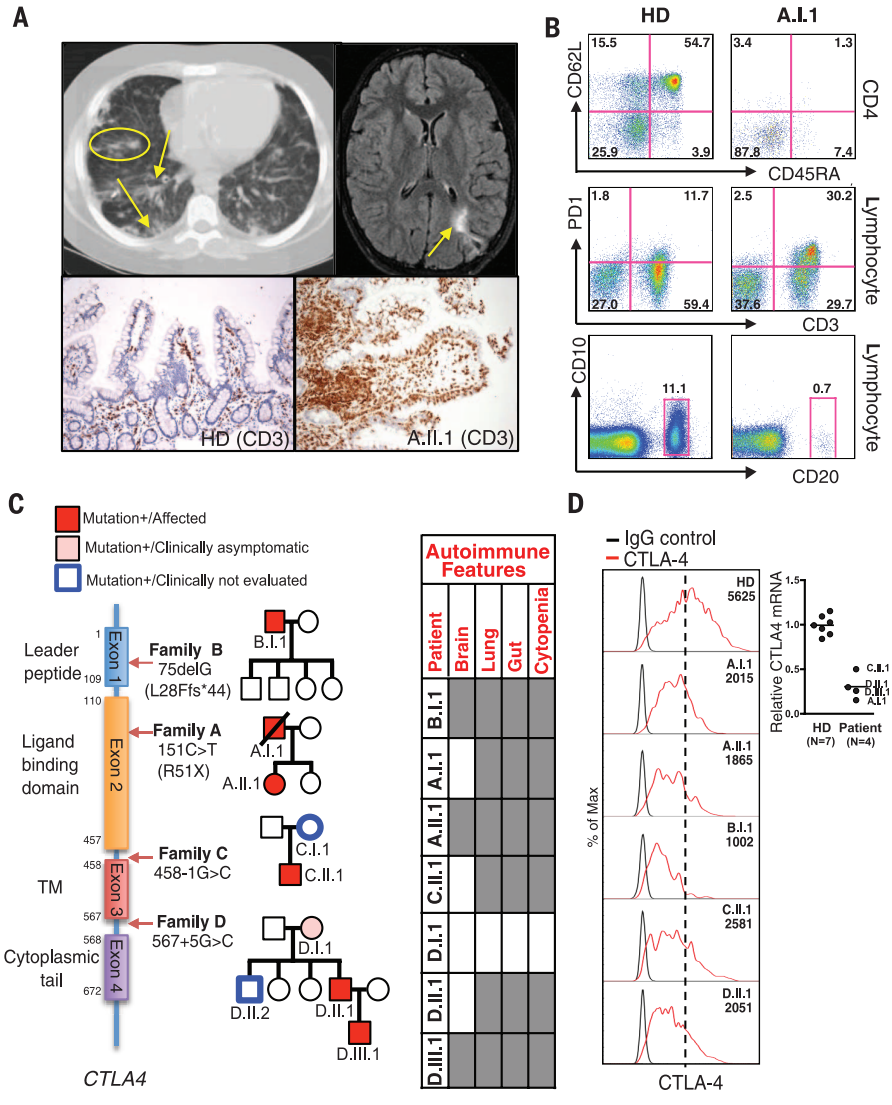

Fig. 2. Abnormal T_{reg} cell phenotype and function in patients. (**A**) Flow cytometric analysis of FoxP3 and CD25 in CD4$^+$ T cells from healthy donor (HD) and patients. (**B**) Mean fluorescence intensity of FoxP3 and CD25 in CD4$^+$ FoxP3$^+$ T cells from healthy donors and patients. Data are means ± SEM of replicates of indicated patient [A.I.1 (N = 7), A.II.1 (N = 1), B.I.1 (N = 2), C.II.1 (N = 2), D.II.1 (N = 4)] and 10 healthy donors. The N values represent number of replicates from each patient. ***P = 0.0007 (Mann-Whitney test). Bar graph: Percentage of CD25$^+$ and CD25$^-$ cells among CD4$^+$FoxP3$^+$ in 10 healthy donors and five patients. (**C**) Autologous and heterologous suppressive activities of T_{reg} cells from five healthy donors and four patients (A.I.1, B.I.1, C.II.1, and D.II.1). The horizontal lines indicate the mean values. Data are from three experiments, with each indicated patient paired with one or two healthy donors. *P = 0.0239, **P = 0.0037 (paired t test).

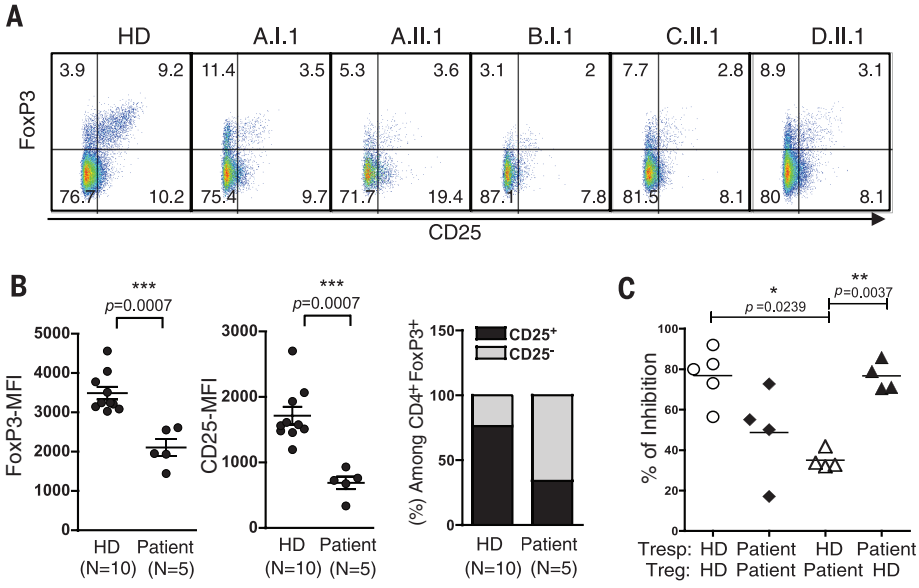

(CVID), had hepatosplenomegaly, autoimmune hemolytic anemia (AIHA), autoimmune thrombocytopenia, pulmonary nodules, and cerebral infiltrative lesions. C.II.1, a 19-year-old male, had childhood-onset EBV$^+$ Hodgkin's lymphoma and developed diffuse lymphadenopathy, splenomegaly, AIHA, autoimmune thrombocytopenia, and enteropathy. His mother (C.I.1), asymptomatic and considered unaffected, consented to genomic studies only. Patient D.II.1 is a 46-year-old male with psoriasis, lymphadenopathy, AIHA, and manifested GI and lung lymphocytic infiltrates. His mother (D.I.1) was unaffected, and his brother (D.II.2) was reportedly healthy but not clinically evaluated; however, his 11-year-old son (D.III.1) had lymphadenopathy, severe AIHA, and lymphocytic brain infiltration. In most patients, GI biopsies revealed histopathology similar to that caused by CTLA-4 blocking antibody treatment in melanoma patients (*17*, *18*).

Both patients in family A had low CD4$^+$ T cells with depleted CD45RA$^+$CD62L$^+$ naïve cells, increased expression of the exhaustion marker PD-1, and a progressive loss of circulating mature B cells (Fig. 1B and table S1). Similar and overlapping immune phenotypes were detected in the additional families (Fig. 1, B to D, and table S1).

We performed whole-exome sequencing using DNA from A.II.1 and identified a heterozygous, nonsense c.151C>T (p.R51X) mutation in *CTLA4*. This was confirmed by Sanger sequencing in the proband and A.I.1 (Fig. 1C). cDNA analyses from A.I.1 T cells showed that the mutant allele mRNA was degraded >95%, consistent with nonsense-mediated decay (table S2). *CTLA4* sequencing in B.I.1 revealed a frameshift deletion (c.75delG; p.L28Ffs*44) (Fig. 1C) that introduced a stop codon in exon 2. Families C and D had mutations in introns 2 and 3 (458–1G>C and 567+5G>C) (Fig. 1C) disrupting the acceptor and donor sites of the second or third introns, respectively. These mutations generated a *CTLA4* mRNA lacking the third exon, putatively encoding a soluble form of *CTLA4* (fig. S2A). Full-length *CTLA4* mRNA, encoding the membrane-bound form, was reduced. Serum-soluble CTLA-4 was comparable in patients and healthy individuals. In an extended cohort, de novo mutants were not identified; however, because B.I.1's parental genotypes are unknown, his mutation could be de novo.

Affected patients had reduced CTLA-4 protein and mRNA expression in sorted T_{reg} cells relative to healthy donors; this reduction persisted after activation (Fig. 1D and fig. S2, A and B). Deletion of *Ctla4* in mice impairs T_{reg} cell suppressive function, causing severe autoimmune disease and early lethality despite normal Foxp3 levels (*11*, *12*). We found that patients had normal percentages of FoxP3$^+$ T_{reg} cells with a CD127$^-$CD45RO$^+$Helios$^+$ phenotype (fig. S3, A and B), but overall expressed significantly less FoxP3 and CD25 [interleukin-2 (IL-2) receptor α subunit and a marker of T_{reg} cells] than T_{reg} cells from healthy donors, and a large proportion of their T_{regs} were CD25$^-$ (Fig. 2, A and B). *FOXP3* mRNA was also reduced in patient T_{reg} cells (fig. S3C). Next, we tested the function of healthy donor or patient T_{reg} cells and found that patient T_{regs} poorly suppressed proliferation of cocultured

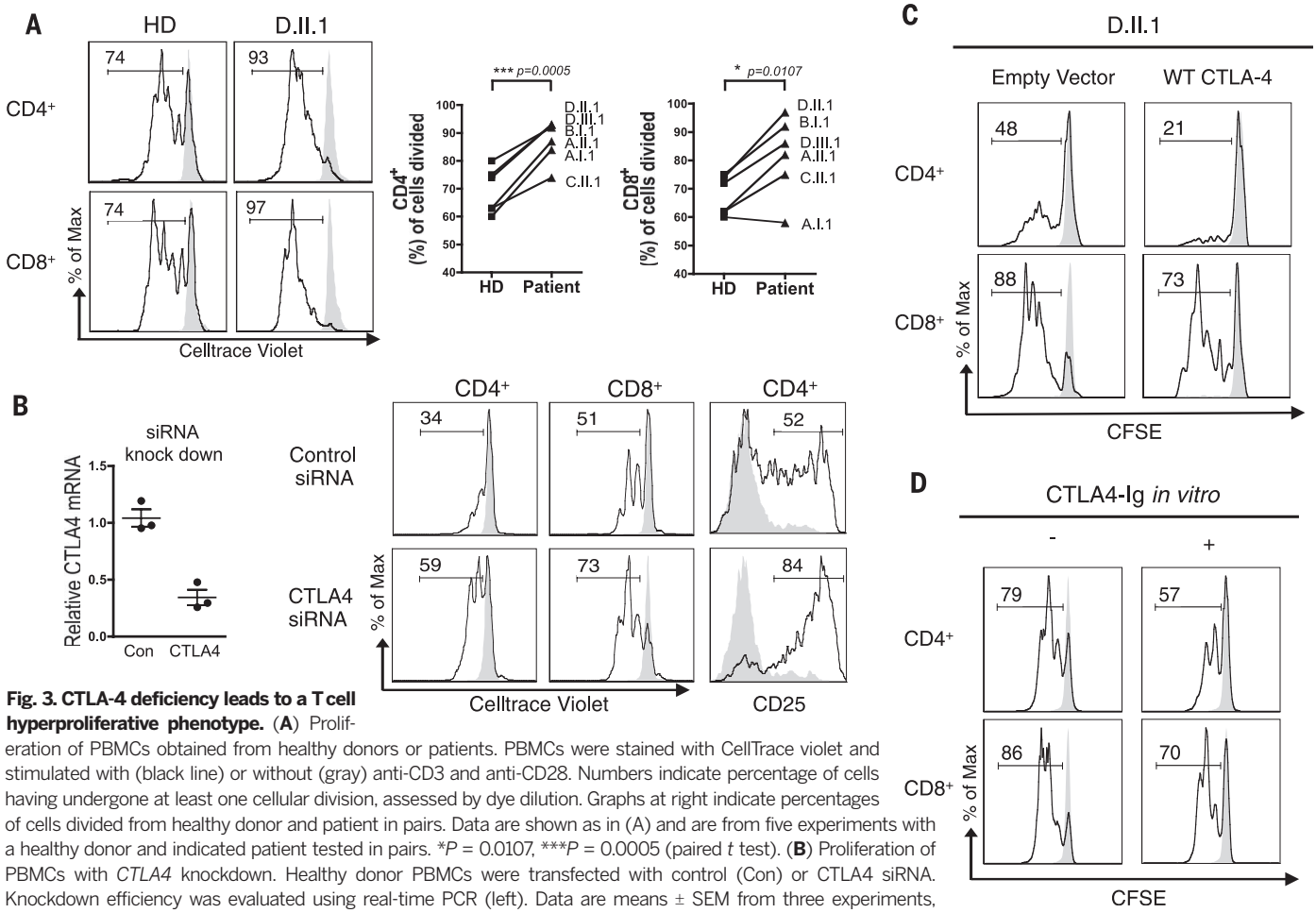

Fig. 3. CTLA-4 deficiency leads to a T cell hyperproliferative phenotype. (**A**) Proliferation of PBMCs obtained from healthy donors or patients. PBMCs were stained with CellTrace violet and stimulated with (black line) or without (gray) anti-CD3 and anti-CD28. Numbers indicate percentage of cells having undergone at least one cellular division, assessed by dye dilution. Graphs at right indicate percentages of cells divided from healthy donor and patient in pairs. Data are shown as in (A) and are from five experiments with a healthy donor and indicated patient tested in pairs. *P = 0.0107, ***P = 0.0005 (paired t test). (**B**) Proliferation of PBMCs with *CTLA4* knockdown. Healthy donor PBMCs were transfected with control (Con) or CTLA4 siRNA. Knockdown efficiency was evaluated using real-time PCR (left). Data are means ± SEM from three experiments, each with a different healthy donor. Cells were then assessed for proliferation and CD25 expression. Data shown are representative of three experiments with three healthy donors tested. (**C**) Reconstitution of wild-type CTLA-4 in patient cells. Patient D.II.1 PBMCs were transfected with control vector (pDsRed-N1) or CTLA-4–DsRed-N1 vector. Proliferation of DsRed$^+$ CD4 and CD8 patient T cells. Data shown are representative of three experiments with a total of three patients (B.I.1, C.II.1, D.II.1). (**D**) Effect of in vitro treatment with CTLA-4–Ig on proliferation of PBMCs. Patient D.III.1 PBMCs were stimulated with anti-CD3 in the presence (+) or absence (−) of CTLA-4–Ig. Data shown are representative of three experiments with a total of three patients (B.I.1, D.II.1, and D.III.1). Percentages of cells having undergone at least one cellular division are indicated in each histogram. Gray peak shows unstimulated cells.

activated autologous or allogeneic T responder cells (Fig. 2C and fig. S3D).

Among the nine subjects harboring *CTLA4* mutations, three relatives were reportedly healthy (C.I.1, D.I.1, and D.II.2). Only one of these unaffected healthy relatives (D.I.1) could be evaluated in detail, and she had no clinical findings similar to CTLA-4–deficient patients. Her T_{reg} cells showed higher expression of CTLA-4 and normal levels of FoxP3 and CD25 (fig. S4, A and B), whereas her effector T cells displayed the same in vitro hyperproliferation observed in affected patients (fig. S4C); these findings suggest that T_{reg} cell dysfunction might be essential for the full disease phenotype.

Consistent with the results of studies in mice (*11*–*13*), CTLA-4–deficient patient T cells were hyperproliferative, with an increased percentage expressing CD25 in response to T cell receptor stimulation (Fig. 3A and fig. S5A). To test whether patient T cell hyperproliferation resulted from reduced *CTLA4* expression, we used small interfering RNA (siRNA) to inhibit *CTLA4* expression in normal peripheral blood mononuclear cells (PBMCs). A factor of ~3 reduction in *CTLA4* recapitulated the hyperproliferative T cell phenotype (Fig. 3B). Moreover, overexpression of wild-type CTLA-4 in patient T cells suppressed the hyperproliferation (Fig. 3C and fig. S5, B and C), indicating that quantitative variations in CTLA-4 controlled the proliferative potential of T cells. CTLA-4–Ig fusion protein also suppressed patient T cell proliferation in vitro (Fig. 3D). Despite hyperproliferation of patient T cells in culture, the patients were lymphopenic. This may be explained by increased FAS (CD95) expression, caspase activity, and apoptosis of patient T cells, or by organ sequestration (fig. S6).

CTLA-4 function in B cells has been investigated, but its role remains unclear (*8*, *12*, *19*). We found that CTLA-4 expression was significantly reduced on activated B cells from patients (fig. S7A). The reduced frequencies of $CD27^+$ class-switched memory B cells and progressive B cell lymphopenia (Fig. 4, A and B), together with known B cell abnormalities in human autoimmune diseases (*20*), prompted us to further investigate B cell maturation and function.

In inflammatory conditions such as systemic lupus erythematosus, rheumatoid arthritis, Sjogren's syndrome, CVID with autoimmunity and lymphoproliferation, and certain chronic infections, a population of B cells expressing reduced levels of CD21 (termed $CD21^{lo}$ B cells) has been identified (*21*–*23*). $CD21^{lo}$ B cells have been viewed as anergic or "exhausted" cells on the basis of observations such as enrichment of self-reactive B cell receptors (BCRs), an activated phenotype, reduced responsiveness to BCR engagement, and increased apoptosis (*22*–*25*). We found that the frequency of $CD21^{lo}$ B cells was greatly elevated in patients' peripheral blood (Fig. 4B) (15 to 90% of B cells in CTLA-4–deficient patients versus <5% in controls). This subset progressively accumulated in patient A.I.1 from 41.5% to >95% of peripheral blood B cells over 3 years. Consistent with the anergic/exhausted state of $CD21^{lo}$ B cells (*22*), we observed heightened apoptosis in patient B cells (fig. S7, B and C) and poor BCR-induced proliferation relative to controls (Fig. 4C). The $CD21^{lo}$ B cells in CTLA-4–deficient patients were $CD19^{hi}CD20^{hi}CD38^{lo}$, distinguishing them from transitional ($CD19^+CD20^{hi}CD38^{hi}$) cells. Flow cytometric analysis revealed that these cells were phenotypically similar to the $CD21^{lo}$ B cell subset in other immune dysregulation disorders (fig. S8A) (*21*, *25*). Accordingly, autoreactive IgG may be produced by the $CD21^{lo}$ B cells, as a greater proportion were IgG^+CD27^- cells, relative to the corresponding cells in healthy donors. Functional analysis in vitro indicated that naïve B cells from CTLA-4–deficient patients secreted IgM and underwent class switching to secrete IgG and IgA robustly (fig. S8B). However, patient $CD21^{lo}$ B cells secreted less Ig than those of healthy donors (fig. S8B). The propensity of $CD21^{lo}$ B cells to exhibit more apoptosis ex vivo (fig. S7C) and their constitutive expression of CD95 (fig. S8A) could explain peripheral B cell lymphopenia and hypogammaglobulinemia in most CTLA-4–deficient patients. Increased frequencies of autoreactive mature naïve B cells have been demonstrated in the blood of patients with immunodysregulation polyendocrinopathy enteropathy X-linked syndrome (IPEX), which is a primary T_{reg} cell defect (*26*); this suggests a role for T_{reg} cells in preventing the accumulation of autoreactive B cells in the periphery. Thus, CTLA-4 haploinsufficiency decreases B cell tolerance and survival either intrinsically or extrinsically because of T_{reg} dysfunction (*26*).

Our data indicate that germline *CTLA4* haploinsufficiency causes lymphoproliferation, lymphocytic infiltration of nonlymphoid organs, autoimmune cytopenias, and B cell abnormalities with an accumulation of $CD21^{lo}$ B cells. These cells may account for antibody-mediated autoimmunity in our patients. In contrast, heterozygous *Ctla4* deficiency in mice shows no obvious phenotype (*12*, *13*). Interestingly, patient D.I.1, who has a *CTLA4* splicing mutation with no apparent somatic reversions or leakiness, is clinically healthy (table S2). This incomplete penetrance in disease may result from other genetic differences

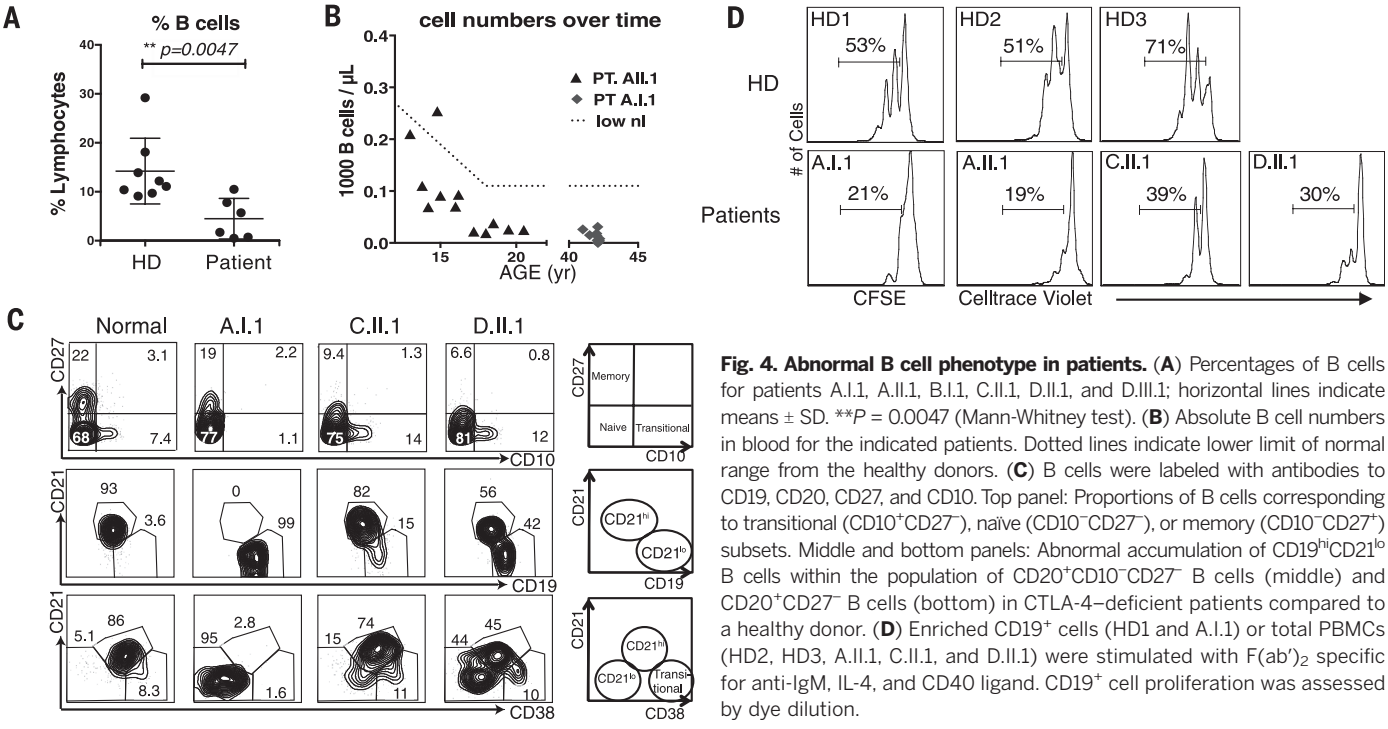

Fig. 4. Abnormal B cell phenotype in patients. (**A**) Percentages of B cells for patients A.I.1, A.II.1, B.I.1, C.II.1, D.II.1, and D.III.1; horizontal lines indicate means ± SD. $^{**}P = 0.0047$ (Mann-Whitney test). (**B**) Absolute B cell numbers in blood for the indicated patients. Dotted lines indicate lower limit of normal range from the healthy donors. (**C**) B cells were labeled with antibodies to CD19, CD20, CD27, and CD10. Top panel: Proportions of B cells corresponding to transitional ($CD10^+CD27^-$), naïve ($CD10^-CD27^-$), or memory ($CD10^-CD27^+$) subsets. Middle and bottom panels: Abnormal accumulation of $CD19^{hi}CD21^{lo}$ B cells within the population of $CD20^+CD10^-CD27^-$ B cells (middle) and $CD20^+CD27^-$ B cells (bottom) in CTLA-4–deficient patients compared to a healthy donor. (**D**) Enriched $CD19^+$ cells (HD1 and A.I.1) or total PBMCs (HD2, HD3, A.II.1, C.II.1, and D.II.1) were stimulated with $F(ab')_2$ specific for anti-IgM, IL-4, and CD40 ligand. $CD19^+$ cell proliferation was assessed by dye dilution.

between family members. This is analogous to that in autoimmune lymphoproliferative syndrome, a human genetic immune disorder with only 60% penetrance among family members harboring the same heterozygous gene mutation (*27*). Contrary to genetic deficiencies in inbred strains of mice, phenotypic variability is commonly observed in human single-gene disorders (*28*). This may explain why D.I.1 has a *CTLA4* mutation, yet is asymptomatic. C.I.1 and D.II.2 are apparently healthy because of incomplete penetrance; however, further immunological testing is required to confirm this assumption. We did not identify any common genetic modifiers in this study, as proven by our cohort analysis (see supplementary text). Also, our analysis of nonsynonymous SNVs in the *CTLA4* coding region showed that CTLA-4 expression and T cell function are comparable to those of wild-type controls (table S3 and figs. S9 and S10). Nonetheless, our findings show that the mutations reported here result in quantitative reductions in CTLA-4 expression, which contribute to a severe loss of tolerance and infiltrative autoimmune disease.

Our results show the spectrum of clinical complications that can be anticipated from CTLA-4–blocking drugs. Consistent with these findings, treatment with the CTLA-4 mimetic, CTLA-4–Ig, suppressed patient T cell hyperproliferation in vitro (Fig. 3D) and could be a potential therapeutic intervention for CTLA-4–deficient patients. Taken together, our results show that heterozygous *CTLA4* mutations in humans are associated with a severe immunoregulatory disorder, which we term CTLA-4 haploinsufficiency with autoimmune infiltration (CHAI) disease.

REFERENCES AND NOTES

1. J. A. Bluestone *et al*., *Nat. Rev. Immunol.* **10**, 797–803 (2010).
2. C. C. Goodnow, *Cell* **130**, 25–35 (2007).
3. S. Sakaguchi, T. Yamaguchi, T. Nomura, M. Ono, *Cell* **133**, 775–787 (2008).
4. S. Z. Josefowicz, L. F. Lu, A. Y. Rudensky, *Annu. Rev. Immunol.* **30**, 531–564 (2012).
5. C. Benoist, D. Mathis, *Cold Spring Harb. Perspect. Biol.* **4**, a007021 (2012).
6. B. T. Fife, J. A. Bluestone, *Immunol. Rev.* **224**, 166–182 (2008).
7. L. Chen, D. B. Flies, *Nat. Rev. Immunol.* **13**, 227–242 (2013).
8. K. Wing *et al*., *Science* **322**, 271–275 (2008).
9. O. S. Qureshi *et al*., *Science* **332**, 600–603 (2011).
10. M. F. Krummel, J. P. Allison, *J. Exp. Med.* **183**, 2533–2540 (1996).
11. E. A. Tivol *et al*., *Immunity* **3**, 541–547 (1995).
12. P. Waterhouse *et al*., *Science* **270**, 985–988 (1995).
13. C. A. Chambers, T. J. Sullivan, J. P. Allison, *Immunity* **7**, 885–895 (1997).
14. G. Herrero-Beaumont, M. J. Martínez Calatrava, S. Castañeda, *Reumatol. Clin.* **8**, 78–83 (2012).
15. M. K. Callahan, J. D. Wolchok, J. P. Allison, *Semin. Oncol.* **37**, 473–484 (2010).
16. H. Ueda *et al*., *Nature* **423**, 506–511 (2003).
17. P. Attia *et al*., *J. Clin. Oncol.* **23**, 6043–6053 (2005).
18. G. Q. Phan *et al*., *Proc. Natl. Acad. Sci. U.S.A.* **100**, 8372–8377 (2003).
19. D. Quandt, H. Hoff, M. Rudolph, S. Fillatreau, M. C. Brunner-Weinzierl, *J. Immunol.* **179**, 7316–7324 (2007).
20. D. A. Kaminski, C. Wei, Y. Qian, A. F. Rosenberg, I. Sanz, *Front. Immunol.* **3**, 302 (2012).
21. M. Rakhmanov *et al*., *Proc. Natl. Acad. Sci. U.S.A.* **106**, 13451–13456 (2009).
22. I. Isnardi *et al*., *Blood* **115**, 5026–5036 (2010).
23. K. Warnatz *et al*., *Blood* **99**, 1544–1551 (2002).
24. C. C. Goodnow, R. Brink, E. Adams, *Nature* **352**, 532–536 (1991).
25. S. Moir *et al*., *J. Exp. Med.* **205**, 1797–1805 (2008).
26. T. Kinnunen *et al*., *Blood* **121**, 1595–1603 (2013).
27. S. Price *et al*., *Blood* **123**, 1989–1999 (2014).
28. M. E. Conley, J. L. Casanova, *Curr. Opin. Immunol.* **30**, 17–23 (2014).

ACKNOWLEDGMENTS

We thank the referring physicians, as well as the patients and families. The data are tabulated in the main paper and in the supplementary materials. Supported by the Intramural Research Program, NIH Clinical Center (H.S.K., T.A.F., J.S., J.E.N., L.R.F.); the Division of Intramural Research, National Institute of Allergy and Infectious Diseases (B.L., Y.Z., V.K.R., H.C.S., Y.R., K.N.O., S.Pr., S.M.H., M.J.L., G.U.); the National Cancer Institute under contract HHSN261200800001E (C.A.F.); National Institute of Allergy and Infectious Diseases grant 5R01HL113304-01 (D.Q.T.); the National Health and Medical Research Council of Australia (E.K.D., S.G.T.); Cancer Council NSW (S.G.T.); and National Institute of Allergy and Infectious Diseases grants AI071087, AI095848, and AI061093 (E.M.). The content of this publication does not necessarily reflect the views or policies of the U.S. Department of Health and Human Services, nor does mention of trade names, commercial products, or organizations imply endorsement by the U.S. Government. The sequencing data are deposited in dbGaP under accession no. phs000797.v1.p1.

SUPPLEMENTARY MATERIALS

www.sciencemag.org/content/345/6204/1623/suppl/DC1
Materials and Methods
Supplementary Text
Figs. S1 to S10
Tables S1 to S3
References (*29*–*35*)

12 May 2014; accepted 2 September 2014
Published online 11 September 2014;
10.1126/science.1255904

Gordon Research Conferences

frontiers of science

2015 "Session I" Meetings will be held between January and May in California and Texas in the United States, and internationally in Lucca (Barga), Italy and Hong Kong, China. A list of preliminary programs appears on the following 9 pages. For detailed programs, fees, site/travel information and online application, visit our web site at **www.grc.org**.

Gordon Conferences are different from other scientific conferences because:

...of their intensity of science, new ideas, discussion, and fun. *(Cliff Kubiak, UCSD)*

Image: *"Tree of Life": A color-coded rendering of cardiac cell orientation.* Courtesy of Patrizia Camelliti, University of Oxford. Submitted by Peter Kohl, Chair, Cardiac Arrhythmia Mechanisms GRC. The Cardiac Arrhythmia Mechanisms GRC will take place March 22-27, 2015 at the Renaissance Tuscany Il Ciocco Resort and Spa in Lucca (Barga), Italy.

Downloaded from www.sciencemag.org on September 26, 2014

2015 "Session I" Preliminary Programs

The list of meetings, session topics and speakers begins below. Discussion leaders are noted in italics.

Gordon Research Seminars (GRS) are listed below their associated Gordon Research Conference. GRSs are 2-day meetings that precede an associated GRC, designed for graduate students, post-docs, and other young scientists to present and exchange new data and cutting-edge ideas. Seed funding for new Gordon Research Seminars is provided by the Kenan Institute for Engineering, Technology & Science at North Carolina State University and Merck & Co., Inc.

Antimicrobial Peptides

Basic and Translational Aspects
May 3-8, 2015
Renaissance Tuscany Il Ciocco Resort, Lucca (Barga), Italy
Chairs: Pieter S. Hiemstra & Julia Dorin
Vice Chairs: Wuyuan Lu & Charles Bevins

- **Keynote Session: The Impact of Dysbiosis, Infection Models and AMPs** (*Gill Diamond* / Richard Flavell / Lalita Ramakrishnan)
- **AMPs and the Microbiome at Epithelial Surfaces** (*Donald Davidson* / Mathias Hornef / Benjamin Marsland / Birgit Schittek / Nita Salzman)
- **AMPs Throughout Evolution** (*Eefjan Breukink, Gudmundur Hrafn Gudmundsson* / Mande Holford)
- **Mechanism of Antimicrobial Action of AMPs** (*William Shafer* / Daniel Wozniak / Shonna McBride / Michaela Wenzel / Kimberly Kline)
- **AMPs as Immune Modulators** (*Anne Van Der Does* / Robert Hancock / Mohini Gray / Henk Haagsman)
- **AMP Dysfunction: Role in Disease** (*Robert Bals* / Edward Hollox / Paul McCray, Jr. / Lhousseine Touqui / Julien Diana)
- **Novel Functions of AMPs** (*Neeloffer Mookherjee, Aaron Weinberg* / Sergio Lira / David Hoskin)
- **Novel AMPs** (*Adrian Gombart, Jens Schroeder* / Marc Devocelle / Michael Otto / Kev Dhaliwal / Peter Nibbering)
- **Applications of AMPs: Putting Them to Work** (*Michael Zasloff, Jan Wehkamp* / Birgitta Agerberth / Victor Nizet)

GRS **Antimicrobial Peptides**
Mechanism, Function and Application
May 2-3, 2015
Chair: Michaela Wenzel
Associate Chair: Anne M. Van Der Does

Cancer Genetics & Epigenetics

Deciphering the Cancer Genome and Epigenome to Develop Novel Therapies
Apr 12-17, 2015
Renaissance Tuscany Il Ciocco Resort, Lucca (Barga), Italy
Chairs: Ricky Johnstone & Stephen B. Baylin
Vice Chair: X. Shirley Liu

- **Keynote Session: The Importance of Cancer Genetics and Epigenetics to the Future of Oncology** (*Ricky Johnstone, Stephen Baylin* / Peter Laird / Scott Lowe / Elaine Mardis)
- **Cancer Genomics and Epigenomics: Hemopoietic Malignancies** (*Jonathan Licht* / Ross Levine / Ari Melnick / Charles Mullighan / Louis Staudt)
- **Cancer Epigenetics: DNA Methylation** (*Peter Laird* / Susan Clark / Joseph Costello / Peter Jones / Wei Li)
- **Cancer Genomics and Epigenomics: Solid Tumors** (*Elaine Mardis* / Matthew Meyerson)
- **Animal Models of Cancer** (*Saverio Minucci* / Eric Baehrecke / Brent Derry / Leisa Johnson / Thomas Look)
- **Novel Cancer Targets** (*Kimberley Stegmaier* / James Bradner / Jacques Neefjes / Johannes Zuber)
- **Cancer Epigenetics: Chromatin Modification** (*X. Shirley Liu* / Yali Dou / Jonathan Licht / Saverio Minucci)
- **Clinical and Biomarker Advances** (*Charles Mullighan* / Alberto Bardelli / Susan Bates / Shyamala Maheswaran)
- **Functional Genetics of Cancer** (*James Bradner* / Bruno Amati / Karen Cichowski / Kimberley Stegmaier)

Cannabinoid Function in the CNS

From Molecules to Disease Mechanisms
May 24-29, 2015
Renaissance Tuscany Il Ciocco Resort, Lucca (Barga), Italy
Chairs: Tibor Harkany & Mauro Maccarrone
Vice Chairs: Joseph F. Cheer & Yasmin Hurd

- **Keynote Session: Endocannabinoid Signaling in the Hypothalamus** (*Ken Mackie* / Tamas Horvath)
- **Molecular Logic of Endocannabinoid Metabolism and Signaling** (*Daniele Piomelli* / Lawrence Marnett / Benjamin Cravatt / Allyn Howlett)
- **From Phytocannabinoids to Cannabinoid Medicines** (*Roger Pertwee* / Raphael Mechoulam / Vincenzo Di Marzo)
- **Endocannabinoids at the Synapse** (*Ivan Soltesz* / Karl Deisseroth / Silvia Marinelli / Masanobu Kano / Chris McBain)
- **From Stemness to Neuronal Circuit Assembly** (*Hui-Chen Lu* / Manuel Guzman / Patrick Doherty)

Gordon Research Conferences: 2015 "Session I" Meeting Schedule and Preliminary Programs

- **Endocannabinoids, Fear and Emotional Control**
  (*Daniela Parolaro* / Andreas Luthi / Beat Lutz / Carsten Wotjak / Rafael Maldonado)
- **Endocannabinoids in Aging and Neurodegeneration**
  (*Nephi Stella* / Elena Cattaneo / Andreas Zimmer / Diego Centonze)
- **Endocannabinoid Signaling in Psychosis, Addiction and Reward**
  (*Pier Vincenzo Piazza* / David Lewis / Larry Parsons / Xia Zhang / Gunter Schumann)
- **Emerging Topics in Endocannabinoid Biology**
  (*Cecilia Hillard* / Claudio D'Addario / Enrico Dainese)

Cannabinoid Function in the CNS
Endocannabinoid Signaling in Neurobiology: From Molecules to Networks
May 23-24, 2015
Chair: Erik Keimpema
Associate Chair: Valerio Chiurchiu

Cardiac Arrhythmia Mechanisms

The Surprising Heart: A Hetero-Cellular, Multi-Physics, and Inter-Disciplinary Challenge
Mar 22-27, 2015
Renaissance Tuscany Il Ciocco Resort, Lucca (Barga), Italy
Chair: Peter Kohl
Vice Chair: Gail A. Robertson

- **Regeneration/Repair and Arrhythmogenesis: Potential and Pitfalls**
  (*Michael Rosen* / Marius Wernig / Nicola Smart)
- **Pacemaking and Conduction**
  (*Toon Van Veen* / Vincent Christoffels / Vadim Fedorov / Peter Mohler / Stacey Rentschler / Eugenio Cingolani)
- **Atrial Arrhythmias**
  (*Nathalie Virag* / Guy Salama / Uli Schotten / Sanjiv Narayan)
- **Ventricular Arrhythmias**
  (*Sian Harding* / Burkert Pieske / Katja Odening / Bettina Cuneo / Peter Schwartz / Natalia Trayanova)
- **Unravelling Arrhythmia Mechanisms: One Channel at a Time (or Two…)**
  (*Jose Jalife* / Dan Roden / Connie Bezzina / Yoram Rudy)
- **Mechanics Matters**
  (*Ursula Ravens* / David Kass / Stephane Hatem / Jeff Holmes / T. Alexander Quinn / Peter Taggart)
- **The Nervous Heart**
  (*Douglas Zipes* / Sami Noujaim / Dominik Linz / Crystal Ripplinger)
- **Techniques that Will Change the Way We Study and Treat Cardiac Arrhythmia Mechanisms**
  (*Igor Efimov* / Paul Blainey / Mario Delmar / Jan Huisken / Marisa Jaconi / Elisa Konofagou)
- **The Surprising Heart: More than Myocytes**
  (*Gail Robertson* / Filip Swirski / Stefanie Dimmeler / Peng-Sheng Chen)

Cardiac Arrhythmia Mechanisms
The Surprising Heart: A Hetero-Cellular, Multi-Physics, and Inter-Disciplinary Challenge
Mar 21-22, 2015
Chair: Eva A. Rog-Zielinska
Associate Chair: David K. Jones

Cartilage Biology & Pathology

Working Together at the Frontiers of Science and Technologies to Eradicate Cartilage Diseases
Mar 22-27, 2015
Hotel Galvez, Galveston, TX
Chairs: Veronique M. Lefebvre & Danny Chan
Vice Chairs: Frank Beier & Elazar Zelzer

- **Recent Breakthroughs in Understanding and Treating Cartilage Diseases**
  (*Linda Sandell* / Christopher Little / Stefan Mundlos)
- **Origin and Regulation of Chondroprogenitors in Development**
  (*Dae-Won Kim* / Vicki Rosen / Lukas Sommer / Michael Underhill / Axel Visel)
- **Identification of Chondroprogenitors to Repair Adult Cartilage Defects**
  (*Martin Lotz* / Cosimo De Bari / George Muschler)
- **Cartilage Growth Plate Function and Regulation in Development and Disease**
  (*Ernestina Schipani* / Audrey McAlinden / Andrew Pitsillides / Philippe Soriano / Wentian Yang)
- **New Approaches to Uncover Disease Causes, Mechanisms and Treatments**
  (*Benoit De Crombrugghe*, *Yingzi Yang* / Jeffrey Esko / Biagio Saitta)
- **Articular Chondrocyte Function and Regulation from Development to Aging and to Adult Disease**
  (*Mary Goldring* / Jang-Soo Chun / Anna Spagnoli / Tonia Vincent)
- **Intervertebral Disc Regulation from Development to Adult Disease**
  (*Makarand Risbud* / Jeffrey Lotz)
- **Structural and Functional Crosstalks Between Cartilage and Other Tissues**
  (*Henry Kronenberg* / Ralf Adams / Cheryle Seguin / Deneen Wellik)
- **Insights from Genome-Wide Studies in Humans and Distant Vertebrates**
  (*Bjorn Olsen* / Joel Hirschhorn / Shiro Ikegawa)

Cartilage Biology & Pathology
Recent Advances and Challenges in Understanding Cartilage Diseases
Mar 21-22, 2015
Chair: Pallavi Bhattaram
Associate Chair: Wilson C.W. Chan

Cell Biology of Megakaryocytes & Platelets

Bridging the Divide Between Megakaryocytes and Platelets
Apr 19-24, 2015
Renaissance Tuscany Il Ciocco Resort, Lucca (Barga), Italy
Chair: Joe Italiano
Vice Chair: Benjamin T. Kile

- **Keynote Session: Thrombopoiesis and Thrombosis: Now and Tomorrow**
  (*Debra Newman* / John Hartwig / Shaun Jackson)
- **Platelets Beyond Hemostasis**
  (*Jerry Ware* / Mark Kahn / Myriam Labelle / John Semple / Simon Foote)
- **Blood Pharming: Making *In Vitro* Platelets**
  (*Beau Mitchell* / Marloes Tijssen / Koji Eto / Alessandra Balduini)
- **Signals that Direct Megakaryocytes and Platelets**
  (*Sanford Shattil* / Wolfgang Bergmeier / Bernard Nieswandt / Ulhas Naik / Michael Holinstat)
- **Seeing Is Believing: Visualizing New Platelet and Megakaryocyte Biology**
  (*Laura Guitierrez* / Steffen Massberg / Harry Heijnen / Renhao Li)
- **Platelet and Megakaryocyte Membrane Dynamics**
  (*Marco Cattaneo* / Martyn Mahaut-Smith / Jonathan Gibbins / Donna Woulfe)
- **Late-Breaking Topics**
  (*Robert Flaumenhaft*)
- **Megakaryocyte and Platelet-Associated Diseases**
  (*Marco Vitale* / William Vainchenker / Heyu Ni / Katya Ravid)
- **Regulating the Trillion Platelets in Our Blood**
  (*Benjamin Kile* / Karin Hoffmeister / Emma Jossefson / James Bussel)

Cell Biology of Megakaryocytes & Platelets
From Cells to Clinics: Megakaryocytes and Platelets in Health and Disease
Apr 18-19, 2015
Chair: Matthew T. Harper
Associate Chair: Kellie R. Machlus

Chemical & Biological Terrorism Defense

Research Synergies for Chemical and Biological Defense
Mar 8-13, 2015
Four Points Sheraton / Holiday Inn Express, Ventura, CA
Chair: Jacqueline Fletcher
Vice Chair: Steven R. Blanke

- **Keynote Session: Global Environmental Change: Impacts on Biosecurity**
  (*Steven Blanke* / James Stack)
- **Countermeasures to Biological Threats**
  (*Petra Oyston* / Catharine Bosio / Lisa Hensley / Daniel Kadouri)
- **Countermeasures to Chemical Threats**
  (*Clement Furlong* / Douglas Cerasoli / Chris Green / Franz Worek)
- **Cutting Edge Research on High Threat Agents**
  (*Anne Boyer* / Adam Bogdanove / Suzanne Kalb / Bryan Krantz)
- **Responding to the NAS Report: New Research Applications to Enhance Microbial Forensic Investigation**
  (*Stephen Morse* / Paul Keim / Ian Lipkin / Karen Wahl)
- **Food Defense: Research to Assure Food Safety and Security**
  (*Jacqueline Fletcher* / Amy Kircher / Eric Johnson)
- **Late-Breaking Topics in Chemical and Biological Terrorism Defense**
  (*Jan Leach*)
- **Host Interactions with Chemical and Biological Agents**
  (*John Hardham* / Barbara Valent / Luis Rodriguez)
- **Real Time Detection and Decontamination of Chemical and Biological Threat Agents**
  (*Thomas Blake* / Ronald Manginell / David Schmale / Yuehe Lin)

Chemical & Biological Terrorism Defense
Applications of Chemical and Biological Defense Research
Mar 7-8, 2015
Chair: Jon M. Daniels
Associate Chair: Katie Margulieux

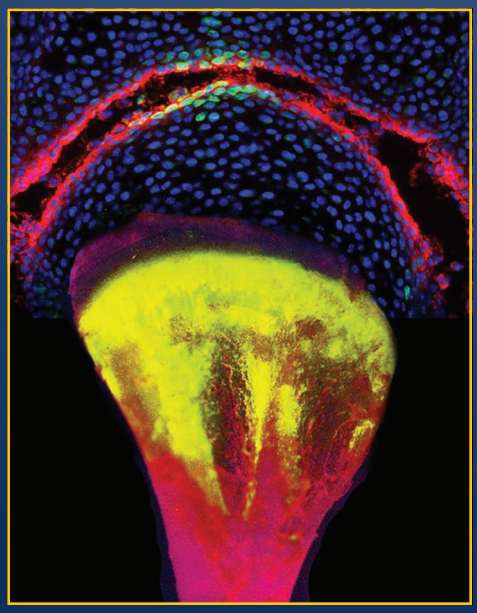

Top: A developing mouse articular joint showing progenitor cells (green) transitioning into differentiated articular chondrocytes (red) at the surface of the nascent joint cavity. Bottom: A mouse embryo scapula highlighting the transition of growth plate chondrocytes into osteoblasts (yellow) to contribute to the developing endochondral bone (red). Courtesy of the Hong Kong University Department of Biochemistry. Submitted by Véronique Lefebvre & Danny Chan, Chairs, Cartilage Biology and Pathology GRC; and Pallavi Bhattaram & Wilson Chan, Chairs, Cartilage Biology and Pathology GRS.

Chemical Reactions at Surfaces

From Model Studies to Complex Real World Systems
Feb 8-13, 2015
Ventura Beach Marriott, Ventura, CA
Chair: Hans-Peter Steinruck
Vice Chair: Andrew J. Gellman

- **Theory (Electronic Structure) - Predictive Power and Limitations**
  (*Manos Mavrikakis* / John Kitchin / Annabella Selloni)
- **Reactions Close to Atmospheric Pressures and Under Electrochemical Conditions**
  (*Mary Jane Shultz* / Hendrik Bluhm / Suljo Linic / Edvin Lundgren)
- **Theory (KMC and MD) - Predictive Power and Limitations**
  (*Axel Gross* / Claudia Draxl / Karsten Reuter)
- **Present Challenges in Catalysis**
  (*Cynthia Friend* / Robert Schloegl / Peter Stair / Simon Bare)
- **Environmental Chemistry**
  (*Bruce Kay* / Vicki Grassian / Kim Prather)
- **New Materials and Synthesis Methods**
  (*Francisco Zaera* / Brian Hayden / Jeong Young Park / Susannah Scott)
- **Chirality in Surface Chemistry**
  (*Georg Held* / Karl-Heinz Ernst / Charles Sykes)
- **Elementary Reaction Steps**
  (*Miquel Salmeron* / Ludo Juurlink / Christian Papp)
- **Organic Surface Layers**
  (*Stacey Bent* / Maki Kawai / Junfa Zhu)

Chemical Reactions at Surfaces
Surface Science Techniques for Addressing Contemporary Issues
Feb 7-8, 2015
Chair: Mathew Payne
Associate Chair: Christoph Gleichweit

Chloroplast Biotechnology

NEW!

Reengineering Photosynthetic Organelles
Jan 18-23, 2015
Ventura Beach Marriott, Ventura, CA
Chair: Pal Maliga
Vice Chair: Ralph Bock

- **Genomes**
  (*Maureen Hanson* / Robert Jansen / Sally Mackenzie / Normand Brisson)
- **Technical Advances**
  (*Ralph Bock* / Anil Day / James Thomson)
- **Transcriptional Regulation**
  (*Toshiharu Shikanai* / Mitsumasa Hanaoka / Takashi Shiina / Thomas Pfannschmidt / David Stern)
- **Posttranscriptional Regulation**
  (*Alice Barkan* / Ian Small / Takahiro Nakamura / Christian Schmitz-Linneweber / Toshiharu Shikanai)
- **Translation and Protein Stability**
  (*Ian Small* / Alice Barkan / Klaas Van Wijk / Zach Adam)
- **Microalgae**
  (*David Stern* / Stephen Mayfield / Saul Purton / Silvia Ramundo)
- **Biotechnology**
  (*Spencer Whitney* / Henry Daniell / Rima Menassa / Inmaculada Farran)
- **Engineering Photosynthesis**
  (*Stephen Mayfield* / Spencer Whitney / Murray Badger / Jane Langdale)
- **Synthetic Biology**
  (*Pal Maliga* / Maureen Hanson / Cheryl Kerfeld / Christopher Voigt)

Cilia, Mucus & Mucociliary Interactions

Translating Assembly and Function to Imaging, Genetics and Therapeutic Discovery
Feb 8-13, 2015
Hotel Galvez, Galveston, TX
Chairs: Steven Brody & David Thornton
Vice Chairs: Elizabeth Smith & Heymut Omran

- **Keynote Session: Cilia, Mucus and Mucociliary Interactions**
  (*Hannah Mitchison* / Richard Boucher / John Wallingford / Heymut Omran)
- **Assembly and Structure**
  (*Colin Bingle* / Julie Brill / Gunnar Hansson / Mary Porter / Benedicte Durand / Olatz Pampliega / Vivek Malhotra)
- **Function and Mucociliary Interactions**
  (*Katharina Ribbeck* / Peter Konig / Bhanu Jena / Brian Button)
- **Advances in Imaging of Cilia, Mucus and Interactions**
  (*Michael Rubenstein* / Ryszard Grygorczyk / Karl Lechtreck / Jung-Chi Liao / Daniela Nicastro / Steven Rowe)
- **Determinants of Surface Fluids and Flow**
  (*Martina Brueckner* / Bridgette Gomperts / Hiroshi Hamada / Paul Quinton / Susana Lopes)
- **Cilia, Mucus and Mucosal Immunity**
  (*Michael McGuckin* / Noam Cohen / Chris Evans / J. Kirk Harris / Jeffrey Whitsett / Katharina Ribbeck)
- **Late-Breaking Topics**
  (*Iain Drummond*, *Judy Voynow*)
- **Genetic Diseases of Mucus and Cilia**
  (*Win Sale*, *David Erle* / Michael Knowles / Cecilia Lo / David Schwartz / Yohannes Tesfaigzi / David Mitchell / Rim Hjeij)
- **Developing Therapeutics for Disorders of Mucus and Cilia**
  (*Matthias Salathe*, *Elizabeth Smith* / Burton Dickey / Susan Dutcher / Michael Holtzman)

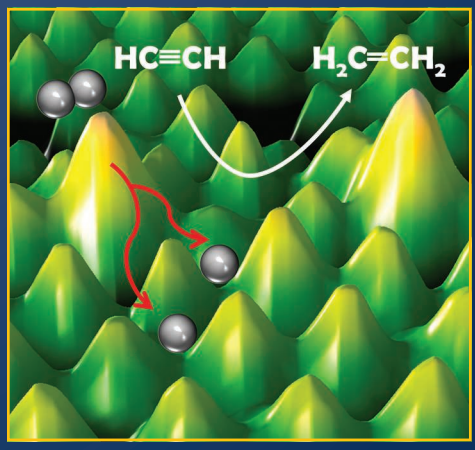

Palladium/copper single atom alloys catalyze the industrially important conversion of acetylene to ethene. Courtesy of the Sykes Group (Tufts University). Submitted by Hans-Peter Steinruck, Chair, Chemical Reactions at Surfaces GRC.

Dendrites: Molecules, Structure & Function

How Development and Experience Shape the Computational Properties of Dendrites
Mar 15-20, 2015
Ventura Beach Marriott, Ventura, CA
Chairs: Hollis Cline & Jeffrey Magee
Vice Chairs: Randy Bruno & Ryohei Yasuda

- **Molecular Trafficking in Dendrites**
  (*Ryohei Yasuda* / Dane Chetkovich / Dax Hoffman / Steven Siegelbaum)
- **Theory and Computational Studies of Dendritic Integration**
  (*Jeffrey Magee* / Robert Guetig / Mate Lengyel / Bartlett Mel / Raoul-Martin Memmesheimer)
- **Dendrite Development and Plasticity**
  (*Ed Rubel* / Kurt Haas / Mineko Kengaku / Jay Parrish / Rachel Wong)
- **Dendritic Integration and Circuit Processing**
  (*Randy Bruno* / Yang Dan / Marla Feller)
- **Synapses**
  (*Hollis Cline* / Cagla Eroglu / Richard Huganir / Shigeo Okabe / Antonie Triller)
- **Spines, Synapses and Plasticity**
  (*Carlos Aizenman* / Yukiko Goda / Christian Hansel)
- **Circuits and Plasticity**
  (*Carlos Aizenman* / Tobias Bonhoeffer / Daniel Feldman / Shaul Hestrin / Yi Zuo)
- **Dendritic Integration During Behavior**
  (*Randy Bruno* / Michael Hausser / Jason Kerr / Takaki Komiyama / Matthew Larkum / Jackie Schiller)
- **Dendritic Integration and Interneurons**
  (*Elly Nedivi* / Brenda Bloodgood / Z. Josh Huang / Sandra Kuhlman / Attila Losonczy)

Dendrites: Molecules, Structure & Function
Development, Function and Disease
Mar 14-15, 2015
Chair: Cody J. Smith
Associate Chair: Trace Henry

Directed Cell Migration

Using a Multidisciplinary Approach to Decipher Cell Migration
Jan 25-30, 2015
Hotel Galvez, Galveston, TX
Chair: Carole Parent
Vice Chair: Denise Montell

- **Keynote Session: At the Forefront of Cell Migration During Epithelial to Mesenchymal Transition**
  (*Carole Parent* / Valerie Weaver / Anna Huttenlocher)
- **Gradient Sensing During Cell Migration**
  (*Orion Weiner* / Peter Devreotes / Richard Firtel / Len Stephens / Pablo Iglesias)
- **Receptor and Calcium Signaling During Cell Migration**
  (*Jeffrey Segall* / Tracy Handel / Narasimhan Gautam / Tobias Meyer)
- **Cytoskeletal Events During Cell Migration**
  (*Daniel Fletcher* / James Bear / Orion Weiner / Gaudenz Danuser / Julie Theriot)
- **Cell Migration and Function**
  (*Michael Sixt* / Jingsong Xu / Daria Siekhaus / Konstantinos Konstantopoulos)
- **Cell Migration in *In Vivo* Settings**
  (*Andrew Ewald* / John Condeelis / Peter Friedl / Michael Sixt / Erik Sahai)
- **Mechanotransduction During Cell Migration**
  (*Xavier Trepat* / Daniel Fletcher / Wolfgang Losert / Michael Sheetz)
- **Collective Cell Migration**
  (*Anna Huttenlocher* / Denise Montell / Eric Theveneau / Darren Gilmour / Pascal Silberzan)
- **Cell Polarity and Adhesion During Cell Migration**
  (*James Bear* / Johanna Ivaska / Gregg Gundersen / Alpha Yap)

Directed Cell Migration
Bridging Biology and Quantitative Analyses
Jan 24-25, 2015
Chair: Ritankar Majumdar
Associate Chair: Shirin Pocha

Gordon Conferences are different from other scientific conferences because:

...of the unique opportunity to learn about exciting unpublished research, to renew old ties and establish new ties, and to interact in a meaningful and substantive way with other scientists. *(Gregory Fu, CalTech)*

Fibronectin, Integrins & Related Molecules

ECM Adhesion Signaling in Context
May 10-15, 2015
Renaissance Tuscany Il Ciocco Resort, Lucca (Barga), Italy
Chair: Valerie M. Weaver
Vice Chair: Charles H. Streuli

- **Keynote Session: ECM Adhesion and Stem Cell Fate**
  (*Charles Streuli* / Fiona Watt / David Cheresh / Sara Wickstrom)
- **From Molecules to Adhesions: A Biophysical Perspective**
  (*Alexander Bershadsky* / Alexander Dunn / Cheng Zhu / David Calderwood / Matthew Paszek / Feng Ye / Haguy Wolfenson)
- **Mechanics, Integrins, and Adhesion Signaling**
  (*Martin Humphries* / Clare Waterman / Corinne Albiges-Rizo / Martin Schwartz)
- **Adhesion Dynamics**
  (*Jim Norman* / James Casanova / Patrick Caswell / Anne Straube / Philippe Chavrier)
- **Adhesion Dynamics and Cell Phenotype**
  (*Jean Schwarzbauer* / Donald Gullberg / Diane Barber / Suresh Alahari / Nicholas Brown)
- **Reciprocal Interplay Between the ECM and Tissue Phenotype**
  (*Viola Vogel* / Thomas Barker / Mercedes Costell / Scott Holley / Matthias Lutolf / Alexandra Naba / Gertraud Orend)
- **ECM, Signaling, and Adhesion in Context**
  (*Mark Ginsberg* / Ellen Van Obberghen-Schilling / Kevin Janes / Otger Campas / Senthil Muthuswamy)
- **Adhesion and Signaling in Tissue Development and Homeostasis**
  (*Reinhard Faessler* / Nasreen Akhtar / Penney Gilbert / Roy Zent / Dean Sheppard)
- **Adhesion and Signaling in Disease**
  (*Johanna Ivaska* / Richard Assoian / Judith Varner / David Schlaepfer / Simon Goodman)

GRS Fibronectin, Integrins & Related Molecules
Regulation of Cell Behavior by Cell-Extracellular Matrix Interactions
May 9-10, 2015
Chair: J. Matthew Barnes
Associate Chair: Matthew C. Jones

Gaseous Ions: Structures, Energetics & Reactions

Ions at Work: From Reaction Dynamics to Macromolecular Structure
Feb 22-27, 2015
Hotel Galvez, Galveston, TX
Chair: Mark A. Johnson
Vice Chair: Julia Laskin

- **Structural Characterization of Macromolecules**
  (*Michael Bowers* / Jennifer Brodbelt / Scott McLuckey)
- **New Developments in Cryogenic Ion Preparation and Characterization**
  (*Dieter Gerlich* / Oleg Boyarkine / Jana Roithova / Gert Von Helden / Daniel Neumark)
- **Ionization and Structure of Biomolecules**
  (*Vicki Wysocki* / Perdita Barran / Zheng Ouyang)
- **Ions in Atmospheric Chemistry**
  (*Albert Viggiano* / Joachim Curtius / Benny Gerber / Francesco Paesani / Ruth Signorell)
- **Ion Spectroscopy: Theory and Experiment**
  (*Anne McCoy* / Steen Nielsen / Ryan Steele)
- **Ionic Clusters and Applications to Catalysis**
  (*Peter Armentrout* / Gereon Niedner-Schatteburg / Stuart McKenzie / Caroline Jarrold)
- **Hydrogen Bonded Systems: Structure, Reactions and Spectroscopy**
  (*Martin Beyer* / Evan Williams / David Russell)
- **Reaction Dynamics and Photochemistry**
  (*Roland Wester* / Philippe Dugourd / Michael Duncan / William Hase / Jan Verlet)
- **Keynote Session: Reflections, Perspectives and Opportunities**
  (*Veronica Bierbaum* / Carl Lineberger)

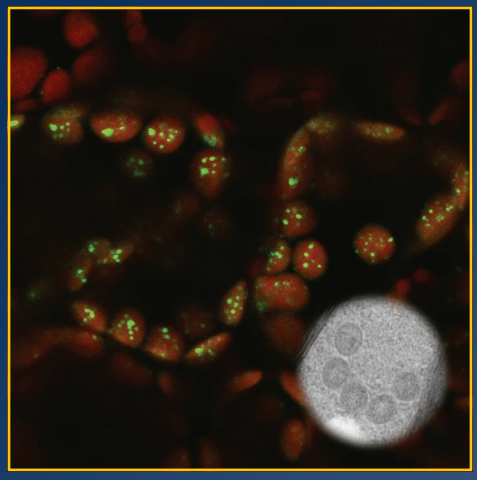

Confocal microscope image of punctate loci (labeled by yellow fluorescent protein) resulting from transient expression of proteins comprising the outer layer of a cyanobacterial β-carboxysome in vascular plant chloroplasts (labeled by red chlorophyll autofluorescence). Spherical microcompartments formed by these carboxysomal proteins within plant chloroplasts were captured with transmission electron microscopy. Courtesy of Myat T. Lin and Maureen R. Hanson (Cornell University), and Alessandro Occhialini and Martin A.J. Parry (Rothamsted Research). Submitted by Pal Maliga, Chair, Chloroplast Biotechnology GRC.

Glial Biology: Functional Interactions Among Glia & Neurons

Glial Cells in Health and Disease
Mar 1-6, 2015
Four Points Sheraton / Holiday Inn Express, Ventura, CA
Chair: Harald W. Sontheimer
Vice Chair: Beth A. Stevens

- **Glia and Nervous System Development**
  (*Nicola Allen* / Gabriel Corfas / David Rowitch / Cagla Eroglu)
- **Glial and Neurodevelopmental Disorders**
  (*Wilma Friedman* / Jonathan Kipnis / Vittorio Gallo / Nenad Sestan / Wenbing Deng / Michelle Olsen / Erik Ullian)
- **Stem Cell Potential of Glia**
  (*Akiko Nishiyama* / Dwight Bergles / Gong Chen / Magdalena Goetz)
- **Glia and Neurodegenerative Diseases**
  (*Byron Ford* / Maiken Nedergaard / Jeffrey Rothstein / Michelle Grey / Joseph El Khoury / Ayodeji Asuni / Baljit Khach)
- **Model Organisms to Study Glia**
  (*Vladimir Parpura* / Shai Shaham / William Talbot / Bruce Apple)
- **Glial Vascular Interactions**
  (*Eric Newman* / Berislav Zlokovic / Katerina Akassoglou / David Attwell / Jessica Filosa / Costantino Iadecola)
- **Glial Axonal Interactions**
  (*Bruce Ransom* / Klaus-Armin Nave / Peter Stys / Patrizia Casaccia)
- **Microglia in Health and Disease**
  (*Monica Carson* / Wenbiao Gan / Olga Garaschuk / Brian Macvicar / Margaret McCarthy)
- **Contribution of Glia to Neuronal Networks *In Vivo***
  (*Philip Haydon* / Anna Devor / James Schummers / Mriganka Sur)

GRS Glial Biology: Functional Interactions Among Glia & Neurons
Glial Cells in Health and Disease
Feb 28 - Mar 1, 2015
Chair: Jeremy C. Petravicz
Associate Chair: Lasse Dissing-Olesen

Glycobiology

Glycans as Mediators of Interactions Between Molecules, Cells and Organisms
Mar 1-6, 2015
Renaissance Tuscany Il Ciocco Resort, Lucca (Barga), Italy
Chair: Markus Aebi
Vice Chair: Michael Tiemeyer

- **Glycans and Evolution**
  (*Markus Aebi* / Pascal Gagneux / Steven Ball / Ajit Varki)
- **Glycobiology of Prokaryotes and Unicellular Organisms**
  (*Michael A. Ferguson* / Elizabeth Hartland / Barbara Imperiali / Malcolm McConville / Chris Whitfield)
- **Glycobiology of the Microbiota**
  (*Thierry Hennet* / Lars Bode / Christine Szymanski)
- **Glycobiology of Plants, Flies and Worms**
  (*Michael Tiemeyer* / Hannes Buelow / Henrik Scheller / Kelly Ten Hagen / Joseph Yost)
- **Glycobiology: A Molecular View**
  (*Karen Colley* / Gideon Davies / Harry Gilbert / Kelley Moremen)
- **Biosynthesis of Carbohydrates; Carbohydrates in Disease**
  (*John Hanover* / Hans Bakker / Taroh Kinoshita / Michael Pierce / Sabine Strahl)
- **Carbohydrate-Binding Proteins**
  (*Anne Imberty* / Takashi Angata / Gabriel Rabinovich / Felix Randow)
- **Glycobiology of Biopharmaceuticals and Vaccines**
  (*Irma Van Die* / Francesco Berti / Richard Cummings / Horst Kunz)
- **Analytical Tools and Big Data**
  (*Nicolle Packer* / Bernard Henrissat / Manfred Wuhrer / William York)

GRS Glycobiology
Glycans as Mediators of Interactions Between Molecules, Cells and Organisms
Feb 28 - Mar 1, 2015
Chair: Robert Gauss
Associate Chair: Melody (Mindy) Perlman-Porterfield

IGF & Insulin System in Physiology and Disease

The IGFs and Insulin System: Emerging Themes in Aging, Diabetes, Cancer and Other Diseases
Mar 8-13, 2015
Ventura Beach Marriott, Ventura, CA
Chair: Briony E. Forbes
Vice Chair: Cunming Duan

- **IGF and Insulin System in Aging**
  (*Cunming Duan* / Andrjez Bartke)
- **Aging**
  (*Marc Tatar* / Nir Barzilai / Yousin Suh / Martin Holzenberger / Coleen Murphy)

- **Molecular Mechanisms Underlying IGF and Insulin Action**
  (*Marek Brzozowski* / Michael Lawrence / Hanudatta Atreya)
- **IGF and Insulin Signaling in Growth, Metabolism and Disease**
  (*Antonino Belfiore* / Andreas Hoeflich / Friedrich Metzger / Shoshana Yakar)
- **IGF-II and the IGF2R**
  (*Bass Hassan* / Andrew Hoffman / Linheng Li)
- **IGF-1R and IR Signaling Pathways**
  (*Shin-Ichiro Takahashi* / Cora O'Neil / Maria Grant)
- **IGF Binding Proteins**
  (*Robert Baxter* / Abishek Kashyap / Janet Martin)
- **IGF and Insulin in Cancer**
  (*Stephen Hursting* / Norbert Tennagels / Roberta Malaguarnera / Douglas Yee)
- **Neurological Diseases / Stem Cells / Progenitor Cells**
  (*Teresa Wood* / Cristina Alberini / Paula Moriera)

Immunology of Fungal Infections

Basic Mechanisms and Translational Implications
Jan 18-23, 2015
Hotel Galvez, Galveston, TX
Chairs: Bruce S. Klein & Bernhard Hube
Vice Chairs: Mihai Netea & George Deepe

- **Keynote Session: Immunogenetics of Fungal Disease**
  (*Jean-Paul Latge* / Steven Holland / Anne Puel / Keynote: Luigina Romani)
- **Components of Innate Immunity to Fungi**
  (*Sarah Gaffen* / Salome Leibundgut-Landmann / Amariliz Rivera / Frank Van De Veerdonk / Tobias Hohl / Christopher Mody / Jessica Quintin)
- **Innate Sensing and Signaling: PRRs and Beyond**
  (*Karl Kuchler* / Gordon Brown / Teunis Geijtenbeek / Jurgen Rhuland / Sarah Gaffen)
- **Structures and Signals that Impact Fungal Immunity**
  (*Mairi Noverr* / Sho Yamasaki / Neil Gow / Jean-Paul Latge / Robert Cramer / Marcel Wuethrich / Karl Kuchler / Robert Wheeler)
- **Adaptive and Maladaptive Immunity to Fungi**
  (*Gordon Brown* / Stuart Levitz / Daniel Kaplan / Liise-Anne Pirofski)
- **Mycobiome, Mammalian Surfaces, and Non-Hematopoietic Lining Cells**
  (*Scott Filler* / David Underhill / Mairi Noverr / Suzanne Noble / Julian Naglik / Teresa Zelante / Terry Wright)
- **Host-Fungal Pathogen Interactions: Systems Biology and Beyond**
  (*Luigina Romani* / Duccio Cavalieri / Marcio Rodrigues / Norman Pavelka / Louise Rollins-Smith)
- **Intracellular Parasitism**
  (*Stuart Levitz* / Jatin Vyas / Robin May / Anita Sil / Thirumala-Devi Kanneganti)
- **Harnessing Immunity to Fungi in the Clinic**
  (*Suzanne Noble* / Agostinho Carvalho / Scott Filler / Michail Lionakis / Jay Kolls)

GRS Immunology of Fungal Infections
Identifying the Common Beneficial Host/Pathogen Interaction
Jan 17-18, 2015
Chair: Teresa Zelante
Associate Chair: Jessica Quintin

Inorganic Reaction Mechanisms

Using Fundamentals to Interface Energy, Biology, Materials and Catalysis
Mar 1-6, 2015
Hotel Galvez, Galveston, TX
Chair: Paul J. Chirik
Vice Chair: Patrick Holland

- **Mechanism as a Tool to Control Reactivity and Selectivity**
  (*John Bercaw* / David Collum / Guy Lloyd-Jones)
- **Mechanism as Applied to Synthetic Methods**
  (*Sebastien Monfette* / Robert Knowles / Timothy Warren / Kyoko Nozaki / Yi Xiao)
- **Mechanisms for Understanding Main Group and Materials Chemistry**
  (*Francois Gabbai* / Brandi Cossiart / Ian Stewart)
- **Mechanisms in Bioinorganic Chemistry**
  (*Justine Roth* / Serena Debeer / Amy Rosenzwig / Michael Green / Andrew Borovik)
- **Mechanisms for Renewable Energy**
  (*Peter Wolczanski* / Kyoung-Shin Choi / Clifford Kubiak)
- **Mechanisms of Materials Synthesis**
  (*Brooke Small* / Susan Schofer / Michael Reynolds / Mircea Dinca / Mahdi Abu-Omar / Gregory Whiteker)
- **Mechanistic Impacts of Ligand Design**
  (*Laurel Schafer* / Jennifer Yang / Milton Smith)
- **Coordination and Organometallic Chemistry**
  (*Suzanne Bart* / Nathaniel Szymczak / Enrique Batista / Bas DeBruin)
- **Mechanisms in Catalysis**
  (*Robert Bergman* / John Hartwig)

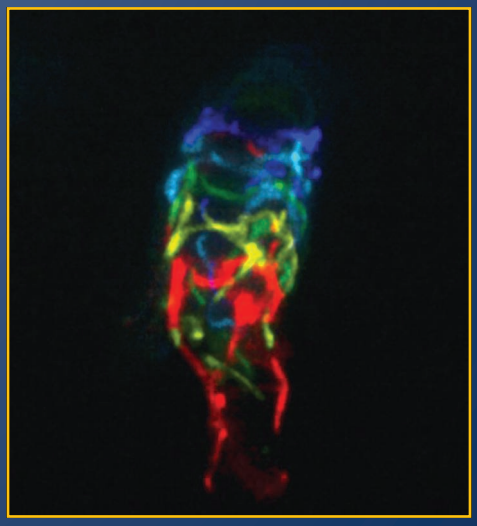

A color evolution time lapse image of a primary neutrophil stained with BODIPY-TR ceramide chemotaxing toward the bacterial peptide fMLP. Images were acquired every 15 seconds and color evolution was assigned from red to blue. Courtesy of Ritankar Majumdar (NCI, NIH). Submitted by Carole Parent, Chair, Directed Cell Migration GRC.

Lysosomal Diseases

Defining Pathogenesis and Therapeutic Strategies for Lysosomal Diseases
Mar 15-20, 2015
Hotel Galvez, Galveston, TX
Chair: Steven U. Walkley
Vice Chair: Andrea Ballabio

- **Keynote Session: Where We Are, and Aren't, on Understanding and Treating Lysosomal Diseases**
  (*Andrea Ballabio* / Beverly Davidson / Tony Futerman)
- **The Lysosomal System as Regulator of Cellular Homeostasis**
  (*Paul Saftig* / David Sabatini / Shawn Ferguson / Carmine Settembre)
- **Lysosomal Dysfunction and Disease Pathogenesis**
  (*Fran Platt* / Stephanie Cherqui / Stephan Storch)
- **Mechanisms of Lysosomal Function and Dysfunction**
  (*Karin Ollinger* / Marja Jaatella / Haoxing Xu / Tamotsu Yoshimori)
- **New Proteins Linked to Lysosomal Dysfunction and Disease**
  (*Thomas Braulke* / Miriam Meisler / Antonella De Matteis)
- **Late-Breaking Topics / Selected Poster Presentations**
  (*Volkmar Gieselmann*)
- **Cell Biological and Clinical Consequences of Heterozygosity in Lysosomal Diseases, Including XCI**
  (*Ellen Sidransky* / Gheona Altarescu / Avi Orr-Urtreger / Matthew Taylor)
- **Innovative Therapeutics for Lysosomal Dysorders**
  (*Elizabeth Neufeld* / William Balch / Peter Lobel)
- **Clinical Trials for Lysosomal Diseases - Ongoing and Upcoming**
  (*Chester Whitley* / Forbes Porter / Luigi Naldini)

GRS Lysosomal Diseases
Defining Pathogenesis and Therapeutic Strategies for Lysosomal Diseases
Mar 14-15, 2015
Chair: Matthew C. Micsenyi
Associate Chair: Chiara Di Malta

Macromolecular Materials

From Synthesis to Application
Jan 11-16, 2015
Four Points Sheraton / Holiday Inn Express, Ventura, CA
Chair: Michael Mackay
Vice Chair: Ronald L. Jones

- **Theory and Simulation**
  (*Arthi Jayaraman* / Amalie Frischneckt / Valeriy Ginsberg)
- **Biomedical Applications**
  (*Lola Eniola-Adefeso* / Matthew Becker / Justin Cooper-White / Kathryn Uhrich)
- **Self Assembly**
  (*Mathew Green* / Svetlana Sukishvili / Brent Summerlin)
- **Synthesis and Utility**
  (*Christine Luscombe* / Luis Campos / Jeff Pyun / Stuart Rowan)
- **Conducting Polymers**
  (*Mark Dadmun* / Timothy Bender / Ryan Murphy)
- **Rheology**
  (*Charles Schroeder* / Eric Furst / Gareth McKinley / Jan Vermant)
- **Processing**
  (*Gila Stein* / Patrick Anderson / Marion McCord)
- **Nanomaterials**
  (*Jill Millstone* / Kenneth Carter / Michael Crawford / Karen Winey)
- **Characterization and Use**
  (*Christopher Kloxin* / Guy Van Assche / Andrew Waterhouse)

GRS Macromolecular Materials
Macromolecules: From Synthesis to Application
Jan 10-11, 2015
Chair: Roddel Remy

Mammalian DNA Repair

Controlling Traffic on the Streets and at the Crossroads of DNA Repair Pathways
Feb 8-13, 2015
Four Points Sheraton / Holiday Inn Express, Ventura, CA
Chair: Orlando D. Scharer
Vice Chair: Wei Yang

- **Keynote Session: DNA Repair and Genome Dynamics**
  (*Orlando Scharer* / Simon Boulton / Tom Mistelli)
- **Cellular Responses to Endogenously Generated DNA Damage**
  (*Leona Samson* / Bruce Demple / Chuan He / Thomas Kunkel / Samuel Wilson)
- **Damage Recognition and Ubiquitin Signaling in Nucleotide Excision Repair**
  (*Bennett Van Houten* / Jung-Hyun Min / Kaoru Sugasawa / Wim Vermeulen)
- **Diverse Mechanisms of Double Strand Break Repair**
  (*Tanya Paull* / Stephen Kowalczykowski / John Tainer / Stephen West / Claire Wyman)
- **Exploiting Genome Instability for Anticancer Therapy**
  (*Mark O'Connor* / John Pascal / Yves Pommier)
- **DNA Damage Signaling at Double Stand Breaks and Replication Forks**
  (*Karlene Cimprich* / Dipanjan Chowdhury / David Cortez / Daniel Durocher / Niels Mailand)
- **Disease Phenotypes Resulting from DNA Repair Defects**
  (*Bevin Engelward* / Winfried Edelmann / Jan Hoeijmakers / Laura Niedernhofer)

Gordon Conferences are different from other scientific conferences because:

...they contain one high caliber presentation after another, complemented by robust discussions of important scientific topics in our field, day after day. It's truly a unique experience. *(David E. Watson, Eli Lilly and Company)*

- **Responding to Obstacles at Replication Forks**
  (*Roger Woodgate* / Dana Branzei / Fumio Hanaoka / Josef Jiricny / Antoine Van Oijen)
- **Fanconi Anemia-Dependent and -Independent Repair of DNA Crosslinks**
  (*Johannes Walter* / Alan D'Andrea / Peter McHugh / John Rouse)

Mammalian DNA Repair
Controlling Traffic on the Streets and at the Crossroads of DNA Repair Pathways
Feb 7-8, 2015
Chair: Julie A. Rageul
Associate Chair: Kareem Mohni

Metals in Biology
The Inorganic Chemistry of Life
Jan 25-30, 2015
Four Points Sheraton / Holiday Inn Express, Ventura, CA
Chair: James M. Mayer
Vice Chair: Joanne Stubbe

- **Deconstructing Enzyme Catalysis**
  (*Stephen Ragsdale* / Marc Fontecave / Judy Hirst)
- **Heme Proteins and Reactivity**
  (*Michael Green* / Emma Raven / Yoshitsugu Shiro / Jeremy Harvey / Matthew Liptak)
- **Imaging and Spectroscopy**
  (*Kara Bren* / Lydia Finney / Zijian Guo / Roberta Pierattelli)
- **Hydrogen and Hydrogenase**
  (*Thomas Rauchfuss* / Anne Jones / Xile Hu / Peter Roach)
- **Bioinorganic Chemistry in the Environment**
  (*Alison Butler* / Jeffrey Gralnick / Jonathan Wilker)
- **Nitric Oxide**
  (*William Tolman* / Elizabeth Boon / Tim Warren)
- **Oxidase and Oxygen**
  (*Shelagh Ferguson-Miller* / Tewfik Soulimane / Peter Brzezinski)
- **Lessons from Small Molecules**
  (*Andy Borovik* / Shinobu Itoh / Franc Meyer / Guochuan Yin / Theodore Betley)
- **The Ubiquity of Heme**
  (*Rachel Austin* / Jay Groves)

Note: Unlike other GRSs, the Bioinorganic Chemistry GRS begins on a Thursday, sharing an evening session with the associated Metals in Biology GRC.

Bioinorganic Chemistry
Biological Inorganic Chemistry: Today and Tomorrow
Jan 29 - Feb 1, 2015
Chair: Thomas J. Lawton
Associate Chair: Kelly Chacon

Micro & Nanoscale Phase Change Heat Transfer
NEW!
Role of Surface Structures
Jan 11-16, 2015
Hotel Galvez, Galveston, TX
Chair: Yoav Peles
Vice Chair: Evelyn N. Wang

- **Research Needs, Challenges, and Opportunities**
  (*Luc Frechette*, *Patrick Phelan* / Yoav Peles / Evelyn Wang / Mark Spector / Avram Bar-Cohen)
- **Liquid to Vapor Phase Change**
  (*Jacopo Buongiorno*, *Gennady Ziskind* / David Cahill / Satish Kandlikar / John Thome / Naomi Halas)
- **Surface Chemistry and Surface Energy**
  (*Daniel Attinger* / Robin Ras / Yasuyuki Takata / Frederic Guittard)
- **Liquid/Vapor/Solid Phase Change Processes**
  (*Andrei Fedorov*, *Amy Fleischer* / John Rose / Dimos Poulikakos / David Quere / Li Shi)
- **Transport Across Thin Films**
  (*Tatiana Gambaryan-Roisman* / Joel Plawsky / Tao Deng / Pawel Keblinski)
- **Physics of Thermal Systems**
  (*Michael Ohadi*, *Acharya Sumanta* / Barbara Carney / Kenneth Goodson / Srinivas Garimella / Anthony Jacobi)
- **Materials at Interfaces**
  (*Samuel Graham*, *Deborah Pence* / Chang-Jin Kim / Pamela Norris / Joanna Aizenberg)
- **Multi Scale Dynamics**
  (*Todd Salamon*, *Mario Trujillo* / Julia Yeomans / Yogendra Joshi / Jayathi Murthy / Steven Wereley)
- **Interfacial Science and Mechanisms**
  (*Vinod Narayanan* / Suresh Garimella / Jungho Kim / Jennifer Lukes)

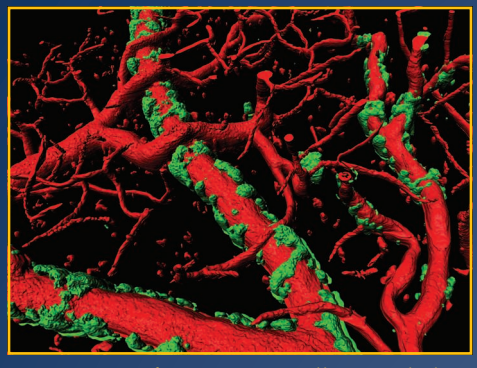

A 3-D reconstruction of an image series acquired by in vivo multi-photon microscopy through a cranial window in a mouse model of Alzheimer's Disease. Blood vessels are labeled with a red vascular dye and the vascular amyloid is labeled in green. Submitted by Harald W. Sontheimer, Chair, Glial Biology: Functional Interactions Among Glia & Neurons GRC.

Molecular Pharmacology
Connecting G Protein-Coupled Receptor Mechanisms to Physiological Functions
Feb 1-6, 2015
Ventura Beach Marriott, Ventura, CA
Chairs: Alan V. Smrcka & Jo Ann Trejo
Vice Chairs: Martin J. Lohse & Jurgen Wess

- **Keynote Session: GPCRs and A(rrestin)CRs: A Tale of Two Transducers**
  (*Michel Bouvier* / Robert Lefkowitz / Shaun Coughlin)
- **GPCR Allostery/Biased Signaling**
  (*Robert Lefkowitz* / Laura Bohn / Patrick Sexton / Jim Wells)
- **GPCR Intracellular Trafficking and Signaling**
  (*Mark Von Zastrow* / Jeff Benovic / Adriano Marchese / Manojkumar Puthenveedu)
- **GPCRs in Addiction and Tolerance**
  (*Emiliana Borelli* / Marc Caron / Charles Chavkin / Brigitte Kieffer)
- **GPCR Signaling in Physiology and Disease**
  (*Paul Insel* / Silvio Gutkind / Joan Heller Brown / Beth Levine / Rick Neubig / Nina Wettschureck)
- **Chemical Targeting/Orphan Receptors**
  (*Jurgen Wess* / Randy Hall / Evi Kostenis / Bryan Roth)
- **G Protein Signaling**
  (*Richard Neubig* / Henrik Dohlman / Heidi Hamm / Gregory Tall)
- **GPCR Signaling Mechanisms and Dynamics**
  (*Martin Lohse* / Marta Filizola / Jonathan Javitch / Jean-Philippe Pin / Gunnar Schulte)
- **Keynote Session: GPCR Structure**
  (*Roger Sunahara* / Brian Kobilka / Fiona Marshall / Georgios Skiniotis)

Molecular Pharmacology
New Frontiers in GPCR Signaling: From Biased Agonism to Disease Progression
Jan 31 - Feb 1, 2015
Chair: Neil J. Grimsey
Associate Chair: Stephanie S. Dusaban

Multi-Drug Efflux Systems
A Paradigm Shift from Fundamental Mechanisms to Practical Applications
Apr 26 - May 1, 2015
Renaissance Tuscany Il Ciocco Resort, Lucca (Barga), Italy
Chairs: Toshihisa Ishikawa & Helen I. Zgurskaya
Vice Chairs: Suresh V. Ambudkar & Melissa H. Brown

- **Keynote Session: Structure and Function of Multi-Drug Efflux Systems**
  (*Victor Ling*, *Hiroshi Nikaido* / Irwin Arias / Eitan Bibi)
- **Multi-Drug Efflux Pumps in Health and Diseases**
  (*Melissa Brown*, *John Schuetz* / Dieter Haeussinger / Ian Paulsen / John Schuetz / Matthias Schwab / Miguel Viveiros / Hannah Wexler)
- **Functional Interactions Between Influx and Efflux in Health and Clinical Conditions**
  (*Deanna Kroetz* / Deanna Kroetz / Tappei Takada / Jashvant Unadkat / Hendrik van Veen)
- **Role of Multi-Drug Efflux in Drug Discovery and Development**
  (*Ed Buurman*, *Olga Lomovskaya* / Per Artursson / Kim Brower / Ed Buurman / Olga Lomovskaya / Larry Sklar)
- **Structure and Molecular Dynamics of Membrane Transporters**
  (*Klaas Pos* / Christian Kandt / Ian Kerr / Osamu Nureki / Klaas Pos)
- **Structure-Function Relationships in Multi-Drug Efflux Pumps from Microbes and Human**
  (*Eitan Bibi*, *Osamu Nureki* / Vassiliy Bavro / David Hooper / John Golin / Cedric Govaerts / Jean-Michel Jault / Iris Maldener)
- **Protein Expression, Folding, and Membrane Trafficking of Membrane Transporters**
  (*Suresh Ambudkar* / Shigeki Higashiyama / Yinan Wei / Suresh Ambudkar)
- **Multi-Drug Efflux Pumps in Environment, Bioengineering and Biofuel Production**
  (*Aindrila Mukhopadhyay*, *Aixin Yan* / Anne-Brit Kolsto / Twan Lammers / Aindrila Mukhopadhyay / Wendy Peer / Aixin Yan)
- **Transporters in Stem Cells and Clinical Implications**
  (*Balazs Sarkadi* / Balazs Sarkadi / Hideyuki Saya / Brian Sorrentino)

Multi-Drug Efflux Systems
Learning from the Past to Innovate the Future
Apr 25-26, 2015
Chair: Jon W. Weeks
Associate Chair: Yu Toyoda

Nanomaterials for Applications in Energy Technology

Energy Conversion, Storage, and Transport
Feb 22-27, 2015
Ventura Beach Marriott, Ventura, CA
Chair: Uwe Kortshagen
Vice Chair: Yi Cui

- **Nano and Energy Science**
  (*Eray Aydil* / Arun Majumdar / Naomi Halas)
- **Electrochemical Energy Conversion and Storage**
  (*Xiaolin Zheng* / Sossina Haile / Jun Liu / Vanessa Wood)
- **Photon Energy Conversion: Plasmonics**
  (*Peter Nordlander* / Albert Polman / Alex Govorov)
- **Materials Design and Synthesis**
  (*Mark Swihart* / Markus Winterer / Suguru Noda / Giulia Galli)
- **Electron Transport for Energy Efficiency**
  (*Alexander Efros* / Cherie Kagan / Matt Law)
- **Thermal and Mechanical Energy Conversion**
  (*Austin Minnich* / Junichiro Shiomi / Zhong-Lin Wang / Qihua Xiong)
- **Sustainability and Environmental Health and Safety**
  (*Robert Hamers* / Christy Haynes / Alison Elder)
- **Photon Energy Conversion: Photovoltaics and Luminescence**
  (*Joseph Luther* / David Norris / Mercouri Kanatzidis / Victor Klimov)
- **Materials Synthesis, Structuring, and Scale-Up**
  (*Lorenzo Mangolini* / Delia Milliron / Bernd Sachweh)

GRS Nanomaterials for Applications in Energy Technology
The Physics and Chemistry of a Sustainable Energy Future
Feb 21-22, 2015
Chair: Lance M. Wheeler

Nitric Oxide

Nitric Oxide Signaling and Therapeutics
Feb 15-20, 2015
Four Points Sheraton / Holiday Inn Express, Ventura, CA
Chair: Harry Ischiropoulos
Vice Chair: Sruti Shiva

- **Keynote Session: Nitric Oxide/Soluble Guanylate Cyclase Signaling**
  (*Harry Ischiropoulos* / Michael Marletta)
- **Nitric Oxide Synthases / sGC Structure-Function**
  (*Dennis Stuehr* / Linda Roman / Elsa Garcin / Dennis Stuehr / C.S. Raman)
- **NO/NOS Interactions with H_2S and NOX**
  (*Bruce Freeman* / Ruma Banerjee / Neil Hogg / Csaba Szabo / Martin Feelisch)
- **NO in the CNS**
  (*Joseph Beckman* / Valina Dawson / Alvaro Estevez / Stuart Lipton)
- **NO Microbial Systems and Inflammation**
  (*Ferric Fang* / Joanne Flynn / Ferric Fang / Andres Vazquez-Torres / Paul Fox)
- **NO, Arginase, Metabolism and Cardiovascular Biology**
  (*Jon Lundberg* / Paul Huang / Brendan Lee / Claudia Morris / Amrita Ahluwalia / Karin Potoka)
- **Late-Breaking Topics**
  (*Sruti Shiva*)
- **NO and Protein PTMs**
  (*Richard Cohen* / Elizabeth Murphy / Steven Tannenbaum / Stacy Wendell / Takaaki Akaike)
- **NO and GNOR Biology**
  (*Andrew Gow* / Limin Liu / Wolfram Goessling)

Oxidative Stress & Disease

The Redox Biology of Age-Related Diseases
Mar 1-6, 2015
Ventura Beach Marriott, Ventura, CA
Chairs: Deborah A. Ferrington & Rajiv Ratan
Vice Chairs: La Dora V. Thompson & Giuseppe Poli

- **Keynote Session: Changing Concepts in Redox Biology**
  (*Deborah Ferrington*, *Rajiv Ratan* / Sue Gho Rhee / Dean Jones)
- **Redox Chemistry and Signaling**
  (*Enrique Cadenas* / Kelvin Davis / Helen Griffiths / Alicia Kowaltowski / Christine Winterbourn)
- **Techniques to Measure *In Vivo* Redox Status**
  (*Holly Van Remmen* / Vsevelod Belusov / Mike Murphy)
- **Altered Redox and Age-Related Eye Disease**
  (*M. Cristina Kenney* / Jonathan Crowston / Ula Jurkunas / Kai Kaarniranta / Kazuo Tsubota)
- **"Omics" and Redox Stress**
  (*Kirsten Lampi* / Christine Vogel / Bing Zhang)
- **Redox Regulation, Stem Cells, and Age-Related Disease**
  (*Margot Mayer-Proschel* / Simone Di Giovanni / Saghi Ghaffari / Mark Noble)
- **Novel Oxidases and Disease**
  (*Michael Tymianski* / Karl-Heinz Krause / Johanna Myllyharju / Christopher Schofield)
- **Redox Regulation as a Therapeutic Strategy**
  (*Linda Van Eldik* / Pinchas Cohen / Stuart Lipton / Alfredo Sadun / Hazel Szeto / Rodney Levine)
- **Functional Regulation by Site-Specific Oxidation of MICAL**
  (*Vadim Gladysheve* / Samie Jeffrey / Jonathan Terman)

GRS Oxidative Stress & Disease
The Redox Mechanisms in Age-Related Degeneration
Feb 28 - Mar 1, 2015
Chair: Megan W. Bourassa
Associate Chairs: Amit Kumar & Nathan Schuld

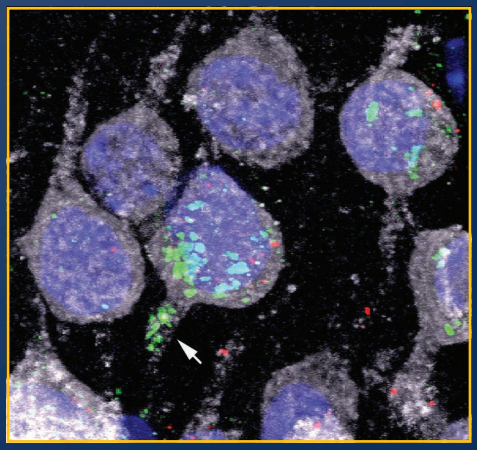

Cortical neurons as viewed in vivo from a mouse model of the lysosomal disease, Niemann-Pick type A (acid sphingomyelinase deficiency). Immunofluorescence labeling shows NeuN-positive neurons (white) with DAPI labeled nuclei (blue) exhibiting aberrant accumulation of the macroautophagy adapter protein p62 (green) and GM2 ganglioside (red). A meganeurite (axon hillock enlargement, arrow) containing p62 is present on one neuron. These neuropathological features are associated with dysfunction of the autophagic-endocytic-lysosomal system and are common hallmarks of many lysosomal diseases. Courtesy of Matthew C. Micsenyi (Walkley laboratory, Albert Einstein College of Medicine) through funding by the NIH, R01 HD045561 (SUW). Submitted by Steven U. Walkley, Chair, Lysosomal Diseases GRC.

Physical Virology

Integrating Global Significance with Atomic Level Understanding
Jan 25-30, 2015
Ventura Beach Marriott, Ventura, CA
Chairs: Trevor Douglas & Nicole Steinmetz
Vice Chairs: Mavis Agbandje-McKenna & Brian Bothner

- **Structure-Based Engineering of Viruses**
  (*Adam Zlotnick* / John Johnson)
- **New Materials by Design**
  (*Jonathan Pokorski* / M.G. Finn / Roman Jerala / Mauri Kostiainen / Christina Wege)
- **Nanomanufacturing**
  (*Suchetana Mukhopadhyay* / Alexander Bittner / Elaine Haberer / Seung-Wuk Lee)
- **Virus Particles in Medicine**
  (*Junghae Suh* / Bryce Chackerian / Steven Lommel / Renata Pasqualini / Polly Roy)
- **Immune Responses**
  (*Nicole Steinmetz* / Martin Bachmann / Alan Davidson / Blake Wiedenheft)
- **Structural Foundations**
  (*Trevor Douglas* / Jose Castion / Peter Prevelige / Phoebe Stewart)
- **Biophysical Methods and Tools**
  (*Bogdan Dragnea* / Martin Jarrold / Aydogan Ozcan / Wouter Roos)
- **Computational and Theoretical Approaches**
  (*Rudi Podgornik* / Charles Brooks / Paul Van Der Schoot)
- **From Basic Principles to Applications**
  (*Peter Prevelige* / Donald L.D. Caspar)

GRS Physical Virology
The Expanding Interface of Viral Characterization & Engineering Application
Jan 24-25, 2015
Chair: Benjamin H. Schwarz
Associate Chair: Amy Wen

Plant Lipids: Structure, Metabolism & Function

Integration of Lipid Metabolism, Signaling and Engineering
Feb 1-6, 2015
Hotel Galvez, Galveston, TX
Chairs: Glenda Gillaspy & Xuemin (Sam) Wang
Vice Chairs: Katayoon Dehesh & Anthony J. Kinney

- **Keynote Session: Emerging Paradigms in Understanding Lipid Metabolism and Function**
  (*Xuemin (Sam) Wang* / Christoph Benning / Donald Jump / Jianbing Yan)
- **New Developments in Lipidomics Technology and Pathway Modeling**
  (*Yonghua Li-Beisson* / Joerg Schwender / Ruth Welti)
- **The Past, Present and Future of Plant Lipids**
  (*Peter Dormann* / Ernst Heinz)
- **Membrane Lipids**
  (*Marina Gavilanes-Ruiz* / Edgar Cahoon / Michael Hothorn / Michael Neff / Ivo Feussner)
- **Lipids in Development**
  (*Yuki Nakamura* / John Browse / Mee Len Chye / Tegan Haslam / Susanne Hoffmann-Benning / Abraham Koo)
- **Lipid Mediators and Signaling**
  (*Erik Nielsen* / Tamas Balla / Ingo Heilmann / Teun Munnik / Imara Perera)
- **Lipids and Stress**
  (*Ana Laxalt* / Ling Guo / Jyoti Shah / Christa Testerink / Katayoon Dehesh)
- **Bioenergy and Industrial Lipids**
  (*Jitao Zou* / Timothy Durrett / John Dyer / Sten Stymne / John Shanklin)
- **Nutritional Lipids and Nutraceuticals**
  (*Basil Nikolau* / Peter Eastmond / Youngsook Lee / Johnathan Napier / Anthony Kinney)

Gordon Conferences are different from other scientific conferences because:

...they stimulate discussion among researchers from industry, academe and government with a wide range of experience from novice to expert.

(Megan Corty, University of Massachusetts Medical School)

GRS Plant Lipids: Structure, Metabolism & Function
Integration of Lipid Metabolism, Signaling and Engineering
Jan 31 - Feb 1, 2015
Chair: Phoebe Williams
Associate Chair: Joy Valenta

Polar Marine Science
Polar Shelves and Shelf Break Exchange in Times of Rapid Climate Warming
Mar 15-20, 2015
Renaissance Tuscany Il Ciocco Resort, Lucca (Barga), Italy
Chair: Paul Wassmann
Vice Chair: Jacqueline M. Grebmeier

- **Keynote Session: Polar Systems in Times of Rapid Climate Change**
  (*Marit Reigstad* / Eddy Carmack / Philip Boyd)
- **Physical Oceanography Shaping the Polar Oceans**
  (*Ursula Schauer* / Rebecca Woodgate / Kikki (Helga) Flesche Kleiven / Isabelle Ansorge)
- **Energy and Gas Exchange at the Ocean-Sea Ice-Atmosphere Interface**
  (*David Barber* / Jean-Louis Tison / Brice Loose)
- **Acidification and Toxins: Sources, Sinks and Pathways**
  (*Lars-Otto Reiersen* / Carlos Duarte / Michiyo Yamamoto-Kawai / Gary Stern)
- **The Many Faces of Changing Ice: From Sea Level Rise to the Marine Carbon Cycle**
  (*Letizia Tedesco* / Ronnie Glud / David Vaugham)
- **Ecosystem Dynamics of Arctic Shelves**
  (*Antje Boetius* / Marcel Barbin / Bodil Bluhm / Susana Agusti)
- **Plankton Dynamics of Antarctic Shelves and Species Evolution**
  (*Hyoung Chul Shin* / Maria Vernet / Jan Strugnell)
- **Carbon Cycling in Arctic and Antarctic Shelves**
  (*Thomas Trull* / Orjan Gustafsson / Jurgen Mienert / Bronte Tilbrook)
- **Higher Trophic Levels**
  (*Daniel Costa* / Akinori Takahashi / Kit M. Kovac)

GRS Polar Marine Science
From Chemistry to Modelling via Biology and Physical Oceanography in the Changing Polar Systems
Mar 14-15, 2015
Chair: Marie Jm. Seguret
Associate Chair: Ingrid Wiedmann

Quantitative Genetics & Genomics
Deciphering the Genetic Basis of Complex Phenotypes for the Benefit of Mankind
Feb 22-27, 2015
Renaissance Tuscany Il Ciocco Resort, Lucca (Barga), Italy
Chair: Michel A. Georges
Vice Chair: Ann E. Stapleton

- **Genomic Architecture of Complex Traits - Uncovering Missing Heritability**
  (*Ed Buckler* / Alkes Price / Jian Yang)
- **From Correlation to Causation - Identifying Causative Variants Underlying Complex Traits**
  (*Manolis Dermitzakis* / Jim Holland / Hailiang Huang / Gil McVean / Augustin Kong)
- **From Correlation to Causation - Identifying Causative Genes Underlying Complex Traits**
  (*Manolis Dermitzakis* / Jonathan Pritchard / Tuuli Lappalainen)
- **From Correlation to Causation - Identifying Networks Underlying Complex Traits**
  (*Ann Stapleton* / Stig Omholt / Ines Thiele / Marc Vidal / Dana Pe'Er)
- **Population Genomics of Complex Traits**
  (*Bruce Walsh* / Piter Bijma / Molly Przeworski)
- **Evolutionary Genomics of Complex Traits**
  (*Bruce Walsh* / Leif Andersson / Kathleen Donohue / Peter Andolfatto / David Stern)
- **Genomics of Host Pathogen Interactions**
  (*Daniel Pomp* / Jeroen Raes / Ran Blekhman)
- **Epigenomics of Complex Traits**
  (*Vincent Colot* / Richard Mott / Erik Miska / Frank Johannes / Sonia Shah)
- **Translational Genomics for Complex Traits**
  (*Chris Schoen* / Mike Goddard / Laurence Moreau / Atul Butte)

GRS Quantitative Genetics & Genomics
Consequences and Evolution of Genomic Variation
Feb 21-22, 2015
Chair: Julia Steinberg
Associate Chair: Frank W. Albert

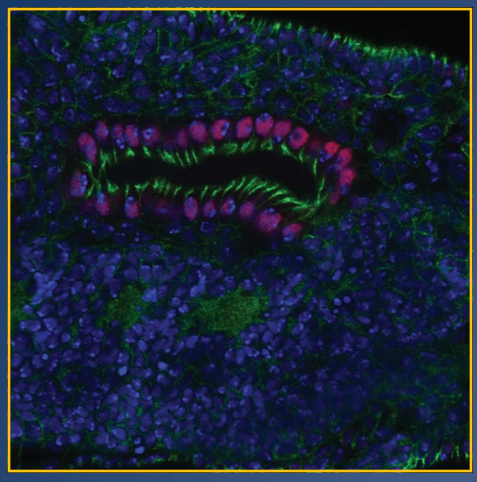

A Drosophila embryonic salivary gland stained with DAPI (blue), antibodies to a nuclear transcription factor (red) and a septate junction marker (green). Courtesy of Deborah J. Andrew and Rebecca M. Fox. Submitted by Deborah J. Andrew & Roberto Weigert, Chairs, Salivary Glands & Exocrine Biology GRC.

RNA Editing
Diversifying the Transcriptome: Consequences for Development and Disease
Mar 8-13, 2015
Renaissance Tuscany Il Ciocco Resort, Lucca (Barga), Italy
Chairs: Jane Jackman & Michael Jantsch
Vice Chairs: Reuben S. Harris & Heather A. Hundley

- **Biogenesis and Diversity of Editing and Modification**
  (*Maureen Hanson* / John Mattick / Anita Hopper / Brenda Bass / Ralph Bock)
- **Toward Describing the Transcriptome**
  (*Heather Hundley* / Mark Helm / Jin Billy Li / Maureen Hanson / Erez Levanon / Gideon Rechavi / Wendy Gilbert)
- **Environmental Adaptation and Tuning of Genetic Information**
  (*Valerie De Crecy-Lagard* / Robert Reenan / Maria Eugenia Armengod / Marie Ohman / Janusz Bujnicki)
- **Editing and Modification in Infection and Pathology**
  (*Nina Papavasiliou* / Catriona Jamieson / Angela Gallo / Charles Samuel / Ruslan Aphasizhev / Jorge Cruz-Reyes / Reuben Harris)
- **Modification, Editing and Immunity**
  (*Mark Helm* / Mary O'Connell / Harold Smith / Nina Papavasiliou / Sebastian Leidel)
- **Catalysis and Target Recognition by Editing and Modification Enzymes**
  (*Mary O'Connell* / Ian Small / Stewart Shuman / Peter Beal / Yi-Tao Yu / Andrea Rentmeister / Peter Dedon)
- **Regulatory Networks and Quality Control**
  (*Jonatha Gott* / Kazuko Nishikura / Eric Phizicky / Pat Limbach / Heather Hundley)
- **Molecular Mechanisms and Macromolecular Machines**
  (*Reuben Harris* / Celia Schiffer / Valerie De Crecy-Lagard / Frederic Allain / Ya-Ming Hou / Ronald Emeson / Thorsten Stafforst)
- **New Horizons for the Transcriptome**
  (*Eric Phizicky* / Juan Alfonzo / Tom Meier / Ronald Micura / Joshua Rosenthal)

GRS RNA Editing
Transcriptome Diversity: Roles in Health and Disease
Mar 7-8, 2015
Chair: Ashanti Matlock

RNA Nanotechnology
NEW!
Converging Disciplines for the Advancement of Inter-RNA Interactions
Feb 1-6, 2015
Four Points Sheraton / Holiday Inn Express, Ventura, CA
Chair: Peixuan Guo
Vice Chair: Neocles B. Leontis

- **Structure and Folding of RNA Nanoparticles**
  (*Eric Westhof* / Eric Westhof / Robert Batey / Thomas Hermann / Hirohide Saito)
- **Physical and Chemical Approaches in RNA Nanotechnology**
  (*Carlo Montemagno* / Paula Hammond / Farzin Haque)
- **RNA Computation and Modeling**
  (*Bruce Shapiro* / Bruce Shapiro / Kirill Afonin / Janusz Bujnicki)
- **RNA Nanoparticles in Therapeutics**
  (*Xing-Jie Liang*, *Xiyun Yan* / Carlo Croce / Mark Evers / Zicai Liang)
- **Importing from DNA Nanotechnology**
  (*Jorgan Kjems* / Paul Rothemund / Hao Yan)
- **RNA Nanoparticles for Rare Diseases**
  (*David Gamm* / Jong Bum Lee)
- **Nanotechnologies Relevant to RNA Research**
  (*Stephanie Morris* / Yuliang Zhao / Dai-Wen Pang / Dennis Bong)
- **Extracellular RNA for Biomarker Development**
  (*Jan Lotvall* / Xandra Breakefield)
- **Extracellular RNA for Therapeutic Development**
  (*Gabriel Lopez-Berestein* / Anil Sood / Judy Lieberman)

Salivary Glands & Exocrine Biology

Development, Homeostasis and Repair of Secretory Organs: Their Microenvironments and the Signals That Control Them
Feb 15-20, 2015
Hotel Galvez, Galveston, TX
Chairs: Deborah J. Andrew & Roberto Weigert
Vice Chairs: Gary A. Weisman & Catherine E. Ovitt

- **Keynote Session: Perspectives, Epithelial Polarity and Gland Morphogenesis** (*Melinda Larsen* / Lawrence Tabak / Elizabeth Knust / Matthew Hoffman)
- **Glycobiology, Mucins and Epithelial Barriers** (*David Yule* / Mary Callaghan Rose / Jerrold Turner / Katharina Ribbeck / Gunnar Hansson)
- **Secretory Organ Development** (*Kenneth Yamada, Darlene Dartt* / Cathrin Brisken / Maria Kukuruzinska / Seung Kim / Ondine Cleaver)
- **Protein Secretion** (*Sarah Hamm-Alvarez* / Ben-Zion Shilo / Duy Tran / Manfred Frick / Antonella De Matteis)
- **Fluid Secretion and Signaling** (*Shmuel Muallem* / Indu Ambudkar / James Sneyd / Mark Donowitz / Hsiao Chan)
- **Cutting Edge Technologies as Applied to Secretory Biology and Disease** (*Ilias Alevizos* / Prashant Mali / Natalie Porat-Shliom / George Patterson)
- **Host-Pathogen Immunity** (*Jay Chiorini, Austin Mercheff* / Dingding An / Olga Baker / Daniel Malamud / Julian Ambrus)
- **Design Flaws - Auto-Immunity in Epithelial Organs** (*Sue Menko* / Denise Faustman / Ammon Peck / Mary Reyland)
- **Keynote Session: Clathrin Mediated Endocytosis** (*Sarah Knox* / Sandra Schmid)

Self-Assembly & Supramolecular Chemistry

From Molecular Information to Function
May 17-22, 2015
Renaissance Tuscany Il Ciocco Resort, Lucca (Barga), Italy
Chairs: Joerg Lahann & Francesco Stellacci
Vice Chairs: Takuzo Aida & Makoto Fujita

- **Keynote Session: Translating Scientific Breakthroughs Beyond Traditional Disciplines** (*Joerg Lahann* / Jeffrey Hubbell)
- **Long-Range Structure Enabled by Complex Self-Assembly** (*Esther Amstrad* / Constantine Evans / Nicholas Kotov / Lee Cronin)
- **Recent Advances with Nanomachines** (*Francesco Stellacci* / Henry Hess / David Leigh / Zvonimir Dogic)
- **Property-Focused Self-Assembly** (*Michael Solomon* / Ashutosh Chilkoti / Ulrich Schubert / Samuel Stupp)
- **Emerging Materials Challenges in Regenerative Medicine** (*Florence Bally* / Jennifer Elisseeff / Molly Stevens)
- **Dynamics of Self-Assembly** (*Sharon Glotzer* / Alexander Katz / Jonathan Nitschke / Michael Solomon / Rienk Eelkema)
- **Broadening the Functionality of Metal Organic Frameworks** (*Makoto Fujita* / Melissa Reynolds / Christian Serre / Christof Woell)
- **Biohybrid Materials** (*Samir Mitragotri* / Kazunori Kataoka / Holger Frauenrath / Tanja Weil)
- **Quasi-Crystalline Materials** (*Takuzo Aida* / Marjolein Dijkstra / Sharon Glotzer / Virgil Percec)

GRS Self-Assembly & Supramolecular Chemistry
From Molecular Assembly to Functional Materials
May 16-17, 2015
Chair: Samuel T. Jones
Associate Chair: Asish Misra

Speciation

NEW!

Modes of Diversification, Ecological Mechanisms, and Genomic Signatures
Mar 15-20, 2015
Four Points Sheraton / Holiday Inn Express, Ventura, CA
Chair: Ulf Dieckmann
Vice Chair: Åke Brännström

- **Biodiversity Crisis and Speciation** (*Roger Butlin* / Michael Rosenzweig / Michel Loreau)
- **Mechanisms of Reproductive Isolation** (*Allen Orr* / Ake Brannstrom / Andrew Hendry / Eva Kisdi)
- **Genetic Constraints** (*Mark Kirkpatrick* / Reinhard Burger / Sergey Gavrilets)
- **Ecological Drivers** (*Ulf Dieckmann* / Dan Bolnick / Joel Brown / Michael Doebeli)
- **Genomic Signatures** (*Jeffrey Feder* / Anna Qvarnstrom / Ole Seehausen)
- **Behavioral Mechanisms** (*Erik Svensson* / Jenny Boughman / Glenn-Peter Satre / Sander van Doorn)
- **Species Cohesion and Hybrid Zones** (*James Mallet* / Kerstin Johannesson / Axel Meyer)
- **Macro-Ecological Explanations of Biodiversity** (*Rampal Etienne* / James Brown / Stephen Hubbell / Akira Sasaki)
- **Toward a Synthetic Understanding of Speciation** (*Simon Levin* / Dolph Schluter / Xavier Thibert-Plante)

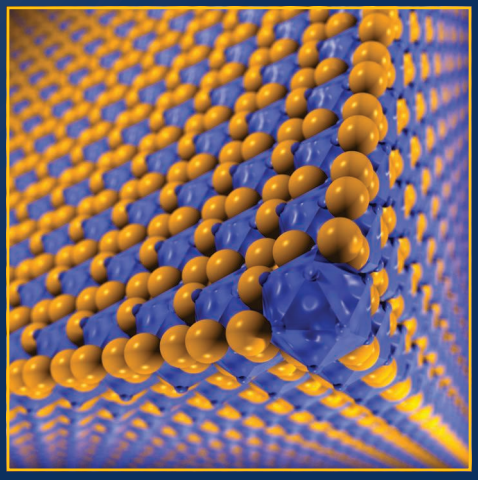

Protein cages, such as virus particles, can be used to form three-dimensional binary superlattices through tunable electrostatic interactions. The image shows a binary superlattice formed from negatively charged cowpea chlorotic mottle virus (blue) and cationic gold nanoparticles (yellow) that adopt an AB_6^{fcc} crystal structure. Courtesy of Mauri Kostiainen & Panu Hiekkataipale. Submitted by Trevor Douglas & Nicole Steinmetz, Chairs, Physical Virology GRC.

Stem Cells & Cancer

Exploring the Heterogeneity of Cancer Cells and Relevance to Therapy
Feb 15-20, 2015
Ventura Beach Marriott, Ventura, CA
Chair: Leonard I. Zon
Vice Chair: Lenhard Rudolph

- **Keynote Session: Cancer Stem Cells and Diversity** (*Leonard Zon* / Leonard Zon / Joan Massague / Luis Parada)
- **Stem Cell Biology** (*Maarten Van Lohuizen* / Hanna Mikkola / Elaine Fuchs / David Traver / Roeland Nusse)
- **Cancer Epigenetics and Stem Cells** (*Hiromitsu Nakauchi* / Margaret Goodell / Emily Bernstein / Maarten Van Lohuizen)
- **Aging and Cancer Stem Cells** (*Emmanuelle Passegue* / Benjamin Ebert / Anne Brunet / Lenhard Rudolph / Ross Levine)
- **Cancer Stem Cell Biology** (*Lenhard Rudolph* / Axel Behrens / Emmanuelle Passegue / Andreas Trumpp)
- **Clonal Evolution and Cell Type of Origin** (*Roeland Nusse* / Derrick Rossi / Douglas Winton / Juergen Knoblich / Tannishtha Reya)
- **Targeting Cancer Stem Cells** (*Catriona Jamieson, David Langenau* / David Langenau / Jane Visvader / Fred De Sauvage)
- **Stem Cell Niches** (*Jane Visvader* / Leanne Jones / Toshio Suda / Amy Wagers / Hiromitsu Nakauchi)
- **Clinical Translation of Cancer Stem Cells** (*David Langenau* / Irving Weissman / Catriona Jamieson / Thomas Rando)

GRS Stem Cells & Cancer
Exploring the Intersection of Stem Cell and Cancer Biology
Feb 14-15, 2015
Chair: Charles K. Kaufman
Associate Chair: Ellen van Rooijen

Stochastic Physics in Biology

Foundations and Current Trends
Jan 11-16, 2015
Ventura Beach Marriott, Ventura, CA
Chair: Steven J. Altschuler
Vice Chair: Jin Wang

- **Stochasticity Across Spatial-Temporal Scales** (*Ken Dill* / Hong Qian / Marc Kirschner / Laura Lavine)
- **Stochasticity in Disease and Cell Fate Networks** (*Daniel Needleman* / Jin Wang / Tanja Kortemme / Hao Li / Sunney Xie)
- **Stochasticity in Signaling Networks** (*Leor Weinberger* / Andre Levchenko / Long Cai)
- **Stochasticity in Cellular Organization** (*Nathalie Balaban* / Daniel Needleman / Amy Gladfelter / Wallace Marshall / Alexander Mogilner)
- **Principles and Consequences of Cellular Heterogeneity** (*Vito Quaranta* / Lani Wu / Nathalie Balaban)
- **Heterogeneity in Tissue Development and Homeostasis** (*Thomas Gregor* / Naama Barkai / Boris Shraiman / Stanislav Shvartsman / Allon Klein)
- **Stochasticity in Pattern Formation of Developing Tissues** (*Zev Gartner* / Claude Desplan / Thomas Gregor)
- **Evolution of Emergent Behaviors in Heterogeneous Cellular Populations** (*Daniel Fisher* / Gabor Balazsi / Peter Robin Hiesinger / Deborah Gordon / Oskar Hallatschek)
- **Evolutionary Design Principles and Dynamics of Genomes and Proteins** (*Marc Kirschner* / Michael Desai / Rama Ranganathan)

Superconductivity

Unconventional Superconductivity: Materials and Mechanisms
May 24-29, 2015
The Chinese University of Hong Kong, Hong Kong, China
Chair: Hai-Hu Wen
Vice Chair: Andrey Chubukov

- **Newly Discovered Superconducting Materials** (*Hidenori Takagi* / Paul Canfield / Brian Maple / Xianhui Chen / Jianlin Luo / Yoshizuka Mizuguchi / Zhuan Xu)
- **Novel Iron-Based Superconducting Materials** (*Paul C. Chu* / Hideo Hosono / Qikun Xue / Donglai Feng / Cedomir Petrovic)
- **Nematicity and Orbital Physics in Iron Based Superconductors** (*Joerg Schmalian* / Rafael Fernades / Hiroshi Kontani / A.N. Pasupathy / Takasada Shibauchi)

- **Gap Symmetry and Phase Diagram of Iron Based Superconductors**
  (*Igor Mazin* / Peter Hirschfeld / Louis Taillefer / Antony Carrington / Jiangping Hu / Yuji Matsuda / Ruslan Prozorov)
- **Pairing Mechanism of Iron-Based and Cuprate Superconductors**
  (*Nanlin Wang* / Bernhard Keimer / Hong Ding / Ilya Eremin / Tetsuo Hanaguri)
- **Feature of Pseudogap in Cuprate Superconductors**
  (*Zheng-Yu Weng* / Martin Greven / Jenny Hoffman / Zhixun Shen / Xingjiang Zhou / Gabriel Kotliar / Richard Greene)
- **Heavy Fermion Superconductors and Quantum Criticality**
  (*Laura Greene* / Piers Coleman / J.C. Seamus Davis / Frank Steglich / Qimiao Si)
- **Superconductivity in Confined and Topological Systems**
  (*Moses H.-W. Chan* / Liang Fu / Yoichi Ando / Ali Yazdani / Ivan Bosovic / Yoshihiro Iwasa / Peter Woelfle)
- **Modern Ideas and Understanding on Unconventional Superconductivity**
  (*Fuchun Zhang* / Dunghai Lee / Tao Xiang / Aharon Kapitulnik / Pengcheng Dai)

Superconductivity
Unconventional Superconductivity: Materials and Mechanisms
May 23-24, 2015
Chair: Xiyu Zhu

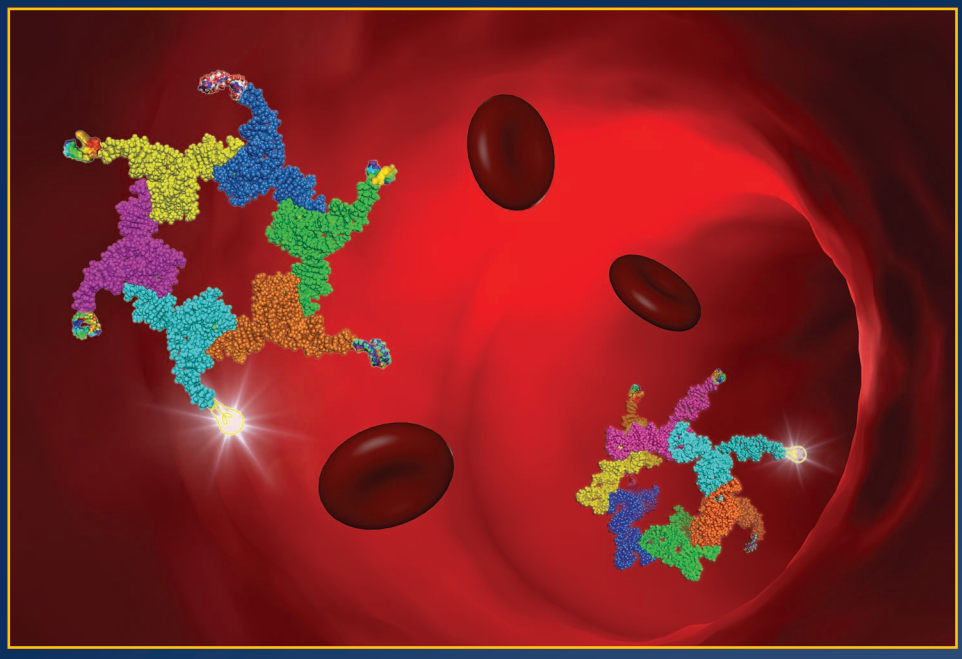

RNA nanotechnology for cancer therapy: Hexameric pRNA nanoparticles harboring targeting, therapeutic and imaging modules tumbling through tumor vasculature. Courtesy of Zhengyi Zhao, Farzin Haque & Peixuan Guo (University of Kentucky). Submitted by Peixuan Guo, Chair, RNA Nanotechnology GRC.

Translation Machinery in Health & Disease

NEW!

Protein Synthesis and Beyond
Feb 22-27, 2015
Four Points Sheraton / Holiday Inn Express, Ventura, CA
Chairs: Xiang-Lei Yang & Jonathan Yewdell
Vice Chair: Sunghoon Kim

- **Keynote Session: New Frontiers in Translation**
  (*Xiang-Lei Yang* / Ada Yonath / Jennifer Doudna)
- **Infectious Diseases and Immunity**
  (*Jonathan Yewdell* / Stephen Benkovic / Robin Fahraeus / Michael Ibba / Babak Javid / Jonathan Yewdell)
- **Inflammatory Diseases**
  (*Melissa Ashlock* / Melissa Ashlock / Ingrid Lundberg / Ehud Razin / Kenneth Stuart)
- **Tumorigenesis**
  (*Sunghoon Kim* / Paul Schimmel / Kun-Liang Guan / Sunghoon Kim / Davide Ruggero / Robert Schneider)
- **Translation Modulation and Metabolic Diseases**
  (*Lluis Ribas de Pouplana* / Anders Bystrom / Rita Horvath / Lluis Ribas de Pouplana)
- **Neurological Disorders**
  (*Susan Ackerman* / Nahum Sonenberg / Susan Ackerman / Jennifer Darnell / Albena Jordanova / Eric Klann)
- **Vascular and Hematologic Disorders**
  (*Paul Fox* / Steven Ellis / Paul Fox / Taisuke Kanaji / Alyson MacInnes)
- **Stress-Induced Adaptive Translation**
  (*Paul Anderson* / Jonathan Weissman / Paul Anderson / Myriam Gorospe / Randal Kaufman / Tao Pan)
- **Translation Machinery as Disease Targets**
  (*Susan Martinis* / Jamie Cate / Karin Musier-Forsyth / Shigeyuki Yokoyama)

Tropical Infectious Diseases

Challenges, Opportunities and Successes
Mar 8-13, 2015
Hotel Galvez, Galveston, TX
Chair: Serap Aksoy
Vice Chair: Jesus Valenzuela

- **Keynote Session: Malaria Control**
  (*Serap Aksoy* / Alan Magill / Terrie Taylor)
- **Challenges for Malaria Control**
  (*Photini Sinnis* / Abdoulaye Djimde / Maria Mota / Dyann Wirth / Jane Carlton / Christopher Plowe)
- **Drug and Insecticide Resistance Management for Malaria Control**
  (*Philip Rosenthal* / Rick Fairhurst / Philip Rosenthal / Hillary Ranson)
- **Dengue and Chikungunya Control**
  (*Scott Weaver* / Scott Weaver / Pattamaporn Kittayapong / Nikos Vasilakis / Alan Rothman / Luciano Moreira)
- **Challenges for Vaccine Development and Efficacy for Tropical Infectious Diseases**
  (*Alan Rothman* / Anne deGroot / Stephen Thomas / Steven Reed)
- **Opportunities in Vector Biology for Control of Tropical Infectious Diseases**
  (*Nora Besansky* / Rebecca Rico Hesse / Nora Besansky / Carolina Barrilas-Mur / Anandasankar Ray / Mike Lehane)
- **Neglected Tropical Diseases and Disease Emergence and Control**
  (*Albert Ko* / Albert Ko / Eric Dumonteil / Andrew Dobson / Grace Murilla / Pauline Mwinzi)
- **Tropical Diseases Targeted for Elimination**
  (*Peter Hotez* / Gary Weill / Charles King / Kingsley Asiedu / Thomas Lietman / Frank Richards / Alison Galvani)
- **Keynote Session: Prospects for Tropical Infectious Disease Control**
  (*Serap Aksoy* / David Sacks / Peter Hotez)

Tropical Infectious Diseases
Challenges, Opportunities and Successes
Mar 7-8, 2015
Chair: Stefanie Trop

Vascular Cell Biology

Frontiers in Basic Science and Clinical Translation
Jan 18-23, 2015
Four Points Sheraton / Holiday Inn Express, Ventura, CA
Chair: Anne Eichmann
Vice Chair: Mark Kahn

- **Keynote Session: Frontiers in Clinical Translation**
  (*Laura Benjamin* / Napoleone Ferrara / Yossi Schlessinger / Hal Dietz)
- **Endothelial Signaling in Development and Disease**
  (*Mark Kahn* / Holger Gerhardt / Elisabetta Dejana / Rosemary Akhurst / Luisa Iruela-Arispe)
- **Vascular Mural Cells**
  (*Gary Owens* / Catherine Hall / Brant Isakson / Joseph McCarty)
- **Vascular Diseases**
  (*Martine Clozel* / Klaus Ley / Jens Titze / David Cheresh / Dwight Towler)
- **Growth Factors/Receptors/Lipid Mediators**
  (*Lena Claesson-Welsh* / Michael Simons / Susan Quaggin / Timothy Hla)
- **Endothelium and Metabolism**
  (*Masataka Majima* / Ulf Eriksson / Calvin Kuo / Zoltan Arany / Stephen Young)
- **Matrix and Biomechanical Signals**
  (*Luisa Iruela-Arispe* / Martin Schwartz / Tatiana Byzova / Mark Ginsberg)
- **Regenerative Biology: Stem Cells and Niches**
  (*Karen Hirschi* / Ralf Adams / Miki De Palma / Fiona Doetsch / Hellmut Augustin)
- **Human Genetic Approaches to Vascular Disease**
  (*Douglas Marchuk* / Sekar Kathiresan / Elisabeth Tournier-Lasserve)

Vascular Cell Biology
Recent Advances and Novel Approaches to Vascular Biology in Development, Homeostasis and Disease
Jan 17-18, 2015
Chair: Steven L. Swendeman

Apply online now at
www.grc.org
and be a part of the experience...

Join us at a GRC or GRS in 2015!

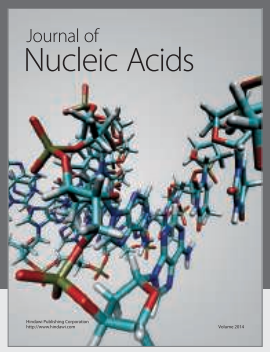

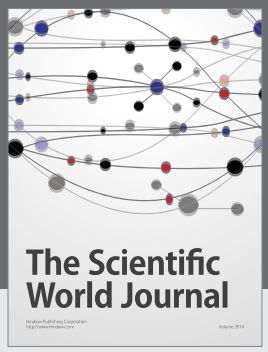

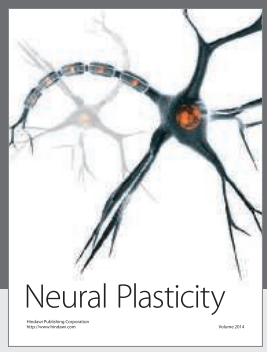

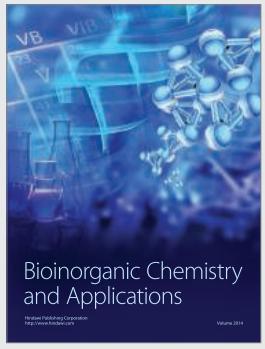

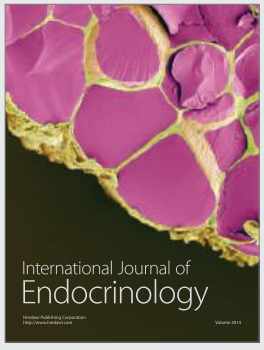

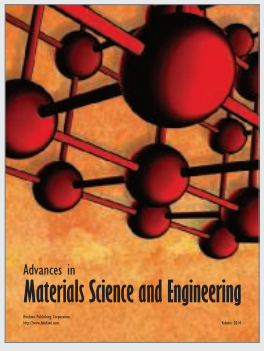

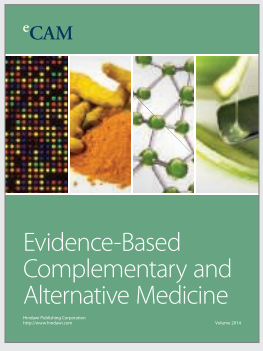

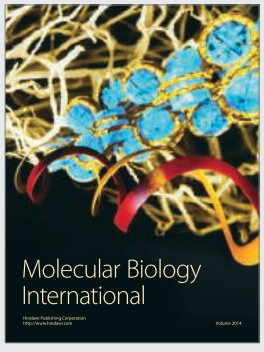

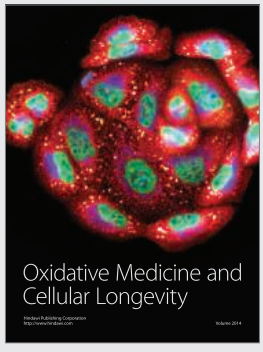

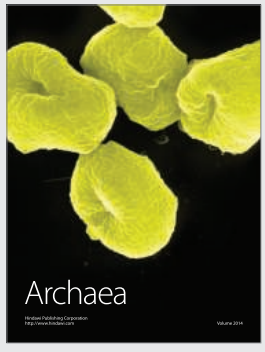

Hindawi

Submit your manuscripts at
http://www.hindawi.com

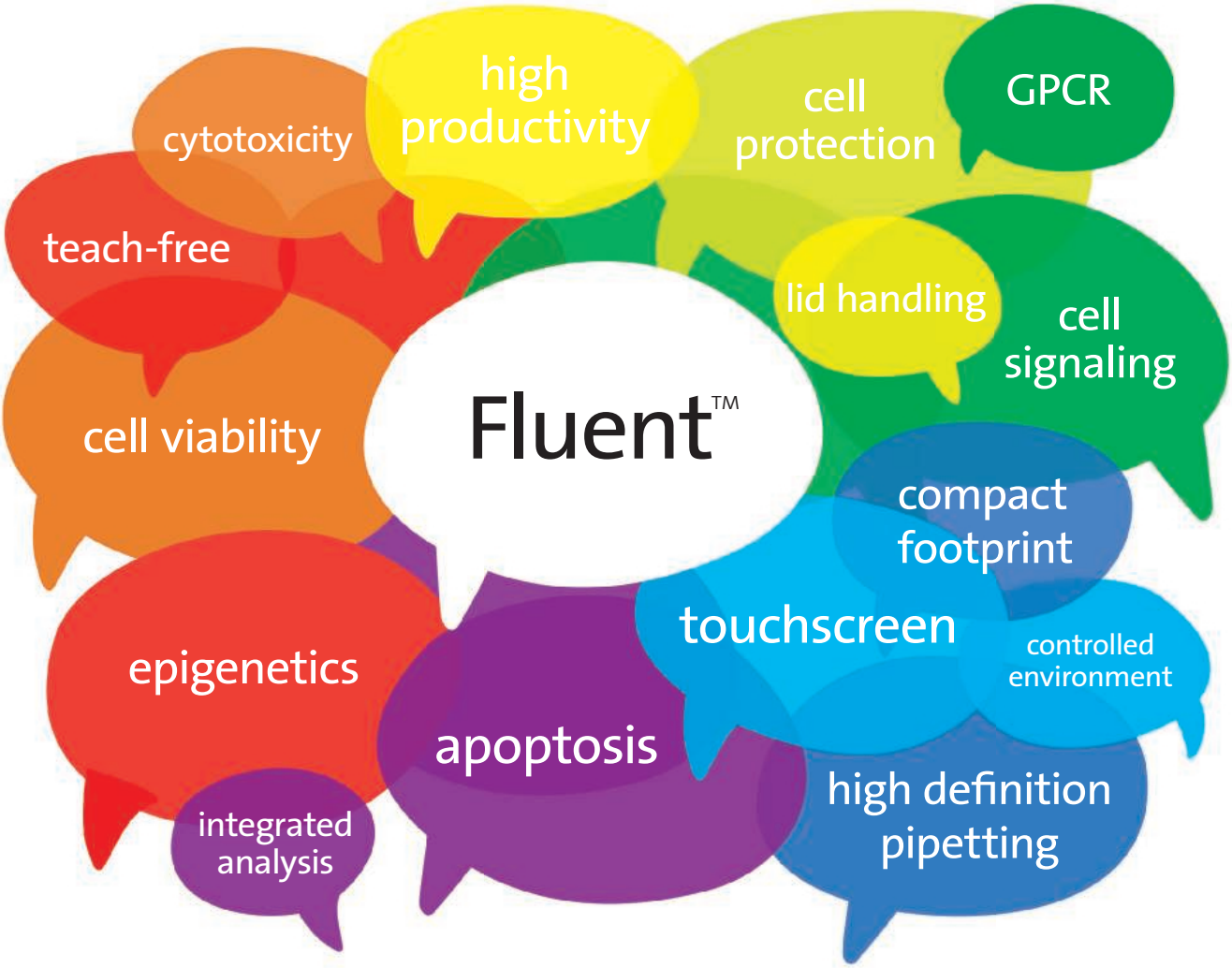

In the lab of the future, everybody will be fluent in cell-based assay automation

Improving productivity for complex cell-based research is a challenge. Processes are complicated, space is in short supply, lab personnel are confronted with more and more difficult tasks, and greater accuracy is always demanded. With the launch of the Fluent laboratory automation solution, all that changes. World-class productivity and simplicity are now within the grasp of every lab.

To see how Tecan is shaping the lab of the future, visit **www.tecan.com/fluent**

Call: The Americas: +1 919 361 5200 Europe: +49 79 5194 170 Asia: +81 44 556 7311
info@tecan.com

© 2014, Tecan Trading AG, Switzerland, all rights reserved.
For disclaimer and trademarks please visit www.tecan.com

TECAN.

Webinar

Part 1: Targeting Cancer Pathways Tumor Resistance

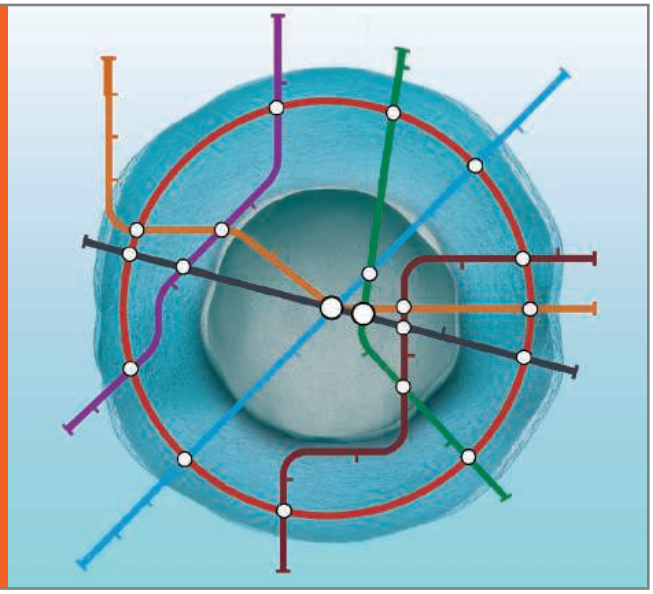

Register Now!

webinar.sciencemag.org

Speakers

Michael B. Yaffe, M.D., Ph.D.
Massachusetts Institute of Technology
Cambridge, MA

Jeffrey Engelman, M.D., Ph.D.
Harvard Medical School
Boston, MA

Michael W. Deininger, M.D., Ph.D.
University of Utah
Salt Lake City, UT

Wednesday, October 22, 2014

12 noon Eastern, 9 a.m. Pacific, 5 p.m. UK, 6 p.m. Central Europe

This webinar is the first in a series focusing on the pathways that allow for cancer development and progression, the emerging research in identifying and targeting these pathways, and the innovations in the development of cancer treatment options. Recent advances in our understanding of cancer have revealed that the disease cannot be understood through simple analysis of genetic mutations within cancerous cells. Instead, tumors should be considered complex tissues in which the cancer cells evolve and communicate with the surrounding cellular microenvironment to promote their own survival and dissemination. Although therapies against specific signaling proteins or pathways have been remarkably successful at treating certain cancers, the tumors frequently develop resistance, leading to even more aggressive forms of the disease.

This webinar will focus on how rewiring of signaling pathways in response to drug treatment contributes to resistance and how this knowledge can be leveraged to develop more effective treatment strategies.

During the webinar, viewers will:

- Gain an understanding of the specific molecules and pathways that are the targets for rationally designed therapies
- Learn about efforts to overcome resistance to the first FDA-approved therapy targeting a hyperactive kinase
- Review mechanisms by which tumor cells resist inhibitors that target cell survival and growth pathways
- Hear how the rewiring of cell death pathways can sensitize cells to traditional chemotherapy agents
- Have their questions answered live by the expert panel.

Webinar sponsored by

Cell Signaling TECHNOLOGY®

KOCH INSTITUTE for Integrative Cancer Research at MIT

Brought to you by the *Science*/AAAS Custom Publishing Office

Science Signaling AAAS

Science AAAS

@SciMagWebinars

Imaging Software

Personalized automation is the key to managing complex multidimensional experiments, and the latest Olympus cellSens imaging software (version 1.11) seamlessly controls motorized hardware to allow effortless setup of complex acquisition sequences and protocols. The unique Graphical Experiment Manager interface allows the user to "draw" their experimental schematic on-screen with familiar "drag and drop" actions, enabling complete control and experimental setup of motorized components and accessories with almost no need for training. The capabilities of this intuitive interface are now expanded to the control of motorized stages, enabling the easy automation of multiposition experiments such as individual scanning protocols performed at different positions on a multiwell plate. Providing insights into a host of biological processes, additional new features of the software include online ratiometric analysis, delivering results in real time and control of rapid focusing devices for fast 3-D applications, while also supporting the latest cameras and image-splitter components.

Olympus
For info: +49-402-3773-5913
www.olympus-europa.com/microscopy

Cell Strainer

Flowmi Cell Strainers are a new choice for processing small volume samples (less than 1,000 µL) for Flow Cytometer and Fluorescence-Assisted Cell Sorting analysis. These new, innovative cell strainers provide fast, efficient filtering with minimal sample loss while providing reduced risk of cytometer clogs. Available in 40 µm porosity, sterile Flowmi Cell Strainers can be used with a wide variety of 1,000 µL pipette tips. Simply press-fit a Flowmi onto the pipette tip containing the sample. After straining, a quick flick of the tip eject button sends the spent tip and strainer to waste collection. For maximum convenience, Flowmi cell strainers are packaged in a compact, covered tray and sealed in a zip-style bag. Product sterility can be maintained when opened and resealed in a laminar flow hood. The tray, which holds 50 Flowmi strainers oriented for immediate access, features a clear, sliding cover for easy, one-handed use.

Bel-Art Products
For info: 800-423-5278
www.belart.com

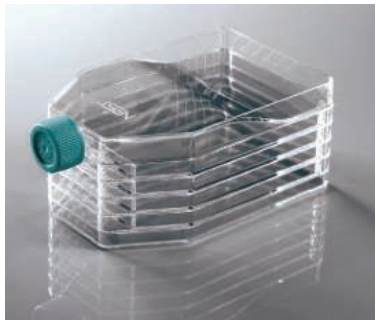

Multilayer Flask

A new five-layer cell culture flask has been developed to fulfill the need of the growing number of applications that require large numbers of cells. While single layer flasks are well proven for small-scale cell culture scale up, their use can become laborious and time-consuming when large numbers of cells are required. Offering a sterile growth area of 870 cm^2 in a compact footprint, the new five-layer cell culture flask offers a high-performance solution to this application need. Porvair cell culture flasks combine the unrivalled optical purity of high-pressure molded 100% USP Class VI virgin crystal polystyrene with a patented low-pressure gas plasma surface treatment that allows cells to adhere more efficiently to the surface by reducing its hydrophobicity. The new five-layer cell culture flasks provide easy pipette access for direct addition of reagents and cells as well as efficient recovery of valuable cells and reagents.

Porvair Sciences
For info: +44-(0)-1978-666239
www.porvair-sciences.com

Automatic Decapper/Capper System

The next generation Automatic Screw Cap DeCapper system is an innovative, easy-to-use device that provides automated decapping/capping of screw cap storage tubes in 96-tube racks in portrait or landscape formats. The device is able to cap or decap 96 Screw Cap tubes, in rows of 8 or 12, in just 60 seconds. The new device is able to provide an automated solution for Micronic screw cap tubes, screw caps, and low-profile screw caps. Micronic low-profile screw caps provide an unmatchable solution for facilities that need a space saving solution for their long-term sample storage at low temperatures. The Automatic Screw Cap DeCapper includes new features such as real-time process monitoring, and torque monitoring for optimal tube sealing, to enhance sample security. An innovative "secure mode" further enhances sample security by decapping and recapping only one row at a time, minimizing the time a tube is open and eliminating the risk of cross contamination.

Micronic
For info: +31-320-277070
www.micronic.com

Superresolution Microscope System

A new pulsed 775 nm STED laser with the superresolution system Leica TCS SP8 STED 3X achieves sub-30 nm resolution through pulsed stimulated emission depletion technology. The laser is an optional enhancement to the system. The Leica TCS SP8 STED 3X is based on stimulated emission depletion (STED) technology. The microscope system is flexible and versatile, and allows researchers to tune resolution in the lateral as well as the axial direction. The 775 nm pulsed STED laser is the most recent addition to the range of multiple STED lasers of different wavelengths. This new pulsed laser leads to a further increase in the resolution capacity of the Leica TCS SP8 STED 3X, revealing details in multicolor co-localization experiments that have never been seen before. The Leica TCS SP8 STED 3X is based on the modular platform Leica TCS SP8.

Leica Microsystems
For info: +49-621-7028-1151
www.leica-microsystems.com

Electronically submit your new product description or product literature information! Go to www.sciencemag.org/products/newproducts.dtl for more information.

Newly offered instrumentation, apparatus, and laboratory materials of interest to researchers in all disciplines in academic, industrial, and governmental organizations are featured in this space. Emphasis is given to purpose, chief characteristics, and availability of products and materials. Endorsement by *Science* or AAAS of any products or materials mentioned is not implied. Additional information may be obtained from the manufacturer or supplier.

Science Advances | AAAS
Significant research. Global impact.

Introducing *Science Advances* – the new, online-only, open-access journal from *Science* and AAAS. Find out how you can be among the first authors published at **scienceadvances.org.**

Promega

Better Biology, Less Work

NAD(P)/NAD(P)H-Glo Assays

The simple add-and-read NAD(P)/NAD(P)H-Glo Assays have unparalleled sensitivity and linearity, making them ideal for metabolic research and HTS research applications. These assays enable direct in-well measurement of total and individual NAD/NADH or NADP/NADPH and can be used in either biochemical or cell-based applications.

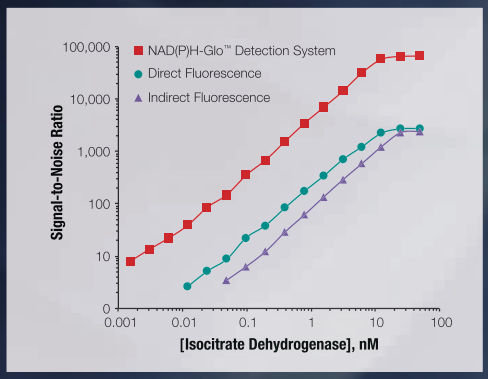

Superior sensitivity compared to fluorescent methods (Total NADH + NADPH measured).

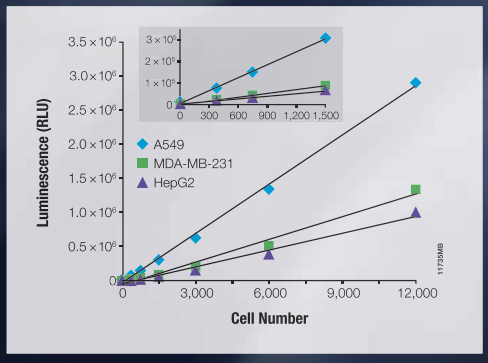

Directly measure total dinucleotide concentrations in multiwell plates using low cell numbers (Total NADP + NADPH measured).

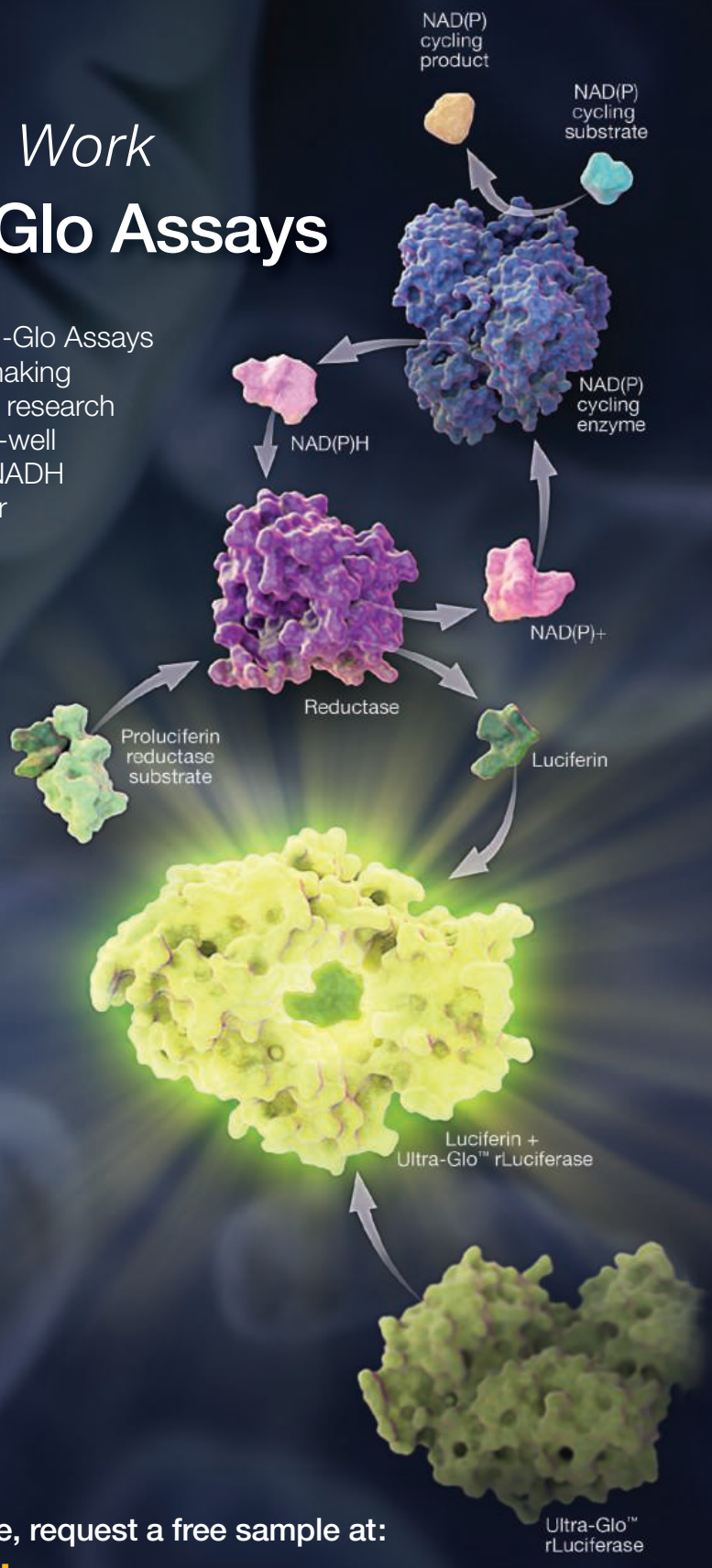

To see how easy better biology can be, request a free sample at:

www.promega.com/TryNADH

©2014 Promega Corporation. All rights reserved. 15110447

Science Careers Advertising

For full advertising details, go to ScienceCareers.org and click For Employers, or call one of our representatives.

Tracy Holmes
Worldwide Associate Director
Science Careers
Phone: +44 (0) 1223 326525

THE AMERICAS

E-mail: advertise@sciencecareers.org
Fax: 202 289 6742

Tina Burks
Phone: 202 326 6577

Nancy Toema
Phone: 202 326 6578

Marci Gallun
Sales Administrator
Phone: 202 326 6582

Online Job Posting Questions
Phone: 202 312 6375

EUROPE / INDIA / AUSTRALIA / NEW ZEALAND / REST OF WORLD

E-mail: ads@science-int.co.uk
Fax: +44 (0) 1223 326532

Axel Gesatzki
Phone: +44 (0) 1223 326529

Sarah Lelarge
Phone: +44 (0) 1223 326527

Kelly Grace
Phone: +44 (0) 1223 326528

JAPAN

Katsuyoshi Fukamizu (Tokyo)
E-mail: kfukamizu@aaas.org
Phone: +81 3 3219 5777

Hiroyuki Mashiki (Kyoto)
E-mail: hmashiki@aaas.org
Phone: +81 75 823 1109

CHINA / KOREA / SINGAPORE / TAIWAN / THAILAND

Ruolei Wu
Phone: +86 186 0082 9345
E-mail: rwu@aaas.org

All ads submitted for publication must comply with applicable U.S. and non-U.S. laws. *Science* reserves the right to refuse any advertisement at its sole discretion for any reason, including without limitation for offensive language or inappropriate content, and all advertising is subject to publisher approval. *Science* encourages our readers to alert us to any ads that they feel may be discriminatory or offensive.

Science Careers
From the journal *Science* AAAS

ScienceCareers.org

ASU SCHOOL OF Life Sciences
ARIZONA STATE UNIVERSITY

Assistant Professor (JOB #10889)

The School of Life Sciences (SOLS) at Arizona State University (ASU) invites applications for a tenure-track faculty position at the rank of Assistant Professor in the area of biomarker research. Anticipated start date is August 16, 2015. We seek imaginative, creative individuals with strong interest in discovery of biomarkers and their mechanistic validation. While all applicants must have a demonstrated record of significant publications within the realm of biomarker research, strong preference will be given to applicants who have particular interests in molecular mechanisms of disease (e.g. infectious, neurodegenerative, metabolic or neoplastic diseases) that complement expertise of existing faculty and who will expand our overall research and instructional capabilities. The successful candidate will be expected to develop an innovative, extramurally-funded, independent research program, fulfill teaching requirements at both the undergraduate and graduate levels and have a commitment to outreach and service at levels within and outside the University community. The successful candidate will be expected to mentor undergraduate and graduate students, postdoctoral trainees, and interact with the multidisciplinary consortium of faculty of SOLS as they interface with other groups on campus such as the Biodesign Institute, Department of Chemistry/Biochemistry, the Schools of Engineering, the Metabolic/Vascular Biology Center at Mayo-Scottsdale, and the NIH-funded Center of Excellence for Membrane Proteins of Infectious Diseases. A competitive start-up package and a teaching load compatible with high research productivity will be provided.

Candidates must have a doctoral degree in biology, biochemistry, engineering, or a related field at the time of appointment and two or more years of relevant postdoctoral experience with demonstrated research and teaching/mentoring excellence.

To apply, send a cover letter, curriculum vitae, three representative publications, separate statements of future research plans and teaching philosophy and interests, and contact information for three letters of reference to be addressed to **Tsafrir Mor, Chair, Biomarker Faculty Search Committee**. Application materials must be sent electronically as pdf files to **solsfacultysearch@asu.edu**. The initial closing date for receipt of applications is **October 31, 2014**; applications will be reviewed weekly thereafter until the search is closed. A background check is required for employment. For additional information on this position and the School of Life Sciences, please visit **http://sols.asu.edu/jobs**.

Arizona State University is an Equal Opportunity/Affirmative Action Employer committed to excellence through diversity. Women and minorities are encouraged to apply (http://www.asu.edu/titleIX/). For more information on ASU's non-discrimination policy, visit ACD 401, http://www.asu.edu/aad/manuals/acd/acd401.html.

ASU SCHOOL OF Life Sciences
ARIZONA STATE UNIVERSITY

Assistant Professor (JOB #10895)

The School of Life Sciences at Arizona State University invites applications for a tenure-track faculty position at the level of Assistant Professor in the area of microbial genomics including metagenomics. Anticipated start date is August 16, 2015. We encourage applications from outstanding candidates who employ an integrated and innovative basic or applied research approach leading to important contributions related to Microbial Genomics. Candidates who focus on a relevant area within Microbial Genomics, including metagenomics, physiology, genetic engineering, biotechnology, bioinformatics, bioprospecting, evolution, microbial interactions, or microbial ecology are preferred. Candidates with a demonstrated record or clear potential to develop a strong, extramurally funded independent research program; to teach at the undergraduate and graduate levels; to successfully mentor undergraduate and graduate students, and postdoctoral associates; and to actively engage in outreach and service within and outside the University are preferred. A competitive start-up package and teaching load compatible with high research productivity will be provided. Arizona State University has a vibrant, interdisciplinary research and education community that the successful candidate will become part of. Examples of relevant centers and initiatives include the Bioenergy and Photosynthesis Center (http://bioenergy.asu.edu), Biodesign (http://www.biodesign.asu.edu/), and Astrobiology (http://astrobiology.asu.edu).

Candidates must have a Ph.D. (or equivalent) in microbiology, genomics or another appropriate field at the time of application. Two years of postdoctoral training, teaching experience, and a record of accomplishment that illustrates strong preparedness for establishing an excellent, independent research program in Microbial Genomics is preferred.

To apply, send a cover letter addressed to **Willem Vermaas, Chair, Microbial Genomics Search Committee**, curriculum vitae, three representative publications, contact information for at least three references, and separate statements of future research plans and teaching philosophy. Application materials must be sent electronically in a single pdf file to **solsfacultysearch2@asu.edu**. The initial closing date for receipt of applications is **October 31, 2014**; applications will be reviewed weekly thereafter until the search is closed. A background check is required for employment. For additional information on this position and the School of Life Sciences, please visit **http://sols.asu.edu/jobs**.

Arizona State University is an Equal Opportunity/Affirmative Action Employer committed to excellence through diversity. Women and minorities are encouraged to apply (http://www.asu.edu/titleIX/). For more information on ASU's non-discrimination policy, visit ACD 401, http://www.asu.edu/aad/manuals/acd/acd401.html.

JAMSTEC

http://www.jamstec.go.jp/e/

FY2015 Recruitment of Scientist or Technical Scientist

Japan Agency for Marine-Earth Science and Technology (JAMSTEC) is recruiting a total of 8 positions as a Scientist or Technical Scientist, who will be engaged in the third medium-term plan.

The successful applicants are expected to join us from April 1, 2015 at Yokosuka, Yokohama or Kochi, Japan.

Required documents must be sent to JAMSTEC by **POST** on or before **October 20, 2014**.

For further information, please visit our website:
http://www.jamstec.go.jp/e/about/recruit/

FY2015 Recruitment of JAMSTEC Postdoctoral Fellow

Japan Agency for Marine-Earth Science and Technology (JAMSTEC) wants to help talented young researchers who have completed a promising PhD thesis to develop their scientific excellence in the field of ocean and earth sciences. For this purpose, JAMSTEC has created a new international postdoctoral fellowship programme.

The successful applicants to this programme will receive a research grant that will enable them to work independently on a research topic of their choosing. During the contract period, they will have access to the necessary facilities and equipment at JAMSTEC.

The successful applicants are expected to join us on April 1, 2015 at Yokosuka, Yokohama, Kochi, or Mutsu, Japan.

Required documents must be sent to JAMSTEC by **POST** on or before **November 5, 2014**.

For further information, please visit our website:
http://www.jamstec.go.jp/e/about/recruit/jinji_20141105.html

Massachusetts Institute of Technology

Come work with us!

Tenure Track Faculty

The Department of Brain & Cognitive Sciences (BCS) (http://bcs.mit.edu) and **The Picower Institute for Learning & Memory at MIT** (http://picower.mit.edu/) are looking to hire up to three (3) tenure-track faculty at the assistant professor level who work in one or more of the following three (3) areas:

i) *Computational* approaches to intelligence, cognition or neuroscience; an experimental component to the candidate's research would be viewed as a positive but is not necessary. An affiliation with Electrical Engineering and Computer Science, the Computer Science and Artificial Intelligence Laboratory (CSAIL), or other allied departments is possible.

ii) *Molecular & cellular:* The Picower Institute is searching for a candidate studying development, function or plasticity of neuronal circuits at the cellular, circuit, and/or systems levels using a multi-faceted approach combining different methodologies and levels of analysis. Candidates with strong cellular/molecular training who are studying development of brain circuits or using stem cell technologies are particularly encouraged to apply.

iii) *Human cognition and/or cognitive neuroscience* using behavioral methods, especially in the areas of language and/or cognitive development OR using fMRI/neuroscience methods.

Successful applicants are expected to develop and lead independent, internationally competitive research programs and to share in our commitment to excellence in undergraduate and graduate education by teaching courses and mentoring graduate and undergraduate research. PhD must be completed by start day of employment and some postdoctoral training is preferred.

Please submit application materials – cover letter, CV, statement of research and teaching interests and representative reprints – online at https://academicjobsonline.org/ajo/jobs/4202. Please state research area in cover letter. To help direct the application, applicants should indicate which of the three areas listed above is their main research area by answering the mandatory questions included in the application. In addition, please arrange to have three letters of recommendation submitted online. Review of applications will begin on November 1, 2014.

MIT is an affirmative action employer, and we encourage applications from women and underrepresented minorities.

http://web.mit.edu

RUTGERS UNIVERSITY

Assistant Professor of Cell Biology and Neuroscience Cryo-Electron Microscopy

The Center for Integrative Proteomics Research (CIPR) and the Department of Cell Biology and Neuroscience within the School of Arts and Sciences (SAS) at Rutgers, The State University of New Jersey, seek to hire an outstanding tenure track assistant professor in the area of Cryo Electron Microscopy. Applicants must have a Ph.D. and/or M.D., a distinguished record of scholarship, a strong commitment to excellence in teaching, and the leadership abilities to develop and support a world-class research program. The successful candidate will be expected to develop and maintain an active, extramurally-funded research program and also to teach undergraduate and graduate courses in cell and structural biology. The Center is housed in a state-of-the-art 75,000-square-foot facility committed to fostering interdisciplinary research in the biological and biomedical sciences using complementary quantitative tools of measurement and analysis. The Department of Cell Biology and Neuroscience is part of the SAS Division of Life Sciences, a group of Rutgers Departments, Centers, Institutes, and core facilities that represent rich opportunities for collaboration. Together the CIPR, the Department, and the expansive Rutgers' biomedical research community provide access to a broad array of excellent state-of-the-art facilities as well as a highly competitive start-up package.

The Center and the Department are located adjacent to the Rutgers Robert Wood Johnson Medical School in Piscataway, and are less than one hour from New York City and Philadelphia.

Applicants with research programs complementing those in the Department, such as neuronal development and function, mRNA processing, and immunology, are strongly urged to apply. Interested individuals should apply online through the Department's recruitment website (**http://cbnsearch.rutgers.edu**) with a curriculum vitae, a brief statement of research plans, and contact information of three individuals who will provide a letter of reference. Applicant review will begin on **October 15th 2014** and continue until the position is filled.

Rutgers University is an Equal Opportunity/Affirmative Action Employer.

MAX-PLANCK-GESELLSCHAFT
zur Förderung der Wissenschaften e.V.

Technische Universität München

Max Planck Research Groups

The Max-Planck-Gesellschaft zur Förderung der Wissenschaften e.V. (MPG) is an independent, non-profit research organisation, whose goal is to promote top quality research at its institutes. The over 80 research institutes of the Max-Planck-Gesellschaft conduct basic research in **Biology** and **Medicine**; **Chemistry**, **Physics** and **Technology**; the **Humanities**, **Social Sciences** and **Law**. In particular, the Max-Planck-Gesellschaft addresses new, innovative and interdisciplinary research areas.

To achieve this, we need you – outstanding postdocs in all fields of research pursued in our organisation. We invite you to work with us and apply for a position as Max Planck Research Group Leader.

Excellent research is irrespective of gender. However, the Max-Planck-Gesellschaft still lacks female scientists and their outstanding talents. We hereby explicitly welcome applications from highly skilled women in all disciplines. We also encourage individuals with disabilities to apply.

The successful candidates will be offered a **Max Planck Research Group** for a period of five years **at a Max Planck Institute of their own choice**. This includes a W2 position equivalent to assistant or associate professor level and additional resources for research positions, budget, and investments. The cumulative amount of funding is competitive with top class start-up packages of international career development programs.

Your application should include a CV, a list of publications, copies of three publications, a one-page summary of scientific achievements, two letters of recommendation, and a two-page research plan.

For detailed information about the advertised positions and for the application form please see

http://www.mprg.mpg.de

The deadline for applications is October 29th, 2014.

Zertifikat seit 2006
audit berufundfamilie

Technische Universität München (TUM) is the first university in Germany to reinforce its recruitment policy by a comprehensive tenure track system. Based on best international standards and transparent performance criteria, TUM FACULTY TENURE TRACK offers performance-based academic career options for high-potential early-career scientists, from the appointment as Assistant Professor through a permanent position as Associate Professor and on to Full Professor.

Successful candidates for a Max Planck Research Group Leader position – see job advertisement of MPG beside – are invited to apply for a position as Tenure Track Assistant Professor at TUM with doctorate granting rights and career options according to the TUM Faculty Tenure Track system.

Therefore, Technische Universität München awards

Tenure Track Assistant Professorships

in all areas of its research and teaching portfolio.

The initial appointment to Assistant Professor (W2 position) will be for 6 years on leave. During this period, the candidate is expected to do top level research at the chosen Max Planck Institute and to establish fruitful collaborations with relevant research groups at TUM.

After positive evaluation at TUM in the final year, the candidate is tenured to Associate Professor (W3 position). In exceptional cases, the tenure evaluation may be initiated after a minimum of three years. Such cases will have to be justified by outstanding achievements of the candidate and when the candidate contributes to strategically shaping the university's profile.

Candidates should be committed to excellence in undergraduate / graduate teaching and in supervising PhD students. Teaching assignments can include courses at TUM in subject area as well as in basic courses and at International Max Planck Research Schools (IMPRS). Teaching load for Assistant Professors at TUM is 5 contact hours per week per semester (SWS).

To be appointed to Professor at TUM the requirements according to Article 7 and 10 III Bavarian Remuneration Act apply. For detailed information about working conditions and TUM FACULTY TENURE TRACK in general please see www.tum.de/tenure-track

As an equal opportunity and affirmative action employer, TUM explicitly encourages applications from women as well as from all others who would bring additional diversity dimensions to the university's research and teaching strategies. Preference will be given to disabled candidates with essentially the same qualifications. TUM Munich Dual Career Office provides support for dual career couples and families.

The Max-Planck-Gesellschaft and the Technische Universität München have developed a joint MPG/TUM career program. This program provides an additional opportunity for Max Planck Research Group Leaders: in addition to your application for a Max Planck Research Group Leader position you can apply for a position as a Tenure Track Assistant Professor at the TUM. Acceptance into this joint program includes doctorate granting rights and career options via Associate to Full Professor according to the TUM FACULTY TENURE TRACK system. This offer is independent of your chosen Max Planck Institute.

Science Careers online @sciencecareers.org

Florida State University

Coastal & Marine Initiative: Geomorphology, Hydrology, Physical Oceanography and Air-Sea Interactions

Florida State University is continuing its *major interdisciplinary initiative in the broadly defined area of Coastal & Marine Research*. During the 2014-15 academic year, the initiative will be recruiting up to five tenure-track faculty members and the search is open with respect to rank. We invite applications from researchers active in coastal system research in the areas of geomorphology, hydrology, physical oceanography and air-sea interactions. Candidates with research interests that bridge across disciplines, including life sciences, are encouraged to apply. The search seeks to complement the existing strengths in coastal and marine research in the Department of Earth, Ocean and Atmospheric Science, the Department of Biological Science and the FSU Coastal and Marine Laboratory. Faculty appointments will be in the Department of Earth, Ocean and Atmospheric Science and can be based at the Coastal and Marine Laboratory. Successful candidates are expected to have a synergistic impact on existing coastal and marine research programs at the University and to contribute to teaching and mentoring at the undergraduate and graduate levels. Successful candidates will be offered highly competitive salaries and start-up packages, high quality research space and access to state-of-the-art instrumentation, computing and facilities in academic and interdisciplinary units.

Applicants are asked to provide a single document in PDF format containing a letter of application, a curriculum vitae, a two page narrative describing their research interests and plans, and a brief teaching statement. Applications must be sent electronically to **coastal-marine2014P.search@fsu.edu**. Applicants should also have three letters of recommendation sent to **coastal-marine2014P.letters@fsu.edu**. The closing date for applications is **November 12, 2014**.

Florida State University is committed to the diversity of its faculty, staff, and students, and to sustaining a work and learning environment that is inclusive. Women, minorities, and people with disabilities are encouraged to apply. FSU is an Equal Opportunity/Access/Affirmative Action Employer.

Florida State University

Coastal & Marine Initiative: Conservation Biology, Fisheries Biology, Population Biology, Community Ecology and Organismal Biology

Florida State University is continuing its *major interdisciplinary initiative in the broadly defined area of Coastal & Marine Research*. During the 2014-15 academic year, the initiative will be recruiting up to five tenure-track faculty members and the search is open with respect to rank. We invite applications in five areas of research of importance to marine and terrestrial coastal areas: (1) conservation biology, (2) fisheries biology, (3) population biology (including demography and population genetics), (4) community ecology (including species interactions and macroecology) and (5) organismal biology (including environmental physiology and functional morphology).We encourage applications from ecologists and evolutionary biologists, empiricists and theoreticians. Habitats of interest include marine habitats (e.g., sea grass, oyster reef, saltmarsh, reefs, open water) and terrestrial systems (e.g., dunes, rivers and streams, maritime forests). Faculty appointments will be in the Department of Biological Science or the Department of Earth, Ocean and Atmospheric Science and can be based at the FSU Coastal and Marine Laboratory. Successful candidates are expected to have a synergistic impact on existing coastal and marine research programs at the University and to contribute to teaching and mentoring at the undergraduate and graduate levels. Successful candidates will be offered highly competitive salaries and start-up packages, high quality research space and access to state-of-the-art instrumentation, computing and facilities in academic and interdisciplinary units.

Applicants are asked to provide a single document in PDF format containing a letter of application, a curriculum vitae, a two page narrative describing their research interests and plans, and a brief teaching statement. Applications must be sent electronically to **coastal-marine2014L.search@fsu.edu**. Applicants should also have three letters of recommendation sent to **coastal-marine2014L.letters@fsu.edu**. The closing date for applications is **November 12, 2014**.

Florida State University is committed to the diversity of its faculty, staff, and students, and to sustaining a work and learning environment that is inclusive. Women, minorities, and people with disabilities are encouraged to apply. FSU is an Equal Opportunity/Access/Affirmative Action Employer.

2014 Annual
Top Employers in Biotech & Pharma

There's only one Science

Special Career Feature: October 17

Ads accepted until October 10 if space is still available.

Who is No. 1 this year?

Science publishes the results of its 13th annual Top Employers Survey on October 17.

Recruit or brand your organization and reach both ACTIVE and PASSIVE job seekers. Here's how:

- Scientists in the biotech/pharma community eagerly anticipate the results of this survey every year.
- Your association with this issue tells prospective recruits that you are among the best. Reach the scientists that your competitors are reaching and promote your advantages.

To book your ad:
advertise@sciencecareers.org
THE AMERICAS
202 326 6582
EUROPE/ROW
+44 (0) 1223 326500
JAPAN
+81 3 3219 5777
CHINA / KOREA / SINGAPORE / TAIWAN
+86 186 0082 9345

Science Careers
From the journal *Science* AAAS
ScienceCareers.org

UT SOUTHWESTERN MEDICAL CENTER

The Department of Molecular Biology at the University of Texas Southwestern Medical Center invites applications for tenure track faculty positions at the level of Assistant, Associate, or Full Professor. We are seeking interactive individuals with strong research programs focused on mechanistic aspects of gene regulation, cell growth and differentiation, development, and stem cell biology, including the use of cellular and animal models to study human disease. Attractive recruitment packages, state-of-the-art core facilities, and exceptional laboratory space are available. UT Southwestern has a vibrant graduate program and an atmosphere of collegiality and collaboration.

Applicants should submit a curriculum vitae containing a summary of past research accomplishments, a statement of future objectives, and names of three references via email to:

Search Committee
Department of Molecular Biology
University of Texas Southwestern Medical Center
MolBioSearch@UTSouthwestern.edu

UT Southwestern Medical Center is an Affirmative Action/Equal Opportunity Employer. Women, minorities, veterans and individuals with disabilities are encouraged to apply.

ILLINOIS
UNIVERSITY OF ILLINOIS AT URBANA-CHAMPAIGN

Faculty Position in Functional Morphology/Biomechanics
Department of Animal Biology in the School of Integrative Biology

The School of Integrative Biology (SIB) and the Department of Animal Biology at the University of Illinois, Urbana-Champaign invite applications and nominations for a full-time, tenure-track faculty position in functional morphology/biomechanics at the rank of Assistant Professor. We seek a functional morphologist that takes multiple approaches to understanding why organismal traits take the forms that they do. We are particularly interested in candidates with research programs that incorporate theoretical, experimental and/or genetic approaches. The successful candidate will show potential to publish in the top disciplinary journals, be expected to develop an externally funded research program, teach at undergraduate and graduate levels, and collaborate with other faculty both within SIB and elsewhere on campus to develop collaborative research initiatives. A Ph.D. in Biology or related discipline is required by start date, and postdoctoral experience is desirable. The anticipated starting date is August 16, 2015; the starting salary is commensurate with qualifications and experience. The successful candidate will have the opportunity to be part of dynamic and well-established communities of integrative biologists with interests spanning a wide range of taxa and to participate in a number of interdisciplinary programs across the campus.

To ensure full consideration, please create your candidate profile through **http://go.illinois.edu/AsstProfFunctMorphology** and upload your application materials: letter of application, curriculum vitae, a representative publication, research statement, teaching philosophy and experience, and contact information for three professional references by **October 17, 2014**. Only applications submitted through the University of Illinois Job Board will be considered. Letters of reference will be solicited during the search process. Applicants may be interviewed before the closing date; however, no hiring decision will be made before October 17, 2014. For further information regarding application procedures or to submit nominations, you may contact **Marty Forrest** at **mjforres@illinois.edu**.

Illinois is an Equal Opportunity Employer and all qualified applicants will receive consideration for employment without regard to race, religion, color, national origin, sex, age, status as a protected veteran, or status as a qualified individual with a disability. Illinois is an Affirmative Action /Equal Opportunity Employer and welcomes individuals with diverse backgrounds, experiences, and ideas who embrace and value diversity and inclusivity. (www.inclusiveillinois.illinois.edu).

Los Alamos NATIONAL LABORATORY EST. 1943

Los Alamos National Laboratory (LANL), a multidisciplinary research institution engaged in strategic science on behalf of national security, has a single opening for a Center Leader position in our National Security Education Center (NSEC). It will be filled either at the Executive Advisor 4 or the R&D Scientist 5 level.

Information Science & Technology Institute

EXECUTIVE ADVISOR 4 **R&D SCIENTIST 5**

The Institute Leader is responsible for establishing a charter, vision and implementation strategy for the institute in collaboration with the relevant Laboratory division leadership that builds on and complements the Laboratory's Information and Science and Technology Pillar. Coordinates external visible workshops and working groups on topics in information science and technology. Manages an active seminar program, coordinates visiting scholars, and represents the Institute at scientific and administrative meetings. Management responsibilities include accountability for quality research, management of financial and human resources, proactive support of Laboratory safety, security, environment and diversity objectives, and the communications/marketing strategy for the Institute.

A Ph.D. degree in a scientific or engineering field relevant to implementation of the Information Science and Technology Strategy or equivalent combination of education and experience is required. Must possess expert knowledge and demonstrated successful experience in one or more of the following disciplines: computational science, high-performance computing, the science of complex networks, computational co-design, data science at scale, and uncertainty quantification.

Applicants may apply to both job postings at **careers.lanl.gov**

EOE

TEMPLE University

Genomics faculty positions (Assistant/Associate Professors)

The Department of Biology at Temple University invites applications for tenured and tenure-track faculty positions in genomics. We are interested in early and mid-career scientists who will integrate concepts, methods, and tools from evolutionary and population genomics to address significant questions in biology and biomedicine. Successful candidates will have a primary focus on large scale analytics and computational science. They will be core faculty of the new Institute for Genomics and Evolutionary Medicine (iGEM) or the Center for Computational Genetics and Genomics (CCGG) at Temple University. We are seeking candidates who will closely complement existing strengths in the Dept. of Biology in the areas of molecular evolution, population genetics, phylogenomics, phylomedicine, biodiversity, and computational biology.

Applicants should submit to **igem@temple.edu** a single pdf containing a cover letter, a detailed curriculum vitae, a summary of current and future research interests, and a statement of teaching philosophy. Please include in the cover letter a link to a Google Scholar profile. Through their research and teaching statements applicants should inform the search committee about the transformative and cross-disciplinary aspects of their work. Review of applications will begin on **November 1, 2014**.

Temple University is located in the heart of historic Philadelphia, and is the sixth largest provider of graduate school education in the USA. Situated in close proximity to New York City and Washington DC, Philadelphia is home to a large biotech industry and has many outstanding academic and research institutions.

Temple University is an Equal Opportunity, Equal Access, Affirmative Action Employer committed to achieving a diverse community (AA, EOE, m/f/d/v).

MICHIGAN STATE UNIVERSITY

MSU-DOE PLANT RESEARCH LABORATORY
http://www.prl.msu.edu
Director Position

Applications for the position of **Director of the MSU-DOE Plant Research Laboratory** at Michigan State University are invited from scientists with an outstanding record of research achievement in the study of photosynthetic organisms. We are especially seeking individuals with research interests that complement existing strengths at the Plant Research Laboratory (PRL). The successful candidate will maintain an active research program, provide scientific leadership and oversee the administration of the PRL. Accordingly, we seek applicants that value and are fluent in both basic and applied research on photosynthetic organisms and have a desire to participate in the formulation and implementation of research activities in these areas. Particular consideration will be given to individuals who will support training in and nourish interdisciplinary approaches that address fundamental biological questions relevant to energy flow between photon capture and the deposition of energy-rich molecules.

The PRL, with significant and long-standing funding from the U.S. Department of Energy, provides an excellent environment for creative research. Michigan State University provides a stimulating atmosphere with world-class colleagues and facilities and an exceptional breadth and depth in the study of photosynthetic organisms. The PRL Director will be appointed as a tenured professor in an appropriate academic department.

Application materials must include a statement of interest highlighting specific strengths related to this position including accomplishments, research interests, broader impacts, future plans, funding history, commitment to diversity and previous administrative experience. Include also a curriculum vitae and names of three references (who will not be contacted without your permission). All materials should be assembled into one PDF and uploaded to **https://jobs.msu.edu** (**position #0147**). To ensure full consideration, materials should be received by **November 1, 2014** but the position will remain open until filled. Questions regarding this position should be directed to prlsrch@msu.edu.

MSU is an Affirmative Action, Equal Opportunity Employer and is committed to achieving excellence through diversity. The University actively encourages applications of women, persons of color, veterans, and persons with disabilities, and we endeavor to facilitate employment assistance to spouses or partners of candidates for faculty and academic staff positions.

COLUMBIA UNIVERSITY
College of Physicians and Surgeons

Columbia Stem Cell Initiative
Tapping the potential of stem cells for human health

Director, Columbia Stem Cell Initiative

Columbia University seeks a leading scientist to direct the Columbia Stem Cell Initiative (CSCI). The successful candidate will be a world leader in the field with an active research program who can develop a strategic vision and research program for the Initiative. The Director will occupy an endowed chair, oversee faculty recruitment and lead an interdisciplinary team of researchers.

The Columbia Stem Cell Initiative (CSCI), established in 2008, now comprises more than 100 teams studying the roles of stem cells in development and regeneration, using them to model disease and screen for new drugs, and to develop advanced technologies for clinical translation. Team members belong to many departments and centers located throughout the medical school campus, Columbia University's main campus and the New York Psychiatric Institute, and have access to state-of the art facilities and technology platforms. There is an outstanding academic environment for scientific interaction and interdisciplinary collaboration, an excellent track record of scientific contributions to the field of stem cell research and a history of continuous extramural funding to the members. This active interdisciplinary environment, together with the resources and space allocated to the new position, will enable the Director to have a major impact in shaping the future of the Initiative.

We invite applications from individuals with outstanding track records of research achievement and the strong leadership qualifications needed to further strengthen stem cell research at Columbia.

Applications should be sent to **Dola Sengupta** (Administrative Director, CSCI, ds2865@columbia.edu).

For more information, please contact: **Joel Stein, M.D., Chair, Department of Rehabilitation and Regenerative Medicine, Columbia University Medical Center, New York NY 10032, USA; Tel: 212-305-4818** E-mail: **js1165@columbia.edu**

Columbia University is an Equal Opportunity/Affirmative Action Employer.

Science Careers

CER

"《科学》职业"已经与赛尔互联(CER)开展合作。中国大陆的高校可以直接联系CER进行国际人才招聘。

请访问
Sciencecareers.org/CER
点得联系信息。

Science
AAAS

Southwest Jiaotong University, P.R.China Anticipates Your Working Application

Southwest Jiaotong University (SWJTU), founded in 1896, situates itself in Chengdu, the provincial capital of Sichuan. It is a national key multidisciplinary "211" and "985 Feature" Projects university directly under the jurisdiction of the Ministry of Education, featuring engineering and a comprehensive range of study programs and research disciplines spreading across more than 20 faculties and institutes/centers. Boasting a complete Bachelor-Master-Doctor education system with more than 2,500 members of academic staff, our school also owns 2 first-level national key disciplines, 2 supplementary first-level national key disciplines (in their establishment), 15 first-level doctoral programs, 43 first-level master programs, 75 key undergraduate programs, 10 post-doctoral stations and more than 40 key laboratories at national and provincial levels.

Our university is currently implementing the strategy of "developing and strengthening the university by introducing and cultivating talents". Therefore, we sincerely look forward to your working application.

More information available at http://www.swjtu.edu.cn/

I. Positions and Requirements

A.High-level Leading Talents

It is required that candidates be listed in national top talents programs such as ***Program of Global Experts, Top Talents of National Special Support Program, "Chang Jiang Scholars", China National Funds for Distinguished Young Scientists and National Award for Distinguished Teacher.***

Candidates are supposed to be no more than 50 years old. The limitation could be extended in the most-needed areas of disciplinary development.

Candidates who work in high-level universities/institutes and reach the above requirements are supposed to be no more than 45 years old.

B. Young Leading Scholars

Candidates are supposed to be listed in or qualified to apply for the following programs:

•National Thousand Young Talents Program

•The Top Young Talents of National Special Support Program(Program for Supporting Top Young Talents)

•Science Foundation for the Excellent Youth Scholars

Candidates should have good team spirit and leadership, outstanding academic achievements, broad academic vision and international cooperation experience and have the potential of being a leading academic researcher.

C. Excellent Young Academic Backbones

Candidates under 40 years old are expected to graduate from high-level universities/institutes either in China or other countries. Those who are professors, associate professors and other equal talents from high-level universities/institutes overseas could be employed as professors and associate professors as well.

D. Excellent Doctors and Post Doctoral Fellows

Candidates under 35 years old are supposed to be excellent academic researchers from high-level universities either in China or other countries.

II. Treatments

The candidates will be provided with competitive salaries and welfares that include settling-in allowance, subsidy of rental residence, start-up funds of scientific research, assistance in establishing scientific platform and research group as well as international-level training and promotion . As for outstanding returnees, we can offer further or specific treatments that can be discussed personally.

III . Contact us:

Contacts: Ye ZENG & Yinchuan LI Telephone number: 86-28-66366202 Email: *talent@swjtu.edu.cn*

Address: Human Resources Department of SWJTU, the western park of high-tech zone, Chengdu, Sichuan, P.R.China, 611756

http://www.swjtu.edu.cn/

Faculty Positions in DUT

Dalian University of Technology (DUT) is located in the beautiful coastal city of Dalian, in northeastern China's Liaoning Province. It is a national key university of the "211" and "985" project directly under the Ministry of Education.

DUT is seeking to recruit excellent expert, scholars (i.e. The Recruitment Program of Global Experts, The Plan for Recruiting 1,000 Professorship for Young Talent, Changjiang Scholar Distinguished Professors and Changjiang Scholar Guest Professors) and faculties from both home and abroad. Qualified applicants of professors, associate professors and lecturers are required to be under the age of 45,40,35 separately, and have obtained a PhD degree in a nation(world)-renowned university or academy of Chinese Academy of Sciences. DUT will provide a good academic environment, competitive salaries at international levels. Potential candidates are encouraged to send your application latter enclosing a current CV to Jiailing or ZhangYan(zhaopin@dlut.edu.cn), indicating in the email subject with "academy + position + applicant`s name".

For more details, please visit the website: http://rc.dlut.edu.

Job Vacancies in China's Universities

赛尔互联 CERNET

Science Careers From the journal *Science* AAAS

赛尔互联：《科学》在中国大陆高校人才引进服务独家合作伙伴

CER is Science' s exclusive agent for recruitment advertisement service in mainland China universities and colleges

China's Rapid Development —— More Opportunities

- South China University of Technology (Guangdong, China)
  http://www2.scut.edu.cn/s/135/t/141/8c/7b/info101499.htm
- Nanchang University (Jiangxi, China)
  http://rsc.ncu.edu.cn/xwgg/16723.htm
- University of Science and Technology of China (Anhui, China)
  http://employment.ustc.edu.cn/cn/
- Nantong University (Jiangsu, China)
  http://rsc.ntu.edu.cn/

For more details, visit http://www.acabridge.cn/

广告联系：赵佳 zhaojia@cernet.com +86 10 62603373

中国教育在线 www.eol.cn 是赛尔互联旗下品牌

Faculty Positions Available at The Institute for Advanced Studies (IAS) and The Medical Research Institute (MRI), Wuhan University, Wuhan, China

武漢大学

Faculty Positions

Two newly founded institutes at Wuhan University in China, the Institute for Advanced Studies (IAS) and the Medical Research Institute (MRI), cordially invite applications for ~50 each, open-rank faculty positions in Biology, Chemistry, Physics, Material Sciences, and Medical Sciences.

All applicants must have a Ph. D or MD and a successful postdoctoral experience. Successful candidates will be expected to establish an active research program in relevant disciplines. We offer internationally competitive recruitment packages.

The applicants should submit, electronically, a full CV, a research statement and contact information of three referees in a single PDF file to wdgyy@whu.edu.cn (for IAS positions) or shuoffice@whu.edu.cn (for MRI positions).

Applications that apply for both institutes at the same time will not be accepted and further processed.

http://hr.whu.edu.cn/

Assistant Professor

Departments of Cancer Biology
Dana-Farber Cancer Institute *and*
Biological Chemistry and Molecular Pharmacology
Harvard Medical School

The Departments of Cancer Biology at the Dana-Farber Cancer Institute and Biological Chemistry and Molecular Pharmacology at Harvard Medical School invite applicants for tenure-track faculty positions at the rank of Assistant Professor or Associate Professor. We are seeking individuals with a demonstrated potential for imaginative research and who propose to work on exciting problems in any area of chemical biology and drug discovery. We are especially interested in candidates who wish to develop prototype drugs against novel targets. The successful candidate will be expected to direct innovative and independent research and participate in the teaching of graduate and/or medical students. Our highly interactive environment provides the opportunity to engage and collaborate with other dedicated researchers both within the Departments and throughout the diverse Harvard research community. Significant scholarly and scientific resources will be made available for this appointment. Applicants will be housed in new space at the Dana-Farber Cancer Institute. For further information about our Department, please see our web page: http://www.dana-farber.org/Research/Departments-and-Centers/Department-of-Cancer-Biology.aspx

Applicants should submit electronic copies of their curriculum vitae, a description of research accomplishments and future research interests (three pages maximum), and ask at least three references to provide letters of recommendation. These materials should be submitted using the following link: https://academicpositions.harvard.edu/postings/5719

Please contact Kim Wilkinson (kim_wilkinson@dfci.harvard.edu) with any questions regarding submission of documents.

Applications must be received by January 31, 2015.

Dana-Farber Cancer Institute and Harvard Medical School are Equal Opportunity/Affirmative Action employers. We are actively committed to increasing the diversity of our faculty. People with disabilities, veterans, women and members of underrepresented minority groups are therefore strongly encouraged to apply.

DANA-FARBER CANCER INSTITUTE
HARVARD MEDICAL SCHOOL

Yale University
School of Medicine

Tenure-Track Faculty Position
Microbial Pathogenesis

The Department of Microbial Pathogenesis of the Yale School of Medicine is seeking applicants for a tenure-track faculty position at the Assistant Professor level. Applications at other ranks from more established investigators with a strong record of accomplishments will also be considered. We are seeking applicants using multidisciplinary approaches to investigate host pathogen interactions. Individuals studying viral, bacterial, or protozoan organisms who are interested in the molecular mechanisms of microbial infection, the immunological response to infection, or the host microbiome are encouraged to apply. The position offers an attractive start-up package, excellent laboratory space and a stimulating scientific research environment. Candidates should have a Ph.D. and/or M. D. degrees, suitable postdoctoral research experience, a strong record of research accomplishments, a commitment to develop independent, innovative research programs, and an interest in graduate and medical education.

Review of applications will begin immediately and will continue until the position is filled. Applicants should submit a curriculum vitae; a statement of current and future research interests and arrange to have three letters of reference sent to: **Chair, Search Committee, Department of Microbial Pathogenesis, Yale School of Medicine, Boyer Center for Molecular Medicine, 295 Congress Av. New Haven, CT 06536**.

Yale University is an Affirmative Action/Equal Opportunity Employer and welcomes applications from women, persons with disabilities, protected veterans, and members of minority groups.

STANFORD UNIVERSITY
DEPARTMENT OF CHEMICAL AND SYSTEMS BIOLOGY

The Department of Chemical and Systems Biology at Stanford University School of Medicine invites applications for a tenure-track position at the **ASSISTANT PROFESSOR** level. We are particularly interested in candidates with a strong interdisciplinary record in the broad areas of chemical biology, systems biology, and/or cellular and molecular biology in normal and disease states. Stanford offers an outstanding environment for creative interdisciplinary biomedical research. The main criterion for appointment in the University Tenure Line is a major commitment to research and teaching. For more information on our department, please visit: **http://chemsysbio.stanford.edu/**.

Candidates should have a Ph.D. and/or M.D. degree and postdoctoral research experience. Applications should include a cover letter addressed to Tobias Meyer, Ph.D., Search Committee Chair; a curriculum vitae, publication list, description of future research plans, and at least 3 letters of reference. All materials should be submitted online to Academic Jobs Online at **https://academicjobsonline.org/ajo/jobs/4602**.

To ensure full consideration, please submit your applications by **December 1, 2014**. Late applications may be considered. Questions should be addressed to **Kathy Johnson, FAA,** at **csbsearch@stanford.edu**.

Stanford University in an Equal Opportunity Employer and is committed to increasing the diversity of its faculty. It welcomes nominations of and applications from women, members of minority groups, protected veterans and individuals with disabilities, as well as from others who would bring additional dimensions to the university's research, teaching and clinical missions.

UF UNIVERSITY of FLORIDA
The Foundation for The Gator Nation

Applications are invited for multiple, newly created, 12-month, tenure-track faculty positions at the Assistant Professor level. The Department of Pharmacology and Therapeutics (http://pharmacology.med.ufl.edu) is expanding under a new Chairman to grow its exceptional programs in neuro-, cardiovascular, muscle and cancer pharmacology with an emphasis on translational and regenerative medicine. The successful candidate(s) must hold a Ph.D. and/or M.D. degree; have at least two years of postdoctoral training; have a record of significant research accomplishments; and present long-term research goals consistent with establishing a highly successful research program. All Department faculty are also expected to contribute to the professional and graduate education programs of the Department. We value a diverse faculty, and particularly encourage applications from women, underrepresented minorities and veterans. The Department offers outstanding laboratories, common research facilities and office space as well as a commitment to develop and enhance faculty members' full potential as researchers, educators and scholars. The University of Florida, located in Gainesville, FL, has state-of-the-art core facilities and numerous other research resources within a vibrant, collegial institution.

Candidates must apply online at **http://jobs.ufl.edu/postings/56892**. Applicants should upload the following five documents: (1) a cover letter, (2) a curriculum vitae, (3) a statement of research interests (past, present, and planned), (4) a statement of teaching philosophy and proficiency, and (5) the names and contact information for at least three references. Applications should be submitted by **November 1, 2014** for best consideration, but applications will be considered until positions are filled. Please direct any inquiries to **admin@pharmacology.ufl.edu**.

The University of Florida is an Equal Opportunity Employer. The selection process will be conducted in accord with the provisions of Florida's 'Government in the Sunshine' and Public Records Laws. Search committee meetings and interviews will be open to the public, and applications, resumes, and other documents related to the search will be available for public inspection.

University of Pittsburgh

Assistant Professors in Learning/Educational Neuroscience

The University of Pittsburgh announces two new positions as part of the University's new Brain Institute. These positions are jointly held in the Learning Research and Development Center (LRDC) and the Department of Psychology, which partner with the Brain Institute in seeking new faculty to be part of collaborative multidisciplinary communities in neuroscience, learning and education, and psychology. LRDC and the Department of Psychology have a strong core of cognitive neuroscience across several specialties, including research related to learning and training.

The research specialty is open. The new faculty will develop research programs consistent with the general goal of the neural-learning component of the Brain Institute, which is to advance understanding of the neural bases of learning, including the brain changes that accompany learning in educational domains, in human development, and in overcoming cognitive impairments.

The successful candidates will be part of the following overlapping research communities:

LRDC (http://www.lrdc.pitt.edu) is an interdisciplinary research center that brings together researchers from several disciplines to advance research on human cognition and learning, the structure of knowledge, effective schooling and training, and educational policy. Laboratory methods, include behavioral, ERP, eye-tracking, MEG, and fMRI. In addition to basic research on the cognitive, motivational, and social bases of knowledge acquisition and use, LRDC is committed to research-based improvement of learning and teaching.

The **Psychology Department** (http://www.psychology.pitt.edu) is committed to excellence in research and in teaching at both the graduate and undergraduate levels. The Department has **34** tenure-stream faculty and houses five graduate training programs: Biological and Health, Clinical, Cognitive, Developmental, and Social, as well as cross-program training opportunities. The interdisciplinary nature of psychological science is reflected in both faculty research interests and training opportunities afforded to graduate students.

The **Brain Institute** is a University-wide initiative whose central mission is to unlock the mysteries of normal and abnormal brain function and to translate the new discoveries that result from this effort into novel approaches for overcoming brain disorders. It is a new institute (Peter Strick, Scientific Director) within the University's large neuroscience communities, spanning the Schools of Medicine, Arts & Sciences, and Engineering.

Tenure for the appointments is in the Department of Psychology. Tenure and promotion are considered according to the research, teaching, and service criteria of the Department, in addition to contributions to the multi-disciplinary research communities represented by the Brain Institute and LRDC.

Applicants should assemble a single PDF document containing a cover letter, CV, statement of research and teaching interests, and up to three papers to **brainint@pitt.edu**. In addition, three letters of recommendation should be sent to this email address with the applicant's last name and the word "recommendation" in the subject line. Applications will be accepted until the positions are filled. However, the search committee will begin reviewing applications on **October 15, 2014**.

The University of Pittsburgh is an Affirmative Action/Equal Opportunity Employer and values equality of opportunity, human dignity and diversity.

UCONN

FACULTY POSITION IN MICROBIOME RESEARCH THE UNIVERSITY OF CONNECTICUT

The Department of Molecular and Cell Biology in the College of Liberal Arts and Sciences and the Institute for Systems Genomics at the University of Connecticut seek applicants for a nine-month, tenure-track faculty position at the assistant professor level at the Storrs campus starting August 23, 2015. Candidates working on microbiomes, host associated microbial communities, or microbiome ecology and evolution are encouraged to apply. For details on this position, qualifications, and application instructions please visit **www.jobs.uconn.edu**.

The University of Connecticut is an EEO/AA Employer.

California State Polytechnic University, Pomona
Biological Sciences Department

TENURE-TRACK FACULTY POSITION
QUANTITATIVE VERTEBRATE ECOLOGIST

The Biological Sciences Department at the California State Polytechnic University, Pomona (Cal Poly Pomona) invites applications for a tenure-track, **ASSISTANT PROFESSOR** position in Quantitative Vertebrate Ecology, beginning September 2015. The area of specialization is open, but candidates who use modern quantitative techniques to study the ecology of vertebrates in freshwater, marine, or terrestrial ecosystems are encouraged to apply. The successful candidate should be engaged in field research in population, community, or ecosystem ecology with a focus on natural populations. A Ph.D. in Ecology or a related field is required. Post-doctoral experience and previous teaching experience are preferred. The successful candidate will have the potential for excellence in teaching, and for developing an externally-funded research program that will involve undergraduate and Master's students. Teaching responsibilities will include introductory and advanced undergraduate and graduate biostatistics, and specialty courses in the candidate's area of expertise in vertebrate biology (ichthyology, herpetology, ornithology, and/or mammalogy), and may involve participation in introductory biology or ecology courses. Cal Poly Pomona is a comprehensive Master's level university with a diverse student body.

The successful candidate will have demonstrated an ability to be responsive to the educational equity goals of the university and its increasing ethnic diversity and international character. Applicants should forward: (1) cover letter that briefly describes the candidate's training, experience, and teaching and research interests (2 pages max); (2) *curriculum vitae*; (3) statement of teaching philosophy (2 pages max); (4) proposed plan of research (2 pages max); (5) three representative peer-reviewed publication reprints; and (6) the names and contact information of three (minimum) to five (preferred) references to: **Chair, Quantitative Vertebrate Ecologist Search Committee, Biological Sciences Department, California State Polytechnic University, 3801 West Temple Avenue, Pomona, CA 91768**. Electronic submission of all application materials as a single PDF file is preferred (**vert_ecologist@csupomona.edu**). Review of applications begins on **December 5, 2014**. Official transcripts and three letters of reference will be required of all finalists. For further information, visit the Department web site at: **http://www.csupomona.edu/~biology.**

California State Polytechnic University, Pomona is an Equal Opportunity, Affirmative Action Employer.

POSITIONS OPEN

CARNEGIE INSTITUTION FOR SCIENCE

POSTDOCTORAL FELLOWSHIPS

The Geophysical Laboratory, Carnegie Institution of Washington, invites applications for postdoctoral fellowships. The Geophysical Laboratory emphasizes interdisciplinary experimental and theoretical research in fields spanning geoscience, microbiology, chemistry, and physics. The Laboratory supports world-class facilities in high-pressure research; organic, stable isotope and biogeochemistry; mineral physics and petrology; and astrobiology.

Please visit **website: https://jobs.carnegiescience.edu/jobs/carnegie-fellowships-for-the-geophysical-laboratory-2/** to view a list of required materials and application instructions. Also, see **website: http://www.gl.ciw.edu/** for a listing of personnel, current research interests, and major facilities.

Completed applications for Carnegie fellowships should be submitted by December 1, 2014.

The Geophysical Laboratory is located in Washington, DC, and is an Equal Opportunity Employer.

ASSISTANT PROFESSOR
Princeton University
Department of Chemistry

The Department of Chemistry at Princeton University invites applications for two tenure-track Assistant Professor positions in chemistry with an emphasis on theory, inorganic materials, and organic chemistry. We seek faculty members who will create a climate that embraces excellence and diversity with a strong commitment to teaching and mentoring that will enhance the work of the department and attract and retain students of all races, nationalities, and genders. We strongly encourage applications from members of all underrepresented groups. Candidates are expected to have completed the Ph.D. in chemistry or a related field at the time of appointment. Applicants should submit a description of research interests, curriculum vitae, a list of publications, and contact information for three references online at **website: http://jobs.princeton.edu/applicants/Central?quickFind=65639.** The deadline for applications is October 15, 2014. *Princeton University is an Equal Opportunity Employer. All qualified applicants will receive consideration for employment without regard to race, color, religion, sex, national origin, disability status, protected veteran status, or any other characteristic protected by law. This position is subject to the University's background check policy.*

POSTDOCTORAL POSITION

A postdoctoral position is available in **Dr. Guo's** laboratory for studying the molecular and physiological mechanisms of Type 2 Diabetes and associated heart failure, focusing on actions of insulin and glucagon in liver or adrenergic receptor signaling in heart. The position requires a M.D. with research experience or Ph.D. in biochemistry, cell biology, and mouse genetics. The candidate must have rich basic research experience in liver metabolism or cardiac biology and strong research publication record, highly motivated for research productivity in our NIH-supported programs. The salary is up to $47,250 plus fringe benefit dependent on experience. The interested candidate will have to apply via **website: http://jobs.tamhsc.edu** and send curriculum vitae, letter of interest, and three references to **Dr. Shaodong Guo, Ph.D. Assistant Professor, Texas A&M University Health Science Center, Department of Medicine. 1901 S. 1st Street, Bldg. 205, Temple, Texas 76504. E-mail: sguo@medicine.tamhsc.edu.**

☑ More scientists agree—we are the most useful website.
ScienceCareers.org

Download your free copy today.

ScienceCareers.org/booklets

From technology specialists to patent attorneys to policy advisers, learn more about the types of careers that scientists can pursue and the skills needed in order to succeed in nonresearch careers.

Science Careers
From the journal *Science* AAAS

JANELIA SPRING CONFERENCES

Spend three days engaged in dialogue with leading scientists at our campus near Washington, DC.

Janelia conferences are small, highly specialized events designed to foster collaborative interactions and the exchange of exciting new ideas.

Highlights
- No registration fee
- Student and travel scholarships available
- Convenient three-day format
- Onsite accommodations at Janelia's innovative campus

Submit an abstract
Janelia.org/conf15

Application Deadline
November 21, 2014, 2:00 p.m. ET

hhmi | janelia Research Campus

March 15–18, 2015
Evolutionary Cell Biology
Organizers: Harmit Malik, Frances Brodsky, Nicole King, Dyche Mullins

March 22–25, 2015
Force-Gated Ion Channels
Organizers: David Corey, Miriam Goodman

March 29–April 1, 2015
Motivational Circuits in Natural and Learned Behaviors
Organizers: Robert Malenka, Scott Sternson

April 19–22, 2015
Insect Vision: Cells, Computation, and Behavior
Organizers: Tom Clandinin, Karin Nordström, Michael Reiser

April 26–29, 2015
Thalamus and Corticothalamic Interactions
Organizers: László Acsády, Jesse Goldberg, Karel Svoboda

May 17–20, 2015
Combining Information from Multiple Modalities Across the Animal Kingdom
Organizers: Dora Angelaki, Gregory DeAngelis, Alexandre Pouget, Marta Zlatic

May 31–June 3, 2015
The Long and Winding Road: Neuronal Trafficking in Physiology and Disease
Organizers: Kang Shen, Erika Holzbaur, Subhojit Roy

Careers in Neuroscience

Special Career Feature
October 31, 2014
Reserve ads by October 14 to guarantee space
Ads accepted until October 27 if space is still available

There's only one Science

This feature examines the areas and regions where the career possibilities are expanding and offers advice for scientists building their career in neuroscience.

Why you should advertise in these issues of *Science*:

Reach: Your job ad is seen by 570,400 readers around the globe

Bonus distributions to:
Society for Neuroscience
15–19 November
Washington, DC

To book your ad:
advertise@sciencecareers.org

THE AMERICAS
202-326-6582

EUROPE/ROW
+44 (0) 1223 326500

JAPAN
+81 3 3219 5777

CHINA / KOREA / SINGAPORE / TAIWAN
+86 186 0082 9345

Science Careers
From the journal *Science* AAAS
ScienceCareers.org

Produced by the *Science*/AAAS Custom Publishing Office.

UCSF
University of California San Francisco
advancing health worldwide™

Associate/Full Professor, In Residence Series
Rudi Schmid Endowed Chair in Neuroscience

UCSF School of Medicine, Department of Neurology

The University of California, San Francisco (UCSF) Department of Neurology and Graduate Program in Neuroscience is seeking candidates for the Rudi Schmid Endowed Chair in Neuroscience, which is supported by a substantial endowment. The successful candidate is expected to lead his or her own major neuroscience research endeavor which should include work relevant to substance abuse, and will hold a primary appointment as Associate or Full Professor in the Department of Neurology, with proposed membership in the UCSF Neuroscience Graduate Program. The holder of this chair will be expected to have a scientific leadership role in the Alcoholism and Addiction Research Group. Outstanding internationally recognized neuroscientists with either Ph.D. or M.D. degrees will be considered.

Interested applicants should send curriculum vitae, a statement of research interests, and the names and complete contact information of three references to: **http://apptrkr.com/519214**

UCSF seeks candidates whose experience, teaching, research or community service has prepared them to contribute to our commitment to diversity and excellence. UCSF is an Equal Opportunity/Affirmative Action Employer.

By **Rodica Stan**

The borders I crossed

I wanted to become a respected scientist, maybe not a Nobel Prize winner but someone who is capable of making a decent contribution. I started by studying biochemistry at the University of Bucharest. I graduated less than a year after the end of Nicolae Ceaușescu's dictatorship. Free to see the world for the first time, I was eager to get a Ph.D. in the United States. My father, a biology teacher who referred to all trees by their scientific names and often explored the neighboring Măcin Mountains with his students, encouraged me to go.

When I was young, borders were serious, scary things. Crossing the first border required a passport—banned during the dictatorship—a student visa, and a one-way ticket that cost the equivalent of my father's yearly income. I bought my ticket, Bucharest to New York, using three bricks of devalued Romanian currency provided by the Soros Foundation. I waved goodbye to my family at the airport. The first border was the hardest; for the rest of my life, I just pushed my way across them.

I became a graduate student at the University of Medicine and Dentistry of New Jersey. For 6 years, I studied relentlessly—signal transduction in yeast—and adapted to a new culture. Crossing the boundary into another discipline, I became a postdoc at Memorial Sloan Kettering Cancer Center (MSKCC). It was—is—an extraordinary place, full of enthusiasm, sharp minds, and state-of-the-art resources focused on understanding and curing cancer. There I met Amore, the postdoc from Rome with pistachio-green eyes. We got married, had a baby, and became permanent residents.

When my research project sank, I moved briefly into medical writing but found that field too remote from my goal. I returned to MSKCC as a research project manager, working in immunology with inspiring clinician-scientists. We rolled out several cancer-research discoveries from the lab into clinical practice.

Amore's research prospered, and he won a coveted independent-researcher position offered by City of Hope, outside Los Angeles, California. I followed him, of course, and my odyssey continued. I worked at City of Hope and then at the John Wayne Cancer Institute, adding pebble after pebble to the cancer-research pyramid. I prepared clinical-trial protocols, grants, and new-drug applications.

In 2009, Amore had an opportunity in Melbourne, Australia. Holding in one hand a one-way ticket and in the other my 8-year-old daughter's hand, I crossed another border. I had a work visa but no work prospects. I started from zero in yet another culture.

"Looking back from midcareer, those borders seem much less scary."

In Australia, many scientists work part-time, especially women. Jobs in academia are scarce, translational research is in its infancy, and the job market is small compared with the one in the United States. I got my first part-time job by responding to a broad "expression of interest" ad placed by a well-known epidemiologist. He saw the value of my skills and relied on my experience to start a high-risk project. Soon after, I got another part-time job, at biotech company Avipep, and then another, at the Ludwig Institute for Cancer Research. In the 4 years I spent in Australia, I worked all the part-time and consulting jobs I could find, sometimes two or three at a time, following my passion and doing whatever I could to stay fully employed.

I left Australia more than a year ago to return to City of Hope for a job I could not refuse. Most of the projects I started in Melbourne had achieved their goal. My family fell apart, but that's another story. I left Amore behind and resettled with my daughter in Los Angeles.

Looking back from midcareer, those borders seem much less scary. I took risks, followed passions, changed visas, packed and unpacked, explored, settled, worked hard, met mentors, and fought to build a career. I made a decent contribution to science—with more to come I hope—placing my own small pebbles, one by one, on the pyramid of research. ■

Rodica Stan is a staff scientist in the Department of Virology at City of Hope's Beckman Research Institute in Duarte, California. For more on life and careers, visit www.sciencecareers.org.

ILLUSTRATION: ROBERT NEUBECKER

Downloaded from www.sciencemag.org on September 26, 2014

Published by AAAS